PALÆOMAGNETISM OF PALÆOGENE STRATA FROM SOUTHERN ZEALANDIA: IMPLICATIONS FOR ICE IN THE GREENHOUSE

Pontus Lurcock

a thesis submitted for the degree of

Doctor of Philosophy

at the University of Otago, Dunedin,

New Zealand

31 October 2011

Abstract

When did the first ice form on Antarctica? Large, stable ice sheets started to appear in the Oligocene, but there may have been earlier, transient Palaeocene glaciations which left only brief traces in the sedimentary record. Correlation of such traces across the New Zealand region requires the accuracy provided by magnetostratigraphic dating. However, the sediments that may contain these traces have extremely weak magnetizations, high glaucony concentrations, and other characteristics which complicate magnetic measurement.

To address these problems, I developed measurement techniques for weakly magnetized samples and wrote a software package called PuffinPlot to process the measurements efficiently. (PuffinPlot is a fully-featured palaeomagnetic data plotting and analysis program also intended for use outside the scope of the thesis.) I also conducted an in-depth rock magnetic study to identify the remanence-bearing minerals and determine the effects of glaucony on magnetic behaviour. The rock magnetic results indicated that the remanence in the glauconitic sediments was carried by single-domain magnetite at extremely low concentrations, and the model I developed for remanence acquisition showed that this magnetite was capable of carrying a stable primary remanence.

Using PuffinPlot and the results from the rock magnetic experiments, I conducted palaeomagnetic studies of early Palaeogene sections at the mid-Waipara River in Canterbury, Fairfield Quarry in eastern Otago, and Campbell Island, 700 km south of New Zealand. At each site I also measured the anisotropy of magnetic susceptibility (AMS) to determine variations in palaeocurrent. The wide spacing of the sites allows regional effects to be distinguished from local ones. The sections had several features in common: very weak magnetization, necessitating special measurement and analysis protocols; poor response to alternating-field demagnetization, necessitating thermal demagnetization; and thermal alteration at relatively low temperatures, necessitating great-circle remagnetization analysis to infer primary remanences.

At Fairfield Quarry, I sampled a 25-metre composite section; 31 of the 58 sites sampled yielded usable data, all of them with reversed polarity. In conjunction with the known location of the K-Pg boundary within the section, this constrained the entire section to the C29r chron. At the mid-Waipara River, 9 sites

(of 21 originally sampled) gave reliable directions, all reversed, constraining a 16-metre continuous section to the c26r chron. At Campbell Island, I sampled two sections in different parts of the island and constructed an integrated stratigraphy from a total of 38 site directions, which expanded the known duration of a major unconformity from around 9.5 Ma to 13.4 Ma.

The improved age constraints on the Campbell Island section allowed the unconformity there to be correlated with a change in palaeocurrent at the mid-Waipara River, with a previously reported Palaeocene horizon of ice-rafted debris from eastern New Zealand, and with known fluctuations in oxygen isotopes during the Palaeocene, implying an extensive glaciation. Some of the glauconitic horizons at Fairfield Quarry may also be linked to earlier transient glaciations. Since Antarctica was still attached to Australia and South America during the Palaeocene, these results imply that circum-Antarctic ocean gateways are unnecessary for Antarctic glaciation.

Acknowledgements

Firstly I must thank my primary supervisor Gary Wilson and secondary supervisor Andrew Gorman. I also owe much to my fellow palaeomagnetists at Otago: Christian Ohneiser, Beth Fox, Bob Dagg, Faye Nelson, and Claudio Tapia, who have assisted me in various roles of field assistantry, software beta-testing, proofreading, and a dozen other things. Christian has been a staunch ally throughout my thesis and I am grateful both for his pragmatic advice and his indomitable spirit. Flatmate and office-mate Beth also deserves thanks for enduring me during the trying months of writing-up mania.

I thank the GNS scientists who laid much of the stratigraphic groundwork for this thesis and with whom I shared some enjoyable days of fieldwork: Chris Hollis, James Crampton, Hugh Morgans, and Percy Strong. The Campbell Island fieldwork was made possible by the efforts of many, including skippers Bill Dickson and Steve Little, cook Julie-Anne Parsons, our guide Billy Wallace, and fellow student Ben Andrew.

I owe thanks to large numbers of students and staff of the department who have abetted this work in greater or lesser ways. John Williams has affably fielded my requests for everything from a hand lens to half a ton of gravel; Brent Pooley prepared my thin sections and gave practical advice on sample preparation; and Damian Walls has provided for all my computational needs. Perhaps most importantly, Angela has supplied delicious cake and biscuits throughout my PhD.

Thank you to my family and friends on the other side of the planet, for kindness and support – especially Natalie Lane for proofreading. Thank you to my friends in Dunedin for helping to keep me fit and sane. Thank you to Eleni, for patience, sympathy, motivation, and cake. And thank you to my parents, for more than I have room to write here.

Contents

Figures

Tables

1 Introduction

… but I should turn mine ears and hear

The moanings of the homeless sea,
  The sound of streams that swift or slow
  Draw down Æonian hills, and sow
The dust of continents to be…

– Alfred, Lord Tennyson, 'In Memoriam' (Tennyson, 1850)

In this chapter I describe the questions that this thesis seeks to answer. I introduce my field areas and explain their significance, and outline the structure of the dissertation.

1.1 Background and motivation

1.1.1 *Early Cenozoic history of the Antarctic ice sheet*

The history and mechanism of Antarctic glaciation is an intensely studied topic, not least because of recent interest in the impact of anthropogenic CO_2 emissions on the Antarctic ice sheets. For several decades the prevailing model for Antarctic glaciation was the *gateway model* (Kennett *et al.*, 1972; Exon *et al.*, 2000), which posits that Antarctic glaciation was initiated by tectonic events: as Australia and South America broke away from Gondwana, an uninterrupted deep-water channel progressively formed around Antarctica. The opening of the Tasmanian Gateway between Antarctica and Australia at around 34 Ma left Antarctica entirely surrounded by ocean (Kennett, 1977). This event led to the initiation of the Antarctic Circumpolar Current (Barker *et al.*, 2007), thermally isolating the circum-Antarctic seas from the rest of the world's oceans. The gateway model identifies this event as the trigger for the growth of the first large-scale Antarctic ice sheets in the early Oligocene (Zachos *et al.*, 1992; Breza and Wise, 1992).

1.1.2 *The case for pre-Oligocene Antarctic glaciation*

Despite the general acceptance of the earliest Oligocene as the time of the first widespread and stable Antarctic glaciation (Lawver and Gahagan, 2003),

there is evidence that smaller, shorter-lived ice sheets may have existed earlier. One line of evidence comes from records of eustatic sea-level fluctuation: the curves of Vail *et al.* (1977), Haq *et al.* (1987), and Miller *et al.* (2005) all contain pre-Oligocene fluctuations of short duration (< 200 kyr) and high amplitude (tens of metres). Changes in global ice volume are the only known mechanism for producing such large, swift variations in eustatic sea level (Pitman and Golovchenko, 1983; Miller *et al.*, 2005).

Global ice volume can also be inferred from stable isotope data: the ratio of oxygen-18 to oxygen-16 in seawater ($\delta^{18}O$), as recorded in foraminiferal tests, is controlled by global ice volume, since oxygen-16 is preferentially sequestered in ice sheets (Miller *et al.*, 1987). Foraminiferal $\delta^{18}O$ is also affected by the water temperature during shell formation (Emiliani and Edwards, 1953); however, the ice-volume signal can be recovered by controlling for temperature using an independent temperature proxy, such as the foraminiferal magnesium/calcium ratio (Rosenthal *et al.*, 1997) and more recently the TEX_{86} proxy (Schouten *et al.*, 2002) based on planktic lipid compositions.

Abreu and Anderson (1998) summarized direct and indirect evidence for Antarctic glaciation throughout the Cenozoic, with the earliest direct sedimentological evidence (a water-lain till recovered from ODP site 742 in Prydz Bay) dated to the mid-Eocene. Direct evidence for earlier glaciations is difficult to find due to a lack of suitable outcrop, but the oxygen isotope record of Abreu *et al.* (1998) suggested that parts of Antarctica may have been glaciated as early as the Early Cretaceous. More recently, Bornemann *et al.* (2008) found evidence for an approximately 200 kyr glacial episode during the Cretaceous supergreenhouse climate; they detected excursions in $\delta^{18}O$ and TEX_{86} values correlated with a eustatic sea-level fall at around 91.2 Ma. They suggested Antarctica as the most likely location for the inferred ice volume of around 18 million km^3. Galeotti *et al.* (2009) also succeeded in correlating Late Cretaceous eustatic sea-level falls with positive $\delta^{18}O$ shifts.

Although data such as those of Bornemann *et al.* (2008) and Galeotti *et al.* (2009) do not directly constrain the location of the inferred ice mass, Antarctica has occupied a southern high-latitude position since the Early Cretaceous (Lawver *et al.*, 1992) and is thus a strong candidate. One piece of direct sedimentological evidence for pre-Oligocene Antarctic glaciation was reported by Leckie *et al.* (1995), in the form of mid-Palaeocene dropstones from a

New Zealand marine mudstone. These were identified as ice-rafted debris (IRD) dropped from the bottom of a drifting iceberg. The presence of IRD implies not merely that Antarctica was glaciated in the Palaeocene, but that there was ice cover all the way to the coastline, suggesting a substantial ice sheet. (Miller *et al.* (2005), in comparison, attempted to reconcile the eustatic evidence for Cretaceous glaciation with the lack of corroborating cold-climate indicators by suggesting that the Antarctic ice sheets did not reach the ocean.) Ice at the Antarctic margin would be expected to influence ocean circulation, for example by the production of cold, dense bottom waters.

1.1.3 *Non-gateway triggers for Antarctic glaciation*

The evidence for partial Antarctic glaciation in the Eocene might be reconcilable with the gateway model: the date of the opening of the Drake Passage, though usually placed at around 31 Ma, is not well constrained (Lawver and Gahagan, 2003). Livermore *et al.* (2007) argued that the Drake Passage may have partially opened as early as 50 Ma, and that the resulting changes in ocean circulation may have sufficed to induce Antarctic glaciation. This explanation, however, cannot account for the evidence for Palaeocene and Cretaceous glaciation.

The *CO_2 model* (Barker and Thomas, 2004) proposes an alternative cause for the initiation of Antarctic ice sheets. In this model, the dominant control on glaciation is the atmospheric concentration of carbon dioxide. DeConto and Pollard (2003b) investigated the effects of CO_2 concentrations and ocean gateways within a general circulation model simulating the initial growth of the East Antarctic Ice Sheet at around the time of the Eocene/Oligocene boundary. They found that the opening of the Drake Passage had only a secondary influence compared to the effect of fluctuations in atmospheric CO_2. In their simulations, glaciation could be controlled by a 280 ppm change in CO_2 concentration, regardless of whether the Drake Passage was open or closed (DeConto and Pollard, 2003a, fig. 5); the seaway only controlled ice volume within a narrow range of intermediate CO_2 levels. This model is consistent with reconstructions of Palaeogene atmospheric CO_2 concentrations, which show a sharp drop at the start of the Oligocene, coinciding with the inception of large-scale Antarctic glaciation (Pagani *et al.*, 2005; Pearson *et al.*, 2009).

Despite the evidence from numerical models and sea-level fluctuations, the relative importance of CO_2 and tectonics in Antarctic glaciation is still contentious (Livermore *et al.*, 2007). A clear sedimentary record of glaciation before any opening of the Drake Passage would provide compelling evidence that ocean gateways are unnecessary for the formation of Antarctic ice sheets. New Zealand is well placed to furnish such a record. Sedimentation around the New Zealand continent is significantly affected by the Antarctic ice sheet: cold, dense Antarctic bottom water (AABW) produced at the Antarctic margin forms the Pacific Deep Western Boundary Current which flows north-eastward along the east side of Zealandia (Carter *et al.*, 2004). In order to find sedimentary evidence for transient pre-Eocene glaciation, it is first necessary to know what forms such evidence would take; fortunately, a more recent glacial episode provides a useful template.

1.1.4 *The Marshall Paraconformity as evidence for glaciation*

What trace would a transient Palaeocene glaciation leave in the sedimentary record of the New Zealand region? Some idea can be gained by examining a more recent, analogous episode, recorded by the *Marshall Paraconformity* (Carter and Landis, 1972; Fulthorpe *et al.*, 1996). The Marshall Paraconformity is a regional, mid-Oligocene unconformity which has been widely correlated at onshore outcrops and offshore wells across the eastern margin of southern New Zealand. On land, it is frequently manifested as a burrowed omission surface overlain by highly bioturbated greensand, with evidence of some localized subaerial exposure (Lewis, 1992). Dating has revealed that it represents a 2–4 Myr hiatus starting at around 32 Ma (Fulthorpe *et al.*, 1996). The timing of this paraconformity coincides with the Oi2 event (Miller *et al.*, 1991), a sharp drop of 15–30 m in eustatic sea level (Haq *et al.*, 1987). The paraconformity is attributed to the early Oligocene onset of Antarctic glaciation and the scouring effect of the resulting bottom-water flow (Carter *et al.*, 2004). The Marshall Paraconformity thus provides a useful model of the sedimentary signals which a Palaeocene glaciation should produce.

1.1.5 *A Palaeocene paraconformity?*

There is some physical evidence for a transient Antarctic glaciation in the early

Palaeocene, manifested in the sedimentary record as a depositional hiatus of regional extent, recorded at widely separated sites on the Campbell Plateau (Hollis *et al.*, 1997) and the East Cape (Hollis and Manzano-Kareah, 2005); this event may also be correlatable with the ice-rafted debris reported by Leckie *et al.* (1995). Zachos *et al.* (1993) showed that nonlinear feedbacks within the Palaeogene climate system led to sudden changes even in the absence of abrupt trigger events, so a sudden, brief glaciation is plausible even if no catastrophic cause can be identified.

1.1.6 *The need for magnetostratigraphy*

The sections studied in this thesis cover a time period from the latest Cretaceous (bottom of Fairfield Quarry section) to the Early/Middle Eocene (top of Limestone Point section on Campbell Island). A greenhouse climate has been inferred for both the late Cretaceous (Bice *et al.*, 2006) and the Early Eocene (Zachos *et al.*, 2008), with the Palaeocene somewhat cooler than the Early Eocene (Zachos *et al.*, 2008). A Palaeocene glacial episode between these periods of warmth would probably have been of relatively short duration. High-resolution dating is thus vital to correlate unconformities at widely dispersed sites with high accuracy, in order to determine whether erosional episodes are attributable to regional rather than local events. Magnetostratigraphy – constrained by lower-resolution biostratigraphy – has the potential to provide this level of resolution in the early Palaeogene. The 17 Myr of the Palaeocene and Early Eocene contain 22 magnetic reversals, many of them at points poorly constrained by biostratigraphy, allowing an average resolution of around 770 kyr. In addition, many southern New Zealand sediments show poor preservation of microfossils (e.g. Hollis and Strong, 2003), limiting the amount of material available for biostratigraphic analysis: for example, the biostratigraphy of the Fairfield Quarry section studied in chapter 5 rests entirely on two dinoflagellate species (McMillan, 1993), providing a resolution of about 3 Myr. In the Palaeogene sediments of Campbell Island, microfossil analysis has proved difficult due to lack of preserved material and the hardness of the Tucker Cove Limestone (Hollis *et al.*, 1997).

1.1.7 *The need for palaeomagnetic analysis software*

The sediments marking the suggested Palaeogene paraconformity are glauconitic, heavily burrowed, and very weakly magnetic. While they do carry a magnetic remanence, they are far from being ideal candidates for palaeomagnetic study. The magnetization may have been affected by bioturbation and diagenesis. The high concentration of glaucony in some of these sediments may affect analysis in unknown ways: the high magnetic susceptibility of glaucony is well known (e.g. Bentor and Kastner, 1965; Odin and Morton, 1988) but no work appears to have been done on its relationship with remanent magnetism. Previous studies of New Zealand marine sediments from the Palaeogene and Neogene have encountered very low natural remanences (e.g. Tinto, 2010, chapter 4), failure to demagnetize under alternating-field (AF) treatment (e.g. Kennett and Watkins, 1974; Pillans *et al.*, 1994), and mineral alteration at low (<300°C) temperatures during thermal treatment (e.g. Wilson and Roberts, 1999). Thus, while palaeomagnetic analysis may be possible, it is unlikely to be straightforward. In the course of this thesis I developed experimental protocols and an associated software package to address the difficulties outlined above. Chapter 4 describes these developments in detail.

1.1.8 *Ocean margins and palaeomagnetism*

Passive ocean margin records are a powerful resource for exploring many aspects of earth history (Nittrouer *et al.*, 2007a): thanks to the continued creation of accommodation space by subsidence, their records can offer the valuable combination of high resolution and extended duration (tens of Myr). Such is the case at the south-eastern margin of the New Zealand continent, where sedimentation was controlled from the Late Cretaceous to the Oligocene by the transgressive phase of a first-order transgressive-regressive megacycle (King, 2000a), as New Zealand rifted from Antarctica and Australia and drifted northward. This rifting resulted in the formation of the Canterbury Basin (Field *et al.*, 1989) and Great South Basin (Cook *et al.*, 1999), which supplied the material studied in this thesis. While the ocean margin records are extensive, their interpretation can be far from straightforward (Mountain *et al.*, 2007); for palaeomagnetic records, many of the difficulties involve understanding the complex depositional and diagenetic processes which contribute to the final magnetiza-

tion. Since the earliest work on sedimentary magnetism by McNish and Johnson (1938), workers have developed a wide repertoire of tools and techniques to address these difficulties (e.g. Collinson *et al.*, 1967; Henshaw and Merrill, 1980; King and Channell, 1991).

Many early sedimentary palaeomagnetic studies (e.g. Creer *et al.*, 1954) tended to concentrate on the natural remanent magnetization (NRM), establishing its reliability using field (Graham, 1949) and laboratory (Bucha, 1963) stability tests; the role of partial demagnetization was often limited to testing the stability of the NRM (Doell and Cox, 1967). Stepwise demagnetization was sometimes employed (e.g. Creer, 1959), but frequently only to establish an 'optimal' cleaning step which could (for suitable samples) remove a secondary magnetization and reveal the primary magnetization (Zijderveld, 1967). This methodology placed limitations on the source material which could be used for palaeomagnetic investigations. In the following decades, the range of sediments suitable for palaeomagnetic study was expanded by a number of developments: the introduction of superconducting rock magnetometers, allowing weaker magnetizations to be measured (Deaver and Goree, 1967; Goree and Fuller, 1976); advances in rock magnetism (Stacey and Banerjee, 1974; O'Reilly, 1984), particularly the development of pseudo-single domain grain theory (Verhoogen, 1959; Stacey, 1962); more attention to depositional and post-depositional mechanisms (e.g. Verosub, 1977; Stober and Thompson, 1979; Brennan, 1993) and the effects of diagenesis (e.g. Tarling, 1976; Karlin and Levi, 1983); and the increasing use of stepwise demagnetization (Channell, 1982) and development of new data analysis techniques (e.g. Zijderveld, 1967; Halls, 1976; Hoffman and Day, 1978; Dunlop, 1979; Kirschvink, 1980; Schmidt, 1982; McFadden and McElhinny, 1988) to isolate multiple components of complex magnetizations.

In all, these developments have fostered a more systematic approach to the determination of palaeomagnetic directions. Rock magnetic and petrological analyses are used to identify remanence carriers, either from whole rock samples or magnetic concentrates. Sedimentological, petrological, rock magnetic, and demagnetization data are interpreted to produce a model of remanence acquisition, which can then be used to interpret the demagnetization data and (where possible) isolate the primary remanence. This paradigm is now routinely applied in studies of sediments from New Zealand (e.g. Roberts and Turner, 1993; Wilson and Roberts, 1999; Turner, 2001) and worldwide (e.g.

Dunlop *et al.*, 1997; Plado *et al.*, 2010).

Palaeomagnetic studies of New Zealand sediments

The development of sedimentary palaeomagnetic studies in the New Zealand region has largely followed the same path as those in the rest of the world. In addition to the large number of magnetostratigraphic studies, there have been numerous palaeomagnetic investigations into the tectonic history of the New Zealand plate boundary zone (e.g. Mumme *et al.*, 1989; Roberts, 1992; Vickery and Lamb, 1995; Hall *et al.*, 2004; Randall *et al.*, 2011).

Early studies (e.g. Kennett *et al.*, 1971; Kennett and Watkins, 1974) tended to use fairly straightforward, one- or two-step demagnetization protocols, with thermal demagnetization (e.g. Kennett and Watkins, 1974; Walcott and Mumme, 1982) generally being found more effective than AF. More recent work (e.g. Turner *et al.*, 1989; Roberts *et al.*, 1994; Wilson and Roberts, 1999) has recognized the need for more elaborate methodology: stepwise thermal demagnetization at small (≤50°C) intervals; monitoring for mineral alteration by susceptibility measurements; and rock magnetic work to constrain the mineralogy of the sampled material. Results from early studies (e.g. Kennett *et al.*, 1971; Lienert *et al.*, 1972) have often proved irreproducible with modern methodology (Turner, 2001), and more recent work has revised some of the original magnetostratigraphies (e.g. Turner *et al.*, 1989; Roberts *et al.*, 1994). From the early 1990s, a number of successful magnetostratigraphic studies have been conducted on Neogene sediments of the eastern South Island and southern and eastern North Island, with attention to both the rock magnetism and mineralogy of the sediments and to their depositional and diagenetic history (e.g. Roberts and Turner, 1993; Wilson, 1993; Roberts *et al.*, 1994; Turner, 2001). In this thesis I have applied similar methodology to the interpretation of palaeomagnetic data.

1.1.9 *Diagenesis and palaeomagnetism in marine sediments*

Reductive diagenesis and iron sulphide formation have long been recognized as a complicating factor in the palaeomagnetic study of marine sediments (Karlin and Levi, 1983).

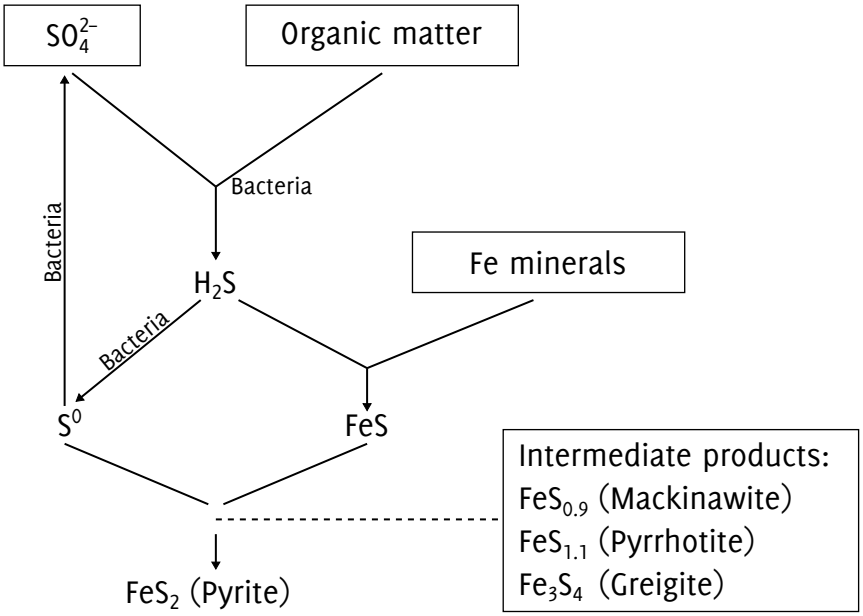

Figure 1.1 An outline of the processes involved in sedimentary pyrite formation, modified from Berner (1972) and Roberts and Turner (1993); intermediate products from Sweeney and Kaplan (1973).

Oxidation of organic matter in marine sediments makes use of the oxidant providing the greatest free energy (Reeburgh, 1983); thus, as diagenesis proceeds, oxidants are used up in a fairly well-established sequence. At the top of the sedimentary column, dissolved oxygen is usually available from the sea-water. Most marine sediments become anoxic at depths below a few centimetres, once this supply has become depleted (Berner, 1984). Near the top of the anoxic zone, ferric iron (including that in magnetite) is reduced (Karlin and Levi, 1983), probably by nitrate-reducing bacteria (Sørensen, 1982). Immediately below the iron-reducing zone lies the sulphate-reducing zone, where bacteria oxidize remaining organic matter using sulphate ions in pore water. The chemical pathways are complex but the overall process can be represented by the equation (Westrich, 1983)

$$2CH_2O + SO_4^{2-} \rightarrow H_2S + 2HCO_3^- \qquad (1.1)$$

where CH_2O represents the organic matter being oxidized. As the equation shows, bacterial sulphate reduction produces hydrogen sulphide, which can susequently react with iron in another complex system of reactions whose final product is pyrite (FeS_2). The iron for this reaction may be a ferrous product of iron reduction in higher in the sediment column (either in solution or as an oxyhydroxide or other iron (II) compound), but Canfield and Berner (1987)

and Karlin (1990b) found that sulphide was also directly involved in the dissolution of magnetite, and that sulphide concentration was a control on the degree of magnetite preservation. In many cases, incomplete pyritization results in sediments containing significant quantities of intermediate iron sulphides – chiefly mackinawite, pyrrhotite, and greigite – of which the latter two are capable of carrying a remanence. Figure 1.1 shows this system of reactions.

Several controls operate on the pyritization system: sedimentation and burial rates control the amount of organic matter in the anoxic zone, since slow sedimentation rates allow time for its consumption by oxic bacteria at the sediment-water interface before burial can occur. In non-permeable sediments, sulphate concentration can also be a control, since sulphate diffusion into the anoxic zone is prevented and the only sulphate supply is from pore water. Iron availability is another potential control, though Berner (1970) considered that in most cases the supply of H_2S would be more limited than the supply of iron.

Pyritization has been widely documented and investigated in marine sediments from New Zealand (e.g. Roberts and Turner, 1993; Wilson and Roberts, 1999; Rowan and Roberts, 2006) and worldwide (e.g. Canfield and Berner, 1987; Karlin, 1990a; Karlin, 1990b; Leslie *et al.*, 1990), and much attention has also been paid to the consequent difficulties for the palaeomagnetic investigation of affected sediments. The initial problem is the loss of some or all of the original magnetite, weakening or erasing the remanence it carries; this is exacerbated by the fact that smaller grains are affected first (Karlin and Levi, 1983), leading to early removal of the single-domain grains which carry the most stable remanences. Although other ferromagnetic minerals may subsequently form and carry remanence, magnetite is generally preferable in palaeomagnetic studies: it is by far the most thoroughly researched and well-understood remanence-carrying mineral, and (at sufficiently small grain sizes) one of the most reliable magnetic recorders (Dunlop, 1995). Another advantage of magnetite as a magnetic recorder is that it does not form authigenically under reducing conditions (Karlin and Levi, 1985 and Karlin, 1990b), making it easier to establish that a magnetite remanence carries a remanence formed at the time of deposition.

Although the detrital magnetite may be dissolved in sulphate-reducing conditions, incomplete pyritization can produce new remanence-carrying minerals with the potential to provide a palaeomagnetic signal. Much recent work

has attempted to improve the rock magnetic and palaeomagnetic interpretation of these minerals, in particular pyrrhotite (e.g. Dekkers, 1988; Dekkers, 1989; Dekkers, 1990; Torii *et al.*, 1996) and greigite (e.g. Hallam and Maher, 1994; Roberts, 1995; Torii *et al.*, 1996; Rowan and Roberts, 2006). Despite these advances, the interpretation of palaeomagnetism in iron sulphides remains much more complex than in spinel oxides. One complicating factor – apart from the less well-understood magnetic behaviour of sulphides – is that reduction and sulphidization processes can occur long after deposition (e.g. Sagnotti *et al.*, 2005; Rowan *et al.*, 2009) making it harder to relate the age of a sample to its remanence.

1.2 Locations of sampling areas

In this section I describe both the current locations of the sections to be studied and their setting at the time of deposition.

1.2.1 *The geological setting of early Palaeogene Zealandia*

New Zealand sedimentation since around 100 Ma has been controlled by a a first-order transgressive-regressive megasequence (King *et al.*, 1999), with the transgressive phase lasting until around 35 Ma. The second and third subsequences of this megasequence, representing the Haumurian to Eocene (80–55 Ma), produced the strata studied in this thesis.

At the end of the Cretaceous, Zealandia was drifting northward from Gondwana, cooling and subsiding as it did so. Passive margin sedimentation was occurring in the eastern basins as marine transgression continued, producing widespread shallow marine strata. In south-eastern New Zealand, this period is recorded in units such as the sandy, coal-bearing Taratu Formation in Otago (underlying the Abbotsford Formation studied in Chapter 5), the non-marine to marginal marine Broken River Formation (Browne and Field, 1985) in Canterbury (below the Waipara Greensand studied in chapter 6), and the coarse sand of the lower Garden Cove Formation at Campbell Island (chapter 7). Zealandia was by this stage tectonically quiescent, and marine sedimentation of progressively deeper-water facies continued into the Palaeocene, producing various fining-upward marine sequences. The conglomerate and sand of the lower

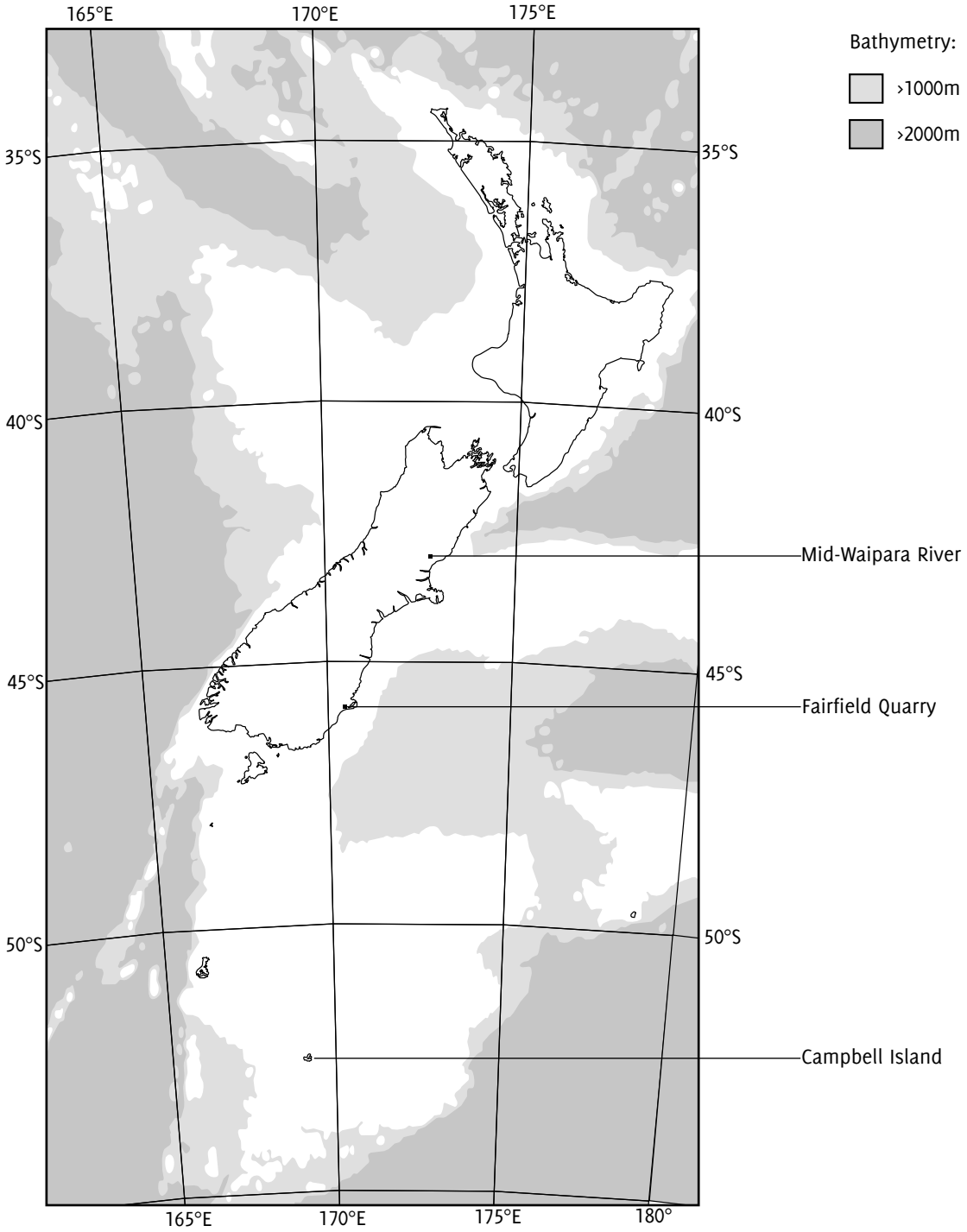

Figure 1.2 Summary of sites sampled for this thesis, shown on a map of the present-day New Zealand coastline and regional bathymetry. The 2000 m isobath delineates the approximate extent of the mostly submerged Zealandia continent. Projection is Lambert Conformal Conic with central meridian at 172°E and standard parallels at 36°S and 46°S. Map data from http://www.naturalearthdata.com.

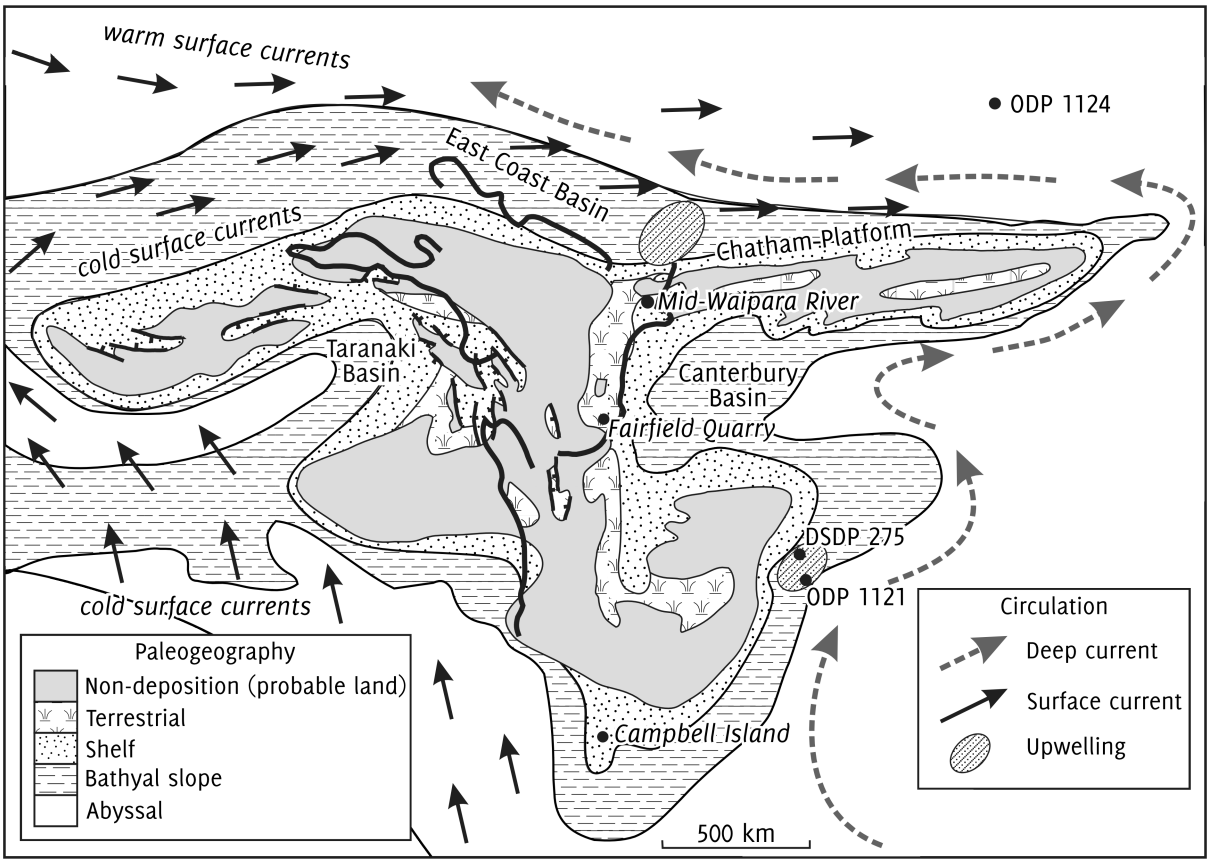

Figure 1.3 Palaeogeography of New Zealand in the latest Cretaceous, showing the locations and settings of the areas investigated in this thesis. After King *et al.* (1999) and Hollis (2003).

Garden Cove Formation graded into mud and silt, and the sandy Taratu formation was succeeded by the muddy Abbotsford Formation. In the Canterbury Basin, the Waipara Greensand was deposited. These are the sediments I investigate in this thesis. The transgression continued throughout the Palaeocene and Eocene, resulting in the deposition of the widespread Amuri Limestone in many of the eastern basins (Lewis, 1992), until sedimentation was interrupted by the early Oligocene Antarctic glaciation which produced the Marshall Paraconformity (section 1.1.4).

1.2.2 *Selection of field areas*

Figure 1.2 shows the locations of my field areas on the present-day New Zealand continent; figure 1.3 shows the same areas located on a palaeogeographic reconstruction of the New Zealand continent at the end of the Cretaceous. Geographically, the sites are widely separated, allowing me to distinguish between local and regional effects: if an event can be correlated across all three sites, its

cause cannot be purely local. As figure 1.3 shows, there is also variation in the depositional settings between the areas: the Campbell Island sediments were deposited in a deep offshore shelf environment, well placed to record changes in ocean current flow; the nearshore environments of the Fairfield Quarry and Waipara River areas were better placed to respond to glacially-controlled short-term variations in eustatic sea level. Thus the site selection provides the opportunity to observe different effects from the same glacial event. Figure 1.4 sketches the stratigraphic relationships between the field areas.

1.3 Thesis outline

1.3.1 *Aims of the study*

This thesis investigates the hypothesis of pre-Oligocene Antarctic glaciation using palaeomagnetic and rock magnetic techniques. The main techniques I apply are magnetostratigraphy (to provide accurate dating, identify depositional hiatuses, and constrain their duration) and the anisotropy of magnetic susceptibility (AMS) (to monitor variations in palaeocurrent flow). AMS is a powerful and sensitive technique for determining grain alignment (and hence current flow at the time of deposition) in sediments; since the Antarctic ice sheets are known to have major effects on ocean circulation patterns, variations in regional palaeocurrent flow can provide evidence for earlier glacial episodes.

A significant portion of the thesis (chapters 2–4) is concerned with the preparatory work necessary for reliable magnetostratigraphy. The sediments studied in the thesis are very weakly magnetized and often highly glauconitic. Weak magnetization makes it difficult to measure sample magnetizations accurately; to overcome this problem I developed special measurement protocols and analysis software, described in chapter 4. Glaucony has the potential to introduce more serious complications: as a diagenetic mineral forming over long time periods, it may hold a remanence from a time significantly after the deposition of the sediments. Such post-depositional magnetization can invalidate magnetostratigraphic work, since the measured remanence direction may not be relatable to the time of deposition. A thorough understanding of glaucony's role in remanence acquisition was thus necessary before reliable magnetostratigraphies can be constructed for the sections I studied. Chapter 3 describes this investigation.

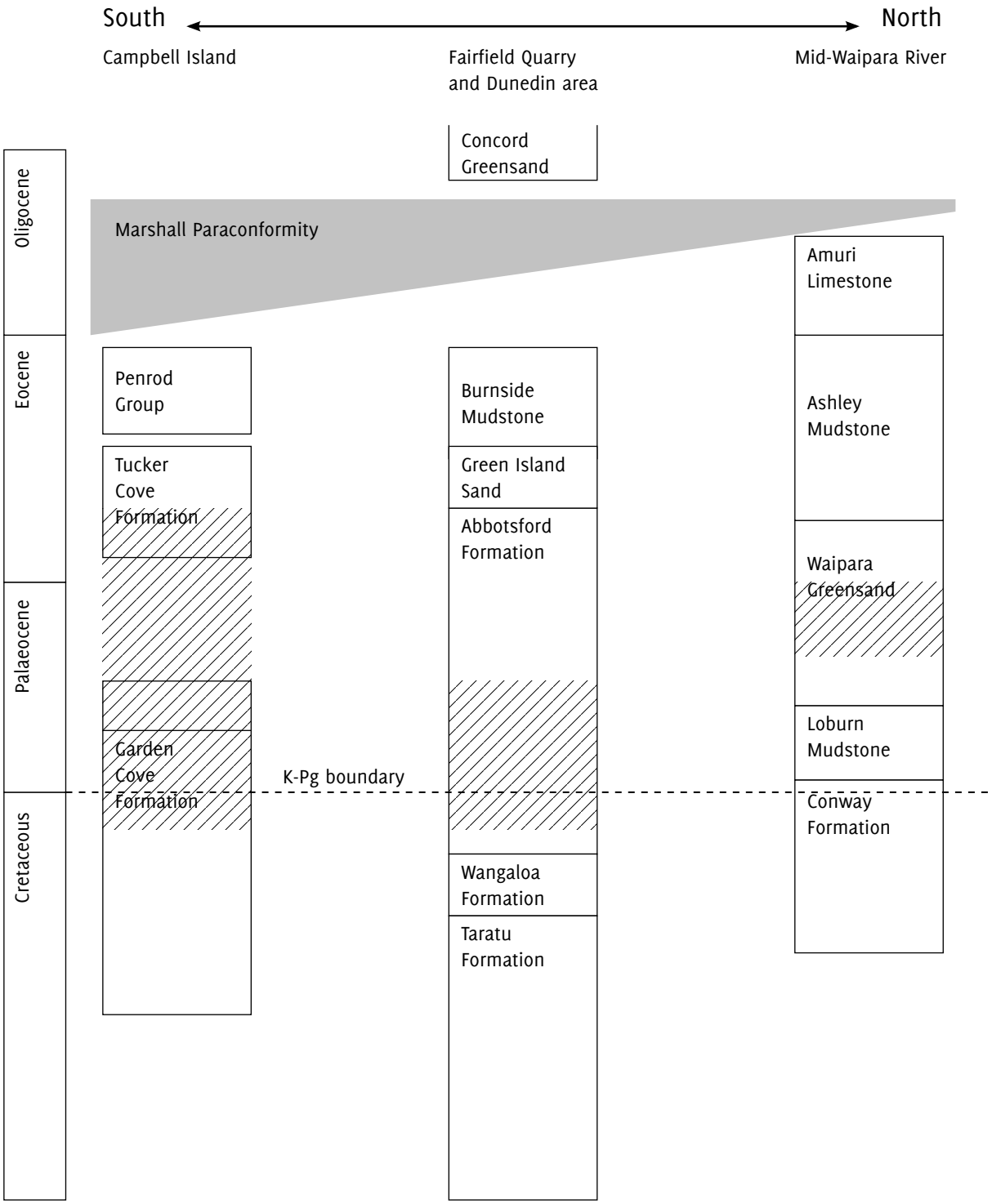

Figure 1.4 Schematic stratigraphic correlation of sections studied in this thesis. Hatched areas indicate the approximate extent of the sections I sampled.

1.3.2 *Structure of the dissertation*

This dissertation comprises nine chapters. This introductory chapter sets out the motivation and background for the problems addressed by this thesis, gives a brief introduction to the geographical and theoretical areas I investigate, and outlines the main aims of the thesis.

Chapter 2 introduces the methods which I use for the rock magnetic and palaeomagnetic studies in the rest of the thesis, including the use of magnetic susceptibility anisotropy to determine palaeocurrent flow. As well as laboratory techniques, it describes the theoretical techniques I use for analysing the data.

Chapter 3 lays the rock magnetic groundwork for the palaeomagnetic studies which follow in chapters 5 to 7. It describes a detailed investigation of the role of glaucony in the magnetic behaviour of sediments sampled at Fairfield Quarry, one of my field areas. As described in the previous section, an understanding of the palaeomagnetism of glaucony is vital to the reliable interpretation of the sediments studied in this thesis.

Chapter 4 describes PuffinPlot, a program I developed in order to conduct the palaeomagnetic analyses in the subsequent chapters. I describe the motivation for its development, the decisions made in its implementation, and the necessary features and capabilities which it provides. PuffinPlot allows quick, interactive, graphical analysis for exploratory investigations of complex behaviours. It also facilitates the analysis of very weakly magnetic samples by automatically combining multiple measurements for a best estimate of a sample's true remanence.

Chapters 5 to 7 present the results of three palaeomagnetic studies I undertook to investigate the questions outlined in this introduction. The studies make use of the techniques, software, and rock magnetic data described in the previous chapters. Chapter 5 describes a Cretaceous-Palaeogene section at Fairfield Quarry near Dunedin; chapter 6 describes a Palaeogene section at the Waipara River north of Christchurch; and chapter 7 describes two Cretaceous-Palaeogene sections at Campbell Island, 700 km south of New Zealand.

Chapter 8 reviews the results of the palaeomagnetic and rock magnetic investigations, and discusses their significance in fulfilling the aims of the thesis. It proposes a remanence acquisition model to explain the unusual magnetic characteristics of the samples, and places the results of the thesis within the context of previous investigations on similar topics.

Chapter 9 provides a concise summary of the most important outcomes of the thesis.

2 Methods

> Though this be madness, yet there is method in't.
>
> – *Hamlet*, II.ii

This chapter introduces the experimental and theoretical methods which I use throughout the rest of the thesis. It contains slightly more detail about the implementation of some techniques than might be expected in a typical palaeomagnetic study. However, this is in keeping with the aims of the thesis: chapter 3 discusses rock magnetism at length, so descriptions of demagnetization and magnetic treatment techniques are useful. Further, since the work of the thesis includes the implementation of a palaeomagnetic analysis software package (chapter 4), it is appropriate to give some detail about the data analysis algorithms which I implement in that chapter.

2.1 Experimental techniques

In this section I briefly describe the palaeomagnetic laboratory techniques which I applied in the rock magnetic and palaeomagnetic investigations of the following chapters. Good overviews of many of these techniques are also given in chapter 3 of McElhinny (1973), chapters 4–5 of Butler (1992), chapter 4 of Opdyke and Channell (1996), and chapters 8–9 of Tauxe *et al.* (2010).

2.1.1 *Demagnetization techniques*

In this section I review the commonly used techniques for progressive demagnetization of palaeomagnetic samples.

2.1.1.1 *Alternating-field (AF) demagnetization*

AF demagnetization, along with thermal demagnetization, is one of the two dominant demagnetization techniques in palaeomagnetic studies. Early accounts were given by Brynjólfsson (1957), As and Zijderveld (1958), and Stacey (1961). AF demagnetization applies an alternating magnetic field, usually at around 200 Hz, to a sample; after initial application, the field is steadily

decreased to zero. This process effectively randomizes the magnetic moments of all samples with coercivity below the peak intensity of the field. By increasing the peak intensity in steps, it is possible to remove progressively higher coercivity components. One potential problem with AF demagnetization is the danger of imparting an anhysteric remanent magnetization if a stray biasing field is present during demagnetization. Some magnetic minerals, for example greigite, may also acquire a remanence (a gyromagnetic remanent magnetization or GRM) during AF treatment even in the absence of a biasing field (e.g. Stephenson, 1980).

AF demagnetization has generally been found to give poor results on New Zealand marine sediments (e.g. Kennett and Watkins, 1974; Roberts and Turner, 1993; Pillans *et al.*, 1994; Wilson and Roberts, 1999), and this thesis was no exception. All the palaeomagnetic studies included a pilot study using AF demagnetization, and in all cases thermal demagnetization was found to perform better.

2.1.1.2 *Thermal demagnetization*

The effectiveness of heating as a demagnetization technique has long been known (Gilbert, 1600, p. 124), but was not given a firm theoretical basis until the work of Néel (1955). Irving *et al.* (1961) gave an early description of partial thermal demagnetization for palaeomagnetic analysis, and the technique has now become standard. Thermal demagnetization exploits the inverse relationship between time and temperature in the Néel equation

$$\tau = \frac{1}{C} \exp\left(\frac{v h_c j_s}{2kT}\right) \tag{2.1}$$

which allows a short period in a field-free space at a higher temperature to unblock a viscous magnetic overprint acquired over a much longer period at a lower temperature. Pullaiah *et al.* (1975) calculated unblocking-temperature curves for magnetite and haematite, allowing estimation of the temperatures required to erase viscous remanent magnetizations; I discuss this work more fully in section 3.5.4 on page 81.

2.1.1.3 *Other demagnetization techniques*

While AF and thermal demagnetization are used in the vast majority of recent

demagnetization studies, other techniques have occasionally been used. Chemical leaching with acid has occasionally been applied as a demagnetization technique (Collinson, 1965; Henry, 1979), but its usage has been limited due to the inconvenience of the procedure and the difficulty of quantifying the degree of treatment. Walton *et al.* (1992) developed a a microwave demagnetization technique, offering many of the advantages of thermal demagnetization while lowering the risk of heating-induced mineral alteration. It has seen limited but successful use in palaeointensity and archaeointensity investigations, for example by Shaw *et al.* (1999). Low-temperature demagnetization, at least for magnetite, has been known to be effective since the work of Ozima *et al.* (1964), but is seldom used in practice (Dunlop, 2003). While none of these techniques were used in the present study, the last two offer promising avenues for future work: I found thermal demagnetization to cause mineral alteration at temperatures as low as 250°C, significantly complicating palaeomagnetic analysis. Both microwave and low-temperature demagnetization can avoid this problem, albeit at the price of introducing other complications.

2.1.2 *Isothermal Remanent Magnetization*

'Isothermal Remanent Magnetization' (IRM) denotes a magnetization imparted by a strong, pulsed, non-alternating magnetic field. In nature it can be imparted by a lightning strike. In the laboratory, it can be imparted using a pulse magnetizer in order to investigate the remanent coercivity of a sample. Within this thesis, all my IRM studies followed the same protocol. I first demagnetized the sample using AF; although, as stated, this is less effective than heating, it avoids the danger of mineral alteration, and the magnetizations imparted by the pulse magnetizer are in any case orders of magnitude greater than those remaining after AF cleaning. I then imparted a series of increasingly intense fields along the same axis of the sample, measuring the magnetization after each step. Generally I used around 33 steps up to a maximum field strength of 1 T, which gave adequate resolution for analysis of the remanent coercivity curve.

In almost all cases my samples were saturated after application of a 1 T field. Starting with this saturated sample, I applied increasingly large pulse fields in the opposite direction to that of the previous fields, measuring the remanence after each step; this process is sometimes called DC demagnetization. I ceased

demagnetization once the initial saturation IRM had been removed entirely. The field strength required for complete DC demagnetization is the *coercivity of remanence*, which I denote by H_{cr} throughout this dissertation.

Sophisticated techniques have been developed for analysis of the IRM acquisition curve; I defer detailed discussion of them to section 3.4.1 on page 50.

2.1.3 *The anisotropy of magnetic susceptibility (AMS)*

AMS is routinely measured as a fast and convenient method of determining petrofabric. Here I give a brief introduction to its application to sedimentary fabrics.

The first investigations into the magnetic susceptibility anisotropy of rocks were focused on sediments, specifically varved clays. The physicist Gustaf Ising analysed samples from southern Sweden in a series of experiments commenced in 1926, though not published until much later (Ising, 1942a; Ising, 1942b). His unsuccessful attempt to use magnetic anisotropy as an indicator of palaeofield led him to the realization that the shape of the anisotropy ellipsoid was almost entirely controlled by the hydrodynamic forces acting on the clay particles during settling and lithification. Like virtually all subsequent workers he described the fabric in terms of a second-order tensor. There was little further work on AMS until Graham (1954) began to advocate its potential. Much subsequent work involved the use of AMS to investigate metamorphic fabrics and igneous flow directions, which I do not discuss here. In the sedimentary domain, Rees (1961) found that current controlled AMS fabric in laboratory redeposition of silt, and Hamilton (1963) found evidence of the same effect in samples of Silurian siltstone; Rees (1965) demonstrated the effectiveness of AMS for current determination in both artificially consolidated and natural specimens. Fuller (1962) found that the susceptibility fabric of till aligned with the dominant visible direction of its clasts. Hamilton and Rees (1970) gave the first review of investigations into the use of AMS to determine palaeocurrent.

Since 1970 AMS has been broadly applied to sediments as a standard technique for palaeocurrent investigation. With the basic relationships between depositional conditions and AMS fabric fairly well understood, research has continued into sedimentary AMS fabrics differing from the 'classic' horizontally aligned pattern. These include: fabrics influenced by coring and sampling

processes (Kent and Lowrie, 1975); inverse fabrics, with the maximum suscptibility axis perpendicular to the bedding plane (Hirt and Gehring, 1991); and fabrics influenced by low levels of tectonic stress on sediments which show no visible evidence of deformation or metamorphosis (Kissel *et al.*, 1986).

2.1.4 *The temperature dependence of magnetic susceptibility (TDMS)*

The temperature dependence of magnetic susceptibility has, over the past twenty years, become a popular technique for investigating magnetic mineralogy (Petrovský and Kapička, 2006). In the basic form of the technique, a sample is heated at a controlled rate from room temperature to a preset maximum temperature, then cooled (again, at a controlled rate) back down to room temperature; throughout the process, the bulk magnetic susceptibility of the sample is automatically measured at intervals of a few seconds. The resulting temperature-susceptibility curves are affected by various aspects of the magnetic mineralogy: paramagnetic minerals exhibit a hyperbolically declining susceptibility in accordance with the Curie-Weiss law; ferromagnetic (*s.l.*) minerals, if heated through their Curie or Néel temperature, show a sharp susceptibility peak (the Hopkinson (1889) peak) followed by a change to paramagnetic behaviour; diamagnetic minerals are unaffected by heating.

In a sample containing a mixture of minerals, the susceptibility curve will be a weighted sum of the individual mineral behaviours, potentially making its interpretation difficult. The situation is further complicated by the fact that the sample – particularly if sedimentary – may alter on heating, changing the magnetic mineralogy. Alteration is easily detected: for an unaltered sample, the heating and cooling curves should be identical, but when alteration occurs the cooling curve will reflect the new mineralogy. Alteration, at least by oxidation, can be reduced by heating in an inert atmosphere, but many heating-induced alterations can occur in the absence of oxygen. Hrouda (2003) described a technique which, while not preventing alteration, allows much more information to be gleaned from alteration-prone samples. This technique involves repeated heatings to progressively higher peak temperatures. By comparing heating and cooling curves, it can easily be determined whether alteration occurred during a particular heating cycle. The temperatures at which alterations occur can thus be constrained between the maximum temperatures of successive heat-

ing cycles. Using this technique allows the alteration itself to become a valuable source of information on mineralogy; for example, greigite experiences a characteristic decomposition at around 200°C (Torii *et al.*, 1996).

2.2 Theoretical techniques

Geological data – especially in palaeomagnetic and rock magnetic studies – very frequently have a three-dimensional character, and the history of directional data analysis is closely tied to these fields.

2.2.1 *Statistics of spherical data*

Palaeomagnetic and rock magnetic data are essentially three-dimensional, and frequently the aspect of interest is a direction in three dimensions (a declination and inclination) rather than a full three-dimensional vector with an associated magnitude. Such is the case, for example, when considering the orientation of an ancient magnetic field, or the orientation of a maximum anisotropy axis along a palaeocurrent flow direction. Palaeomagnetism, while far from the only field to make use of spherical statistics (Fisher *et al.*, 1987), has heavily influenced its development.

2.2.1.1 *Parametric statistics*

Traditional Gaussian statistics, developed for Euclidian spaces, are poorly equipped to analyse directional data, which are constrained to the non-Euclidean space corresponding to the surface of a sphere. Fisher (1953), motivated by the need to analyse remanent magnetization orientations in rocks, developed the first statistical framework for spherical directions. The Fisher distribution is essentially equivalent to an angular Gaussian distribution, with points distributed symmetrically about a central direction. Its broad applicability and relative straightforwardness have ensured its wide popularity up to the present day (e.g. Lawrence *et al.*, 2009, §20). Further developments in spherical statistics addressed situations where the distribution is not symmetrical about the mean, but has wider dispersion in one direction than another, giving a spread equivalent to an ellipse rather than a circle on the sphere's surface. The Kent (1982) distribution is one formulation of such a distribution: its mean is

the same as a Fisher mean of the same data, but its parameters encode two axis lengths and an orientation for an ellipse, rather than just the radius of a circle.

2.2.1.2 *Nonparametric statistics*

The increase in computing power during the late twentieth century permitted new developments in statistics. Efron (1979) devised the *bootstrap*, a statistical technique which allows data to be analysed without having to assume that it conforms to a known, parametrized distribution. A bootstrap is performed by taking a large number of artificial 'pseudosamples' – random selections from the measured data – and using them to construct a distribution for the entire, unknown data set. The technique is further described in Efron (1982).

Fisher and Hall (1989) applied the bootstrap to spherical data; their techniques produce irregular, contoured confidence regions which give more detail than traditional parametric confidence intervals but are for this reason difficult to express concisely. Tauxe *et al.* (1991), in developing the approach for palaeomagnetic analysis, observed that palaeomagnetic bootstrap confidence regions could be adequately described by ellipses; their approach thus used bootstrap statistics to determine a confidence interval, but expressed it in terms of a Kent (1982) ellipse.

2.2.2 *The analysis of demagnetization data*

Numerous techniques have been applied to the analysis of magnetization vector paths from stepwise demagnetization experiments; Kirschvink (1980) provides references to the most popular. Here I describe only the two techniques that I apply in this thesis.

2.2.2.1 *Principal component analysis (PCA)*

Sometimes it is useful or necessary to consider full three-dimensional vectors rather than just directions; this is often the case when fitting a path to remanence vectors from a sequence of demagnetization steps. Kirschvink (1980) applied the classic statistical technique of principal component analysis (Pearson, 1901) to demagnetization data. To carry out PCA, the data points are first translated so that their centroid coincides with the origin. The translated

data are used to construct an orientation tensor (Scheidegger, 1965). An eigendecomposition of this tensor produces, as its eigenvectors, least-squares fits for three orthogonal axes through the centroid of the data. The maximum axis corresponds to a best-fitting line through the data, while the minimum axis gives the pole to a best-fitting plane. The planar fit can be useful when analysing a demagnetization path with two overlapping magnetization components, although more sophisticated analyses (such as the remagnetization great circles analysis described in section 2.2.2.2) are required to separate the components. It is also possible, when performing a PCA, to 'anchor' the fit, producing a line or plane which is constrained to pass through the origin. This constraint is useful when it is known that only one component is present (or two, in the case of a planar fit), and that it must therefore be demagnetizing towards the origin. Anchoring is achieved by simply omitting the initial translation of the centroid to the origin.

2.2.2.2 *Great-circle remagnetization paths*

PCA is a simple and effective analysis technique when a magnetic component can be isolated and its points fitted; unfortunately this is not always the case. If a natural remanence consists of a hard primary magnetization combined with a soft viscous overprint, it is sometimes possible to demagnetize the soft component to the hard component's starting point, then demagnetize the hard component to the origin. In this case PCA can be applied to the second component. This technique works even if demagnetization cannot be completed all the way to the origin, provided it can be seen that the second vectors are trending towards the origin.

In some cases, however, the hard component may not even be reached, either because the available equipment cannot provide sufficient demagnetization, or – in the case of a thermal demagnetization study – because heating has induced mineral alteration, destroying or altering the remaining magnetization. It is, however, still possible to infer the direction of the hard component.

While the soft component is demagnetizing, its demagnetization path forms a line in three-dimensional space pointing towards the direction of the hard component. Ignoring the magnitude of the magnetization vectors and projecting them onto a sphere, this line is equivalent to a great circle. Even if the hard component is demagnetizing, the great-circle path is still followed since

the hard component is only demagnetizing towards the origin. The direction of the hard component, then, lies somewhere along the great circle. Unless the soft component demagnetizes completely, it is impossible to know where on the circle the hard component lies. However, if several samples are taken from a site, their demagnetization circles can be combined. Ideally, all the circles will intersect at the same point, which must be the direction of the hard component.

In reality, it is unlikely that all the circles will converge perfectly, since various sources of error and noise will affect the exact orientation of the circles. Various techniques have been devised for determining the best estimate of a final direction from imperfectly intersecting great-circle paths, along with associated confidence intervals and goodness-of-fit parameters. In this thesis I use the algorithm described by McFadden and McElhinny (1988); amongst other advantages, their technique also allows stable end-points to be integrated into the analysis, which is useful if analysing a site where the final component could be resolved for some samples but not for others.

2.2.3 *The analysis of AMS data*

AMS is expressed as a second-order tensor defined by six parameters, and may be visualized as an oriented three-dimensional ellipsoid, the length of each axis corresponding to the susceptibility along that axis. Analysis of AMS tensors frequently simplifies matters by treating the shape (relative axis lengths) and orientation (directions of axes) separately. I discuss these aspects in turn. I also describe a statistical test for the reliability of AMS measurements.

2.2.3.1 *Shape analysis of AMS*

Many workers have defined parameters describing the relative magnitudes of the three anisotropy axes, in order to quantify such properties as lineation, foliation, and the degree of anisotropy. Such parameters make it easier to analyse the shape of anisotropy tensors (more strictly, of their associated ellipsoids) in isolation from their orientations. Unfortunately, there has been more creativity in defining new parameters than consensus in applying existing ones, resulting in an impressive parametric proliferation. Tarling and Hrouda (1993) compiled a summary of 26 of the more common parameters, and even this

was not exhaustive, omitting for example the intensity parameter defined by Lisle (1989). Cañón-Tapia (1994) produced a survey of 28 parameters, and conducted an investigation into their usefulness. He showed that many of them carry the same information (with varying degrees of efficiency) and made clear recommendations as to the most useful ones.

In this thesis, following recommendations by both Tarling and Hrouda (1993) and Cañón-Tapia (1994), I routinely apply two parameters: P', the *corrected anisotropy degree*, and T, the *shape factor*, both defined by Jelínek (1981). Their formal definitions are:

$$P' = \exp\sqrt{2[(\eta_1 - \eta_m)^2 + (\eta_2 - \eta_m)^2 + (\eta_3 - \eta_m)^2]} \tag{2.2}$$

and

$$T = \frac{2\eta_2 - \eta_1 - \eta_3}{\eta_1 - \eta_3} \tag{2.3}$$

where

$$\eta_i = \ln K_i \quad ; \quad \eta_m = \sqrt[3]{\eta_1\eta_2\eta_3}$$

Here, K_1, K_2, and K_3 denote the magnitudes of the maximum, intermediate, and minimum principal axes of the anisotropy ellipsoid, respectively.

The corrected anisotropy degree P' is also sometimes denoted by P_J (Tarling and Hrouda, 1993) or P_j (Borradaile and Jackson, 2004). It takes a value of 1 for a perfectly isotropic fabric (a spherical anisotropy ellipsoid), with larger values indicating increasing anisotropy. The shape factor T describes the shape of the anisotropy ellipsoid, with a value of 1 denoting a perfectly oblate shape (a symmetrical disc) and -1 denoting a perfectly prolate shape (a symmetrical rod). For primary sedimentary fabrics, typical ranges are $1.01 < P' < 1.1$ and $0.2 < T < 0.8$ (Tarling and Hrouda, 1993, figure 5.14).

2.2.3.2 *Orientation analysis of AMS*

Statistical analysis of AMS tensor orientations has much in common with the spherical statistics of single directions discussed in section 2.2.1.1. If the directions of the three axes are considered independently, exactly the same techniques can be applied; the Watson-Scheidegger distribution (Scheidegger, 1965) is sometimes used instead of the Fisher distribution. One obvious problem with this technique is that the resulting directions may not be orthogonal,

(Ernst and Pearce, 1989); thus, the 'average' produced for a set of tensors is not itself a tensor, which can make further interpretation difficult.

Jelínek (1978), building on earlier work by Hext (1963), advocated a different approach which produced a 'mean normalized tensor' – an estimate of the AMS tensor which would hypothetically be produced by measuring the entire rock body from which the samples were taken. Unfortunately, the actual implementation of the Jelínek (1978) technique required some simplification for mathematical tractability, which could compromise the accuracy of its estimated confidence intervals. Constable and Tauxe (1990) used a variant of the directional bootstrap statistics described in section 2.2.1.2 to provide better confidence intervals, and it is their procedure that I use for AMS directional statistics within this thesis.

2.2.3.3 *Distinguishing weak AMS data from noise*

Many of the samples measured in this thesis are very weakly anisotropic; it is therefore necessary to consider, when making a measurement, whether the measured anisotropy reflects genuine properties of the sample or whether it is simply an artefact of machine noise. In many cases, correlation between samples gives confidence that a measured anisotropy orientation is not spurious: if tens of samples, drilled at varying orientations, all show the same alignments of anisotropy axes *after* correction for sample orientation, it is extremely likely that the inferred direction represents a signal from the lithology rather than the equipment. This verification technique is not ideal, however: it cannot determine the fidelity of a single, isolated sample measurement; it cannot be applied when there is little variation between sample orientations; and it cannot distinguish cases where there is genuine randomly varying anisotropy.

Fortunately, Jelínek (1996) developed a statistical test (the *F-test*) which allows genuine and spurious anisotropy to be distinguished at the sample level. He defined a parameter F in terms of the measured anisotropy levels and the estimated error reported by the AGICO kappabridge during measurement; F is essentially a measure of the likelihood that a measured anisotropy is due to a genuine signal rather than random noise. Jelínek (1996) derived a threshold of $F > 3.9715$ for a 95% probability that a measurement is genuine. I apply this test throughout the thesis and do not undertake any further analysis on samples with an F-value below the threshold.

3 Rock magnetism of glauconitic sediments

Magnetic Atoms, such as Iron, keep
Unpaired Electrons in their middle shell,
Each one a spinning Magnet that would leap
The *Bloch* Walls whereat antiparallel
Domains converge. Diffuse Material
Becomes *Magnetic* when another Field
Aligns domains like Seaweed in a swell.
How nicely microscopic forces yield,
In Units growing visible, the World we wield!

– John Updike, 'The Dance of the Solids' (in Updike, 1969)

3.1 Introduction

This study was designed to identify and characterize the remanence carriers in glauconitic sediments, and in particular to investigate the specific role of glaucony in the preservation of palaeomagnetically significant, stable magnetization. In this section I describe the aims of the study and the significance of the glaucony facies, and give a brief outline of the chapter.

3.1.1 *Aims of the study*

Given the widespread occurrence of glaucony in New Zealand sediments (Field *et al.*, 1989, pp. 59–63) and worldwide (Odin and Matter, 1981), and its usefulness in stratigraphic and palaeoenvironmental interpretation (Amorosi, 1995), an understanding of its significance in palaeomagnetic studies would be valuable.

For this study, I chose to concentrate on a single glauconitic unit; although this limits the ease with which the results can be generalized, it permitted me to apply a broad range of techniques to characterize more fully the magnetic mineralogy. In the palaeomagnetic studies described elsewhere in this thesis, I applied a more focused selection of rock magnetic techniques, allowing me to relate the samples' magnetic behaviours to the results in this chapter without conducting further full-scale rock magnetic studies.

The goal of the study was to produce two comparisons of magnetic behaviour:

1. A comparison between glauconitic and non-glauconitic sediments. I did this by investigating samples from within and just outside a glauconitic horizon.

2. A comparison between the glauconitic and non-glauconitic components of glauconitic sediments. I did this by applying standard glaucony extraction techniques (Odin, 1982; Amorosi *et al.*, 2007) to material from a glauconitic horizon and analysing the glauconitic and non-glauconitic fractions separately. Glaucony has a high magnetic susceptibility (Bentor and Kastner, 1965; Odin and Morton, 1988), and these techniques use magnetic separation to concentrate glaucony by isolating the high-susceptibility grains in powdered samples.

Using these data, along with more general petrological characteristics of the samples, I created a model of how these sediments acquired their NRM, and what relation this magnetization might have to the geomagnetic field during deposition and lithification. In particular, I wished to investigate the magnetic properties of the glauconitic grains themselves: whether they carry a significant remanence, and if so, whether it could be linked to the field in which the glauconitization process took place.

The impetus for this rock-magnetic investigation is the interpretation of palaeomagnetic data from glauconitic sediments: if the process by which the magnetization is acquired is understood, its palaeomagnetic fidelity and usefulness can be assessed. The role of glaucony in remanence acquisiton is important both in selecting suitable sediments for palaeomagnetic study and in interpreting the data when glauconitic sediments are sampled.

3.1.2 *The significance of the glaucony facies*

The significance of the glaucony facies in stratigraphy and the determination of palaeoenvironments has long been recognized. Goldman (1922) described the association of glauconitic horizons with hiatuses in deposition, and inferred that glaucony formation is a diagenetic process at or near the sea-floor which can only occur in the absence of significant sedimentary input. This assessment has been borne out by subsequent research. For much of the twentieth century, the study of glaucony was complicated by loose application of the term 'glauconite' and by the lack of a generally accepted model for glaucony formation.

Both problems were addressed by Odin and Matter (1981), whose 'verdissement' model of glauconitization is now generally accepted. Odin and Matter (1981) also reformed the terminology surrounding glaucony, deprecating the term 'glauconite' in favour of more precise mineral specifications such as 'glauconitic mica', and coining the term 'glaucony' for the facies. This reform has not been universally adopted, but throughout this thesis I follow the practice of Odin and his co-workers in using the term 'glaucony' to refer to the facies and to glauconitic grains. Odin and Morton (1988) gave well-defined criteria for distinguishing glaucony from other similar grains.

The more thorough understanding of glauconitic evolution provided by Odin allowed more sophisticated interpretations of glaucony within sedimentary sequences. These have included methods of distinguishing autochthonous and allochthonous glaucony (Amorosi, 1997; Amorosi *et al.*, 2007) and reassessment of the palaeoenvironmental conditions required for its formation (Huggett and Gale, 1997). Despite these developments, the basic interpretation of glaucony remains unchanged; a horizon of authigenic glaucony in a sedimentary sequence indicates a hiatus in deposition.

Although the evolution of glauconitic minerals is now fairly well understood, little is known concerning their magnetic behaviour. Odin (1982) and Amorosi (1993) attested that paramagnetic susceptibility is strongly correlated with K_2O content and thus with maturity, but it seems that, prior to this thesis, no work has been done on their relationship with palaeomagnetism.

3.1.3 *Chapter outline*

Section 3.2 describes the samples I used for the study and the experimental techniques I applied to them. Section 3.3 describes and plots the data obtained from the experiments. Section 3.4 applies analytical techniques to the raw data of the previous section in order to determine the magnetic mineralogy of the samples and its relationship to glaucony. Section 3.5 discusses the significance of these analyses, proposes a model for the remanence acquisition of the sampled sediments, and assesses their suitability for palaeomagnetic studies. Section 3.5 also discusses the effects of viscous magnetization and possible alternative methods of separation.

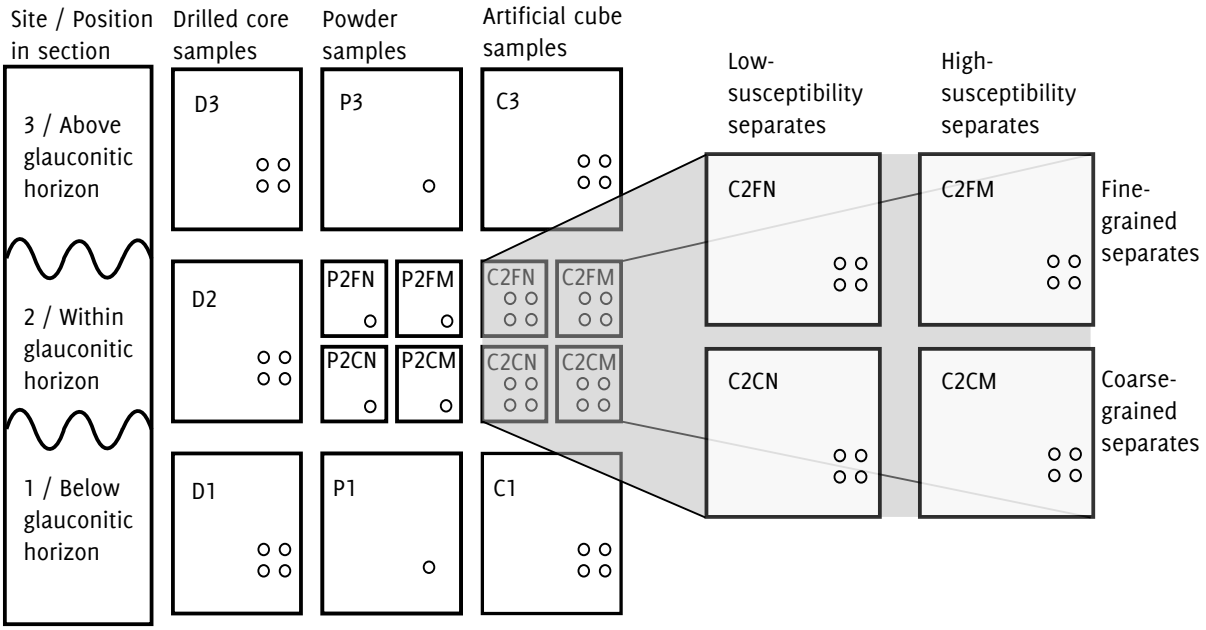

Figure 3.1 Summary of the sample groups used for the rock magnetism study (see text for full explanation). Each box corresponds to a uniform sample group; the C2 samples are depicted twice, to allow annotation of the size and magnetic susceptibility fractions. Each small circle corresponds to a single physical specimen. The high-susceptibility separates were expected to contain higher concentrations of glaucony than the low-susceptibility separates.

3.2 Experimental procedure

In this section I describe the samples that I took, how I prepared and processed them, and the experimental techniques I applied to them.

3.2.1 *Description of samples*

I selected a well-defined glauconitic horizon from the lower Abbotsford Formation at Fairfield Quarry, and took bulk and oriented samples from below the horizon (site 1; height 24.5 m), within it (site 2; 25.5 m), and above it (site 3; 29.5 m). The stratigraphic heights of the sites are measured from the datum used for the section log in chapter 5, which also gives background information on the Abbotsford Formation and the sampling locality. The study involved three types of sample: standard palaeomagnetic drill cores; powder samples, prepared directly from crushed bulk samples or from separates; and artificial cube samples made from cemented powders. Producing artificially cemented cubes allowed me to apply a range of bulk magnetic techniques requiring discrete, orientable specimens. Identical treatment protocols could now be

applied to the unprocessed drill cores and the cubes, allowing direct comparisons of behaviour between bulk material and separates. The samples are summarized in figure 3.1 and table 3.1.

Samples are identified by a short code of 2–4 characters, constructed as follows:

1. Sample type: D drill core, C cube, P powder.

2. Position in section: 1 below glauconitic horizon, 2 within it, 3 above it.

3. Size fraction (only for position 2): F fine, C coarse.

4. Susceptibility fraction (only for position 2): M high susceptibility (glauconitic), N low susceptibility (non-glauconitic).

Each sample code (except for the P series powder samples) actually denotes a set of four sister samples; unless otherwise stated, all numerical results presented in this chapter for 'C' and 'D' samples represent the mean for the four samples corresponding to the sample code.

Sample	Site	Type	Volume (cm^3)	Grain size (μm)	Mag. sus.
D1	1	Drilled core	10.3	—	—
C1	1	Cemented cube	4.0	—	—
P1	1	Loose powder	0.25	—	—
D3	3	Drilled core	10.3	—	—
C3	3	Cemented cube	4.0	—	—
P3	3	Loose powder	0.25	—	—
D2	2	Drilled core	10.3	—	—
P2	2	Loose powder	0.25	—	—
C2FN	2	Cemented cube	4.0	62–180	Low
P2FN	2	Loose powder	0.25	62–180	Low
C2FM	2	Cemented cube	4.0	62–180	High
P2FM	2	Loose powder	0.25	62–180	High
C2CN	2	Cemented cube	4.0	180–500	Low
P2CN	2	Loose powder	0.25	180–500	Low
C2CM	2	Cemented cube	4.0	180–500	High
P2CM	2	Loose powder	0.25	180–500	High

Table 3.1 Summary of samples used in the rock magnetism study. The sample volumes are nominal.

3.2.2 *Sample preparation*

The D series samples (drill cores) were drilled from the outcrop using a water-cooled rock drill with a diamond-tipped non-magnetic 25 mm barrel, and cut to 22 mm lengths using a circular saw with diamond-edged brass blades.

I prepared the P and C series samples by powdering material taken from the outcrop. For the samples from sites 1 and 3, the powder was not fractionated; for site 2, I prepared four different fractions as described in section 3.2.2.1. The P samples consisted solely of disaggregated powder; I produced the C samples by cementing the powder into solid cubes, as described in section 3.2.2.1.

The steps for glaucony separation followed approximately the procedure described by Amorosi *et al.* (2007), although the disaggregation procedure used in that paper did not prove necessary due to the softness of the sediments I was working with. This separation procedure uses magnetic fractionation to extract glaucony, which has a relatively high magnetic susceptibility. In this aspect it bears some resemblance to procedures developed to extract and concentrate remanence carriers for analysis, such as those discussed by Hounslow and Maher (1996). In this study, however, the goal was separation of glaucony rather than concentration of ferrimagnetic particles.

3.2.2.1 *Disaggregation and fractionation*

I disaggregated the samples by crushing the material, dry, between a wooden board and PVC pipe, exercising care to minimize damage to the glaucony grains. I then subjected the glauconitic material from site 2 to further procedures to separate the glauconitic grains: I wet-sieved the disaggregated material using a 62 μm mesh and dried the coarse fraction at room temperature. I then dry-sieved this material to separate it into 62–180 μm and 180–500 μm fractions (all the grains being below 500 μm). Performing size fractionation allowed me to investigate the effect of grain size on magnetic properties; for dry magnetic separation techniques, narrowly sizing the material also increases the efficiency of separation (Odin, 1982, p. 392; Jones, 1987, p. 41; Svoboda, 2004, p. 96).

I performed magnetic separation of the fine and coarse fractions of the glauconitic material using a Frantz-type isodynamic separator with a current of 0.55 A, a longitudinal dip of 15°, and a transverse tilt of 8°.

3.2.2.2 *Cementing*

Most of the rock magnetic laboratory procedures in my experimental plan required discrete, orientable specimens with a volume of around 1–10 cm^3. To produce these from disaggregated material, I mixed the material with aqueous sodium silicate solution to form a paste, using a ratio of approximately 7 cm^3 of dry material to 12 cm^3 of 50% sodium silicate solution. Sodium silicate solution (also known as 'water glass') dries to a strong, clear, heatproof cement with negligible saturation magnetization. It has frequently been used in palaeomagnetic and archaeomagnetic studies to stabilize friable specimens (e.g. Gómez-Paccard *et al.*, 2006) or to produce solid samples from unconsolidated material (e.g. Dankers, 1981). While Kostadinova *et al.* (2004) raised concerns about its effect on the thermal variation of magnetic susceptibility, they found no effect on remanence. I did not use sodium silicate in the preparation of the 'P' series of samples, so its effect on thermal susceptibility variation was not a concern.

In order to monitor for any effects due to sodium silicate impregnation or other aspects of sample preparation, I produced artificial cube samples for sites 1 and 3 using disaggregated but otherwise untreated bulk material. Any effects from the process of producing cube samples should thus be visible as a deviation between the behaviour of the drilled cores and the corresponding cemented cubes.

I packed the paste firmly into plastic moulds constructed from IODP sample cubes (the 'Japanese cube' described by Richter *et al.*, 2007). I modified the cubes by removing the bottom and drilling 93 evenly spaced 1.5 mm holes in the sides and lid, to allow sufficient air circulation for the paste to dry. I used the lid as a removable bottom, allowing easier extraction of the dried samples, and lubricated the moulds using silicone spray.

I left the paste to dry in the moulds for 24–48 hours at room temperature in a field-free (<150 nT) room before extracting the moulded cubes. The resulting cubes had a measured volume of approximately 4 cm^3.

3.2.3 *Measurements and analyses*

In this section I describe the experimental protocols and techniques I applied. Specific details of the equipment I used are given in Appendix C on page 329.

3.2.3.1 *Magnetic methods: cylinder and cube samples*

I subjected all the drill-core and cube samples to the following treatments:

1. Stepwise AF demagnetization of any remanent magnetization, using steps of 0, 5, 10, 15, 20, 25, 30, 35, 40, 45, 50, 60, 70, 80, 90, 100, 110, 120, 130, 140, and 150 mT. (I also used these steps for subsequent stepwise AF and anhysteretic remanent magnetization (ARM) treatments.) The synthetic samples were not expected to have any initial remanence, but I included them in this treatment to ensure uniformity of treatment across all samples.

2. Stepwise acquisition of an ARM with a bias field of 45 μT, followed by stepwise AF demagnetization of the resulting remanence.

3. Stepwise IRM acquisition. IRMs were imparted using a pulse magnetizer, with steps of 0, 5, 10, 15, 20, 25, 30, 35, 40, 45, 50, 55, 60, 65, 70, 75, 80, 85, 90, 100, 110, 120, 130, 140, 150, 160, 180, 200, 250, 300, 350, 400, 450, 500, 600, 800, and 1000 mT.

4. Stepwise IRM backfield application (also called DC demagnetization), using the same steps, until the previously acquired IRM was erased.

5. Stepwise AF demagnetization of a 1 T IRM.

6. The coercivity analysis technique devised by Lowrie (1990); this comprises thermal demagnetization of three different, orthogonal IRMs, and is described in more detail below.

The Lowrie (1990) technique is a well-established method for efficiently measuring the thermal unblocking spectra of grain populations with varying coercivities. Three IRMs of decreasing intensity (in this study: 1, 0.4, and 0.12 T) are successively imparted at orthogonal angles to each other; lower-coercivity grains will be realigned with one of the weaker fields, while the grains of highest coercivity will retain the alignment imparted by the initial, strong field. The samples are then subjected to stepwise thermal demagnetization, in this case from 25°C to 775°C in 25°C steps, with a heating time of 40 minutes at each step. The decreases in remanence along the three IRM directions allow determination of a separate unblocking spectrum for each of the coercivity classes.

3.2.3.2 *Magnetic methods: powder samples*

The P series of powder samples was only used for temperature-dependent magnetic susceptibility measurements. I made these measurements using a 716 A/m, 976 Hz field in an argon atmosphere (99.999% purity) with a flow rate of 100 ml per minute. The temperature range was 40°C to 700°C, with a heating rate of 11°C per minute and an average measurement interval of about 6°C, resulting in around 245 measurements per sample.

Correction of TDMS data

The CS-3 furnace apparatus used for the measurement consists of a water-circulating cooling unit containing a glass sample tube, into which is inserted a probe which acts both as heating element and thermometer. Unfortunately the furnace assembly itself undergoes changes in magnetic susceptibility with temperature, and it is thus necessary to correct the raw data to compensate for this. A procedure for this is described in Hrouda (1994), and is in essence very simple: a set of 'free-furnace' measurements is taken without a sample in the tube; for each sample measurement, the free-furnace measurement is subtracted. Since the exact measurement temperatures vary slightly from one run to the next, it is necessary to interpolate the free-furnace data to obtain the furnace susceptibility for the sample measurement temperatures. I modified the procedure described by Hrouda (1994) in two ways:

1. The susceptibility variation of the sample tube is small compared to that of the probe and water jacket; Hrouda (1994) thus found it sufficient to correct for the water jacket and probe, and to regard the sample tubes as interchangeable. With time and use, however, the tubes can become slightly contaminated with residue from previous measurements, altering their magnetic behaviour. I thus chose to correct each sample measurement using a free furnace measurement made using the same sample tube.

2. Hrouda (1994) smoothed and interpolated the free-furnace data using a five-point moving average; following the recommendation of Takezawa (2006), I instead used a cubic smoothing spline (Silverman, 1985).

Progressive heating cycles

Heating-induced mineral alteration is a frequent problem in thermomagnetic investigations of all kinds, including measurement of the temperature dependence of magnetic susceptibility (TDMS). Hrouda (2003) discussed this problem and recommended repeated heating of the sample to progressively higher temperatures. While this does nothing to prevent alteration occurring, it does make it easier to see how much alteration occurs within each temperature interval; when constrained like this, the alteration temperatures themselves can become useful clues to the sample mineralogy. I adopted this protocol, using 100°C intervals up to 700°C. I also attempted to limit oxidation of samples by heating them in an argon atmosphere. Significant alteration still occurred, however.

3.2.3.3 *Non-magnetic methods*

Polished thin sections were made from a drill core from each of the three sampled positions within the section. Four polished mounts were also made from the four sets of grain separates. I examined these sections microscopically under transmitted and reflected light, and using secondary and backscattered electron imaging. I used an energy dispersive X-ray spectroscopy (EDS) microprobe to investigate compositions of individual mineral grains in an attempt to identify remanence carriers visually.

3.3 Results

In this section I present experimental results with a minimum of interpretation; discussion and analysis is deferred to the next section. The magnetic data files, micrographs, and microprobe analyses are included on the data CD-ROM (appendix D).

3.3.1 *Rock magnetic parameters*

Values for several common rock magnetic parameters for the samples are given in table 3.2. χ is positively correlated with glauconitic content. Both the SIRM and χ_{ARM} are negatively correlated with glaucony, indicating a lower concentration of remanence carriers in the glauconitic samples. The H_{cr}, H'_{cr}, and MDF

parameters show relatively little variation overall, indicating similar coercivity spectra for all the samples.

Sample name	H_{cr} mT	H'_{cr} mT	MDF mT	SIRM mA/m	χ SI $\times 10^{-4}$	χ_{ARM} SI $\times 10^{-4}$
D1	42.8	48.5	28.3	163	2.1	2.3
C1	43.0	49.5	28.5	199	2.1	2.4
D3	42.3	48.2	27.9	162	1.6	1.9
C3	41.5	47.7	27.6	170	1.9	1.9
C2CN	44.5	51.8	28.8	127	3.8	1.2
C2FN	44.6	52.0	29.4	110	3.5	1.1
D2	41.1	47.1	25.4	86	5.8	0.90
C2CM	46.7	56.0	28.9	52	4.7	0.39
C2FM	42.1	49.7	26.8	66	5.5	0.53

Table 3.2 Rock magnetic parameters for sample sets

3.3.2 *IRM, backfield IRM, and AF demagnetization of IRM*

Figure 3.2 shows individual plots of IRM acquisition and DC demagnetization by backfield IRM. The samples show significant variation in saturation isothermal remanent magnetization (SIRM), but all have similar, low, coercivities. Figure 3.3 shows the stepwise AF demagnetization of a 1 T IRM.

3.3.3 *ARM acquisition and demagnetization*

Figure 3.4 shows stepwise ARM acquisition curves for all the samples and AF demagnetization curves for the imparted ARMs. The initial values of the AF demagnetization curves are a little lower than the final values of the acquisition curves; this is most probably due to viscous decay of magnetization during the period between the two experimental runs (30–90 minutes).

The most noticeable feature of the ARM acquisition curves is the anomalously low remanence acquired by the C1 and C3 sample groups during the first five (0–20 mT) steps. I interpret this as experimental error, for the following reasons: the fact that the C1 and C3 samples were measured in the same experimental run, and were the only samples in that run; the lack of agreement with other samples undergoing the same treatment (particularly the mineralogically identical D1 and D3 sets); the lack of corresponding artefacts in any of the

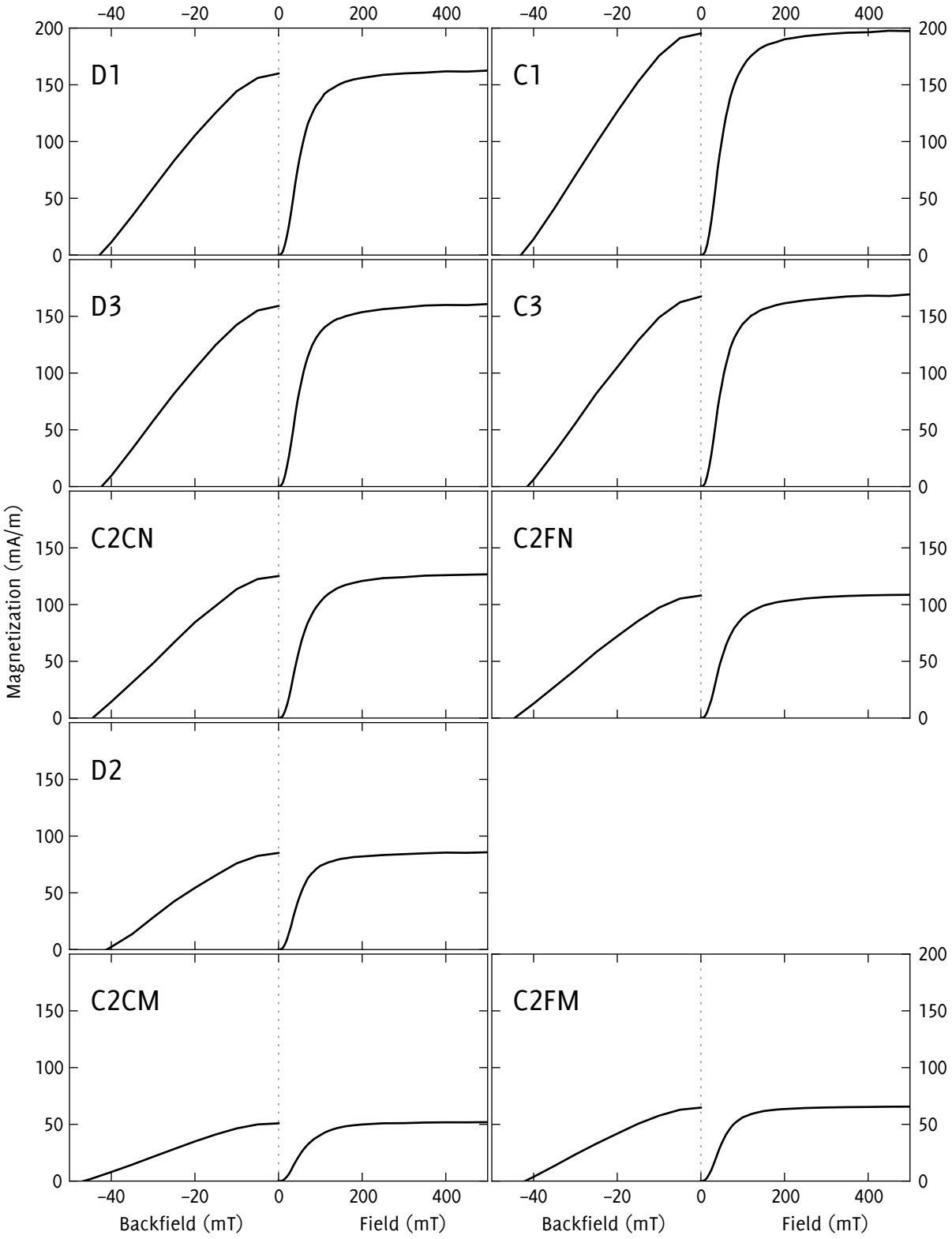

Figure 3.2 IRM acquisition and backfield demagnetization for all sample sets. Each plot shows the acquisition curve on the right and the backfield curve on the left, using different horizontal scales. IRM acquisition fields up to 1 T were applied, but the acquisition curves are truncated at 500 mT since all samples had acquired over 98% of their saturation magnetization at this field.

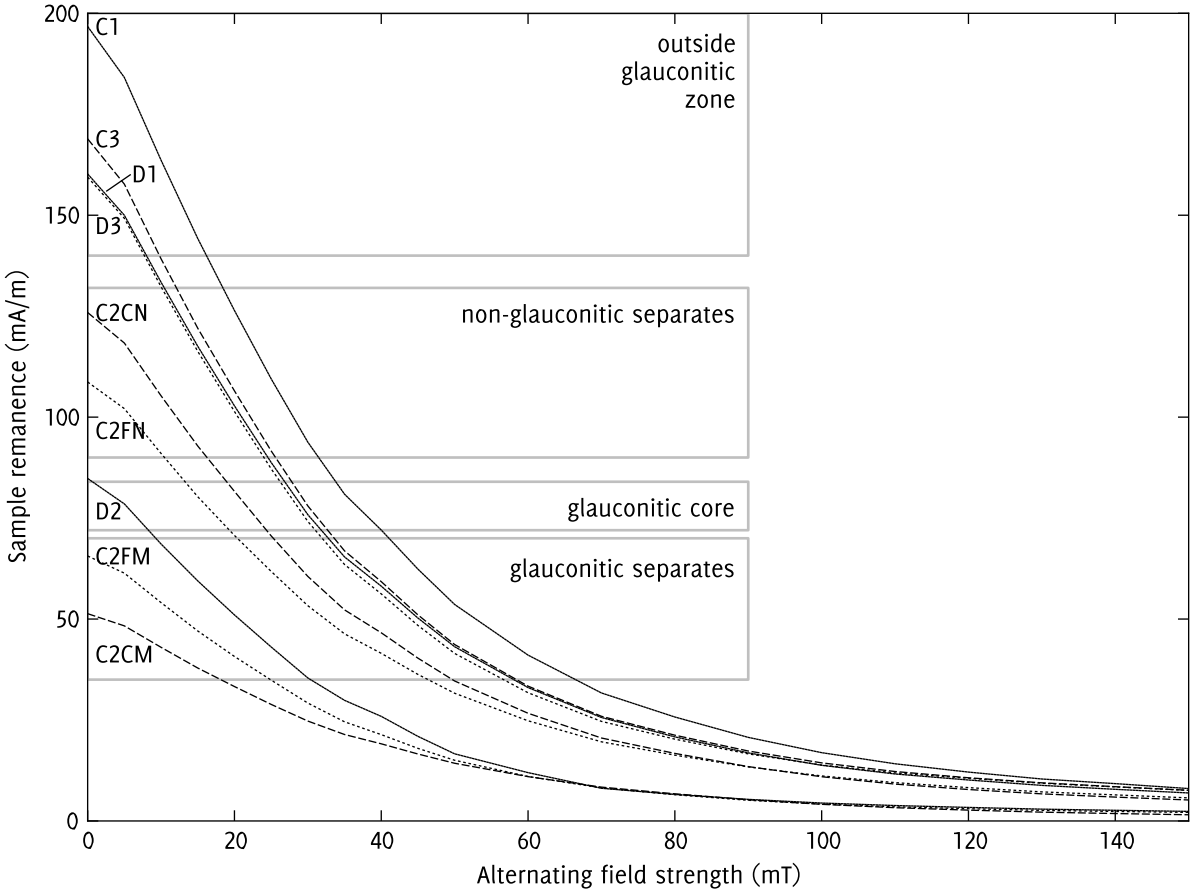

Figure 3.3 AF demagnetization of a 1 T IRM

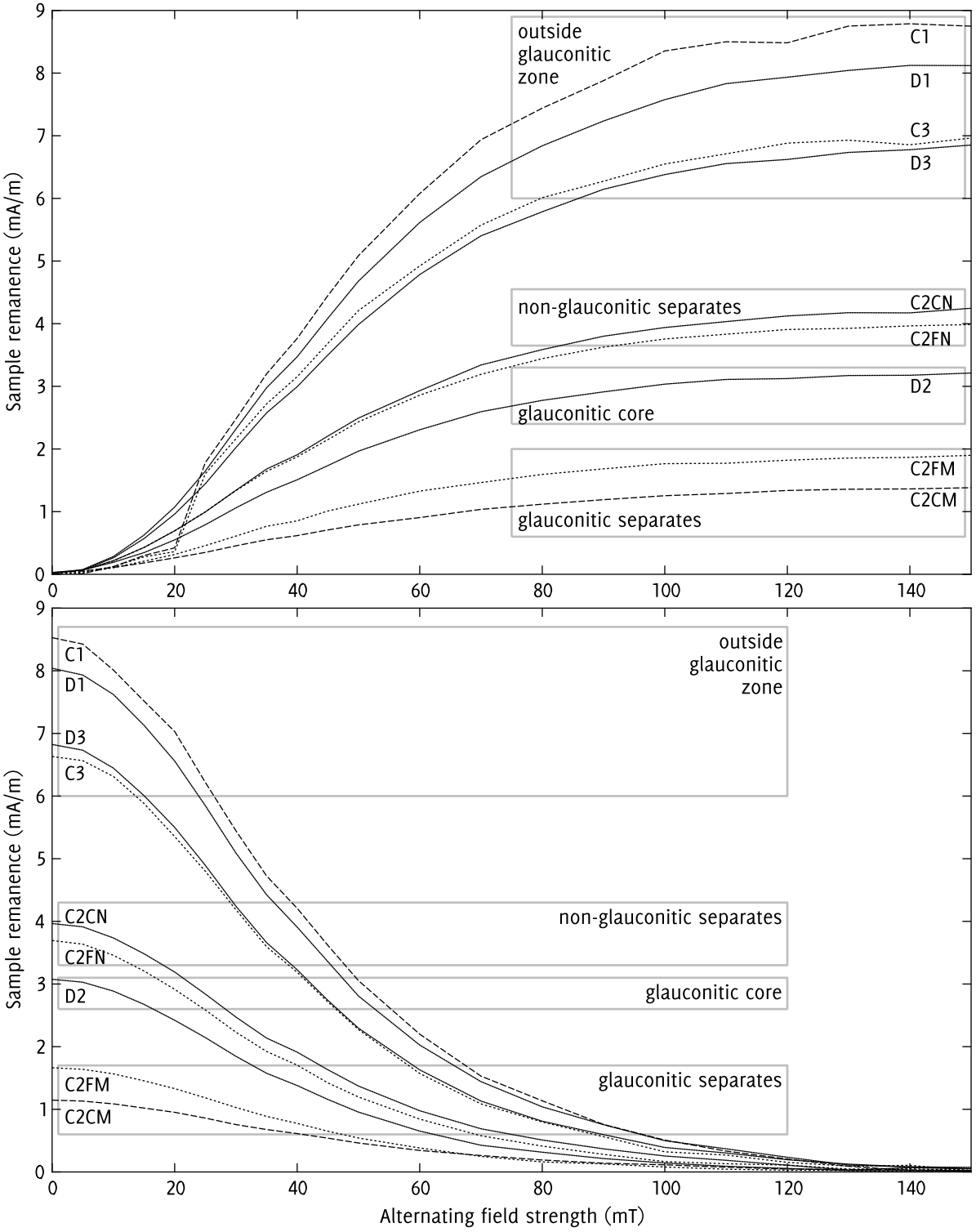

Figure 3.4 ARM acquisition (top) and AF demagnetization of ARM (bottom) for all sample sets.

other AF or IRM experiments on the C1 and C3 samples, in particular the AF demagnetization of the acquired ARM; and the very sharp difference between the readings at 20 mT and 25 mT. The most likely explanation is a flux jump in the z-axis SQUID of the cryomagnetometer.

3.3.4 *Thermal demagnetization of IRM*

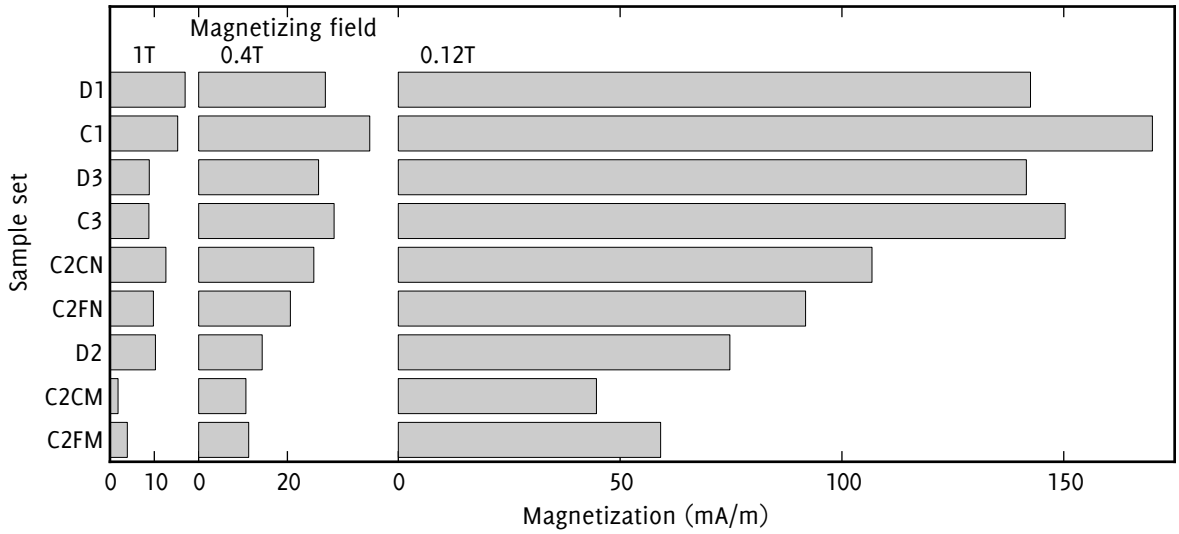

Figure 3.5 Initial magnetizations of the three coercivity components

Figure 3.5 shows the relative initial IRMs of the three components. The results of the thermal demagnetization are shown in figure 3.6. As would be expected given the low coercivities suggested by the IRM acquisition curves, the majority of the remanence was aligned with the 0.12 T field in all the measured samples. Typically the 0.12 T component accounted for around 75% of the total remanence, with the 0.4 T component giving 15–20% and the 1 T component 5–10%.

3.3.5 *Magnetic susceptibility measurements*

3.3.5.1 *Initial susceptibilities*

I measured the volume-normalized room-temperature magnetic susceptibilities of the drill-core and cube samples using the MFK-1A kappabridge. The results are show in table 3.2; the values for D2 and the glauconitic separates agree well with the glaucony susceptibilities given in figure 5 of Bentor and Kastner

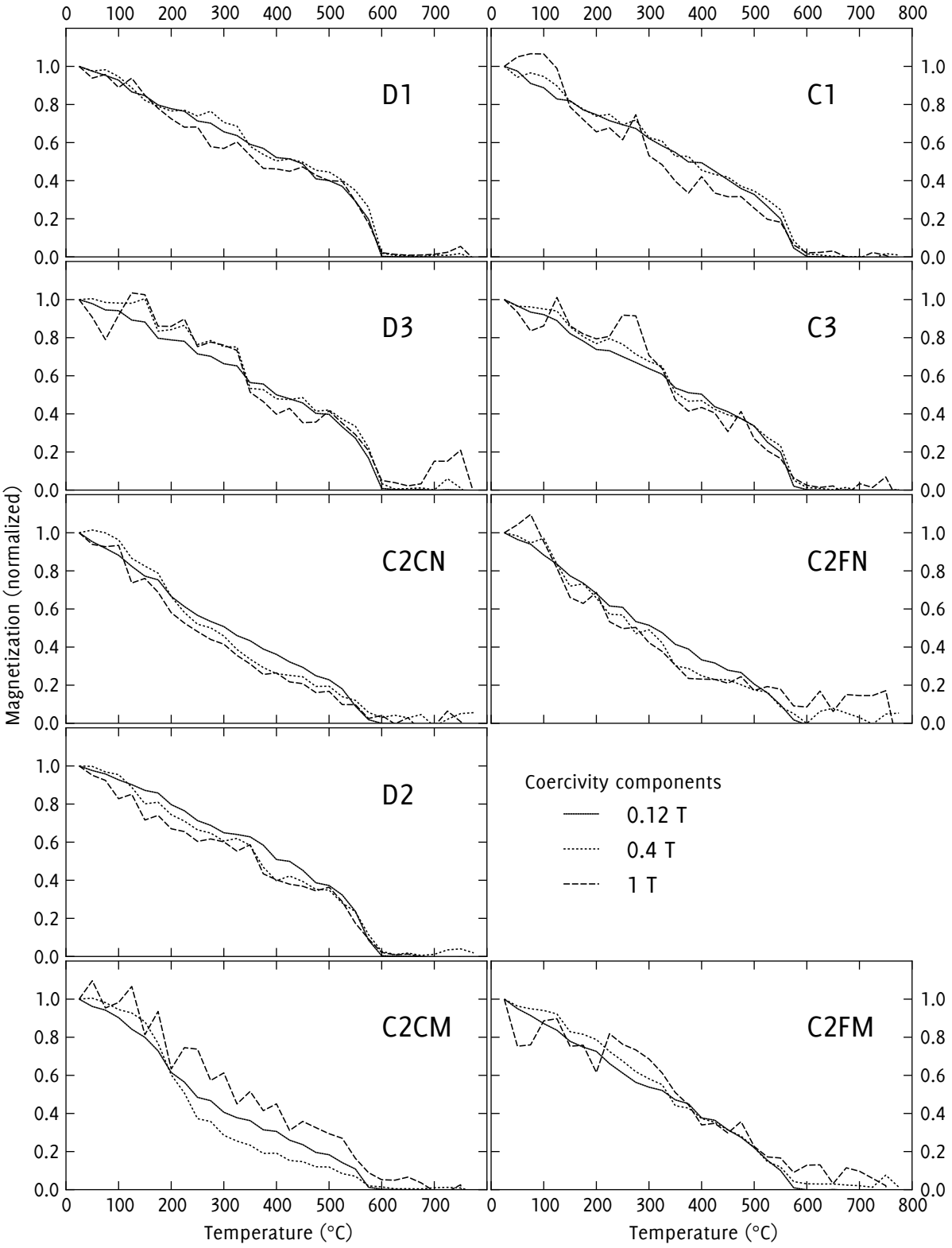

Figure 3.6 Thermal demagnetization of the triaxial magnetization in 25°C steps from 25°C to 775°C. For each sample set, the three coercivity components are individually normalized and plotted on the same graph. The apparent higher noise levels for the 0.4 T and 1 T components are due to their lower remanences.

(1965). As would be expected, the less glauconitic sites 1 and 3 show lower susceptibilities compared to the glauconitic site 2, and the glauconitic separates have higher susceptibilities than the non-glauconitic separates. One unexpected result is that the whole-rock D2 samples have slightly greater susceptibility than the glauconitic separates C2CM and C2FM. The most likely explanation is that the fine, sub-62 μm particles in the drill-core were slightly paramagnetic and contributed to the susceptibility, whereas the separates are cemented with diamagnetic sodium silicate.

3.3.5.2 *Results*

The results of the TDMS experiments are shown in figure 3.7 (p. 48). All the samples show large, irreversible increases in magnetic susceptibility, indicating significant heating-induced mineral alteration. The combined plots are dominated by the high susceptibilities caused by alteration in the 500–600°C range, which obscures the possibly more informative behaviour just below 600°C. In figure 3.8 (p. 49) I plot the 600°C heating step with an expanded vertical scale which shows this behaviour more clearly.

3.3.6 *Optical microscopy*

Optical study of the thin sections revealed various opaque, reflective mineral phases, including framboidal pyrite up to 1 mm in diameter. Other opaques appeared euhedral with sizes ranging from 10 μm down to the optical resolution limit of the microscope (around 1 μm); these grains were sometimes embedded in glauconitic and polycrystalline siliciclastic grains, but were most often observed in the matrix.

3.3.7 *Electron microprobe analysis*

I subjected around 50 of the opaque, reflective grains identified in thin section to electron microprobe analysis; they were all identified as pyrite. Due to the limitation imposed by the diameter of the probe beam, all the analysed grains were above 5 μm in size. Figure 3.9 (p. 50) shows an example of pyrite crystals in a polycrystalline grain.

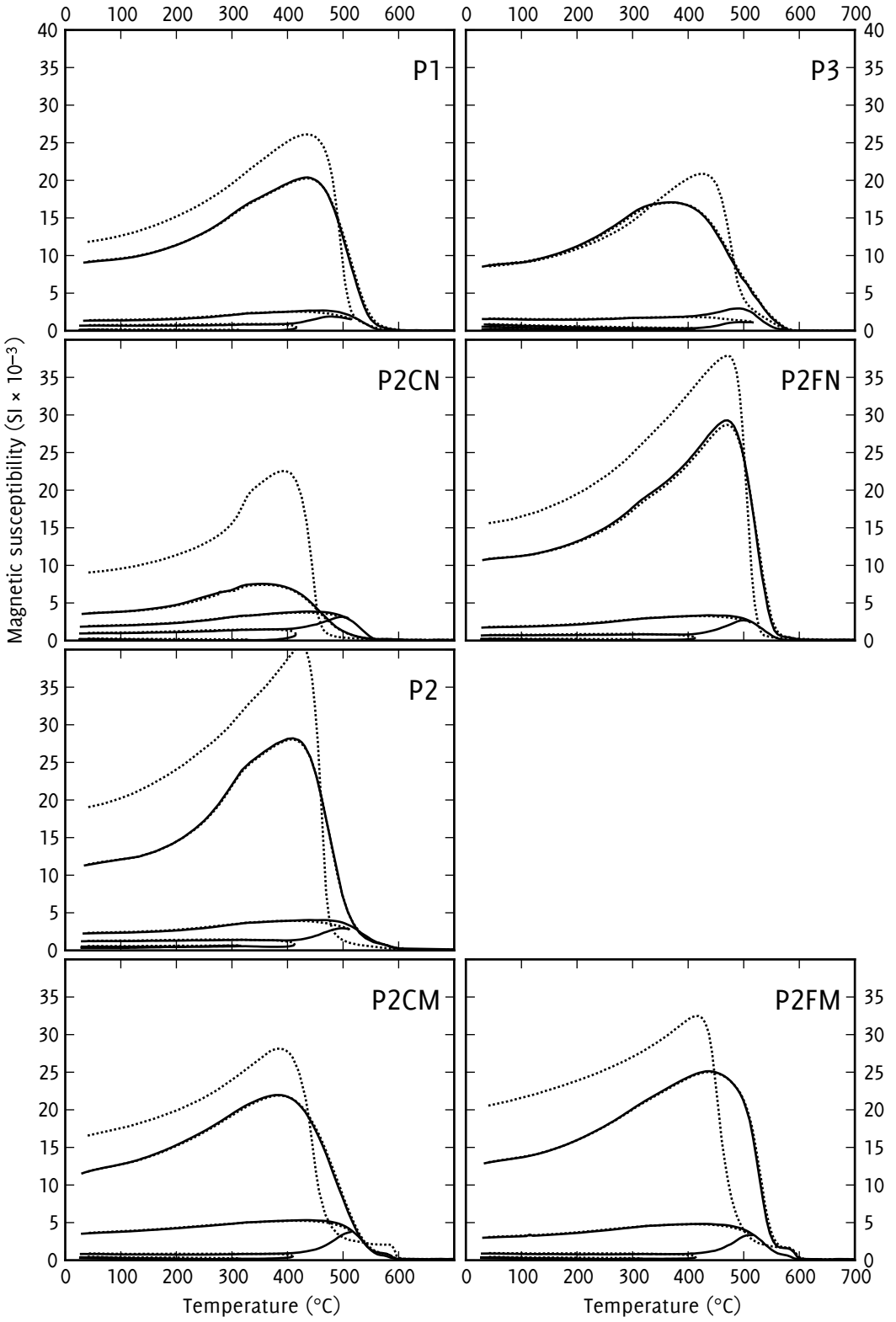

Figure 3.7 Variation in susceptibilities across successive heating cycles. Solid lines show heating; dashed lines show cooling. The cooling line for a temperature step T_1 is always replicated by the heating line for the next temperature step T_2, since all the possible alteration up to T_1 has already taken place.

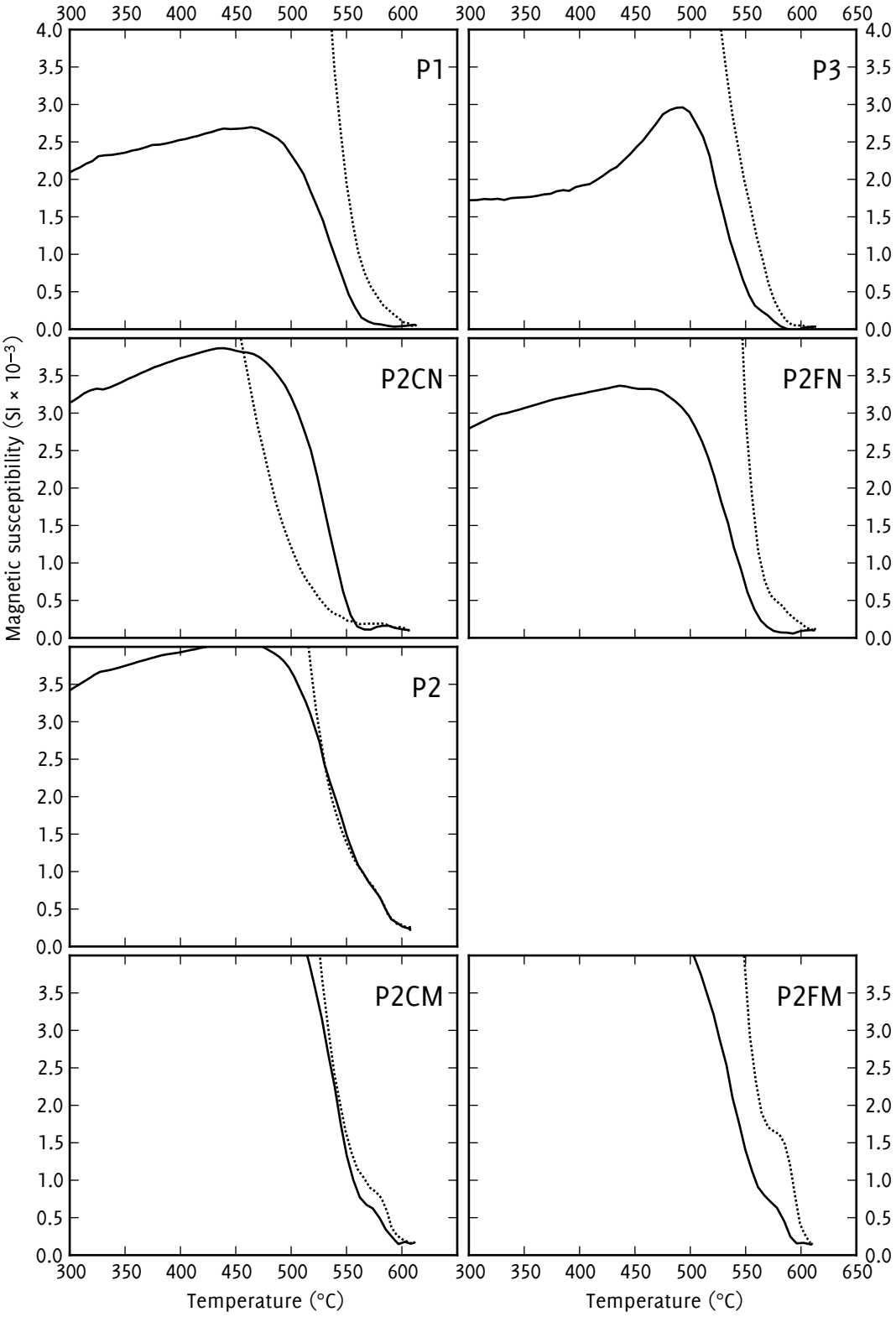

Figure 3.8 Susceptibility variation in the 600°C heating step, showing a steep decrease at around 550–600°C for each sample.

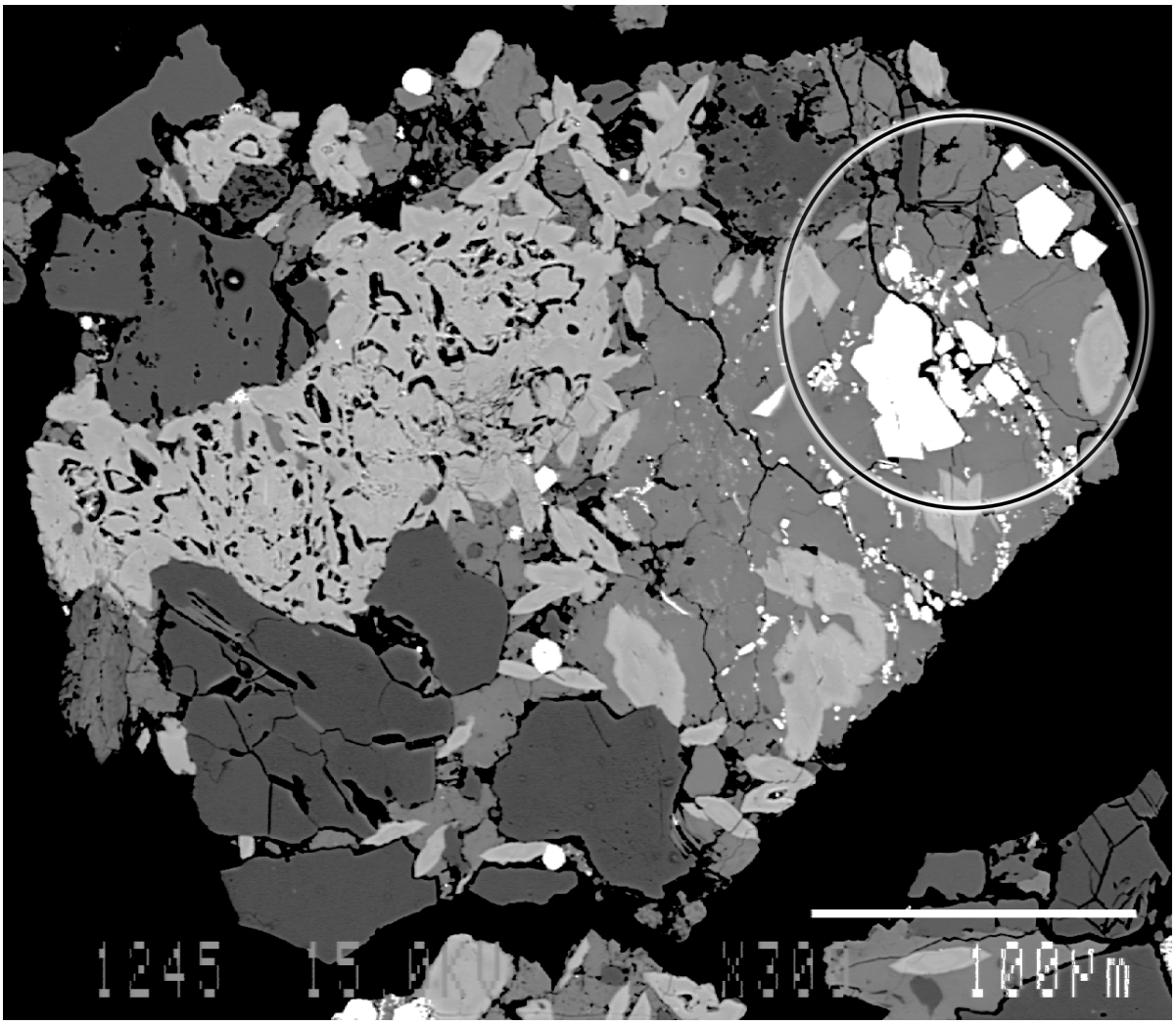

Figure 3.9 A complex polycrystalline grain imaged with electron backscatter. The bright grains in the upper right-hand region (circled) were identified as pyrite by EDS.

3.4 Analysis of results

In this section I analyse and interpret the raw experimental results presented in the previous section in order to determine the magnetic mineralogy of the samples.

3.4.1 *IRM acquisition curves*

The normalized IRM curves all had very similar shapes, suggesting that while the remanence carriers varied in concentration, there was little change in bulk magnetic mineralogy across the horizon. In all cases the material was dominated by low-coercivity remanence carriers: in progressive IRM magnetization

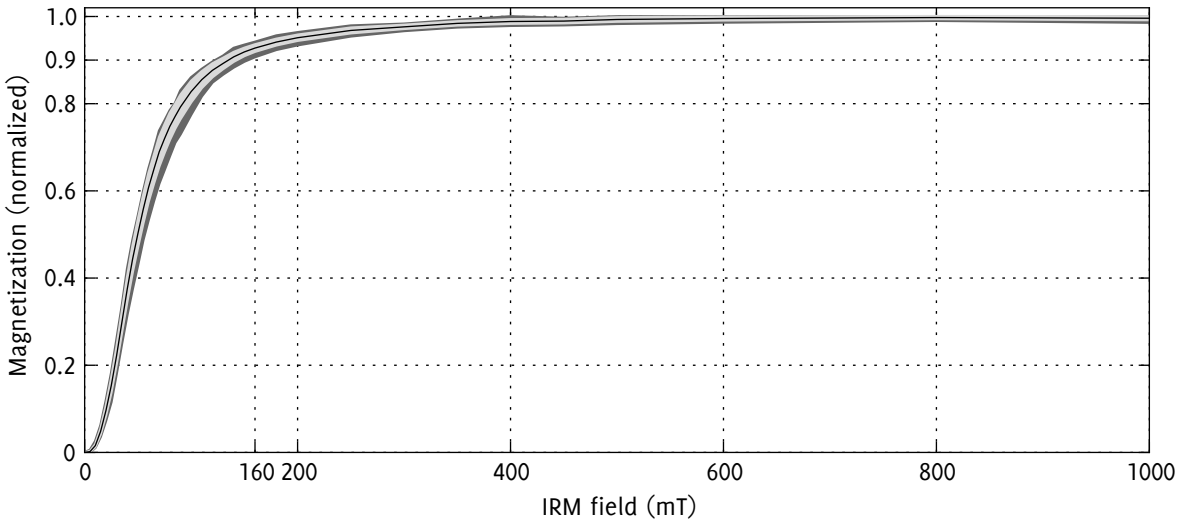

Figure 3.10 Similarity of normalized IRM curves across all 36 drill-core and cube specimens in the study. The dark grey area shows the full range of values; the light grey area shows one standard deviation either side of the mean; the black line shows the mean. The samples acquired over 90% of their saturation remanence by 160 mT.

to 1 T, all samples acquired over 90% of their magnetization by 160 mT. Figure 3.10 shows the narrow range of IRM behaviours among the samples.

The non-normalized IRM acquisition curves in figure 3.11 show the relative SIRMs of the different sample sets. The D1 and D3 sets have practically identical curves, indicating very similar magnetic mineralogies and concentrations.

Theoretically – assuming that the sampled material is homogeneous and that the cube preparation has no effect on magnetic properties – the non-normalized IRM curves for the drilled samples D1 and D3 should be identical to those for their corresponding cube samples C1 and C3. In the case of site 3 (above the glauconitic horizon), the correspondence is very good, but at site 1 (below the glauconitic horizon) there is a significant discrepancy in SIRM between D1 and C1. The shapes of the D1 and C1 curves, however, are practically identical (a linear regression gives $R^2 = 1.000$, as compared to a mean R^2 of 0.997 across all possible pairs of curves) so the variation is only in the apparent concentration of magnetic minerals. The most likely causes for this variation are miscalculation of the cube volumes and small-scale inhomogeneity in the concentration of remanence carriers.

There is a clear difference in SIRM between the samples within the glauconitic horizon (site 2) and those either side of it (sites 1 and 3), with the SIRM of the latter being about twice as large. Within the samples from site 2, the core samples D2 plot, as would be expected, close to the mean of the mineral separates (the C2 samples). Interestingly, the most remanence seems

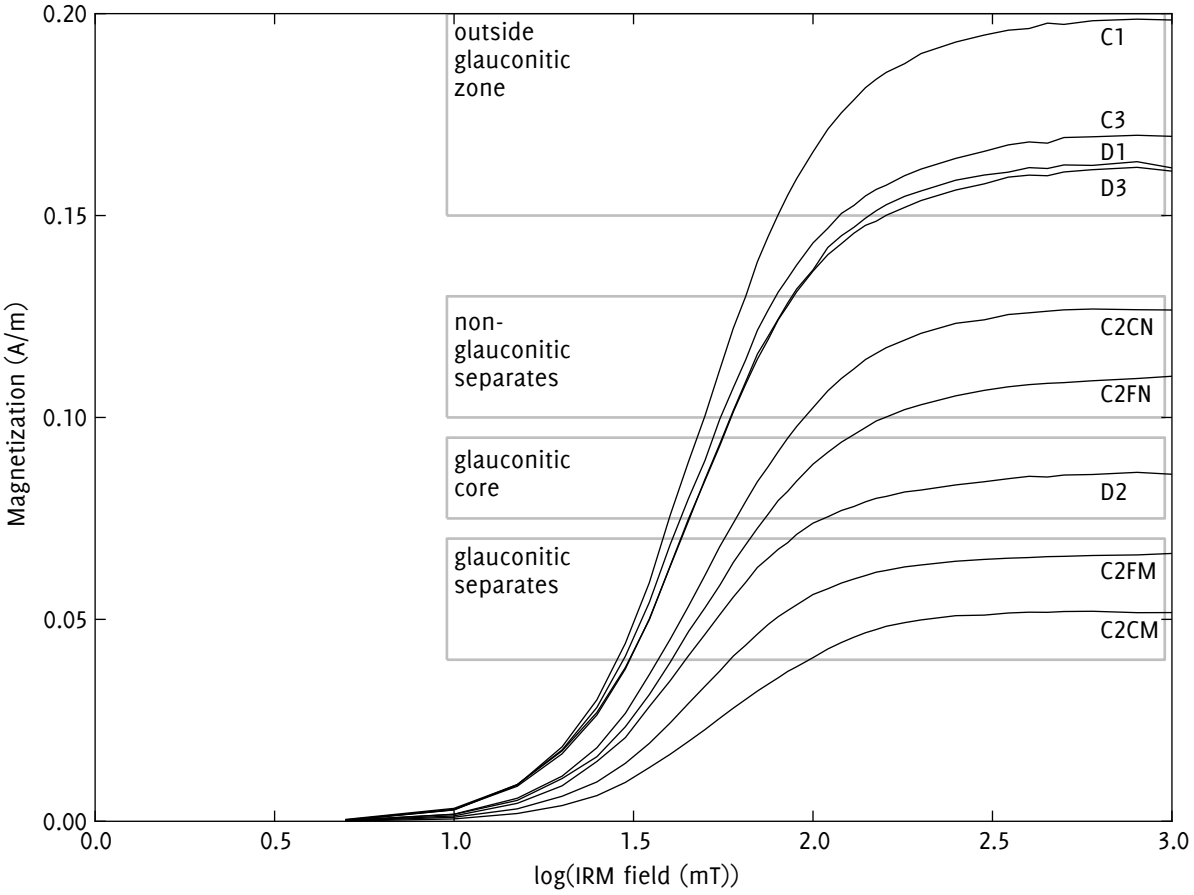

Figure 3.11 Mean IRM acquisition curve for each sample set; note the logarithmic scale on the x axis.

to be carried by the *less* magnetically susceptible fractions C2FN and C2CN. Since most of the common remanence-carrying minerals (magnetite, titanomagnetite, maghaemite, titanomaghaemite, monoclinic pyrrhotite) have high magnetic susceptibilities (0.6–6 SI units), this inverse relationship between susceptibility and SIRM is uncommon – indeed, in cases where magnetite concentration is sufficiently high and the matrix of low susceptibility, magnetic susceptibility has successfully been used as a linear measure of magnetite concentration (e.g. Shandley and Bacon, 1966 and Puranen, 1977). Haematite and goethite have lower susceptibilities, but their saturation magnetizations are correspondingly lower, and they may in any case be ruled out here since they both have coercivities much higher than any observed in these samples (France and Oldfield, 2000). The inverse correlation between susceptibility and SIRM must thus be attributed to the well-known high paramagnetic susceptibility of glauconony (Odin, 1982, p. 389) and a higher concentration of ferrimagnetic particles in the non-glauconitic grains.

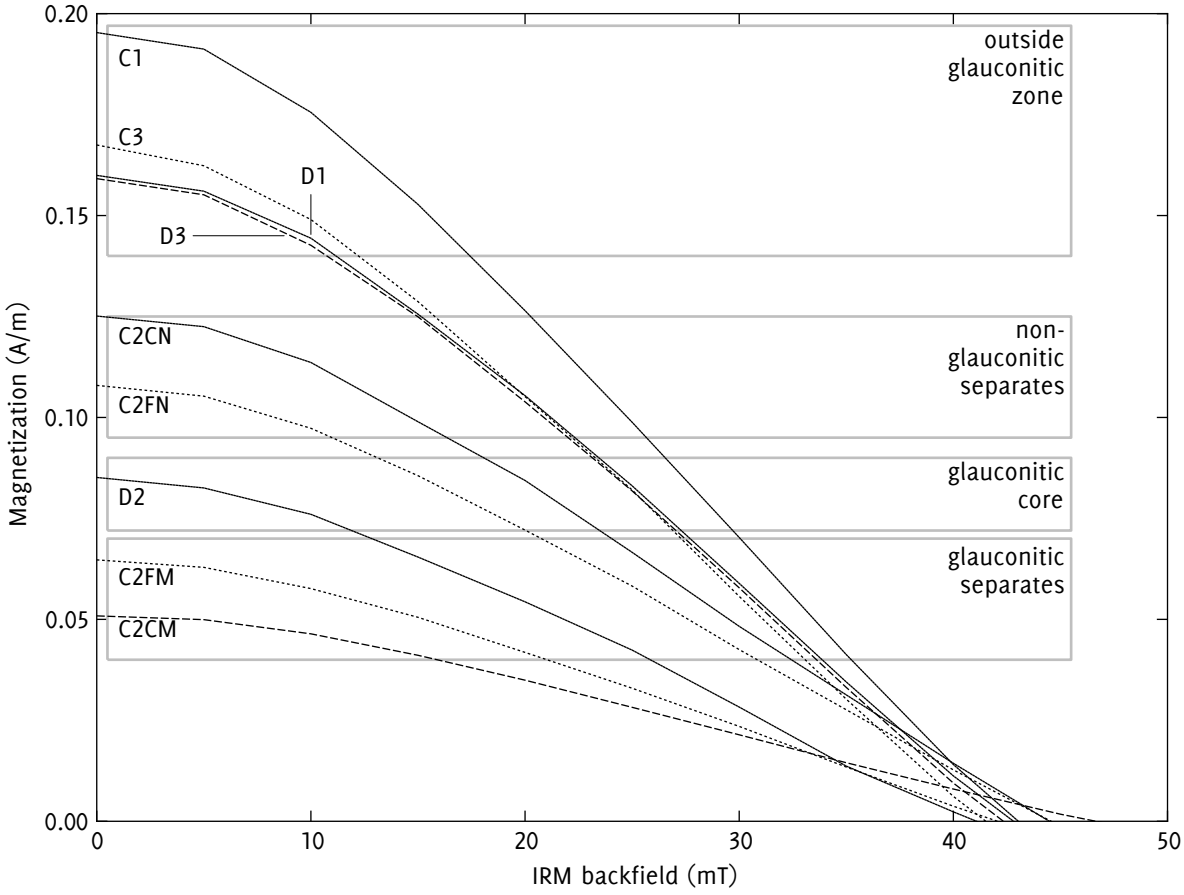

Figure 3.12 Remanence decrease on application of IRM backfield

It seems plausible that the carriers are sub-micron crystals incorporated within larger polycrystalline grains. The magnetic susceptibility of pure magnetite has been variously measured as 1–5.7 SI (Hunt *et al.*, 1995), and has a theoretical upper bound of around 20 SI (Dunlop and Özdemir, 1997, p. 139). All my non-magnetic separates had a susceptibility above 3.3×10^{-4} SI. A 25 μm-diameter diamagnetic quartz grain containing a 1 μm magnetite crystal would have a susceptibility below 3×10^{-4} SI and could thus enter the non-magnetic fraction. This model requires, of course, that the concentration of remanence-carrying ferromagnetic grains in the magnetically susceptible glaucony fractions is far lower than in the non-glauconitic fractions. The encapsulation of magnetite grains would also explain how they escaped the widespread pyritization evident in the samples.

3.4.1.1 *IRM backfield*

On progressive application of an IRM backfield, all samples reached zero reman-

ence at 40–50 mT. The demagnetization behaviour is shown in figure 3.12. I calculated precise H_{cr} values by linear interpolation across the zero-remanence line; they are shown in table 3.2 (p. 41).

3.4.2 *Log-Gaussian modelling of IRM curves*

IRM acquisition curves are a powerful tool for determining a sample's coercivity spectrum and hence its magnetic mineralogy. Two useful plotting conventions have developed as variations of the straightforward field-remanence plot:

1. The *x* axis is made logarithmic; this gives more space to the lower-coercivity regions where remanence acquisition is usually most rapid.

2. The *slope* of the remanence acquisition curve, rather than the remanence itself, is used as the *y* co-ordinate (e.g. by McIntosh *et al.*, 1996). This practice has a simple physical interpretation: for two magnetizing fields $H_1<H_2$, the incremental IRM IRM(H_1)–IRM(H_2) acquired between them is due to the particles magnetized by H_2 which were not magnetized by H_1; the slope (IRM(H_1)–IRM(H_2))/(H_1–H_2) thus represents the coercivity of that fraction of the sample. In the limit as $H_1 \to H_2$, the slope of the line at H_1 represents the relative fraction of particles with a coercivity of H_1. The derivative graph thus provides a clear visual representation of the coercivity spectrum. (Dunlop (1972) employed a lower-resolution version of this technique, plotting incremental remanence at 0.1 T intervals.)

Early studies, such as that of Dunlop (1972), employed IRM analyses which were to some extent qualitative. A major step toward more quantitative modelling of IRM acquisition was made by Robertson (1993), who found that the IRM acquisition curves of individual magnetic mineral phases could be expressed as cumulative Gaussian functions of the logarithm of the magnetizing field; the technique was described more thoroughly by Robertson and France (1994). Multiple magnetic phases in a sample can thus be resolved by decomposing the IRM acquisition curve into a sum of cumulative log-Gaussian (CLG) functions. The saturation magnetization of an individual CLG curve will of course depend on the concentration of the associated mineral phase as well as its saturation magnetization. However, the position and width of the Gaussian peak

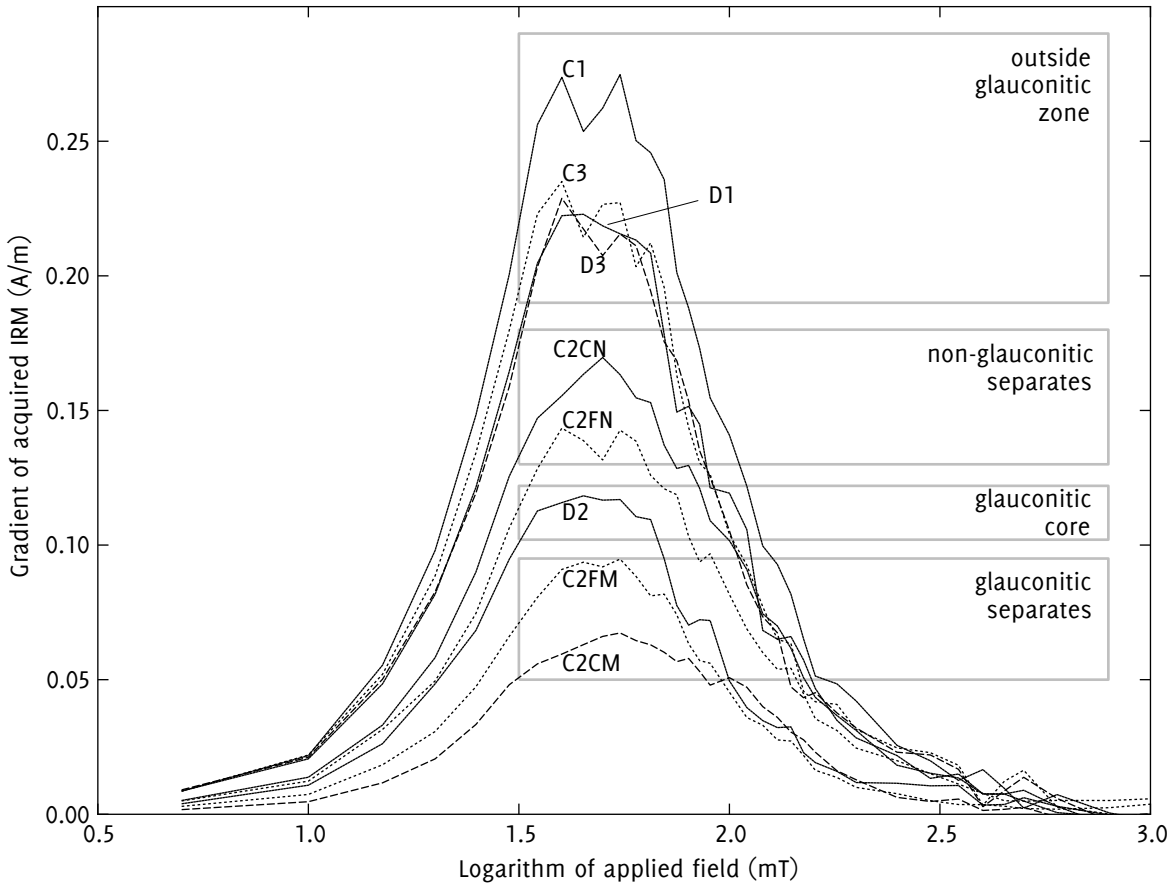

Figure 3.13 Plot of gradient of magnetization vs. log(applied field) for the samples in the study. Each line shows the mean magnetization of four or five sister samples.

(corresponding respectively to the mean coercivity and the variation in coercivities) are independent of concentration and can thus be diagnostic of a mineral phase.

In early applications of CLG fitting (e.g. Robertson (1993) and McIntosh *et al.* (1996)), the component curves were fitted by eye. Stockhausen (1998) developed mathematical criteria to assess goodness of fit and an interactive computer program to aid in manual fitting. Kruiver *et al.* (2001) developed more objective statistical tests for goodness of fit. Heslop *et al.* (2002) developed a program which can automatically fit a set of CLG functions to a dataset, using an expectation-maximization algorithm (Dempster *et al.*, 1977).

3.4.2.1 *Application of CLG model*

As a first step towards CLG modelling of my IRM data, figure 3.13 plots the gradi-

ents of IRM remanence against the logarithm of the applied field. Although there are major differences in the magnitude of the magnetizations, the shapes of the curves are very similar, both between the glauconitic and non-glauconitic sites and between the glauconitic and non-glauconitic separates. This similarity indicates that the remanence carriers are largely the same in all the samples, with the main variation being in their concentration.

I used the program described by Heslop *et al.* (2002) to fit CLG functions to the IRM curves of my samples; the results are shown in figure 3.14 (p. 57). While there is some noise in the data, the two-component CLG model provides a very reasonable fit to the measured IRM acquisition curves. The two components overlap heavily; component 1 carries most of the remanence in every sample, and compared to component 2 it has a slightly lower mean coercivity and a narrower coercivity spectrum. The figure also shows the results of a single-component fit, which in most cases is noteiceably worse than the two-component fit. I now consider the validity of these models.

3.4.2.2 *Validity of cumulative log-Gaussian models*

Heslop *et al.* (2004) raised doubts about the universal applicability of CLG models to IRM acquisition curves. Using a Preisach-Néel (Spinu and Stancu, 1998) model of magnetic grain behaviour, they identified three effects which might cause deviation from Gaussian behaviour:

1. Interaction of magnetic grains. Interaction is unlikely to cause significant effects in this study: the magnitude of the SIRM for the studied samples indicates a very low concentration of magnetizable minerals. Robertson and France (1994) calculated that interaction effects should only become significant when the separation of the magnetizable grains is close to their own diameters, which should be far from being the case here. It is possible that the magnetite grains are clumped, which might result in interaction despite the overall low concentration; however, Heslop *et al.* (2004) showed that interaction should result in a negatively skewed distribution, whereas the distributions given by my samples are all positively skewed.

2. Initial magnetization state of the sample. In this study, samples were subjected to complete triaxial AF demagnetization before application of the

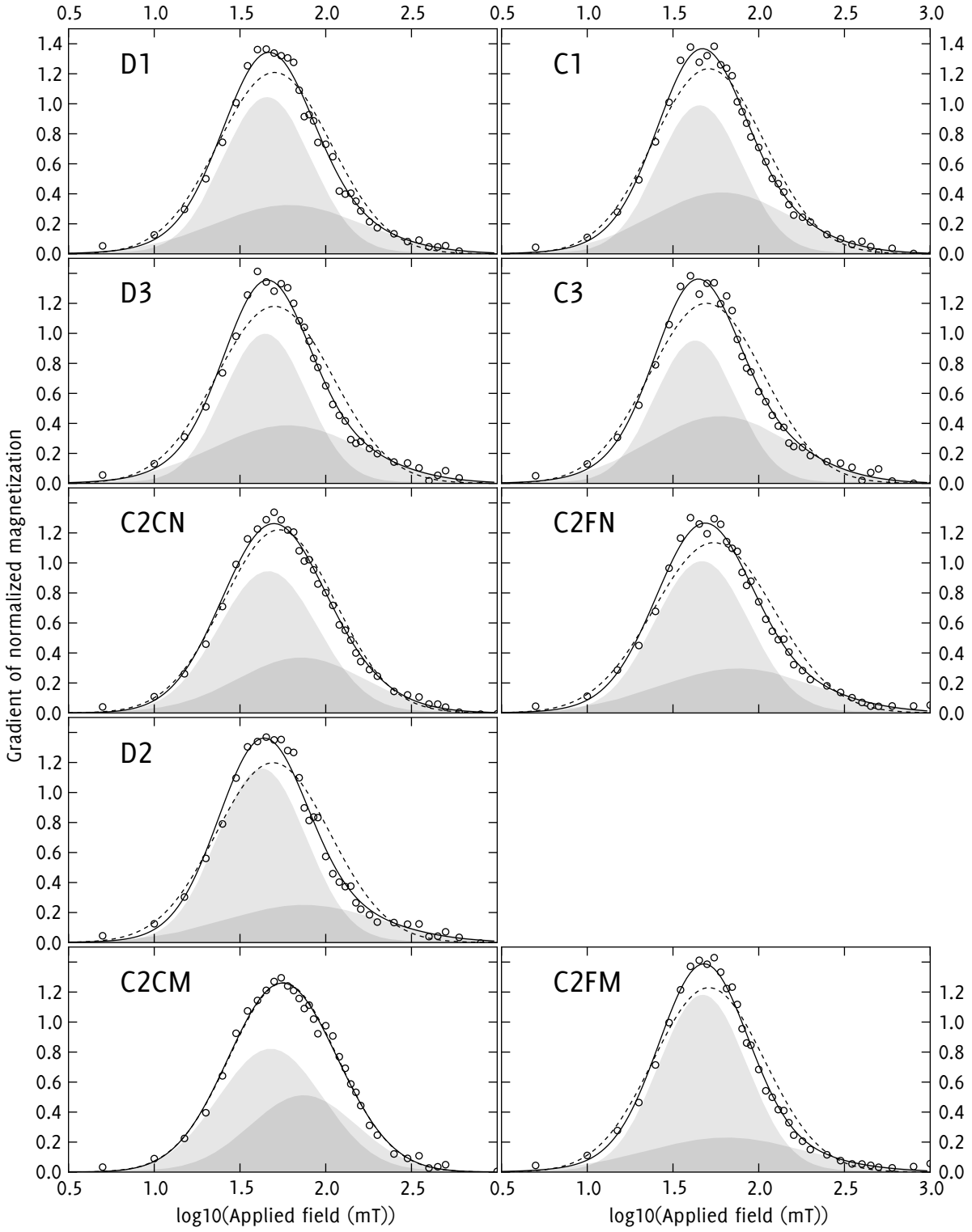

Figure 3.14 Normalized logarithmic plots of IRM acquisition curve gradients, fitted as a sum of two Gaussian functions. Points show IRM gradient averaged across sister samples; shaded curves show individual Gaussian functions for a 2-component fit; solid line shows sum of Gaussians; dashed line shows the best-fitting single Gaussian curve. Within each plot, the larger peak represents component 1; the smaller represents component 2.

IRM; this procedure is strongly recommended by Heslop *et al.* (2004) as it minimizes the chance of distorting the log-normal distribution.

3. Thermal relaxation. Unlike the two preceding effects, thermal relaxation cannot easily be discounted *a priori*. However, Heslop *et al.* (2004) observed that '[t]hermal relaxation and magnetic interaction result in negatively skewed distributions. This indicates that positively skewed distributions should be interpreted along the lines of mixed mineralogy'. All the distributions in the present study are positively skewed.

It thus seems reasonable – on consideration of the IRM data alone – to provisionally interpret the CLG fits as a reflection of two actual mineral phases rather than an experimental artefact. Heslop *et al.* (2004) warned, however, that the EM algorithm 'can produce quite variable results for multicomponent systems where major and minor components are almost completely overlapping'. Quantitative interpretation of the two-component fit should therefore be undertaken with caution, and checked against the results of other analysis techniques; it is possible that the single-component fit, though noticeably poorer for most samples, is a more accurate reflection of the true mineralogy. In the remainder of this section, I apply other analyses to constrain the ambiguities of the CLG model.

3.4.2.3 *Application and interpretation of CLG models*

A Gaussian curve can be characterized entirely by three parameters; adapting the notation of Heslop *et al.* (2002), the Gaussian function can be written as:

$$f(B) = \frac{M_{\mathrm{ri}}}{DP\sqrt{2\pi}} \exp\left(\frac{(B - B_{½})^2}{2DP^2}\right) \tag{3.1}$$

Where: B is the base-10 logarithm of the field for which the function is to be evaluated; M_{ri} is the relative contribution of the component to the total remanence; $B_{½}$ is the logarithm of H'_{cr}, the field at which this component has acquired half its remanence, corresponding to the mean of the distribution curve; and DP is the dispersion parameter, corresponding to one standard deviation of the distribution.

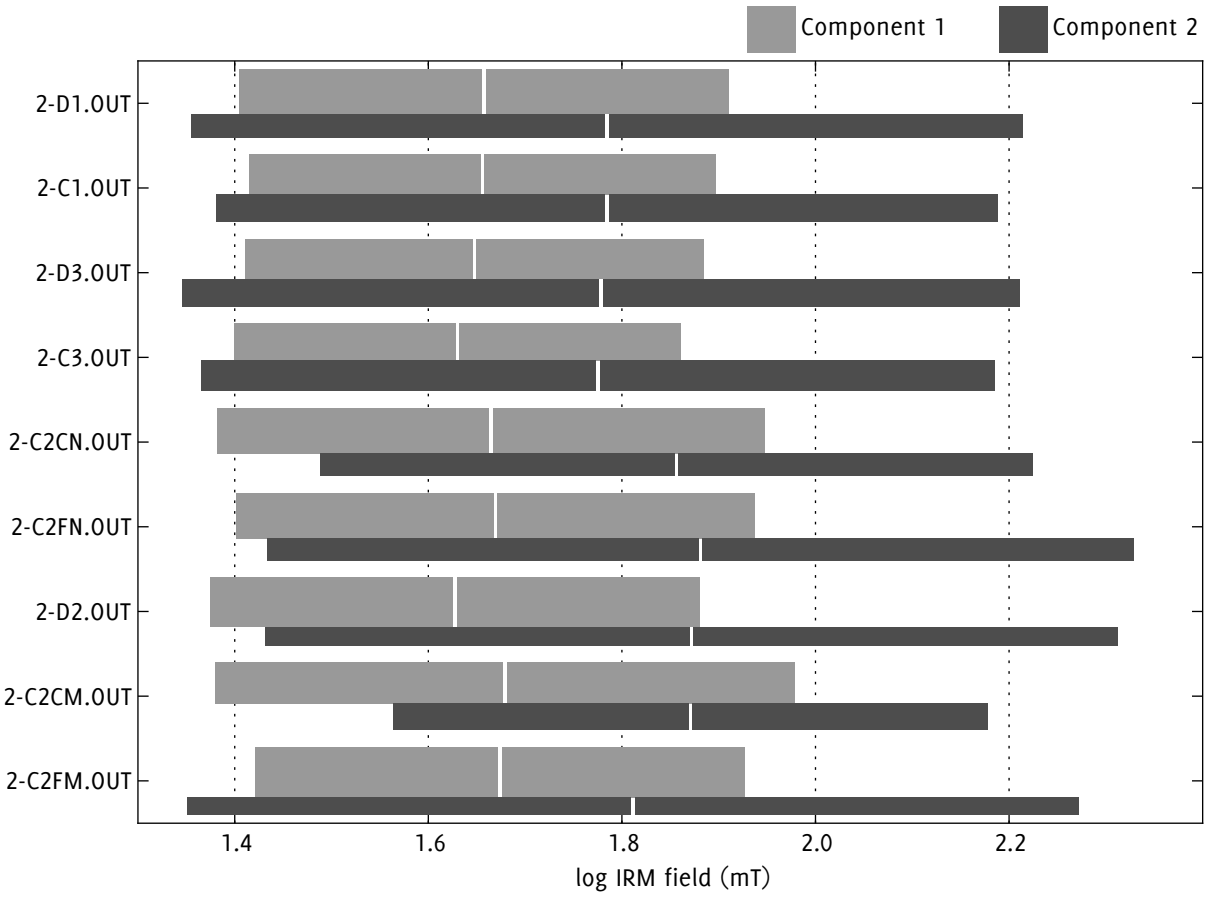

Figure 3.15 Box-plot of CLG curve parameters. Each sample-set is represented by two boxes, one for each of the two modelled components. The extent of the box shows the range of one standard deviation either side of the mean (*DP*); the white stripe gives the location of the mean ($B_{½}$); within each pair, the relative heights of the boxes are proportional to the relative areas of the curves (M_{ri}).

Figure 3.15 displays these parameters more directly than the curves, allowing variations in composition to be evaluated more easily. From this figure it can be seen that:

1. Drill-core samples have compositions practically identical with the equivalent cube samples, as would be hoped.

2. The magnetic composition of sites 1 and 3 is the same.

3. The D2 samples differ slightly from those at sites 1 and 3: component 1 is stronger, and component 2 shows a slightly higher mean coercivity and a broader spectrum.

4. Amongst the separates from site 2, component 1 is strongest in C2FM and weakest in C2CM.

5. The only notable correspondence between CLG parameters and either magnetic or size fractionation is the slightly higher *DP* in the fine fractions.

6. Despite these variations, the coercivity spectra of the two components remain fairly uniform across the sample sets. The variation in their relative abundances is far greater: the contribution of component 2 to the total IRM ranges from 26% in C2FM to 45% in C3.

7. Component 2 is more prominent in the coarse fractions C2CM and C2CN.

3.4.2.4 *Identification of components*

Symons and Cioppa (2000) collated published data to produce type curves for IRM magnetization and AF demagnetization of magnetite, pyrrhotite, haematite, and goethite in a variety of domain states. Since these reference curves are empirically derived from published data, they do not incorporate the assumption that a mineral phase can be modelled by a CLG curve. Using these curves – rather than simply comparing the curve parameters themselves with reference values given by Robertson and France (1994) and elsewhere – thus provides an extra check on the validity of the CLG modelling technique.

As would be expected from a mixture of mineral phases, the measured IRM acquisition data (prior to unmixing) can not be fitted to any of the type curves. However, the inidividual log-Gaussian components can be integrated back into cumulative distribution functions described by the function

$$\frac{1}{2}\left[1 + \operatorname{erf}\left(\frac{B - B_{½}}{\sqrt{2DP^2}}\right)\right] \tag{3.2}$$

corresponding to the IRM acquisition curves which would be obtained if the two components were physically separated and individually analysed. These 'virtual' IRM acquisition curves for components 1 and 2 are plotted in figure 3.16 (p. 61) and figure 3.17 (p. 62) against the type curves for magnetite and pyrrhotite respectively.

From these correspondences the two components can be interpreted as single-domain (SD) or pseudo-single-domain (PSD) magnetite, and PSD pyrrhotite. Symons and Cioppa (2000) also includes type curves for AF demagnetization curves; however, since it is not clear that AF demagnetization curves

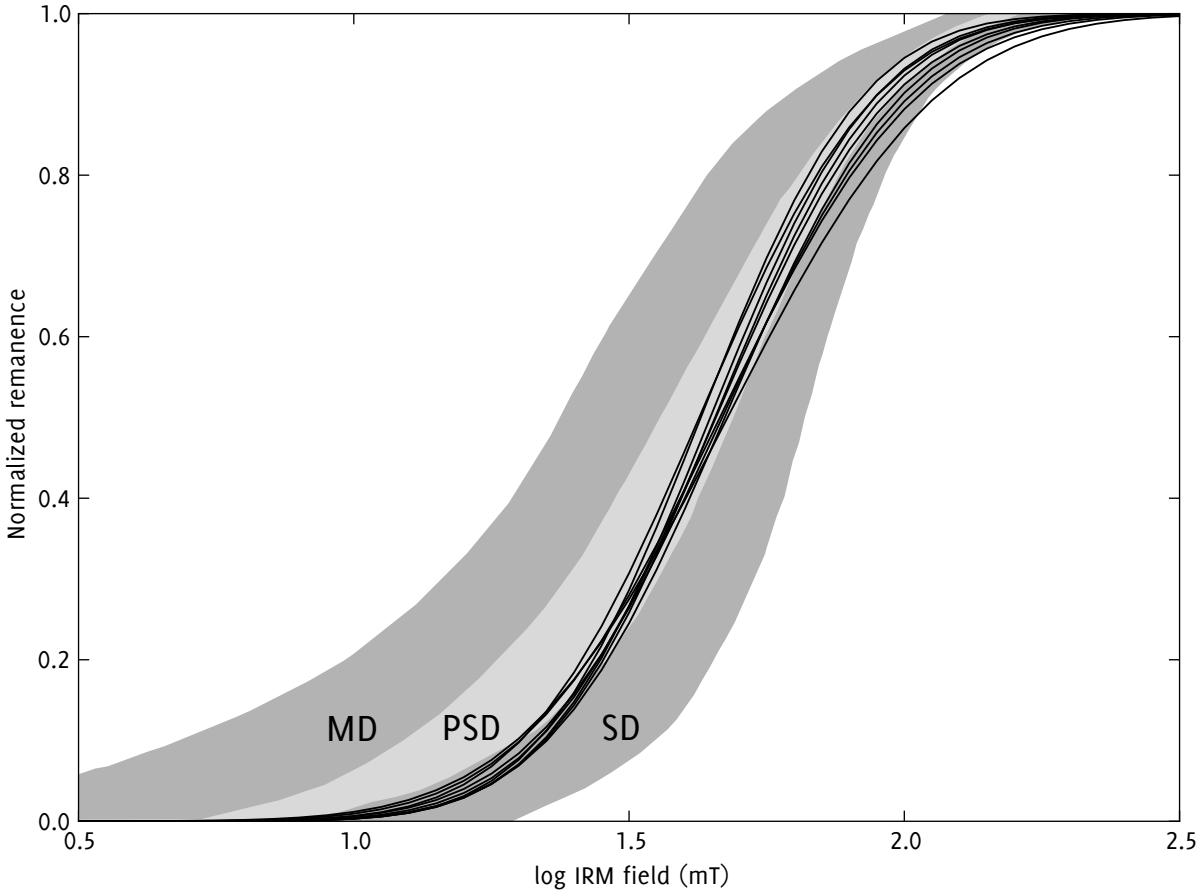

Figure 3.16 Component 1 of each sample set plotted against type curves for magnetite. Shaded areas represent zones of multi-domain (MD), pseudo-single-domain (PSD), and single-domain (SD) behaviour.

can be unmixed in the same way as IRM acquisition curves, it is not possible to produce meaningful virtual component plots for AF demagnetization.

Given the heavy overlap between the magnetite and pyrrhotite fields, these plots alone cannot definitively determine the mineralogy. Magnetite coercivity can be increased by the dominance of shape anisotropy in irregularly shaped grains (Dunlop and Özdemir, 1997, p. 56); in sediments, bacterial magnetosome chains can give rise to this effect (Moskowitz *et al.*, 1993). However, the IRM data still provide important and well-defined constraints which can be combined with those imposed by other experiments.

3.4.3 *IRM acquisition and DC demagnetization*

A comparison between IRM acquisition and the 'DC demagnetization' applied by a backfield IRM can be useful in constraining a sample's mineralogy. Wohlfarth (1958) calculated relations between SIRM, IRM, backfield IRM, and par-

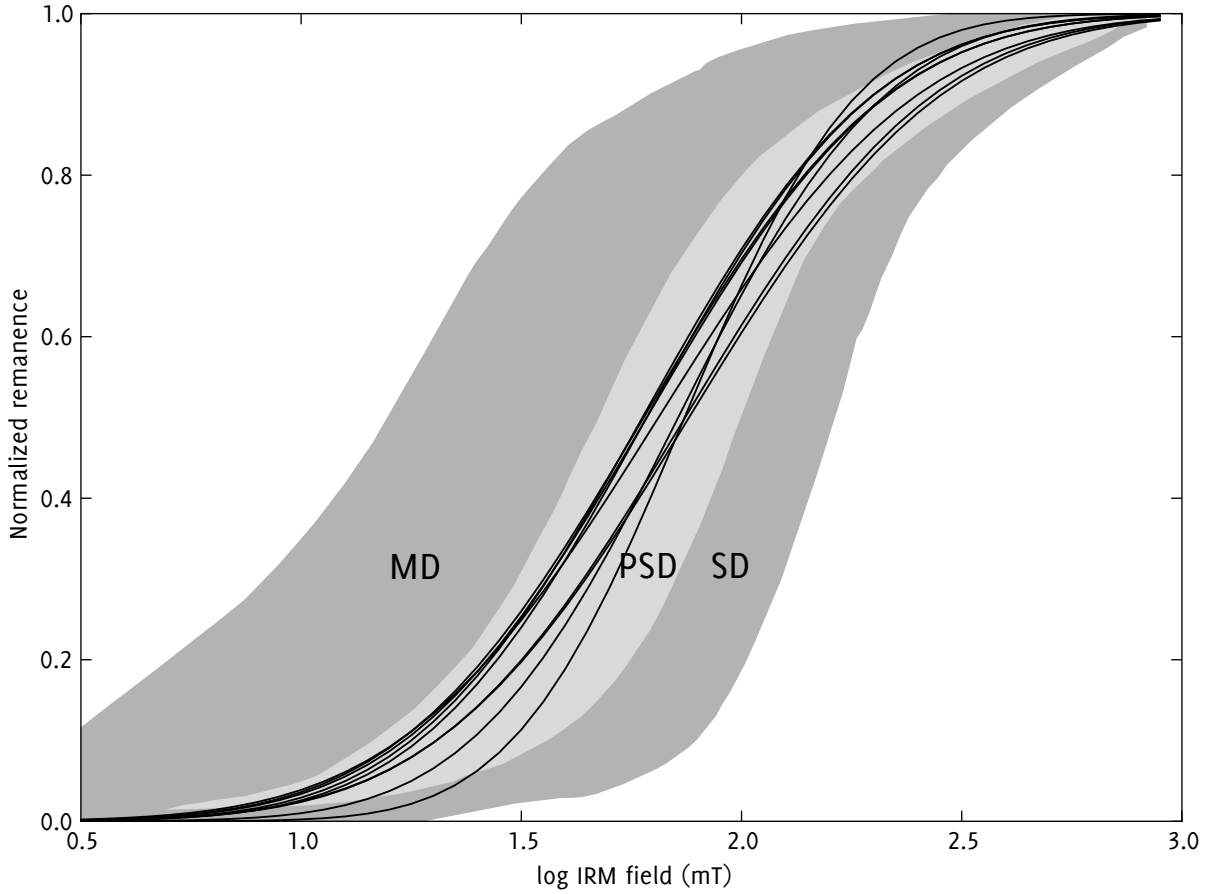

Figure 3.17 Component 2 plotted against type curves for pyrrhotite. Shaded areas represent zones of multi-domain (MD), pseudo-single-domain (PSD), and single-domain (SD) behaviour.

tially AF-demagnetized IRM for a theoretical assemblage of non-interacting, stable single-domain magnetic grains. By measuring these magnetizations for a sample and comparing their relations to those predicted by Wohlfarth's equations, deviations from 'ideal' non-interacting stable single-domain (SSD) behaviour can be seen.

For an ideal grain population and any field H below the saturating field, the following relation should hold between the $\mathrm{IRM_A}$ acquired from a demagnetized state, the saturation $\mathrm{IRM_S}$, and the backfield $\mathrm{IRM_B}$:

$$\mathrm{IRM}_A(H) = \mathrm{IRM}_S - 2\,\mathrm{IRM}_B(H) \tag{3.3}$$

This relation can be understood by considering the sub-population of grains aligned by a particular field H. Before initial IRM acquisition, the grains are magnetized in random directions, giving a net zero remanence; the application of H imparts a net remanence M to the grains. Applying the backfield $-H$ to the sample will affect exactly the same sub-population of grains. This time,

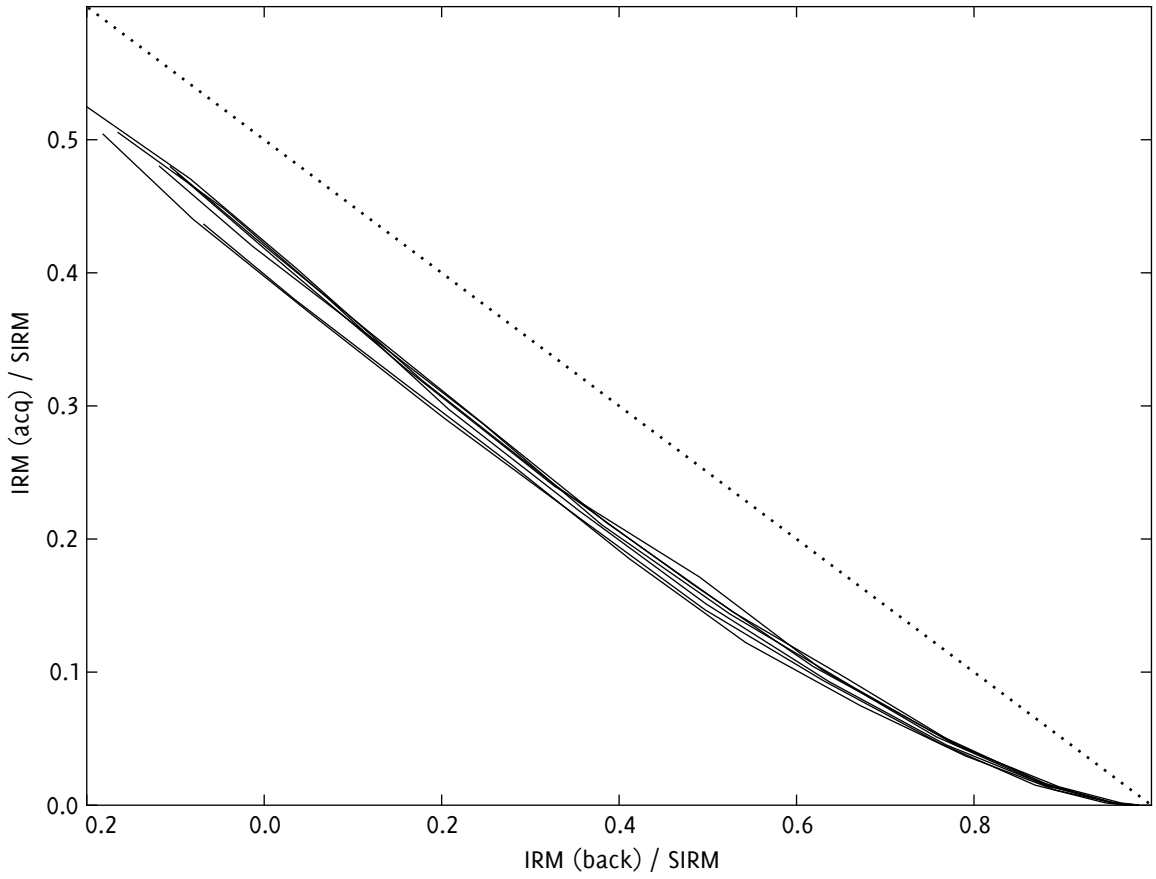

Figure 3.18 Partial Henkel (1964) plot for all sample sets, showing the relationship between IRM acquisition and backfield response for the same applied fields. The dotted line shows the theoretical ideal behaviour for an assemblage of non-interacting SD grains according to the equations of Wohlfarth (1958).

however, they are initially aligned anti-parallel to the field, so their remanence changes from M to $-M$. The ideal backfield curve thus has the shape of the acquisition curve, inverted and scaled by a factor of two.

Henkel (1964) devised a plot of acquisition IRM versus backfield IRM (for the same field strength, both remanences normalized to SIRM) which can show deviation from SSD non-interacting behaviour. Samples plotting above the $y = \frac{1}{2}(1-x)$ line would indicate positive interaction; this behaviour is hardly ever observed (Jackson, 2007). Samples plotting below the line indicate either negative interaction between single-domain particles or multi-domain behaviour. Modelling by Muxworthy *et al.* (2003) suggested that interaction effects should only be significant when magnetic particles are separated by less than twice their grain size. A rough bound on particle separation can be calculated from the SIRM: my most magnetic sample set, C1, acquired a SIRM of around 0.2 A/m. Even if all the remanence were carried by monoclinic pyrrhotite, which has

a saturation magnetization of 80 kA/m, this would imply a concentration of about 2.5 ppm, giving an average particle spacing tens of times greater than the grain size.

A full Henkel plot requires IRM backfield remanences to be measured all the way to reverse saturation. I only applied backfields until the remanence reached zero, but even a partial Henkel plot of this data (figure 3.18) shows the samples' behaviour adequately. Once more, the behaviour of all the samples is fairly similar, with $\mathrm{IRM}_A / \mathrm{IRM}_B$ falling below the SSD reference line. Given the unlikelihood of interaction effects, this probably indicates the presence of multi-domain grains, although it is difficult to draw any conclusions as to the relative abundances of SSD, PSD (pseudo-single domain), and MD (multi-domain) grains.

Cisowski (1981) devised another means of comparing IRM acquisition with AF demagnetization: a *crossover plot* with applied field on the x axis, and both IRM acquisition and backfield demagnetization (rescaled by one-half) on the y axis. In this case, ideal behaviour would produce a symmetrical graph. Since a crossover plot conveys essentially the same information as a Henkel plot, I have not produced one here.

3.4.4 *ARM acquisition and AF demagnetization*

Theoretically, the shape of an ARM acquisition curve should be practically identical to an AF demagnetization curve for the acquired remanence: since the bias field is small relative to the AF field, the population of grains aligned at any given AF field during ARM application should be the same as the population which is randomized by the same alternating field strength during AF demagnetization. I calculated a linear regression between the magnetization and demagnetization curves of each sample to test this relationship; in every case the R^2 value was above 0.99, indicating that the samples' behaviour closely follows the theoretical model. The slope of the regression lines varies from −0.84 to −0.97, differing from the 'ideal' value of −1 due to viscous decay of remanence before demagnetization.

I used the saturation (or near-saturation) magnetizations at 150 mT to calculate ARM susceptibility values, which are shown in table 3.2. They follow the same trends as the saturation IRMs. An interesting difference between ARM and IRM behaviours is evident both in the magnetization graphs and in com-

parisons between SIRM and χ_{ARM} the sodium silicate treatment appears to have less effect on ARM behaviour. The ARM behaviour of the D1 and D3 drill-core samples is almost identical to that of the corresponding cubes. In contrast, the drill-cores from sites 1 and 3 respond almost identically to IRM, but the cube samples (especially from site 1) acquire a higher remanence.

χ_{ARM} is often used in conjunction with χ to estimate magnetic grain size, using the method of King *et al.* (1982) or subsequent modifications such as that of Maher (1988); however, this method actually requires measurement of the susceptibility of the ferrimagnetic, ARM-carrying component in isolation. In many cases, the paramagnetic susceptibility of a sample is negligible and the bulk susceptibility is a good approximation to the ferrimagnetic susceptibility; such is not the case here. Since the paramagnetic and ferrimagnetic susceptibility contributions cannot be resolved without the use of hysteresis measurements, χ_{ARM} cannot be used in this case to confirm the grain-size estimates derived from the IRM curve shapes.

3.4.5 *AF demagnetization of IRM*

The AF demagnetization curves of saturation IRM in figure 3.3 give indications of the domain state of the remanence-carrying grains. Reference plots of AF demagnetization (e.g. Dunlop and Özdemir, 1997, p. 291; Symons and Cioppa, 2000) show that, at least for magnetite, single-domain or pseudo-single-domain grains give a sigmoidal curve, with an initially flat or shallow slope, steepening for the first half of the curve before inflecting and shallowing out as the remanence approaches zero. Multi-domain grains, in contrast, give rise to a more hyperbolically shaped curve with an initially steep slope which flattens out progressively without inflection. The samples in this study all produce curves with the sigmoidal, single-domain shape.

3.4.6 *Temperature dependence of susceptibility*

All the samples showed complex behaviour during the successive heating cycles, with major heating-induced mineral alteration (manifested as irreversible temperature-susceptibility curves) in the 500-700°C range.

3.4.6.1 *Determination of Curie and Néel points*

Temperature-susceptibility curves can often be used to determine the disordering temperature (Curie or Néel point) of a ferromagnetic (*sensu lato*) mineral. If alteration occurs during heating, the measured disordering temperature may be that of an alteration product rather than a component of the original sample. Though this may preclude precise identification of the original minerals, it can still provide a valuable constraint. For example, a transition to paramagnetic behaviour below 600°C would rule out haematite as a component – regardless of any alteration – since haematite is thermally stable up to and beyond its Néel point of 675°C.

The approximate disordering temperature of a mineral can easily be seen on a temperature-susceptibility curve, usually appearing as a spike in susceptibility – the Hopkinson (1889) peak – followed by a sharp decline to a near-zero value as the ferromagnetic susceptibility disappears, leaving only a weak paramagnetic signal. However, since the disappearance of ferromagnetism is not instantaneous, the exact disordering temperature is not self-evident.

Before the wide availability of equipment for TDMS measurement, disordering temperatures were usually determined from temperature-*magnetization* curves, most usually by the two-tangent method of Grommé *et al.* (1969). This technique has subsequently been applied to temperature-*susceptibility* curves, for example by de Wall and Nano (2004). Petrovský and Kapička (2006) pointed out that, due to the inequivalence of magnetization and susceptibility, this practice can produce significant (>50%) errors; this criticism is applicable to any magnetization-specific method applied to susceptibility data, such as the 'extrapolation' method of Moskowitz (1981) or the 'differential' method of Tauxe (1998). Petrovský and Kapička (2006), while cautioning that it is 'practically impossible to determine the Curie point precisely' from susceptibility data, describe three methods which can give acceptable accuracy under certain conditions. (In the following discussion I follow the terminology of Petrovský and Kapička (2006) in referring only to Curie points, but their arguments apply equally well to Néel points.)

1. Analysis of the paramagnetic portion of the curve above the Curie point: χ^{-1} is plotted against temperature, which should give a linear increase in accordance with the Curie-Weiss law. A fit to the linear portion of the curve

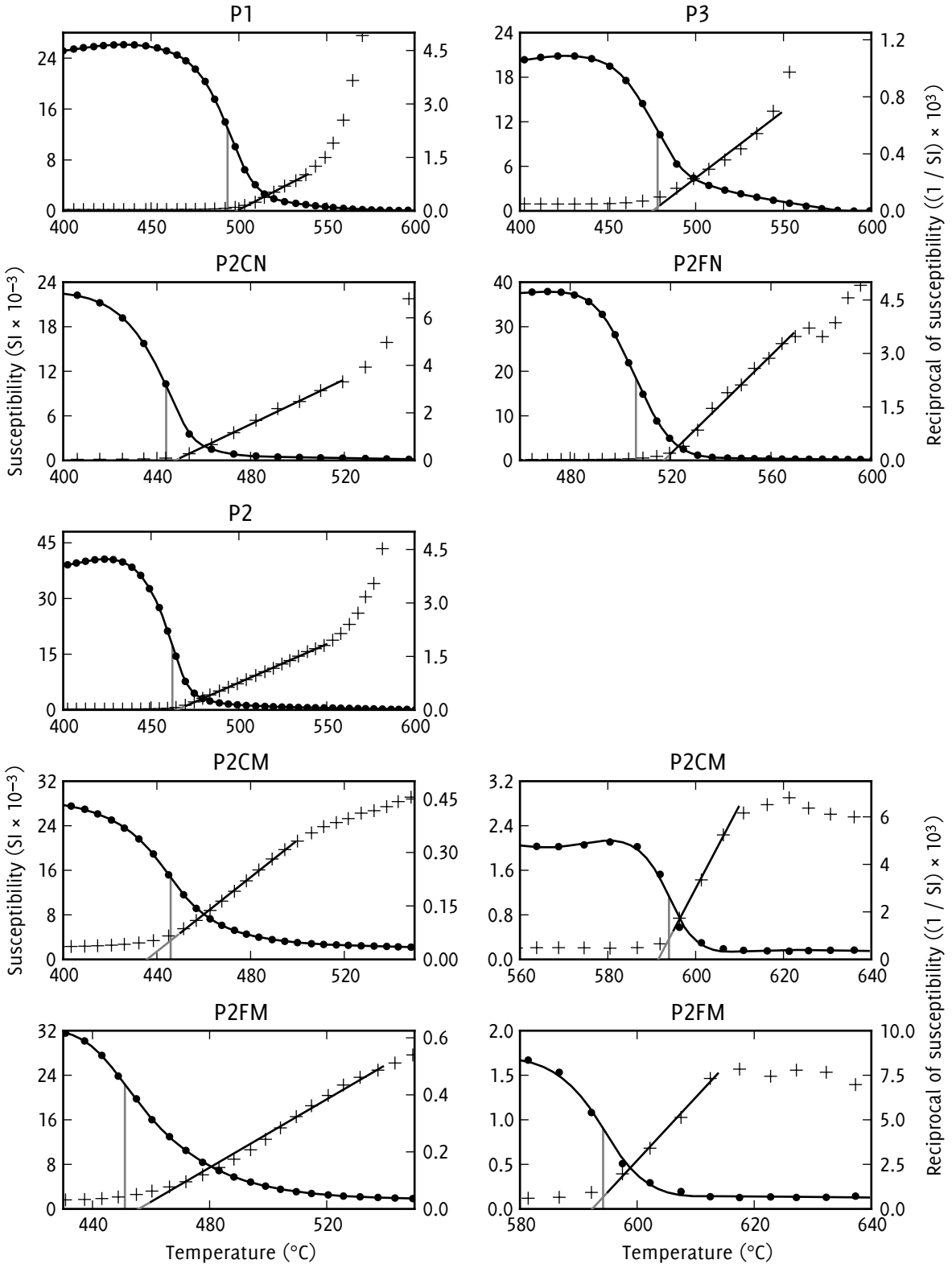

Figure 3.19 Disordering temperatures, determined by two methods. The solid dots show the susceptibility; the vertical grey line connects the inflection point to the x axis; the crosses show inverse susceptibility; the solid straight lines show the least-squares linear fit and the range to which it was applied. The two estimates of the disordering temperature are thus given by the intersection of the two grey lines with the *x* axis. Note that, for each of the samples P2CM and P2FM, two disordering temperatures (corresponding to two different mineral phases) are determined.

is extrapolated to the χ^{-1} line, and the intersection gives the Curie point. Apart from its accuracy, this method has the advantage that its reliability can be checked on a case-by-case basis by evaluating the goodness of the linear fit. If the fit is poor (perhaps due to a mixture of different mineral phases) another method can be applied.

2. A 'sharp' Hopkinson peak can be used as the Curie point. (The Hopkinson peak is usually observed to occur just *below* the Curie point – e.g. by Radhakrishnamurty and Likhite (1970) – but this technique is presumably intended for cases where the subsequent susceptibility decline is near-vertical, so the difference will be negligible.)

3. If a broad susceptibility peak is observed, the inflection point on the high-temperature side of the peak can be taken as the point at which paramagnetic behaviour becomes dominant. The theoretical justification for this technique is not as clear as that for the inverse-susceptibility technique, but for my samples the two methods showed reasonable agreement – in most cases to within 5°C (see table 3.3).

For this investigation I used both the first (inverse susceptibility) and third (inflection point) techniques on each sample, allowing me to cross-check the accuracy of the estimates. The second (Hopkinson peak) technique was not used since none of the samples produced sufficiently sharp peaks. The results are shown in figure 3.19 (p. 67) and table 3.3 (p. 69).

3.4.6.2 *Heating-induced alteration*

The temperature-susceptibility curves for the powder samples are shown in figure 3.7 (p. 48). As with the IRM acquisition curves, most of the differences between samples are quantitative rather than qualitative. Almost all samples show little or no alteration below 400°C; in the 400–700°C temperature range, most of the alteration takes place between 500 and 600°C (except in P2CN). The changes are summarized in figure 3.20 (p. 70).

3.4.6.3 *Interpretation of disordering temperatures*

One obvious feature of the curves is the minimal susceptibility above 600°C,

		Disordering temperature (°C)		
Sample	R^2	paramagnetic	inflection	mean
P1	0.995	499	494	496
P3	0.972	475	478	477
P2CN	0.997	448	444	446
P2FN	0.990	517	506	512
P2	0.999	465	462	463
P2CM	0.999	436	446	441
P2CM	0.998	591	594	593
P2FM	0.988	456	451	453
P2FM	0.993	592	594	593

Table 3.3 Disordering temperature determinations using two methods: least-squares linear fit to paramagnetic inverse susceptibility, and inflection point of the high-temperature side of the Hopkinson peak. The R^2 value is for the linear fit; there is no goodness-of-fit parameter for the inflection-point technique. The rightmost column gives the mean of the temperatures calculated by the two methods. Note that two temperatures were calculated for each of P2CM and P2FM

indicating the absence of haematite. This lack of susceptibility also indicates an absence of any minerals which would alter to haematite below 700°C.

The calculated disordering temperatures in the 440-520°C range are interesting mineralogically, but they do not correspond to a remanence carrier originally present in the mineral: the Hopkinson peaks do not appear until the cooling curve of the 600°C step, showing that they correspond to a mineral formed by alteration in the 500–600°C range. This fact is confirmed by thermal IRM demagnetization curves of the corresponding D- and C-series samples. If the mineral inferred from the TDMS studies were initially present in the samples, the loss of its IRM should be visible as a steeper slope (corresponding to a more rapid loss of remanence) in the temperature region just below the disordering temperature; no such behaviour is observable in the IRM thermal demagnetization curves (figure 3.6, p. 46), which show a fairly steady decline to around 600°C.

These disordering temperatures are too high to be attributed to any iron sulphide or oxyhydroxide; the only minerals with disordering temperatures above 400°C are magnetite, maghaemite, and haematite. In their pure forms they all have disordering temperatures too high to fit with those measured here, but cation substitution can reduce these temperatures significantly (Readman

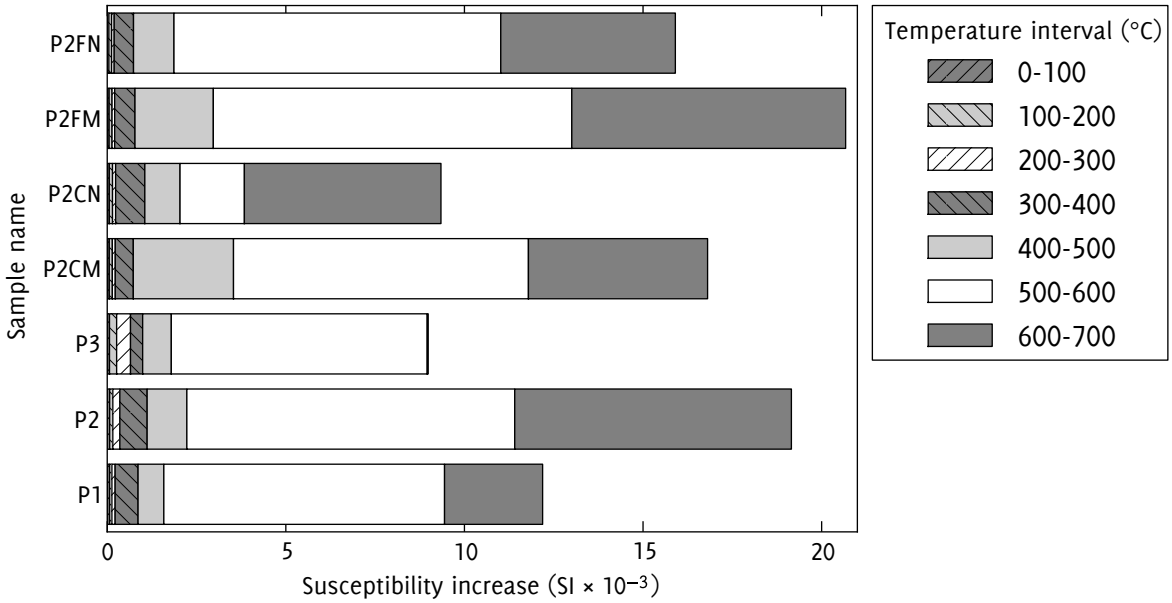

Figure 3.20 Summary of increases in room-temperature susceptibility with successive heating cycles.

and O'Reilly, 1972). Given the high aluminium content of glauconite (Bentor and Kastner, 1965), aluminium is a strong candidate for the substituting cation in this case. Cation substitution by aluminium of glauconitic origin would be consistent with the fact that P2 gives a lower temperature than the less glauconitic P1 and P3.

All the samples show less dramatic but more palaeomagnetically interesting Hopkinson peaks in the 550–600°C range (figure 3.8, p. 49). Since this is close to the Curie temperature of magnetite (580°C), the coercivity spectra indicate magnetite, and magnetite is unlikely to alter upon heating to 600°C in an inert atmosphere, these temperatures may well correspond to magnetite present in the original samples. Unfortunately, with the exception of P2CM and P2FM, the curves are too complicated and the remanences too low for exact determination of disordering temperatures, and their calculated positions may be affected by the presence of alteration products. Nevertheless, they provide some further support for the magnetite mineralogy which can be more definitely inferred from the IRM acquisition and thermal demagnetization experiments.

Note also that almost all samples in figure 3.8 show sharp kinks in the temperature-susceptibility curve shortly before minimum susceptibility is reached, which may indicate the presence of two similar but distinct mineral phases.

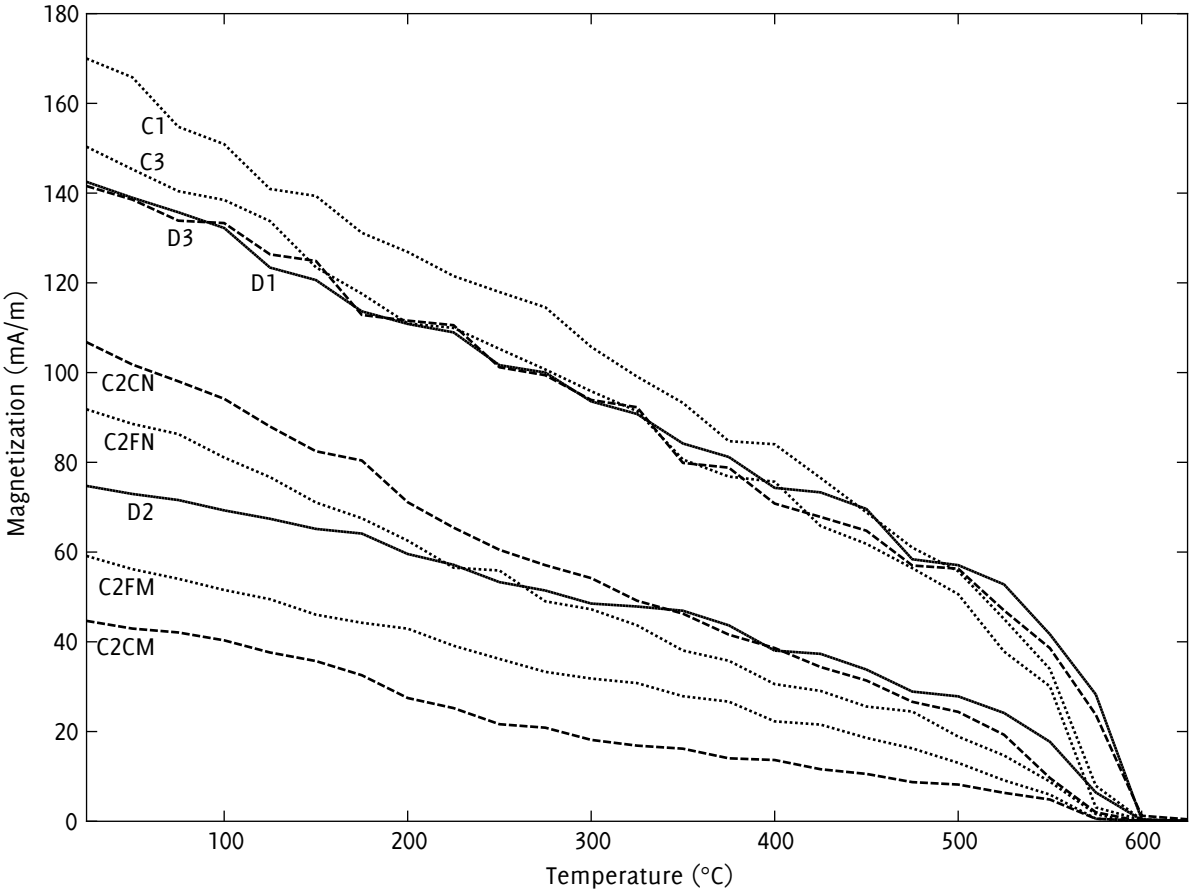

Figure 3.21 Thermal demagnetization of the 0.12 T component of a triaxial IRM for all sample sets.

3.4.7 *Thermal demagnetization*

Like most of the other experimental methods, thermal demagnetization of a triaxial IRM produces fairly uniform behaviour between the samples (figure 3.6, p. 46). In general there is a more or less linear decline in magnetization with heating, with the line steepening suddenly at around 550°C to reach zero just below 600°C. This point is close to the Curie temperature of magnetite, with little or no deviation due to oxidation or cation substitution. It is interesting to note the contrast between these results and those of the TDMS study: in the susceptibility experiments, the high-temperature curves were dominated by huge Hopkinson peaks produced by thermal alteration products, making it difficult to distinguish the Curie points of the pre-existing minerals. In these IRM demagnetization experiments, thermal alteration undoubtedly occurred, and was accompanied by obvious colour changes in the samples. However, since the demagnetization took place in a shielded oven within a field-free room, the new minerals acquired no remanence, and did not obscure the

demagnetization behaviour of the original mineralogy.

Although demagnetization behaviour was mostly uniform, there were some deviations suggestive of small variations in mineralogy. Most noticeable is C2CM, for which the 0.4 T component has a significantly steeper segment spanning the 150–250°C range. It is possible that this corresponds to the thermal decomposition of greigite (Torii *et al.*, 1996), but if so, it is a minor component. The shape of the overall curve still corresponds largely to magnetite, and the D2 samples did not show any gyroremanent behaviour during AF treatment, which would be expected if there were significant quantities of greigite (Snowball, 1997).

Figure 3.21 (p. 71) plots the 0.12 T components of all the samples together. It is noticeable that only some samples show the 'shoulder' caused by a steepening demagnetization curve from 500–600°C; specifically, the cubes made from sieved separates do *not* have a shoulder. It is possible that the shoulder represents a finer-grained component lost during sieving; however, this high-unblocking-temperature component's remanence is small compared to that of the main component, and the Curie temperature indicates that they both consist of magnetite.

3.4.8 *Mineral composition*

In this section I will attempt to synthesize the results of the various rock magnetic experiments to deduce the most likely composition of the remanence carriers and other magnetically important minerals in the samples.

3.4.8.1 *Iron oxides*

The IRM data, as discussed in section 3.4.2, is consistent with reference data for magnetite. This diagnosis is also supported by the analyses performed by Hutton and Turner (1936, p. 266) on samples from the Abbotsford Formation, which showed minor to rare amounts of magnetite. However, the IRM data cannot constrain the mineralogy precisely. Magnetite forms part of a complex solid-solution series which is usually represented in a ternary diagram spanning FeO (wüstite), TiO_2 (rutile, anatose, or brookite), and Fe_2O_3 (haematite or maghaemite); however, iron may also be substituted with cations of other elements. Identification by magnetic techniques alone is thus necessarily impre-

cise. Since I was unable to find any grains for direct microprobe analysis, the exact mineralogy of component 1 could not be determined. It is possible to give some constraints, however.

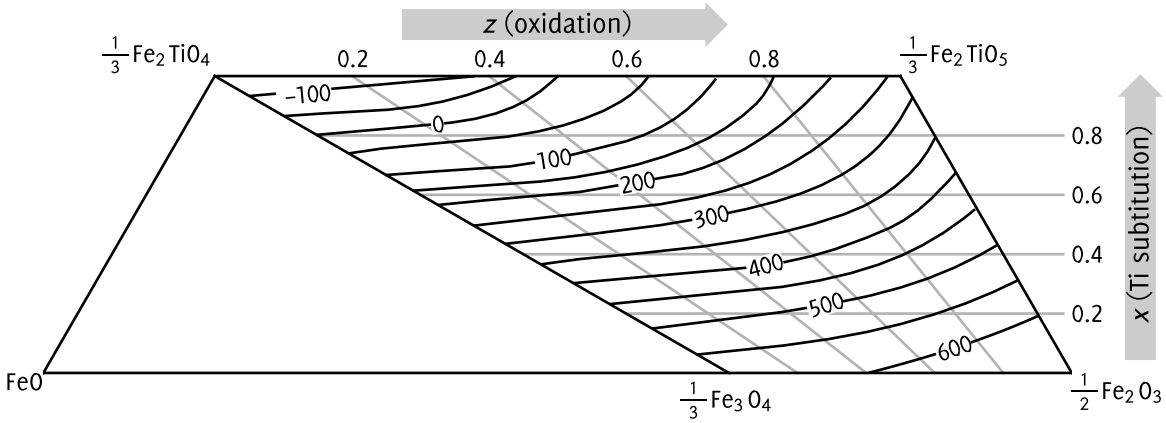

Figure 3.22 Contours of equal Curie temperature (in degrees Celsius) on the lower part of the TiO_2–FeO–Fe_2O_3 ternary diagram. Horizontal grid lines show *x*, the degree of titanium substitution; diagonal grid lines show *z*, the oxidation parameter. Redrawn after Readman and O'Reilly (1972).

Degree of oxidation

Pure and cation-substituted magnetites can undergo oxidation, producing (in the case of pure magnetite) cation-deficient spinels spanning a continuous range from Fe_3O_4 to γ-Fe_2O_3 (maghaemite). Oxidized magnetites retain, along with the spinel structure, similar magnetic properties to unoxidized magnetite, making discrimination by purely magnetic means difficult (Evans and Heller, 2003, p. 46; Oldfield, 1999, p. 105). Discrimination by remanent coercivity spectrum is impossible, as can be seen from the type curves of Dunlop (1972). Neither is susceptibility a useful diagnostic measure: the range of reported susceptibilities for maghaemite is contained entirely within the range for magnetite (Hunt *et al.*, 1995), and in any case the unknown concentration of the spinel and the presence of other strongly susceptible minerals would make susceptibility-based discrimination highly impractical in this study.

One useful diagnostic property is the inversion temperature: the cation-deficient spinel structure of γ-Fe_2O_3 is metastable and can alter under heating (Verwey, 1935) or pressure (O'Reilly, 1984) to the corundum structure of α-Fe_2O_3 (haematite). This inversion causes a sharp drop in susceptibility, since haematite's mass-normalized susceptibility is 2–3 orders of magnitude lower than that of maghaemite (Hunt *et al.*, 1995). Kushiro (1960) gave a

(very approximate) inversion pressure of 15 MPa at 0°C, corresponding to a water depth of 1500 m; given the probable near-shore depositional environment, maghaemite can thus not be ruled out on this basis. Heating-induced inversion has been reported at a wide range of temperatures; the survey in Dunlop and Özdemir (1997) found a range of 250–900°C from eleven published sources. Only three of these sources report inversion temperatures above 700°C, so it is probable (given the lack of inversion during my TDMS studies) that maghaemite is not present, but it cannot be ruled out entirely on this basis alone. However, the Curie point offers another clue. Published measurements vary (mainly because direct measurement is usually prevented by inversion below the Curie point) but Dunlop and Özdemir (1997) considered 645°C the 'best present estimate', with 675°C the highest published estimate. Thus, if maghaemite is present in my samples, and if it does not invert to haematite on heating to 700°C, it should show a Hopkinson peak and subsequent susceptibility drop within this temperature range; no such behaviour is evident, so maghaemite can be ruled out in this case.

The most direct way to determine the oxidation state would be microprobe analysis; unfortunately none of the mineral grains I analysed were remanence carriers. The most reliable magnetic techniques for detecting oxidation of magnetite rely on low-temperature behaviour. Stoichiometric magnetite undergoes a Verwey (1939) transition at 110–120 K, which can be detected as a sharp decrease in SIRM above the transition temperature. Torii *et al.* (1996) observed the transition even for trace concentrations of magnetite. The Verwey transition is suppressed by oxidation (Özdemir *et al.*, 1993), and can thus be useful as a diagnostic test for oxidation. (A sharp susceptibility increase above the Verwey transition has also been observed in MD magnetites (Moskowitz *et al.*, 1998 and Muxworthy, 1999) but Muxworthy (1999) found that this was absent for an acicular SD magnetite.) Low-temperature facilities are not available at the Otago Palaeomagnetic Research Facility OPRF so I have not attempted any of these techniques.

Degree of cation substitution

Titanium is the most common substituting cation in magnetite, and by far the most extensively studied, but the spinel structure can also accommodate other elements, including aluminium, chromium, magnesium, manganese,

and nickel (Dunlop and Özdemir, 1997, p. 79). One significant effect of titanium substitution is a rapid decrease in the Curie point, as can be seen from figure 3.22 (p. 73). Since no disordering temperatures are observed below 500°C, titanium substitution must be below 0.2 (assuming no or negligible oxidation).

Curie temperature constraints

If the Curie points just below 600°C (figure 3.8, p. 49) represent original sample mineralogy rather than alteration products, they give tighter constraints on the degree of magnetite substitution. The complex shapes of the curves make exact Curie points hard to infer, but they all appear to be above 550°C, corresponding to a substitution parameter below 0.1. Since the coercivity spectra provide strong evidence for magnetite, and since magnetite does not alter on heating to 600°C, it is probable that these Curie points do indeed correspond to magnetite in the original samples. The inferred lack of oxidation and the high Curie temperatures constrain cation substitution to a very low level, less than 0.1 if titanium is assumed and the contours in figure 3.22 (p. 73) are used. Since the goal of these rock magnetic investigations is to assess palaeomagnetic suitability, such a constraint is probably sufficient: even if not entirely pure, a single-domain magnetite with only slight oxidation or subtitution will carry a stable remanence.

3.4.8.2 *Sulphides*

Several iron sulphides are capable of carrying remanence. Their potential palaeomagnetic significance has become clear only in the past two decades – a recent development compared to the long history of iron oxide investigations – but much work has been done in that time. Even sulphides which do not directly carry a remanence can exhibit distinctive magnetic properties and alterations during laboratory treatment, and they must thus be considered during rock magnetic investigations. Snowball and Torii (1999) gave a useful overview of the magnetic properties and significance of iron sulphides.

Pyrrhotites

The term ‘pyrrhotite’ denotes a range of iron sulphides with iron:sulphur ratios

from 1:1 (troilite) to 9:11 (smythite) and various crystal structures (hexagonal, monoclinic, or rhombic). Monoclinic pyrrhotite (Fe_7S_8) is the only palaeomagnetically significant phase: although hexagonal pyrrhotites with higher Fe:S ratios can sometimes carry a weak (compared to the monoclinic form) defect ferrimagnetism (Dekkers, 1988 and Snowball and Torii, 1999), they have never been reported as palaeomagnetic remanence carriers.

Pyrrhotite is a plausible candidate for coercivity component 2, as the coercivity curve matches the reference curves of Symons and Cioppa (2000), (figure 3.17). Clark (1984) also gave magnetic parameters for pyrrhotite, including H'_{cr}; taking a rough average of 63 mT for the H'_{cr} of component 2, the reference tables of Clark (1984) give a grain size of around 15 μm. This value falls well within the 2–40 μm PSD region given by Dekkers (1988) and thus agrees with the PSD magnetic grain size inferred from the Symons and Cioppa (2000) curves.

Pyrrhotite has also been reported to alter to magnetite on heating to 600°C (Bina *et al.*, 1991). This behaviour (with some cation substitution in the magnetite) could correspond to the alteration seen in my high-temperature susceptibility experiments. Apart from this, however, the thermal experiments offer little support for the pyrrhotite hypothesis. Pyrrhotite as a significant remanence carrier should give rise to a steepening of the demagnetization curve in the 200–300°C region as pyrrhotite's Curie temperature of 320°C is approached; Torii *et al.* (1996) applied the Lowrie (1990) technique to pyrrhotite-bearing sediments and observed this behaviour in the 0.12 T and 0.4 T axes. In figure 3.6 (p. 46), the C2CM samples do faintly show similar behaviour in the 0.4 T axis (and even more faintly in the 0.12 T axis), but it is too indistinct to be conclusive and not paralleled in any of the other samples.

In the thermal susceptibility study, the P2 sample has a very slight peak at around 300°C during the 400°C heating step (not visible in figure 3.7 (p. 48) due to the small vertical scale), but again it is too faint to be definitive and not visible in the other samples. Furthermore, the coercivity-inferred grain size of 15 μm means that pyrrhotite grains should have been large enough to be seen and analysed during the electron microscope and microprobe investigation, but all the grains I analysed were pure pyrite. My microprobe investigation was necessarily not exhaustive, so it is possible that pyrrhotite grains were present but not analysed, possibly as intergrowths within very large pyrite framboids.

Overall, however, the evidence seems to be against pyrrhotite as a remanence carrier, and for the identification of component 2 with a separate population of higher-coercivity magnetite. The suggestion in figure 3.8 (p. 49) of two different disordering temperatures also supports this hypothesis. Although the diagnosis of magnetite as the high-coercivity component is not supported by the reference plots of Symons and Cioppa (2000), Peters and Dekkers (2003) gave a range of magnetite H'_{cr} values (10–63 mT) which accommodates most of the component-2 coercivities of the core samples. Moreover, the fitted coercivity values may be somewhat inaccurate, as discussed in section 3.4.2.2 (p. 56).

Greigite

Like pyrrhotite, greigite has a coercivity range which overlaps with that of magnetite, but is generally higher (Roberts, 1995); this makes it another candidate for coercivity component 2. The other room-temperature magnetic properties of greigite are also similar to those of magnetite and pyrrhotite, making discrimination difficult (Evans, 2005, p. 47; Peters and Thompson, 1998); in this case the high paramagnetic susceptibility of the glaucony further restricts the magnetic parameters which can usefully be applied.

Once again, thermal studies provide more reliable discrimination: Torii *et al.* (1996), using the Lowrie (1990) technique, described a major loss of remanence from the 0.12 T and 0.4 T components in the 200–250°C range, which they attributed to thermal decomposition rather than unblocking. Hallam and Maher (1994) reported a similar remanence loss during the thermal demagnetization of a 300 mT IRM. No corresponding feature is evident in my thermal demagnetization curves, so greigite can be excluded from consideration as component 2.

Pyrite

Large amounts of pyrite were identified by optical microscopy and electron microprobe. Pyrite is paramagnetic at room temperature and thus plays no part in remanence acquisition. However, it is still important to consider it, both for its implications about the depositional environment and for its behaviour during laboratory treatment.

The prevalence of pyrite in the sampled sections indicates a reducing environment during deposition, which would explain the low magnetite concentrations. Pyritization was complete in all the analysed grains, with no pyrrhotite, greigite, or other intermediate minerals found. The mystery then becomes not the low concentration of magnetite but the fact that there is any evidence for magnetite at all – especially considering that the small inferred magnetic grain sizes would give a high surface area to volume ratio and hence high susceptibility to chemical alteration. I return to this question in section 3.5.

Laboratory heating of pyrite in air has been found to cause magnetite formation (Tudryn and Tucholka, 2004); however, the argon atmosphere used in my temperature-dependent susceptibility studies makes this transformation less likely.

3.4.8.3 *Oxyhydroxides*

Goethite (α-FeOOH) is the only oxyhydroxide with direct magnetic significance (Evans, 2005, p. 41) – that is, the only one capable of carrying a noticeable remanence. Its Curie point has been assigned various values between 100°C (Stacey and Banerjee, 1974) and 150°C (Maher *et al.*, 1999), most commonly 120°C (e.g. by Dunlop and Özdemir, 1997 and Opdyke and Channell, 1996); the magnetic susceptibility curves show no Hopkinson peak or subsequent susceptibility drop around this temperature, and none of the thermal demagnetization curves show a particularly abrupt loss of remanence in the 100–150°C heating steps. Goethite also has a high coercivity (France and Oldfield, 2000) and alters to haematite in the temperature range 250–370°C (Dekkers, 1990 and Gehring and Heller, 1989); neither of these properties is evident in my samples. The presence of goethite (at least in magnetically significant quantities) can thus be ruled out with confidence.

Ferrihydrite ($Fe_2O_3 \bullet 0.5H_2O$, $FeOOH \bullet 0.4H_2O$, $Fe_5O_3(OH)_9$) does not carry a remanence, but can alter under heating: Weidler and Stanjek (1998) observed alteration to haematite commencing above 125°C and complete by 325°C. Campbell *et al.* (1997) heated ferrihydrite with varying admixtures of glucose as a reductant, and obtained mixtures of magnetite, maghaemite, and haematite depending on the reduction conditions; in all cases, major alteration occurred by 505°C. Since my samples show little alteration below 500°C,

large amounts of ferrihydrite seem unlikely. In any case, its presence would not affect the remanent magnetization of the samples.

Lepidocrocite (γ-FeO(OH)) carries no remanence, but alters to maghaemite by 300°C (O'Reilly, 1984) with a further alteration to haematite by 500°C (Dunlop and Özdemir, 1997 and Gehring and Hofmeister, 1994). Maghaemite's mass-normalized susceptibility is 600–1200 times greater than that of lepidocrocite (Hunt *et al.*, 1995), so the lack of a significant room-temperature susceptibility increase on heating to 300°C indicates that significant quantities of lepidocrocite are not present. As with ferrihydrite, lepidocrocite would not affect the remanence and is chiefly of interest in interpreting thermal demagnetization behaviours.

3.4.8.4 *Other minerals*

Siderite ($FeCO_3$) is paramagnetic at room temperature, but it may be implicated in the thermal alteration products with disordering temperatures in the 440–520°C range: Housen *et al.* (1996) found that a siderite-bearing chalk formed a mineral with a disordering temperature around 450°C on heating to 700°C, which they hypthesized to be a Mn-ferrite, the manganese originating from traces of rhodocrosite in the siderite. The anisotropy of susceptibility measurements from the same section in chapter 5 (section 5.4.2.2 on p. 137) show an inverse fabric, also suggestive of the presence of siderite.

3.4.9 *Magnetic grain sizes*

The coercivity spectrum of component 1 is consistent with magnetite in the SSD/PSD range (figure 3.16, p. 61). No magnetite grains were visible under the electron microscope, indicating that any magnetite present was probably under 1 μm in diameter. Since the SSD/PSD transition for magnetite is at around 70 nm and the PSD/MD transition at around 2 μm (Maher, 2007, p. 253), this is also consistent with a SSD/PSD grain size.

3.5 Discussion

In this section I discuss the differences between the samples (both the whole-rock drill cores and the separates); I propose models for the acquisition of natural remanence, and the palaeomagnetic implications of these processes.

3.5.1 *Comparisons between glauconitic and non-glauconitic samples*

Samples from within and outside the glauconitic horizon have similar magnetic mineralogies, as identified by coercivity spectra, unblocking temperatures, and temperature dependence of magnetic susceptibility. The most striking difference is that the samples from the glauconitic horizon have only about half the saturation magnetization of the other samples. Dilution of the remanence carrying component is thus associated with an increase in glauconitic content, suggesting that the glaucony grains themselves play no part in holding the magnetic remanence.

3.5.2 *Comparisons between separated extracts*

The comparative behaviour of the separates is consistent with that of the whole-rock drill cores: the high-susceptibility glauconitic components carry a lower remanence, both in IRM and ARM studies. This relationship provides further confirmation that, in spite of high susceptibility, the glauconitic grains themselves carry little or no remanence. Since all the separates have sizes above 62 μm the results also show that a significant portion of the remanence is carried by these larger grains. Microprobe observation and the lack of multidomain magnetic behaviour makes it clear that there are no entire magnetic grains of this size; the magnetic mineral grains themselves must therefore be embedded within these larger grains.

3.5.3 *Depositional magnetization*

The samples, while extensively pyritized, hold a small but appreciable remanence attributable to magnetite (and, possibly, a less significant pyrrhotite component). The magnetite has escaped pyritization, either by being physically shielded from the environment, or because it was formed or deposited at a later point, when a pyritizing environment no longer prevailed. It appears that much of the magnetite is associated with low-susceptibility grains larger than 62 μm; the low overall susceptibility and spontaneous magnetization of these grains indicates a very low magnetite concentration, and the coercivity spectrum indicates magnetite grains smaller than 2 μm.

These observations correspond well to a model comprising a low concentration of small magnetite grains embedded in larger, polycrystalline, siliciclastic grains with negligible susceptibility. The coercivity spectrum indicates magnetite; the low susceptibility and saturation magnetization indicates a low concentration; and the fact that the magnetite grains survived pyritization indicates that they were protected from the immediate environment, which can be explained by embedding in a larger grain. The IRM and AF data indicate that the magnetite is of single-domain or pseudo-single-domain grain size, and thus capable of holding a stable remanence.

The actual fidelity of depositional or post-depositional remanent magnetization depends on the order of events during deposition and lithification of the sediments: if the magnetite grains were able to settle individually, were locked into their 'host' grains, and were subsequently lithified with no further disturbance, they should provide a reasonable magnetic record. However, if the host grains were disturbed after incorporation of the magnetite, they are unlikely to record a field direction: the overall remanence of a large particle with a tiny magnetite concentration would not be enough to affect the alignment of the particle during settling. It is impossible to determine the actual order of events from rock magnetic measurements; however, palaeomagnetic measurements of the NRM from a larger suite of samples would quickly establish whether there is a consistent directional component to the remanence.

3.5.4 *Viscous remanent magnetization (VRM)*

After acquisition and lock-in of depositional remanent magnetization, sediments begin to acquire a viscous remanent magnetization, imparted at ambient temperatures by the Earth's magnetic field. When considering a palaeomagnetic study, it is useful to consider the effect of this VRM on the total magnetization, and how it might be removed by partial demagnetization. I here consider a simple, approximate model of VRM acquisition and removal for the samples in this study.

Pullaiah *et al.* (1975) calculated theoretical relations between unblocking times and temperatures for magnetite and haematite, using the equations of Néel (1949). For any magnetic grain (and thus by extension any group of grains), they derived the equation:

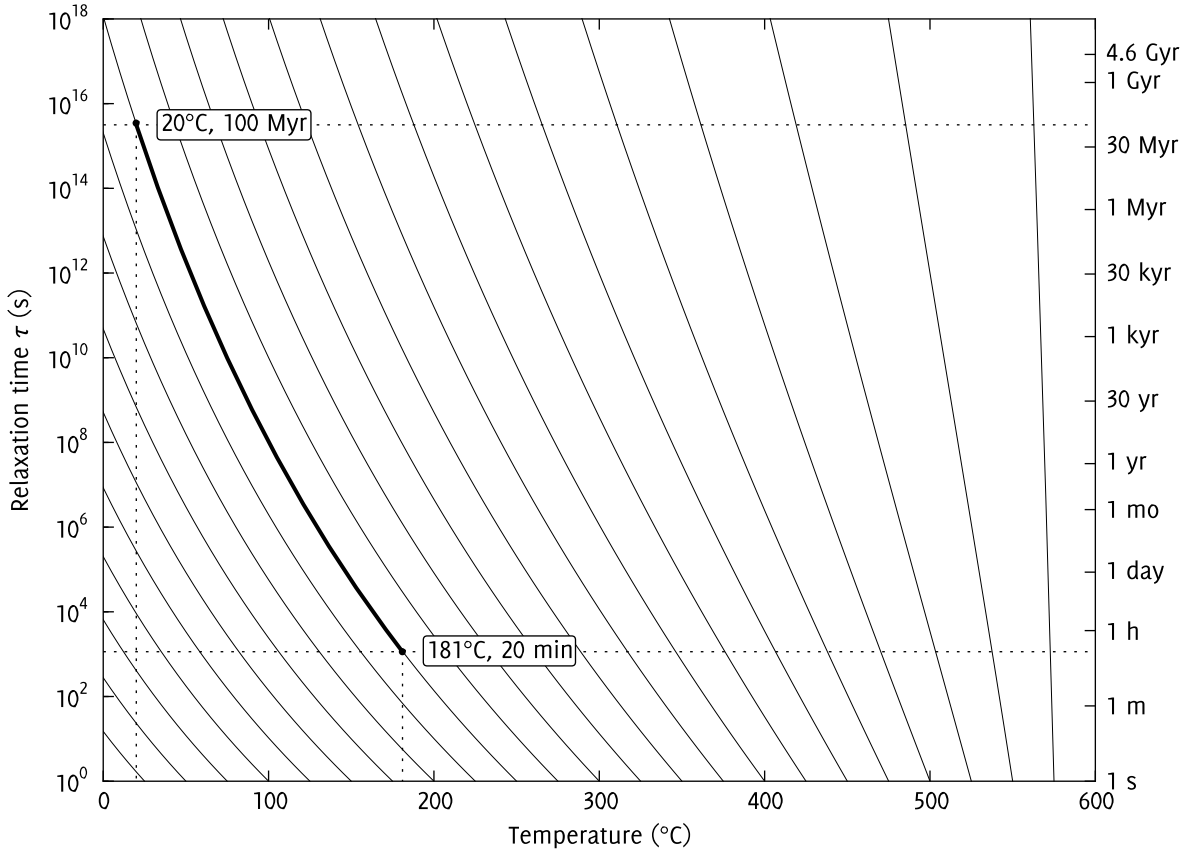

Figure 3.23 Theoretical nomogram of unblocking time/temperature curves for magnetite, after Pullaiah *et al.* (1975). The heavy line represents a grain population which acquired a VRM at 20°C over 100 Myr, and could be unblocked by heating to 181°C for 20 minutes. The parameters used to construct the nomogram are identical to those specified for the calculation in the text.

$$\frac{T_1 \ln(C\tau_1)}{M_s(T_1)H_c(T_1)} = \frac{T_2 \ln(C\tau_2)}{M_s(T_2)H_c(T_2)} \tag{3.4}$$

Here, C is a frequency factor (Néel, 1955), the reciprocal of the atomic reorganization time τ_0 (Dunlop and Özdemir, 1997, p. 202). T_1 and T_2 are any two temperatures below the Curie point of the magnetic material; τ_1 and τ_2 are the respective relaxation times. $M_s(T)$ is the saturation magnetization at temperature T, and H_c the coercive force. For magnetite, Pullaiah *et al.* (1975) used the approximation $H_c(T) \propto M_s(T)$ based on the dominance of shape anisotropy, allowing the formula to be simplified to

$$\frac{T_1 \ln(C\tau_1)}{M_s^2(T_1)} = \frac{T_2 \ln(C\tau_2)}{M_s^2(T_2)} \tag{3.5}$$

Several experimental determinations have been made of the variation of M_s with T for magnetite (by Pauthenet and Bochirol, 1951; by Moskowitz in Baner-

jee, 1991; by N. Sugiura and by W. Williams, both in Newell *et al.*, 1990), and this data has been used (e.g. by Moskowitz, 1981) to constrain the theoretically derived relation given by equation 3.6:

$$M_S(T) = M_S(T_0)\left(\frac{T_C - T}{T_C - T_0}\right)^{\gamma} \tag{3.6}$$

where T_0 is a temperature below the Curie point for which the saturation magnetization has been determined. Moskowitz (1981) proposed a value of 0.5 for γ. Dunlop and Özdemir (1997) found that 'γ = 0.43 gives the best fit' (to the experimental data cited above), whereas Tauxe *et al.* (2010) suggested a value of 'about 0.36–0.39'.

I now use formula 3.5 to give an estimate of the thermal treatment required to unblock the VRM acquired by this study's sediments since their deposition. I use high estimates of 100 Myr for τ_1 and 20°C for T_1, and take τ_2 to be 20 minutes (a reasonable estimate of the minimum time samples spend at the target temperature during 40 minutes of heating in the rock oven). I take γ = 0.4, using an average between the values of Dunlop and Özdemir (1997) and Tauxe *et al.* (2010), and set $C = 10^9$ (McNab *et al.*, 1968 and Egli and Lowrie, 2002). Substituting the M_S terms using equation 3.6 allows the $(T_C - T_0)$ and $M_S(T_0)$ terms to cancel out, so there is no need to supply empirical values for them. This leaves T_2, the laboratory unblocking temperature, as the only unknown. Substituting equation 3.6 into formula 3.5, supplying the specified parameters, rearranging and simplifying gives:

$$\frac{T_2}{(T_C - T_2)^{2\gamma}} = \frac{T_1 \ln(C\tau_1)}{(T_C - T_1)^{2\gamma} \ln(C\tau_2)} \approx 3.764 \tag{3.7}$$

Solving numerically for T_2 using a bisection method gives an unblocking temperature of about 181°C.

This calculation can also be represented graphically using a temperature/time nomogram like that produced by Pullaiah *et al.* (1975). Figure 3.23 (p. 82) shows such a nomogram, constructed using the parameters given above, with the solution overlaid as a contour line.

These calculations are not, of course, intended to be an accurate determination: the Pullaiah *et al.* (1975) equations are not directly derived from empirical data (although Dunlop and Özdemir (1993) provided experimental confirmation for the case of non-interacting single-domain magnetite). I have used high estimates for the age of the material and the temperature of VRM acquisition,

and a low estimate of the unblocking time (as well as disregarding the effects of previous unblocking steps and of the samples' heating and cooling periods), all of which will tend to produce a higher estimate of the required unblocking temperature. Despite the inevitable inaccuracy, this model is still useful in giving a rough idea of the temperature range at which a VRM signal might cease to be significant.

3.5.5 *Glaucony, palaeomagnetism, and rock magnetism*

At least for the samples studied here, glaucony plays no role in palaeomagnetic behaviour: the glaucony grains carry negligible remanence, so the chief influence is to dilute the magnetic signal carried by other minerals.

Glaucony also has an impact on the applicability of various standard rock magnetic techniques: many traditional magnetic parameters and plots involve the use of magnetic susceptibility, often under the assumption that the susceptibility due to the paramagnetic or diamagnetic matrix will be negligible compared to that due to the remanence carriers. In this case, the very small concentration of ferrimagnetic grains and the large paramagnetic susceptibility of the glauconitic components mean that the samples do not conform to this assumption. For example, an attempt to apply the King *et al.* (1982) plot for grain size determination (χ_{ARM} vs. χ) to the data from this study would yield a grain size of over 200 μm. King *et al.* (1982) did consider this issue, and noted that such errors 'can be readily corrected by measuring high-field hysteresis loops to determine the χ of the non-magnetic matrix.', but this negates the chief appeal of such techniques, which is their speed and convenience, and as Yamazaki and Ioka (1997) pointed out, it is seldom done in practice.

Similarly, Peters and Thompson (1998) presented a useful diagnostic biplot of SIRM/χ vs. H_{cr} for determination of magnetic mineral composition; the samples from this study plot well outside the magnetite/titanomagnetite field.

Such diagnostic plots are of course never intended by their authors to be used blindly, with no consideration for unusual characteristics of the samples. In this case the results are anomalous enough that they would hardly be taken at face value, but it is easy to imagine cases where plausible but incorrect results would be produced.

3.5.6 *Magnetic separation*

In this section I discuss the magnetic separation techniques applied in this chapter and their somewhat unusual results in relation to the mineralogies of the studied sediments. I also review other magnetic separation methods and their potential usefulness for sediments like the ones studied in this thesis.

3.5.6.1 *Magnetic separation techniques*

The magnetic separation methods employed in this chapter were modelled on standard methods for separating glaucony, as employed by Odin (1982) and Amorosi *et al.* (2007). Separation had the primary purpose of investigating the relationship between glaucony and rock magnetic properties, with a secondary aim of concentrating remanence carriers sufficiently for direct investigation by scanning electron microscopy (SEM), electron probe microanalysis (EPMA), or X-ray diffraction (XRD) analysis, if possible. The separation methods, relying on the high magnetic susceptibility of glaucony, were effective in concentrating the glaucony grains. The subsequent rock magnetic analyses showed that the actual remanence carriers were not concentrated in the high-susceptibility fractions; in fact, the less-susceptible fractions held more remanence than the highly susceptible, glauconitic fractions. This result provides a strong indication that the glauconitic components do not contribute to the remanence; however, even the low-susceptibility fractions did not contain a sufficient concentration of remanence carriers to allow direct identification using SEM and microprobe analysis. Since the lack of remanence carrier concentrates meant that magnetic mineralogy had to be largely inferred from bulk rock magnetic data, it is worth considering whether other extraction techniques might have had more success in isolating remanence carriers.

Early attempts to concentrate magnetic minerals for direct analysis (e.g. Løvlie *et al.*, 1972; Kent and Lowrie, 1974) used, like the standard glaucony separation techniques, a Frantz isodynamic magnetic separator, albeit with the material in suspension. Extraction efficiency was low, and Petersen *et al.* (1986) noted that, in particular, sub-micron grains were usually not extracted – a significant problem, given that this size fraction encompasses most or all of the stable single-domain range for magnetite (Maher, 1988). Several versions of this technique have been employed, two of the main variations being the

use of a peristaltic pump for recirculation (e.g. Papamarinopoulos *et al.*, 1982; Freeman, 1986) and the substitution of a permanent magnet for the Frantz separator (e.g. Papamarinopoulos *et al.*, 1982; Canfield and Berner, 1987; Karlin, 1990a). Hounslow and Maher (1996) termed these techniques 'magnetic edge' methods, their common feature being the use of magnetic field gradients produced by relatively high (>100 mT) fields at the pole pieces of permanent magnets or electromagnets.

Another type of extraction method, described by Petersen *et al.* (1986) and also used by Vali *et al.* (1989), involves the use of a magnetic probe within a recirculating system usually driven by a peristaltic pump. As described by Hounslow and Maher (1999), the probe is a plastic-sheathed steel pin temporarily magnetized by contact with a supermagnet. While the absolute field at the probe tip is low (<100 mT), the probe geometry produces a high field gradient; Petersen *et al.* (1986) considered that these parameters would bias extraction towards permanently magnetized (as opposed to merely highly susceptible) particles. The low field strength means that several days can be required to produce an extract. Hounslow and Maher (1996) use the term 'magnetized probe' for this method.

A third method, the 'high-gradient' procedure, was developed by Schulze and Dixon (1979) for use with soils and subsequently applied by Hughes (1982), Righi and Jadault (1988), and Sun and Jackson (1994), among others. It makes use of very high (>1 T) magnetic fields usually produced by an electromagnet; the sample suspension is passed through a steel wool filter within the field, with the sharp edges of the wool also providing a high gradient. These factors allow high-gradient separation to extract paramagnetic fractions not separated by other methods. For this reason, high-gradient separation is seldom used in attempts to isolate remanence carriers, and is more commonly applied (e.g. Righi and Jadault, 1988) in separating diamagnetic and paramagnetic components. Sun and Jackson (1994) used high-gradient extraction in an attempt to isolate remanence carriers from Palaeozoic carbonates; however, most of the magnetite was inadvertently dissolved during sample preparation, making the effectiveness of the subsequent magnetic separation hard to evaluate.

Hounslow and Maher (1996) made a systematic investigation of the extraction techniques described above, evaluating their effectiveness quantitatively

with rock magnetic measurements before and after separation. For the separation of ferrimagnetic particles from paramagnetic and antiferromagnetic particles, they considered magnetized probe separation the most suitable; however, even with this technique, they reported the presence of some antiferromagnetic, paramagnetic, and even diamagnetic grains in the magnetic extracts.

Roberts and Turner (1993) concentrated samples for EPMA, XRD, and thermomagnetic Curie balance analysis using a variant of the magnetic-edge technique of Papamarinopoulos *et al.* (1982), with partial success. In both the XRD and EPMA studies, magnetic carriers were identified from only a few samples, due to insufficiently pure separates, and only three sites produced sufficient magnetic extract for thermomagnetic analysis. Wilson and Roberts (1999) used a combination of dry separation in a Frantz separator and wet magnetized probe separation with a system similar to that of Petersen *et al.* (1986). No discrete ferromagnetic (*s.l.*) grains were isolated; the separates contained abundant paramagnetic ilmenite, and the remanence was attributed to sub-micron, iron-enriched zones within the ilmenite grains.

Separation, inclusions, and heterogeneous grains

Magnetic separation methods can perform poorly on samples containing grains of non-uniform composition – either due to discrete inclusions (e.g. Hounslow *et al.*, 1995) or to compositional variations within a single crystal (e.g. Wilson and Roberts, 1999). In such cases the remanence carriers may be embedded at low concentration within in a paramagnetic or diamagnetic grain, meaning that the overall susceptibility of the grain is insufficient for magnetic extraction. The problem is that magnetic separation, when used to isolate remanence carriers, effectively makes use of magnetic susceptibility as a proxy for ferromagnetic (*s.l.*) behaviour. This technique works well in cases where the remanence carriers are iron spinel oxides and are concentrated in discrete grains, giving rise to susceptibilities typically at least an order of magnitude above those of most paramagnetic or diamagnetic minerals (Hunt *et al.*, 1995, table 1). The overall susceptibility of an inhomogeneous grain is determined by the sum of all the susceptibilities of its components, weighted by their concentrations. Thus, if the concentration of highly susceptible remanence carriers is sufficiently low, they will make a negligible contribution to the overall susceptibility, and susceptibility-based separation techniques will be ineffective.

The problem is compounded if the material being separated contains a fraction with a high paramagnetic susceptibility, as in the glauconitic samples studied in chapter 3; in this case, the paramagnetic susceptibility can exceed the 'diluted' ferromagnetic susceptibility of the remanence carriers. Thus, for the samples of chapter 3, the magnetic susceptibility was effectively inverted: the remanence carriers were concentrated in the less susceptible fraction.

Hounslow *et al.* (1995) described a case where ferrimagnetic inclusions within quartz grains carried a stable remanence in Triassic sandstones from the North Sea. They produced magnetic extracts using a combination of magnetic edge and magnetized probe separation techniques, and found that the susceptibility of their samples was controlled by paramagnetic minerals, and that the separates contained a large proportion of diamagnetic silicate grains. They concluded, on the basis of rock magnetic and mineralogical analyses, that the silicate grains contained magnetite inclusions. Their rock magnetic results suggested that the inclusions were of sub-micron size, producing stable single-domain magnetic behaviour. Similar inclusions have been reported from Pleistocene North Sea sediments by Maher and Hallam (2005), and from a wide variety of sedimentary rocks from the British Isles by Hounslow and Morton (2004). I discuss magnetic inclusions and their relationship to palaeomagnetism in more detail in section 8.2.6.

Efficacy of separation in other studies

Magnetic separation has had variable success in producing representative concentrates of remanence carriers. It has long been appreciated (e.g. Lowrie and Heller, 1982) that a magnetic extract is by no means guaranteed to be representative of the original sample, with biases introduced by factors such as paramagnetic susceptibility and the distribution of grain sizes. Hounslow and Maher (1996) made a systematic study of separation techniques and their effectiveness, quantifying extraction efficiency by comparing rock magnetic measurements on the original samples and the extracts. They used a composite separation technique (described in more detail by Hounslow and Maher, 1999) incorporating magnetic edge, magnetized probe, and high-gradient techniques, allowing them to assess the particular strengths of each method. They achieved extraction efficiencies above 70% in the best cases, but noted that efficiency was reduced for samples with high paramagnetic susceptibility and by

ferrimagnetic inclusions within paramagnetic and diamagnetic silicates; many of the samples studied in this thesis have one or both of these characteristics.

The use of separation has been uncommon in New Zealand palaeomagnetic studies. Roberts and Turner (1993), using the magnetic edge technique of Papamarinopoulos *et al.* (1982) produced separates from Neogene sediments of the South Island Awatere Group, with limited success: XRD analysis showed large amounts of chlorite and quartz, masking potential remanence carrier peaks, and potential remanence carriers were only identified at two of the ten analysed sites; only three sites produced sufficiently concentrated separates for Curie balance analysis. A high-coercivity remanence carrier detected in IRM acquisition studies on bulk samples was undetectable by XRD on the corresponding separates, demonstrating the potential higher sensitivity of rock magnetic methods on weakly magnetic samples. Wilson and Roberts (1999) produced two sets of separates from sediments from Pliocene sediments from the Wanganui basin; the first set of separates was made with a Frantz separator, and the second with a magnetized probe apparatus similar to that of Petersen *et al.* (1986). Rock magnetic results suggested that the extracts were representative of the original magnetic mineralogy, but BEI and EPMA analyses did not identify any ferromagnetic (*s.l.*) minerals. Given the results of these previous magnetic extraction experiments, it is not clear that more elaborate sepration protocols would have succeeded in isolating the remanence carriers of the sediments studied in this thesis.

3.6 Conclusions

In order to interpret the palaeomagnetism of the glauconitic sediments studied in this thesis, a solid understanding of the magnetic mineralogy of glauconony was necessary. Since glaucony forms diagenetically over periods which can exceed 100 kyr, any remanence carried by the glaucony grains themselves would require careful interpretation with regard to the timing of its acquisition.

In this chapter, I described the rock magnetic analysis of glauconitic sediments taken from a horizon at Fairfield Quarry. I produced glauconitic and non-glauconitic separates by sieving and magnetic separation, and performed all experiments on a sample suite containing both whole-rock samples and separates. For analyses requiring solid, discrete samples, I produced artificial cubes from the separates, cemented with sodium silicate.

For all the samples, I measured IRM acquisition curves, AF and DC demagnetization of IRM, ARM acquisition and demagnetization, and the TDMS. I applied the technique of Lowrie (1990), which involves the application of three different orthogonal IRMs followed by stepwise thermal demagnetization. I also examined thin sections of the samples by optical and electron microscopy, and analysed their compositions with an electron microprobe.

The most useful analysis techniques proved to be IRM acquisition and TDMS. I analysed the IRM curves using the log-Gaussian modelling technique of Heslop *et al.* (2002); the results showed the presence of magnetite and the possibility of pyrrhotite. TDMS results showed no evidence of pyrrhotite, indicating a magnetite-dominated magnetic mineralogy with SD or PSD grain size. The sediments were extensively pyritized and I did not directly observe any remanence carrying minerals during microprobe analysis; IRM results indicated a magnetite concentration below 1 p.p.m., so this was unsurprising.

Comparisons between glauconitic and non-glauconitic sediments showed that the remanence was carried by the non-glauconitic fraction and that the timing of glaucony formation should therefore have no bearing on the acquisition of NRM. Since magnetite is unlikely to form authigenically under the reducing conditions responsible for the abundant pyrite, this means that the sediments are capable of retaining a primary depositional magnetization, albeit an extremely weak one.

4 Palaeomagnetic analysis software

> On two occasions I have been asked – 'Pray, Mr. Babbage, if you put into the machine wrong figures, will the right answers come out?'… I am not able rightly to apprehend the kind of confusion of ideas that could provoke such a question.
>
> – Charles Babbage, *Passages from the Life of a Philosopher* (Babbage, 1864)

4.1 Introduction

This chapter describes the palaeomagnetic analysis software which I developed to investigate the palaeomagnetic data collected for this thesis. The program is also intended to be generally useful to other palaeomagnetists, and is already in use by other workers at Otago University (e.g. Ohneiser, 2011; Nelson, 2011) for both discrete and long core data analysis and plotting.

4.1.1 *Requirements for this thesis*

Chapter 3 described the magnetic properties of glauconitic sediments from Fairfield Quarry; similar behaviours are shown by most of the sediments studied in this thesis. One consistent feature is the extremely low concentration of remanence carriers, leading to a very low NRM. With such low remanences, minimizing the effects of noise during measurement becomes critical for useful analysis. The facilities provided by the 'Long Core' software provided with the 2G magnetometer in use at Otago proved inadequate for the task, and I started to develop a software package for more accurate and convenient analysis of the magnetometer data.

The characteristics of my samples dictated various other functionality required in the analysis software: great-circle remagnetization analysis; bulk analysis using uniform parameters for similar groups of samples; interactive refinements of analysis parameters for a single sample or an entire suite to allow quick optimization of results; and several other features. The feature set of my new software is described in more detail in section 4.5, which also explains the requirements motivating the features.

4.1.2 *Other requirements*

Other workers at the OPRF also had an interest in using an improved analysis program, which led to the inclusion of other features – chiefly the ability to analyse long core as well as discrete data.

4.1.3 *Scope of this chapter*

This chapter describes the requirements for the software, the choices made in its implementation, the theoretical background of some of the algorithms used, and the relationship to the material studied in this thesis. Details on the practical use of the software are given in the user manual in appendix A.

4.2 Background

In this section I briefly review existing palaeomagnetic software.

4.2.1 *History of palaeomagnetic software*

The fields of palaeomagnetism and software engineering both came of age in the second half of the twentieth century, and given the volumes of numerical data produced by many palaeomagnetic studies it is unsurprising that computer-aided analysis has rapidly become more or less indispensable. Early analysis software was seldom published, but in the past two decades it has become more common to release software publicly, for a number of reasons:

1. Computer systems have become both more prevalent and more standardized. In the early years of electronic computing, the usage of a published program was not only restricted by the small number of computers worldwide, but by the fact that only a subset of them would be compatible with the machine used to develop the software. Now personal computers in use number in the hundreds of millions, and the dominance of a small number of operating systems and hardware platorms has reduced compatibility problems.

2. The complexity of the software is increasing, due both to more sophisticated analysis techniques and more elaborate user interfaces. It is thus

becoming decreasingly practical for each laboratory to develop internal, ad-hoc software for its data processing needs.

3. The increasing availability and speed of internet connections has provided an excellent method of software distribution. Some early, specialized analysis programs were published as papers with the complete source code included (e.g. Facer, 1976 and Rao and Krishna, 1994) but when the source code runs into thousands of lines this becomes impracticable. Distribution of physical media by mail has of course always been another option, but is slow, labour-intensive, unreliable, and expensive compared to distribution over a computer network.

4.2.2 *List of palaeomagnetic analysis packages*

Table 4.1 gives a brief and fairly comprehensive checklist of previously published palaeomagnetic analysis software. The table only lists integrated palaeomagnetic analysis packages – that is, programs or suites of programs which integrate multiple forms of display and/or analysis rather than performing a single, specialized function such as principal component analysis. Though many of these packages are very capable, none provide all the facilities required for this thesis.

4.3 Data visualization and analysis

The theoretical and historical background of the most commonly employed palaeomagnetic data analysis techniques was described in section 2.2. In this section I describe the most popular plots used to analyse and present palaeomagnetic data.

The most commonly employed plot types in palaeomagnetism are the demagnetization-remanence biplot, showing the change in intensity sample remanence with successive treatment steps; the Lambert azimuthal equal-area projection, showing changes in the direction of the magnetization vector; and the Zijderveld plot, which shows both direction and magnitude of the magnetization vectors.

Name	Platforms	Reference	Notes
CryoMag	LWX	Wack (2010)	written in Python
IAPD-99	W	(none known)	By Torsvik et al., 1999. Appears no longer to be available.
Paleomac	C	Cogné (2003)	Includes tectonic reconstruction facilities.
Paleomag	C	Jones (2002)	New (cross-platform) version currently in development.
Paleomag	W	Zhang and Ogg (2003)	Based on an earlier DOS program.
Palmag	W	Maier and Bachtadse (1998)	Dos-based command-line tools.
Palaeomag-Tools	W	Hounslow (2001)	Extensive functionality.
Plotcore	W	McCormack (2005)	Written in Visual Basic.
Pmag	LWX	Tauxe *et al.* (1998)	A suite of command-line tools written in Fortran; superceded by PmagPy.
PmagPy	LWX	Tauxe *et al.* (2010)	A suite of command-line tools written in Python.
PMGSC	W	Enkin (2008)	Dos version also available.
UPmag	LWX	Xuan and Channell (2009)	Matlab-based program for long core data.
Zplot	C	(none known)	Written by Stephen Hurst in 1986 (last updated in 1999).
Zplotit	LX	Acton (2011)	For bulk plotting of large data-sets.

Table 4.1 List of palaeomagnetic analysis software. Platform codes: W Windows (including DOS); C Mac Classic; X Mac OS X; L Linux.

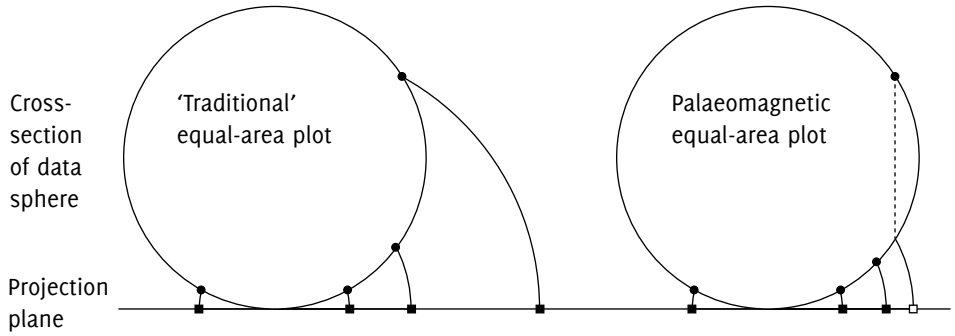

Figure 4.1 Construction of the Lambert azimuthal equal-area projection. Circular points represent points in 3-dimensional space; square points are their projections onto the plane. The diagram represents a vertical cross-section and thus effectively shows the projection of inclinations; projected declinations are identical to the original declination. Note that, in the 'palaeomagnetic' version of the plot, upper-hemisphere points are reflected into the lower hemisphere and projected from there. Ambiguity in reading the plot is avoided by using filled points for the lower hemisphere and unfilled ones for the upper hemisphere.

4.3.1 *Demagnetization-remanence plot*

The demagnetization-remanence plot is the simplest plot commonly used in palaeomagnetic analysis. It is a biplot where the x axis gives the current treatment step (usually expressed in degrees Celsius for thermal demagnetization, or in millitesla for AF demagnetization) and the y axis gives the volume-normalized intensity of magnetization (in A/m) after the application of that step.

For thermal demagnetization studies, it is also useful to overlay, on the same axes, a plot of the bulk magnetic susceptibility of the sample. Large changes in magnetic susceptibility indicate mineral alteration and are thus important in the interpretation of the magnetic data.

4.3.2 *Lambert azimuthal equal-area projection*

The Lambert azimuthal equal-area projection (often referred to simply as the 'equal-area projection') was first devised by Lambert (1772) as a map projection, and during the 20th century it has become popular as a method of representing three-dimensional directional data in cases where preservation of area is more important than preservation of angular relationships. Prior to the projection's use in palaeomagnetic studies, it was widely employed as a representation for three-dimensional data in petrofabric and structural analysis, largely due to its popularization by Schmidt (1925). Howarth (1996) wrote a concise history of the usage of this projection (and others) in geology. As

employed for data projection in Cartesian co-ordinates, the projection equation can be expressed as:

$$\begin{pmatrix} x \\ y \\ z \end{pmatrix} \mapsto \frac{\sqrt{1-|z|}}{\sqrt{x^2+y^2}} \begin{pmatrix} mx \\ my \end{pmatrix} \tag{4.1}$$

Strictly, the plot commonly used in palaeomagnetism is not a single Lambert projection, but two overlaid lower-hemisphere projections: the lower hemisphere is projected as is, and the upper hemisphere is reflected into the lower and projected as a lower hemisphere, distinguished by different plotting symbols. This arrangement gives a far more intuitive display than a strict Lambert projection, which would show the upper hemisphere as a ring-shaped region surrounding the lower-hemisphere projection. Figure 4.1 gives a graphical representation of the Lambert projection.

4.3.3 *Zijderveld plot*

The Zijderveld plot consists of two orthographic projections of the three-dimensional demagnetization data onto mutually orthogonal planes; it has also been referred to as the vector component diagram, vector end point diagram, and orthogonal projection diagram (Butler, 1992, p. 85). One of the planes is horizontal, and the other is a vertical plane oriented either east-west or north-south. The projections are plotted at the same scale and overlaid on the same plotting area; each axis may thus represent two different directions in three-dimensional space, although it is common to arrange the plot such that one of the axes represents the line common to both the projection planes. This method of plotting was first described by Zijderveld (1967), though single, non-overlaid orthographic projections were in use earlier (Wilson, 1961). Dunlop (1979) wrote a thorough discussion of the history, usage, advantages, and limitations of the Zijderveld plot.

Butler (1992) described an alternative form of this diagram, sometimes referred to (e.g. by Haubold, 1999) as a 'modified Zijderveld' plot. In this variation, the standard vertical projection is replaced by a representation where each point is projected in a vertical plane defined by the origin and the point itself – in effect, a different orthographic projection is used for every point. This procedure has the advantage of showing the true inclination of the point on

the vertical plot, and is popular in cases where the sample's declination itself is unknown – principally in vertically drilled long cores. Tauxe *et al.* (2010, p. 175) argued against this modification, calling it 'confusing and misleading', but it continues to be widely used.

4.3.4 *Other plot types*

Other types of plot have occasionally been employed in palaeomagnetism. The stereographic (equal-angle) plot has sometimes been used instead of the Lambert azimuthal equal-area plot (e.g. by Tarling *et al.*, 1976) but the equal-area plot remains by far the more popular. Goguitchaichvili (1999) pointed out that Zijderveld diagram is not readily comprehensible to non-palaeomagnetists. He attempted to remedy the situation by devising a new plot in which demagnetization step is plotted on the x axis, and plots of inclination, declination, and intensity are overlaid on the y axis. This method of data display has so far seen limited use.

4.4 Implementation

4.4.1 *Implementation requirements*

Below, I list the most important requirements for the software used in this thesis. Some are general to scientific software or to palaeomagnetic analysis software, and some are specific to the scope of this thesis.

Multi-platform support Academic environments tend to be diverse in operating systems, with Windows, Mac OS, and Linux (amongst others) all being present in significant propertions; this, at least, is the case at the University of Otago where PuffinPlot was conceived. The program should run on as many operating systems as possible, to avoid excluding potential users (especially since the potential total user base of palaeomagnetists is fairly small).

Future-proofing The program should be not only operational, but amenable to revision and improvement by the original programmer or by others, for many years into the future. This requirement is connected in part to

multi-platform support, since a program tied to a single operating system becomes largely unusable if the operating system itself becomes obsolete; palaeomagnetic analysis programs written for Mac OS Classic have suffered this fate.

Open source code The source code needs to be freely available for inspection and modification. Open source code is a requisite for future-proofing: if the source code is not released, no bug-fixes or improvements can be made unless the original developer has sufficient time, skill, and motivation. Readable source code is also important in demonstrating that the program's results are reliable. When results are published, the program's source code constitutes the most specific possible documentation of the algorithms used, and allows other researchers to assure themselves that the implementations are correct. The dangers arising from unobtainable source code are demonstrated in a discussion of the Bingham (1974) probability distribution by Tauxe *et al.* (2010, p. 234): '… many published descriptions of the Bingham calculation… have errors in them. The source code for calculating Bingham statistics in widely used paleomagnetic data reduction programs is generally not available, and it is unknown whether these programs contain bugs.'

Interactive operation New Zealand sediments frequently have complex, noisy, multi-component magnetizations requiring careful individual interpretation and analysis. While bulk analysis tools such Zplotit (Acton, 2011) and PmagPy (Tauxe *et al.*, 2010) are excellent for rapidly analysing large volumes of data with fairly uniform behaviour, analysis of 'difficult' data-sets can be better served by an interactive graphical user interface allowing rapid exploration of the data.

Batch operation While interactive analysis is certainly desirable, batch analysis is (as stated above) also desirable for many data-sets, and the program should thus support both types of usage. In most cases, a combination will be desirable: initial interactive exploratory data analysis of representative samples, in order to determine the most suitable parameters for a batch analysis of the entire data-set.

Scriptability A graphical interface is the most useful for data exploration and

more intuitive for most users. However, a command-line interface allows a program to be integrated into more complex workflows. It can be used as one component in a series of automated processing steps. Ideally, the program should offer bother graphical and command-line interfaces.

Offset origins One specific requirement for the program (and one absent in its predecessor at the OPRF) is the ability to determine directions for components which do not trend towards the origin. In samples with multiple demagnetization components, this allows analysis of components other than the final one; this is particularly useful for samples where the primary component is not the one with the highest coercivity or blocking temperature.

Publication-quality output As well as high-quality on-screen output, the program needs to produce output in a vector graphics format. Vector output allows publication-quality reproduction at any scale and – for most vector graphics formats – also allows the output file to be further edited by the user if necessary.

Facilities for weakly magnetized samples When working on very weakly magnetized sediments, the remanence of the magnetometer's measuring tray becomes significant. The program needs facilities to correct the measured data for the remanence of the sample tray, and to combine multiple measurements of weak samples to produce a single, more accurate measurement.

4.4.2 *Choice of programming language and environment*

The choice of programming language and software platform is important when implementing a new software package. I took the following aspects into account.

Power As the sole developer of this software, I required a high-level language with sufficient expressive power to implement the program single-handed within the time-frame of the thesis.

Stability Ideally, it should be possible to develop a program for years or even decades after its original release. It is inevitable that bugs will be found

and new features required; if the programming language has become obsolete or unavailable in the interim, it becomes impossible to remedy these problems without a complete rewrite. Several published rock magnetic and palaeomagnetic analysis programs are no longer practically usable due to the obsolescence of their implementation languages (e.g. Noël and Rudnicki, 1988; Sherwood, 1989; Facer, 1976).

Popularity The popularity of an implementation language is important for two main reasons: firstly, a program written in a popular language has a large potential pool of people able to work on it and improve it; secondly, a popular language is likely to remain available and supported for a long time.

Library support It is easier and more reliable to develop software using a language with extensive and reliable standard libraries, which remove the need to develop parts such as graphical user interfaces from scratch, leaving more time to concentrate on the primary goals of the application.

Availability If other developers are to work on a program after its initial release, it is important that the language and libraries are not difficult or expensive to acquire. For a commercially marketed language, the cost of the language can become a barrier to working on the software.

Operating system support As discussed in section 4.4.1, the program needs to run on multiple operating systems; this means that the language and platform need to support those operating systems. It should also be possible to develop the software on a single operating system while deploying it on others.

Ease of deployment Packaging and distributing software on multiple platforms can be complex and time-consuming, especially when frequent new versions are being released to testers. Packaging should be quick, and it should be possible to cross-compile and package the program for all supported operating systems from a single development environment on a single operating system.

Speed This is perhaps the least critical consideration on this list. For data-intensive applications such as seismic processing and rheological model-

> ling, speed is often important. Palaeomagnetic data sets, however, are generally small enough that, in most cases, almost any modern language will give acceptable performance. The question is not 'is it the fastest' but 'is it fast *enough*', and for most languages the answer is 'yes'.

Taking these criteria into consideration, I evaluated a number of programming languages and environments; below I describe some of the stronger candidates.

Fortran (Backus *et al.*, 1957) has a long and successful history of use within the physical sciences, dating back to its original inception in 1953. It satisfies the criteria of speed, stability, availability, and platform support. The major weaknesses are library support and cross-platform deployment: while there are excellent, cross-platform numerical libraries, it is harder to find interactive graphics libraries fulfilling the same criteria. And while Fortran compilers are available for most modern operating systems, cross-compilation is difficult: that is to say, the program must usually be separately compiled on each operating system for which it is released.

Python (Beazley, 2009) has many appealing features, including its popularity for scientific software and wide variety of libraries (especially for numerical and scientific applications). I wrote a prototype version of PuffinPlot using Python, but found deployment to be complicated: while Python itself is an interpreted language, the most popular powerful GUI libraries (wxPython and PyQT) are not written in Python. This fact complicates deployment significantly: the program must be individually built for each target operating system, and may require the user to install additional software.

Java (Arnold *et al.*, 2005) was my final choice for an implementation language. It fulfils most of the stated criteria admirably: it is stable and well-established, having first been released in 1995; it is in wide use, ranking among the three most popular programming languages in the world; it is freely available for a wide variety of operating systems, including Windows, OS X, and Linux; it includes extensive libraries (most importantly, in this case, for vector graphics and graphical user interfaces); and it is more than fast enough for palaeomagnetic data analysis. Perhaps the most appealing feature is the ease of deployment: Java is a 'write-once, run-anywhere' language: the same package can be run unmodified on any platform with a Java runtime environment (JRE) installed. The JRE need only be installed once, and is in wide enough use that it is already installed on most personal computers (on OS X, it is prein-

stalled with the operating system). Java has seen previous use in geoscience applications, particularly in cases where interactive visualization is required (e.g. Spreitzhofer *et al.*, 2004; Reed *et al.*, 2006; Zervas *et al.*, 2009). Another advantage is that, in addition to Java, various scripting languages can run in the JRE, allowing users to write short scripts or more extensive programs which build upon PuffinPlot's features.

4.5 PuffinPlot: a new palaeomagnetic analysis program

Motivated by the considerations described in the previous section, I implemented a new, cross-platform, Java-based analysis program which I have named PuffinPlot. PuffinPlot evolved steadily throughout the thesis as I added features to deal with various particular requirements of the sections I studied. I added other features in response to requests by other users. At present, PuffinPlot consists of around 11,000 lines of Java code (excluding third-party libraries) and constitutes a complete, user-friendly palaeomagnetic plotting and analysis system.

4.5.1 *Choice of name*

It is perhaps necessary to give some justification for the choice of name. It is true that the term 'puffin' has little direct connection to the program's functionality. However, I believe it is more important for a program to have a short, simple, and unique name than one which thoroughly describes the functionality. The uniqueness of the name can be important for potential users attempting to locate and install the software; a Google search for the program 'paleomag' (Jones, 2002), the other program 'paleomag' (Zhang and Ogg, 2003), or 'zplot' (Stephen Hurst, no reference known) results in tens of thousands of spurious results. As the two 'paleomag's show, an entirely descriptive name also risks duplicating the name of an existing program. Highly specific descriptive names can also become unwieldy: for example, Facer (1976) described a program for palaeomagnetic analysis using Fisherian statistics which bore the logical but slightly ponderous name PALMAGFISHERANAL.

Although 'puffin' was a mostly arbitrary choice (the chief factors being brevity, alliteration, and uniqueness), it is pleasing to note that several million

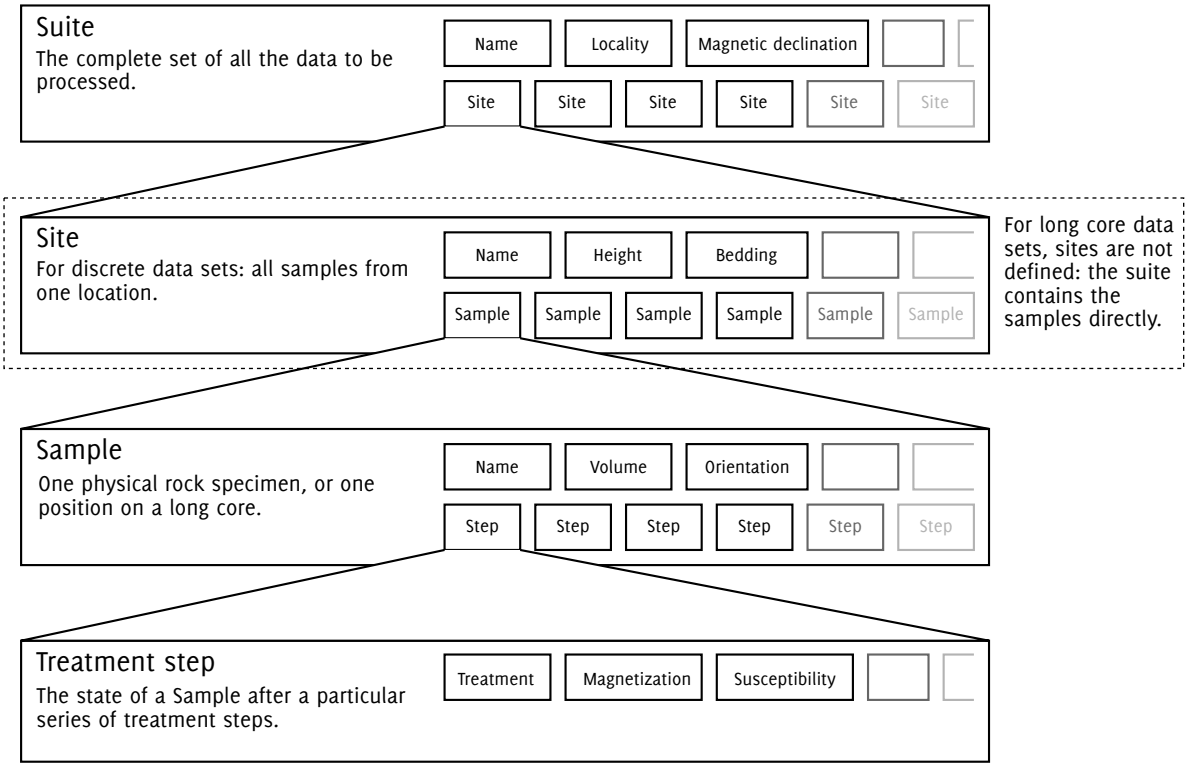

Figure 4.2 PuffinPlot's hierarchical data model. Each layer (except the lowest) contains multiple instances of the following layer.

puffins breed in Iceland, whose lava flows provided important early evidence for geomagnetic field reversals (Hospers, 1951); this evidence was corroborated by the magnetic anomalies which stripe the seafloor beneath the Atlantic Puffin's feeding grounds (Vine and Matthews, 1963).

4.5.2 *Data model*

PuffinPlot uses a hierarchical data structure, with higher levels containing multiple instances of each lower level. The structure is summarized in figure 4.2. At the top is the *suite*, which contains all the data to be analysed as part of a particular study. For a discrete specimen study, this will typically correspond to a section in the field; for a long core study, it will correspond to a core. A suite is initially created by opening one or more data files from a magnetometer; it is saved as a file in PuffinPlot's own format. In a discrete study, a suite contains multiple *sites*. A site corresponds to a set of samples taken from one spot in a section. A site's associated data can include such things as bedding attitude and stratigraphic height, as well as calculated parameters such as the mean

palaeomagnetic direction for all the samples at the site. For a long core study, sites are not defined: samples are contained directly within the suite.

Each site (or, for long core data, the suite) contains multiple *samples*. A sample corresponds to a small physical volume of rock. For a discrete study, this will usually be a typical palaeomagnetic 25 mm cylinder or IODP cube sample. For long cores, it is the portion of the core at a particular depth.[1] The data associated with a sample consists of information specific to this physical unit which does not change with the application of demagnetization techniques – for example, a sample code or name (or, for long cores, a depth), the field orientation of the sample, and its volume. For discrete samples this data can also include a tensor representing AMS, which is imported separately from an AGICO kappabridge datafile and collated with the magnetization data by matching the sample names. The sample can also contain calculated parameters, such as a direction fitted by principal component analysis, or a best-fitting great circle.

Each sample contains multiple *demagnetization steps*. A *step* represents a sample at a particular point during the treatment protocol. Its associated data thus includes details of the treatment: the type (thermal, AF, IRM, etc.) and parameters (temperature, field strength, etc.). The data also includes the state of the sample itself – most importantly, the measured magnetization vector. For thermal studies, the magnetic susceptibility is usually also recorded after every heating cycle, and is also stored as part of the step.

The three-dimensional vector representing the magnetization of a particular sample at a particular point is of course the fundamental 'atom' of palaeomagnetic data. The layers sitting above it in the hierarchy can be seen as the bookkeeping necessary for the useful interpretation of the raw magnetic data.

4.5.3 *Weakly magnetized samples*

A major requirement for PuffinPlot was to allow more accurate analysis of weakly magnetized samples. In this section I describe the features I implemented to achieve this goal.

---

[1] A long core is typically measured at intervals shorter than the length of core which influences the sensors (the 'effective sensor length'). Neighbouring portions of core will thus affect the reading at a particular point, so the reading at a particular point cannot strictly be said to correspond to any well-defined segment of the core. Deconvolution techniques can partially overcome this problem (Weeks *et al.*, 1993), but PuffinPlot does not yet provide such facilities.

4.5.3.1 *Magnetic moment measurement*

The 2G magnetometer software allows the user to specify a number of successive SQUID[2] readings which will be combined whenever taking a magnetic moment measurement, in order to average out random noise and improve precision. In this section I use the term *reading* to refer to a single raw magnetic moment determination from a SQUID unit (never explicitly reported to the user); I use the term *measurement* to refer to the composite magnetic moment value produced by combining a number of readings. My tests showed that increasing the number of readings per measurement from one to three improved both precision and accuracy dramatically. Repeatedly measuring the same sample, I found that, for very weak magnetizations, the standard deviation of the measurement was reduced by over an order of magnitude. Further tests, in which I measured the same samples in different orientations to cancel out any systematic bias, confirmed that the three-reading measurement was more accurate as well as more precise. Increases to more than three readings produced less dramatic improvements in precision.

4.5.3.2 *The tray correction*

The 'Long Core' software provided with the 2G magnetometer at the Otago allows for a sample tray correction to be applied: before any samples are measured, the remanence of the sample tray is first measured at each sample position. The tray remanence is then automatically subtracted from subsequent sample measurements.

As implemented in the 2G software, the tray correction facility proved to have several problems in practice. Perhaps the most serious problem is the fact that the tray reading *always* uses only one reading per moment measurement; thus, any improvements in sample measurement accuracy from using a multiple-readings measurement are effectively negated by the high noise levels from the tray correction. Other measurement parameters, such as tray movement speed and drift correction, are also 'hard-wired' for a tray measurement,

[2] SQUID is an abbreviation for Superconducting Quantum Interference Device, the magnetic moment sensor used in a cryomagnetometer.

which may cause further deviations from the configuration for the sample measurement.

Another problem stems from the fact that the tray reading is not recorded in the same way as a sample measurement: it is stored in a separate file using a different format, making it hard to determine the effectiveness of the correction after an experimental run. This arrangement is of particular concern if the tray measurement is repeated during a run: to determine which tray correction was applied to a particular sample measurement, the time-stamps or run numbers must be analysed.

4.5.3.3 *An improved tray correction*

The obvious solution to many of the tray correction problems is to ignore the 'official' tray correction entirely, and instead perform an extra sample measurement with an empty tray. This procedure ensures that the tray is measured using exactly the same measurement settings as the samples themselves. PuffinPlot can automatically subtract this tray measurement when loading a 2G file, making its implementation entirely transparent to the user.

PuffinPlot also allows a more precise tray correction protocol, using repeated tray measurements. In this protocol, the tray is remeasured before each sample measurement. This procedure allows correction for changes in the tray remanence caused by, for instance, contamination by fragments of friable samples. I found this procedure to produce significant improvements over a single tray measurement. Although this doubles the number of measurements which have to be made, the extra effort involved is relatively little in a thermal study, since the tray must in any case be unloaded and reloaded with different sample batches at every heating step.

4.5.3.4 *Drift correction*

The calibration of SQUID sensors tends to drift over timescales of less than a minute. The 2G software can correct for this by applying a drift correction. Correcting for drift involves taking a calibration measurement before and after measuring the tray of samples; a linear fit is made between the two calibration measurements and subtracted from each sample measurement. PuffinPlot offers a refinement of this procedure: one or more sample slots is left empty

and specified as a calibration point. This system allows PuffinPlot to calculate the change in the measured moment at the same sample slot between the tray measurement run and sample measurement run, and correct all the sample measurements by that amount.

In effect, while the built-in 2G drift correction corrects for drift *within* a single measurement run, my drift correction corrects for the drift that occurs *between* a tray measurement and the subsequent sample measurement. I found this to increase precision, even when also using 2G's drift correction.

4.5.3.5 *Multiple sample orientations*

PuffinPlot includes facilities to combine sample measurements taken in different orientations. This procedure ensures accuracy as well as precision. If, for example, there is a constant bias to the x-axis moment measurement, it can be negated by measuring a sample twice: once in standard orientation, and once with the sample rotated 180° about the y or z axis, so that the x axis becomes inverted. In this case the bias will offset the x measurement in opposite directions, and combining them will cancel it out. In addition, multiple measurements should help to cancel errors produced by inaccurate sample positioning. I devised various measurement protocols along these lines, using up to four different sample orientations to cancel errors in all axes. When combined with the other protocols described above, this gave further improvements. However, the protocol is extremely time-consuming. While it may be suitable for a study with a small number of very weakly magnetized specimens, it was impractical for the hundreds of samples studied in this thesis.

4.5.4 *Analysis of multicomponent magnetizations*

New Zealand sediments frequently exhibit multiple magnetization components of detrital, post-detrital, thermoviscous, and chemical origin, often with significant overlaps in coercivity or unblocking spectra. Since cases have been described where the final component does not represent the primary remanence (e.g. Turner, 2001), accurate characterization of non-final components is often important for New Zealand magnetostratigraphy. In this section I describe some of the facilities which PuffinPlot provides to separate and analyse these components.

4.5.4.1 *Interactive and bulk analysis*

PuffinPlot aims to combine the most useful aspects of two styles of analysis: interactive and bulk. Interactive analysis allows rapid exploration of data, and might (for palaeomagnetic data) consist of repeatedly attempting PCA fits to various sets of data points for a single sample in an attempt to find the most plausible demagnetization range defining a component. For this kind of exploratory analysis, it is important to be able to repeatedly re-run an analysis with various modifications to their parameters, in order to determine the most effective ones. PuffinPlot aids this kind of exploration by offering mouse-controlled point selection, instant visual feedback on analyses, and hotkeys for a wide range of functions such as running a PCA calculation, changing plot projections, hiding and showing points, selecting and deselecting points, etc.

The disadvantage of interactive analysis is that it is time consuming; if sample behaviour is fairly uniform throughout a suite, it is needlessly repetitive to manually analyse each sample. Thus, PuffinPlot also provides facilities for bulk analysis: if a group of data points has been selected for one sample, the corresponding points can be automatically selected across a chosen range of samples, or the entire suite. Calculations such as PCA and MDF can then be done on all the chosen samples at once. This feature allows the user to first investigate the behaviour of one or a few samples in detail, in order to determine the paramaters for the analysis, then quickly apply it to a large number of samples.

For further automation of the analysis process, PuffinPlot can be controlled by a script; section 4.5.10 gives an example of this.

4.5.4.2 *NRM histogram*

In addition to the standard palaeomagnetic plots, PuffinPlot provides a histogram of NRM intensities. The histogram gives a useful quick view of the magnetizations within a suite: the number of modes in the distribution can show groupings of different magnetic mineralogies, and outliers can easily be spotted.

4.5.4.3 *Principal component analysis (PCA)*

Principal component analysis is a standard workhorse of palaeomagnetic ana-

lysis, providing a best-fitting line and plane through any set of data points. Section 2.2.2.1 presents the theoretical basis for PCA. PuffinPlot provides a PCA implementation based on the formulation of Kirschvink (1980), including his Maximum Angular Deviation (MAD) parameters for linear and planar goodness of fit. Importantly for the analysis of non-final components, PuffinPlot allows for unanchored PCA fits, where the line of best fit is not constrained to pass through the origin.

4.5.4.4 *Great circle remagnetization analysis*

PCA works well when components do not overlap excessively, and when the component of interest can be directly observed as a collinear sequence of points. Great circle remagnetization analysis, as described in section 2.2.2.2, allows a final component to be determined when its demagnetization path extensively or entirely overlaps that of the previous component, or even when the final component is not demagnetized at all. The price of this capability is that multiple samples from a site are required to establish a palaeomagnetic direction. In many cases, unanchored PCA and great circle analysis can play complementary roles, with PCA identifying the softer components, and great-circle analysis identifying the final, hardest component using the same demagnetization paths for which PCA yields the penultimate component.

Great circle remagnetization analysis is frequently required for New Zealand sediments: thermal demagnetization is often necessary due to a poor response to AF demagnetization, but alteration at relatively low temperatures (300–400°C) means that the final component is often not demagnetized (e.g. Wilson and Roberts, 1999; Rowan *et al.*, 2005).

4.5.4.5 *User-defined annotation*

Despite the numerical algorithms available for palaeomagnetic analysis, it still requires a significant amount of human judgement and qualitative assessment, particularly in the early stages. PuffinPlot provides facilities for the user to log and tabulate assessments of the data, by means of so-called annotations. The user may specify any number of annotation headings for a data suite, with each heading corresponding to an observation that might be made about a sample,

for example 'estimated number of components' or 'approximate alteration temperature'. The user can then provide these annotations for each sample as part of the data analysis process. While the same functionality could be provided by making notes in, say, a spreadsheet or text editor (or indeed using a pencil and paper), it is far more efficient to integrate this functionality with the main analysis program: firstly, the user does not need to switch between different programs, and secondly there is no need to integrate the annotations with the numerical results after they have been made. PuffinPlot saves the user's annotations along with the other data, and exports them along with the results of sample calculations.

4.5.4.6 *Point hiding*

One fairly basic but surprisingly useful feature of PuffinPlot is the ability to hide selected data points, preventing them from appearing on the plots. The later stages of stepwise demagnetization, whether thermal or AF, frequently lead to large, random increases in remanence. These 'chaotic' data points can easily obscure the data at lower demagnetization steps if they are not hidden, both by directly overlaying the useful data on a graph, and (in the case of the Zijderveld plot) by forcing a small scale for the graph in order to accommodate the outlying points. Hiding points is also useful for removing occasional meaningless, high-intensity data points produced by flux jumps during measurement of long cores.

Like most of PuffinPlot's other features, point hiding can easily be applied across an entire sample selection or suite, so that – for example – demagnetization steps above 450°C can be hidden for every sample in a suite with only a few clicks of the mouse.

4.5.4.7 *AMS data import*

PuffinPlot can import AMS data and integrate it automatically with the corresponding demagnetization data. This integration allows AMS and remanence data to be viewed side-by-side and compared easily, which is useful for investigating possible relationships between AMS axes and magnetization directions. Analysing both types of data in the same program also simplifies the application of corrections for sample and formation orientation and local magnetic

declination, since the same corrections are used for AMS and palaeomagnetic data.

4.5.4.8 *Ternary plot of orthogonal intensities*

I implemented an experimental ternary plot type to display data from the Lowrie (1990) triaxial demagnetization technique, described in section 3.2.3.1 on page 38. The position of a point on the plot shows the relative intensities of the low-, intermediate-, and high-coercivity components of magnetization, and the path of successive points during demagnetization thus shows the relative effect of thermal demagnetization on the components.

4.5.5 *Other features*

As well as features specifically motivated by the requirements of this thesis, PuffinPlot includes a fairly standard array of other data analysis facilities, summarized below.

- Calculation of Fisher (1953) statistics on a per-site or per-suite basis.
- Calculation and display of Median Destructive Field (MDF).
- Printing of diagrams, and export of diagrams in Scalable Vector Graphics (SVG) format.
- Editing and application of corrections for sample orientation, bedding orientation, and local magnetic declination.
- Reversals test (Cox and Doell, 1960).
- Hext (1963) and bootstrap (Constable and Tauxe, 1990) statistics on AMS data, using the PmagPy programs of Tauxe *et al.* (2010).

4.5.6 *Display layout*

The standard triptych of palaeomagnetic data display consists of a Zijderveld plot of projected vectors, a Lambert azimuthal equal-area plot of vector directions, and a simple biplot of demagnetization degree against intensity of remanence. Laying these out in a reasonable manner – along with possible further

tables and plots – is not always easy. For example, a Zijderveld plot can often consume a large rectangle of space while leaving one or more of its quadrants entirely empty of data. When space is constrained (as in a short journal article) this is wasteful, and authors frequently make use of overlapping layouts, with individual plots encroaching upon the blank portions of their neighbours (e.g. Wilson and Roberts, 1999, fig. 2; Turner *et al.*, 2005, fig. 5; Plado *et al.*, 2010, fig. 4). Furthermore, during routine analysis, data plots vary in importance depending on the character of the data and the goal of the analysis. For these and similar reasons, a flexible layout system is vital.

In normal usage of PuffinPlot, the plots are anchored to particular positions on the page. User interaction with the graphs themselves is limited to selecting points for analysis. However, the display can be customized by selecting Move plots from the Edit menu. Each plot is now labelled and highlighted with translucent orange borders, allowing them to be resized, repositioned, and overlapped at will. Once the plots are suitably positioned, the user deactivates Move plots and the plots are once more anchored in place. The plot locations are saved along with the user's other settings, so they persist if the program is closed and restarted. User settings can also be exported to and imported from external files, so multiple plot layouts can be saved and the user can switch between them as needed.

PuffinPlot also allows plots to be deactivated (hidden), so that the display is not cluttered by plots that the user does not require.

4.5.7 *Data import*

PuffinPlot was designed primarily to work with data from the 2G Enterprises cryogenic magnetometer at the OPRF, which is controlled by the 'Long Core' software supplied with the instrument. PuffinPlot was also designed to replace the previous analysis software in use at Otago, Steve Hurst's Zplot. PuffinPlot was thus designed from the start to be able to read the file formats of these two programs. PuffinPlot can also import ASC files of susceptibility anisotropy data, as produced by AGICO's Safyr program from kappabridge measurements. The file loading code is heavily modularized so it is easy to add support for other file formats.

PuffinPlot's own data format has evolved from the 2G file format, which is a simple table of data containing a line for each demagnetization step. The

PuffinPlot file contains the raw demagnetization data (sample and formation corrections are calculated on-the-fly, so corrected orientations are not stored) with various extra items, such as details of PCA and great-circle fits, and which points are currently selected or hidden.

4.5.8 *Equal-area projections*

The Lambert equal-area projection is used in several contexts within PuffinPlot; in this section I list the different applications and briefly describe the implementation of the projection.

Types of equal-area plot in PuffinPlot

PuffinPlot implements several equal-area plots:

1. A sample demagnetization plot shows the direction of the magnetization vector for each demagnetization step in a graph, possibly with a best-fitting great circle overlaid.

2. A site mean direction plot shows the sample demagnetization directions (either points giving PCA directions, or great circles showing demagnetization trends), and the best-fitting site mean direction determined by Fisher (1953) statistics or McFadden and McElhinny (1988) remagnetization great circle analysis.

3. A formation mean direction plot shows the site mean directions for all the sites, with a formation mean direction for the entire suite (or two formation mean directions if two polarities are present in the site mean directions).

4. If AMS data has been imported, an AMS plot shows the directions of the principal AMS axes for all the selected sites. This plot also shows the principal axes of the mean tensor and their confidence regions, if they have been calculated.

Implementing an equal-area projection

When projecting individual points in a Lambert equal-area projection, the mathematics is fairly straightforward: the three-dimensional Cartesian data

are corrected for sample and formation orientation with rotation matrices, and the resulting vector is fed into equation 4.1. However, an equal-area plot also requires great circle segments to connect points, entire great circles to show planar fits, and elliptical regions on the sphere's surface to show confidence intervals. All these structures are first constructed in three-dimensional space as sequences of points, then projected point-by-point onto the plot surface; provided that enough points are used, the ensuing multi-segment line has the appearance of a smooth curve. The most common case is the production of a great-circle segment, since these are used to connect successive points on a demagnetization path. To produce these paths I implemented the 'slerp' spherical interpolation algorithm described by Shoemake (1985), which interpolates points at constant angular intervals along an arbitrary great-circle path.

To produce elliptical confidence regions on the sphere, I use a standard parametric ellipse equation to produce an appropriately shaped ellipse in a default position on the surface of the sphere. (The region is technically only an ellipse within the two-dimensional space of the sphere's surface; in three-dimensional space it is of course curved around the sphere.) Three-dimensional rotation matrices are then applied to move the ellipse to the correct position and orientation, after which it is projected onto the plot. For an AMS plot an extra step is necessary: since AMS data is projected in the lower hemisphere only, any portion of the confidence ellipse protruding into the upper hemisphere is reflected onto the corresponding lower-hemisphere portion before projection.

4.5.9 *Data export*

PuffinPlot allows the export of all data produced by its analyses, for further processing or plotting. Data are exported in the standard comma separated value (CSV) format, readable by the vast majority of spreadsheets, graphing programs, databases, and programming environments. Separate files are produced for data at the sample, site, and suite levels. User-defined annotations are included in the sample data export file.

PuffinPlot's own data format is a straightforward tab-separated text file with a fairly self-explanatory format, which means that, if required, it can also be read and written by external programs.

4.5.10 *Scriptability*

PuffinPlot's graphical desktop interface is intended to be the primary way to interact with the program. However, it is often useful to be able to interact with a program using a scripting language, in order to extend its capabilities, integrate it conveniently with other programs, or process large amounts of data without manual intervention. The Java platform upon which PuffinPlot is built supports a number of scripting languages which can easily interface with PuffinPlot. Perhaps most usefully, an implementation of the Python programming language – named Jython (Juneau *et al.*, 2009) – has been developed for the Java platform. Since Python is widely used in scientific programming and scripting, and familiar to a large number of scientists, this should provide a convenient route for anyone wishing to integrate PuffinPlot with other data processing steps. Using Jython, PuffinPlot can be controlled either from a pre-written script, or interactively from a command shell which accepts and executes commands one at a time from the user.

Figure 4.3 (p. 116) shows a very simple script demonstrating the use of PuffinPlot from within a Python environment. The script opens a data file, calculates the mean NRM, and produces a file containing a PCA direction for each sample. Note that virtually all of PuffinPlot's data and functionality is available to the Python script, so far more complex examples are possible.

4.6 Conclusions

The samples analysed in this thesis had several uncommon features, perhaps most significantly very low NRMs. PuffinPlot was conceived primarily to extract useful data from these samples, but has also been developed to a point where it is useful for general palaeomagnetic analysis. For the purposes of this thesis, its most vital feature is the ability to combine multiple sample measurements, tray measurements, and measurements of empty sample slots in order to compensate for the high noise levels encountered when measuring samples at the limit of a magnetometer's sensitivity. Another important feature is the capability for fast, interactive, graphical analysis, which is of particular use in the early, exploratory stages of data analysis: different selections of demagnetization steps and analysis techniques can be tried out rapidly to see what yields the most reliable results. The 'cut-and-paste' feature for point selection is also use-

```
### Import the required libraries.
from net.talvi.puffinplot import PuffinApp
from net.talvi.puffinplot.data import Suite
from java.io import File

### Start PuffinPlot and open a data file.
puffin = PuffinApp()
input_file = File("example.ppl")
suite = Suite([input_file])
samples = suite.getSamples()

### Calculate and display the mean NRM.
total_nrm = sum([sample.getNRM() for sample in samples])
print total_nrm / suite.getNumSamples()

### Perform a PCA calculation for each sample.
for sample in samples:          # do this for each sample:
    sample.selectAll()          # select all points in the sample
    sample.useSelectionForPca() # and mark them for use in PCA
suite.doSampleCalculations()    # perform PCA for each sample

### Save the results of the PCA calculation.
output_file = File("example-results.csv")
suite.saveCalcsSample(output_file)
```

Figure 4.3 A simple Python script to demonstrate the use of PuffinPlot from a scripting environment. This script first opens a data file. It then calculates the mean NRM of all the samples and displays it. Then it calculates a PCA direction for each sample in the suite, and saves the results to a CSV file. Explanatory comments in the script are preceded by the character #.

ful in this regard, allowing an analysis to be instantaneously applied to a large group of samples. A large number of data plots were needed for this thesis, creating the requirement that PuffinPlot allow flexible graph layout and produce publication-quality vector graphic output. PuffinPlot also includes the unusual feature (for a palaeomagnetic program) of being able to handle AMS data. Conceivably, the AMS results could have been plotted by a separate, existing program, but adding this capability to PuffinPlot made it far more easier to relate the AMS data to magnetostratigraphic analyses of the same samples.

PuffinPlot offers other facilities beyond those specifically required for this thesis: the ability to run on all major desktop operating systems; the analysis

of long core as well as discrete samples; and the inclusion of a scripting interface allowing its capabilities to be extended without needing to modify the program itself. PuffinPlot's freely released source code also permits other researchers to build upon the program, or simply to assure themselves that important algorithms are implemented correctly.

5 Fairfield Quarry

> … look unto the rock whence ye are hewn, and to the hole of the pit whence ye are digged.
>
> – Isaiah 51:1

5.1 Introduction

Fairfield Quarry is situated roughly 8 km west of the city of Dunedin on New Zealand's South Island, at 45° 53′ 34″ S, 170° 24′ 36″ E (New Zealand map grid reference GR 144 086 764); figure 5.1 (p. 120) shows Fairfield Quarry from above. It exposes an approximately Haumurian-Teurian (late Cretaceous to early Palaeogene) sedimentary sequence about 40 m in height (McMillan, 1993). This chapter aims to establish a magnetostratigraphy for the central portion of this sequence (including the Cretaceous-Palaeogene boundary), informed by the detailed rock magnetic study undertaken in chapter 3. The rock magnetic work was mainly done to constrain the magnetic mineralogy and allow reliable interpretation of the palaeomagnetic data. I also used rock magnetism to investigate the depositional environment; in particular, I made AMS measurements in order to determine palaeocurrent flow and direction during deposition.

5.1.1 *Stratigraphy*

The Fairfield Quarry section comprises a part of the eastern Otago sedimentary sequence, a succession laid down from approximately 80 Ma to 14 Ma atop a basement of Haast Schist (McKellar, 1990). The Haumurian (Late Cretaceous) Taratu Formation exposed at the bottom of the Fairfield Quarry section, and the marine beds overlying it, have a regional dip of 5–7° to the south-east (McKellar, 1990, p. 42). The site has long been of geological interest, and was originally operated as a coal mine from the 1860s (Lindsay, 1867). It later became a sand quarry and is mentioned as 'Shiels' Sand-Pit' by Ongley (1939). Sections at Fairfield Quarry were described by Daniel (1961) and Situmorang (1978). The exact lithostratigraphic classification and nomenclature of Teurian (Palaeocene) and Haumurian sediments in the Dunedin area has varied somewhat

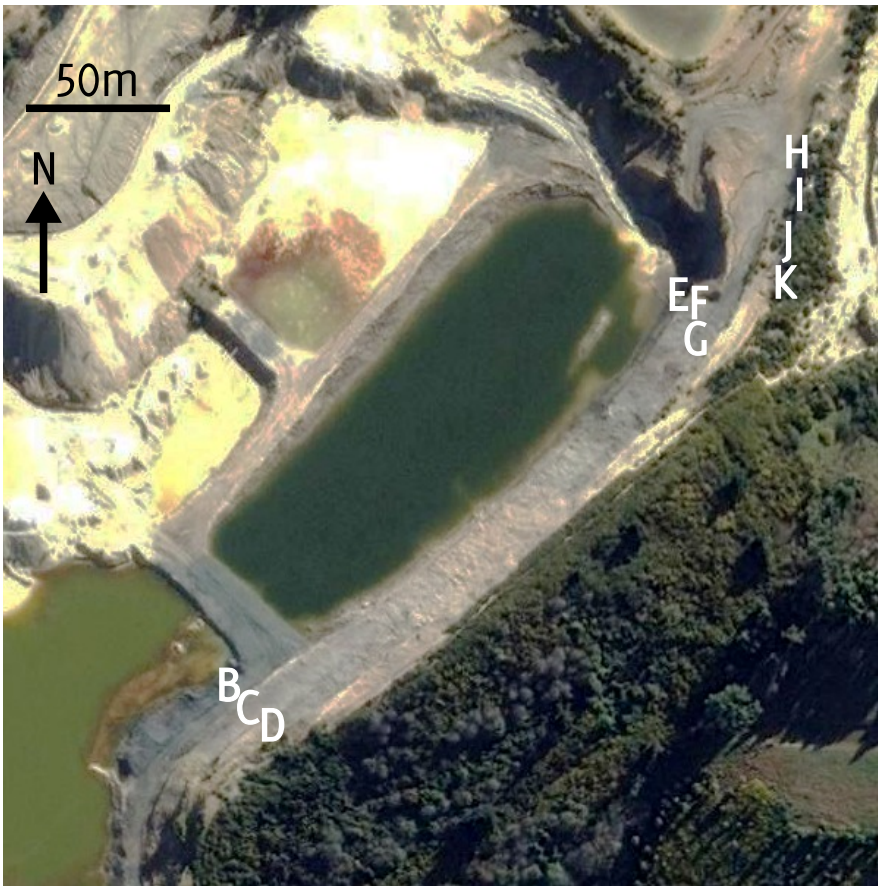

Figure 5.1 Aerial view of Fairfield Quarry on 4 July 2010, showing approximate locations of sampled sub-sections. Photograph courtesy of Google Earth.

over the years (e.g. Benson, 1968; Webb, 1973b; Carter, 1988b); here I follow the stratigraphy given by McMillan (1993).

At Fairfield, the bottom of the section exposes the Taratu Formation, which is topped by the 3 m thick Fernhill Sand Member, variously assigned to the Taratu Formation (McKellar, 1990, p. 14) and the regional Wangaloa Formation (Carter, 1988b). The next and thickest part of the section consists of the lowest 40 m of the 300 m thick Abbotsford Formation (Park, 1910, p. 121; McMillan, 1993), containing the Fairfield Greensand, Saddle Hill Siltstone, Steele Greensand, and Quarries Siltstone members; the Abbotsford Formation has previously been known as the Abbotsford Sandstone (Park, 1910) and Abbotsford Mudstone (Grange, 1921; Fleming, 1959). The exposure at Fairfield is topped by a few metres of colluvium and loess. Figure 5.2 summarizes this stratigraphy.

Some studies of the Fairfield sediments have attempted to establish the

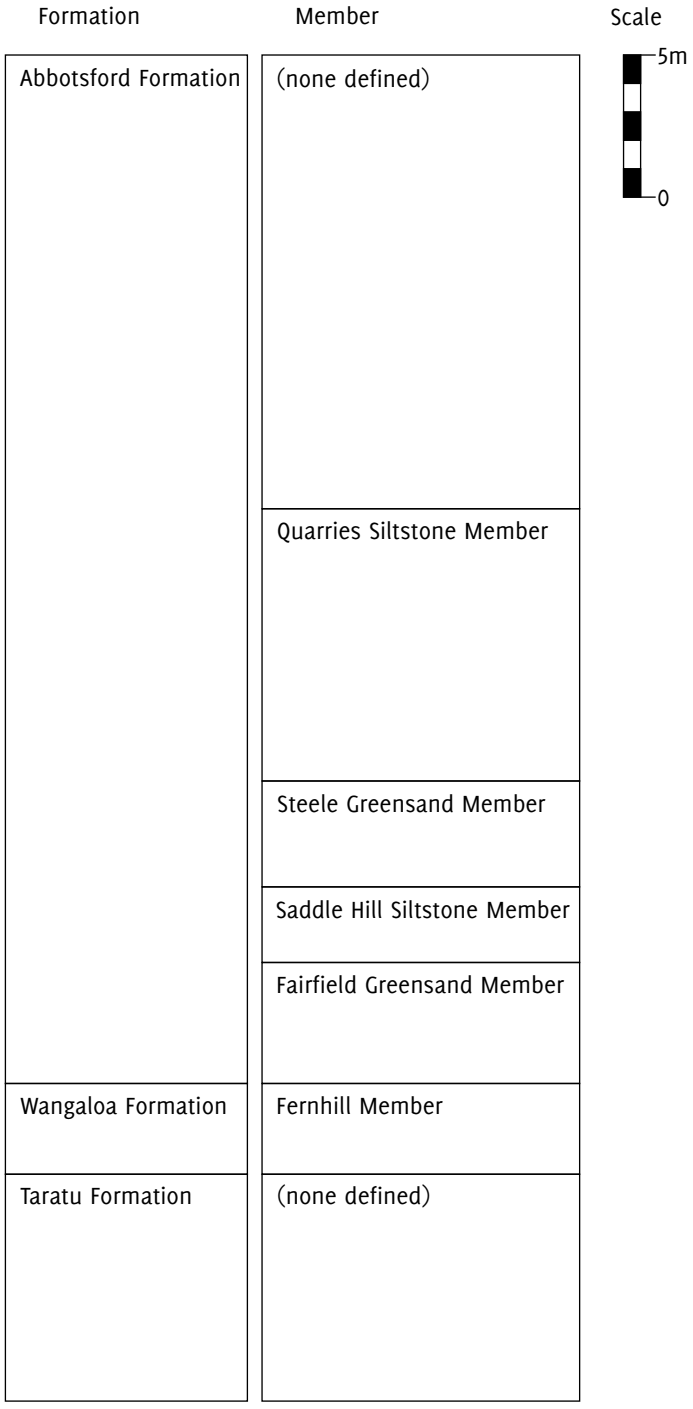

Figure 5.2 Summary lithostratigraphy of the Fairfield Quarry section, after McMillan (1993). The Taratu Formation and most of the Fernhill Member are no longer exposed at the quarry face.

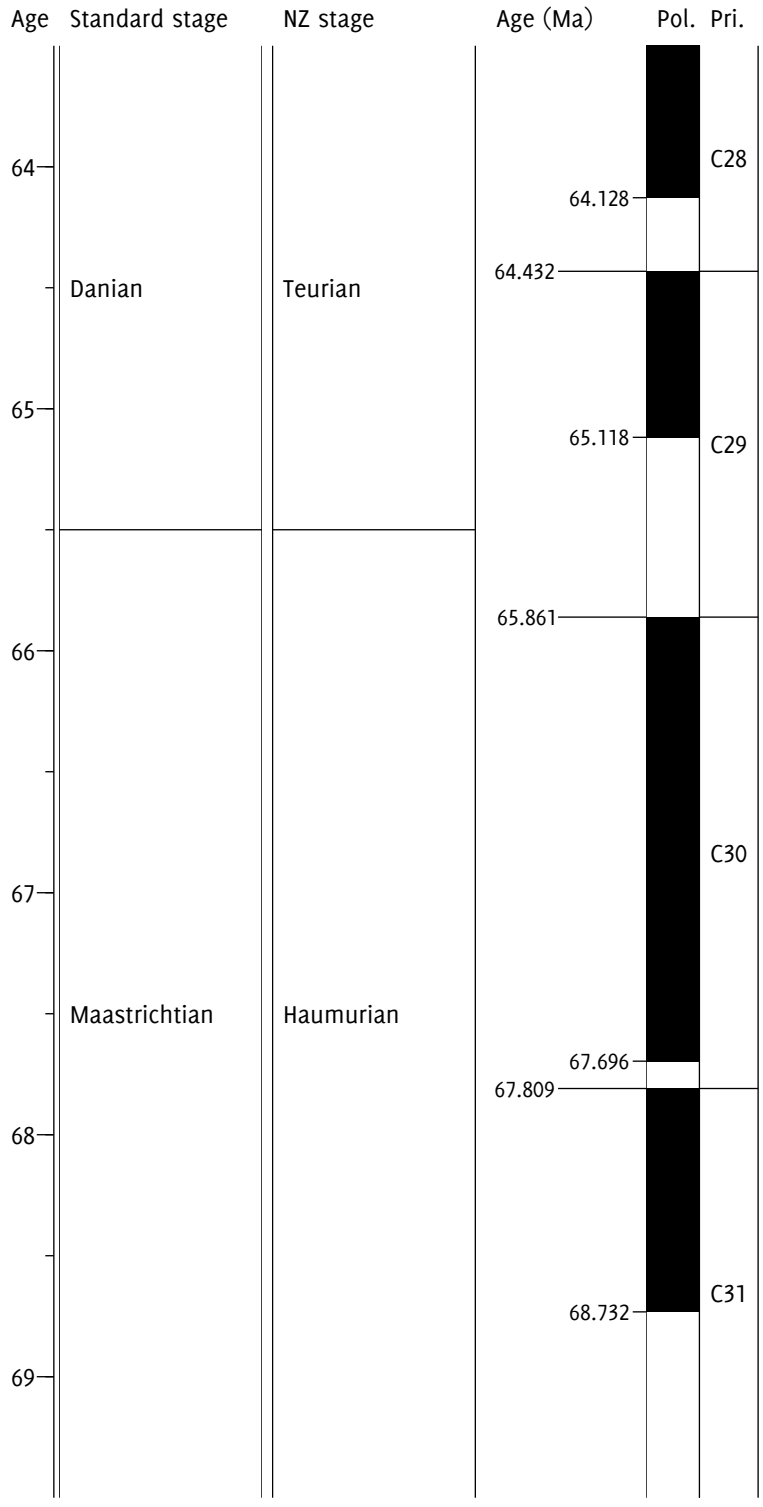

Figure 5.3 Timescale for the age range of the Fairfield Quarry section as constrained biostratigraphically by McMillan (1993).

position of the K-Pg boundary within the section, a task complicated by the absence of the geochemical signature (Fordyce *et al.*, 2009) frequently found in K-Pg boundary sections (Alvarez *et al.*, 1980). Webb (1973a) made a micropalaeontological investigation of sediments from the nearby ASH 17 drillhole (GR 144 088 752) and placed the boundary at the top of the Saddle Hill Siltstone member, about 7 m above the top of the Fernhill Sand. This position suggested a correlation of the overlying Steele Greensand Member with the Wangaloa Formation (Webb, 1973b), but this interpretation turned out to be at odds with subsequent dinoflagellate dating of samples from the quarry itself (McMillan, 1993).

McMillan (1993) has given the most thorough description of the Fairfield sediments to date. His study included a dinoflagellate biostratigraphy which located a transition between a *Manumiella druggii* (late Haumurian) zone and a *Trithyrodinium evittii* (basal Teurian) zone; this constrained the K-Pg boundary to a 3 m interval in the upper part of the section, some 14 m above the position suggested by Webb's (1973a) work on the ASH 17 core. McMillan (1993) provisionally placed the K-Pg boundary at a burrowed discontinuity around 15 m from the top of the section; this identification was confirmed by an additional dinoflagellate study reported by Wilson and McMillan (1996). The depositional setting of the Abbotsford Formation sediments at Fairfield was identified as estuarine/bay to inner offshore by McMillan and Wilson (1997) and as nearshore marine by Willumsen and Vajda (2010).

5.1.2 *Magnetostratigraphic and geomagnetic setting*

Roncaglia *et al.* (1999) placed the start of the *M. druggii* zone in the latest early Maastrichtian – corresponding to about 69.5 Ma in the timescale of Gradstein *et al.* (2004) – and the end of the zone at the K-Pg boundary. The *T. evittii* zone ranges from the K-Pg boundary to a poorly constrained youngest age of 63.5 Ma (Hollis, 2003). Magnetostratigraphically, this period encompasses the C31r to C28n chrons. The C29r chron is fairly brief, spanning 64.745–65.578 Ma (with the K-Pg boundary at 65.0±0.3 Ma) in the Cande and Kent (1995) chronology used for the Cenozoic portion of the current New Zealand geological timescale (Cooper, 2004) and 65.118–65.861 Ma (K-Pg boundary at 65.5±0.3 Ma) in the updated stratigraphy of Gradstein *et al.* (2004). Since the palynologically constrained age range contains seven reversals and the K-Pg

boundary has been located within the section, magnetostratigraphy has the potential to determine the ages of the surrounding sediments quite precisely. Figure 5.3 (p. 122) shows the geomagnetic polarity timescale (GPTS) for the time period.

The present geomagnetic field at Fairfield, calculated from the 10th generation International Geomagnetic Reference Field model (Macmillan and Maus, 2005), has an inclination of −70° and a declination of 25°. When considering the thermoviscous magnetic overprint which might have been imparted during the current Brunhes normal chron, it is useful also to calculate the time-averaged field produced by a geocentric axial dipole (GAD) model. In this case, the declination is of course zero, and the inclination I is −64°, as calculated from the latitude λ by the formula $\tan I = 2 \tan \lambda$ (Opdyke and Channell, 1996).

5.1.3 *Tectonic history and palaeogeography*

To interpret any depositional remanent magnetization from the Fairfield sediments, it is necessary to determine the latitude and orientation of the site at the time of deposition. The New Zealand microcontinent broke away from Gondwana at around 85 Ma (Ballance, 1993a) and by the end of the Cretaceous period was drifting northward and subsiding. The reconstructions of Cook *et al.* (1999) suggested a palaeolatitude of 55–70°S at the start of the Cenozoic, corresponding to a GAD field inclination between −70° and −80°.

Tectonic rotation of New Zealand in the Cenozoic has been investigated by Sutherland (1995) and King (2000b). King (2000b) gave a rotation of 40° clockwise from the current position for the area corresponding to the present eastern South Island at 40 Ma; Sutherland (1995) calculated a similar rotation of around 50° at 45 Ma. The calculated rotations are for the Pacific plate relative to the Australian plate. Plate reconstructions for earlier time periods are less definite due to the lack of surviving ocean crust, but since the Pacific-Australian plate boundary associated with the more recent rotation did not form until around 45 Ma, it is reasonable to assume that there was less significant rotation during the first 20 Ma of the Cenozoic, making a rotation of 45–60° plausible for the end of the Cretaceous.

Figure 5.4 South-east face of Fairfield Quarry, showing positions of sampled sub-sections. The magnified insets show the locations of the upper sub-sections at the northern end of the quarry.

5.2 Sampling and logging

I visited Fairfield Quarry for a total of around four weeks during a period from May 2007 to May 2010, collecting oriented palaeomagnetic cores and logging magnetic susceptibility and sedimentary features.

There is extensive exposure on the east face of the main quarry pit, but there is no section which is both continuous and practically accessible for palaeomagnetic sampling: the upper parts of benches are inaccessible (especially with palaeomagnetic drilling equipment) and the lowest parts are buried in slumped material. I therefore sampled ten sub-sections[3] (designated with letters from B to K) to produce a nearly continuous composite section; figure 5.4 (p. 125) shows the positions of the sub-sections within the quarry, and figure 5.1 (p. 120) shows their approximate locations in an aerial view. This section covers the bottom 24 m of the Abbotsford Formation, from the base of the Fairfield Greensand Member to 8 m above the position of the K-Pg boundary as determined by McMillan and Wilson (1997).

5.2.1 *Structure*

An accurate determination of the formation dip was necessary to integrate the sampled sub-sections reliably. It is impossible to measure the formation orientation directly at Fairfield, since the extensive bioturbation has eradicated any small-scale bedding structures. Fortunately, the extensive exposure and clearly visible glauconitic beds allowed me determine the dip at a larger scale. I selected a well-defined glauconitic concretionary horizon visible across the entire eastern face of the quarry. For each of several points along this bed, I measured its distance and inclination from a fixed vantage point using a laser range-finder with inclinometer, and its azimuth using a field compass. I converted these measurements into points within a three-dimensional Cartesian co-ordinate system and calculated their moment of inertia as described by Fernández (2005) to give a best-fitting plane (the technique is a development of the three-point method described by e.g. Groshong (2006), p. 52). The indices of co-planarity (M = 14.55) and co-linearity (K = 0.60) indicated a reliable fit

[3] Another sub-section (sub-section A) was also drilled at the same stratigraphic height as sub-section B, but its samples were only used in pilot demagnetization studies.

based on the threshold values (M>4, K<0.8) determined by Fernández (2005). The result was a dip of 6.3° with dip direction 132°, in good agreement with the regional dip of 6–7° south-east given by McKellar (1990).

5.2.2 *Oriented core sampling*

I picked palaeomagnetic sampling sites at 20–50 cm vertical intervals along the studied sub-sections. The sampling intervals were intended to provide sufficient resolution to be sure of detecting the relatively short chrons around the K-Pg boundary, although accessibility, exposure, or lithology sometimes necessitated larger intervals. From each sampling site I drilled three to five 25 mm cores using a water-cooled petrol or electric rock drill. I oriented the cores using a Pomeroy orienting fixture and transported them to the field-free laboratory in mu-metal shields. In total I drilled 165 cores at 60 sites. I measured heights both as tape-measured distances along the face and as actual vertical heights established with a laser range-finder. Heights were measured from a local datum for each sub-section; I calculated stratigraphic offsets between sub-sections using range-finder measurements and later integrated them into a composite section.

5.2.3 *Section logging*

For the seven uppermost sub-sections (E–K) I logged the magnetic susceptibility at 5cm intervals using a Bartington MS2 meter connected to an MS2F surface point probe. For the four uppermost sub-sections (H–K) I also created a detailed sedimentary log at 10 cm resolution, allowing unambiguous correlation with the corresponding section of the log made by McMillan (1993). This log also allowed me to locate the K-Pg boundary precisely in relation to my sampling sites. The lower parts of the section showed less complex variation (especially in the Quarries Siltstone Member, which is around 8 m thick and largely undifferentiated) so detailed logging was not required here for correlation: I confined myself to noting obvious sedimentological features and boundaries between lithostratigraphic members.

5.3 Laboratory work

I processed and analysed the samples at the OPRF. Details of the equipment I used are given in Appendix C.

5.3.1 *Sample preprocessing*

I cut the drilled cores into standard-sized (25 mm diameter, 22 mm height) palaeomagnetic sample cylinders and labelled them for identification and orientation. I reassembled broken cores and samples using a non-magnetic glue (UHU contact gel). The cores yielded around 400 oriented samples in total.

5.3.2 *Stepwise demagnetization*

I conducted a brief pilot demagnetization study using AF treatment. AF proved ineffective as a demagnetization technique: rather than producing discernible trends in magnetization corresponding to the gradual removal of a component, the successively larger field strengths produced apparently random changes in magnetization. A thermal demagnetization pilot study proved more successful, and I used thermal treatment for all subsequent demagnetization. Figure 5.5 (p. 129) shows typical results for AF and thermal demagnetization.

I used 201 of the oriented samples for a comprehensive thermal study, with 3–4 samples per drilling site. I applied stepwise thermal demagnetization at 30°C intervals to samples from sites B1 to F4; for all subsequent samples, I used 25°C steps. I measured the samples' susceptibility after each heating step and stopped treatment when there was a large (twofold or greater) increase in susceptibility, indicating mineral alteration.

5.3.3 *Magnetic susceptibility*

I used a kappabridge to measure AMS for all the oriented samples. These measurements also provided accurate determinations of the initial room-temperature bulk susceptibility of the samples. For selected sites spaced throughout the section, I also measured the temperature dependence of magnetic susceptibility, using progressive 100°C heating steps from 100°C to 700°C in an argon atmosphere.

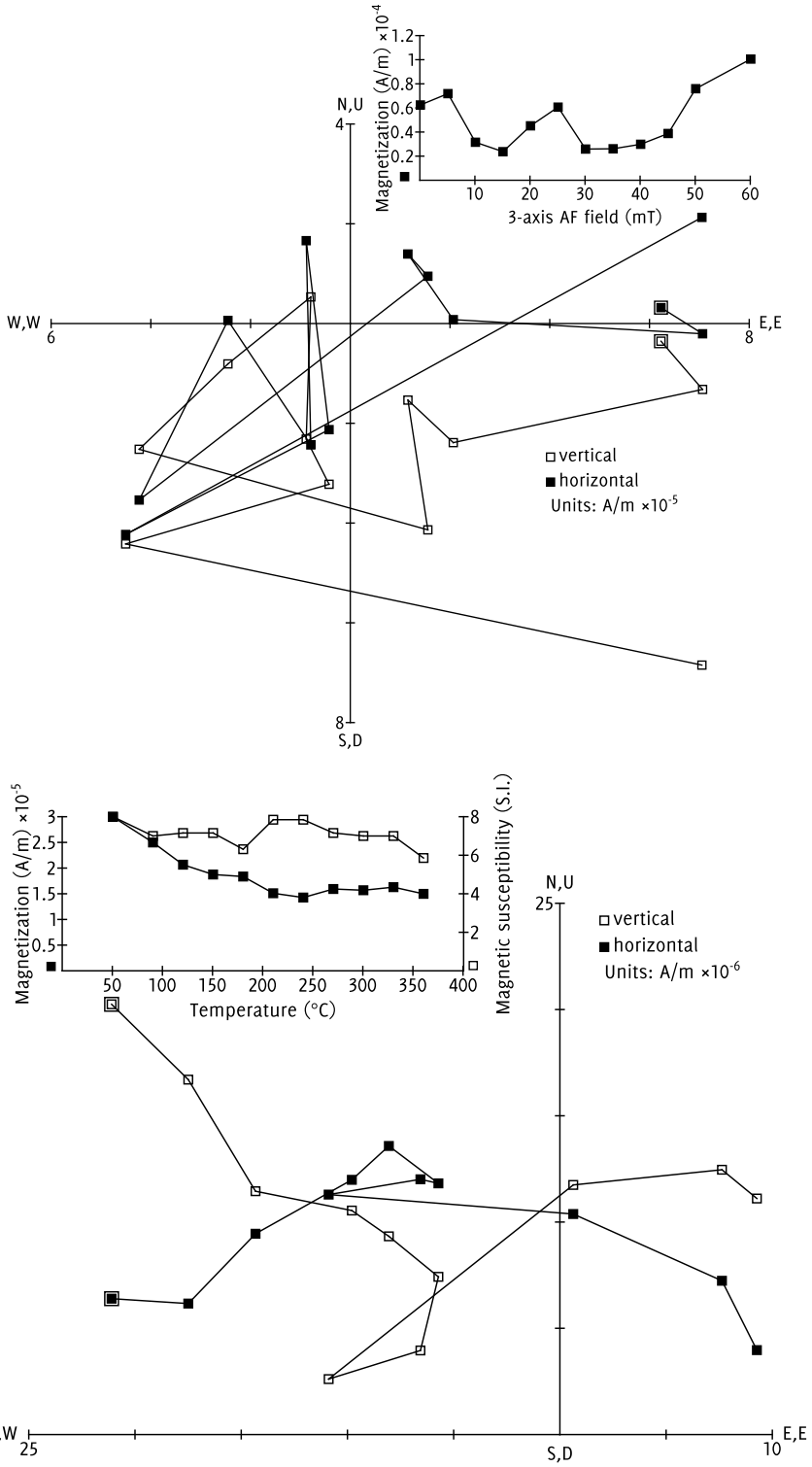

Figure 5.5 Typical results of AF (top; sample A0203.2) and thermal (bottom; sample A0204.2) demagnetization on Fairfield samples. Both samples are from the Fairfield Greensand Member at stratigraphic height 6.3 m.

5.3.4 *Isothermal remanent magnetization*

I undertook an IRM acquisition study using eight samples selected from sites B to I (I already had IRM data for sites I, J, and K from the study in chapter 3). I imparted IRMs in 33 steps from 0 to 1 T, with field strength increasing in approximately exponential fashion. This distribution of field intensities is recommended by Heslop *et al.* (2002) to maximize the efficacy of the IRM analysis techniques applied in section 5.4.3.

5.4 Results

In this section I present the sedimentological and magnetic results of the Fairfield Quarry study. Data files for all the magnetic analyses are included on the data CD-ROM (appendix D).

5.4.1 *Stratigraphy*

An integrated graphic log, summarizing the most important sedimentological and magnetic properties of the studied sections, is given as a one-page overview in figure 5.6, and in detail in figures 5.7 to 5.11 (pages 131 to 136). Heights are from an arbitrary datum below the sampled section, and range from 5.5 m to 29.5 m. The bottom 16 m of the section are given at a scale of 8 metres per page; the remainder of the section is shown at 3 metres per page to give room for display of the high-resolution sedimentary data.

The lower parts of the section show clear alternation between the glauconitic and non-glauconitic units but otherwise little variation in lithology, excepting a prominent, sulphur-rich horizon of soft, very fine sand at around 10 m (top of Saddle Hill Siltstone Member). The uppermost eight metres of the section, starting above the Quarries Siltstone member, show complex variations in glaucony content, with horizons of fossilized wood fragments and arthropod (mainly *Thalassinoides*) burrows. The section is mottled throughout with poorly defined burrow textures, which are distinguished in the log from the distinct burrows in the uppermost part.

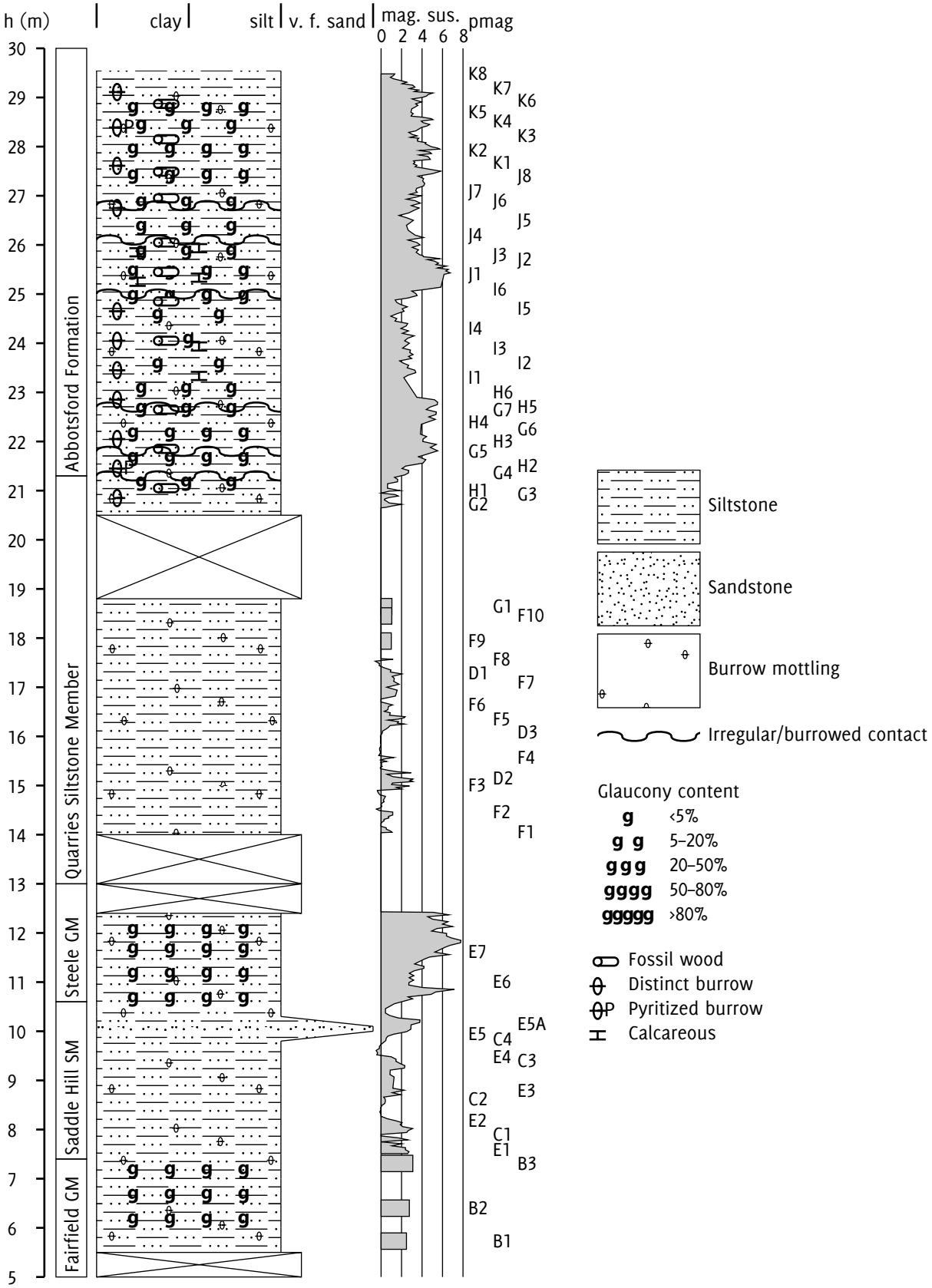

Figure 5.6 Stratigraphic log of the entire Fairfield Quarry section in overview. Magnetic suseptibility units: SI × 10^{-4}; where no field readings for susceptibility are available, site readings from sampled cores are shown as bars. The 'pmag' column lists palaeomagnetic sampling sites. Further details are given in the text in section 5.4.1.

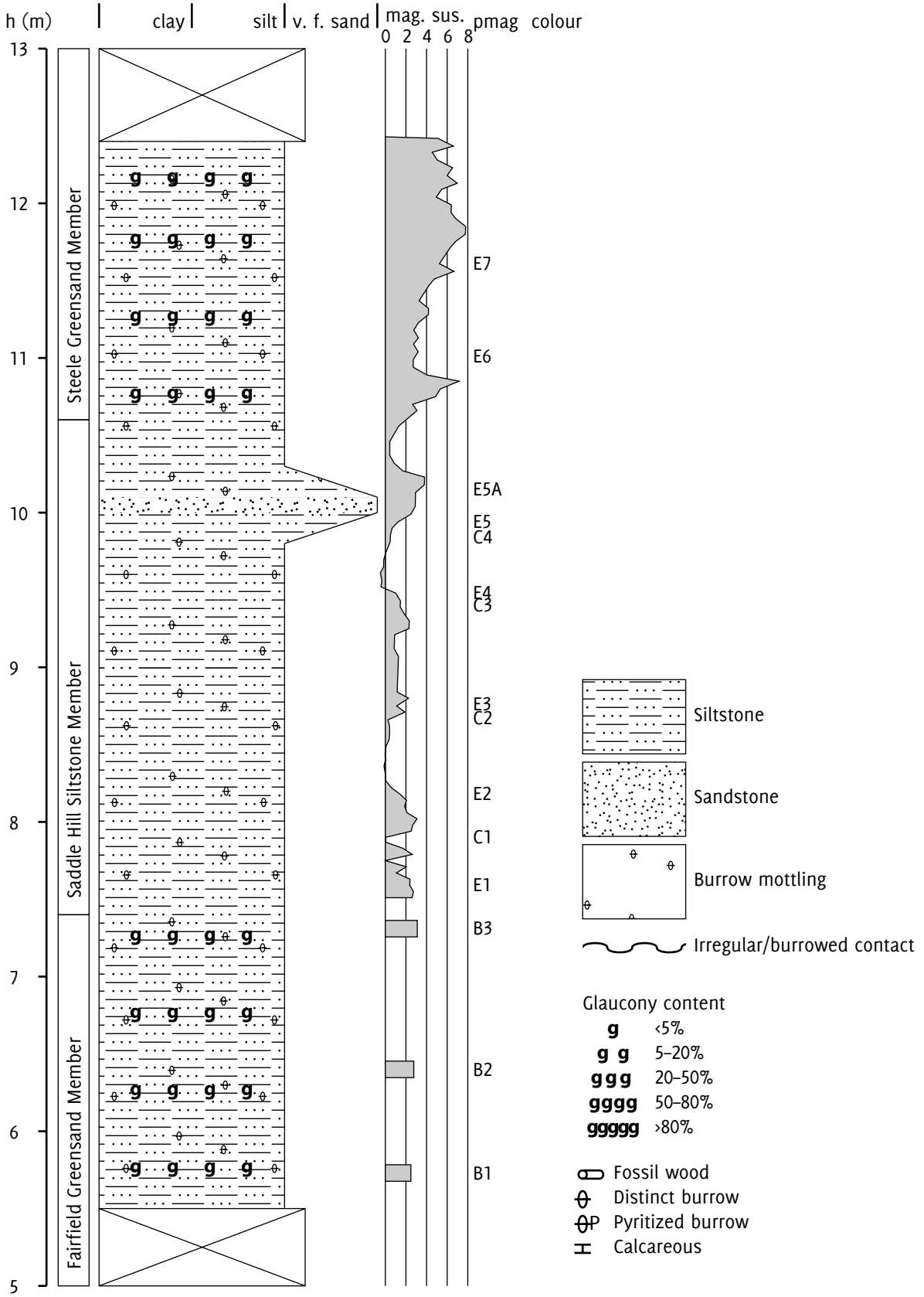

Figure 5.7 Stratigraphic log of the Fairfield Quarry section, 5–13 m. Magnetic suseptibility units: SI $\times 10^{-4}$; where no field readings for susceptibility are available, site readings from sampled cores are shown as bars. The 'pmag' column gives the codes of sites where oriented palaeomagnetic cores were obtained. Further details are given in the text in section 5.4.1.

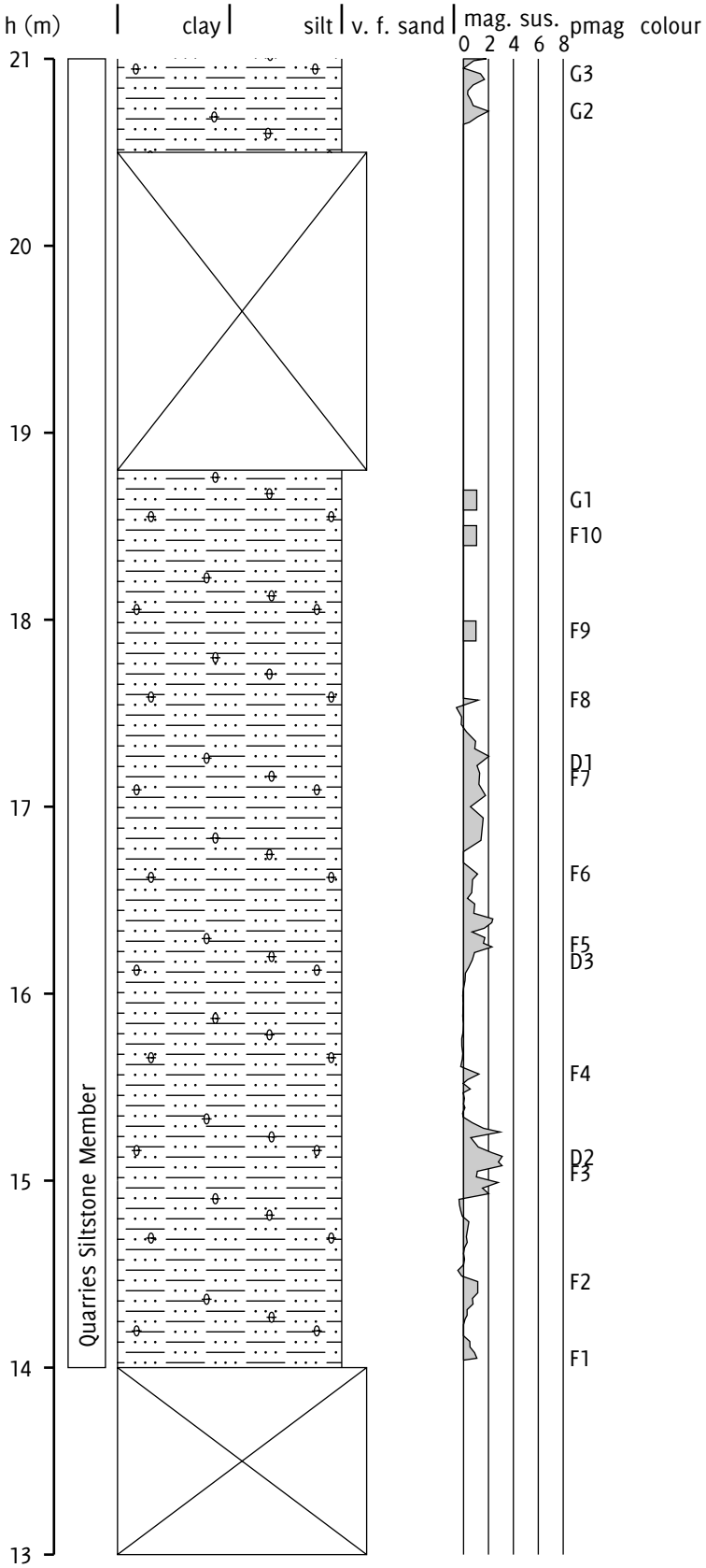

Figure 5.8 Stratigraphic log of the Fairfield Quarry section, 13–21 m. Key and notes on page 132.

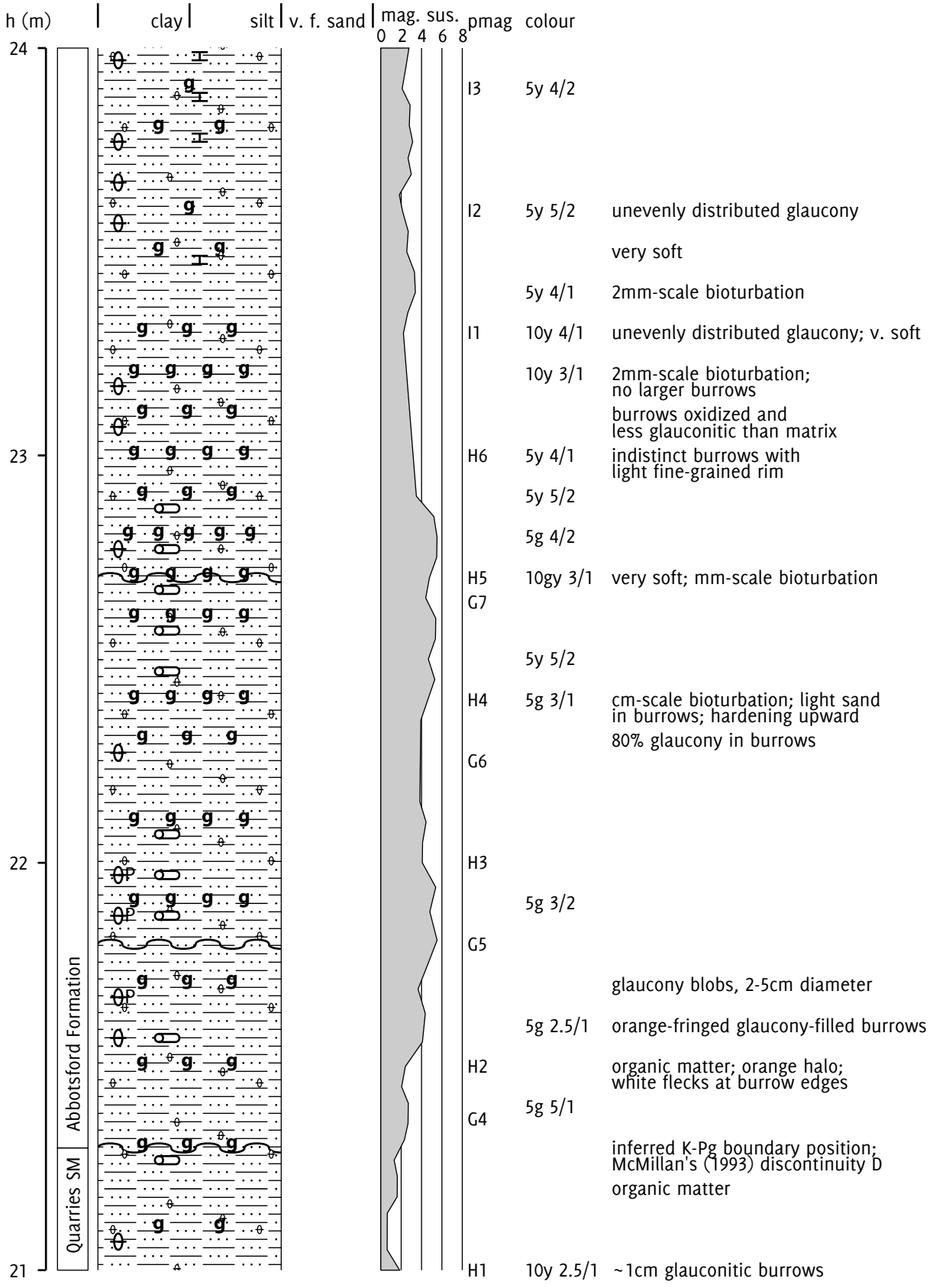

Figure 5.9 Stratigraphic log of the Fairfield Quarry section, 21–24 m. Colours are in the Munsell system. Key and notes on page 132.

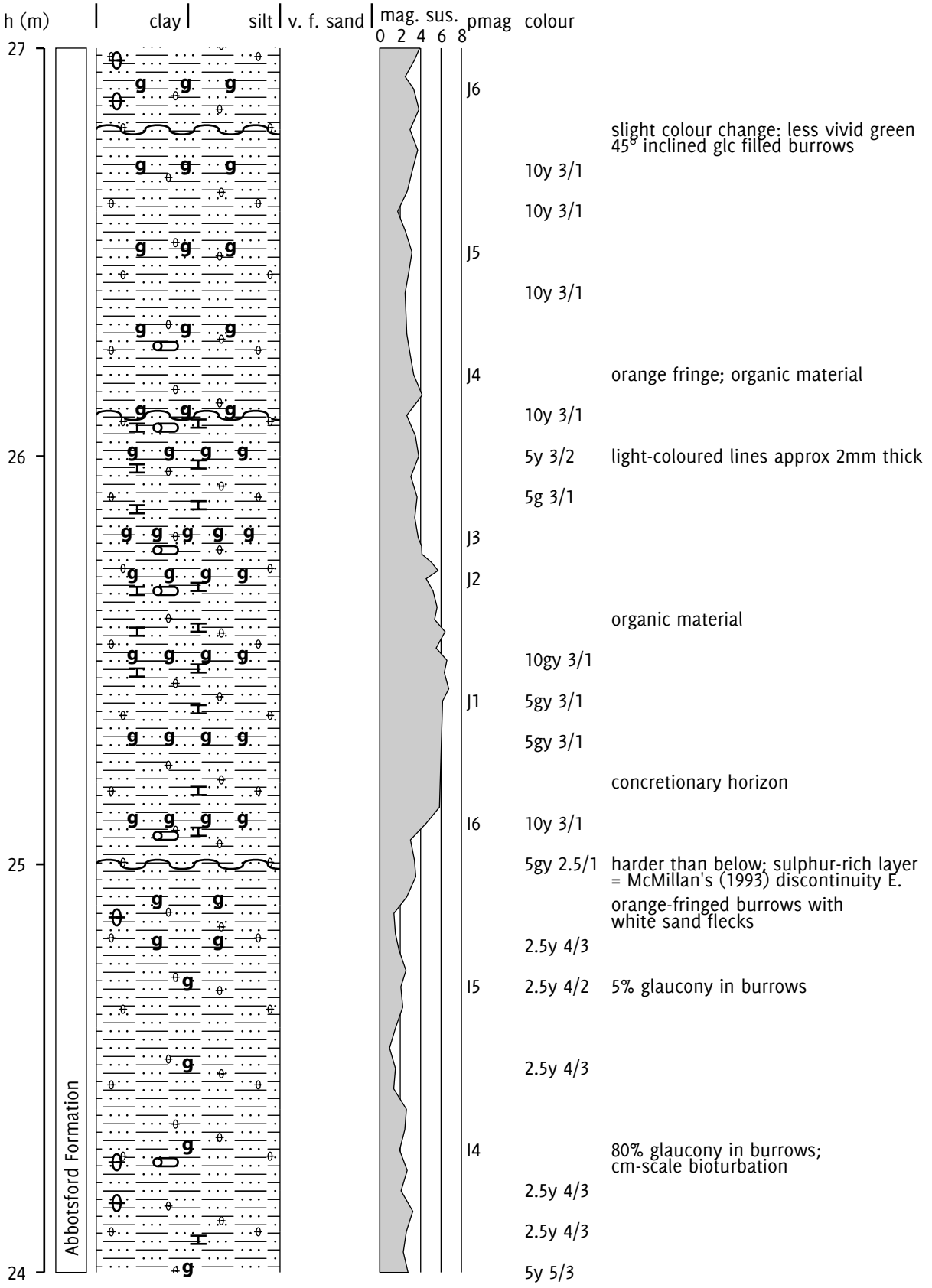

Figure 5.10 Stratigraphic log of the Fairfield Quarry section, 24–27 m. Colours are in the Munsell system. Key and notes on page 132.

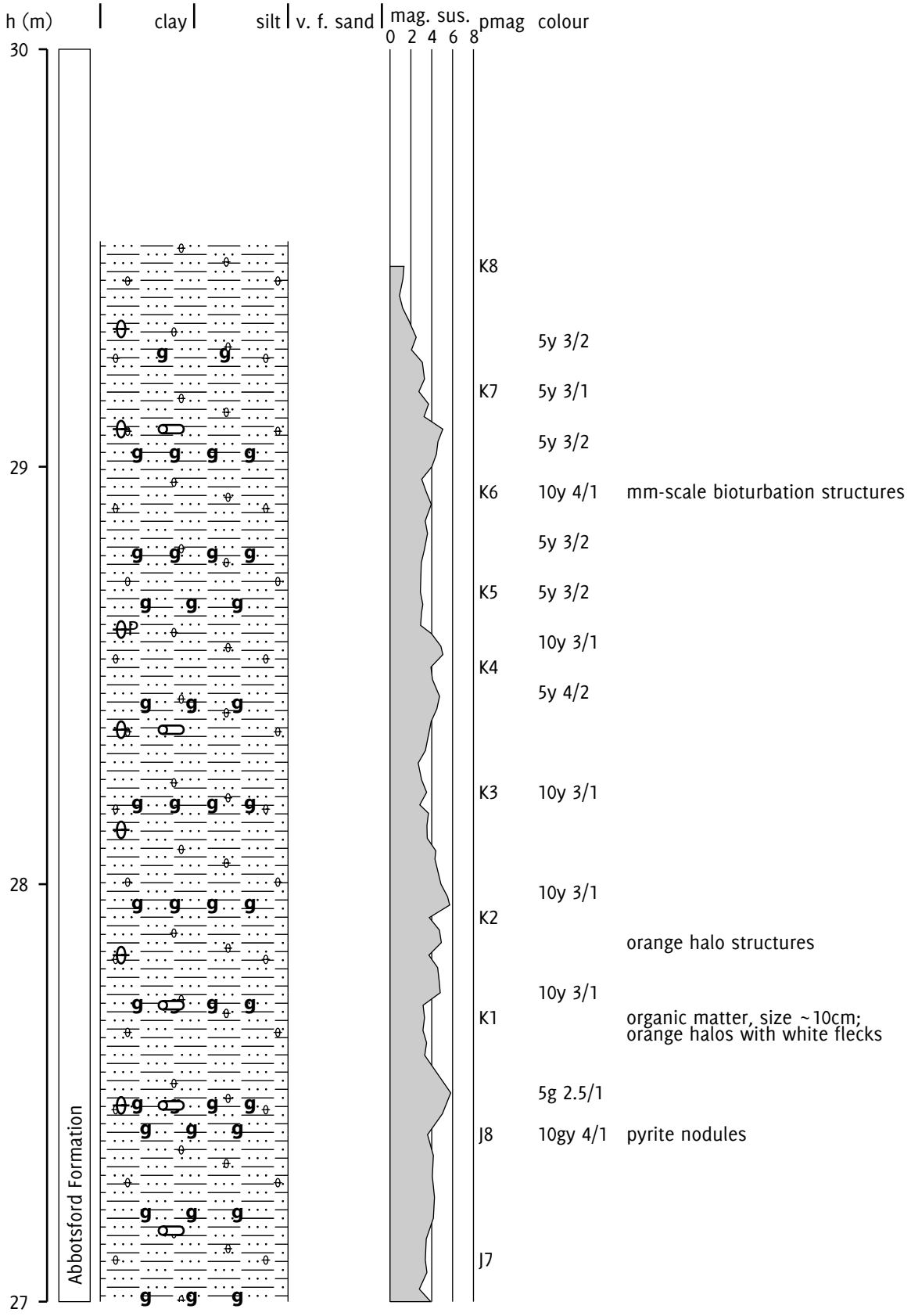

Figure 5.11 Stratigraphic log of the Fairfield Quarry section, 27–30 m. Colours are in the Munsell system. Key and notes on page 132.

5.4.2 *Magnetic susceptibility*

In this section I describe the results of bulk, anisotropy, and thermal susceptibility measurements on the kappabridge. Susceptibility changes during stepwise thermal demagnetization are described in section 5.4.5.

5.4.2.1 *Bulk susceptibility*

I determined an average bulk susceptibility for each site by taking the mean of the volume-normalized susceptibilities of individual samples as measured on the kappabridge. The site susceptibility is thus a mean value for some tens of cm^3 of material, sampled non-contiguously from a bulk of at least several hundred cm^3; it can thus reasonably be expected to average out any inhomogeneities caused by centimetre-scale bioturbation.

There were two problems with the field measurements of magnetic susceptibility collected at 5 cm intervals with the Bartington system: firstly, sensor drift occasionally caused gradual deviation of the measured values; secondly, the point sensor (diameter 15 mm) is small enough to be affected by the inhomogeneous nature of the sediments. I thus took the laboratory site susceptibilities as absolute, reliable measurements, and used the field measurements to interpolate between them and increase the spatial resolution of sampling.

Bulk susceptibility is positively correlated with glauconitic content, as can be seen from the log in figures 5.6 to 5.11.

5.4.2.2 *Anisotropy of magnetic susceptibility*

For analysis of AMS, I divided the samples into four sets spanning ranges between the heights 5.5, 7.5, 9, 12, and 29.5 m within the measured section; I will refer to these sets as A1–A4 in order of increasing height. The uppermost set, A4 (12–29.5m), is by far the largest: I analysed all these samples as a single set because they all exhibited the same inverse fabric, as described in more detail below. All directions are given relative to the bedding plane.

I performed statistical analyses on the anisotropy tensors using the techniques described by Constable and Tauxe (1990) and Tauxe *et al.* (1998) (an overview is given in chapter 13 of Tauxe *et al.*, 2010), which apply the computational Monte-Carlo bootstrap technique of Efron (1979) to the spherical

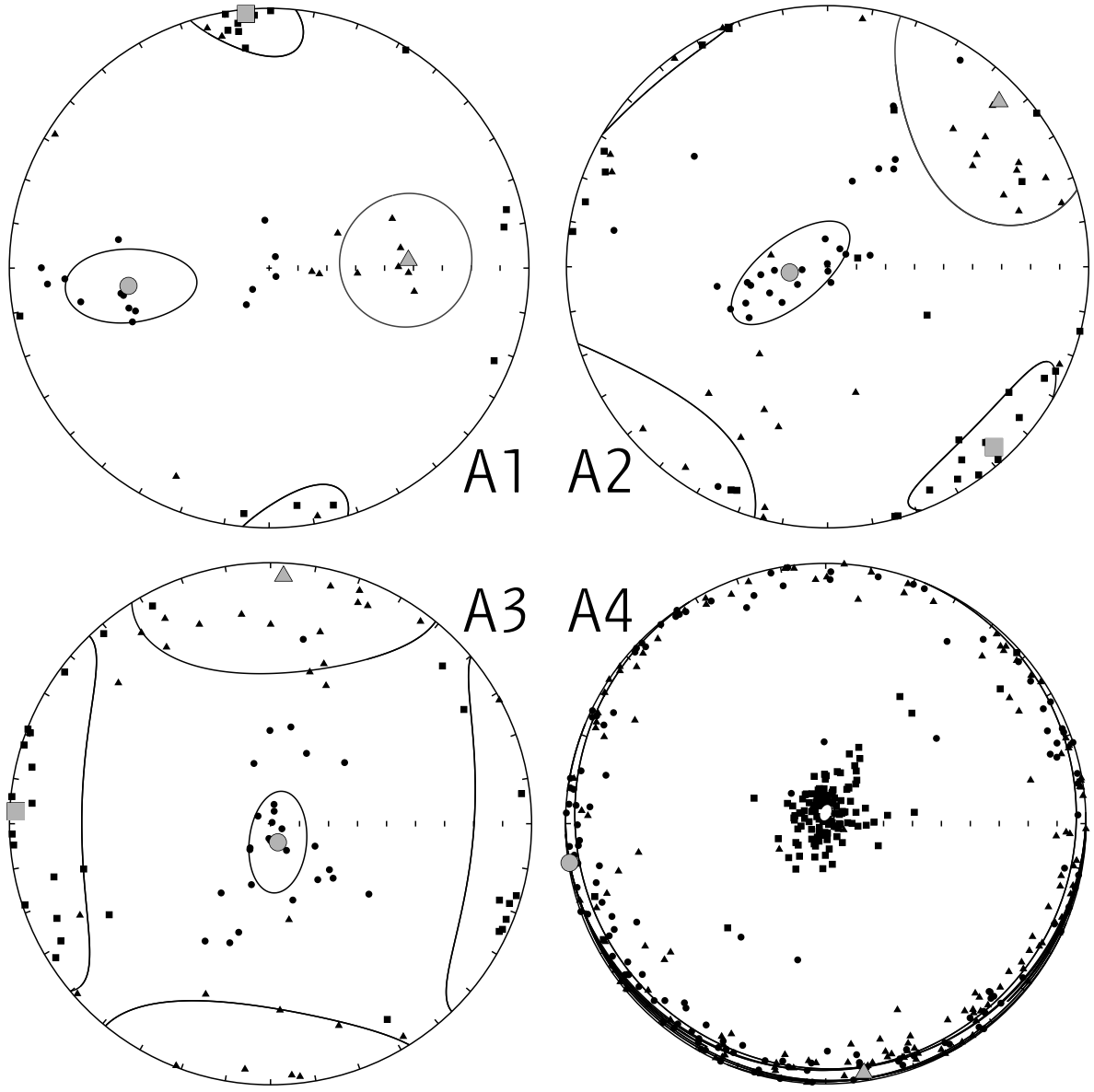

Figure 5.12 Lower hemisphere equal-area plots of principal axes from Fairfield AMS data. Sample height ranges for plots: A1 5.5–7.5 m, A2 7.5–9 m, A3 9–12 m, A4 12–29.5 m. Point shapes: squares show maximum anisotropy axis, triangles intermediate axis, and circles minimum axis. Corresponding large, grey shapes show mean directions. Ellipses show 95% confidence regions determined by parametric (plots A1–A3) or nonparametric (plot A4) bootstrap statistics; further details are given in the text. On the A4 plot the maximum axis confidence region is shown as a filled white ellipse near the centre, and the mean direction marker is omitted since it would be larger than the confidence region. Numerical values for the statistical parameters are given in table 5.1.

Set	Height (m)	N	Axis	D	I	η	D_η	I_η	ζ	D_ζ	I_ζ
A1	5.5–7.5	15	Max.	354.8	2.0	10.8	262.9	29.1	19.4	121.2	54.6
			Int.	86.8	45.4	19.3	353.0	4.1	22.5	258.9	44.9
			Min.	262.8	44.6	10.6	354.8	2.1	22.4	86.9	44.7
A2	7.5–9	28	Max.	137.3	6.7	23.9	46.2	5.9	11.1	278.8	80.4
			Int.	46.1	9.7	28.3	311.0	21.9	38.4	169.9	62.7
			Min.	261.5	78.1	9.9	141.8	6.2	22.5	50.7	10.2
A3	9–12	28	Max.	272.8	2.6	43.3	181.6	4.1	25.8	60.5	82.2
			Int.	3.0	5.6	34.2	103.3	43.0	38.4	259.9	44.5
			Min.	158.4	83.8	8.9	275.5	2.9	15.9	5.8	5.3
A4	12–29.5	140	Max.	0.2	86.6	1.4	111.7	1.2	2.3	201.8	3.3
			Int.	171.3	3.4	75.9	261.0	0.6	2.4	0.4	86.5
			Min.	261.3	0.5	233.4	122.0	2.0	4.2	1.6	86.1

Table 5.1 Statistical parameters for Fairfield AMS data. The *N* column gives the number of samples used in the analysis. Each dataset is described in three lines, one for each of the maximum, intermediate, and minimum axes. *D* and *I* give the mean declination and inclination respectively. η and ζ are the semi-angles subtended by the ellipse of 95% confidence. The *D* and *I* values for a confidence interval are the declination and inclination of the associated axis of the confidence ellipse. All angular quantities are in degrees. Details of the statistical analysis techniques used are given in the text. The same data are shown graphically in figure 5.12.

Set	Height (m)	N	$\overline{P'}$	$\sigma(P')$	$\overline{T}$	$\sigma(T)$
A1	5.5–7.5	15	1.002	0.001	0.477	0.298
A2	7.5–9	28	1.004	0.001	0.198	0.493
A3	9–12	28	1.004	0.002	0.213	0.426
A4	12–29.5	140	1.013	0.008	−0.673	0.241

Table 5.2 Heights and anisotropy parameters for AMS sample sets. N is the number of samples. P' is the corrected anisotropy factor and T the shape parameter (Jelínek, 1981). $\overline{x}$ and $\sigma(x)$ denote mean and standard deviation respectively.

statistical framework of Hext (1963) and Jelínek (1981). I used the 'bootams' program described in appendix F of Tauxe *et al.* (2010) to perform the analyses, producing Kent (1982) confidence ellipses for the principal axes of each set. I used the PuffinPlot program described in chapter 4 of this thesis to correct the data for sample and bedding orientation before analysis, and to plot the results figure 5.12 (p. 138). For sample set A4 (140 samples), I used a nonparametric ('naïve') bootstrap. The other sets contained fewer than 30 samples each, close to the limit given by Tauxe *et al.* (2010) for the reliability of the nonparametric approach; for these I therefore used a parametric bootstrap.

Fabric shapes

Table 5.2 gives, for each sample set, the mean and standard deviation of the AMS parameters P' (the corrected anisotropy degree) and T (the shape factor) (Jelínek, 1981). I describe these parameters in more detail in section 2.2.3.1.

Table 5.2 shows that all the samples have very weak anisotropy, with P' values low even as compared with other undeformed sediments (Tarling and Hrouda, 1993, figure 5.14); however, they all pass the F-test of Jelínek (1996) (described in section 2.2.3.3), indicating that the measured anisotropy is not merely an artefact of machine noise. Sets A1–A3 have oblate fabric shapes, with T values falling within the expected range for undeformed sediments (Tarling and Hrouda, 1993). Despite the overall oblate shape, they have sufficient prolation to distinguish the major and intermediate axes consistently, as is clear from the grouping visible in figure 5.12 (p. 138). Set A4 is strikingly different, with a strongly prolate shape which cannot be attributed to a primary sedimentary fabric; the probable cause is discussed in more detail below.

Fabric orientations

All samples in A1 have a primary susceptibility axis with a near-horizontal orientation, consistent with a primary sedimentary fabric. The mean declination is also well-constrained (around 20° at 95% confidence), indicating alignment with a palaeocurrent direction. The orientations of the intermediate and minimum axes, however, are puzzling, with mean inclinations around 45°. They cannot be due to current- or slope-controlled imbrication, which tends to incline the major axis rather than the other two (Hamilton and Rees, 1970). Metamorphism, even at grades too low for visual identification, can alter sedimentary fabric shape (Tarling and Hrouda, 1993) but in this case the very low anisotropy factors P_J (well below any reported by Hrouda and Janák (1976) in their study on the effects of metamorphism on AMS fabric) and the strongly oblate shape rule out any such influence. The intermediate and minor axes are poorly constrained in the plane normal to the major axis, giving a weak vertical/east-west girdle distribution.

The AMS fabrics of sets A2 and A3 have more classically sedimentary fabric shapes: the 95% confidence intervals for the minor axes both contain the vertical direction, while the confidence ellipses for the major and intermediate axes intersect the horizontal plane. A comparison of the lower three sets shows a progressive change in palaeocurrent orientation, from north/south at A1 to east/west at A3. The increasing spread of major axis directions also indicates a weakening of current with time. The current direction (as opposed to orientation) is not evident at A1 or A3, but the 6.7° south-eastward inclination of the major axis in set A2 implies a palaeocurrent flowing to the northwest (Hamilton, 1963). (Since these directions are determined in the present-day tectonic configuration, the original declinations would have been rotated approximately 45° clockwise – see section 5.1.3).

Samples in the A4 set (the uppermost 17.5 m of the section) have a strongly prolate inverse magnetic fabric – that is, the K1 axis is normal to the bedding plane, rather than parallel as is more usually observed. Inverse fabrics in sedimentary rocks have previously been attributed to uniaxial single-domain magnetite (Potter and Stephenson, 1988), ferroan calcite (Ihmlé *et al.*, 1989), and siderite (Hirt and Gehring, 1991). Márton *et al.* (2010) described a strongly prolate inverse fabric in Oligocene sediments from the Outer Western Carpathians. Like the Fairfield sediments, the samples of Márton *et al.* (2010) were pyr-

Sample	SIRM	H_{cr}	H'_{cr}	— Component 1 —			— Component 2 —		
	mA/m	mT	mT	M_{ri}	$B_{½}$	*DP*	M_{ri}	$B_{½}$	*DP*
B03	62.4	40.6	45.9	0.53	1.63	0.23	0.47	1.73	0.4
C01	144.4	40.7	46.1	0.65	1.63	0.24	0.35	1.77	0.44
E02	138.8	41.0	46.5	0.64	1.63	0.24	0.36	1.77	0.44
E05	185.7	40.9	46.2	0.66	1.63	0.24	0.34	1.78	0.44
F07	177.7	41.2	46.6	0.77	1.63	0.26	0.23	1.87	0.5
G05	110.7	40.4	46.3	0.66	1.62	0.26	0.34	1.8	0.43
H01	204.1	41.5	46.9	0.63	1.64	0.25	0.37	1.75	0.41
I02	159.9	43.0	49.2	0.59	1.65	0.25	0.41	1.77	0.41

Table 5.3 IRM parameters for Fairfield samples. SIRM is saturation IRM; H_{cr} is the reverse field needed to remove SIRM; H'_{cr} is the field needed to magnetize to half the SIRM; see section 3.4.2 (p. 54) for details of component parameters.

itized glauconitic quartz siltstone; the inverse fabric was found to be due to the presence of siderite.

In this case, single-domain magnetite can probably be discounted, since the rock magnetic investigations of chapter 3 indicated that the predominant magnetite grain size is pseudo-single domain and that the susceptibility is not controlled by magnetite. The inverse fabric of the Fairfield sediments is most likely to be due to siderite, which was found throughout the section by McMillan (1993). The high degree of prolateness (with values of Jelínek's (1981) shape parameter *T* usually below –0.7) also corresponds well with the value for siderite given in figure 2.11 of Tarling and Hrouda (1993) (the degree of anisotropy cannot be correlated in the same way, since, unlike the shape parameter, it is affected by dilution within an isotropic matrix). Siderite was also detected in the Teurian Abbotsford Formation at the nearby Fairfield Estates Drillhole (McMillan, 1995). The inverse fabric made it impossible to determine palaeocurrent direction from the AMS measurements.

5.4.3 *Isothermal remanent magnetization*

The IRM study showed very similar remanent coercivity spectra throughout the section, but significant variation in saturation magnetization, indicating strong variability in the concentration of remanence carriers. As in the mineralogical

study of chapter 3, saturation IRM was inversely correlated with glaucony concentration. The lowest SIRM was from site B3 in the highly glauconitic Fairfield Greensand Member, and the highest from site H1 at the top of the non-glauconitic Quarries Siltstone Member. Figure 5.13 (p. 144) shows the IRM acquisition and DC demagnetization curves.

I modelled the IRM data as the sum of cumulative log-Gaussian functions using the Irmunmix program of Heslop *et al.* (2002); full details of the technique are given in section 3.4.2. Figure 5.14 (p. 145) shows the fits of the CLG models to the gradients of the acquisition curves, and table 5.3 lists IRM parameters, including the parameters for the CLG components. In each case, a two-component fit was sufficient to give good agreement with the experimental data. The parameters of the two components were similar for every sample: a dominant softer component (component 1) and a less pronounced, slightly higher-coercivity component (component 2) with a much broader peak. The relative contributions of the components were around 65:35, except in samples B3 (53:47) and F7 (59:41).

The parameters of the two components are very similar to those determined for the whole-rock samples in the rock magnetic study of chapter 3 (figure 3.15, p. 59). Again, component 1 appears to be SD/PSD magnetite, based on comparison with the reference values given by Robertson and France (1994) and the type curves of Symons and Cioppa (2000). Component 2 fits the Symons and Cioppa (2000) type curves and Clark (1984) H'_{cr} values for PSD pyrrhotite. However, given the lack of corroboration for a pyrrhotite component for the samples in the rock magnetic study, I am wary of accepting this interpretation without further evidence: it is also possible that component 2 represents a separate magnetite population with an increased coercivity due to the influence of shape anisotropy, as discussed in section 3.4.2. A single-component fit, also shown figure 5.14, is noticeably poorer but may (given the other constraints) be a better reflection of the true mineralogy.

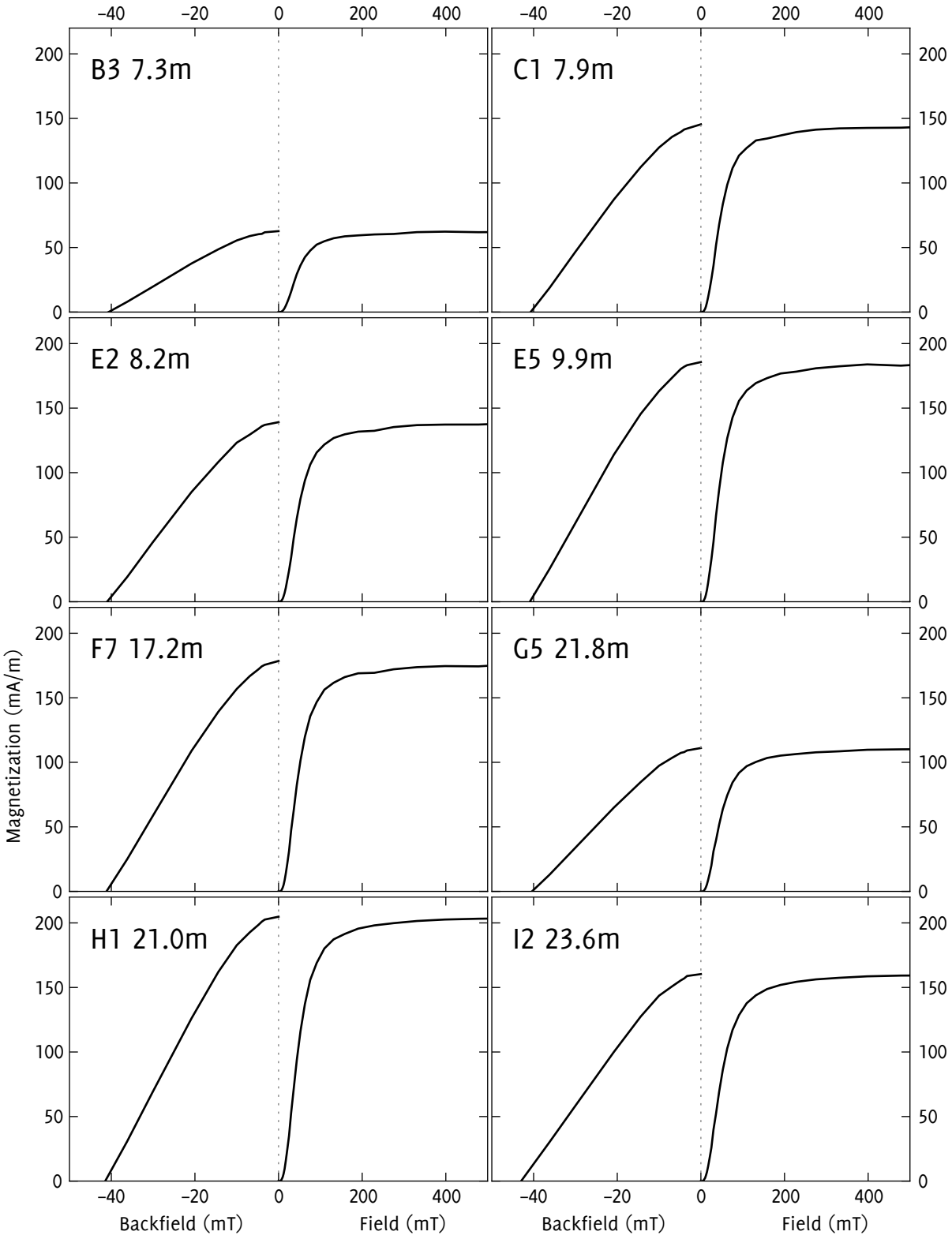

Figure 5.13 IRM magnetization (right sides of plots) and DC demagnetization (left sides) for selected Fairfield Quarry samples; the graphs are labelled with the site code and the height within the overall section. Acquisition continued up to 1 T but graphs are truncated at 500 mT since no appreciable increase in remanence occurred beyond this point. Note the differing x-axis scales for magnetization and demagnetization.

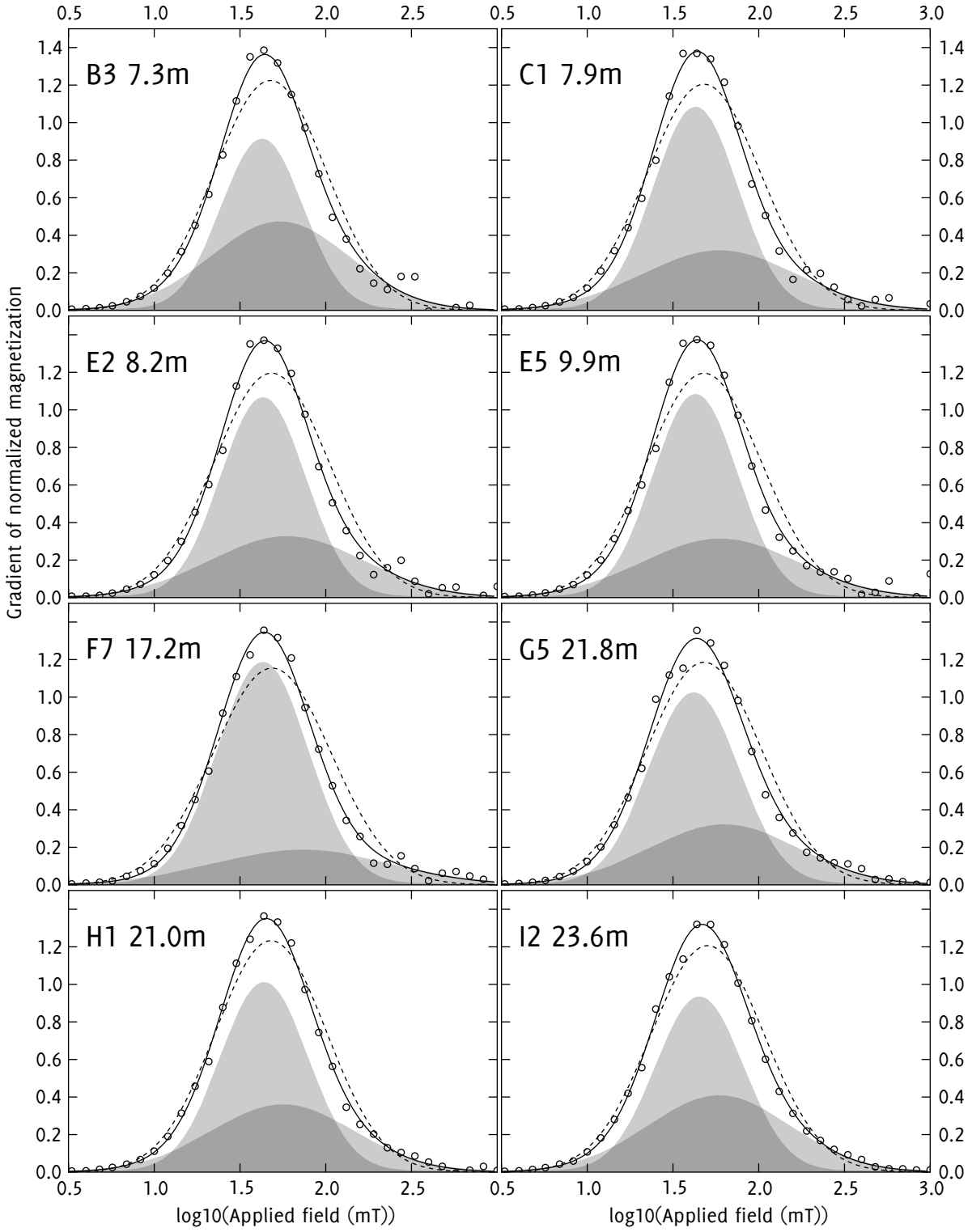

Figure 5.14 Normalized cumulative log-Gaussian fits for Fairfield IRM acquisition data. The circular points show the gradient of the experimentally determined IRM acquisition curve. The superimposed shaded curves are modelled log-Gaussian functions, and the black line is the sum of these two components. The dashed line shows the best fitting single Guassian curve.

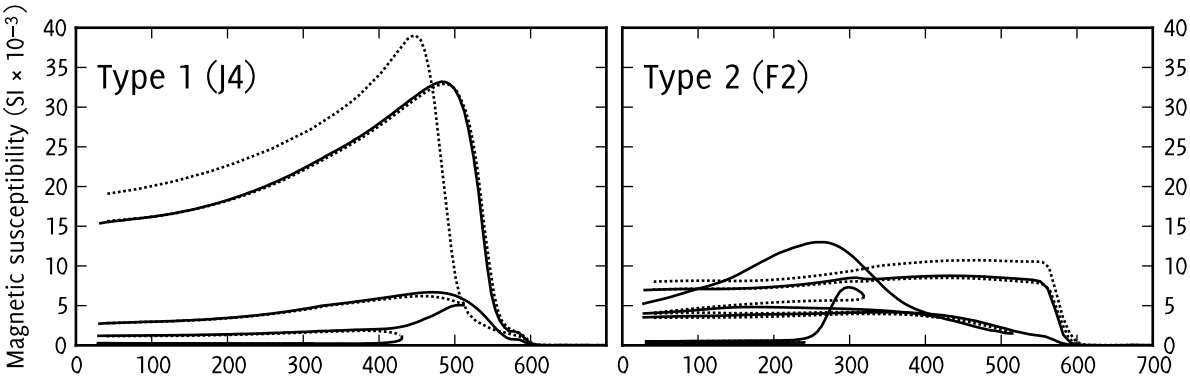

Figure 5.15 Temperature/susceptibility plots showing the two types of behaviour.

5.4.3.1 *Temperature dependence of susceptibility*

I measured the temperature dependence of susceptibility for ten samples spaced through the section. The behaviours fell into two categories which I refer to as types 1 and 2, illustrated in figure 5.15. Most of the samples (type 1) showed behaviour similar to the three whole-rock samples from the rock magnetism study figure 3.7 (p. 48). For these samples, there was little or no detectable alteration in susceptibility up to 400°C. The 400–500°C heating step produced major (twofold or greater) irreversible increases in susceptibility, indicating mineral alteration. The 500–600°C step created huge (two orders of magnitude) increases in room-temperature susceptibility, indicating the creation of a ferromagnetic mineral. The altered samples showed strong Hopkinson peaks in the 500°C region just below 600°C, suggesting that the alteration product was magnetite (possibly with a small degree of oxidation or cation substitution). The complete lack of susceptibility above 600°C indicates that the samples contained no haematite, nor any minerals which would alter to haematite on heating to 700°C.

The type 2 samples begin to alter at a lower temperature, with susceptibility increases from around 250°C, and undergo a complex series of alterations up to 600°C, at which point susceptibility drops (as for the type 1 samples) to near zero. It is tempting to interpret the susceptibility increase at 250°C and subsequent peak at 300°C as evidence for pyrrhotite (Curie temperature 320°C), in keeping with the IRM results in section 5.4.3, but on closer examination this conclusion is tenuous: the peak does not appear on the cooling curve, suggesting that it is associated with the formation of a new mineral phase rather than the Curie point of a mineral which was initially present. The peak does

not appear on the next heating step; since Wehland *et al.* (2005) found that pyrrhotite was stable up to 420°C, this is evidence against its presence. Additionally, if pyrrhotite is present it should be associated with a higher contribution from the magnetically harder component 2 in the IRM data; however, site 12 shows type-1 thermal susceptibility behaviour despite a 41% contribution from coercivity component 2.

5.4.4 *Summary of magnetic mineralogy*

Overall, the magnetic mineralogy of the samples is fairly consistent throughout the section, showing the same characteristics as the samples studied in detail in chapter 3. The coercivity spectra confirm the presence of magnetite, but their cumulative log-Gaussian decomposition suggests that pyrrhotite is also present. The thermal susceptibility curves confirm the presence of (possibly slightly altered) magnetite, but do not show any evidence for pyrrhotite. Once more I interpret the second component as a high-coercivity magnetite population; while this does not fit the type curves of Symons and Cioppa (2000), the H'_{cr} values are mostly within the larger range (10–63 mT) given by Peters and Dekkers (2003). (The IRM sample from site F7 has a second component with $H'_{cr} = 74.1$, but – given the weakness of the second component in this sample, and the caveats of Heslop *et al.* (2002) concerning the accuracy of fits for overlapping components – it can probably be reconciled with the values of Peters and Dekkers (2003).)

5.4.5 *Thermal demagnetization*

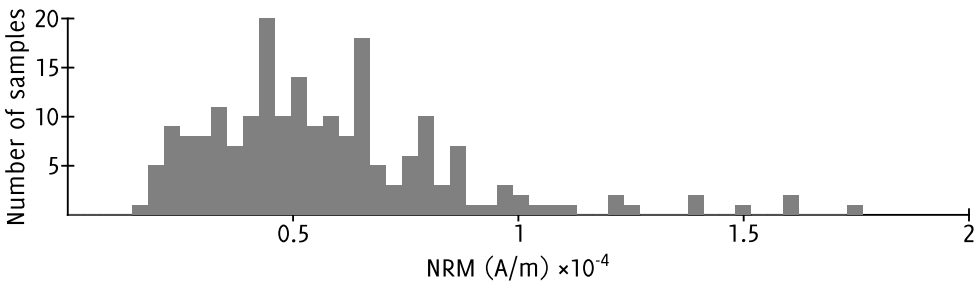

Figure 5.16 Histogram of NRMS of Fairfield Quarry samples

The samples presented significant challenges for palaeomagnetic analysis. They all had very weak NRM intensities, in the range 15–180 μA/m (mean 56 μA/m,

standard deviation 28 μA/m). As figure 5.16 (p. 147) shows, the distribution of NRMs was uneven and strongly positively skewed. Only 12 of the samples had NRMs exceeding 100 μA/m, of which 9 are from the sites 13–15 (heights 23.9–24.7 m). The high NRMs correlate with a decrease in glaucony, consistent with the inverse correlation between glauconitic content and saturation remanence found in chapter 3. However, glaucony cannot be the only control on NRM, since samples from the non-glauconitic Quarries Siltstone Member in the lower section do not show higher NRMs than the glauconitic parts of the section. Chapter 4 describes the techniques I used to increase the accuracy of magnetic moment measurements.

As in the temperature-dependent susceptibility experiments, the samples underwent thermal alteration at relatively low temperatures: usually alteration happened in the 200–400°C range, in most cases at around 300°C. The temperatures are slightly lower than for the TDMS studies on average, possibly because of the argon atmosphere used in the latter. Alteration was indicated by sharp increases in susceptibility, usually accompanied by major excursions in remanence. Since alteration occurred long before demagnetization was complete, I used the great circle remagnetization analysis technique described by McFadden and McElhinny (1988) to determine the characteristic remanences of the samples. This method is introduced in section 2.2.2.2 (p. 26).

5.4.5.1 *Demagnetization behaviours*

General characteristics

During progressive thermal demagnetization, mineral alteration was indicated unambiguously by susceptibility increases, but in many cases the sample magnetizations began to vary randomly some tens of degrees before the susceptibility spike. I attribute this variation to the onset of mineral alteration: given the low magnetizations of all the samples, a very small amount of alteration would be sufficient to disrupt the demagnetization curve. The Bartington loop sensor used to monitor thermal alteration during demagnetization has a relatively low sensitivity, and may thus be incapable of detecting the earlier stages of alteration.

A few samples showed a sharp change in the direction of the demagnetization path at the second or third point (50–75°C). I took this to be the effect

of slight VRM imparted during sample collection or preparation, and excluded the initial point or points from analysis where it occurred.

Due to the low initial remanences, all demagnetization paths showed a significant amount of random noise. However, trends in the demagnetization paths were still discernible in most cases.

Viscous overprinting

In most cases, initial demagnetization paths were directed strongly downward, consistent with the erasure of a viscous overprint acquired during the current normal chron. I tested this hypothesis by examining the directions of the first demagnetization steps of all the samples; the mean direction was 352.8° declination, −68.3° inclination (direction not adjusted for bedding, on the assumption that the tilting occurred prior to the Brunhes–Matuyama reversal). Although the data are very noisy, the direction of the site GAD field (0° declination, −64° inclination) is well within the nonparametric bootstrap 95% confidence interval of the PCA directions (an ellipse with semi-axis lengths of 20.5° and 17.8°). The direction confirms that this initial portion of the demagnetization curve is due to a Brunhes normal viscous magnetization.

Types of demagnetization behaviour

I classified the demagnetization behaviours of the samples into one of four types, which are detailed below.

Type SN: single component, not origin directed

SN was the dominant behaviour type, shown by 60% (120 out of 201) of the samples studied. The demagnetization path described a single straight line in three-dimensional space, directed towards a point other than the origin. I took this point to correspond to the primary depositional or post-depositional remanence of the sample, which had not begun to demagnetize noticeably by the time mineral alteration halted the study. The actual demagnetization endpoints were not reached during demagnetization, but could be inferred by great-circle path analysis when enough samples were available from a single site. Figure 5.17 (p. 150) shows three examples of type SN behaviour.

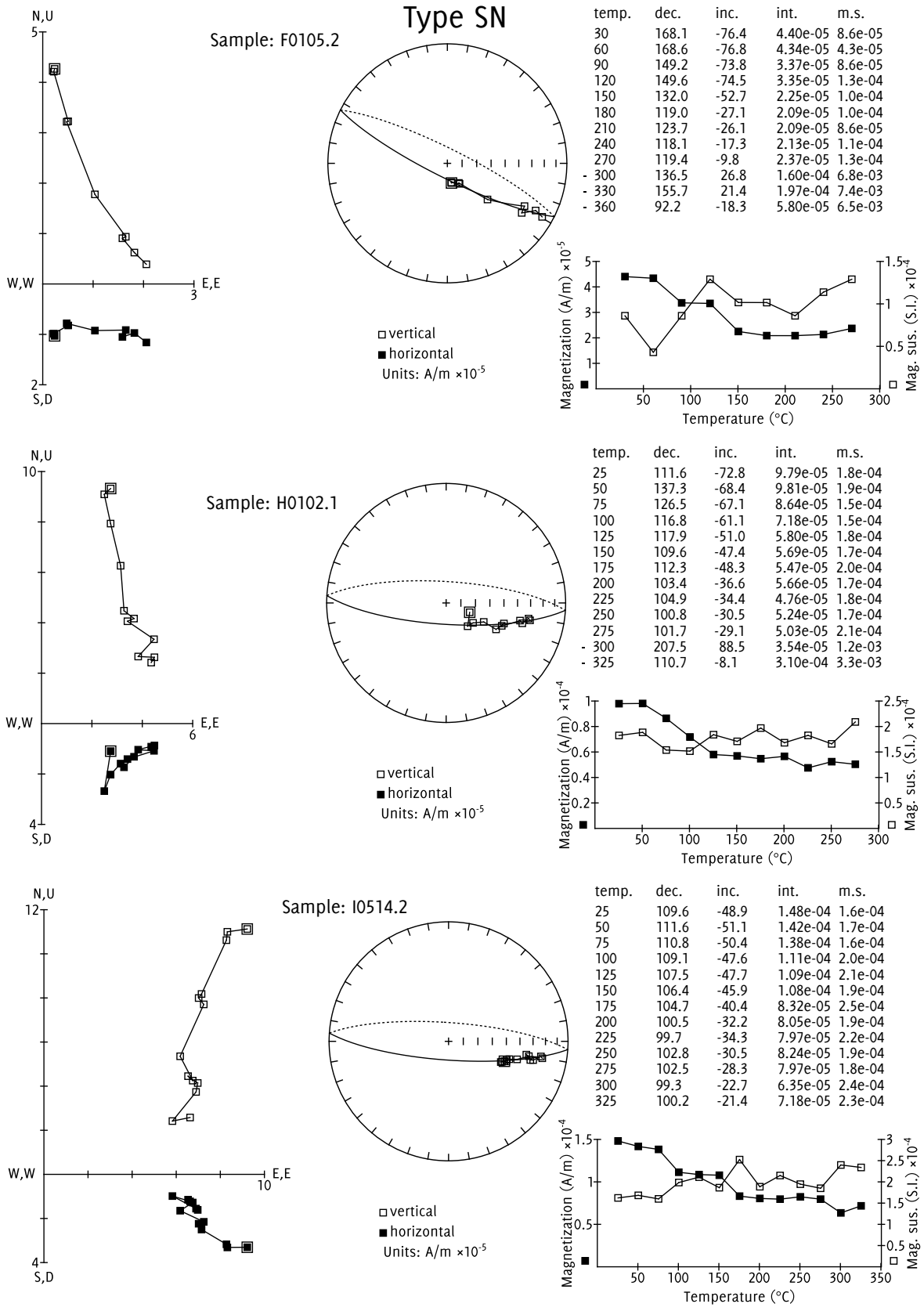

Figure 5.17 Type SN demagnetization behaviour, from sites F01, H01, and I05. Great-circle fits are shown on the equal-area plots.

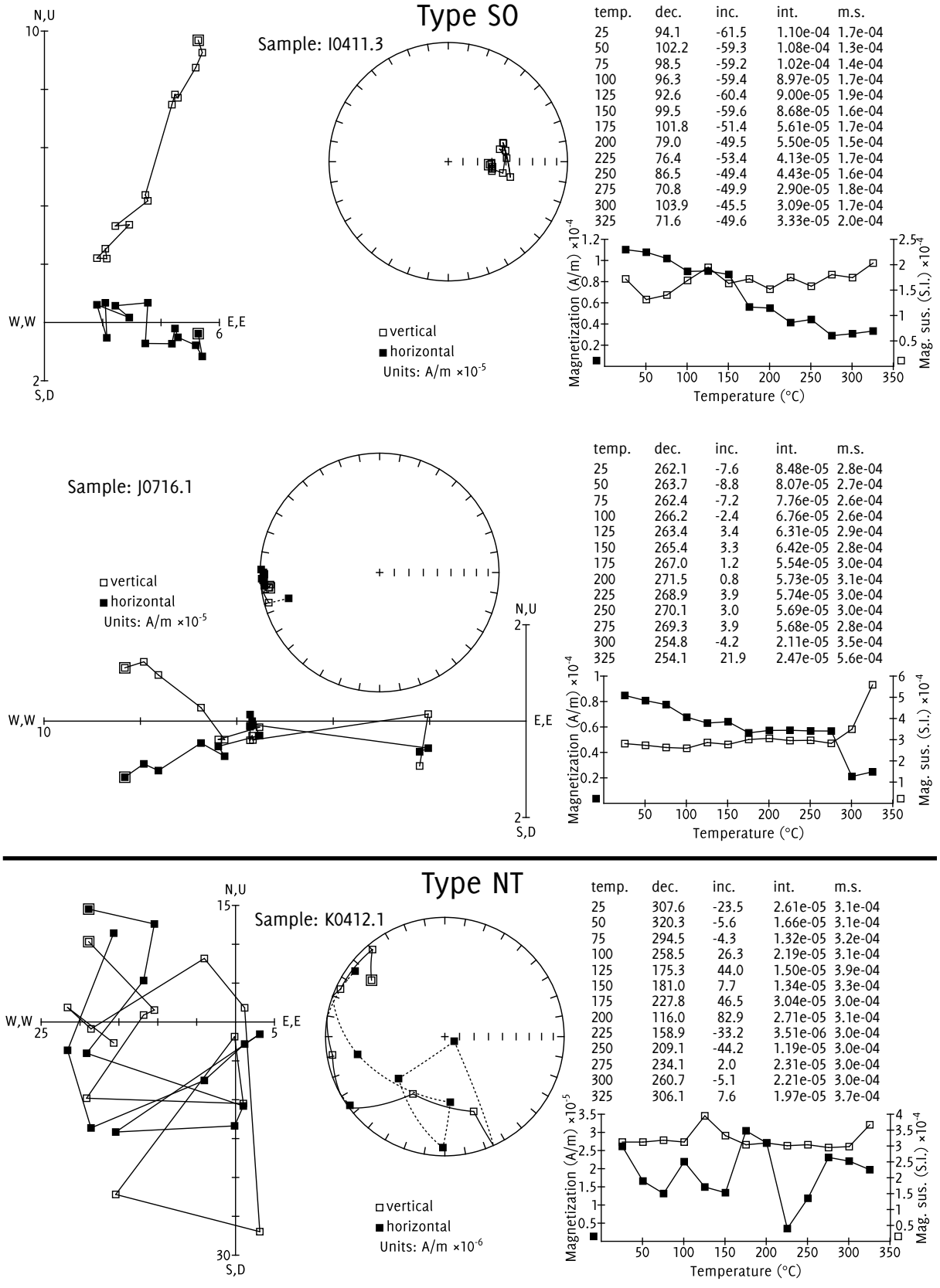

Figure 5.18 Demagnetization behaviours: type so (top and centre) and type NT (bottom)

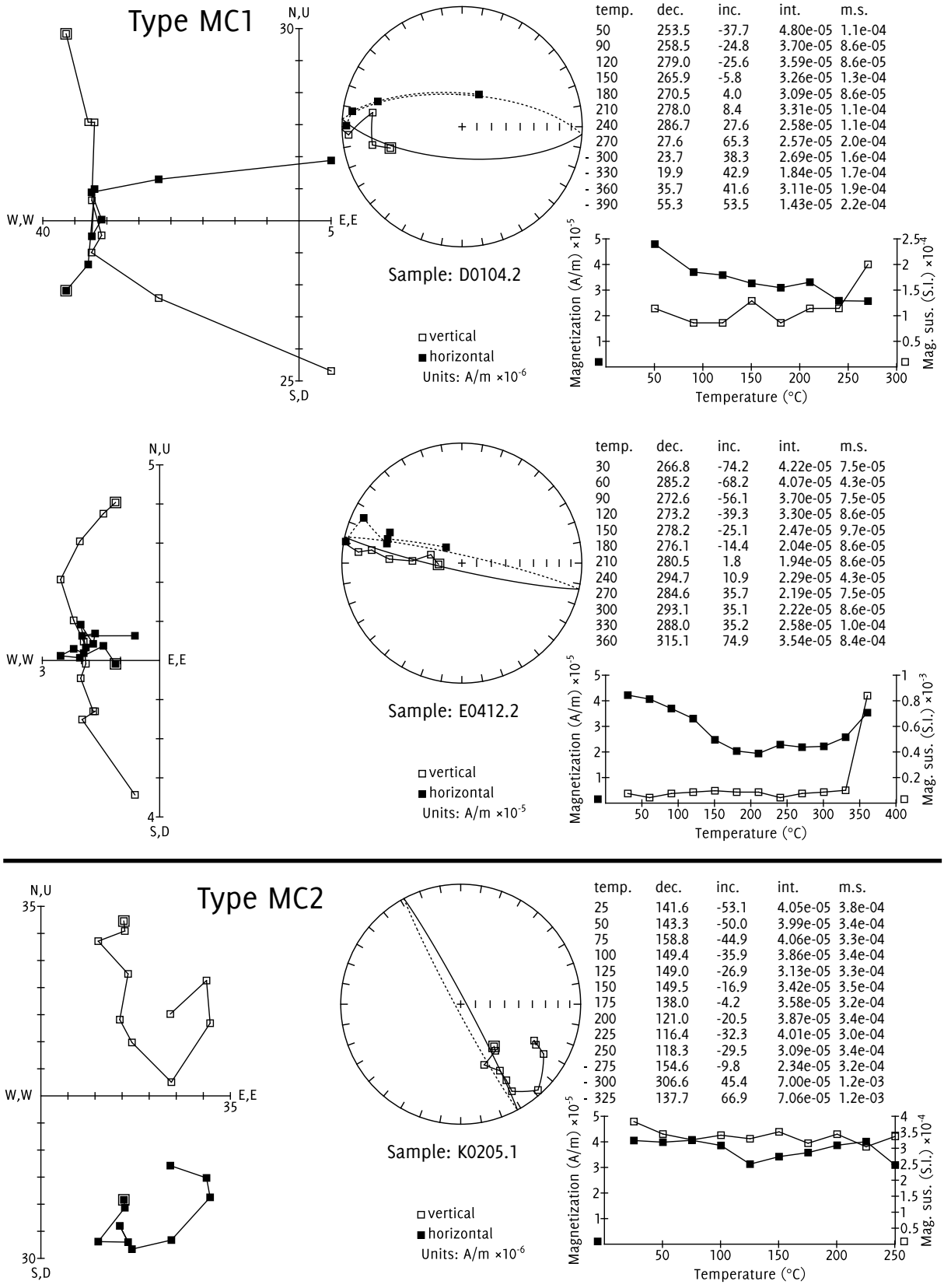

Figure 5.19 Type MC1 demagnetization behaviour (top and centre), and MC2 demagnetization behaviour (bottom). Great-circle fits are shown; in the bottom figure, the great-circle fit is to the first component only.

Type SO: single component, origin directed

17% (34⁄201) of the samples fell into this category. These samples had demagnetization paths trending approximately towards the origin. The direction of the demagnetization trends did not correspond to the current geomagnetic field at Fairfield, nor to any plausible ancient magnetic field direction from the latest Cretaceous or early Palaeocene. I interpreted these directions as representing a secondary remanence, with the primary magnetization either entirely absent due to lack of magnetic material, removed or replaced by chemical alteration, or too weak to be detectable beneath the stronger secondary signal. No palaeomagnetic direction could be determined from these samples. Figure 5.18 (p. 151) shows examples of this behaviour.

Type MC: two components

In 9% (19⁄201) of the samples, two demagnetization components were identifiable. The second component generally appeared at around 180–220°C and was thus usually obscured by alteration after 3–4 heating steps. There was often overlap between the two components, indicated by a demagnetization path describing a continuous curve in three dimensions rather than two straight segments. For 3% of all samples (type MC1; 7 samples) the plane of the two demagnetization components contained the origin, and the path of the *normalized* demagnetization vectors thus followed a single great-circle segment despite the two different directions. For 6% of all samples (type MC2, 12 samples), the two components did not both occupy a plane through the origin, and the normalized vector path thus contained two great-circle segments. The MC1 samples were in most cases amenable to great-circle remagnetization analysis, since the two vectors could effectively be treated as one. The MC2 samples presented greater difficulties: usually no great circle could be fitted, either because the number of points representing the second component was insufficient for reliable determination, or because of overlapping demagnetization spectra. Figure 5.19 (p. 152) shows examples of these behaviours.

Type NT: no discernible components

This type comprised 14% (28⁄201) of the samples. The magnetization of these samples changed in a disordered manner: in some cases the demagnetization

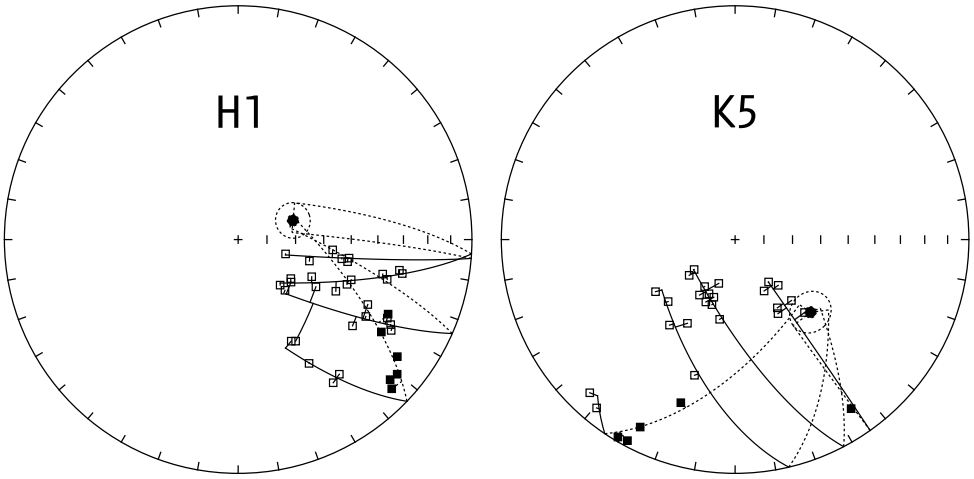

Figure 5.20 Illustrative great-circle intersections from Fairfield Quarry demagnetization data at sites H1 and K5. The round dot shows the best-fitting site mean direction at each site. The small circle around the dot does not show the α_{95} vaue determined by the algorithm (which is 0.9° at H1 and 1.3° at K5), but the greatest perpendicular distance between a great-circle demagnetization path and the site mean direction.

paths seemed almost random; in others there were faint suggestions of trends, but insufficient collinear or coplanar points to pick directions with any degree of confidence. Figure 5.18 (p. 151) shows an example of type NT behaviour.

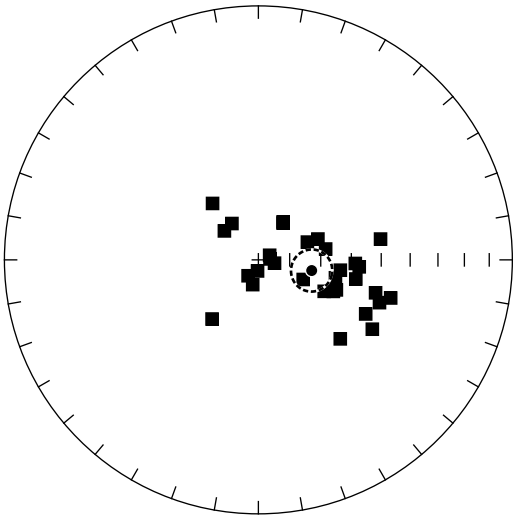

Figure 5.21 Formation mean direction for Fairfield Quarry section. Square points are site means, circular point is formation mean, and dashed circle shows Fisherian 95% confidence region.

5.4.5.2 *Palaeomagnetic directions*

None of the sample remanences in this study reached the origin during demagnetization, due to the early onset of mineral alteration. I attempted a great-circle fit to each sample's demagnetization data, but in several cases the data were so noisy that no interpretation was possible. I applied the McFadden and McElhinny (1988) algorithm to any site where three or more great circles were successfully determined. I then discarded any sites where the k value, as determined by the algorithm, was below 10. After this winnowing, 31 usable sites remained out of the 58 originally sampled.

Figure 5.20 shows two examples of site mean directions determined by the intersection of great-circle paths. Table 5.5 gives the parameters for all 31 sites for which a reliable fit was possible. All the inferred final directions for the sites lay in the lower hemisphere, most of them in the south-eastern quadrant with inclinations above 50°, indicating a reversed palaeofield and anticlockwise tectonic rotation. Since none of the sites showed a normal polarity, a reversal test cannot be performed.

Dec.	Inc.	α_{95}	k
101.3	72.6	6.7	16.1

Table 5.4 Formation mean direction for Fairfield Quarry

I determined a mean vector and error ellipse for the directions using Fisher (1953) statistics. The results are shown in figure 5.21 (p. 155) and table 5.4. The inclination of 72.6°, with a 95% confidence interval of about 65–80°, is an excellent fit with the palaeofield at New Zealand's inferred location at the end of the Cretaceous (see section 5.1.3). The declination of 101.3° implies a tectonic rotation of around 70° since the time of deposition, somewhat greater than the 45–60° suggested in section 5.1.3. However, the orientation of the eastern South Island prior to 45 Ma is poorly constrained, and the 95% confidence region would allow for a rotation as low as 55°. Since the sampled section spans the K-Pg boundary which lies within the C29r chron, a reversed direction is to be expected at least for the samples from the immediate region of the boundary. Figure 5.22 (p. 158) shows this chron in the context of the surrounding international and New Zealand stages and GPTS.

5.5 Conclusions

5.5.1 *Results of the study*

Despite the low magnetizations and noisy demagnetization data of the Fairfield samples, magnetostratigraphy – in conjunction with the known position of the K-Pg boundary within the section – was successful in constraining the entire studied section within the narrow (65.118–65.861 Ma) range of the C29r chron. The previous bound for the bottom of the section, based on the range of *M. druggii*, was around 69.5 Ma. The previously known uppermost age, as determined by the range of *T. evittii*, was around 63.5 Ma, but this limit is poorly dated (Hollis, 2003, p. 310).

The oriented drill samples, as well as providing the material for the magnetostratigraphy, allowed me to determine palaeocurrent flow and its variation through the lower part of the section through measurements of AMS.

Figure 5.23 (p. 161) shows a summary stratigraphy of the section, marking only the sites for which a reliable site mean direction could be obtained.

Site	H (cm)	N	T_1 (°C)	T_2 (°C)	Dec.	Inc.	α_{95}	k
K5	2870	4	25–75	150–250	134.0	53.1	24.9	51.5
K3	2822	3	25	175–325	80.8	68.1	23.5	799.9
K2	2792	4	25–50	150–225	70.1	73.3	58.2	10.3
K1	2768	4	25	150–275	113.6	74.3	15.8	125.6
J6	2690	3	25	175–200	105.3	44.3	36.4	248.8
J3	2580	3	25–75	200–325	218.1	65.9	149.7	35.9
I3	2390	3	25–75	225–275	320.9	66.6	86.8	70.7
H6	2300	4	25	150–250	310.4	75.7	30.9	33.7
H5	2270	4	25–50	175–275	112.8	63.8	31.1	33.3
H4	2240	4	25–50	150–250	85.4	86.3	47.3	15.0
H3	2200	3	25–50	275–325	324.0	75.6	72.2	96.0
H1	2100	4	25–75	200–275	70.7	69.8	17.4	104.4
F8	1757	4	25	150–250	33.8	75.8	27.8	41.3
D1	1721	4	50	270	33.1	75.5	33.9	28.2
F7	1718	4	25	175–225	101.1	57.9	10.5	286.5
F6	1664	3	25–50	175–200	184.3	86.5	2.9	51013.3
D3	1621	3	50	180–240	97.2	63.4	10.8	3768.5
F4	1557	4	30–120	180–270	212.9	84.0	30.5	34.6
D2	1511	4	50	180–240	105.7	50.4	30.3	34.9
F3	1505	4	30–90	180–270	192.9	81.9	5.3	1092.9
F2	1446	4	30–90	150–270	67.8	86.1	22.5	62.6
F1	1405	4	30–120	210–270	116.8	50.9	21.4	69.1
C4	984	3	50–120	270	80.3	49.6	110.8	66.5
E4	948	4	30	210–300	101.6	84.7	20.4	75.7
C3	940	4	50	270–330	93.9	57.3	24.4	53.6
E3	875	3	30	210–270	115.5	66.6	40.8	273.4
C2	870	4	50–120	240–300	121.3	46.4	29.2	37.6
E2	818	4	30	210–270	111.1	63.1	22.3	64.0
C1	790	4	50	210–240	103.1	64.5	5.6	1006.5
B3	731	4	50	210–270	109.5	48.1	28.8	10.1
B2	640	3	50	210–240	92.1	58.7	32.3	429.3

Table 5.5 Site demagnetization data. H is the height in the section. N is the number of great circles used in the fit. T_1 is the temperature of the lowest demagnetization step used for great-circle fitting; if different temperatures were used for different samples within the site, the range is given. T_2 is the highest temperature (or range of temperatures) for great-circle fits. Dec and Inc are the declination and inclination of the inferred magnetization component. α_{95} is the 95% confidence angle and k the estimated precision parameter; see text for notes on their interpretation.

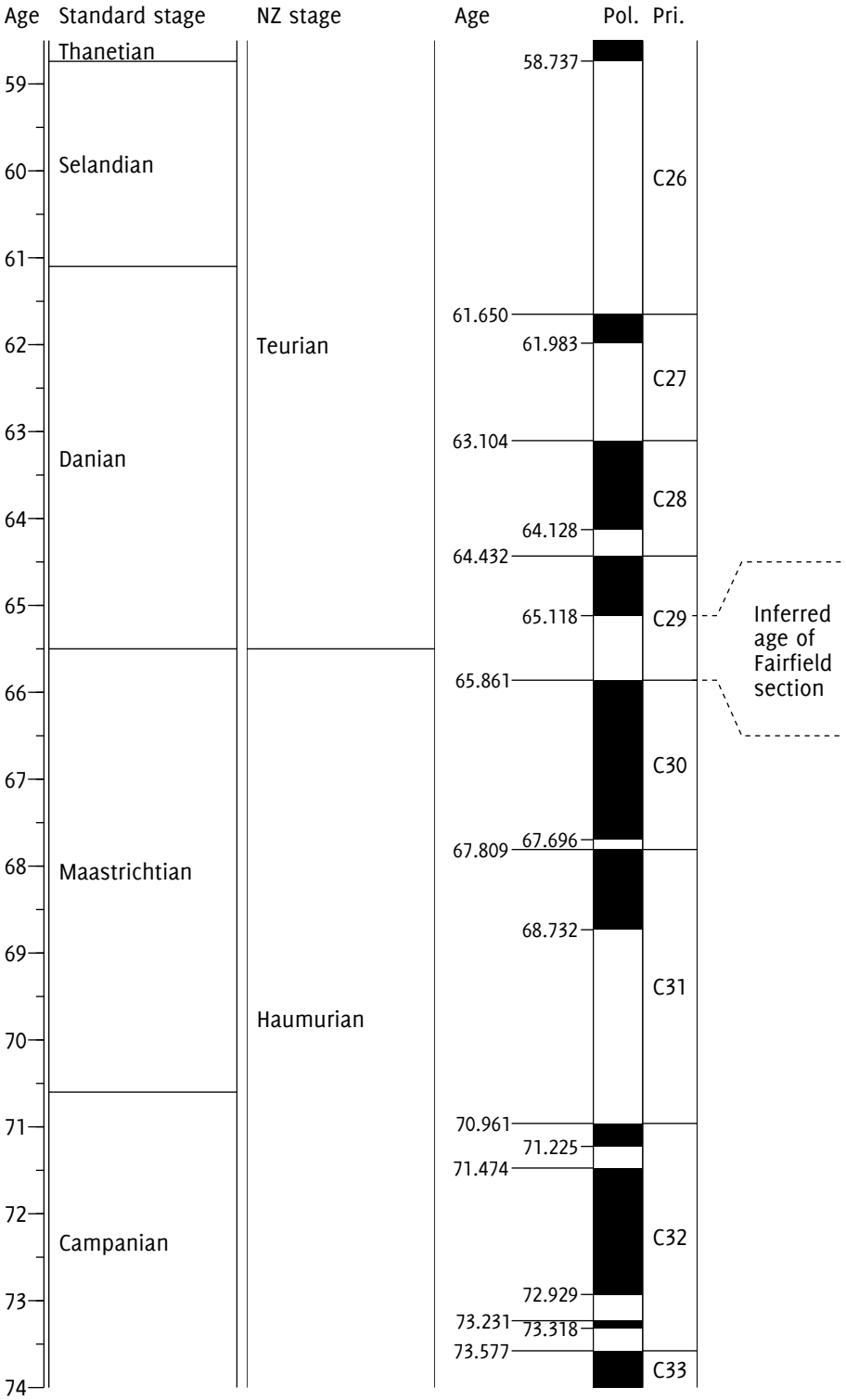

Figure 5.22 Timescale showing the age of the Fairfield Quarry section as determined by reversal magnetostratigraphy and (via correlation with the sedimentary log of McMillan, 1993) by dinoflagellate biostratigraphy.

The figure also shows the location of the K-Pg boundary as determined by McMillan (1993). Sedimentation rates can be constrained by relating the magnetostratigraphy to the stratigraphic height. In the portion of the section above the K-Pg boundary, 8 m of sediment has been deposited in less than 382 kyr, implying a minimum mean sedimentation rate of only 21 mm/kyr; it is likely, however, that two of the unconformities suggest periods of non-deposition or erosion (see section 5.5.2) and that the actual depositional sedimentation rate may thus have been somewhat higher. If (as discussed in section 5.5.2) the top of the sampled section in fact corresponds to C28r rather than C29r, the estimate for the minimum sedimentation rate is not greatly affected: the duration of C28r (302 kyr) is similar to that of the Palaeogene portion of C29r.

Below the K-Pg boundary, a maximum of 361 kyr of time is represented by 16 m of sediment, giving a minimum sedimentation rate of 44 mm/kyr. Again, there is a discontinuity – between the Saddle Hill Silstone Member and the Steele Greensand Member – which accounts for an unknown amount of time and may imply a higher depositional rate. In interpreting the magnetostratigraphy, it is also necessary to consider the two gaps, from 10–14 m and 18–21 m, in the sampling sites for which directions were determined. Would it be possible for one or both of these gaps to contain a normal chron, altering the magnetostratigraphy? A comparison of the log in figure 5.23 with the magnetostratigraphy in figure 5.22 (p. 158) shows that this is implausible: the gap would have to contain at least the whole C30n chron, representing 1.835 Ma; this would require a sudden change to a sedimentation rate of under 2.2 mm/kyr, for which there is no evidence in the lithology. It is also unlikely that the unexposed sections mask additional unconformities, since McMillan (1993) reported none in the corresponding parts of his log.

Current directions were only determined for the lowermost 12 m, due to the inverse fabric of the upper section. Within the lower part, however, there is a clear rotation of current direction as determined by principal axis orientation (from north-south to east-west in present-day tectonic orientation) and a weakening of the current intensity (as determined by wider dispersion of directions).

The formation mean direction determined for the section agrees with the rough constraints provided by the known tectonic history of the region (see section 5.1.3), but the declination (102° with a 95% confidence interval of ±12°)

implies a tectonic rotation, relative to the GAD field, of at least 66°; this is at the high end of the rotation extrapolated from the reconstructions of Sutherland (1995).

5.5.2 *Ambiguities of the magnetostratigraphic interpretation*

The assignment of the entire section to the C29r chron is the simplest and most obvious interpretation of the palaeomagnetic data. In view of the unconformities within the section, however, some caveats are necessary.

There are six unconformities in the uppermost 9 m of the section. McMillan (1993), however, considered that only two of these (the K-Pg boundary at 21.2 m, and the unconformity at 25 m) constituted parasequence boundaries. These unconformities correspond to the two earliest Teurian unconformities (U/C5.2 and U/C5.3) discussed by McMillan and Wilson (1997) in their allostratigraphy of coastal southern Otago. McMillan (1993) attributed the other four unconformities to storm-induced emplacement, on the basis of sedimentological evidence such as grit and gravel clasts and absence of corresponding unconformities in nearby sections. These unconformities should therefore not represent any significant amount of time.

The two significant unconformities, however, may encompass enough time to affect the magnetostratigraphic interpretation. The dinoflagellate study of Willumsen (2003) did not find that basal Paleocene *C. cornuta* Interval Subzone at Fairfield Quarry, implying a missing time interval at the start of the Palaeocene. It is thus possible that this hiatus contains the C29n chron, and that the reversed magnetozone above the K-Pg unconformity in fact corresponds to C28r rather than C29r. Correspondence with C27r or any younger chron is unlikely, since this would conflict with the *T. evitti* age reported by McMillan (1993) and confirmed by Willumsen (2003); for the same reason I consider it unlikely that the unconformity at 25 m conceals the C28n chron.

5.5.3 *Possible further work*

It is unfortunate that palaeocurrent determinations were only possible for the lowermost 12 m of the section, particularly since the K-Pg boundary is contained within the upper part. It may be possible to recover a primary, depositional fabric from the rock despite the dominance of the inverse fabric due to

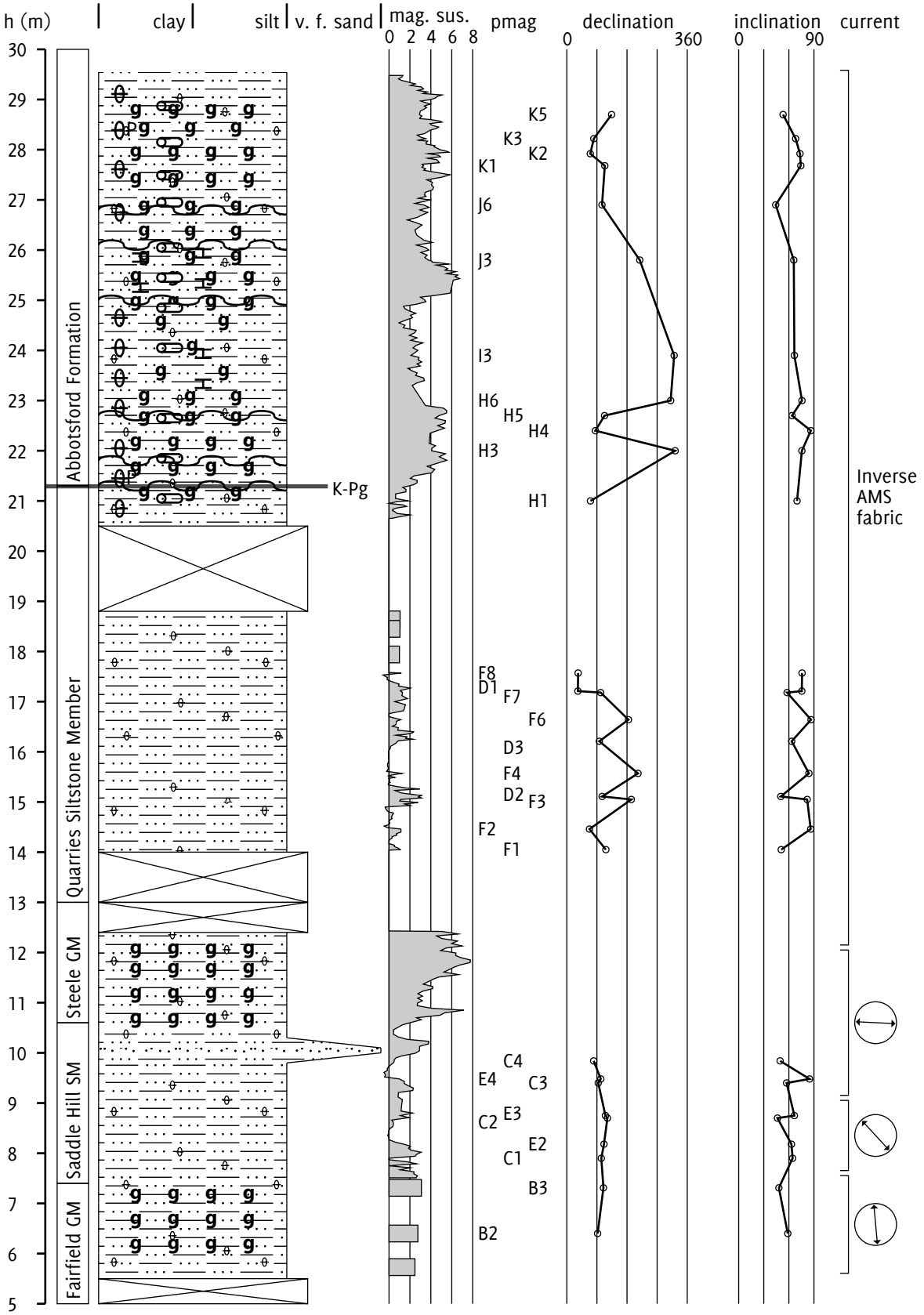

Figure 5.23 Section log showing only palaeomagnetic sites for which a valid site mean direction was determined. All successfully determined site mean directions were reversed. Rightmost column shows maximum AMS axis as indicator of palaeocurrent. Note the K-Pg boundary at 21.2 m

siderite. Heating has been found to be capable of isolating different elements of a composite fabric (e.g. Henry *et al.*, 2003). Hirt and Gehring (1991), investigating ironstone samples, succeeded in transforming a siderite-dominated inverse fabric into a normal fabric by heating to 500°C. AMS data has also been combined with measurements of the anisotropy of anhysteric remanent magnetization (AARM) to separate ferromagnetic and paramagnetic fabrics (Borradaile *et al.*, 1999). Such studies require careful interpretation of the sample mineralogy, but can be a powerful tool for separating composite fabrics (Urrutia-Fucugauchi, 2007).

I did not sample the uppermost 10 m of the Fairfield Quarry section, because it was impossible to find an exposure which was both accessible with palaeomagnetic drilling equipment and amenable to correlation with the rest of the section. With the use of ropes, however, it may be possible to extend sampling to the top of the section, and perhaps to locate the start of the C29n chron. Sampling past the chron boundary would improve the accuracy of the dating and allow the use of a palaeomagnetic reversal test as a further check on the fidelity of the formation mean directions. It may also allow the extension of the palaeocurrent record further into the Palaeocene, if the inverse fabric problem can be resolved.

It may also be possible to extend sampling downward. The Taratu Formation exposure on the south-east face of the quarry – showing about 12 m of exposure in a 1980 photograph in McKellar (1990) – is now submerged beneath a tailings pond. However, further sampling may be possible on the west side of the quarry where the bedding dip elevates the Taratu Formation to a more accessible height, though it is not certain that the coarse-grained lithology would be suitable for palaeomagnetic study.

6 Mid-Waipara River Section

> Before starting again for a longer journey into the Southern Alps, I wished to examine the interesting region of the Middle Waipara… . In the geological portion of this Report some details will be found on this district, of which it can truly be said that it offers us the key to unravel the relations in which our young secondary and old tertiary beds stand to each other.
>
> – Julius von Haast, *Geology of the Provinces of Canterbury and Westland, New Zealand* (Haast, 1879)

6.1 Introduction

This chapter presents a palaeomagnetic analysis of Palaeocene sediments exposed as part of the of the Cretaceous-Cenozoic mid-Waipara river section. Within this section, I took samples from a 56 m, Palaeocene section of the lower Waipara Greensand, and analysed them for magnetostratigraphy and rock magnetic properties. Figure 6.1 (p. 165) shows the sampling area. The goal was to integrate the palaeomagnetic samples with an integrated biostratigraphic analysis from the same sites to improve the age resolution for palaeoclimatic interpretations of the section. My rock-magnetic analysis included the measurement of anisotropy of magnetic susceptibility to provide an indication of the palaeocurrent at time of deposition.

6.1.1 *Background*

The Waipara River region is situated on the eastern South Island of New Zealand north of Christchurch, to the east of the Doctors Range and Mount Grey area. The area has been the subject of geological interest for well over a century, beginning with the brief description of the Kowai River outcrops by Forbes (1855). Investigation of the mid-Waipara River itself followed swiftly, and T. H. Cockburn Hood discovered plesiosaur bones there in 1859 (Owen, 1861; Hood, 1870). Much work in the region followed in the 1860s and 1870s, with Haast (1871) producing the first map. A few decades later, Thomson (1920) was able to catalogue 35 publications on the area and allude to 'many other visits by those who have not published their observations'. The first detailed general map and description of the region was produced by Wilson (1963), who also provided a thorough review of previous publications. Subsequent work

on the mid-Waipara River section has sought to constrain, biostratigraphically and geochemically, the position of the Cretaceous-Palaeogene boundary (e.g. Strong, 1984; Brooks *et al.*, 1986), now placed with certainty at the base of a glauconitic sandstone at the top of the Conway Formation (Hollis and Strong, 2003). The section has played an important role in palaeoclimatic investigations of the latest Cretaceous and early Palaeogene in the New Zealand region (e.g. Vajda and Raine, 2003; Hollis *et al.*, 2009). Scientists from the Institute of Geological and Nuclear Sciences (GNS) undertook thorough palaeontological and biostratigraphic sampling of the mid-Waipara River in early 2003, helping to resolve earlier stratigraphic ambiguities and gaps. The collections were detailed by Morgans *et al.* (2005), who also gave a brief review of previous micropalaeontological and palynological work on the section. The section described in this chapter forms one part of the section described by Morgans *et al.* (2005).

6.1.2 *Location*

The field area is shown in figure 6.1 (p. 165). The sampling sites are spaced along the true right bank of the Waipara River's middle branch, in the region of 43° 03′ 30″ S, 172° 35′ 35″ E. The sampling area corresponds to column 2 (west side of horseshoe bend) in the sampling scheme of Morgans *et al.* (2005), and the sampling locations were tied geographically and stratigraphically to the collections described in that report.

6.1.3 *Stratigraphy*

Almost all the mid-Waipara River outcrops are part of the Haumurian-Whaingaroan (late Cretaceous to Oligocene) Eyre Group (Field *et al.*, 1989), the exception being the Amuri Limestone at the top. The section sampled in this investigation comprises the lowermost 25 m of the Waipara Greensand, within the Mt Ellen Member, starting approximately 50 m (stratigraphic) above the Cretaceous-Palaeogene boundary. Two sites (D11 and D12) are somewhat higher stratigraphically, around 50–60 m from the bottom of the Waipara Greensand.

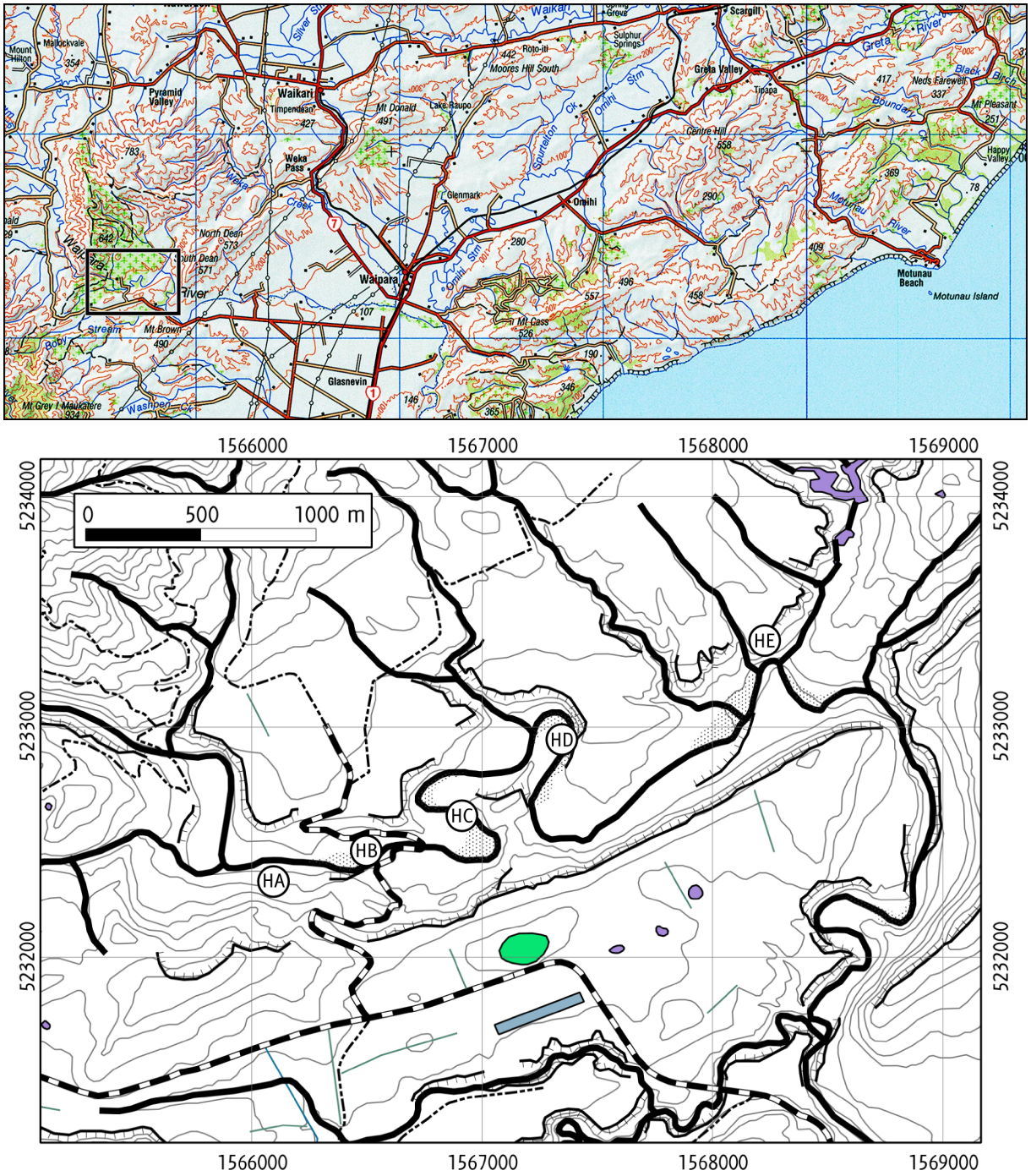

Figure 6.1 Map of the mid-Waipara River field area. The lower map magnifies the marked area on the upper map. The markers HA–HE correspond to the sections A–E described by Hollis and Strong (2003). The K-Pg boundary is exposed at section HA. Sample suites C and D, discussed in this chapter, were both obtained at section HC. Map datum: New Zealand Geodetic Datum 2000. Projection: New Zealand Transverse Mercator 2000. Topographic data are from LINZ Topo50 map BV24 (Waipara), edition 1.0 (2009). Crown copyright reserved.

6.2 Fieldwork

I made two visits to the section to collect oriented palaeomagnetic cores, in January 2008 (suite C, 10 sites, 38 cores) and January 2010 (suite D, 11 sites, 44 cores). (12 sites were actually drilled for suite D, but no oriented core was recovered from the first; the 11 sites used in this study are thus numbered D2–D12.) Samples were drilled with electric or petrol hand drills, most often at or near to the waterline at the time of sampling. Sampling site locations were logged with a handheld GPS unit, and on a stratigraphic column produced by Hugh Morgans of GNS. Full details of field equipment are given in Appendix C. At the time of the 2010 sample collection, the river stage and flow were approximately 0.35 m and 0.2 m^3/s respectively, as reported by the Environment Canterbury monitoring station at Waipara White Gorge, about 2 km downstream of the section.

Figure 6.2 (p. 167) shows a stratigraphic log (after Morgans *et al.*, 2005) of the sampled section, annotated with the positions of the palaeomagnetic sampling sites.

6.3 Laboratory work

I processed the samples at the OPRF; full details of equipment used are given in Appendix C.

6.3.1 *Sample preparation*

Many of the cores in suite C consisted of very friable, poorly lithified glauconitic sand; some were entirely disaggregated either by transport to the laboratory or by attempts to cut them into 22 mm samples. I used large amounts of adhesive (Aremco Ceramabond 571-L) to stabilize many of the surviving samples. The samples carried a very weak magnetization (usually around 50 μA/m) and the adhesive turned out to have sufficient magnetic remanence to contaminate its measurement. In the end, six of the ten sampled sites – almost all from concretionary horizons – yielded enough cohering, non-contaminated samples for palaeomagnetic measurement. All the samples from suite D were drilled from concretionary horizons and thus did not suffer the same problems: all eleven

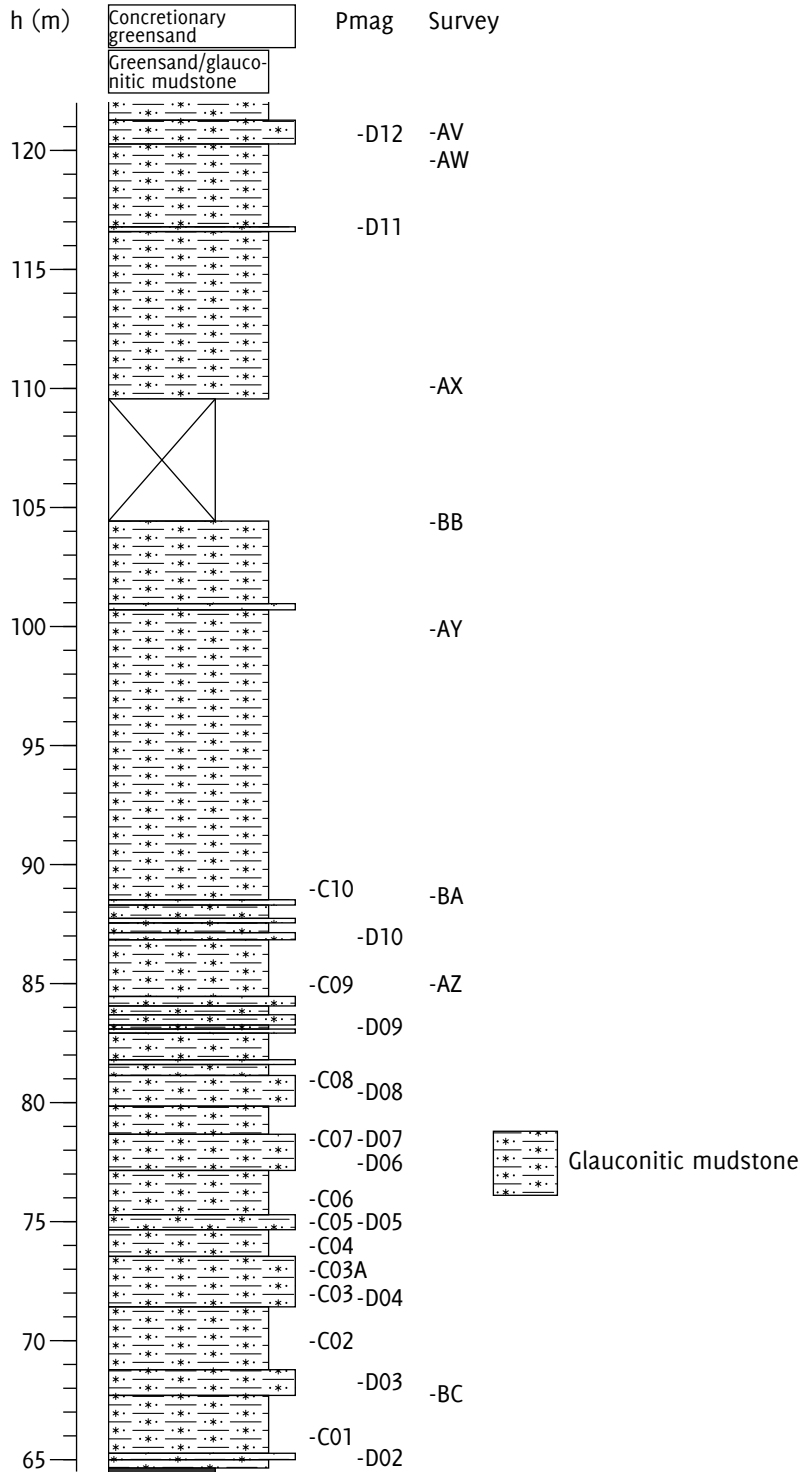

Figure 6.2 Stratigraphic log for the mid-Waipara River section, showing heights of palaeomagnetic sampling sites. Lithology and section heights are taken from figure 5 in appendix 1 of Morgans *et al.* (2005). The 'Pmag' column shows the heights of the palaeomagnetic drill sample sites, and the 'Survey' column marks the survey points defined by Morgans *et al.* (2005).

sites from suite D were used in the palaeomagnetic study. In total, the two sets of cores yielded around 170 samples.

6.3.2 *Isothermal remanent magnetization*

I conducted an IRM study to determine the remanent coercivity spectra of eight representative samples taken from sites throughout the studied section. I imparted remanences using a pulse magnetizer in 32 steps to a maximum field of 1 T. I then applied a series of increasing fields in the opposite direction, progressively erasing the previously imparted IRM, until the magnetization of the sample reversed in polarity. This procedure allowed me to determine the bulk remanent coercivity directly.

6.3.3 *Magnetic susceptibility*

For 150 oriented samples taken from both suite C and suite D, I measured the bulk magnetic susceptibility and the anisotropy of magnetic susceptibility in a kappabridge. I also measured the temperature dependence of magnetic susceptibility for nine powder samples taken from sites throughout the section (C01, D02–D09). I subjected each sample to seven cycles of heating followed by cooling to room temperatures, with peak temperatures of 100–700°C, increasing in 100°C steps. This procedure allowed me to check for room-temperature susceptibility changes indicating heating-induced mineral alteration. Samples were heated in an argon atmosphere and susceptibility measured in a 716 A/m field.

6.3.4 *Stepwise demagnetization*

I conducted a pilot study using AF demagnetization; this did not prove an effective technique (further details are given in section 6.4.3). I therefore used thermal demagnetization for the main study, in 25°C intervals from room temperature to 600°C. The demagnetization study used 80 oriented samples, comprising 4-5 samples from each of 17 sites.

6.4 Results

In this section I present the rock magnetic, palaeomagnetic, and magnetostratigraphic results of the Mid-Waipara River study. Data files for all the magnetic analyses are included on the data CD-ROM (appendix D).

6.4.1 *Isothermal remanent magnetization*

Figure 6.3 (p. 171) shows IRM acquisition and DC demagnetization curves for all eight samples in the IRM study. The samples are magnetically soft, reaching over 90% of saturation remanence by 0.2 T, which indicates a probable magnetite mineralogy and a definite absence of haematite or goethite (Peters and Dekkers, 2003, table 1). Table 6.1 (p. 170) shows the saturation magnetization, coercivity of remanence, and remanent acquisition coercive force for the samples. The saturation magnetization is very low – around 20 mA/m for most of the samples. I assume that the magnetization is carried by magnetite with a grain size in the range 0.02–10 μm, which encompasses the full size range of SSD and PSD behaviours (Maher, 2007, p. 253); then the volume-normalized saturation of the magnetite must be at least 21 kA/m (Peters and Dekkers, 2003, fig. 2b), implying a volume magnetite concentration below about one part per million. The magnetization is even lower than that of the glauconitic separates in the rock magnetism study of chapter 3 (figure 3.11, p. 52). All these samples are highly glauconitic, suggesting that here too the remanence carriers are diluted by the purely paramagnetic glaucony grains.

I analysed the coercivity spectra by using the Irmunmix program of Heslop *et al.* (2002) to express them as a sum of cumulative log-Gaussian functions (the technique is fully explained in section 3.4.2 on page 54). As with the samples from Fairfield Quarry, all the samples are well fitted with a superposition of two low-coercivity functions; figure 6.4 (p. 172) shows the fits graphically, and table 6.1 gives the parameters of the curves.

Each sample consists of the same two components, as shown by the similar positions and widths of the two peaks in each plot. The proportions of the components vary, but with the exception of the sample from site C01, each always accounts for at least 40% of the total magnetization. Component 1 shows lower $B_{1/2}$ and *DP* values, corresponding to both a lower coercivity and a lower range of coercivities; component 2 has a higher coercivity and a greater range, giving

Sample	SIRM	H_{cr}	H'_{cr}	— Component 1 —			— Component 2 —		
	mA/m	mT	mT	M_{ri}	$B_{½}$	DP	M_{ri}	$B_{½}$	DP
C01	50.5	34.3	41.6	0.77	1.58	0.30	0.23	1.85	0.48
D02	23.7	45.8	52.1	0.42	1.64	0.26	0.58	1.82	0.46
D02	23.7	45.8	52.1	0.42	1.64	0.26	0.58	1.82	0.46
D03	19.7	42.3	48.7	0.59	1.62	0.27	0.41	1.84	0.46
D05	20.9	44.5	50.7	0.40	1.63	0.25	0.60	1.80	0.44
D07	22.7	45.3	51.2	0.59	1.60	0.29	0.41	1.96	0.42
D09	17.4	46.6	54.0	0.57	1.61	0.30	0.43	1.98	0.41
D11	19.7	44.4	50.6	0.52	1.63	0.26	0.48	1.85	0.45
D12	23.0	45.6	51.3	0.55	1.66	0.25	0.45	1.81	0.45

Table 6.1 IRM parameters for Waipara River samples. SIRM is saturation magnetization; H_{cr} is coercivity of remanence; H'_{cr} is the remanent acquisition coercive force. See section 3.4.2, page 54 for details of component parameters.

a broader peak at a position further along the x axis. The separation between the two peaks is small compared to their widths, giving a large amount of overlap between them.

As in the study of chapter 3, the most obvious identifications are magnetite for the softer component and pyrrhotite for the harder. However, the small separation of the peaks, and the lack of other evidence for pyrrhotite found in the studies of chapter 3, lead me to believe that magnetite is also a plausible candidate for component 2, or that the two-component fit is in fact merely an artefact of the modelling technique and does not accurately reflect the mineralogy. Figure 6.4 also shows a single-component log-Gaussian model; although it gives a slightly poorer fit than the two-component model, it may be a better reflection of the mineralogy.

6.4.2 *Magnetic susceptibility*

The samples had a mean susceptibility of 3.55×10^{-4} (SI) (standard deviation 5.64×10^{-5} SI). To investigate the relationship of susceptibility with the remanence carriers, I assume that the remanence is carried by magnetite with a grain size in the range 0.01–10 μm; within this range the maximum recorded susceptibility of magnetite is around 6 SI units (Peters and Dekkers, 2003, fig. 2a;

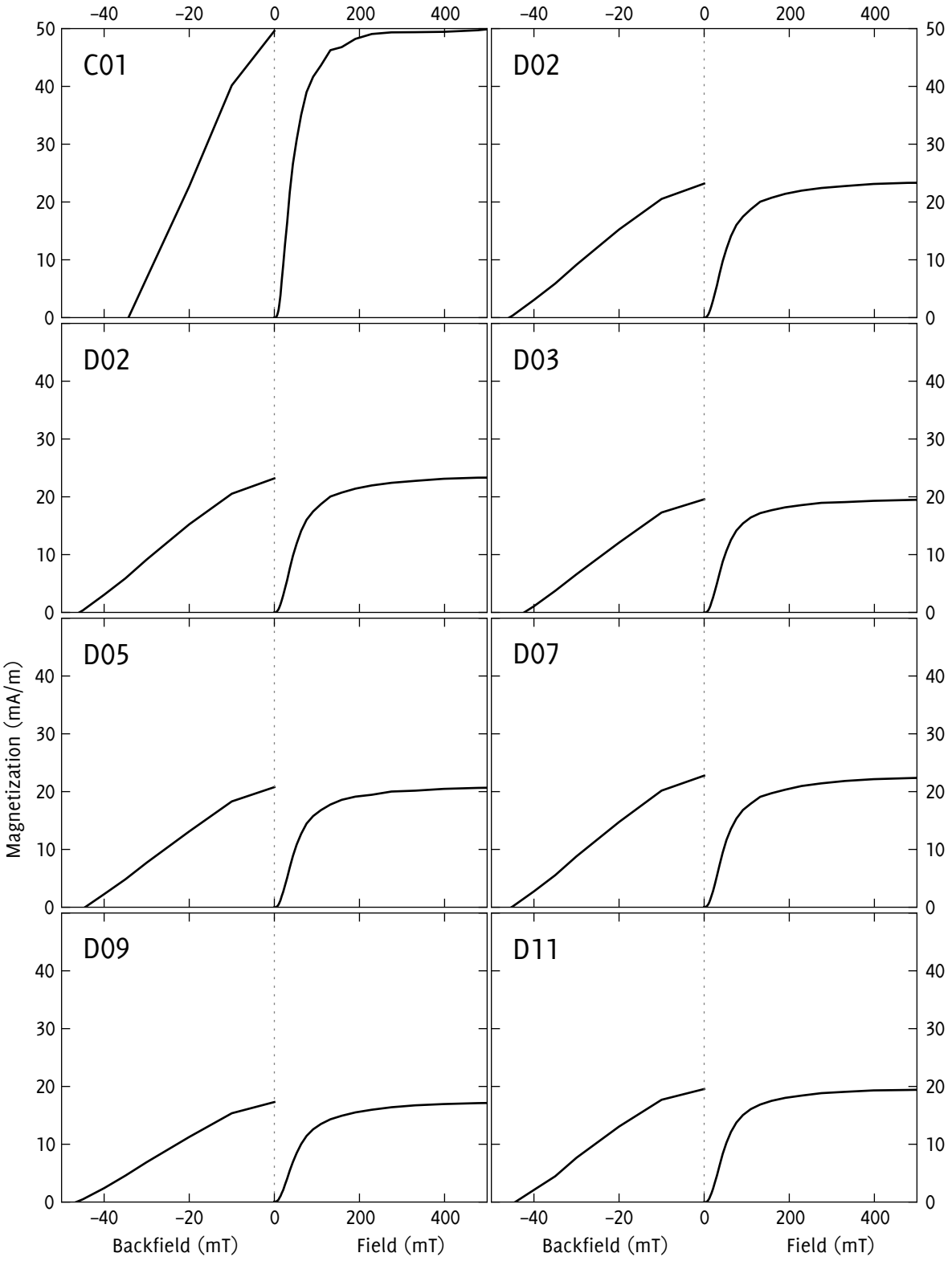

Figure 6.3 IRM acquisition and DC demagnetization curves for Waipara samples, shown respectively on the right and left parts of the graphs. IRM acquisition continued up to 1 T, but the x axis is truncated at 500 mT since minimal remanence is acquired beyond this point. Note the differing scales on the left and right portions of the x axes.

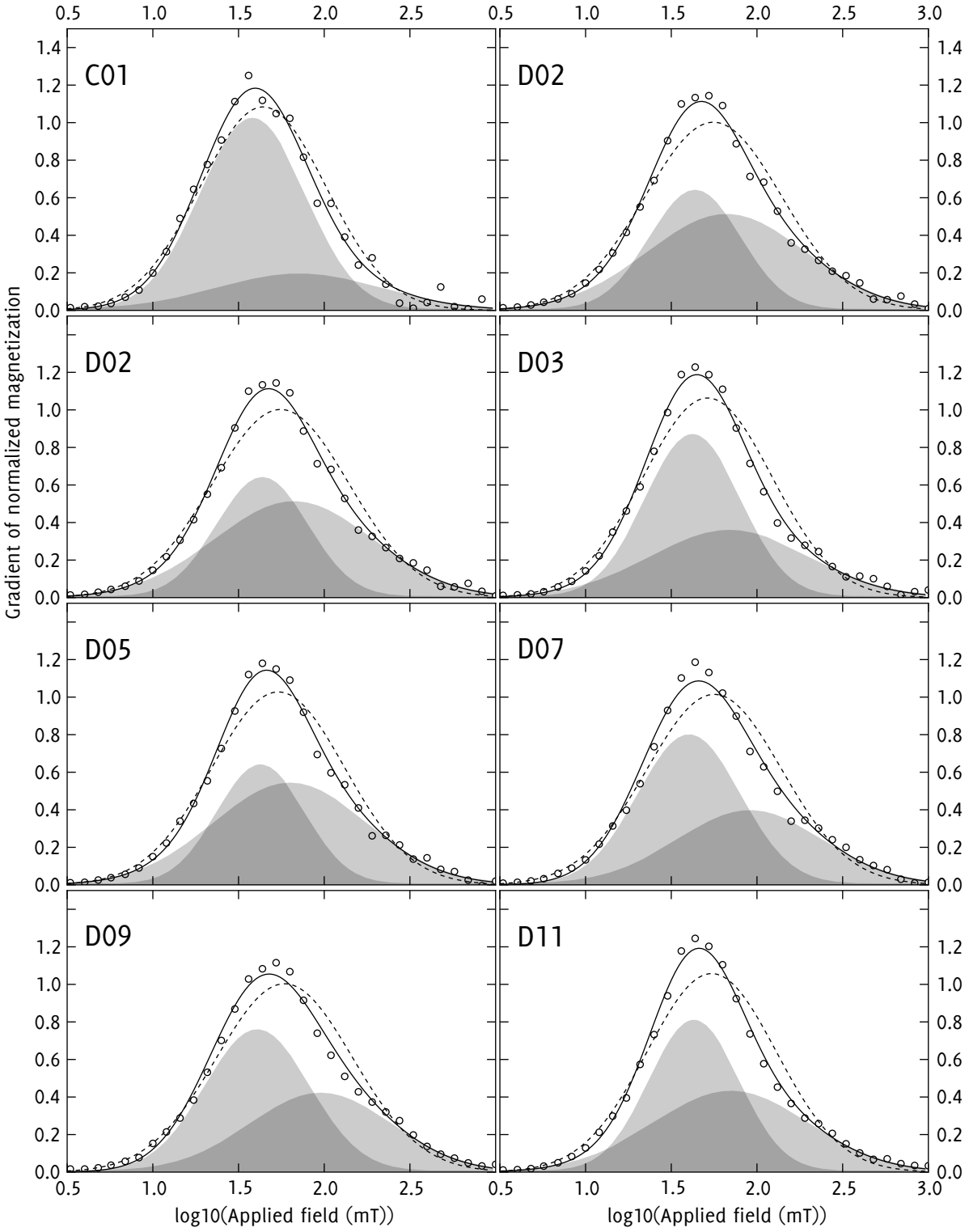

Figure 6.4 IRM acquisition gradient curves for Waipara River samples, fitted to the sum of two log-Gaussian functions. The circular points show the gradient of the experimentally determined IRM acquisition curve. The superimposed shaded curves are modelled log-Gaussian functions, and the black line is the sum of these two components. The dashed line shows the best fitting single Guassian curve.

Hunt *et al.*, 1995, table 1). Multiplying this by the magnetite concentration of 1 p.p.m. estimated in section 6.4.1 gives a volume susceptibility below 6×10^{-6} SI, so (given these assumptions) the susceptibility is not due to the remanence carrying component. The samples all contained over 50% glaucony, which is likely to be largely responsible for the susceptibility value: the measured susceptibilities are consistent with the range of $2.7–4.3 \times 10^{-4}$ SI for pure glaucony given by Bentor and Kastner (1965).

6.4.2.1 *Anisotropy of magnetic susceptibility*

The anisotropy of susceptibility was, in general, very low, in some cases below the noise level of the kappabridge. Jelínek (1996) described a statistical test (the F-test) to distinguish genuinely anisotropic samples from apparent anisotropy resulting from machine noise. I excluded all samples with an F value below 3.9715, corresponding to a 95% confidence level that the sample is anisotropic; 88 of the 150 samples passed the test. These samples had a mean corrected susceptibility factor P' of 1.002 (standard deviation 0.002). The shape factor T varied widely, with a mean of −0.019 and standard deviation of 0.411. The only clear trend in anisotropy parameters appeared at site C04, which had a strongly prolate fabric and significantly higher overall anisotropy. This site was the only one in the study not drilled from a concretion, suggesting that the fabric of the other samples is to some extent controlled by the concretionary material. Figure 6.5 plots P' against T for all 88 samples.

Despite the low anisotropy, the significantly anisotropic ($F > 3.9715$) samples from suite D show clear trends in orientation related to sedimentary bedding (the suite C samples appear more or less randomly distributed, possibly due to contamination by the adhesive used). The samples from the lower sites D02–D06 have a major axis in the horizontal plane aligned approximately NE/SW. The intermediate and minor axes are smeared towards a girdle distribution, but with the minor axis clustering towards the vertical and the intermediate axis towards the horizontal. This orientation distribution is consistent with a primary sedimentary fabric deposited in the presence of a NE/SW current (cf. e.g. Ellwood, 1980). The upper part of the section, comprising sites D07–D12, shows a more vaguely defined fabric with an approximately horizontal girdle distribution for the major and intermediate axes, and a near-vertical direction for the minor axis.

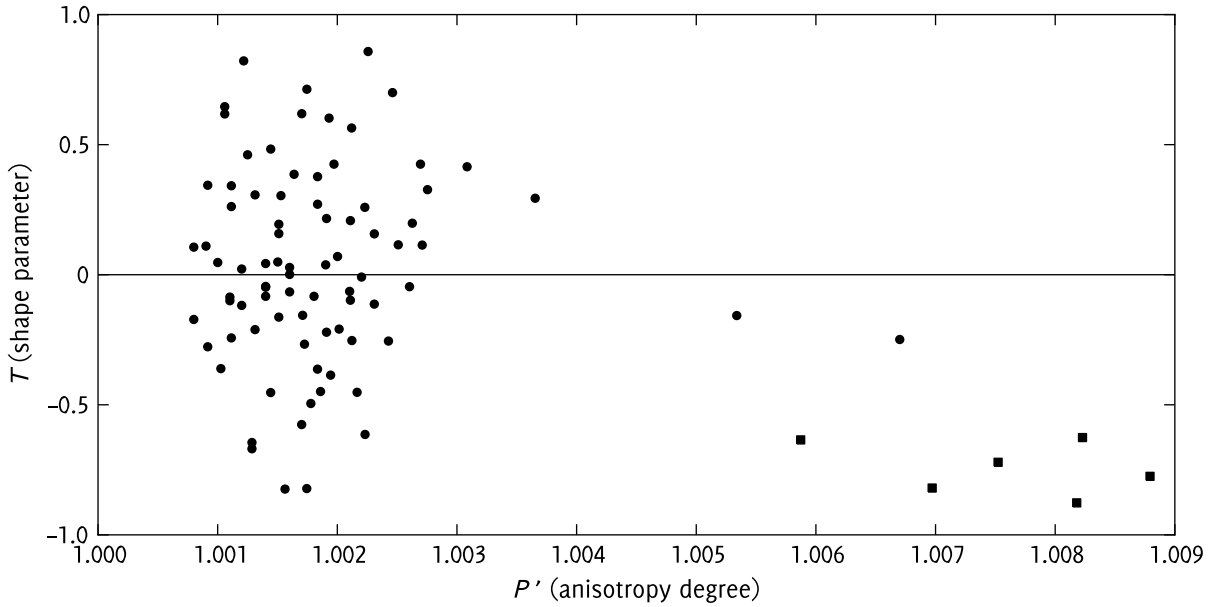

Figure 6.5 *P′–T* plot of anisotropy parameters for Waipara River samples. Samples from site C04 are shown as squares, all others as circles.

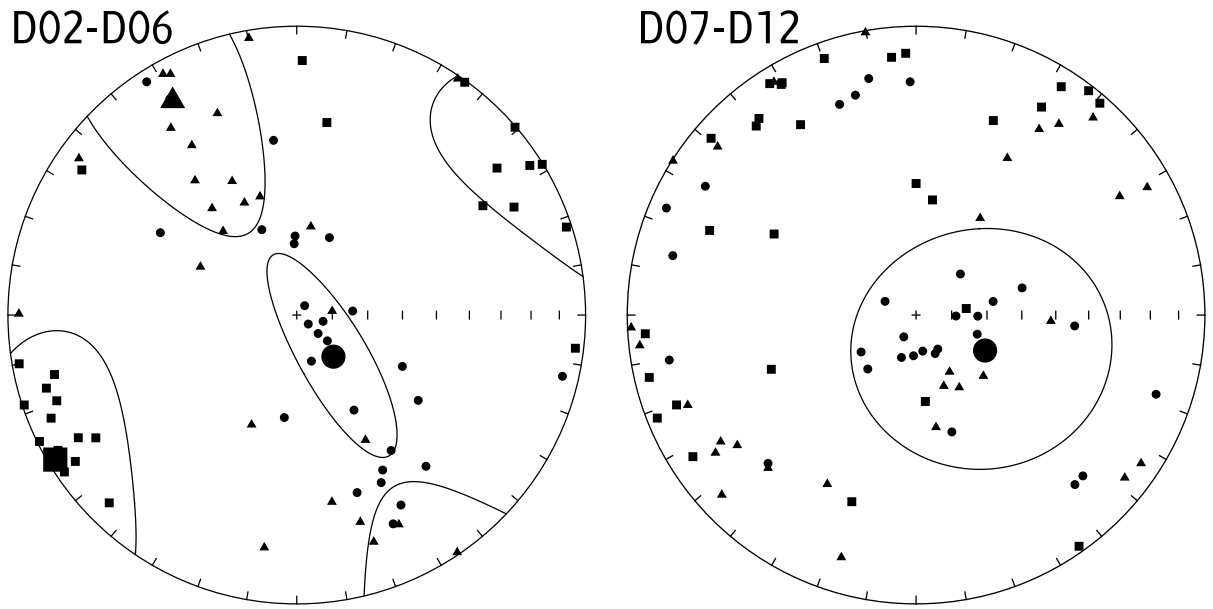

Figure 6.6 Principal axes of AMS data for all sites in suite D, divided into upper and lower subsets. Data are shown on equal-area projections. Squares denote the major axis, triangles the intermediate, and circles the minor. Mean directions are shown by large symbols. 95% confidence ellipses were calculated based on a parametric bootstrap calculation. Mean directions and confidence ellipses for the intermediate and major axes are not shown on the plots for sites D07–D12, as the confidence intervals are very large.

Figure 6.6 (p. 174) shows the distribution of AMS principal axes for the upper and lower parts of the section, with confidence ellipses determined by a parametric bootstrap algorithm. Table 6.2 (p. 175) gives the statistical para-

Set	N	Axis	D	I	η	D_η	I_η	ζ	D_ζ	I_ζ
D02–D06	27	Max.	239.1	2.9	21.8	145.2	35.1	33.8	341.6	53.8
		Int.	329.9	15.4	17.6	60.2	0.4	47.7	151.3	68.0
		Min.	138.6	74.4	9.5	239.4	3.1	33.3	330.2	15.1
D07–D12	29	Max.	323.3	19.9	125.6	217.4	6.1	44.2	115.7	62.2
		Int.	230.0	8.9	243.5	8.9	15.6	134.4	115.2	45.2
		Min.	117.2	68.1	33.9	2.1	8.3	37.7	269.4	18.2

Table 6.2 Statistical parameters for AMS data

meters for the fits.

6.4.2.2 *Temperature dependence of magnetic susceptibility*

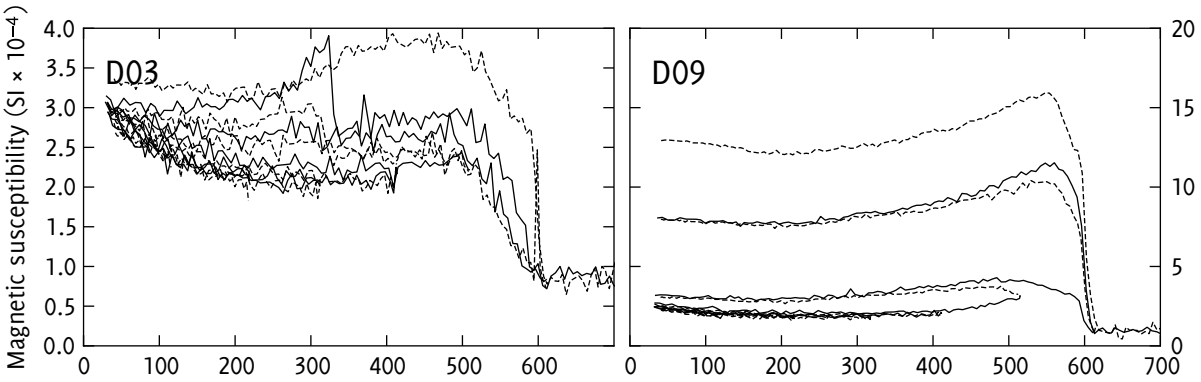

Figure 6.7 Temperature-susceptibility curves for two of the nine samples studied; note the different y-axis scales. Solid lines show heating curves, and dashed lines show cooling curves. D03 had the weakest susceptibility among the studied samples; its uneven susceptibility curves are due to susceptibilities close to the noise level of the kappabridge. Both samples show a sharp decline just below 600°C (magnetite) and D03 shows a Hopkinson peak at around 320°C after heating to 600°C (pyrrhotite produced by thermal alteration).

Most of the samples showed gently declining susceptibility, consistent with paramagnetic behaviour, up to 400°C, followed by significant irreversible susceptibility increases in the 400–700°C range, indicating heating-induced alteration. All the samples showed sharp drops to near-zero susceptibility around 600°C, often preceded by a visible Hopkinson peak. This behaviour was probably due to magnetite: although the magnetite contribution to room-temperature susceptibility is negligible, the susceptibility increase at the Hopkinson peak is sufficient to make it visible. (The slight variation of the observed susceptibility drops from magnetite's Curie temperature of 580°C can be accoun-

ted for by small degrees of oxidation and/or cation substitution). After the final heating step the susceptibilities of all samples (except the sample from site D03) had increased by a factor of 2–10. In general, both the increase in room-temperature susceptibility and the strength of the Hopkinson peaks was far less than than observed in the Fairfield samples (see figure 5.15 (p. 146), although the general pattern of behaviour was similar.

Due to the evidence of mineral alteration below the Curie point of magnetite, it is not certain that all the magnetite indicated by the Hopkinson peaks was present in the original samples. However, since the coercivity spectra also indicate magnetite, and since no Curie points are evident below that of magnetite, it is reasonable to conclude that not all the magnetite was an alteration product.

Apart from showing the presence of magnetite, the temperature-susceptibility curves are important in ruling out the presence of pyrrhotite, which if present would show a Hopkinson peak at its Curie point of 320°C. Five of the samples (from sites C01, D03, D04, D06, and D07) do in fact show pyrrhotite as an alteration product, appearing on the cooling curve of the 600°C step, and disappearing (probably due to alteration to magnetite) at the 700°C step. The clear visibility of the heating-derived pyrrhotite in the temperature-susceptibility curve gives confidence that any pyrrhotite present in the original sample would have been evident in the 400°C heating step.

The only sample to show alteration below the 500°C step was D08, which showed an irreversible doubling of susceptibility at around 260°C; further alteration occurred in the 500–600°C interval, and a susceptibility drop just below 600°C indicated that the alteration product was magnetite. This behaviour could be due to the decomposition of a non-magnetic mineral into magnetite, but it is also consistent with the behaviour reported for greigite by Roberts (1995); I will discuss the possible presence of greigite further in section 6.4.3.

Figure 6.7 (p. 175) shows results from two of the studied samples. In sample D03, the Curie point of magnetite is visible as a sharp drop with no clear peak preceding it. This curve shape is due to the superposition of the Hopkinson peak on the hyperbolically decreasing curve of the paramagnetic component. Evidently, in the 300–500°C region, the paramagnetic decrease and ferrimagnetic increase are of similar magnitude, giving a nearly horizontal susceptibility curve. In the sub-300°C portion of the curve, before the Hopkinson effect

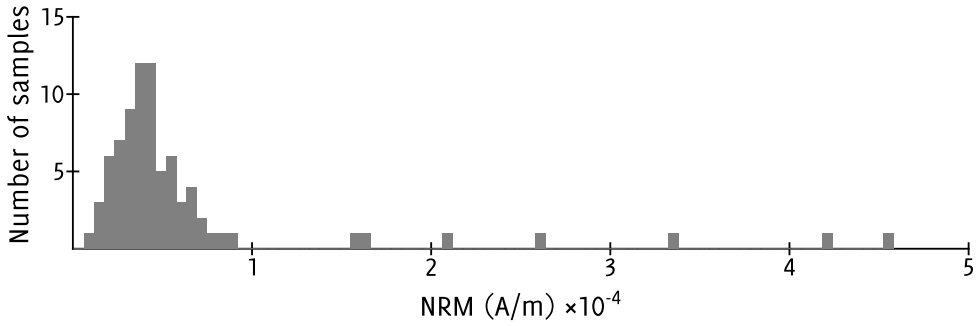

Figure 6.8 Histogram of initial remanences of Waipara samples

becomes significant, the paramagnetic decline can be discerned despite the high noise levels.

6.4.3 *Stepwise demagnetization*

The samples in the thermal demagnetization study had a mean NRM intensity of 59.5 μA/m, with a standard deviation of 78.5 μA/m. However, these parameters were skewed by seven outliers with much higher remanences than the majority of the samples; figure 6.8 shows the distribution of NRM intensities as a histogram. There is no discernible trend to the distribution of these higher remanences, which are more or less evenly spaced throughout the section. As with Fairfield Quarry samples of chapter 5, the more weakly magnetized of these samples approach the sensitivity limits of the OPRF magnetometer.

6.4.3.1 *AF demagnetization*

Despite the generally poor results of AF demagnetization on New Zealand sediments (see section 2.1.1.1), I performed a brief AF pilot demagnetization study on seven samples from set C. As for the Fairfield material, AF treatment appeared to have a randomizing rather than a demagnetizing effect on the weak remanences of the samples.

I considered the possibility that the noisy character of the AF demagnetization data might be due to a gyroremanent component in the mineralogy of the samples; the thermal susceptibility data from site D08 suggested the presence of greigite, which has been found to exhibit gyromagnetic behaviour (Hu *et al.*, 1998). Since gyromagnetic remanence is imparted perpendicular to the axis of demagnetization (Dankers and Zijderveld, 1981), it should be easy to detect by

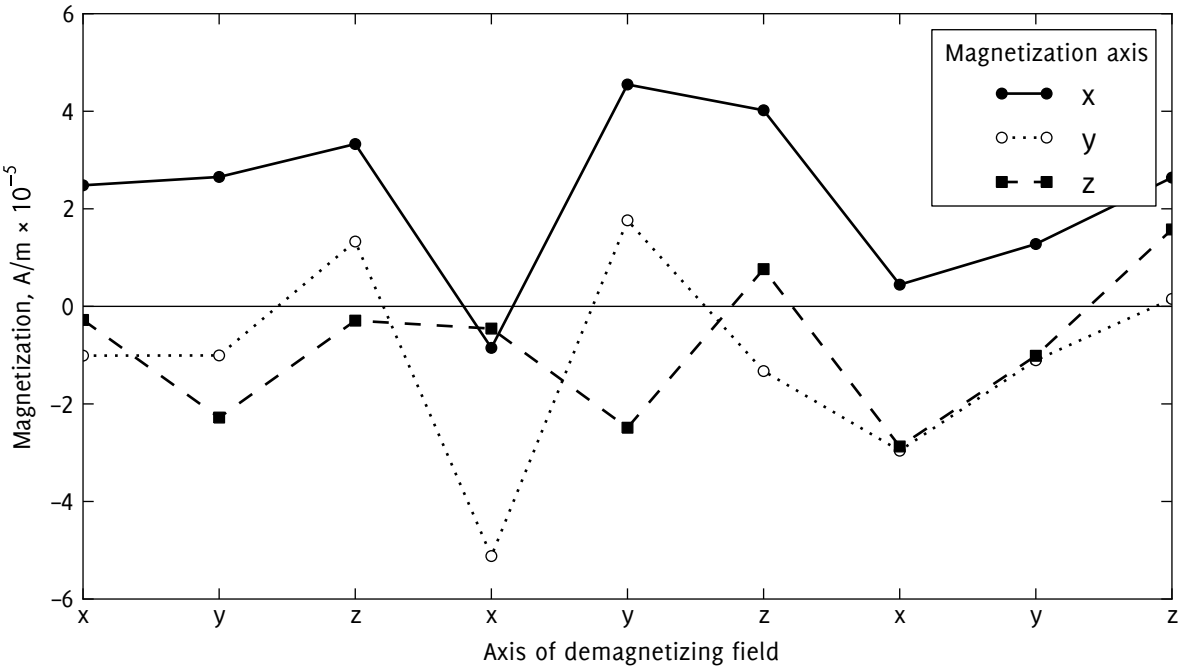

Figure 6.9 Test for GRM in mid-Waipara River samples. AF fields were applied sequentially in the directions labelled along the *x* axis. If GRM were being imparted, it would be expected that a field applied in, say, the *x* axis would erase most of the magnetization in that axis while imparting a magnetization in one or both of the orthogonal axes. No such behaviour is visible here.

applying AF demagnetization successively along three orthogonal axes. Each axis should then show a decline in remanence after demagnetization in that axis, and increases after demagnetization in the other axes.

I conducted a study on six samples from suite C, applying a sequence of nine uniaxial demagnetizations, cycling the AF field direction between three orthogonal axes. I used a field of 100 mT, since gyromagnetism has been found to be more pronounced at higher field strengths (Dankers and Zijderveld, 1981).

The results of this experiment (of which figure 6.9 gives an example) showed no clear evidence for GRM: the magnetization intensities along each axis appeared to fluctuate more or less at random in the range of 1–5 × 10^{-5} A/m. This lack of GRM argues against the presence of palaeomagnetically significant amounts of greigite in the samples.

6.4.3.2 *Thermal demagnetization behaviour*

I continued demagnetization up to 575°C, since no order-of-magnitude increases in magnetic susceptibility occurred during heating. However, examination of the demagnetization data revealed that significant mineral altera-

tion generally commenced at around 300°C, producing a two- or threefold susceptibility increase usually occurring over several heating steps. In most cases, this was followed by a decline in susceptibility from around 500°C; the most obvious interpretation is an intermediate thermal alteration product which underwent further alteration to a less susceptible phase – probably haematite, which has a high thermal stability and a lower magnetic susceptibility than many magnetic minerals. This behaviour differs from the thermomagnetic data obtained from the kappabridge, where alteration did not commence until 400°C and room-temperature susceptibility increased rather than falling in the 500–600°C heating step. The discrepancy can be explained by the argon atmosphere used in the kappabridge experiments, which would restrict oxidation. The palaeomagnetic samples acquired a reddish colour by the final heating step, whereas the kappabridge samples were dark grey after heating to 700°C, lending support to the haematite hypothesis.

There was evidence for alteration in the remanence data as well as the susceptibility data: beyond about 300°C (and sometimes at lower temperatures), the magnetization path generally became chaotic, with large jumps in random directions and no discernible trend.

Despite the fact that the samples had similar NRM intensities to those from Fairfield Quarry, the demagnetization paths were noticeably noisier in the Waipara samples. The fluctuations in the demagnetization trends can therefore not be entirely attributed to measurement noise: they are at least partly caused by a degree of random variation in the actual sample magnetizations.

6.4.3.3 *Types of demagnetization behaviour*

I classified the demagnetization behaviours of the 80 samples into four types.

Type SN: single component, not origin directed

SN was the most common behaviour type, shown by 57% (46/80) of the samples. The sequence of demagnetization vectors proceeded along a single (albeit often noisy) line in three-dimensional space; in no case did the magnetization path reach or point directly towards the origin. I interpreted the path as representing the progressive demagnetization of a secondary remanence component,

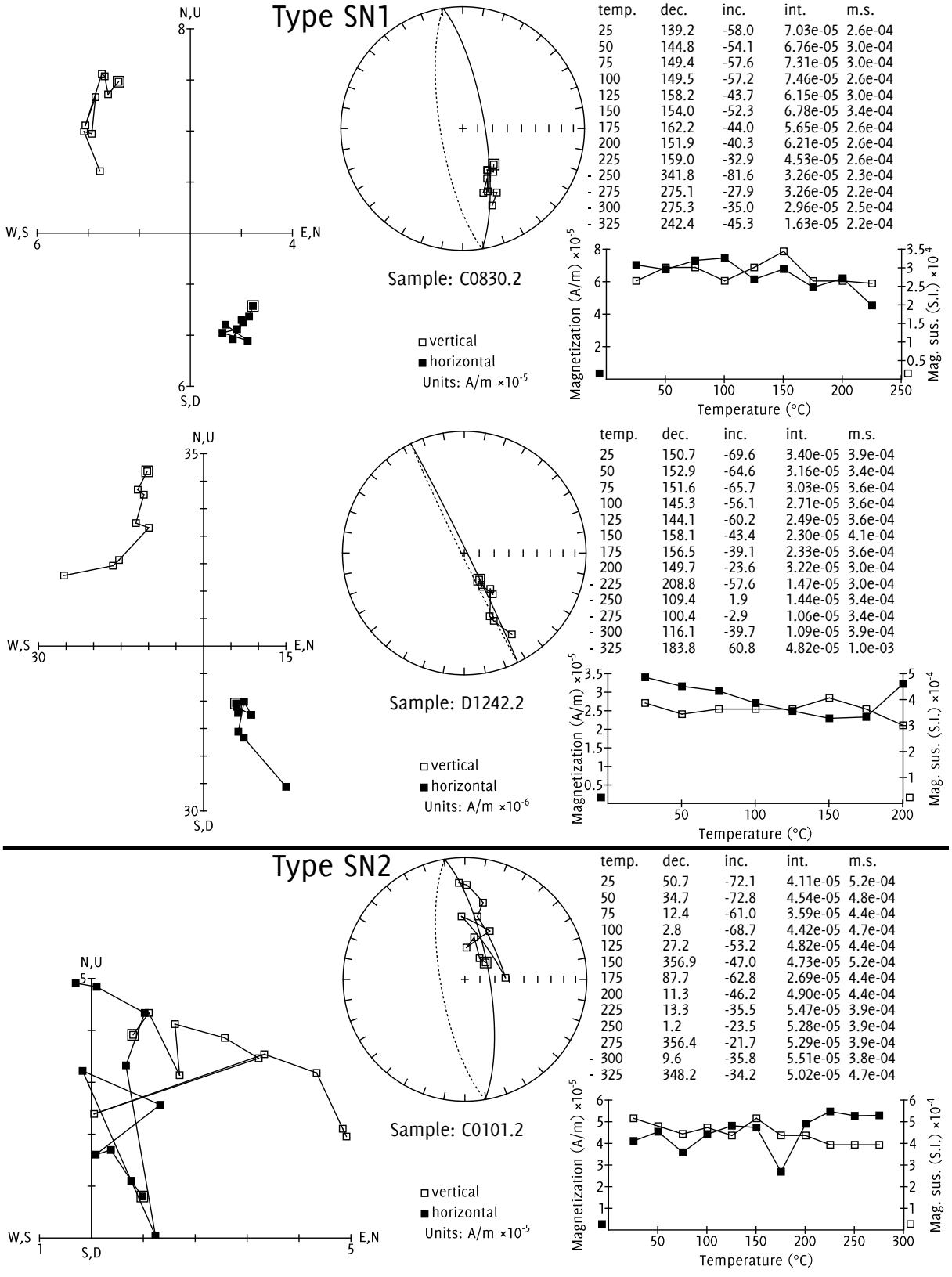

Figure 6.10 Demagnetization behaviours: type SN. Top and centre figures show type SN1 (distinct single component); bottom figure shows type SN2 (indistinct single component). Best-fit great circles are shown on the equal-area plots.

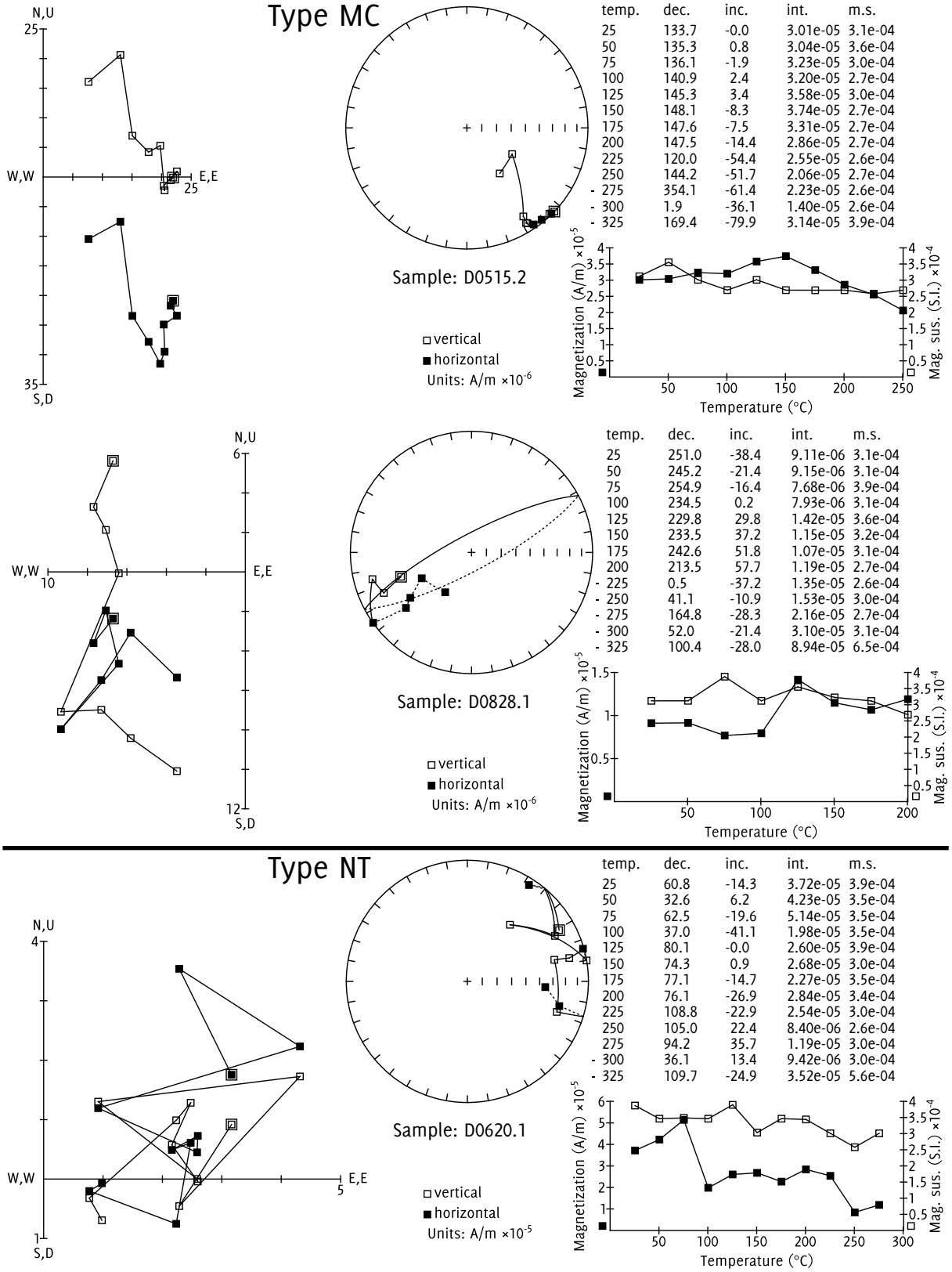

Figure 6.11 Demagnetization behaviours: types MC and NT. Top: type MC, two components in a plane not through the origin, no great-circle fit attempted. Centre: type MC, two components in a plane through the origin, great circle fitted. Bottom: type NT, no discernible trend, no fit attempted.

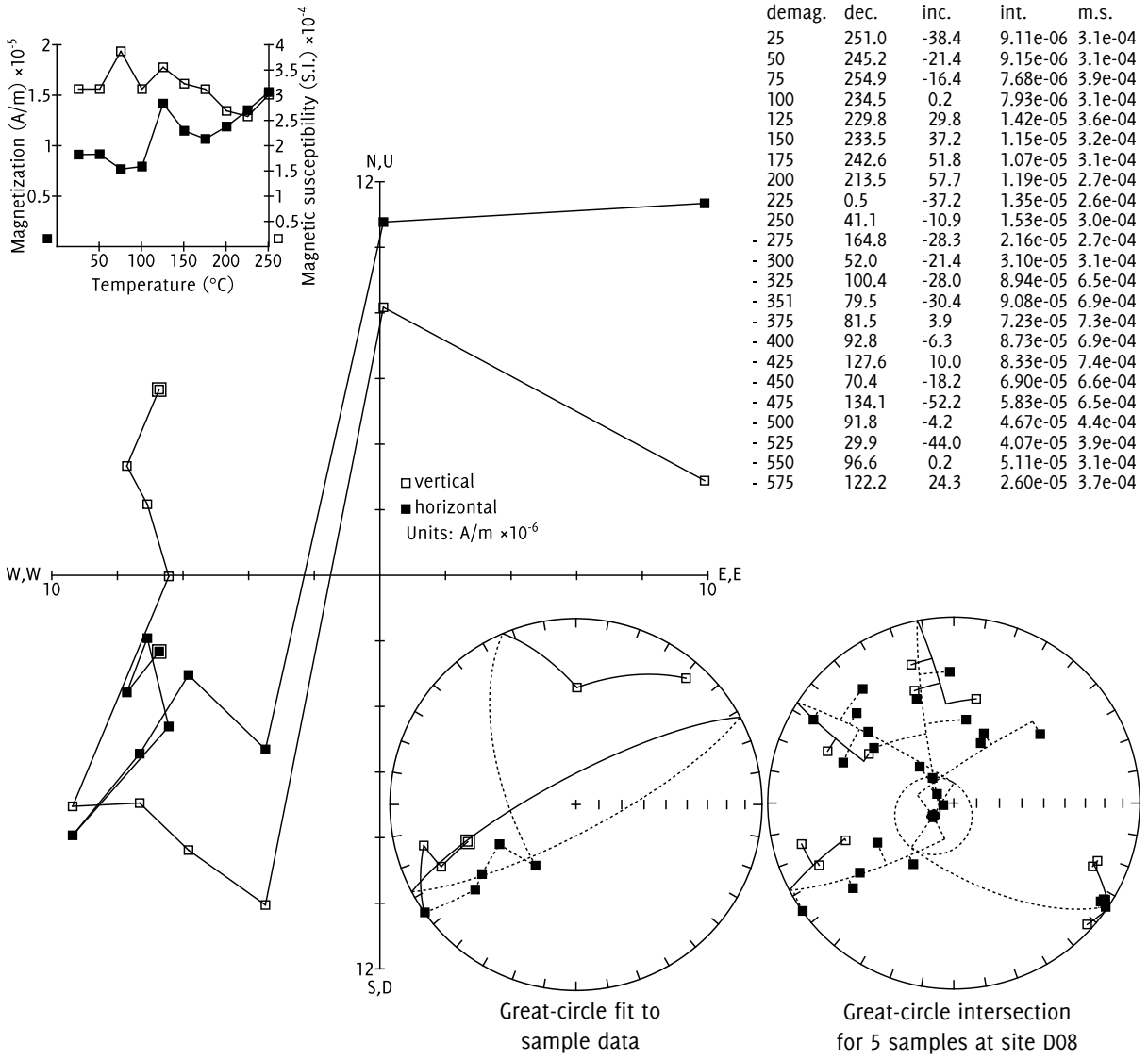

demag.	dec.	inc.	int.	m.s.
25	251.0	-38.4	9.11e-06	3.1e-04
50	245.2	-21.4	9.15e-06	3.1e-04
75	254.9	-16.4	7.68e-06	3.9e-04
100	234.5	0.2	7.93e-06	3.1e-04
125	229.8	29.8	1.42e-05	3.6e-04
150	233.5	37.2	1.15e-05	3.2e-04
175	242.6	51.8	1.07e-05	3.1e-04
200	213.5	57.7	1.19e-05	2.7e-04
225	0.5	-37.2	1.35e-05	2.6e-04
250	41.1	-10.9	1.53e-05	3.0e-04
- 275	164.8	-28.3	2.16e-05	2.7e-04
- 300	52.0	-21.4	3.10e-05	3.1e-04
- 325	100.4	-28.0	8.94e-05	6.5e-04
- 351	79.5	-30.4	9.08e-05	6.9e-04
- 375	81.5	3.9	7.23e-05	7.3e-04
- 400	92.8	-6.3	8.73e-05	6.9e-04
- 425	127.6	10.0	8.33e-05	7.4e-04
- 450	70.4	-18.2	6.90e-05	6.6e-04
- 475	134.1	-52.2	5.83e-05	6.5e-04
- 500	91.8	-4.2	4.67e-05	4.4e-04
- 525	29.9	-44.0	4.07e-05	3.9e-04
- 550	96.6	0.2	5.11e-05	3.1e-04
- 575	122.2	24.3	2.60e-05	3.7e-04

Figure 6.12 Sample demagnetization data for sample D0828.1 from site D08. Demagnetization steps above 200°C are not plotted; the great circle is fitted to the 25–200°C steps. The equal-area plot at bottom right shows the demagnetization direction for the entire site, determined by intersection of great-circle demagnetization paths. The calculated best-fit direction is shown as a circle. The dotted small circle has a radius equal to the *greatest* distance between a demagnetization path and the best-fit direction, and does not correspond to the calculated α_{95} value of 2.5°; see the text for notes on goodness-of-fit parameters.

moving towards a point representing a undemagnetized harder primary remanence. In no case could the primary remanence be deduced from a single sample, since the early onset of mineral alteration obscured the end of the demagnetization path. However, provided enough SN-type samples were available at a site, I was able to use great-circle remagnetization analysis (McFadden and McElhinny, 1988) to constrain the primary direction.

I further divided SN-type behaviour into SN1 (distinct single component; 29% (23⁄80) of the samples) and SN2 (indistinct single component; 29% (23⁄80) samples). SN1 samples, though usually noisy, showed a clearly visible trend. SN2 samples had a larger proportion of superimposed noise; however, great-circle fits to them were stable – adding or removing one or two points to the fit did not significantly change the orientation of the circle. A further test of palaeomagnetic fidelity was provided by the goodness-of-fit parameters for the intersection between the individual great circles at a site, which is further discussed below; the application of these two tests allowed me to discard unreliable fits.

Figure 6.10 (p. 180) shows examples of SN-type behaviour.

Type MC: multiple components

This behaviour occurred in 24% (19⁄80) of the samples. They showed evidence of two (or, in one case, three) magnetization components with different orientations and different thermal unblocking spectra. In no case was the final component directed towards the origin, so I interpreted the demagnetization paths as the result of multiple non-primary (chemical or thermoviscous) components. In most cases analysis was impossible, due to the small number of data points per component, high noise levels, and low remanences. In some cases the two component directions were both within a plane containing the origin, and the normalized vector path thus lay along a single great circle. In this case, I fitted a great circle to the path on the assumption that it was trending towards a primary magnetization vector. Where this was not the case, the second component was too short and noisy to give an acceptable fit on its own. Figure 6.11 (p. 181) shows examples of MC-type behaviour.

Type NT: no discernible trend

This behaviour occured in 19% (15⁄80) of the samples, which were characterized

Site	H (m)	N	T_1 (°C)	T_2 (°C)	Dec.	Inc.	α_{95}	k
D12	121	4	50–100	200–225	5.5	81.9	65.6	8.3
D11	117	5	50	150–200	131.3	55.5	22.4	25.5
Do8	80.5	5	25–50	200	237.9	79.4	33.7	11.6
Do7	78	5	25–75	175–250	186.6	30.9	29.5	15.0
Co5	75	4	25–75	175–250	158.9	45.4	70.3	7.4
Do4	71.5	5	25–100	200–275	134.2	69.6	48.3	6.0
Do3	68	5	50	200	124.7	71.3	33	12.2
Co1	66	4	50–75	200–275	180.7	35.4	41.7	19.0
Do2	65	4	50	200	196.6	46.2	56.2	11.0

Table 6.3 Site mean directions determined by great-circle remagnetization analysis for all suitable sites (see text for selection criteria). Columns: H stratigraphic height in metres; N number of circles used in fit; T_1 range of initial temperature steps for fitted points; T_2 range of final temperature steps for fitted points; α_{95} nominal radius of 95% confidence cone; k estimate of precision parameter κ. α_{95} values are as produced by the algorithm of McFadden and McElhinny (1988); they indicate relative goodness of fit and should not be taken as literal 95% confidence regions. The declination for sample D12 may appear anomalous, but its high inclination means that small measurement errors can produce large variations in declination.

by a lack of any consistent direction in the demagnetization path and apparently random variations in direction and magnitude of the magnetization vectors. I did not attempt to determine any directions from these samples. Figure 6.11 (p. 181) shows an example of NT-type behaviour.

6.4.3.4 *Site mean directions*

Due to the relatively low alteration temperatures, none of the samples reached a stable endpoint, and all site mean directions were established using intersection of great-circle remagnetization paths as described by McFadden and McElhinny (1988) and in section 2.2.2.2. The weak NRMs resulted in high noise levels, so many of the great-circle fits contained points which deviated by a few degrees from the inferred path. However, four or five samples were available at each site, which gave reasonable confidence in the inferred final direction. Figure 6.12 (p. 182) shows an example of a great-circle fit to a sample demagnetization path and a site mean direction determined by the fitted circle and other great circles from the same site.

Not all the sites had sufficient data to calculate a direction. I excluded any sites where fewer than four great-circle paths could be fitted[4]. I also excluded

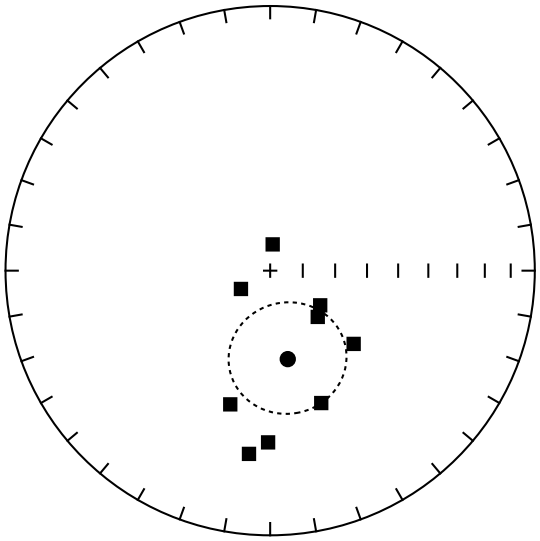

Figure 6.13 Formation mean direction for mid-Waipara River section. Square points show site mean directions; round point shows formation mean direction. Declination 168.7°; Inclination 62.1°; α_{95} = 17.6°; k = 9.5.

any great-circle intersections for which $\alpha_{95} > 75$ or $k < 5$. Under these criteria nine of the 17 sites were found acceptable. Table 6.3 shows the calculated final directions and goodness-of-fit parameters for these sites. Despite the low k-values, the consistency of directions between sites gives confidence in the soundness of the great-circle analysis.

The calculated site mean directions have a fairly large spread, but all are in the lower hemisphere, indicating a reversed magnetic field direction during deposition, and they cluster in the southeast quadrant, consistent with the degree of tectonic rotation of the eastern South Island since the early Palaeogene.

Figure 6.14 (p. 187) gives a summary log of the mid-Waipara River section, showing palaeomagnetic directions at the sites for which site mean directions could be reliably determined. The lowermost 16 m is relatively densely sampled, giving reasonable confidence that all the reversed directions lie within the same chron. The two uppermost sites, D11 and D12, are also reversed, but there is a

[4] Ideally, three circles should be sufficient to determine a site direction: two circles give an intersection point, and the third provides independent confirmation (if the three circles do not converge, there is clearly a problem). In the case of the mid-Waipara data, the demagnetization paths themselves were so noisy that I considered four circles to be a more prudent criterion.

Dec.	Inc.	α_{95}	k
168.7	62.1	17.6	9.5

Table 6.4 Formation mean direction for mid-Waipara River

37 m (stratigraphic height) gap between them and the rest of the samples, so it is possible that they lie within a different chron.

Figure 6.14 also shows the palaeocurrent direction determined for the lowermost 12 m of the section. In the upper part of the section, the AMS has a typical primary sedimentary fabric with no preferred direction for the major axis, implying a weakening or cessation of bottom current during its deposition.

6.4.3.5 *Formation mean direction*

Figure 6.13 shows the formation mean direction of the site mean directions, with 95% confidence interval determined by Fisher (1953) statistics. Its parameters are shown in table 6.4.

As described in section 5.1.3, the latitude of the eastern South Island during the early Palaeogene gives an expected geomagnetic field inclination of 70–80°; the estimated (but poorly constrained) tectonic rotation of around 50° would correspond to a local magnetic declination of around 130°. The calculated formation mean direction shows a slightly flatter inclination and more southerly declination than might be expected from these constraints, but the expected direction is within the 95% confidence region.

6.4.3.6 *Age determination*

The calcareous nannoplankton species *Chiasmolithus bidens* has been located in a sample 4 m from the base of the Waipara Greensand (68.5 m on the section log, approximate height of sample D03) (Chris Hollis, pers. comm.). *C. bidens* is an NP4 marker with a first occurrence at 61.45 Ma, which places sample D03 within the C26r chron. The samples D02–D08 form a closely spaced group and are all of reversed polarity, placing them all within the same chron. While the samples D11 and D12 are also reversed, the 36.5 m gap between D08 and D11 means that they cannot be constrained to the same chron: there is ample room

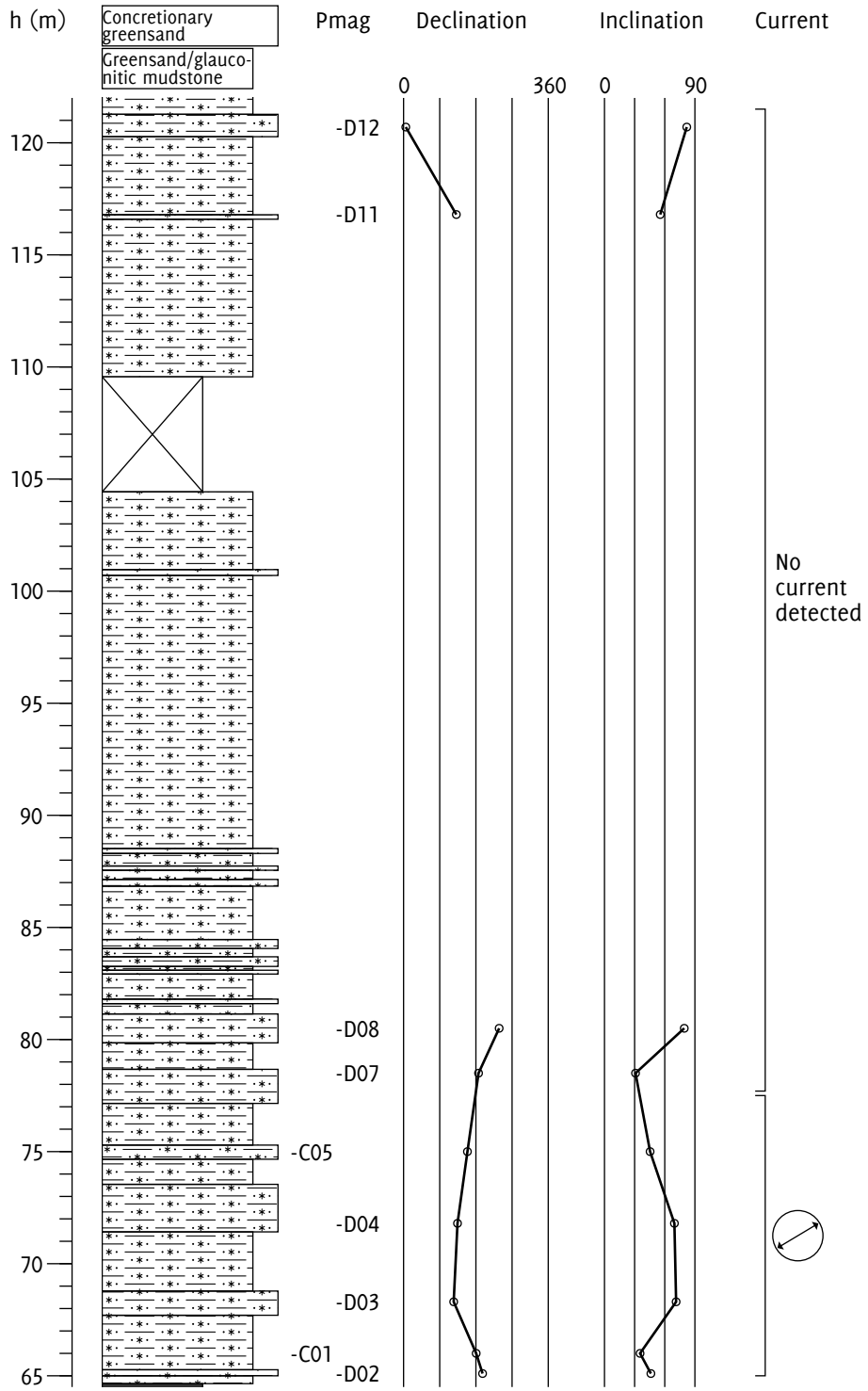

Figure 6.14 Log of mid-Waipara River section, showing only palaeomagnetic drill sites for which directions could be reliably determined; all directions were reversed. Site mean direction declinations and inclinations are plotted alongside. Palaeocurrent direction, estimated from AMS, is also shown.

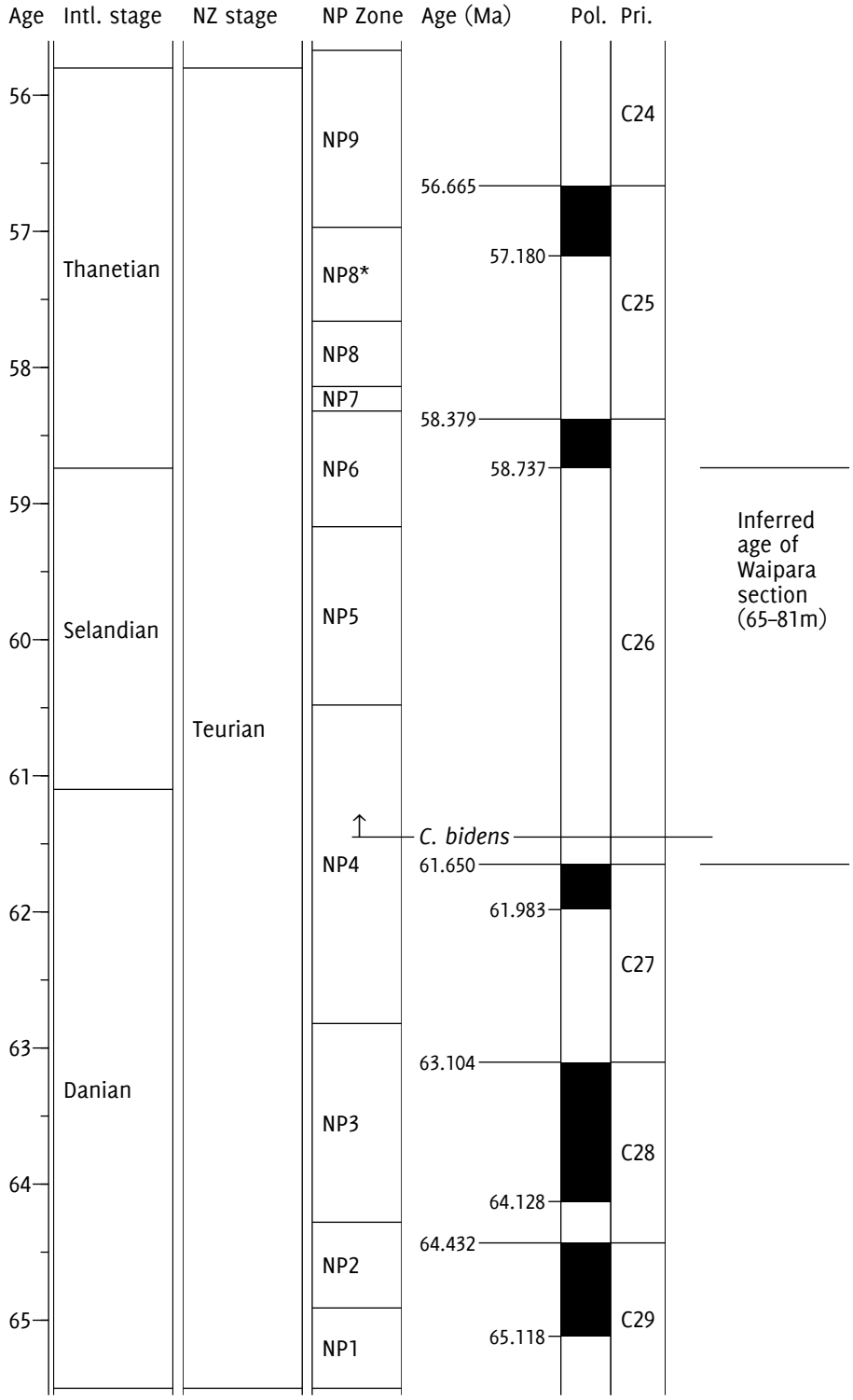

Figure 6.15 Timescale for mid-Waipara River section, showing age determination based on palaeomagnetism and calcareous nannoplankton.

in the sampling gap for the C25n normal chron. Figure 6.15 (p. 188) shows the magnetostratigraphic/biostratigraphic age determination.

6.5 Conclusions

6.5.1 *Results of the study*

A magnetostratigraphy was established for a 16 m continuous section at the mid-Waipara River, consisting entirely of reversed polarity and placed within the C26r chron based on biostratigraphic constraints. The duration of this chron (2.9 Ma), in conjunction with the thickness of the sampled sediments, implies a minimum mean sedimentation rate of approximately 5.5 mm/kyr. This low constraint is consistent with the presence of glaucony throughout the section, which is commonly associated with sedimentation rates of similar magnitude (e.g. Huggett and Gale, 1997). It is also comparable to the 7–18 mm/kyr sedimentation rates determined by Hollis *et al.* (2005) for the same time period at the Mead Stream site, some 150 km to the north-east. The low sedimentation rate may be related to the AMS orientations observed through most of the section: for sites D02–D06, the primary AMS axis has a clear and consistent horizontal orientation indicative of a sustained bottom current aligning the grains. A strong current flow would have the effect of limiting the sedimentation rate.

The reconstructed sedimentation rate only gives a mean value: a magnetostratigraphically derived estimate cannot detect fluctuations within a single chron. The mean rate itself only gives a minimum value, derived from the fact that the entire thickness was laid down during the time-span of the C26r chron; it is not possible from this data to reconstruct a maximum value. It is thus possible that the actual sedimentation rate was significantly higher than 5.5 mm/kyr.

Not all the sampled material contributed to the magnetostratigraphy. Sampling continued upward for another eight metres, but none of these samples yielded a reliable remanence direction. More intensive sampling of this zone might yield enough samples to establish reliable polarities, and there is a reasonable chance that C26r/C26n boundary may be located in this zone.

The mean palaeomagnetic direction established for the section is roughly consistent with the known tectonic constraints; the mean inferred rotation of

around 11° is less than expected from the reconstructions of Sutherland (1995). However, the high inclination and substantial scatter of site means gives a large 95% confidence region, spanning almost 80° of declination, so the result is still reconcilable with expected tectonic rotation. In addition, the small number of samples may mean that secular variation has been inadequately averaged so that the mean direction does not properly represent a geocentric axial dipole.

6.5.2 *Possible further work*

The results of this chapter constitute the first successful palaeomagnetic study of this important section. The methods applied here open the door to magnetostratigraphy of the entire Cretaceous-Palaeogene sequence at the mid-Waipara River. This prospect is appealing because of the significance of the sequence and the extensive published work on its biostratigraphy and palaeoenvironment: a magnetostratigraphic study could at once be integrated with the large body of existing data, aided by the thorough mapping published in Hollis and Strong (2003).

One limitation of my study was the friability of the sediments: almost all the successfully analysed samples were from concretionary horizons. Non-concretionary samples generally fell apart before I could complete demagnetization. However, this problem could be overcome with the application of sodium silicate solution to stabilize the samples before transport (see section 3.2.2.2). It would probably be impractical to stabilize the sampling sites *it situ* before drilling, since they are saturated with water; however, impregnation of the drilled cores with sodium silicate solution should allow far more of them to survive the subsequent processing steps. This stabilization would remove the restriction of only sampling the concretions, and allow future magnetostratigraphies to be sampled at higher resolution.

7 Campbell Island

> … we found ourselves on the brink of a tolerably elevated cliff, nearly in the centre of a circular basin, open to the ocean, whose configuration resembled the vast ruins of some gigantic ancient Coliseum. The sea had in every direction excavated, rent, and sculptured the rock, respecting only its hardest portions: the latter stood out in bold relief on the face of the cliffs, like so many antique pillars which Time had not yet been able to overthrow.
>
> – Thomas Musgrave and François Raynal explore Campbell Island (Raynal, 1875)

7.1 Introduction

This chapter presents the results of a magnetostratigraphic and rock magnetic study of Late Cretaceous to early Palaeogene sediments from the Garden Cove and Tucker Cove formations at Campbell Island in the Pacific Ocean south of New Zealand. The work is based on stratigraphic logging and palaeomagnetic sampling at two sections on different parts of the island. There is a large stratigraphic overlap between the sections, allowing correlation of their lithostratigraphies and magnetostratigraphies. As well as producing a magnetostratigraphy, I have used the anisotropy of magnetic susceptibility to determine palaeocurrent flow.

7.1.1 *Setting*

Campbell Island is the southernmost landmass of the Zealandia continent. It has an area of 114 km² and is situated at 52°33′S, 169°8′E, around 700 km south of the South Island of New Zealand. Physiographically, Campbell Island is a volcanic dome extensively dissected by marine, fluvial, and glacial[5] erosion, with the Miocene igneous rock overlying Late Cretaceous to Palaeogene marine sediments atop a scarcely exposed schist basement.

The geological history of Campbell Island, as established by Oliver (1950) and Beggs (1976), began with the deposition, metamorphosis, uplift, and peneplanation of the basement during the Paleozoic and Mesozoic. Sedimentation recommenced during a Cretaceous marine transgression, and continued until

[5] Marshall and Browne (1909) and Oliver (1950) reported evidence for glaciation; this was disputed by Morris (1976) but confirmed by recent geophysical studies (Fraser, 2009).

the Oligocene; the lack of deposition beyond this point is associated with the establishment of the Antarctic Circumpolar Current (Kennett, 1977). In the Miocene, localized volcanism uplifted the island and covered it with lavas, which have since been partially removed by erosion.

The Campbell Island sedimentary sequence is geologically important: it constitutes the only on-land exposure of Cretaceous and Palaeogene strata between New Zealand and Antarctica, and the southernmost such exposure in the Pacific Ocean (Hollis *et al.*, 1997). The area is well placed to record variations in bottom-water flow influenced by Antarctic glaciation.

Figure 7.1 (p. 193) shows the geography of Campbell Island and the locations of the sections described in this chapter.

7.1.2 *Previous work*

The remote location of Campbell Island has limited geological investigations in the two centuries since its discovery. Raynal (1870) briefly mentioned unsuccessful mineral prospecting there in 1863, but the first serious geological work was done by Filhol (1885) during a French expedition to observe a transit of Venus in 1874; there were also short notes on the geology by Buchanan (1884), Reisheck (1889), Chapman (1890), and Hector (1896). The next significant investigation was by Marshall and Browne (1909) who, from a five-day expedition in 1907, produced a general geological map and descriptions of most of the rock units of the island (they were unable to locate the schist basement, although they knew of it from the description by Filhol). The first comprehensive geological treatment was the detailed map and report made by Oliver (1950) based on work done while he was posted to the island as a coast-watcher during the Second World War. Oliver *et al.* (1950) contains this work and two short palaeontological reports; Oliver's observations were also briefly summarized by Bailey and Sorensen (1962).

A two-month Lands and Survey Department expedition in 1975–6 resulted in new descriptions of the igneous (Morris, 1976) and metamorphic and sedimentary (Beggs, 1976) geology. Beggs (1976) refined Oliver's stratigraphy and made detailed logs of the metamorphic and sedimentary units; this work was later published in Beggs (1978).

Much of the subsequent work on Campbell Island has focused on improving the biostratigraphy of the late Cretaceous-Palaeogene sedimentary

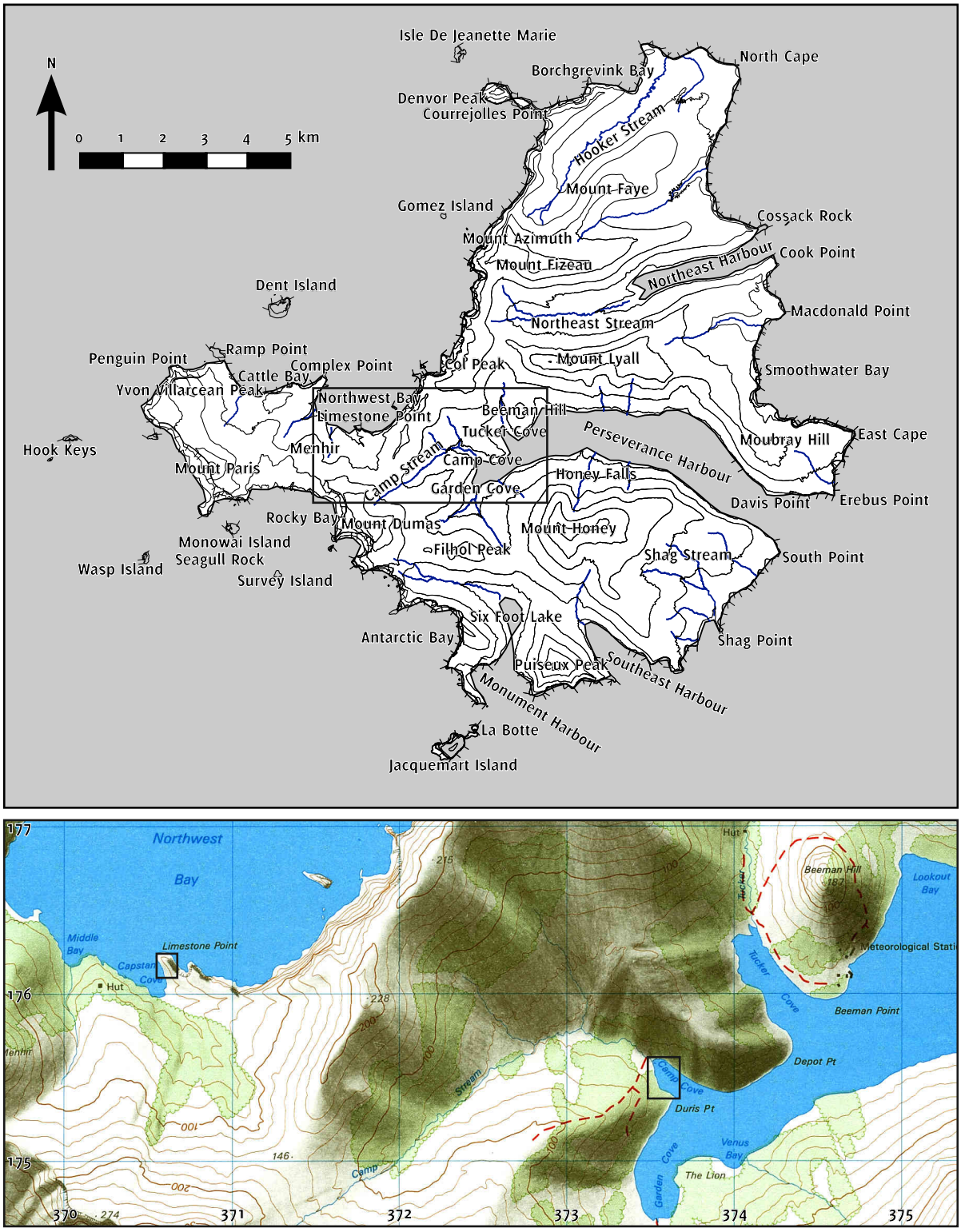

Figure 7.1 Map of Campbell Island sampling localities. The upper map marks the general sampling area within the whole island, and the lower map marks the two sampled sections within this area. Both maps are projected onto the Universal Transverse Mercator Zone 59 grid, and the northings and eastings on the lower map are in kilometres on that grid. Contours on upper map are at 20 m, 100 m, and at 100 m intervals thereafter. Map data and lower map image from Land Information New Zealand. Crown copyright reserved.

sequence in order to better relate it to other regional on- and offshore data. Hollis *et al.* (1997) gave a summary of biostratigraphy to date and presented new results from samples collected in 1995–1997.

7.1.3 *Stratigraphy*

Overview

The basement at Campbell Island consists of low-grade metamorphic rocks of the Complex Point Group (Beggs, 1976) – previously the Complex Point Formation (Oliver, 1950) and Complex Point Schist (Fleming, 1959). It is unconformably overlain by sediments of the Campbell Island Group (Beggs, 1976), comprising the Garden Cove and Tucker Cove formations (Oliver, 1950), which are the subject of this study and are described in more detail below. The Campbell Island Group is succeeded by the Shoal Point Formation, consisting of Miocene pyroclastic material; they are separated by an unconformity which Beggs (1978) tentatively identified with the Marshall Paraconformity of Carter and Landis (1972) (described in section 1.1.4, page 4 of this thesis). Volcanic flow rocks of Miocene age cover the sedimentary sequence across most of the island. Figure 7.2 (p. 195) shows a summary of this stratigraphy.

Garden Cove Formation

The Garden Cove Formation was defined by Oliver (1950) and incorporated into the Campbell Island Group defined by Beggs (1976). Oliver (1950) described a 16 m exposure west of North-West Bay consisting of quartz pebbles in the lower parts, carbonaceous sandstone near the top, and irregular interbeddings of these two lithologies, as well as quartz sand, in the intermediate part. Fleming (1959) nominated an exposure at the head of Perseverance Harbour (presumably the Camp Cove section described later in this chapter) as the type locality. Beggs (1976) logged a 30 m measured section west of Complex Point, preferring this to Fleming's type section due to the superior exposure and lack of intrusions.

Finlay (1950) gave a Teurian (Palaeocene) age for the upper Garden Cove Formation, based on foraminiferal analysis of a single sample from the Camp

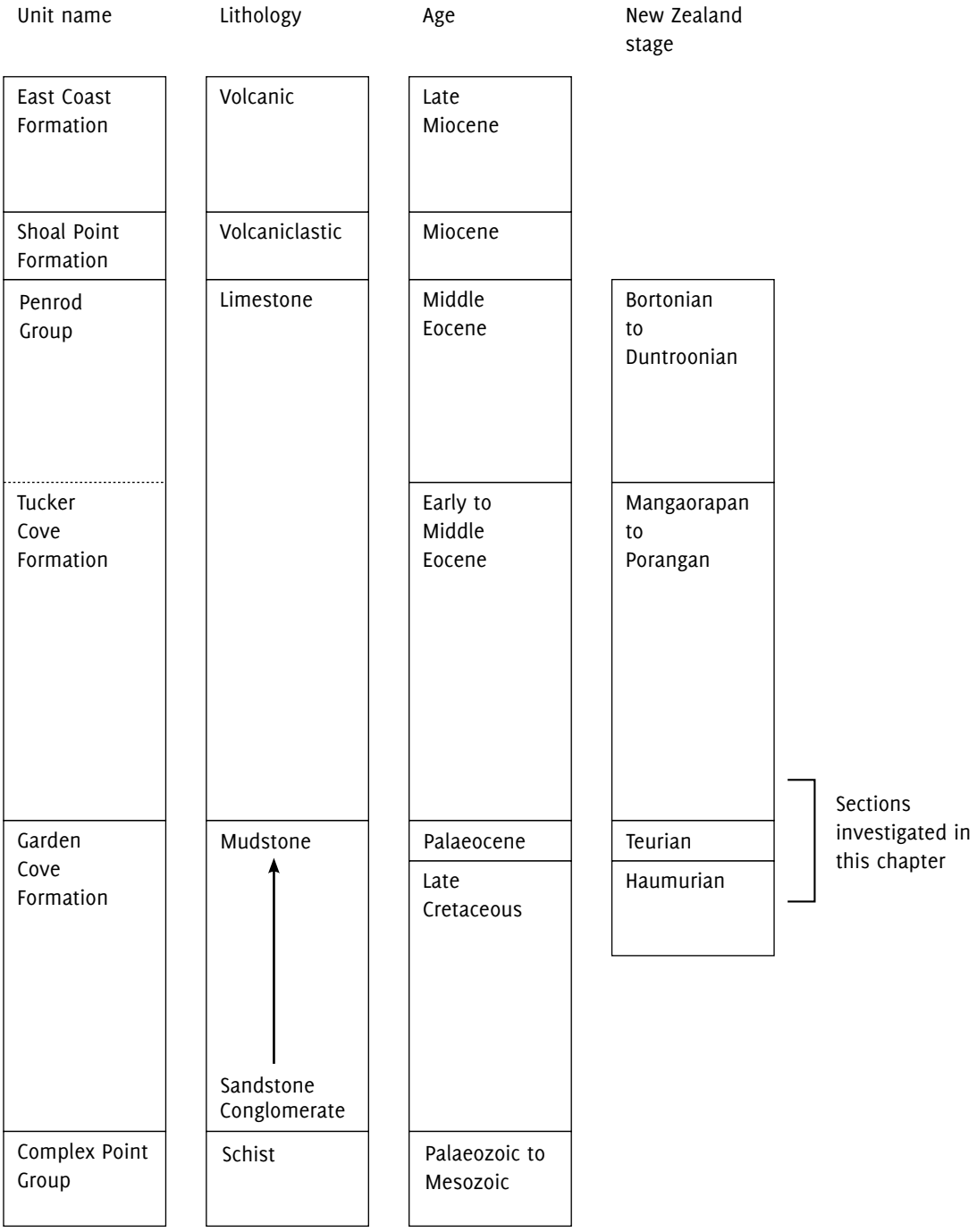

Figure 7.2 Sketch of Campbell Island stratigraphy, simplified from Hollis *et al.* (1997) and Beggs (1976). Following the redefinition of Cook *et al.* (1999), the Tucker Cove Formation is truncated at the Porangan-Bortonian unconformity.

Cove outcrop[6]. Wilson (1967) analysed another sample from the same section, finding that it was 'Paleocene (Teurian) despite the occurrence of some Cretaceous elements', but later revised this to Haumurian (Maastrichtian) (Wilson, 1972). He noted that Finlay's sample was 'likely to be stratigraphically higher', implying for the first time that the Cretaceous-Palaeogene boundary might be found in the Garden Cove Formation. Hollis *et al.* (1997) gave a more thorough biostratigraphy of the Garden Cove and Tucker Cove formations at both Perseverance Harbour and the northwestern outcrops, reliably locating the K-Pg boundary in the upper part of the Garden Cove Formation.

Tucker Cove Formation

Like the Garden Cove Formation (which it overlies unconformably), the Tucker Cove Formation was defined by Oliver (1950) (as the Tucker Cove Limestone), named for an inlet within Perseverance Harbour, and incorporated into the Campbell Island Group of Beggs (1976). Oliver described it as 'a white, fine-grained, foraminiferal limestone' with stylolitic bedding and horizons of chert nodules; the maximum thickness is around 200 m. Beggs (1978) nominated a cliff section between Complex Point and Penguin Bay as a type locality and gave the age as middle Early Eocene to early Late Oligocene. He estimated that the limestone was deposited at a minimum depth of 250 m; Hollis *et al.* (1997, p. 11) revised this to 1500 m for the lower part of the formation.

Hollis *et al.* (1997) summarized and synthesized previous work on the Tucker Cove Formation and gave an improved biostratigraphy from new sample collections. Cook *et al.* (1999, p. 55) redefined the Formation to include 'only sediments beneath the unconformity surface that separates Eocene from early Oligocene[7] strata (Hollis *et al.*, 1997)', placing the sediments above the unconformity in the undifferentiated Penrod Group.

The Tucker Cove Formation has been correlated with a Palaeogene nannofossil ooze from DSDP hole 277 (Kennett *et al.*, 1975, p. 48). It is also equivalent,

---

[6] At the time of Finlay's writing, the Teurian was regarded as part of the Late Cretaceous Mata Series, but it was subsequently moved to the Palaeogene Dannevirke Series (Hornibrook, 1962).

[7] Hollis *et al.* (1997, p. 33) actually dated the unconformity as Porangan-Bortonian (Middle Eocene to Middle–Late Eocene), but this does not materially affect Cook's redefinition (which appears to be based on the unconformity surface itself rather than age).

though not identically aged, to the Amuri Limestone at the mid-Waipara River section (Cook *et al.*, 1999).

7.1.4 *Aims of the study*

A primary aim of this study was to produce a magnetostratigraphy for the topmost Garden Cove and lowest Tucker Cove formations at two sampled localities. In conjunction with integrated biostratigraphic sampling, this should provide accurate dating of the unconformity between the two formations, and a better constraint on the position of the K-Pg boundary within the Garden Cove Formation. Additionally, rock magnetic data can provide information about the depositional environment; in particular, the anisotropy of magnetic susceptibility can indicate current flow at the time of deposition.

7.2 Fieldwork

I visited Campbell Island twice, in November 2007 and February 2009, in both cases as a part of a multidisciplinary scientific expedition aboard the University of Otago vessel *Polaris II*.

7.2.1 *Summary*

During the 2007 expedition, Gary Wilson and I sampled a 9.5-metre (stratigraphic thickness) section at Limestone Point (suite C), containing the contact between the Garden Cove and Tucker Cove formations. Chris Hollis and James Crampton of GNS logged the section and took biostratigraphic samples.

In 2009, Bob Dagg and I extended the Limestone Point sampling further upward (suite D) into the Tucker Cove Formation. We also sampled another section on the west side of Camp Cove (suite A and suite B), which exposed the top 35 m of the Garden Cove Formation and the bottom 2 m of the Tucker Cove Formation. Ben Andrew mapped and logged the Camp Cove section; Steve Little of the *Polaris II* provided field support. Suite A is from a continuous four-metre exposure near the head of Camp Cove containing the contact between the Garden Cove and Tucker Cove formations; suite B is from the Garden Cove Formation exposure along the shoreline to the east of this contact zone (about 30 m stratigraphic thickness).

Prefix	Unit	Location	Date	Notes
A	Garden Cove Fmn./ Tucker Cove Fmn.	Camp Cove	2009	Dense sampling across contact.
B	Garden Cove Fmn.	Camp Cove	2009	Along shoreline east of contact, below suite A.
C	Garden Cove Fmn./ Tucker Cove Fmn.	Limestone Point	2007	Mostly Garden Cove Formation.
D	Tucker Cove Fmn.	Limestone Point	2009	Immediately above suite C.

Table 7.1 Sample suite prefixes and details.

In total 100 oriented cores were recovered at Limestone Point, and 134 at Camp Cove. The lowermost Tucker Cove Formation was poorly lithified and the sampled portion of the Garden Cove Formation was friable and heavily jointed, so most of the drilled cores were shorter than 10 cm.

Figure 7.3 (p. 200) and figure 7.4 (p. 201) show a graphic log for the Limestone Point section; figure 7.5 (p. 202) and figure 7.6 (p. 203) give one for the Camp Cove section.

7.2.2 *Description of sample suites*

The four suites of samples, denoted by the letters A–D, are described below; Table 7.1 summarizes this information. For the remainder of this chapter, sites are denoted by a single prefix letter for the suite followed by a two-digit number for the site within that suite.

A. 58 cores were drilled at 12 densely spaced (around 15 cm) sites on a single outcrop in Camp Cove which exposed the contact between the Garden Cove and Tucker Cove formations. Sampling extended approximately 1 m below the contact and 1.5 m above it.

B. 76 cores were drilled from the uppermost Garden Cove Formation at 10 sites along the western shoreline of Camp Cove. The sampling covered a stratigraphic height of 26 m. Sampling density was dictated by the limited exposure and accessibility of the section; most sites were spaced at less than

3 m of stratigraphic thickness, but there was a gap of 9 m between sites B05 and B06.

C. 79 cores were drilled from 28 sites covering 11 m of stratigraphic thickness at Limestone Point; the bottom of the section was a gently sloping wave-cut platform, steepening to a cliff at the top. The lowermost 24 sites were in the uppermost Garden Cove Formation, and the top three in the lowermost Tucker Cove Formation.

D. 21 cores were drilled from the Tucker Cove Formation at Limestone Point at stratigraphic heights of 1–4 m above the contact with the Garden Cove Formation.

7.3 Laboratory work

All laboratory work was performed at the OPRF; details of equipment are given in appendix C.

7.3.1 *Isothermal remanent magnetization*

I selected eight samples from the sampled sections on Campbell Island: four each from the Camp Cove and Limestone Point sections. Within each section, both the Tucker Cove and Garden Cove formations were represented. I conducted an IRM study to determine the remanent coercivity spectra of these samples. I pulse magnetized them in 32 exponentially increasing steps up to a maximum field of 1 T. I then applied a series of increasing fields in the opposite direction until the magnetization of the sample reversed in polarity, allowing me to determine the bulk remanent coercivity directly.

7.3.2 *Magnetic susceptibility*

I measured the TDMS of 19 samples spaced throughout the Camp Cove section, and of 5 samples across the Limestone Point section. As for the other TDMS studies in this thesis, I used repeated heating cycles with increasing peak temperatures (100°C to 700°C in 100°C steps) in order to monitor thermally induced mineral alteration; section 2.1.4 gives more details of the technique. I

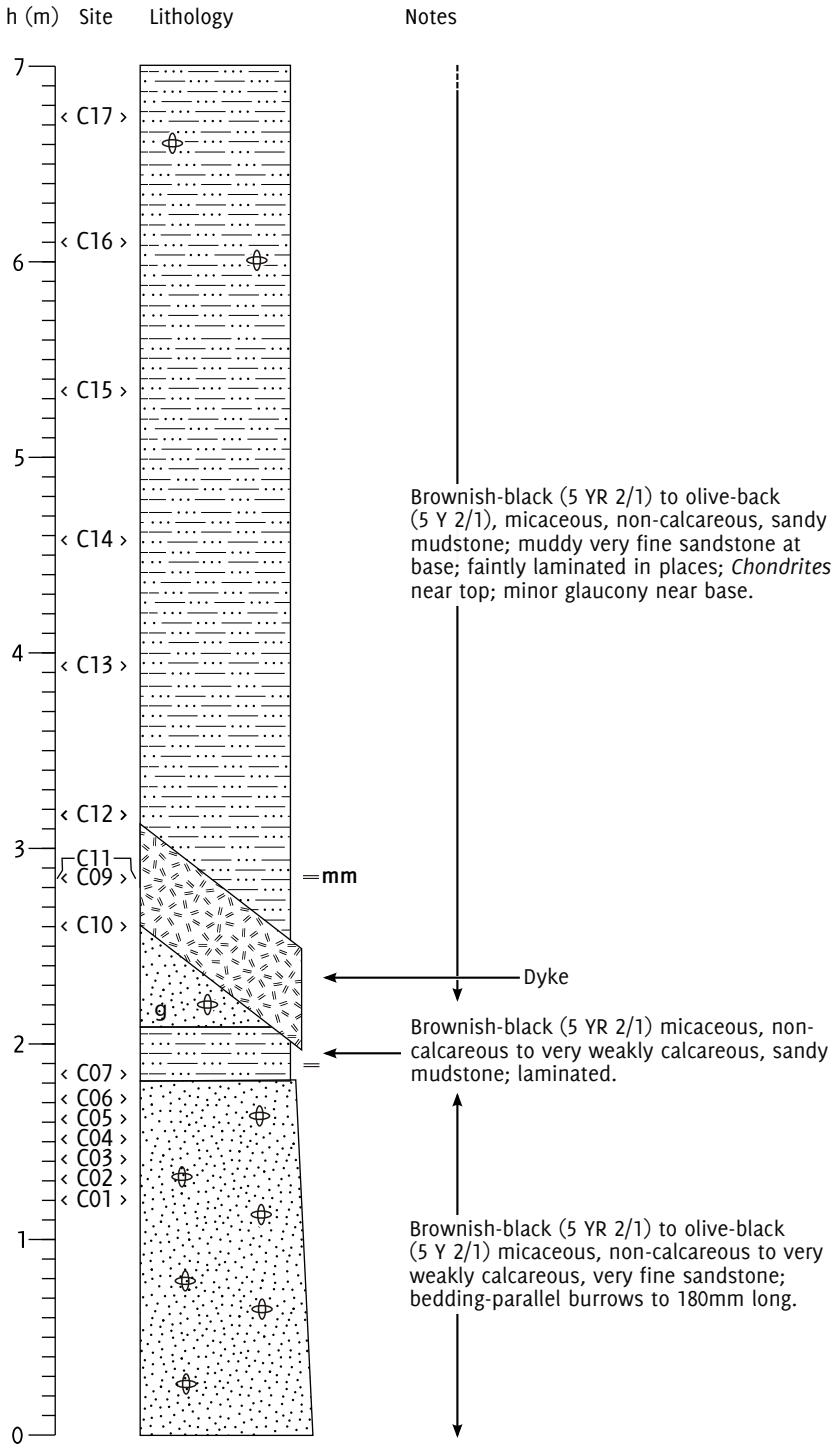

Figure 7.3 Limestone Point log, 0–7 m. After a log by James Crampton and Chris Hollis, November 2007.

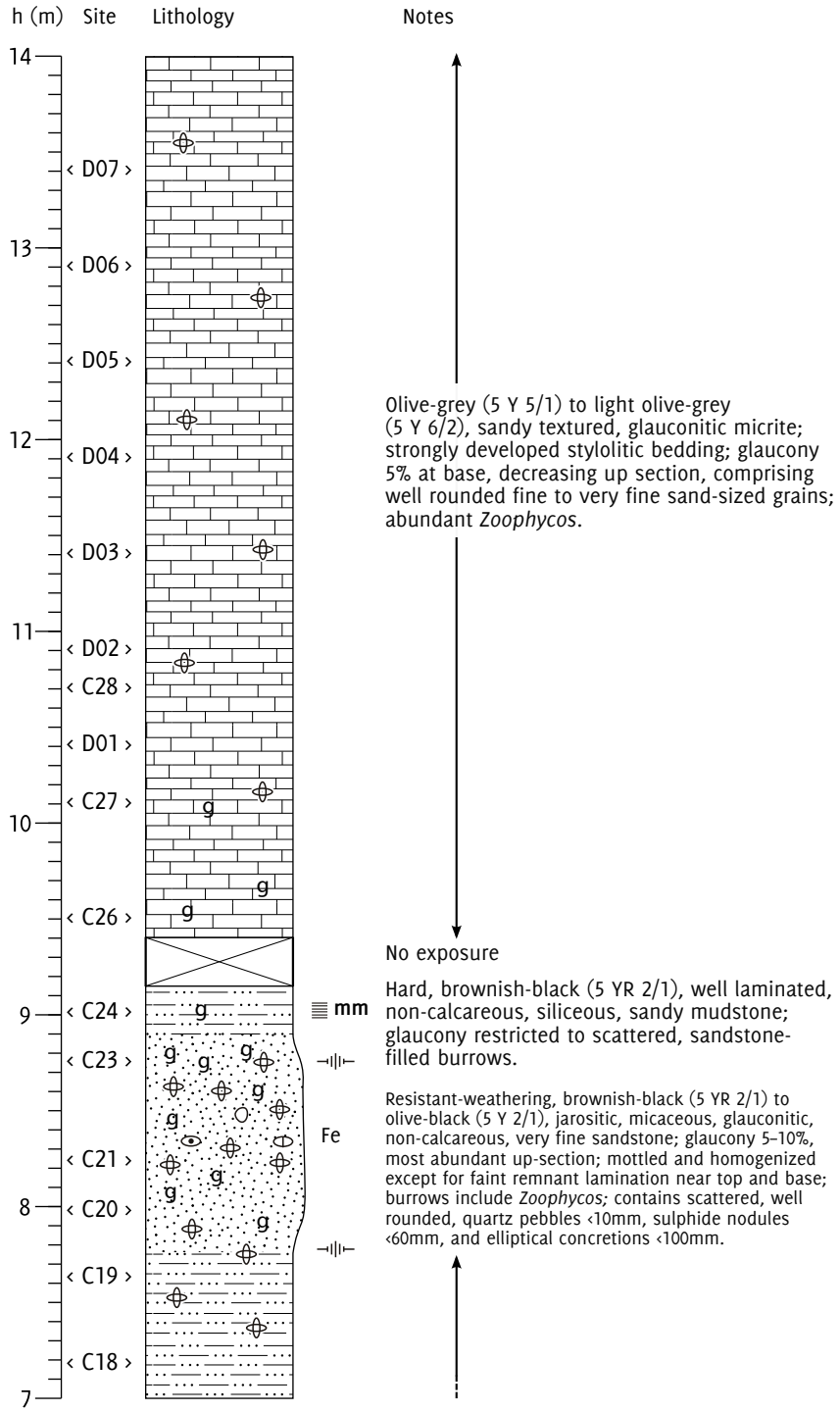

Figure 7.4 Limestone Point log, 7–14 m. After logs by James Crampton and Chris Hollis (November 2007) and Ben Andrew (February 2009).

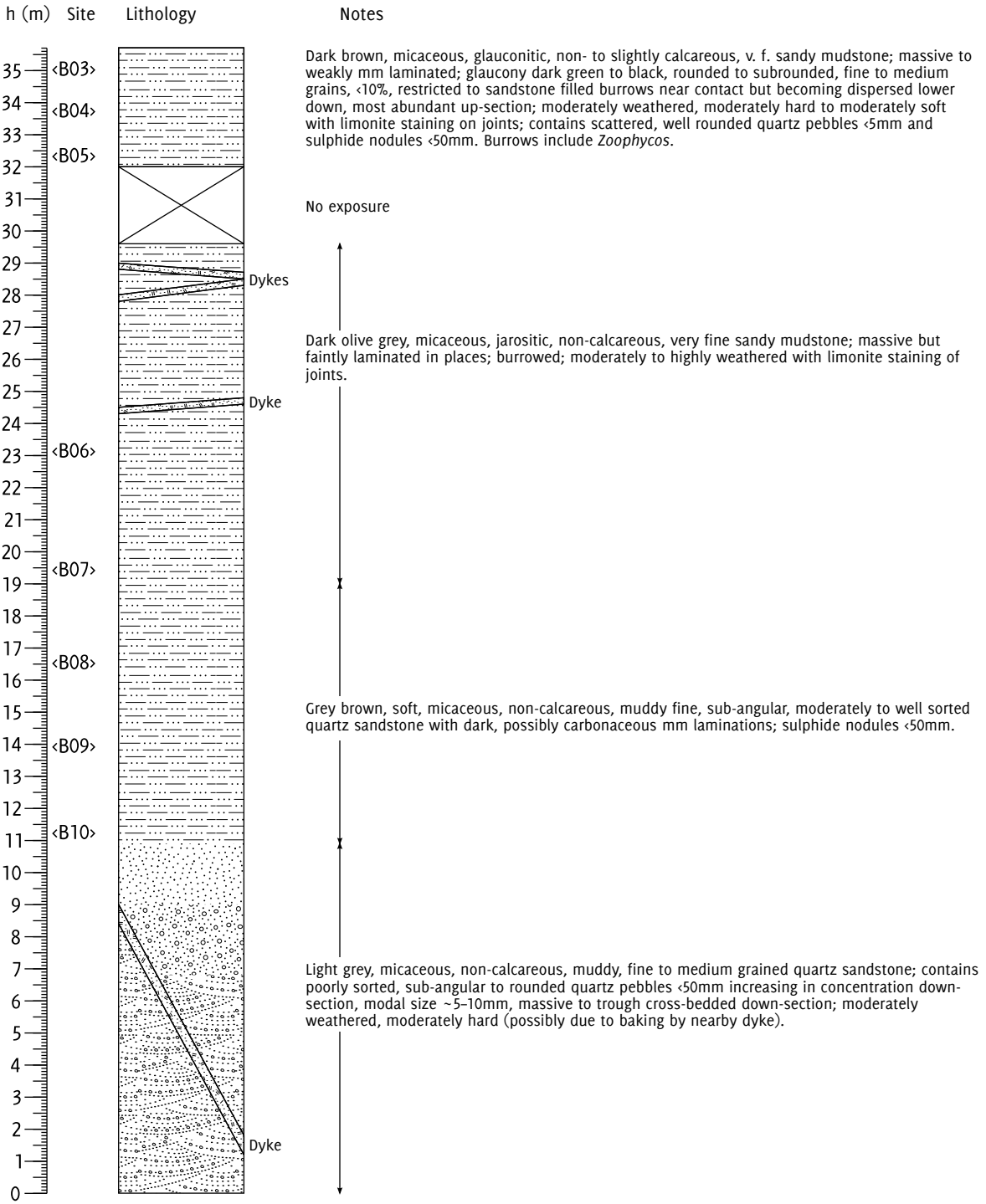

Figure 7.5 Camp Cove log, 0–35.7 m. Redrawn after a log by Ben Andrew and Bob Dagg, February 2009.

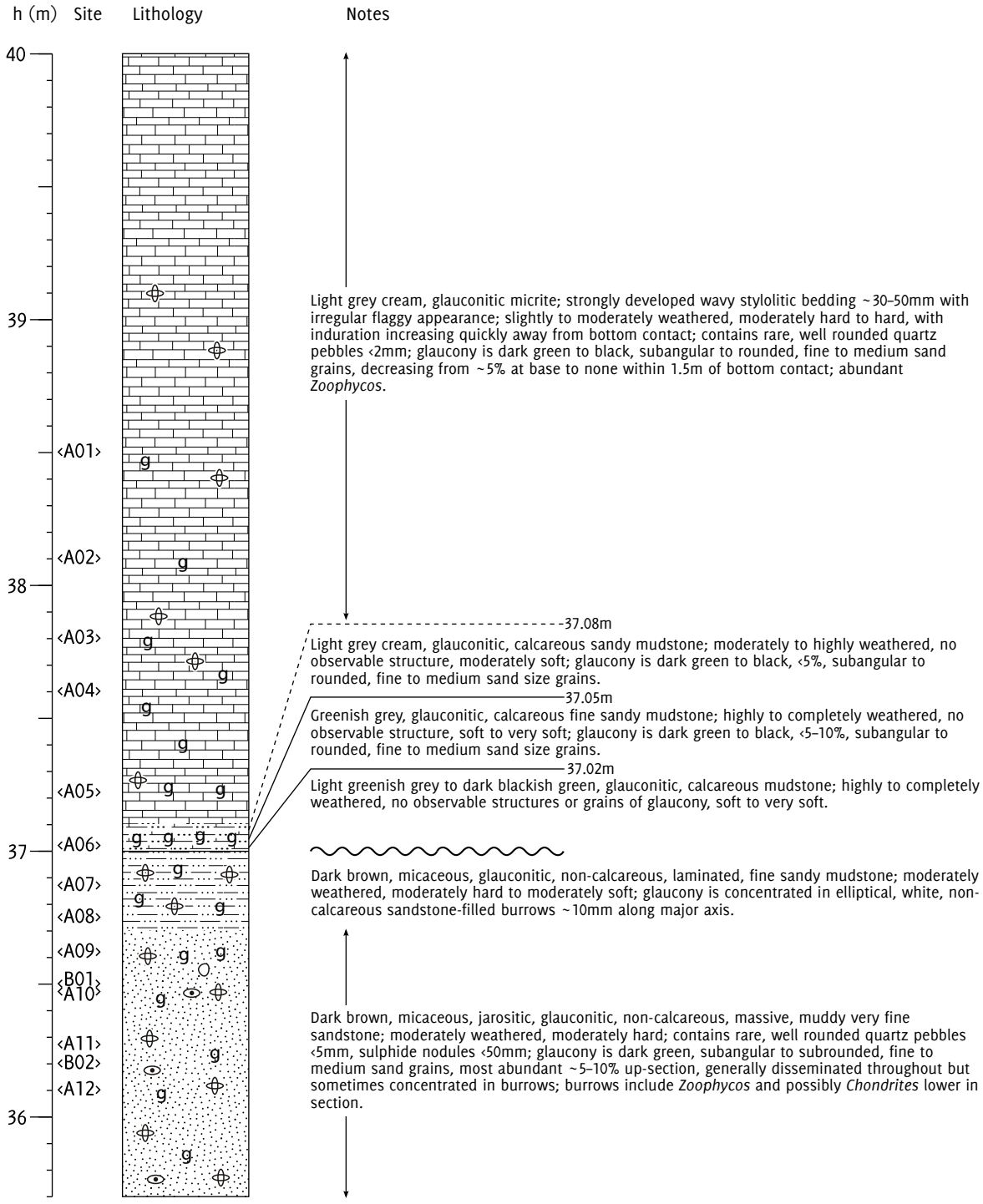

Figure 7.6 Camp Cove log, 35.7–40 m. Redrawn after a log by Ben Andrew, February 2009.

also measured the AMS of all samples in suites A, B, and D in order to determine palaeocurrent directions.

7.3.3 *Stepwise demagnetization*

Here I give details of the thermal demagnetization protocols I used for the four suites. The maximum demagnetization temperatures were not determined in advance: for each study, I stopped performing heating steps when heating-induced mineral alteration obscured the demagnetization signal. I determined this by monitoring magnetic susceptbility and magnetization intensity: alteration was indicated by large (twofold or greater) susceptibility increases and/or random variation or large increases in magnetization.

A. I demagnetized 45 samples (3 each from sites A06, A08, and A12; 4 from the other 9 sites) to 450°C in 25°C steps.

B. I used 40 samples (4 from each of 10 sites) and demagnetized them to 400°C in 25°C steps.

C. I used 75 samples for the thermal demagnetization study (3 from each of 25 sites; no oriented core was recovered from sites C08, C22, or C25, so these sites were excluded from the study). I demagnetized them in 30°C intervals to 600°C.

D. I used 28 samples for the thermal demagnetization study (4 from each of 7 sites) and demagnetized them in 25°C steps up to 400°C.

7.4 Rock magnetic results

In this section I present the rock magnetic results of the Campbell Island study. Data files for all the magnetic analyses are included on the data CD-ROM (appendix D).

7.4.1 *Isothermal remanent magnetization*

With the exception of D03 (from the Tucker Cove Formation at Limestone Point), the samples all showed a soft coercivity spectrum typical of magnetite

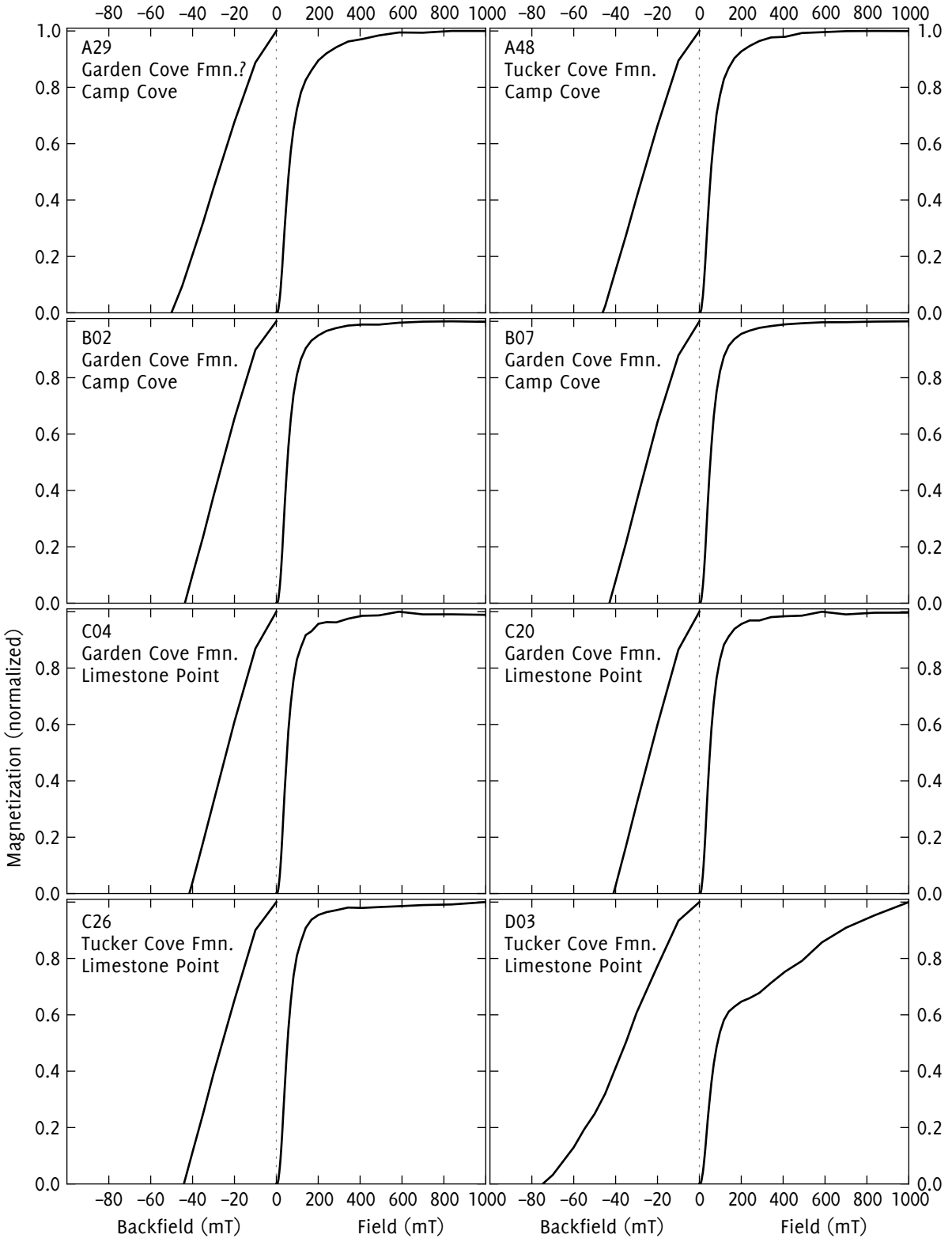

Figure 7.7 Isothermal remanent magnetization acquisition (right side of each subplot) and DC demagnetization (left side) for Campbell Island samples. Due to the wide range of saturation magnetizations, the magnetization curves are normalized. Note also the differing horizontal scales for the magnetization and demagnetization curves.

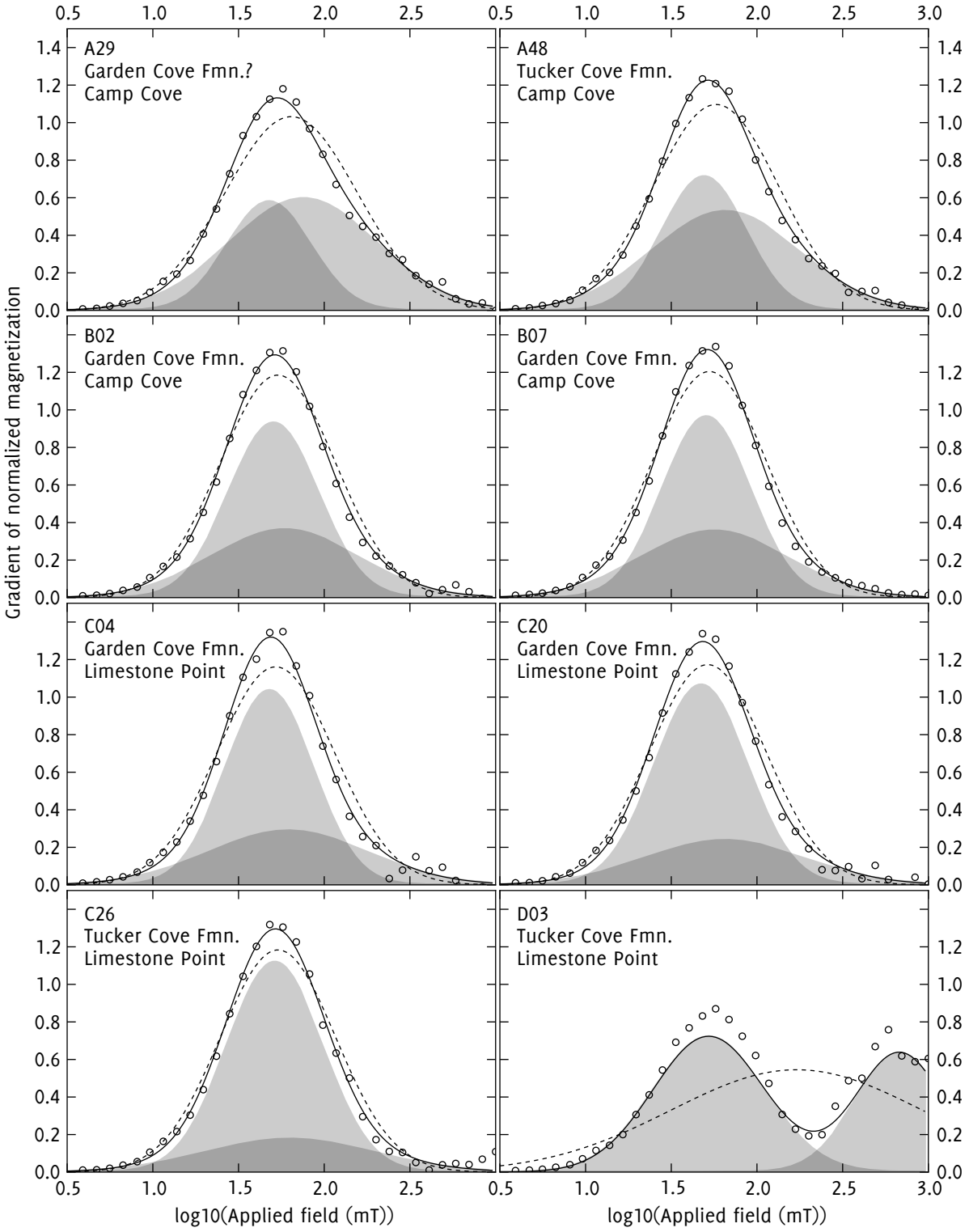

Figure 7.8 Cumulative log-Gaussian fits to IRM acquisition curves. The small circles show the measured gradient of the acquisition curve at each point. Within each subplot, the shaded areas show log-Gaussian components for a two-component fit, and the solid line shows the sum of these components. The dotted line shows the best-fitting single log-Gaussian curve.

mineralogy, as can be seen from the plots in figure 7.7 (p. 205). They achieved 95% saturation below 350 mT (in most cases at around 200 mT) and were saturated or very nearly saturated by 1 T. Bulk coercivities of remanence were in the 40–50 mT range, well within the limits for magnetite given by Peters and Dekkers (2003). The clear exception to this behaviour is sample D03 from the lower Tucker Cove Formation at Limestone Point: it has an initial soft coercivity component, which can be seen from the steep gradient of the acquisition curve in the first 100 mT. Beyond this point, the slope of the acquisition curve suddenly becomes flatter and remanence acquisition continues at a near-linear rate up to 1 T. Unlike the other samples, D03 does not appear to have reached saturation at 1 T. The most likely candidates for such a high-coercivity component are goethite and haematite.

Cumulative log-Gaussian analysis of IRM data

Figure 7.8 (p. 206) shows fits of the IRM acquisition gradient curves to log-Gaussian functions; table 7.2 shows the parameters for the fits. The theory and practice of this technique is discussed in detail in section 3.4.2 on page 54. Leaving D03 aside for the moment, the curve fits look similar to those from the other IRM studies in this thesis (figure 3.14, p. 57; figure 5.14, p. 145; figure 6.4, p. 172). There is a large (usually dominant) peak with low mean coercivity (component 1), heavily overlapping a weaker peak with a slightly higher mean coercivity (component 2). In the Campbell Island samples, however, there is usually very little difference between the mean coercivities of the two peaks. It is possible (as in the previous IRM studies in this thesis) that the two-component model – although it gives a noticeably better fit to the data than a single component – cannot be justified here. Figure 7.8 shows the IRM acquisition gradient curves with the best-fitting 2-component and single-component log-Gaussian models. Without independent confirmation of distinct mineral phases, it is difficult to justify the inclusion of two components.

The case for sample D03 is very different: a single-component model appears inadequate, and a two-component fit, although not perfect, shows two well-defined peaks with little overlap. Component 2 has $B_{½} = 2.83$, giving a H'_{cr} value of $10^{2.83} = 676$ mT. This value falls within the range of 28–769 mT given for haematite by Peters and Dekkers (2003), and does not match the coercivity of any other known magnetic mineral (goethite coercivities are much higher).

Sample	SIRM	H_{cr}	H'_{cr}	— Component 1 —			— Component 2 —		
	mA/m	mT	mT	M_{ri}	$B_{½}$	DP	M_{ri}	$B_{½}$	DP
A29	160.8	50.1	59.8	0.36	1.68	0.24	0.64	1.88	0.43
A48	23.2	46.2	55.1	0.43	1.69	0.24	0.57	1.82	0.43
B02	67.2	43.7	52.6	0.61	1.70	0.26	0.39	1.77	0.43
B07	245.8	43.0	52.1	0.62	1.70	0.26	0.38	1.75	0.42
C04	117.9	41.6	51.0	0.66	1.68	0.26	0.34	1.79	0.46
C20	152.8	41.0	50.1	0.72	1.67	0.27	0.28	1.81	0.46
C26	25.0	44.1	53.1	0.78	1.71	0.28	0.22	1.80	0.49
D03	14.5	74.8	86.6	0.59	1.72	0.33	0.41	2.83	0.26

Table 7.2 IRM parameters for Campbell Island samples

I attempted to find further confirmation for haematite by taking subsamples from D03 for TDMS analysis; one of the samples contained a dark grey 2 mm nodule with a dark orange rim, and the other consisted entirely of pale cream coloured limestone. Neither sample provided any evidence for haematite during heating, with both samples showing a Hopkinson peak and complete loss of susceptibility at around 600°C. One explanation for this is that the haematite was unevenly distributed; it is also possible that the concentration was simply too low to be detected. Even compared to the other sediments investigated in this thesis, the Tucker Cove Formation has a very low saturation magnetization and thus a low concentration of remanence-carrying grains. Haematite's volume-normalized saturation magnetization is around 5×10^{-3} times that of magnetite (Dunlop and Özdemir, 1997, p. 51), whereas its volume susceptibility can be as little as 10^{-4} times that of magnetite (Hunt *et al.*, 1995). Thus, in a case such as this where the haematite component has a lower saturation magnetization than the magnetite component, its susceptibility contribution may be in the region of ⅟₅₀ that of the magnetite. It is also possible that the high-coercivity component is not pure haematite but a haemo-ilmenite, which would have a lower disordering temperature due to substitution of titanium ions.

7.4.2 *Temperature dependence of magnetic susceptibility*

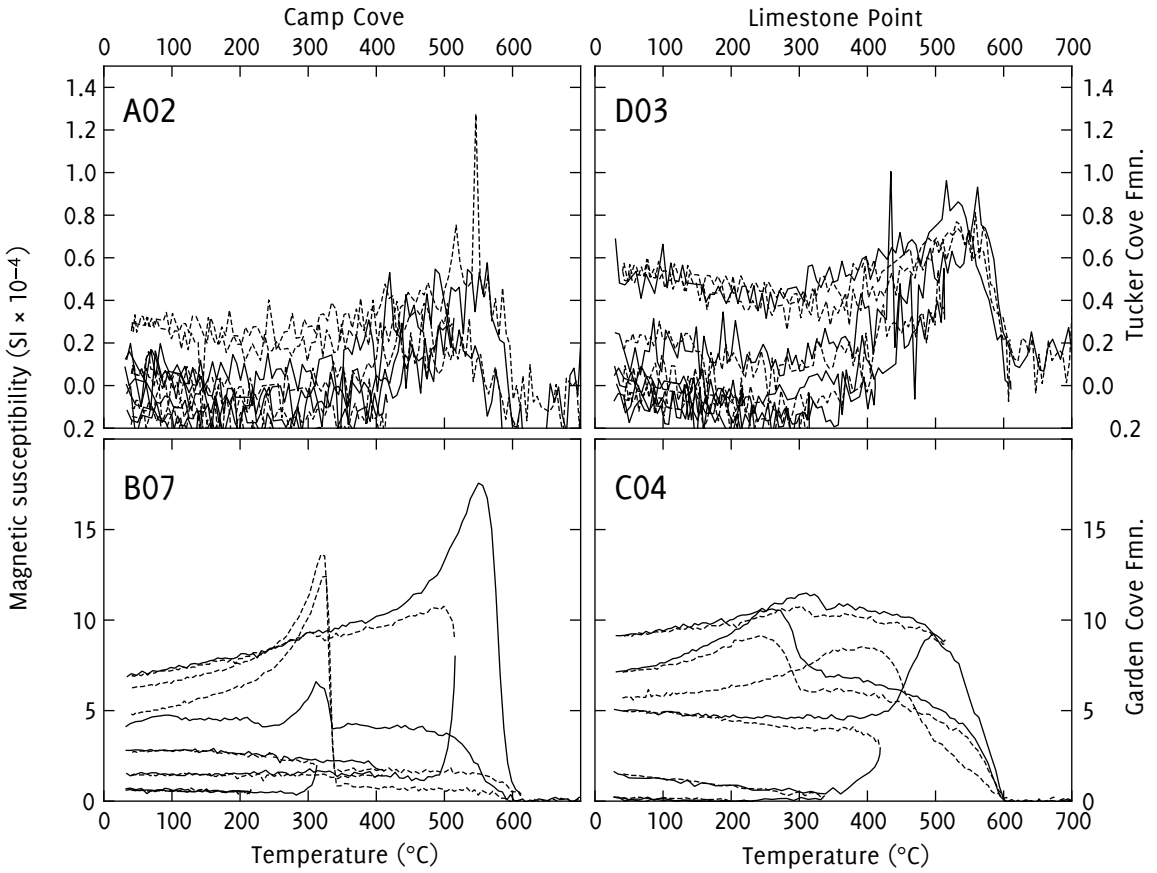

Figure 7.9 Specimen TDMS behaviours for samples from Tucker Cove and Garden Cove formations at Limestone Point and Camp Cove.

There was significant variation among the measured samples, but they all displayed the common feature of a Hopkinson peak followed by a sharp drop in susceptibility just below 600°C, indicative of a magnetite mineralogy. Some of the samples (mostly from the Tucker Cove Formation) had extremely weak susceptibilities, and in these cases the Hopkinson peak itself was sometimes obscured by the simultaneously declining susceptibility of paramagnetic components. However, even for these samples, the disordering temperature could be inferred from the sharp drop in susceptibility after the peak. Figure 7.9 (p. 209) shows examples of TDMS curves from both sections and both formations.

Despite the argon atmosphere, all samples showed irreversible increases in susceptibility – indicating mineral alteration – in the 300–400°C range. Alteration continued at subsequent heating steps. It is thus not possible to state with certainty that all the magnetite inferred from the Hopkinson peaks around

600°C was initially present; however, the consistent lack of susceptibility above 600°C rules out haematite, and the lack of pre-alteration Hopkinson peaks at 320°C rules out pyrrhotite. (After thermal alteration at 400–600°C, a peak corresponding to pyrrhotite does in fact appear in most of the Garden Cove Formation samples, which suggests that if there had been pyrrhotite present initially, the TDMS results would have shown it.)

7.4.3 *Anisotropy of Magnetic Susceptibility*

I measured AMS for all samples in suites A, B, and D.

Suite A

Figure 7.10 (p. 213) shows AMS directions for suite A. Most samples from this suite showed a well-constrained horizontal maximum susceptibility axis, consistent with an orientation produced by current flow at the time of deposition. The orientation of the other two axes is more unusual: the intermediate axis is steeply inclined to above 50°, with the minimum axis close to the bedding plane. These orientations are an inversion of the usual relationship between these axes in sedimentary fabrics, as described by e.g. Rees (1961): the commonly observed sedimentary fabric has a minimum axis perpendicular, or nearly so, to the bedding plane. Other origins for the magnetic fabric must thus be considered. Metamorphism can affect AMS fabrics at grades too low to produce visible changes (Hrouda and Janák, 1976); however, there are strong grounds for ruling out metamorphic influence on the fabric. Firstly, the corrected anisotropy factors P' of all the samples are below 1.02; this is well below the value of 1.05 given by Tarling and Hrouda (1993, p. 148) as a diagnostic threshold for the detection of metamorphic influence. Secondly, the fabric orientation varies significantly between sites just 30 cm apart in outcrop; it is hard to imagine that metamorphism could produce such extremely localized variation. A more likely candidate for the unusual fabric is diagenesis. Schieber and Ellwood (1988) reported similar fabric shapes arising from the diagenetic growth of dolomite within shales. By comparison with macroscopic current indicators, they established that despite the rotation of the intermediate and minor axes, the maximum axis orientation still gave a reliable record of palaeocurrent. The association of the maximum axis here with current flow is also

supported by the fact that it is in all cases very close to the horizontal, and that the direction for sites A11–A12 agrees with that for the sites B01–B02, which are at the same stratigraphic height and display an unmodified sedimentary fabric.

The only samples from suite A not to show this directional fabric were those from sites A05 and A06. These samples had a typical (but very weakly defined) sedimentary orientation, with an approximately bedding-normal minimum axis. The poorly constrained minimum axis may be due to bioturbation. The other two axes were randomly oriented, suggesting a lack of palaeocurrent and possible bioturbation. These samples are from just above (within 20 cm) the contact between the Garden Cove and Tucker Cove formations, and the change in AMS fabric is presumably associated with the hiatus in deposition at this contact.

Suite B

The samples from suite B (shown in figure 7.11, p. 214) had a clear primary sedimentary fabric controlled by palaeocurrent direction. Minimum axes directions were all bedding-normal; the other axes were both in the bedding plane. The declination of the major axis varied with section height, indicating changes in current flow. At site B10, the sedimentary fabric is visible, but much more weakly defined than at the higher sites. Even here, though, a weak north-south palaeocurrent direction is evident.

Variations in palaeocurrent flow are evident with increasing height through the section: in the lower sections (B07–B10) the primary axes are oriented north-south to northeast-southwest, with mean directions varying slightly between site groups. At B05–B06, there appears to have been a cessation of current, as indicated by the randomly oriented major and intermediate susceptibility axes. This inferred hiatus may be due to ocean circulation changes associated with the K-Pg boundary event: at this site, the boundary has been placed at around 10 m below the Garden Cove Formation / Tucker Cove Formation contact, between the heights of B05 and B06. Above B05, current flow resumes in a west-east orientation, rotating to a more nearly north-south orientation at the top of the section.

Suite D

Figure 7.10 (p. 213) shows the AMS directions measured for suite D. These samples showed two distinct behaviours: at sites 1–6, a near-horizontal maximum susceptibility axis oriented roughly north-south showed a probable palaeocurrent direction; at site 7, a less easily interpretable fabric appeared, with a tightly clustered minimum axis and the other two axes in a girdle distribution.

7.5 Palaeomagnetic results

In this section I present the results of the stepwise demagnetization experiments. I first describe (section 7.5.1) four *types* of demagnetization behaviour (distinct from the four *suites* of samples defined in table 7.1, p. 198). With reference to these behaviour types, I then describe the palaeomagnetic results from Camp Cove (section 7.5.2) and from Limestone Point (section 7.5.3). Within each of these two sections, I first classify the demagnetization behaviours according to the defined types, then present the site mean directions and formation mean directions obtained by analysing these behaviours. Demagnetization data files are included on the data CD-ROM (appendix D).

7.5.1 *Demagnetization behaviours*

Type SO: single component, origin directed

Type SO samples have an NRM with inclination steeper than −70° and a northward declination. On demagnetization they show a single, albeit frequently noisy, component trending approximately towards the origin, with a maximum temperature usually in the range 360–420°C, after which the magnetization vector varies at random. I interpreted this as the superposition of a normal depositional remanent magnetization and a viscous overprint from the present-day normal chron. Ideally, these would be resolvable as two different directions, since the DRM was imparted at a different latitude and tectonic rotation. However, the expected difference in inclination is only a few degrees, and the high inclination means that variations in declination cause little change in the overall magnetization vector. The difference between a present-day normal magnet-

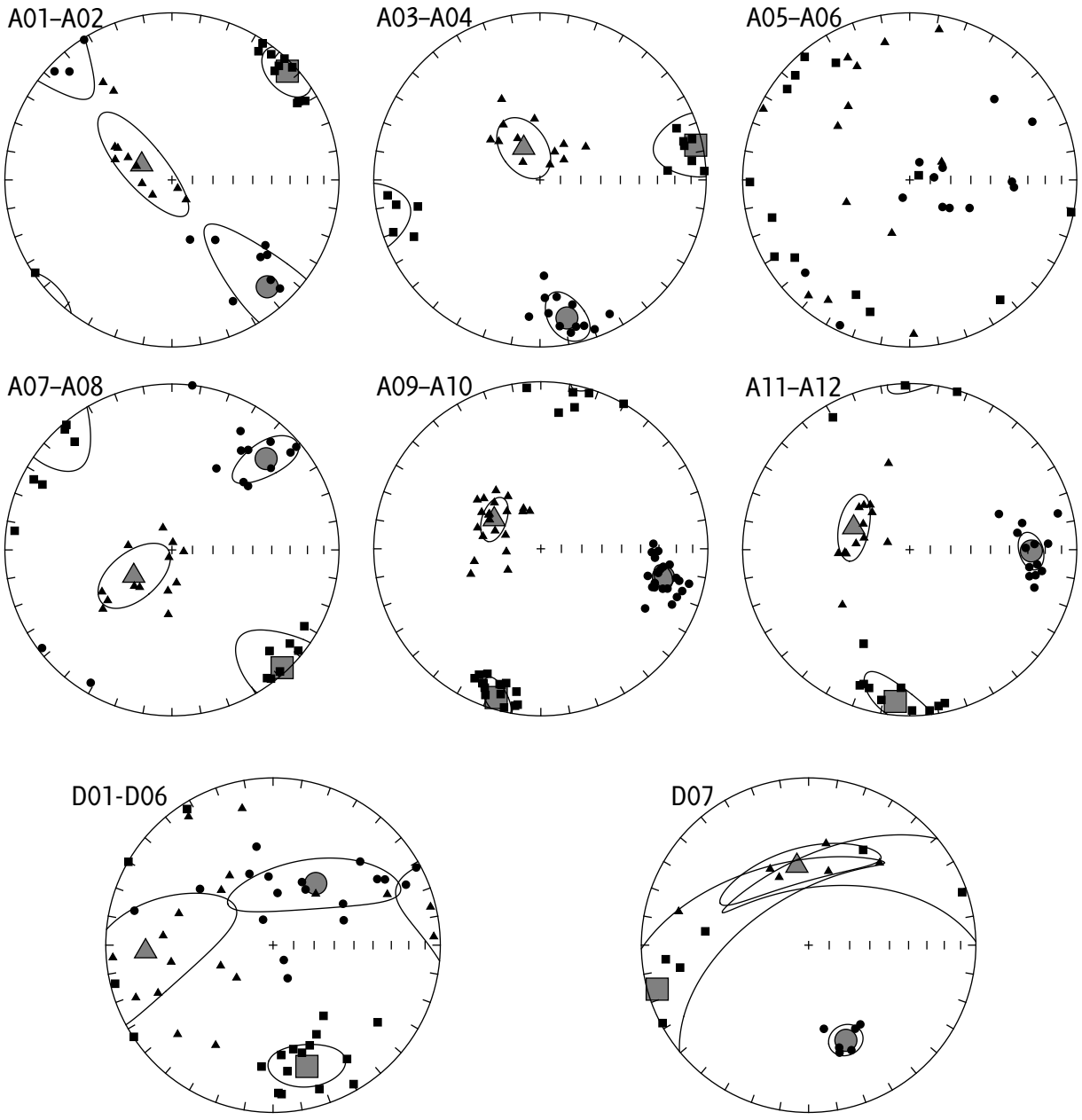

Figure 7.10 AMS directions for suites A (top) and D (bottom). Parametric bootstrap 95% confidence intervals are shown, but may be too small due to the low number of samples.

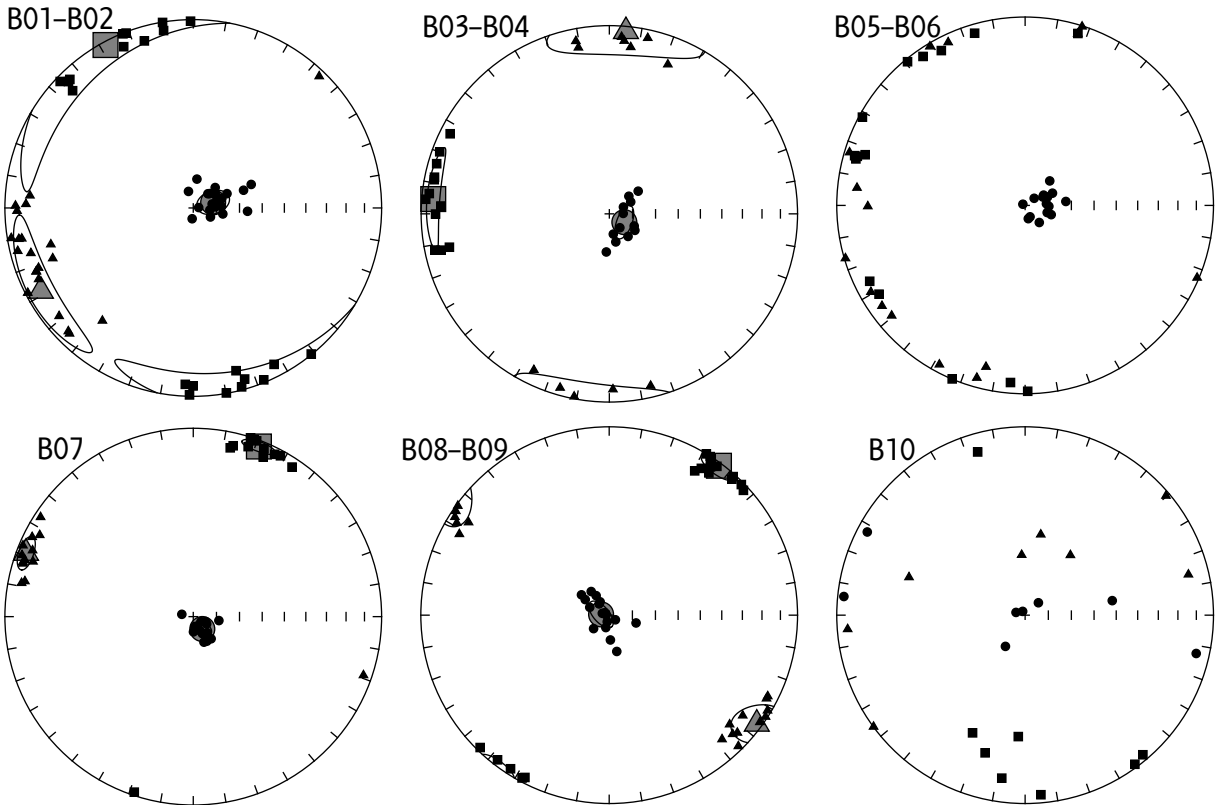

Figure 7.11 AMS directions for suite B. Parametric bootstrap 95% confidence intervals are shown, but may be too small due to the low number of samples.

ization and a normal magnetization from the time of deposition would thus be less than the noise level in the measurements. For analysis purposes I therefore treat these samples a having a single component. I analysed type SO samples by performing a principal component analysis, anchored to the origin, on the points comprising the trend, and taking the Fisher (1953) mean of the PCA directions within each site.

Type SN: single component, not origin directed

Type SN samples showed a single demagnetization trend directed strongly downward towards a point other than the origin. The trend is usually visible up to 200–300°C, after which magnetization varies randomly with subsequent demagnetization steps. I interpreted this behaviour as the progressive removal of a present-day viscous magnetic overprint, with the offset from the origin being due to a depositional remanent magnetization with a higher unblocking temperature. I interpreted the random variation at higher temperatures as the consequence of thermally induced mineral alteration. I analysed these samples by fitting a great circle to the trend, and using the great-circle remagnetization analysis technique of McFadden and McElhinny (1988) to combine the great circles at each site and determine an extrapolated endpoint, which I took to be the DRM.

Type NT: no discernible trend

The magnetization vectors of NT-type samples showed no discernible trend during demagnetization, and varied apparently at random. I interpreted this behaviour as the result of random noise in the measurement process obscuring the signal produced by the sample magnetization. I did not attempt to determine any palaeomagnetic directions from these samples.

Type ND: no demagnetization

Type ND samples show no variation in the magnetization direction with increasing demagnetization steps, except for a slight random variation attributable to measurement noise. This behaviour continues either until the highest heating

step, or until mineral alteration occurs and magnetization begins to vary randomly. I did not attempt to determine palaeomagnetic directions from type-ND samples.

7.5.2 *Palaeomagnetism of the Camp Cove section*

In this section I present the demagnetization behaviours and mean directions from the Camp Cove suites (A and B).

7.5.2.1 *Camp Cove demagnetization behaviours*

The NRMs of the Camp Cove samples were bimodally distributed, which was unsurprising given the two distinct lithologies comprising the section: within suite A, the 23 samples from the limestone of the Tucker Cove Formation had a mean NRM of 46 μA/m; the 22 samples from the Garden Cove Formation mudstone had a mean NRM of 120 μA/m, probably reflecting higher terrigenous input.

Type SN: single component, not origin directed

Although the initial remanence directions of the samples varied widely, the demagnetization behaviours were fairly uniform. 98% ($^{83}/_{85}$) of the samples conformed to type SN (single component, not origin directed). During initial demagnetization, the remanence vector moved steadily downward, with relatively little change in the horizontal components of magnetization. Occasionally the 25–50°C step was in a different direction. In no case was the trend directed towards to origin. At heating steps higher then 200°C, the magnetization vector began to fluctuate seemingly at random with each successive demagnetization step. Occasionally this transition to chaotic behaviour occurred at a slightly different temperature step (175–250°C). Figure 7.12 (p. 217) and figure 7.13 (p. 218) show examples of SN-type behaviour.

I interpreted the initial component to be a viscous overprint from the present-day Brunhes normal polarity chron, based on its low unblocking spectrum and downward-directed demagnetization trend. An analysis of the directions of the 25–200°C curves for suite A supports this: I determined best-fit directions by unanchored principal component analysis and calculated a

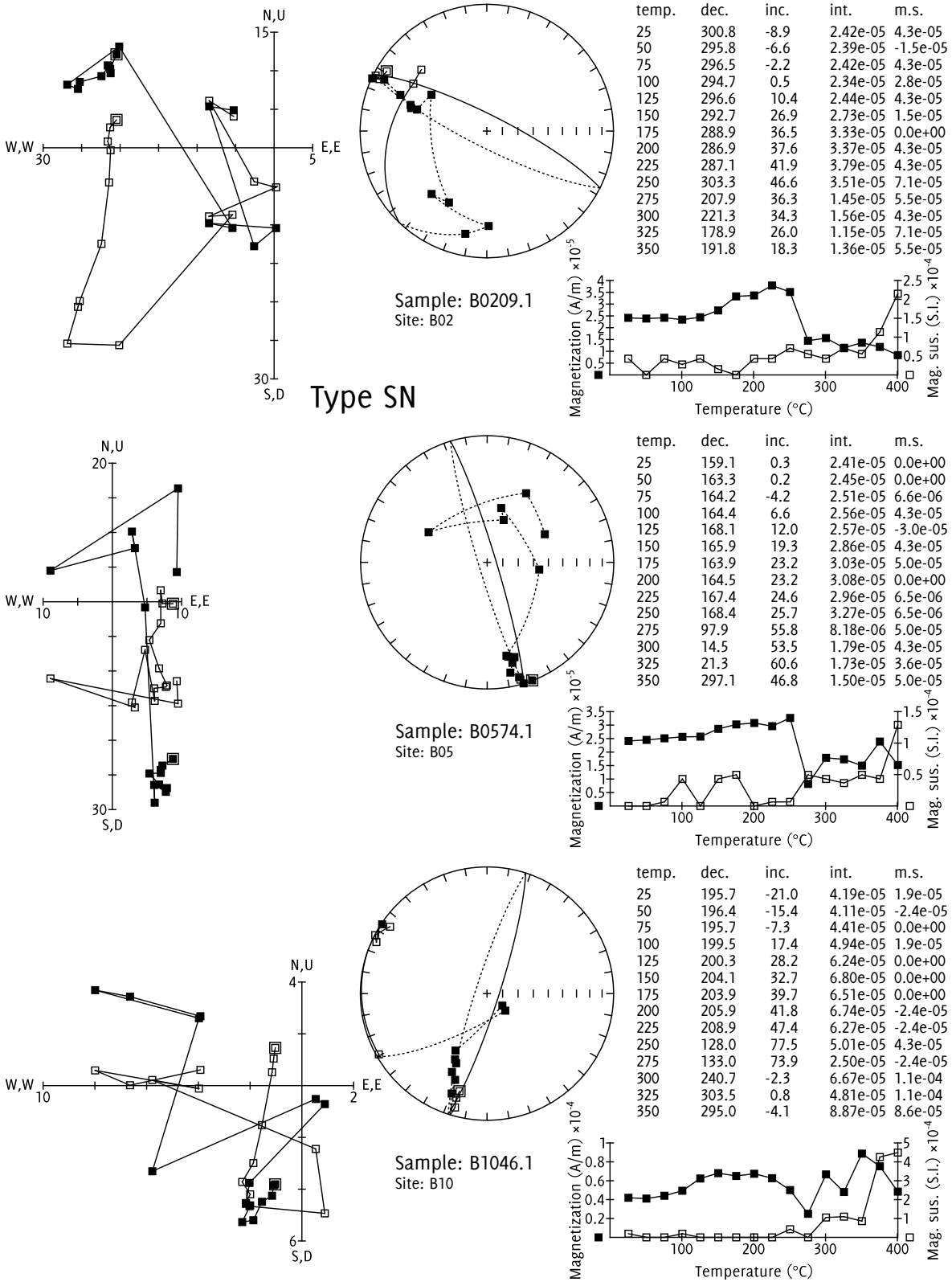

Figure 7.12 Demagnetization behaviours for Camp Cove samples. All samples are type SN, showing a single demagnetization component from 25–200°C followed by random variation. Best-fit great circles are shown, fitted to the 25–200°C points.

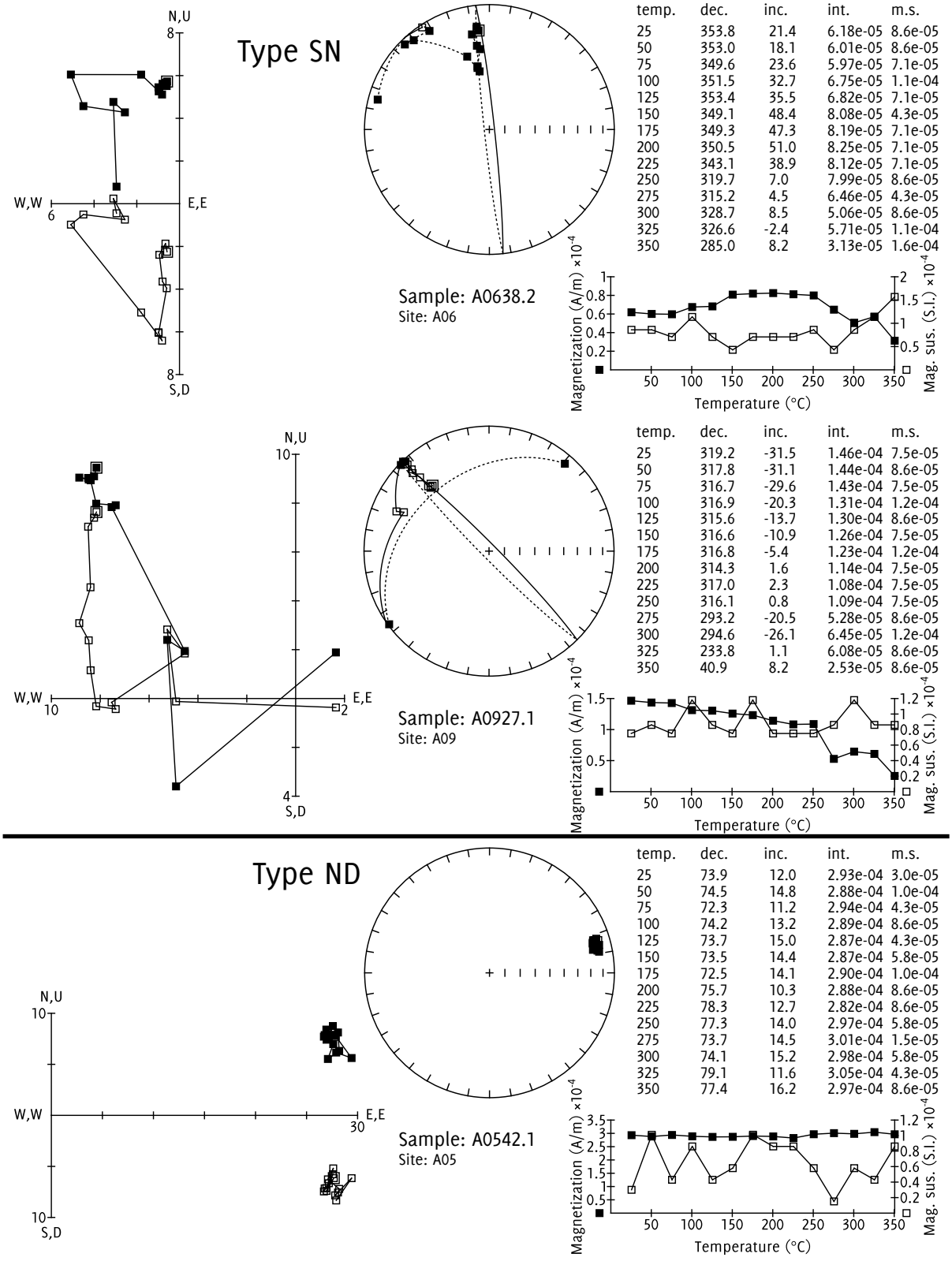

Figure 7.13 Demagnetization behaviours for Camp Cove samples. The top and centre samples are type SN, with a single component from 25–200°C, followed by random variation. Best-fit great circles are shown, fitted to the 25–200°C points. The bottom sample shows type ND (non-demagnetizing) behaviour; no demagnetization components could be determined from it.

Fisher mean for them. The result (I=−67.9°, D=24.3°, α_{95}=9.2°, k=6.4) was close to the current normal GAD field at the site (I=−69°). Since this trend was not origin-directed, I inferred that it was directed towards a stable depositional or post-depositional component carried by magnetite which had not yet begun to unblock to a measurable extent. I took the higher-temperature chaotic behaviour to be due to the onset of heating-induced mineral alteration. The inferred alteration temperature is slightly lower than the alteration temperatures determined by the TDMS experiments, which might be due to the inert argon atmosphere used for those experiments. It may also be that magnetization is in this case more sensitive to mineral alteration than susceptibility.

Type ND: no demagnetization

Type ND behaviour was evident in 2% (2/85) of the samples: A0542.1 and A0544.1, both from site A05. The samples displayed no significant demagnetization at all, the magnetization vector fluctuating slightly around a single point. In A0544.1 this behaviour was succeeded by random variation at 350°C, while in A0542.1 the magnetization vector remained approximately constant up to the maximum temperature of 450°C. Figure 7.13 (p. 218) shows an example of ND-type behaviour.

7.5.2.2 *Camp Cove site mean directions*

Many of the angular demagnetization paths were fairly short – in the worst cases around 10° – but for all the samples (except the two non-demagnetizing ones described above) stable great-circle fits proved possible. I fitted a great circle to the 25–200°C portion of each sample's demagnetization path. There was strong evidence that the great circles were trending towards stable and consistent remanence directions: at each site, three or four circles were fitted, and in most cases they converged on an area less than 10° in diameter (figure 7.14, p. 221). The McFadden and McElhinny (1988) formulae gave $k \geq 14.4$ for all the great-circle fits and $\alpha_{95} \leq 50°$ in all but three cases; in most cases the fit parameters were significantly better than this, with 71% of the samples showing $\alpha_{95} \leq 31°$ and $k \geq 51.5$. Stable remanence directions were determined for all sites except A05, where the two non-demagnetizing samples left only two samples for which a great circle could be fitted.

Site	H (m)	N	Dec.	Inc.	α_{95}	k
A01	38.5	4	159.9	76.4	19.4	84.1
A02	38.1	4	193.0	67.0	12.6	198.7
A03	37.8	4	256.6	77.2	12.7	195.0
A04	37.65	4	66.6	63.7	21.8	66.5
A06	37	3	188.9	71.8	25.1	703.5
A07	36.87	3	167.3	79.3	90.9	65.6
A08	36.77	3	168.2	78.6	67.1	109.0
A09	36.6	4	213.2	81.5	16.5	115.9
B01	36.5	4	237.7	73	48.4	14.4
A10	36.45	4	44.5	84.6	32	31.5
A11	36.3	4	26.0	80.1	16.5	116.1
B02	36.2	4	189.2	79.3	2.7	4177.5
A12	36.1	3	216.4	77.3	122.6	43.4
B03	35	4	252.8	66.9	18.7	89.8
B04	33.7	4	311.2	66.2	20.2	77.6
B05	32.3	4	210.6	75.7	40.4	20.2
B06	23.1	4	211	83.6	15.4	132.8
B07	19.4	4	277.3	80.2	24.9	51.5
B08	16.5	4	345.1	64.9	30	35.7
B09	13.9	4	250	79.8	30.6	34.4
B10	11.2	4	208.9	62.9	14.3	153.3

Table 7.3 Site mean directions determined by great-circle remagnetization analysis for samples from the Camp Cove section. *N* is the number of great circles fitted at each site; Dec and Inc are the inferred final declination and inclination; α_{95} and *k* are the 95% confidence semi-angle and estimated precision parameter produced by the algorithm of McFadden and McElhinny (1988). Due to the small number of samples, the confidence angles are probably unrealistically small. All great circles were fitted from the 25–200°C demagnetization steps. No direction was determined for site A05 since only two of its samples were successfully demagnetized (see text for details).

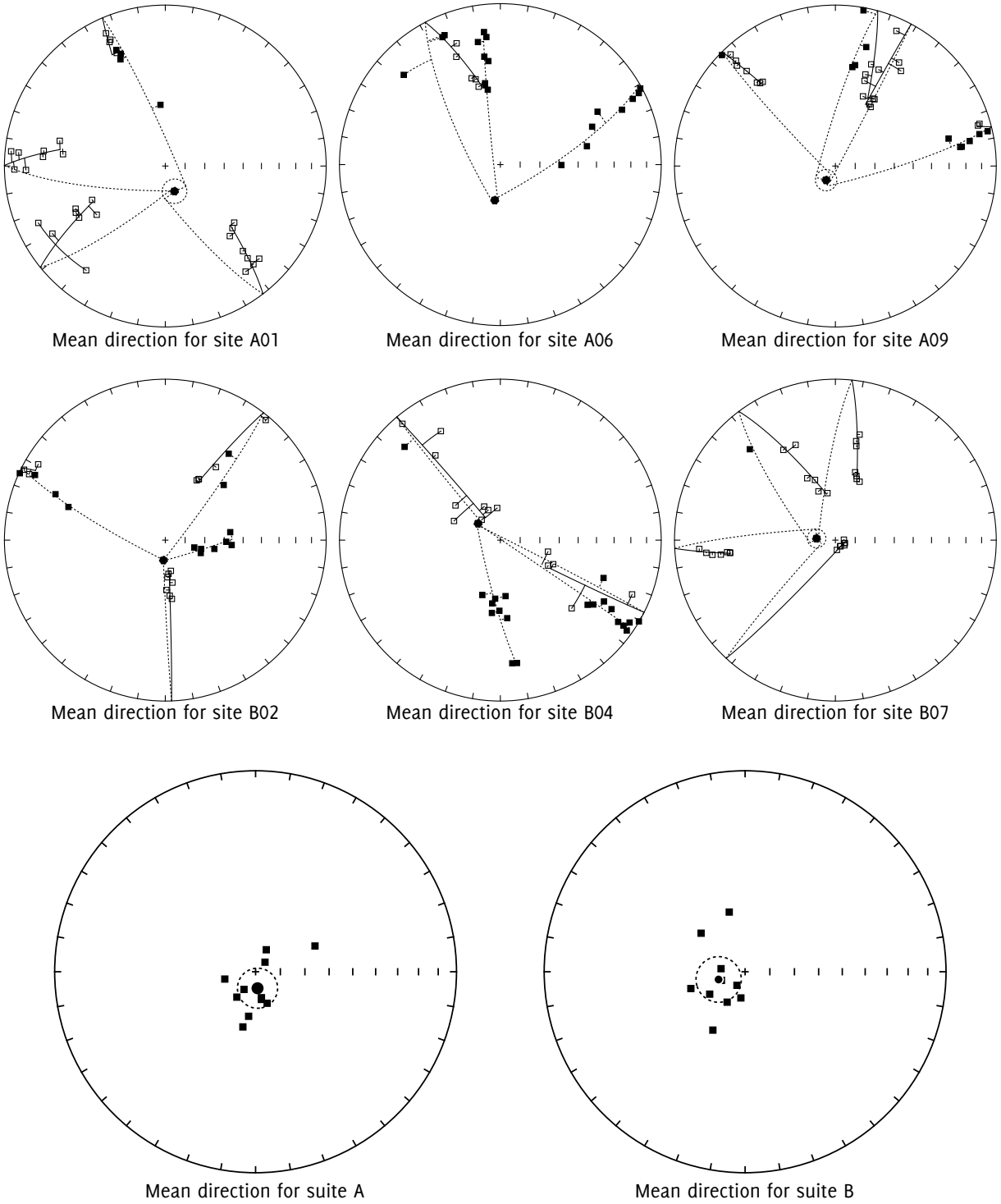

Figure 7.14 Site mean directions and formation mean directions for suite A and suite B at the Camp Cove section. On site mean plots (top and middle), square points show demagnetization steps, round points show site means, lines show best fit great circles, and small circle around site mean shows the largest distance to any of the great circles. On formation mean plots (bottom), squares points show site means, round points show formation means, and small circles show Fisher 95% confidence regions.

The site mean directions, as determined by great-circle intersection, all lay in the lower hemisphere, indicating a reversed geomagnetic field during deposition. Table 7.3 (p. 220) shows details of the Camp Cove site mean directions. Figure 7.15 (p. 223) and figure 7.16 (p. 224) show the inclinations and declinations of the site mean directions, as well as the palaeocurrent directions inferred from AMS, overlaid on the graphic logs shown previously.

7.5.2.3 *Camp Cove formation mean directions*

I have chosen to calculate formation mean directions separately for suite A and suite B, since their site mean directions appear to form two fairly distinct, though closely spaced, clusters. Below, I discuss possible reasons for this appearance of two different directions in stratigraphically overlapping suites of samples.

Suite	Declination	Inclination	α_{95}	k
A	173.2	83.3	8.1	32.8
B	253.7	78.8	9.2	28.7

Table 7.4 Formation mean direction s for Camp Cove

The formation mean directions, calculated using Fisher (1953) statistics, are shown in table 7.4. These directions, and the site mean directions from which they are derived, are shown in figure 7.14 (p. 221). The inclinations of the poles are both in good agreement with the known tectonic constraints in the latest Cretaceous and earliest Palaeogene (Cook *et al.*, 1999), which put the latitude of Campbell Island at approximately 70–75° South.

The declinations of the formation mean directions must be interpreted with caution, since the high inclinations mean that even small directional errors can result in large variations in declination. At site A, the Fisherian 95% confidence circle encompasses the pole, meaning that technically no constraints on the declination at all can be established at the 95% confidence level. However, a northward-pointing declination would require an almost vertical inclination, which would give a tectonically impossible latitude (>85°), so it is reasonable to conclude that the true palaeopole lies in one of the southern quadrants.

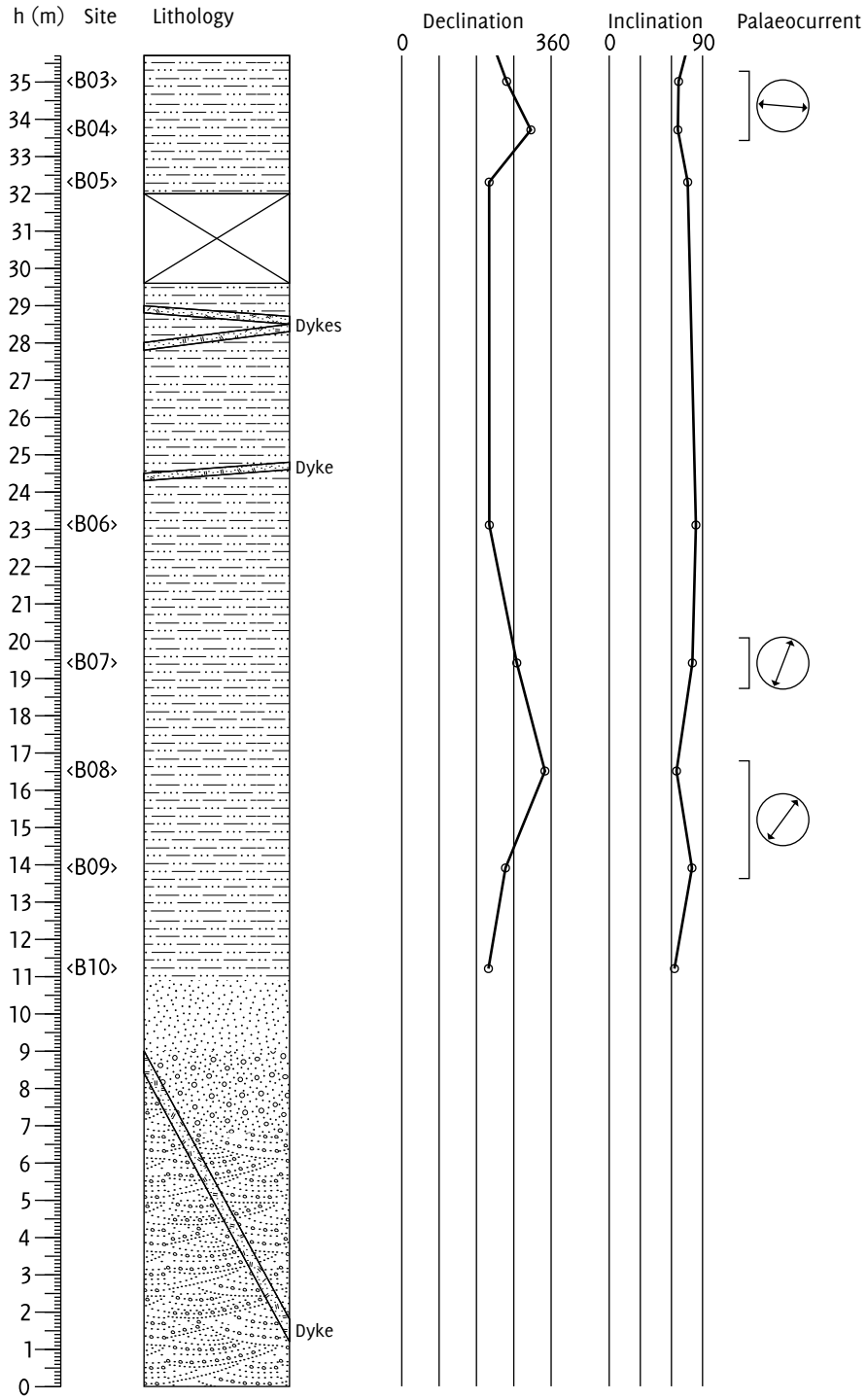

Figure 7.15 Site mean directions on the Camp Cove log, part 1

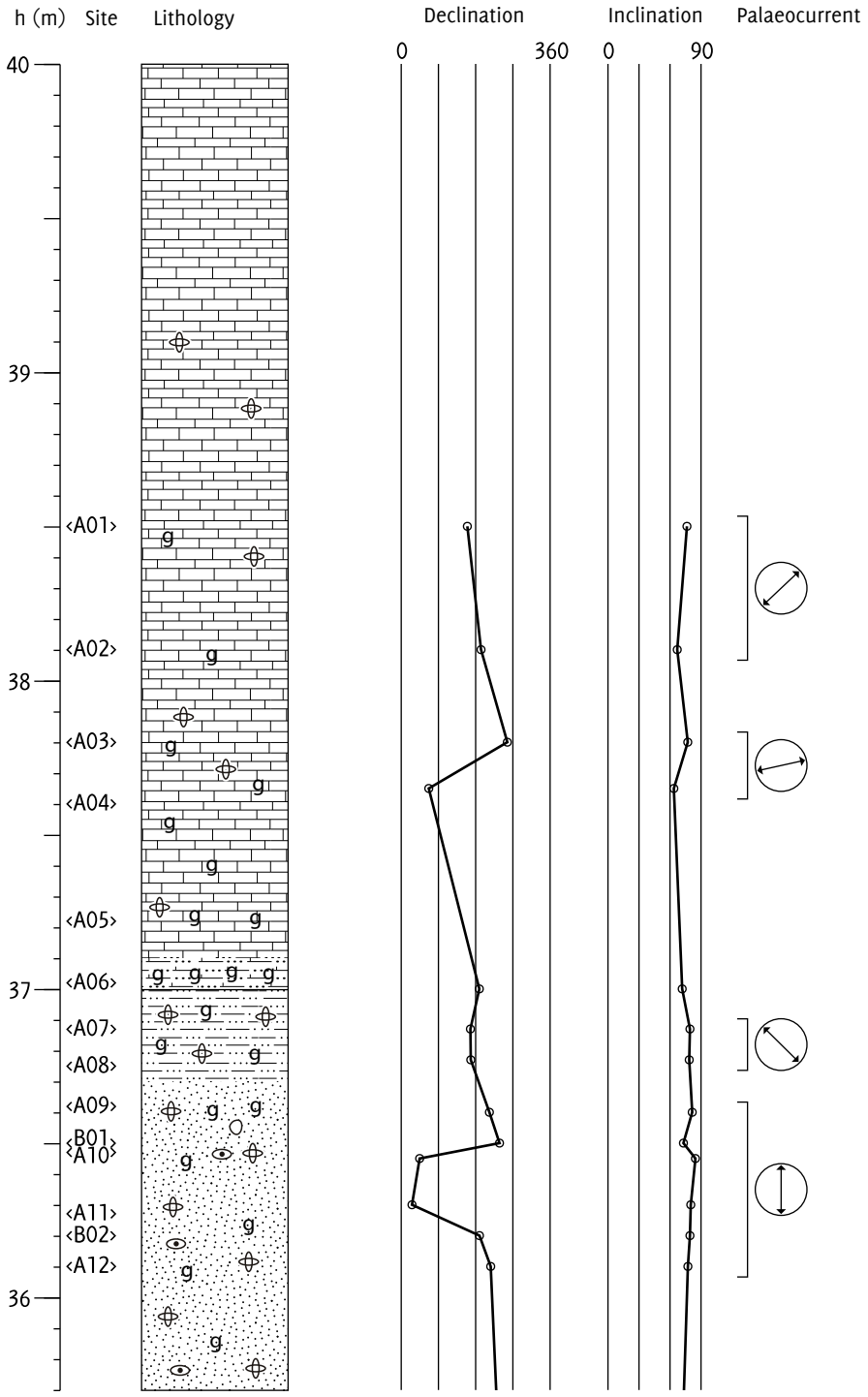

Figure 7.16 Site mean directions on the Camp Cove log, part 2

The mean declination of the suite A palaeopole is in reasonable agreement with the known tectonic constraints: although the mean declination of 173.2° would imply a much smaller rotation than the >40° determined by Sutherland (1995), the expected declination and inclination are well within the 95% confidence interval.

The declination of the suite B palaeopole is more difficult to account for: the mean direction is almost due west, far from the expected south-eastern quadrant, and the confidence interval is too small to contain the expected direction. One possible explanation for this anomaly is an error in the measurement of the bedding orientation: no clear bedding structures were evident in the Garden Cove Formation at Camp Cove, so I used the measured bedding attitude of the overlying Tucker Cove Formation to correct the directions. If there is a slight angular unconformity between these formations at Camp Cove, this would produce an error in the Garden Cove Formation site mean directions; due to the high inclinations, only a slight bedding error would be sufficient to alter the declination by a large amount.

7.5.3 *Palaeomagnetism of the Limestone Point section*

In this section I present the demagnetization behaviours and mean directions from the Limestone Point suites (C and D).

7.5.3.1 *Limestone Point demagnetization behaviours*

The Limestone Point samples comprise two suites, C and D. The demagnetization data from suite C were difficult to analyse, for a number of reasons. Firstly, like all the sediments studied in this thesis, they had weak remanent magnetizations: excluding the dyke at site 9, the mean NRM intensity was 330 μA/M. Secondly, they were the first samples I analysed in the course of this thesis, and at the time of the study I had not developed the software tools and protocols for treatment of weak samples which I describe in chapter 4. The high noise levels in the suite C data prompted me to develop the methods which I applied to subsequent palaeomagnetic studies; unfortunately the methods could not be applied retrospectively to suite C, since they require extra measurements during the demagnetization process. Thirdly, I only demagnetized three samples

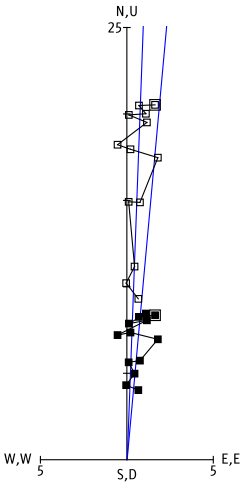

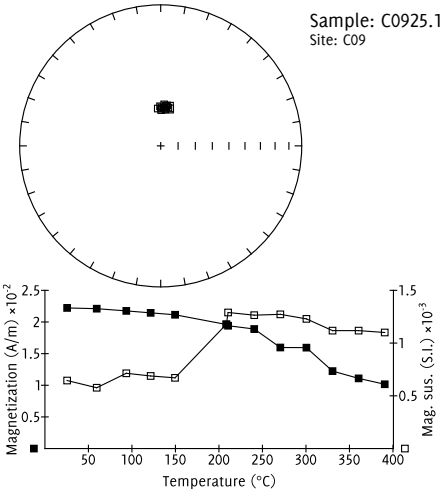

temp.	dec.	inc.	int.	m.s.
25	10.9	-67.5	2.22e-02	6.5e-04
59	4.7	-68.0	2.21e-02	5.8e-04
93	7.2	-66.9	2.18e-02	7.1e-04
121	0.6	-68.5	2.14e-02	6.9e-04
149	8.0	-67.3	2.11e-02	6.7e-04
208	355.5	-68.3	1.96e-02	1.2e-03
210	1.4	-67.7	1.94e-02	1.3e-03
240	14.2	-67.6	1.89e-02	1.3e-03
270	7.3	-68.8	1.60e-02	1.3e-03
300	0.8	-69.3	1.59e-02	1.2e-03
330	4.8	-65.9	1.22e-02	1.1e-03
360	359.1	-67.1	1.11e-02	1.1e-03
390	9.0	-66.3	1.02e-02	1.1e-03
- 420	3.1	-67.0	6.42e-03	1.3e-03
- 450	8.3	-68.0	4.50e-03	1.7e-03
- 480	71.3	-83.0	1.54e-03	7.4e-03
- 510	321.4	36.5	2.28e-03	2.0e-02
- 540	67.4	35.1	2.11e-03	2.6e-02
- 570	358.3	-74.7	7.73e-04	2.8e-02
- 600	97.7	-63.1	1.69e-03	3.3e-02

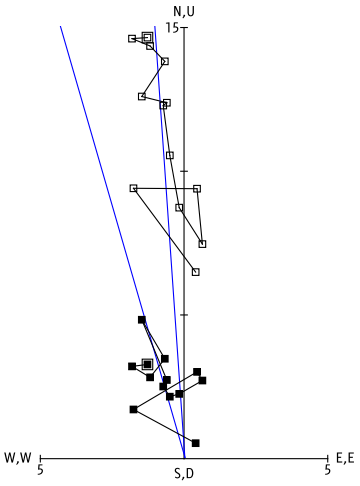

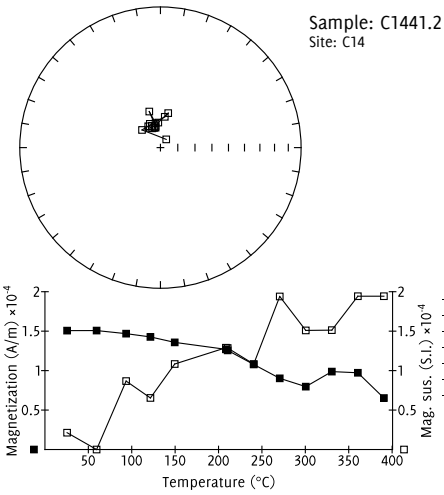

temp.	dec.	inc.	int.	m.s.
25	338.4	-76.5	1.51e-04	2.1e-05
59	330.2	-75.8	1.51e-04	0.0e+00
93	336.9	-77.9	1.47e-04	8.7e-05
121	348.7	-75.6	1.43e-04	6.5e-05
149	342.8	-68.1	1.36e-04	1.1e-04
208	347.1	-77.2	1.27e-04	1.3e-04
210	343.4	-78.0	1.26e-04	1.3e-04
240	346.4	-78.1	1.08e-04	1.1e-04
270	355.1	-75.5	9.02e-05	1.9e-04
300	12.7	-69.5	7.97e-05	1.5e-04
330	8.0	-72.0	9.88e-05	1.5e-04
360	313.8	-75.3	9.73e-05	1.9e-04
390	35.1	-84.2	6.52e-05	1.9e-04
- 420	96.5	-69.7	5.47e-05	2.6e-04
- 450	206.3	-34.8	3.70e-05	6.5e-04
- 480	179.8	-49.2	1.32e-04	8.0e-04
- 510	64.0	9.3	9.84e-05	8.2e-04
- 540	98.6	-11.7	6.67e-04	9.9e-04
- 570	110.9	-31.4	1.25e-03	1.4e-03
- 600	154.4	-25.1	5.35e-03	1.8e-03

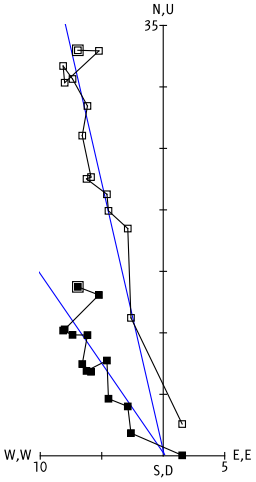

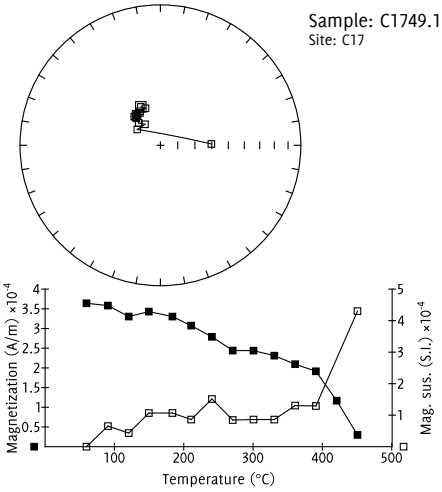

temp.	dec.	inc.	int.	m.s.
- 25	307.2	-68.2	7.25e-04	-1.4e-06
59	333.0	-64.9	3.64e-04	-2.2e-05
90	338.0	-66.8	3.58e-04	6.5e-05
120	321.8	-66.7	3.30e-04	4.3e-05
149	321.1	-67.6	3.43e-04	1.1e-04
183	322.9	-68.1	3.30e-04	1.1e-04
210	327.6	-67.8	3.07e-04	8.6e-05
240	318.3	-69.0	2.79e-04	1.5e-04
270	319.0	-68.2	2.44e-04	8.5e-05
300	317.6	-67.5	2.44e-04	8.6e-05
330	329.1	-67.0	2.31e-04	8.6e-05
360	315.8	-72.0	2.09e-04	1.3e-04
390	323.7	-74.9	1.91e-04	1.3e-04
420	304.5	-73.8	1.17e-04	NaN
450	88.5	-60.3	2.98e-05	4.3e-04
- 480	214.1	-16.0	1.68e-04	5.0e-04
- 510	21.8	-76.0	2.23e-04	6.2e-04
- 540	279.0	41.7	4.25e-04	7.1e-04
- 570	4.5	-24.7	2.53e-03	1.1e-03
- 600	254.5	-10.9	1.72e-03	1.2e-03

Figure 7.17 Limestone Point demagnetization behaviours: type S0, Projections of the origin-anchored linear PCA fit are overlaid on the Zijderveld plots. The topmost sample (C0925.1) is from the dyke, hence the strong NRM intensity.

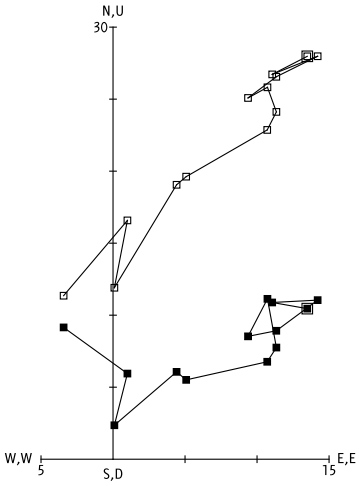

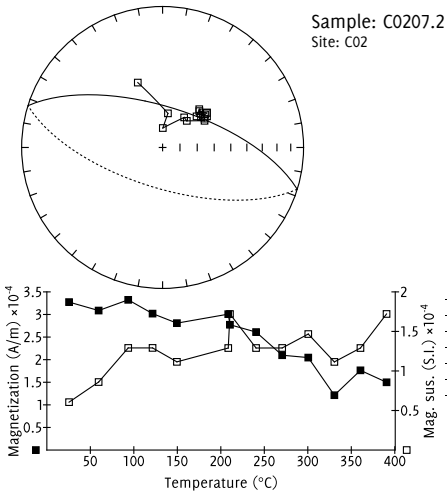

temp.	dec.	inc.	int.	m.s.
25	52.1	-58.7	3.27e-04	6.1e-05
59	45.3	-59.9	3.09e-04	8.6e-05
93	52.0	-57.3	3.32e-04	1.3e-04
121	51.6	-61.6	3.02e-04	1.3e-04
149	47.5	-63.3	2.81e-04	1.1e-04
208	43.7	-59.2	3.01e-04	1.3e-04
210	55.5	-60.4	2.77e-04	1.7e-04
240	57.5	-61.1	2.61e-04	1.3e-04
270	42.3	-69.2	2.10e-04	1.3e-04
300	35.6	-68.6	2.05e-04	1.5e-04
330	0.7	-78.8	1.21e-04	1.1e-04
360	8.9	-70.0	1.76e-04	1.3e-04
390	339.1	-49.2	1.50e-04	1.7e-04
- 420	19.8	-54.2	1.08e-04	2.2e-04
- 450	322.9	-34.5	1.68e-04	1.6e-03
- 480	2.3	-15.1	3.87e-04	2.0e-03
- 510	270.8	-35.6	1.06e-03	2.7e-03
- 540	318.4	5.8	9.59e-04	3.7e-03
- 570	109.8	-29.4	9.54e-04	3.7e-03
- 600	0.6	14.2	1.45e-03	3.6e-03

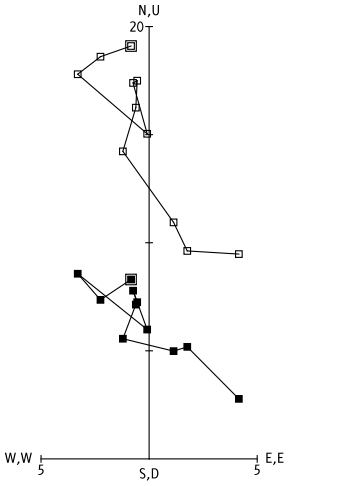

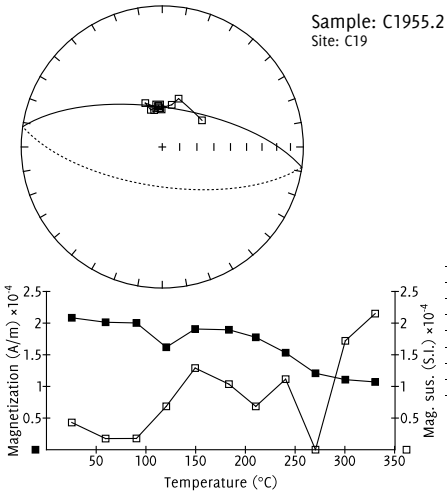

temp.	dec.	inc.	int.	m.s.
25	354.2	-66.4	2.08e-04	4.3e-05
59	342.9	-67.5	2.01e-04	1.8e-05
90	338.8	-62.7	2.00e-04	1.8e-05
120	359.0	-68.3	1.62e-04	6.9e-05
149	354.4	-65.8	1.91e-04	1.3e-04
183	355.5	-67.4	1.89e-04	1.0e-04
210	355.0	-66.2	1.78e-04	6.8e-05
240	347.5	-68.2	1.53e-04	1.1e-04
270	12.6	-65.0	1.21e-04	4.4e-08
300	18.7	-60.4	1.11e-04	1.7e-04
330	56.1	-62.3	1.07e-04	2.2e-04
- 360	105.3	-68.0	8.98e-05	2.8e-04
- 390	25.2	-23.2	5.08e-05	3.4e-04
- 420	63.8	-6.8	6.24e-05	NaN
- 450	289.2	-22.0	2.18e-04	8.4e-04
- 480	53.3	15.2	1.06e-03	9.3e-04
- 510	22.1	29.1	1.56e-03	1.2e-03
- 540	33.4	8.6	1.81e-03	1.2e-03
- 570	44.8	-1.4	2.86e-03	1.2e-03
- 600	46.5	-12.4	2.56e-03	1.3e-03

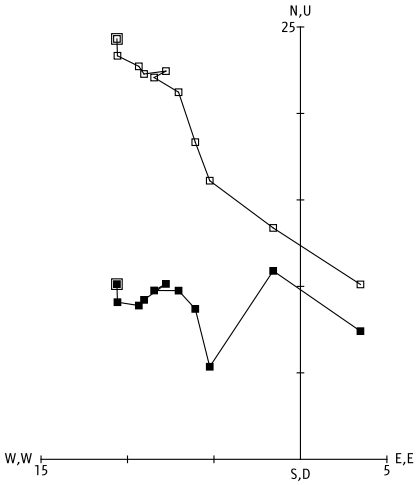

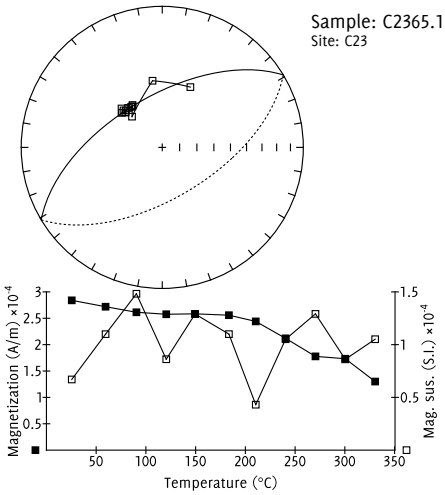

temp.	dec.	inc.	int.	m.s.
25	313.6	-58.9	2.84e-04	6.7e-05
59	310.6	-59.1	2.72e-04	1.1e-04
90	313.5	-60.4	2.61e-04	1.5e-04
120	315.5	-59.9	2.58e-04	8.6e-05
149	322.5	-60.3	2.58e-04	1.3e-04
183	319.0	-59.7	2.56e-04	1.1e-04
210	324.1	-60.4	2.44e-04	4.3e-05
240	325.0	-59.9	2.12e-04	1.1e-04
270	315.5	-65.0	1.78e-04	1.3e-04
300	351.7	-50.5	1.73e-04	8.6e-05
330	25.0	-51.0	1.30e-04	1.1e-04
- 360	354.8	-72.1	5.89e-05	1.3e-04
- 390	358.1	-38.6	1.06e-04	1.3e-04
- 420	25.1	-49.2	7.62e-05	NaN
- 450	9.5	-20.0	6.75e-05	8.4e-04
- 480	3.6	-1.1	6.96e-05	1.0e-03
- 510	349.2	-32.1	8.59e-05	1.2e-03
- 540	51.6	-31.0	7.97e-05	1.3e-03
- 570	67.7	-29.4	1.22e-04	1.4e-03
- 600	23.8	58.6	1.07e-04	1.6e-03

Figure 7.18 Limestone Point demagnetization behaviours: type SN. Great circles are fitted to the single, non-origin-directed, component.

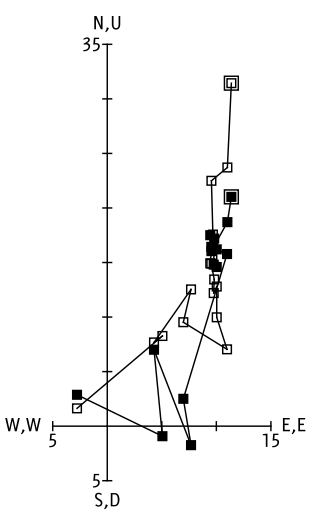

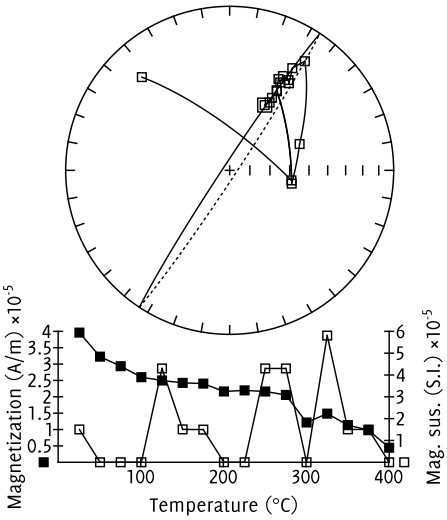

Sample: D0103.2
Site: D01

temp.	dec.	inc.	int.	m.s.
25	28.2	-52.8	3.96e-05	1.5e-05
50	30.3	-47.6	3.23e-05	-2.8e-05
75	30.5	-50.3	2.94e-05	-1.3e-05
100	30.4	-42.8	2.60e-05	-1.3e-05
125	28.1	-37.0	2.50e-05	4.3e-05
150	29.9	-38.2	2.43e-05	1.5e-05
175	29.5	-34.3	2.40e-05	1.5e-05
200	33.1	-34.7	2.16e-05	-2.8e-05
225	34.2	-36.0	2.20e-05	-1.3e-05
250	31.5	-27.8	2.16e-05	4.3e-05
275	34.6	-20.3	2.06e-05	4.3e-05
300	69.4	-52.4	1.22e-05	-2.8e-05
325	102.1	-58.3	1.49e-05	5.8e-05
350	30.9	-43.2	1.14e-05	1.5e-05
375	99.2	-58.7	9.79e-06	1.5e-05
400	316.7	-23.0	4.45e-06	0.0e+00

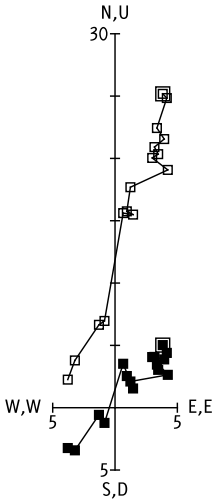

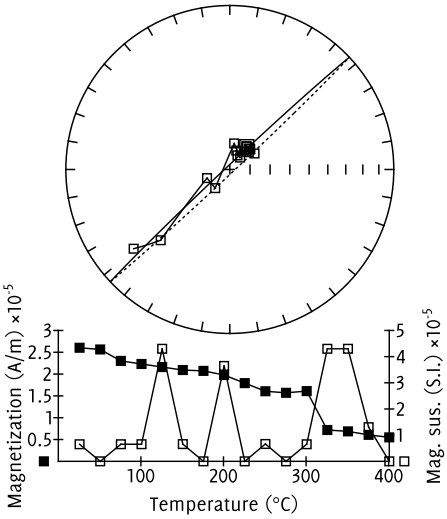

Sample: D0515.2
Site: D05

temp.	dec.	inc.	int.	m.s.
25	36.6	-75.9	2.60e-05	6.5e-06
50	42.6	-76.3	2.56e-05	0.0e+00
75	43.2	-77.9	2.30e-05	6.5e-06
100	44.6	-75.6	2.23e-05	6.5e-06
125	36.9	-76.1	2.16e-05	4.3e-05
150	47.7	-77.3	2.09e-05	6.6e-06
175	35.3	-75.9	2.07e-05	0.0e+00
200	57.1	-75.4	1.98e-05	3.6e-05
225	28.5	-82.1	1.79e-05	-3.6e-05
250	18.9	-80.1	1.61e-05	6.6e-06
275	40.9	-82.2	1.57e-05	-3.6e-05
300	9.5	-76.9	1.61e-05	6.5e-06
325	218.0	-78.3	7.18e-06	4.3e-05
350	249.3	-77.9	6.87e-06	4.3e-05
375	224.3	-39.5	6.07e-06	1.3e-05
400	230.5	-25.0	5.49e-06	0.0e+00

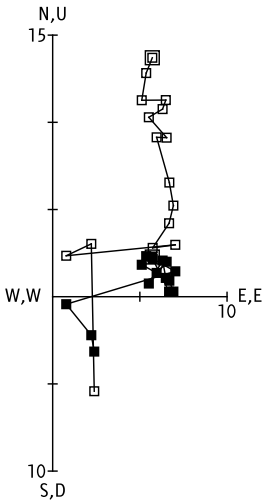

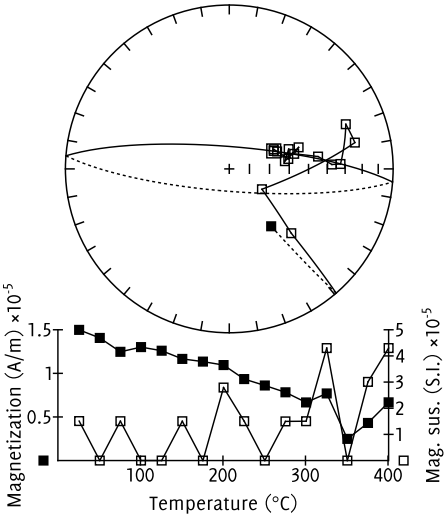

Sample: D0616.1
Site: D06

temp.	dec.	inc.	int.	m.s.
25	68.0	-66.1	1.50e-05	1.5e-05
50	66.2	-65.8	1.41e-05	0.0e+00
75	70.0	-64.6	1.25e-05	1.5e-05
100	80.4	-60.1	1.30e-05	-2.8e-05
125	71.6	-58.6	1.26e-05	0.0e+00
150	82.1	-62.0	1.17e-05	1.5e-05
175	72.7	-53.5	1.13e-05	0.0e+00
200	76.9	-56.6	1.10e-05	2.8e-05
225	82.1	-44.5	9.34e-06	1.5e-05
250	87.5	-37.4	8.61e-06	-2.8e-05
275	87.5	-32.6	7.83e-06	1.5e-05
300	69.0	-24.8	6.67e-06	1.5e-05
325	78.2	-22.8	7.70e-06	4.3e-05
350	121.9	-70.9	2.49e-06	0.0e+00
375	136.0	-44.7	4.31e-06	3.0e-05
400	143.9	54.3	6.68e-06	4.3e-05

Figure 7.19 Limestone Point demagnetization behaviours, type SN. All samples display a single demagnetization component starting at 25°C and ending at 275–400°C. Best-fit great circles are shown, fitted to the single component.

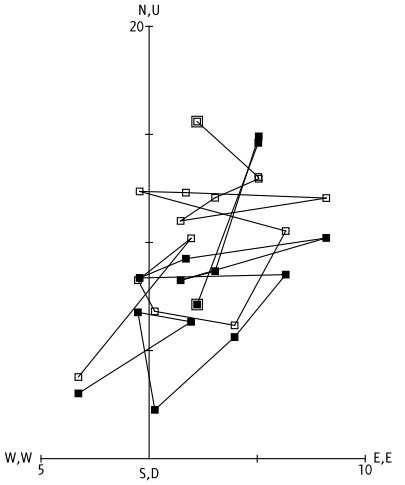

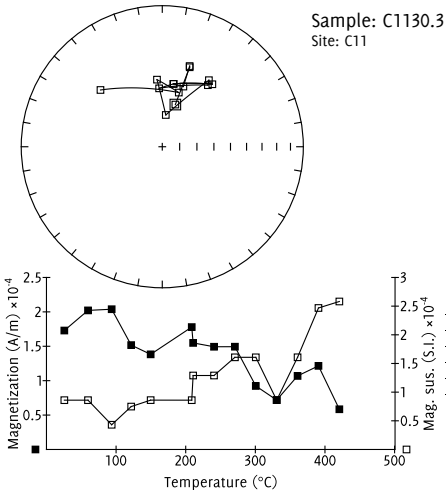

temp.	dec.	inc.	int.	m.s.
25	17.2	-64.4	1.73e-04	8.6e-05
59	19.0	-40.1	2.02e-04	8.6e-05
93	18.7	-39.4	2.04e-04	4.3e-05
121	19.3	-52.7	1.52e-04	7.5e-05
149	9.9	-52.7	1.38e-04	8.6e-05
208	38.7	-42.7	1.78e-04	8.6e-05
210	10.3	-52.6	1.55e-04	1.3e-04
240	356.9	-55.9	1.49e-04	1.3e-04
270	36.5	-44.8	1.49e-04	1.6e-04
300	35.0	-41.9	9.23e-05	1.6e-04
330	6.3	-71.6	7.18e-05	8.6e-05
360	355.5	-50.6	1.07e-04	1.6e-04
390	16.9	-57.0	1.22e-04	2.5e-04
420	312.6	-40.2	5.84e-05	2.6e-04
- 450	203.1	42.9	6.67e-05	1.1e-03
- 480	286.6	-18.5	3.69e-04	2.0e-03
- 510	25.4	3.2	3.99e-04	2.5e-03
- 540	25.4	-34.3	3.59e-03	2.5e-03
- 570	58.7	7.1	1.30e-03	2.4e-03
- 600	300.8	55.6	7.68e-04	2.4e-03

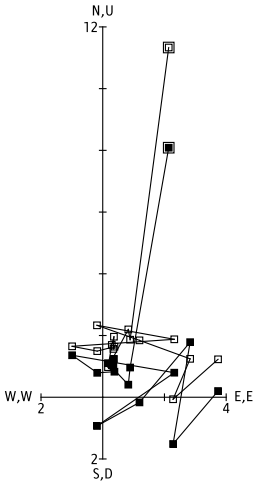

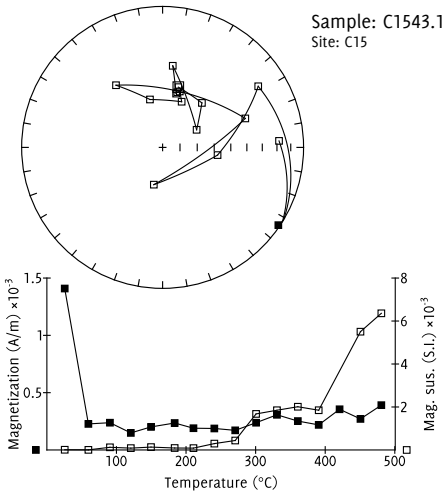

temp.	dec.	inc.	int.	m.s.
25	14.6	-53.6	1.41e-03	9.8e-06
59	41.5	-55.4	2.27e-04	4.9e-06
90	62.6	-67.9	2.38e-04	1.2e-04
120	7.1	-41.3	1.49e-04	8.6e-05
149	14.1	-57.7	2.01e-04	1.3e-04
183	14.9	-56.7	2.35e-04	9.1e-05
210	17.1	-55.9	1.90e-04	8.6e-05
240	22.6	-61.3	1.87e-04	3.0e-04
270	345.2	-61.2	1.71e-04	4.4e-04
300	323.1	-44.1	2.38e-04	1.7e-03
330	70.7	-37.9	3.07e-04	1.8e-03
360	193.3	-67.9	2.52e-04	2.0e-03
390	98.0	-57.7	2.19e-04	1.8e-03
420	57.4	-20.6	3.55e-04	NaN
450	123.9	1.2	2.71e-04	5.5e-03
480	86.8	-18.4	3.91e-04	6.4e-03
- 510	8.0	-24.3	7.93e-04	4.8e-03
- 540	1.3	-7.3	1.28e-03	5.4e-03
- 570	75.7	41.5	1.65e-03	5.2e-03
- 600	58.5	-2.7	1.57e-03	5.5e-03

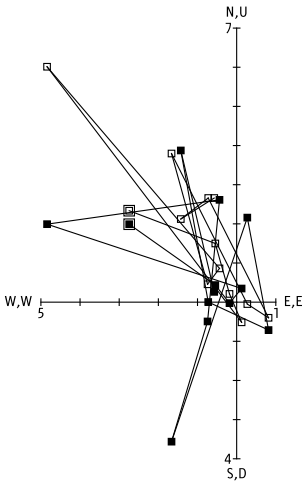

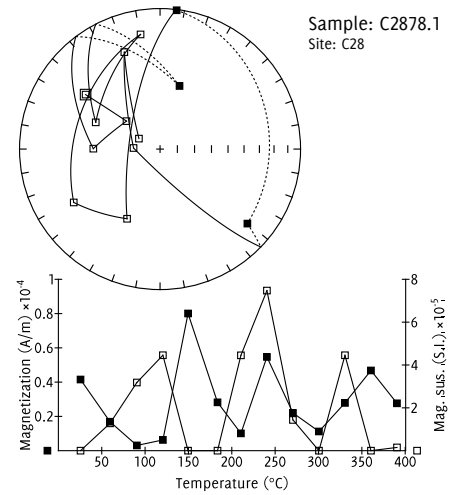

temp.	dec.	inc.	int.	m.s.
25	306.2	-34.7	4.15e-05	0.0e+00
59	309.8	-64.6	1.69e-05	1.3e-05
90	270.4	-50.7	3.06e-06	3.2e-05
120	17.2	51.2	6.26e-06	4.5e-05
149	292.6	-49.0	8.01e-05	0.0e+00
183	350.3	-18.4	2.82e-05	-3.0e-05
210	238.3	-28.6	1.01e-05	4.5e-05
240	205.3	-44.3	5.47e-05	7.5e-05
270	6.8	0.6	2.20e-05	1.4e-05
300	130.5	19.4	1.12e-05	-1.1e-05
330	272.3	-74.6	2.79e-05	4.5e-05
360	339.8	-27.3	4.68e-05	-4.1e-05
390	296.4	-76.4	2.76e-05	1.5e-06
420	199.4	23.7	2.67e-05	6.4e-05
450	202.2	13.3	1.81e-05	6.4e-05
480	217.5	-26.2	4.28e-05	8.9e-05
510	142.3	76.0	1.08e-03	1.1e-04
540	204.9	-16.9	5.22e-05	7.6e-05
570	176.5	-50.6	2.88e-05	1.1e-04
600	114.0	58.7	2.04e-05	1.5e-04

Figure 7.20 Limestone Point demagnetization behaviours: type NT. No clear demagnetization trends are visible.

per site; when applying great-circle remagnetization analysis, this is the minimum number required to determine a site mean direction. Thus if any of the three samples from a site is uninterpretable, no direction can be determined. For suite D, the new protocols proved effective and all the samples yielded useful data.

I classified the demagnetization behaviours of the 103 Limestone Point samples into one of three types. The general characteristics of these types are described in more detail in section 7.5.1.

Type SO: single component, origin directed

This behaviour was shown by 14% (14/103) of the samples. These samples have a highly inclined, north-directed NRM, demagnetizing towards the origin. I interpreted this as the superposition of a normal depositional remanent magnetization (or, in the case of the samples from site C09, within the dyke, a thermal remanent magnetization) and a viscous overprint from the present-day normal chron. I determined directions from these samples using anchored linear PCA. Figure 7.17 (p. 226) shows examples of SO-type demagnetization behaviour in Limestone Point samples.

Type SN: single component, not origin directed

This behaviour was shown by 59% (61/103) of the samples.

Their demagnetization trend is usually apparent up to around 200–350°C, beyond which it is succeeded by random behaviour, which I attributed to heating-induced mineral alteration. The only exception was sample D0515.2, where the demagnetization trend continued all the way to the final heating step of 400°C. The samples all had an upward-pointing NRM; with successive heating steps, the magnetization vector moved downward, usually with relatively little change in the horizontal components. I analysed these samples using the great-circle remagnetization technique. Figure 7.18 (p. 227) and figure 7.19 (p. 228) show six examples of SN-type demagnetization behaviour.

Type NT: no discernible trend

Type NT behaviour was shown by 27% (28/103) of the samples. All suite C samples from sites C26–C28, in the limestone of the Tucker Cove Formation, showed

Set	Polarity	Dec.	Inc.	α_{95}	k
C	R	166.6	69.7	7.1	61.9
C	N	339.8	−75.9	6.8	1355.6
D	R	201.5	74.2	7.4	67.5

Table 7.5 formation mean directions for Limestone Point

this behaviour, almost certainly due to their low natural remanence (mean intensity 66 μA/m) and the less sophisticated experimental protocol. (By comparison, suite D samples from the same lithology were all successfully analysed as type SN with the new protocol.) I did not attempt to perform any palaeomagnetic analysis on NT-type samples. Figure 7.20 (p. 229) shows examples of NT-type behaviour.

7.5.3.2 *Limestone Point site mean directions*

Table 7.6 shows details of the site mean directions at Limestone Point. Figure 7.23 (p. 235) shows examples of the determination of site mean directions by intersecting great-circle remagnetization paths. Figure 7.21 (p. 232) and figure 7.22 (p. 233) show the inclinations and declinations of the site mean directions on a graphic log, as well as the palaeocurrent directions inferred from AMS for the samples near the top of the section.

7.5.3.3 *Limestone Point formation mean directions*

At Limestone Point, as at Camp Cove, the site mean directions of the two suites from this section appear to cluster around slightly different directions, so I have once again calculated two formation mean directions. The formation mean directions are listed in table 7.5 (p. 231).

7.5.4 *Field tests for palaeomagnetic stability*

To verify that the directions I determined did indeed correspond to primary remanences, I carried out two types of well-established field test on them.

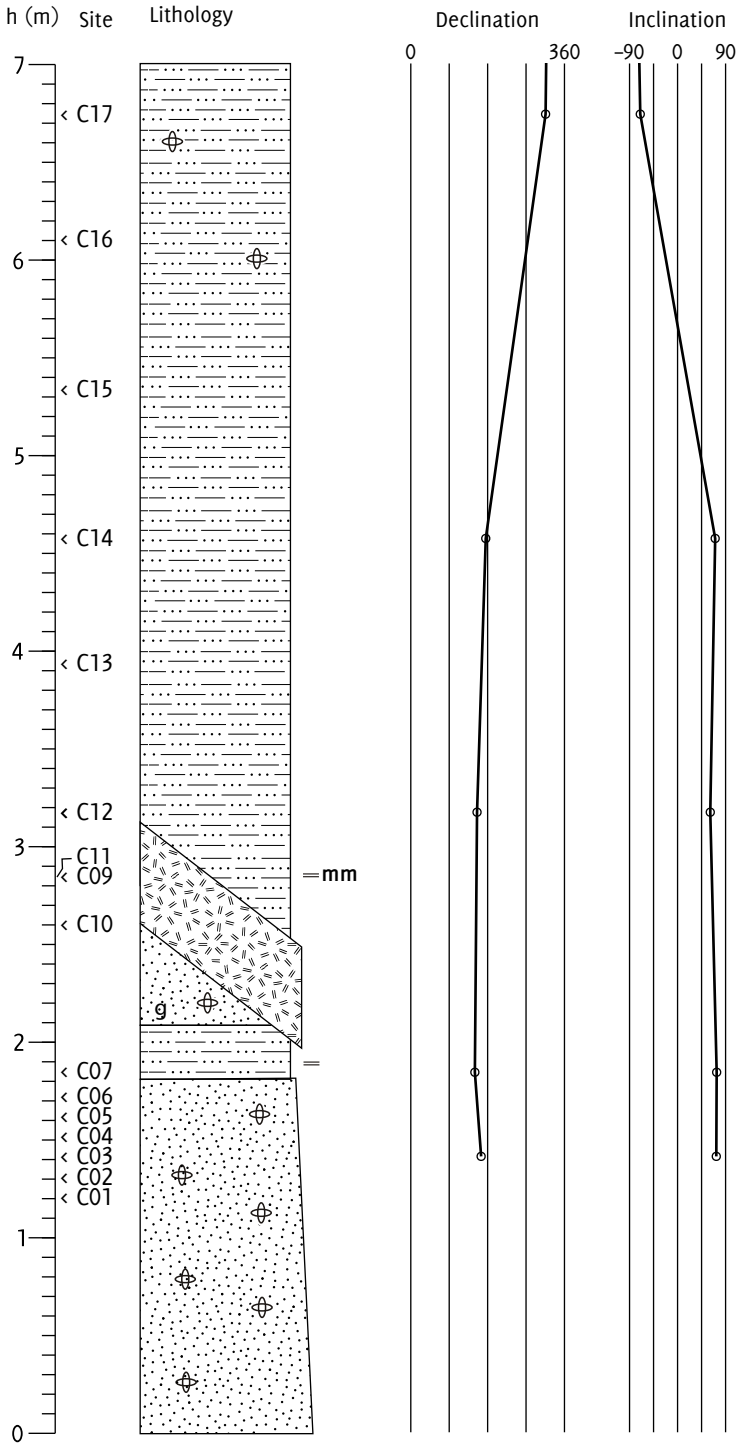

Figure 7.21 Site mean directions for lower Limestone Point section

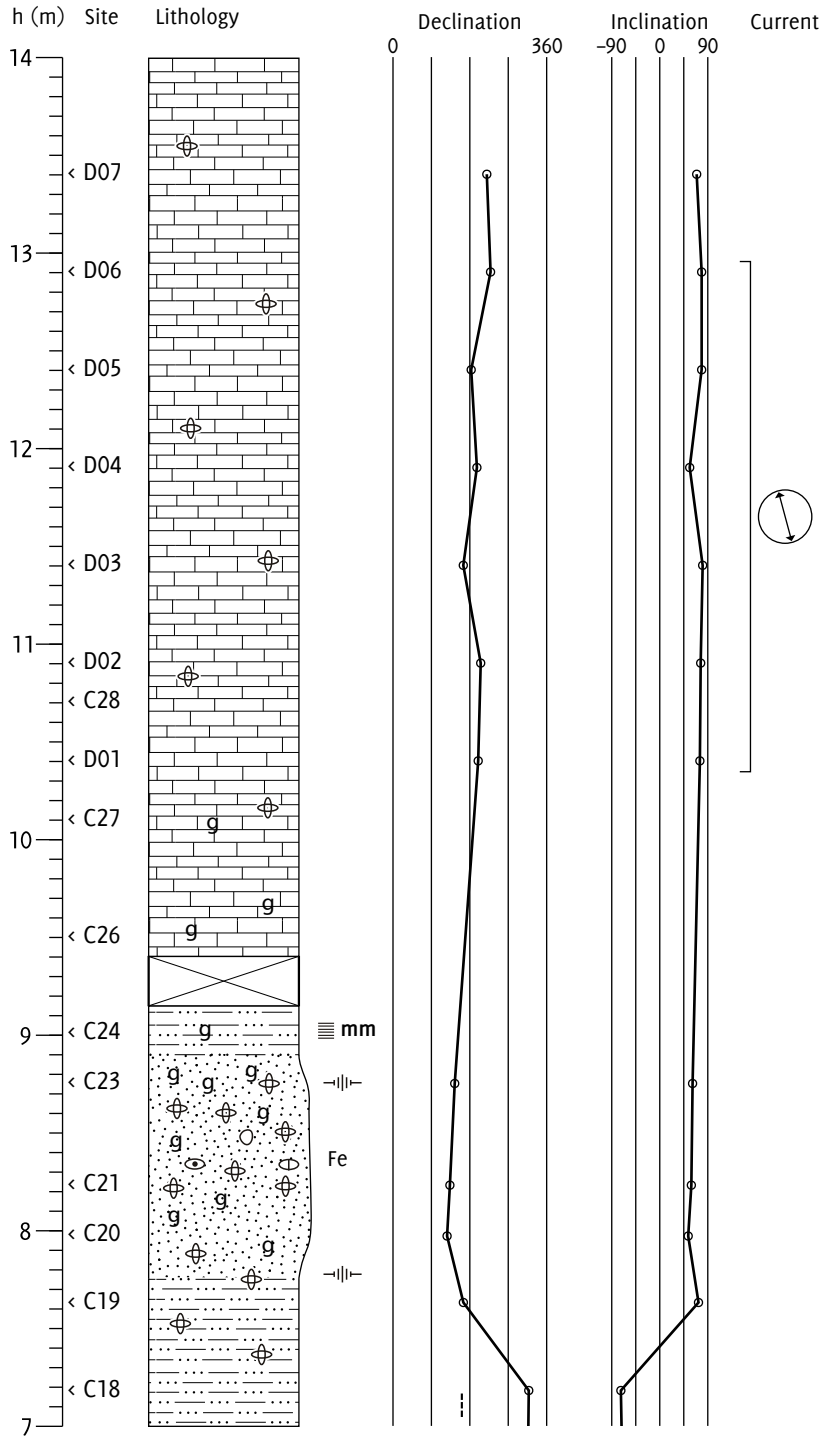

Figure 7.22 Site mean directions for upper Limestone Point section

Site	H (m)	Fit	N	T_1 (°C)	T_2 (°C)	Dec.	Inc.	α_{95}	k
D07	13.40	c	4	25	275	219.8	69.2	22.1	65.2
D06	12.90	c	4	25	225	228.6	78.5	10.1	307.9
D05	12.40	c	4	25	225	183.2	78.5	19.7	81.3
D04	11.90	c	4	25	225–275	196.6	56.1	14.2	155.4
D03	11.40	c	4	25	225	164.7	80.4	19.9	79.6
D02	10.90	c	4	25	225	205.5	76.7	6.7	688.1
D01	10.40	c	4	25	225	199.6	75.2	1.8	9518.9
C23	8.75	c	3	25	270–330	158.5	65.6	25.0	712.3
C21	8.23	c	3	25	330–390	144.3	64.7	62.7	123.2
C20	7.97	c	3	25	300–330	134.3	59.6	35.7	150.4
C19	7.63	c	3	25–60	330–390	191.1	73.1	22.4	879.6
C18	7.18	f	3	25	330–360	344.1	−77.1	14.3	75.7
C17	6.74	f	3	25–60	270–420	336.2	−74.7	7.0	314.8
C14	4.57	c	3	25	300	197.8	69.8	39.9	286.3
C12	3.17	c	3	25	210–300	169.9	64.0	98.5	58.1
C07	1.84	c	3	25–149	270–300	178.0	75.8	7.2	8437.6
C03	1.41	c	3	25	270–330	191.0	73.2	61.0	129.1

Table 7.6 Site mean directions for samples from the Limestone Point section. 'Fit' gives the method used to determine the site mean direction: 'c' for remagnetization great circles analysis, 'f' for Fisherian mean of origin-anchored linear PCA fits. *N* is the number samples used to determine the site mean direction; Dec and Inc are its declination and inclination; α_{95} and k are the 95% confidence semi-angle and estimated precision parameter produced by the formulae of Fisher (1953) or McFadden and McElhinny (1988). T_1 and T_2 are respectively the ranges of minimum and maximum temperature steps used for the site mean direction determinations at a site.

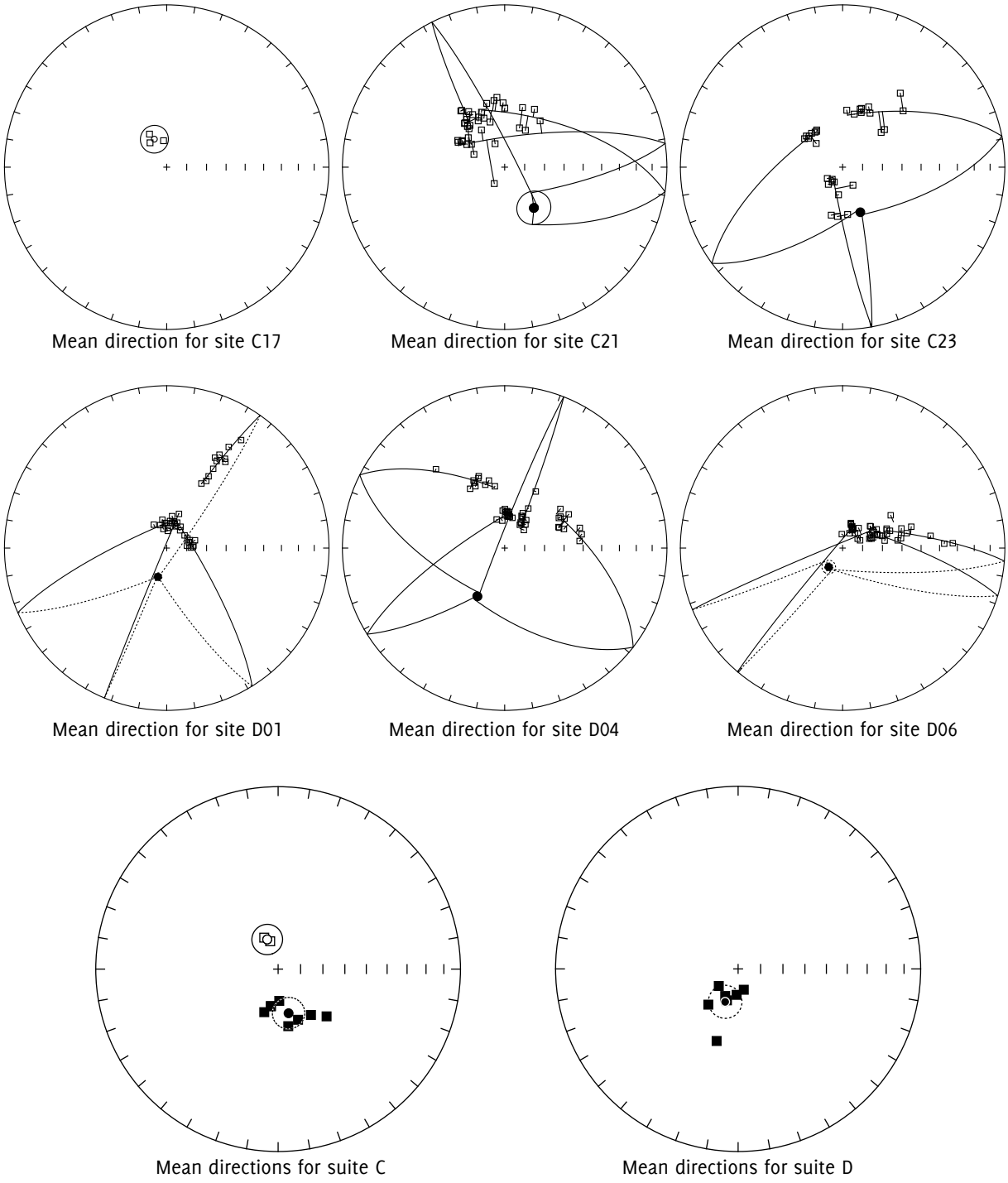

Figure 7.23 Illustrative site mean directions and formation mean directions for suite C and suite D at Limestone Point. On site mean plots (top and middle), square points show demagnetization steps, round points show site means, lines show best fit great circles, and small circle around site mean shows the largest distance to any of the great circles. On formation mean plots (bottom), squares points show site means, round points show formation means, and small circles show Fisher 95% confidence regions.

7.5.4.1 *Reversals test on Limestone Point poles*

Since the lower Limestone Point section (suite C) shows two polarities, it is possible to perform a reversals test (Cox and Doell, 1960) to indicate whether the remanence is primary. The magnetic field of the earth, averaged over periods of thousands of years, corresponds to a geocentric axial dipole (GAD). Thus, with a sufficient number of samples to average out secular variation, the reversed directions from a section should point in the opposite direction to the normal directions, to within a reasonable confidence interval. I reflected the mean reversed palaeopole into the upper hemisphere and used the standard formula

$$\arccos(\sin i_1 \sin i_2 + \cos i_1 \cos i_2 \cos(d_2 - d_1)) \tag{7.1}$$

to calculate the angular distance between the poles. The formula gave a distance of 6.0°, within the 95% confidence intervals of both the reversed (6.3°) and normal (6.8°) pole. The data thus passes the reversals test. It is true that the normal pole is only represented by two data points. However, this would be more likely to increase than to decrease the deviation from dipolarity, since a small data set is more influenced by secular variation.

7.5.4.2 *Fold test*

Since the sediments of Campbell Island have been domed upward by Neogene volcanic activity, the sections at Camp Cove and Limestone Point have different bedding orientations: the Camp Cove beds dip 14° with a down-dip azimuth of 2°, and the Limestone Point beds at 8° towards 272°. This difference in bedding attitude allows a fold test (Graham, 1949) to be applied to the combined collection of site directions from the two sections. In a fold test, samples are taken from two equivalent-age but differently oriented sections; the distribution of the site mean directions is then examined before and after correction for bedding orientation (usually referred to as 'unfolding'). The directions should cluster more tightly in the configuration in which the remanences were originally acquired: if they are primary remanences, they should cluster more tightly after unfolding.

While the principle of the fold test is intuitive, some statistical work is required to apply it quantitatively and assign a confidence level to the claim that the clustering is significantly better in one configuration or the other. In

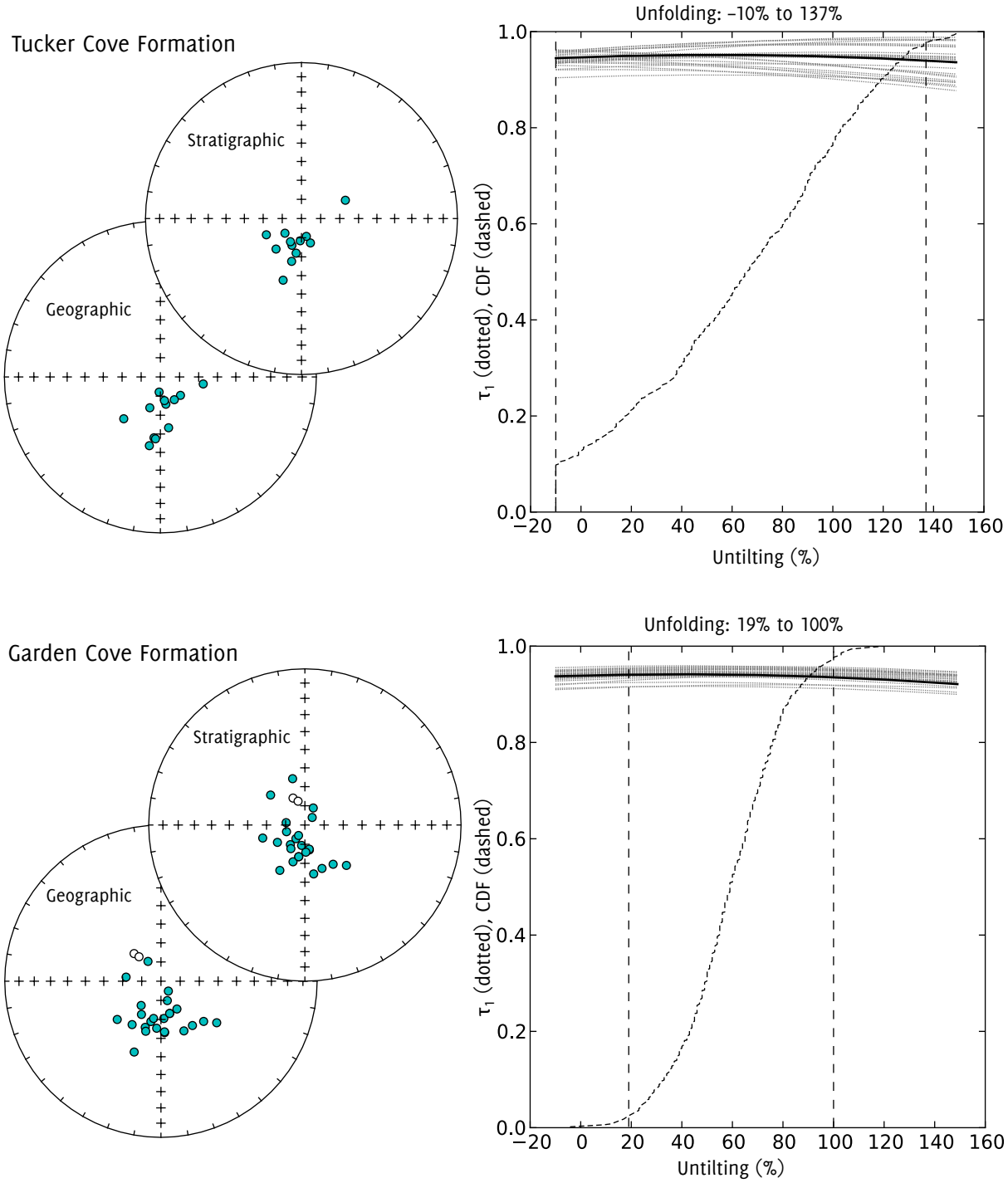

Figure 7.24 Application of a fold test to the Campbell Island sections.

this case I used the technique described by Tauxe and Watson (1994), which uses nonparametric bootstrap statistics like those described in section 2.2.1.2 (p. 25) to produce confidence intervals. I applied the test using the 'foldtest.py' program from the PmagPy suite described by Tauxe *et al.* (2010).

Because of the apparent difference in formation mean directions between the Tucker Cove Formation and Garden Cove Formation samples at Limestone Point (figure 7.23, p. 235), I applied the fold test separately for the two formations. Figure 7.24 shows the results.

For the Tucker Cove formation, the test is entirely inconclusive: the 95% confidence interval for the optimal degree of unfolding runs from −10% to 137%. This range is skewed slightly towards the fully unfolded (100%) end of the scale, but no conclusions can be drawn from it.

The fold test on the Garden Cove formation is slightly more useful: the confidence interval of 19% to 100% covers a wide range, but definitely excludes the possibility of entirely post-folding remanence acquisition and (barely) includes the possibility of entirely pre-folding remanence acquisition. It thus supports, albeit weakly, the proposition that the remanence is primary.

7.6 Magnetostratigraphy

I constructed a composite stratigraphy from the two sampled sections, and combined the polarity data with known biostratigraphic constraints. Figure 7.25 shows this stratigraphy. Ages are constrained by biostratigraphic data from Hollis *et al.* (1997) and the 2007 expedition. Some of the assignments of magnetozones to polarity chrons are tentative.

Garden Cove Formation

The top of the Garden Cove formation has been constrained as Danian, probably older than 61.7 Ma, based on the last occurrence of the dinoflagellate cyst *Palaeoperidinium pyrophorum* (Chris Hollis, pers. comm. 2011). Since the top of the Garden Cove Formation yielded reverse magnetized samples, this gives the possibility of C27r or C28r as the corresponding chron. I selected C28r as this allows the normal chron C29n to be correlated both to the normal zone at Limestone Point and to an unexposed part of Camp Cove, which in turn can tie the stratigraphy to the K-Pg boundary at that section.

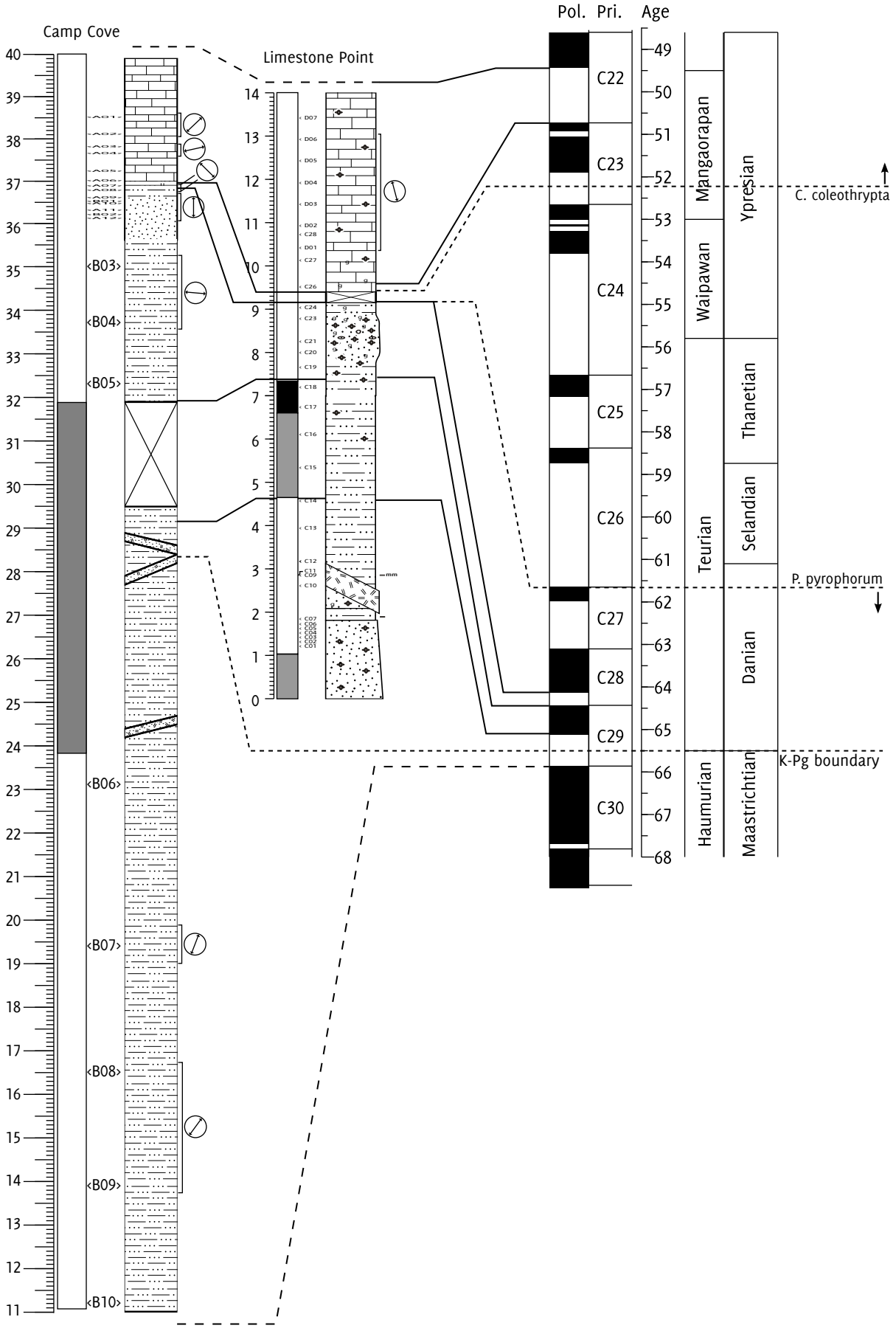

Figure 7.25 Campbell Island combined stratigraphy, based on biostratigraphic constraints and magnetic polarities. See text for details.

At Camp Cove, the biostratigraphically constrained position of the K-Pg boundary at just above 28 m allowed the lower part of the section to be identified with the C29r chron. The long duration of the C30n chron, and the very short reversed chron between it and the C31n chron, make it unlikely that a normal magnetozone has been missed, despite the sparse sampling. The K-Pg boundary falls in an 8 m gap where no palaeomagnetic sampling was possible. I infer the existence of a normal magnetozone corresponding to C29n between the K-Pg boundary and the first sample above it (B05, reversed), which I also correlate with the normal zone at Limestone Point. The reversed zone continues from B05 up to the top of the Garden Cove Formation at Camp Cove, and I correlate it with C28r.

Tucker Cove Formation

The base of the Tucker Cove Formation has been dated biostratigraphically as Mangaorapan (Early Eocene) in Perseverance Harbour and Mangaorapan–Heretaungan (Early Eocene to early Middle Eocene) on western Campbell Island (Hollis *et al.*, 1997). A maximum age limit is given by the presence of the dinoflagellate cyst *Charlesdowniea coleothrypta*, with a first occurrence at about 52.2 Ma (Gradstein *et al.*, 2004). At both sections, the sampled thickness of the Tucker Cove Formation was entirely reversed, and I have assigned it to the C22r chron. There is, however, a possibility that the reversed zone may represent the topmost part of C23r. I chose C22r on the grounds that it provides a much greater length of time than the approximately 200 kyr between the first occurrence of *C. coleothrypta* and the start of C23n.

7.7 Conclusions and further work

In this section I briefly summarize the findings of the chapter and their immediate implications; broader discussion is deferred to the next chapter. I also suggest ways in which the work could be extended.

7.7.1 *Conclusions*

Sedimentation rates

The magnetostratigraphy allows some inferences about sedimentation rates.

The bottom part of the Camp Cove section was deposited between the start of C29r at 65.861 Ma and the K-Pg boundary 65.5 Ma, giving a minimum sedimentation rate of around 47 mm/ka. Above the K-Pg boundary, the top of the Garden Cove Formation is constrained to C28r, giving a much lower sedimentation rate of around 7–8 mm/kyr at Camp Cove. This figure, however, only gives a minimum mean sedimentation rate, corresponding to deposition occurring right up until the end of the C29r chron. It is possible that deposition ceased before the end of this chron and that the actual deposition rate was thus significantly higher. The identification of the C29n chron at Limestone Point provides an additional constraint on the sedimentation rate. Since the bottom of the chron was not identified with certainty, the mean rate may be anywhere between ~1 mm/kyr and ~4.4 mm/kyr. Even the upper end of this range, however, is well below the estimate for the Cretaceous Garden Cove Formation from the Camp Cove section.

For the Tucker Cove Formation, the sampling at Limestone Point gives a minimum sedimentation rate of 3 mm/kyr if the identification of the magnetozone with the C22r chron is correct; if it is assigned to the portion of C23r after the first occurrence of *C. coleothrypta*, a higher minimum bound of around 13 mm/kyr is produced. Since the top of the magnetozone was not located, these are once again only minimum rates.

Tectonic setting

The latitude of Campbell Island in the early Palaeogene was around 60–75°S (Cook *et al.*, 1999), giving an expected GAD field inclination of around 74–83°. The inclinations of the calculated formation mean directions are mostly fall within this range, although the inclination of suite C (69.7°) is slightly lower than expected. The range of declinations is more puzzling: given the anticlockwise rotation of the region at around 1°/Myr through much of the Cenozoic (King, 2000b), reversed mean directions would be expected to be in the southeast quadrant; this is the case for suites A and C, but the declinations for suites B and D would be more consistent with *clockwise* rotation. I discuss these discrepancies in more detail in chapter 8 (section 8.4, p. 275).

Palaeocurrent

The AMS measurements provide a long record of palaeocurrent flow through the upper Garden Cove Formation and lower Tucker Cove Formation. The suite A and suite B measurements imply consistently directed (at timescales of >10 kyr) current flow through the latest Cretaceous and earliest Palaeocene, with gradual changes in flow direction through the section. At the unconformity between the two formations, AMS directions showed random orientation, suggestive of either a cessation of flow or significant bioturbation. The second explanation seems more likely, since the AMS foliation was noticeably disrupted: simple cessation of current flow should remove the AMS lineation, but retain a bedding-parallel foliation.

In the lower Tucker Cove Formation, AMS directions were determined at both the sections, giving the opportunity to compare them. As can be seen in figure 7.25, the Tucker Cove Formation directions are different at Limestone Point and Camp Cove. The most likely explanation for this is simply that the Camp Cove AMS data are simply stratigraphically lower than those at Limestone Point, and that the almost north-south direction determined from the D-series Limestone Point samples represents a further evolution of the directions at the top of the Camp Cove section, rather than a contradiction of them. It is interesting that the younger AMS data at Limestone Point are more stable than those obtained from the older samples at Camp Cove. From this it appears that there was significant fluctuation in bottom-water currents immediately after the unconformity, later giving way to a more stable system.

7.7.2 *Further work*

While the studied sediments were weakly magnetized and their demagnetization paths short, great-circle analysis proved successful in most cases. The site mean directions determined at Campbell Island were in general more reliable than those at Fairfield Quarry or the mid-Waipara River, and the remainder of the Tucker Cove and Garden Cove formations offer attractive targets for magnetostratigraphy. Their exposures have been well-documented and dated biostratigraphically by previous workers (e.g. Hollis *et al.*, 1997), so magnetostratigraphy could easily be integrated with the published work. Palaeomagnetic work on the Garden Cove Formation may be limited by the coarse-

grained nature of its lower part, which may not prserve a depositional magnetization. In the upper parts of the Tucker Cove Formation, evidence for thermal alteration has been reported (Beggs, 1976); this may limit palaeomagnetic work by imparting a thermoviscous overprint. Great-circle remagnetization analysis may still recover depositional remanences from overprinted sites, but with sufficient temperature and time the original magnetization may be obscured entirely. However, even these limits leave at minimum tens of metres of stratigraphic thickness suitable for palaeomagnetic study.

8 Discussion

> There are two ways to understand complicated things as a complicated machine. Either can the master, who has built the machine, show you what he has done and how the machine works. Or you can investigate every single part and – to begin with – understand them individually. Thereafter, you must also put all the individual parts together in order to understand how they work in coherence.
>
> – Steno (1665), translated by Hansen (2009)

In this chapter I discuss the rock magnetic and palaeomagnetic results presented in the preceding chapters, and relate them to previously published data on Cenozoic marine sediments from Zealandia. I then discuss the implications of my results for the hypothesis of one or more Palaeogene paraconformities in the New Zealand region, and for the pre-Oligocene history of Antarctic glaciation. Various aspects of individual results and methods have already been discussed in the corresponding chapters; this chapter focuses on integrating those results which are relevant to more than one chapter.

The discussion comprises five major themes: experimental and theoretical methods and their effectiveness; the palaeomagnetic behaviour of the studied sediments, and the construction of a model to explain it; the stratigraphies constructed in the palaeomagnetic investigations; the relationship between the measured palaeomagnetic directions and the tectonic setting; and, finally, the implications of the findings for the possibility of Palaeocene unconformities and pre-Oligocene Antarctic glaciation.

8.1 Rock and palaeomagnetic methods

Various experimental and theoretical techniques were applied in the rock and palaeomagnetic investigations of the preceding chapters. In this section I discuss their efficacy and compare their implementations and results with those described in the published literature.

8.1.1 *Magnetic separation*

Magnetic separation was successful in separating glauconitic and non-glauconitic minerals for rock magnetic analysis. It did not, however, succeed in producing sufficient concentrations of remanence carrying minerals for direct observation. This failure was largely due to the high paramagnetic susceptibility and

low magnetite concentration of the samples and to the fact that the remanence carriers were apparently encapsulated within larger, low-susceptibility grains. Section 3.5.6 (p. 85) discussed the effect of this lithology on separation, and the possibility of applying other separation techniques to concentrate the remanence carriers.

8.1.2 *Rock magnetic analysis methods*

No remanence-carrying minerals were directly observed during the microscope and microprobe studies. This outcome is not unusual when studying heavily pyritized, weakly magnetic sediments (e.g. Sun and Jackson, 1994; Wilson and Roberts, 1999; Turner, 2001); in these cases rock magnetic measurements, combined with sedimentological data from direct analyses, have often proved effective in constraining the magnetic mineralogy sufficiently for palaeomagnetic interpretation. In this section I summarize the rock magnetic techniques I have used in this thesis and compare them with the methodology used in similar previous studies.

8.1.2.1 *Isothermal remanent magnetization*

IRM acquisition curves have frequently been used in studies of New Zealand sediments (e.g. Roberts and Turner, 1993; Roberts and Pillans, 1993; Wilson and Roberts, 1999; Vickery and Lamb, 1995; Turner, 2001). However, unmixing techniques, such as the cumulative log-Gaussian analysis applied throughout this thesis, have not previously been used, limiting the quantitative interpretation of IRM data: when more than one population of remanence carrying grains is present, reference data such as H_{cr} values (e.g. Peters and Dekkers, 2003) or type curves (e.g. Symons and Cioppa, 2000) are less helpful, since such reference data are usually only produced for single minerals. Interpretations of IRM acquisition have therefore tended to be semi-qualitative, with the chief use being to distinguish between ferrimagnetic and antiferomagnetic minerals, which tend respectively to have relatively low and high remanent coercivities (e.g. Roberts and Pillans, 1993; Wilson and Roberts, 1999).

Unmixing allows the reference data to be applied to the composite mineral assemblages often found in nature. The Heslop *et al.* (2002) unmixing technique also has the advantage that remanent coercivity parameters can be

estimated even for minerals which do not reach saturation; this is particularly useful for distinguishing between haematite and goethite, which both saturate well above 1 T (the highest field achievable with many laboratory pulse magnetizers) but tend to have distinctively differing coercivity spectra (France and Oldfield, 2000). Thus, for example, Roberts and Turner (1993) inferred the presence of 'an antiferromagnetic mineral, such as haematite or goethite' from a sample which did not saturate by 800 mT, but could not make a more specific diagnosis.

While the IRM software of Heslop *et al.* (2002) certainly provided more quantitative analysis of the IRM data in this thesis, it was not a panacea: in particular, the pyrrhotite component suggested by the unmixed remanent coercivity spectra was not confirmed by thermal experiments. Similar mineralogical uncertainties appeared in a paper by Vickery and Lamb (1995), in which magnetic mineralogy was inferred from IRM acquisition curves and demagnetization characteristics. They reported 'magnetites and haematite (± goethite)' from Palaeocene–Oligocene Amuri Limestone samples; 'titanomagnetite ± pyrrhotite' in a Miocene siltstone; and data which 'suggest[ed] the presence of both magnetite and pyrrhotite' from a Pliocene siltstone. These ambiguous diagnoses demonstrate the difficulty of differentiating minerals of similar coercivity using IRM acquisition, even when thermal demagnetization data is also available. In the Vickery and Lamb (1995) experiments, demagnetization was undertaken at approximately 50°C intervals, limiting the resolution to which disordering and alteration temperatures could be determined. My investigations were helped in this regard both by the use of smaller (usually 25°C) demagnetization steps and by separate TDMS experiments allowing the monitoring of thermal effects at a temperature resolution of around 6°C.

Since doubts have been raised about the validity of CLG IRM models, I did not simply match the curve parameters against published values: I re-integrated the individual components into 'virtual' IRM acquisition curves, which could then be checked against empirically derived reference curves for various minerals (section 3.4.2.4, page 60). In section 8.2.1 (p. 253) I discuss in more detail the ambiguities in interpretation of the unmixed IRM data.

8.1.2.2 *Thermomagnetic studies*

TDMS studies proved extremely useful for all the palaeomagnetic investigations

within this thesis, as well as for the rock magnetic study of chapter 3. Like IRM studies, TDMS studies have proved effective with extremely low concentrations of magnetic minerals: the dramatic susceptibility increase caused by the Hopkinson (1889) effect can allow the identification of the Curie point even when the room-temperature susceptibility of the mineral is too low to be measured precisely. Some of the least magnetic samples studied in this thesis were from the Tucker Cove Limestone on Campbell Island; sample D03, for example had a saturation IRM of 14.5 mA/m, corresponding to a magnetite concentration below 1.4 parts per million[8]. Nevertheless, its Curie point was clearly visible on the TDMS graph (figure 7.9, p. 209).

There are two main difficulties in the interpretation of TDMS data. The first is the inevitable ambiguity of Curie temperature determinations: a single Curie (or Néel) temperature may be associated with several minerals. In particular, iron oxide spinels show continuous variations in Curie temperature with varying oxidation and cation substitution parameters (figure 3.22, p. 73), from below room temperature to around 645°C for maghaemite. For this reason TDMS data must be interpreted in conjunction with the results of other types of analysis.

The second problem is heating-induced mineral alteration, which can be recognized by a non-reversible susceptibility curve (i.e. a cooling curve which differs from the corresponding heating curve). Alteration occurred in all TDMS studies in this thesis. This alteration complicates the interpretation of any subsequently observed behaviour, since it is hard to tell whether the behaviour is due to the original sample mineralogy or to an alteration product. On the other hand, alteration itself (or lack thereof) can be a valuable diagnostic of mineralogy, especially when heating is applied in successive heating-cooling cycles with increasing peak temperatures (Hrouda, 2003); examples include the inversion of maghaemite to haematite (Verwey, 1935) and the thermal decomposition of greigite (Dekkers *et al.*, 2000).

While TDMS studies alone cannot unambiguously determine mineralogy, they can significantly constrain the possible range of mineral components; for example, a complete loss of susceptibility below 675°C excludes not only haematite but a number of minerals known to alter to haematite upon heat-

[8] In making this estimate I assumed a maximum pure-magnetite SIRM value of 21 kA/m, as discussed in section 6.4.1 (p. 169)

ing (e.g. Henry, 2007). TDMS studies work particularly well as a complement to IRM studies, since it is uncommon for two different minerals to have both a similar remanent coercivity spectrum and similar disordering/alteration temperatures (Lowrie and Heller, 1982; McElhinny and McFadden, 2000, §3.5.2).

Relatively few palaeomagnetic studies of New Zealand marine sediments have made use of continuous thermomagnetic experiments, and none appear to have made use of the stepwise heating technique used in this thesis to constrain alteration temperatures. Roberts and Turner (1993), using high-temperature Curie balance measurements, were able to infer the presence of greigite in Neogene sandstones of the Awatere Group. Their results were obtained on separates (limiting the technique to the three sites for which sufficiently magnetic separates could be produced), whereas the kappabridge used for this thesis was sufficiently sensitive that raw, unconcentrated material could be used. Wilson and Roberts (1999) performed TDMS experiments on both bulk samples and magnetic extracts from Pliocene sediments of the Wanganui Basin, with results reminiscent of those generally seen in this thesis: initial low susceptibility, with a much higher susceptibility component produced from thermal alteration. The alteration did not occur in the magnetic extract, indicating that it was associated with non-remanence carrying components of the mineralogy, probably clay minerals. Turner (2001) performed thermomagnetic experiments on Neogene sediments of the Wanganui River Valley using a variable frequency translation balance, and found an argon atmosphere effective in suppressing thermal alteration. Measured magnetizations were very weak but were sufficient to rule out the presence of iron sulphides on the basis on Curie point determination.

Low-temperature techniques were not used in this thesis, but have great potential for reliable discrimination between several ferrimagnetic mineral phases. The SIRM of magnetite drops sharply at the Verwey (1939) transition at around 110 K, allowing it to be distinguished from maghaemite (Özdemir *et al.*, 1993) and titanomagnetite. Pyrrhotite also displays a low-temperature transition, at around 30 K (Dekkers, 1989). Torii *et al.* (1996) found that thermal unblocking of a remanence imparted at 5 K enabled reliable detection of both these minerals in natural samples, even (at least for magnetite) at trace concentrations. Greigite exhibits no low-temperature transition (Roberts, 1995). Although they are not entirely unambiguous (Moskowitz *et al.*, 1998), low-

temperature magnetization measurements are thus useful for distinguishing between magnetite, pyrrhotite, and greigite, which all have similar remanent coercivity spectra and are all potential remanence carriers in pyritized sediments.

8.1.2.3 *Triaxial IRM demagnetization*

Since the development of the Lowrie (1990) triaxial thermal demagnetization technique from the earlier Hirt and Lowrie (1988) biaxial technique, it has been extensively applied in palaeomagnetic and rock magnetic studies worldwide. Like the combination of IRM acquisition and TDMS experiments, it exploits the fact that minerals with similar coercivities tend to have different thermomagnetic behaviours, and *vice versa*. The technique consists of successively magnetizing the sample with three orthogonal DC fields of decreasing intensity, followed by a stepwise thermal demagnetization of this composite IRM. Measurement of the initial magnetization provides, in effect, a very crude remanent coercivity spectrum; the subsequent demagnetization isolates the thermal behaviour of the three different coercivity components.

Hounslow *et al.* (1995), for example, used triaxial thermal demagnetization to unravel mixed magnetic mineralogies varying lithologies of some North Sea sandstones. Sagnotti *et al.* (2005) successfully used it to distinguish between magnetite and an iron sulphide (greigite or pyrrhotite) in a Ross Sea mudstone. In New Zealand, the technique has been applied by Roberts and Pillans (1993) to Pleistocene Wanganui basin sediments, giving evidence of a titanomagnetite-dominated magnetic mineralogy. The results from my Fairfield Quarry samples, presented in figure 3.6 (p. 46), show similarities with many results from these studies – in particular, the dominance of the low-coercivity component, and the magnetite or near-magnetite final unblocking temperature of all the components.

8.1.2.4 *Stepwise demagnetization*

Although AF demagnetization has occasionally been used (e.g. Kennett *et al.*, 1971; Mumme and Walcott, 1985; Seward *et al.*, 1986)[9], most palaeomagnetic

[9] Seward *et al.* (1986), unusually, reported 'little difference between results achieved with AC [i.e.

studies of New Zealand sediments have found thermal demagnetization to produce more reliable palaeomagnetic directions (e.g. Kennett and Watkins, 1974; Wright and Vella, 1988; Turner *et al.*, 1989; Roberts and Pillans, 1993; Turner *et al.*, 2007), to the extent that some more recent studies (e.g. Turner and Kamp, 1990; Roberts and Turner, 1993; Roberts *et al.*, 1994; Wilson and Roberts, 1999) have omitted even pilot experiments with AF treatment and proceeded directly to thermal demagnetization. For all the sites sampled in this thesis, pilot studies showed better results from thermal demagnetization, despite the frequent low alteration temperatures, and all the main studies were therefore conducted using thermal demagnetization. As is common in thermal demagnetization studies, I measured room-temperature susceptibility after each step to detect mineral alteration. The main purpose of this procedure is to assess the reliability of the magnetic moment measurements, but the susceptibility data itself constitutes useful rock magnetic data and helps to constrain the mineralogy of the samples. Roberts and Turner (1993), for example, noted that the room-temperature susceptibility of greigite-bearing samples tends to decrease after heating steps in the 200–350°C range. The lack of this behaviour in my thermal demagnetization experiments was useful in confirming the absence of greigite.

8.1.2.5 *Microscope and microprobe analysis*

No remanence carriers were identified by optical or electron microscopy or by electron microprobe analysis. This circumstance was due in part to the ineffectiveness of the separation techniques in concentrating the ferrimagnetic grains, as discussed in section 3.5.6.1 (p. 85), and in part to the small (submicron) magnetite grain size, as inferred from remanent coercivity spectra. As in other studies (e.g. Wilson and Roberts, 1999), microscope and microprobe analyses were nevertheless useful in providing information about the mineralogy. Optical microscopy was effective in identifying potential remanence carriers by opacity under transmitted light and brightness under reflected light, and bulk electron imaging easily picked out the higher atomic weights of iron compounds from the surrounding silicates. Electron microprobe analysis was successful in accurately determining the composition of the pyrites in

---

AF] or thermal cleaning'.

the sample; quantitative assessment of the iron/sulphur ratio was particularly important in distinguishing paramagnetic pyrite from ferrimagnetic greigite or monoclinic pyrrhotite. Had any of the sub-micron magnetite grains been found, however, the accuracy of EPMA analysis would probably have been compromised by the diameter of the electron beam.

8.1.2.6 *Sample preparation for rock magnetic analysis*

Many of the rock magnetic procedures used in chapter 3 required discrete, orientable samples to be produced from disaggregated separates. There were various constraints on the choice of sample mounting system. Firstly, it must be non-magnetic; that is, its initial NRM, and the artificial remanences induced by any laboratory procedures, must be negligible compared to the corresponding remanences of the mounted grains. Given the low magnetizations of the sediments, this was a difficult requirement to meet. Turner *et al.* (2007) used plaster of Paris to mount magnetic grains for IRM treatment, and Wilson (1961) used plaster to jacket friable specimens. For my samples, preliminary experiments showed that both plaster of Paris and dental stone held too much remanence to be of use. My mounting material also needed to be heatproof. Poly (methyl methacrylate) (a.k.a. Perspex, Lucite, or Plexiglas) has also been used to mount separates for rock magnetic analysis (e.g. Collinson, 1977; Wilson and Roberts, 1999), but my experiments included thermal demagnetization up to (potentially) 775°C, and the melting point of Poly(methyl methacrylate) is around 160°C (Smith and Hashemi, 2006). In the end, my solution was to mould cubes using a paste made from sample grains and sodium silicate solution, as described in section 3.2.2.2 (p. 37). This method satisfied both the main requirements of negligible magnetism and good heat resistance.

8.1.2.7 *Testing for gyroremanence*

In section 6.4.3.1 (p. 177), I considered the possibility that the poor AF demagnetization results may be due to small quantities of greigite, which is known to acquire a gyroremanent magnetization in an alternating field (Snowball, 1997 and Hu *et al.*, 1998) and has been observed to exhibit this behaviour in New Zealand marine sediments (e.g. Rowan, 2006; Ohneiser *et al.*, 2008). A strong GRM can usually be recognized as a clear, progressive increase in magnetic

intensity with increasing demagnetization field (e.g. Snowball, 1997, fig. 8), but I wished to test for the possibility of a mixed mineralogy producing a minor GRM component overlaid on a stronger overall demagnetization trend. The test I devised for this, using successive orthogonal uniaxial demagnetizations of constant field strength, did not show the behaviour expected from a GRM.

8.2 Palaeomagnetic behaviours

In this section I discuss the magnetic mineralogy and demagnetization behaviours of my samples, and compare them with similar sediments from eastern Zealandia. There has been relatively little published work on Palaeogene–Eocene sediments from this region, and my discussion also includes palaeomagnetic studies from throughout the Palaeogene and Neogene; given the persistence of regional passive-margin sedimentation through much of the Cenozoic (Carter, 1988a; King *et al.*, 1999; Cook *et al.*, 1999), the younger sediments should provide useful comparisons with those examined in this thesis.

8.2.1 *Magnetic mineralogies in this thesis*

Despite the variations in geographical location, lithology, and age, the samples studied in this thesis were remarkably uniform in magnetic mineralogy, as determined chiefly by IRM acquisition curves and temperature dependence of magnetic susceptibility.

For all the palaeomagnetic studies, as well as the detailed rock magnetic study of chapter 3, I analysed the IRM acquisition curves using the technique of Heslop *et al.* (2002). This technique involves decomposition of the acquisition curve into cumulative log-Gaussian functions using an expectation-maximization algorithm, on the assumption that each log-Gaussian function corresponds to a single mineral phase. For most samples in this thesis, this model gave two strongly overlapping components with mean coercivities at or slightly above commonly reported values for magnetite. The harder components might be interpretable as pyrrhotite, and the temperature-dependent susceptibility studies were valuable in ruling out this possibility. The Curie temperatures determined by TDMS curves also indicated that the magnetite had suffered negligible cation substitution and oxidation. However, there is still ambiguity as

to how the two IRM components should be interpreted; there are two main possibilities:

1. The two components represent two distinct populations of ferrimagnetic grains, with different mineralogical characteristics leading to different remanent coercivity behaviour. Dunlop (1986) noted that, for submicron magnetites, finer grains tend to have higher coercivities, so the two components may represent two size fractions.

2. There is only a single population of magnetite grains, and the two components are an artefact of the Gaussian model originally proposed by Robertson and France (1994) and employed by Heslop *et al.* (2002); this would imply that a cumulative log-Gaussian function is not always sufficient to describe the IRM acquisition of a mineral phase. Heslop *et al.* (2002) gave caveats about the accuracy of CLG fitting when (as in this case) there is extensive overlap between the components, and Egli (2003) questioned the universal applicability of CLG IRM modelling.

The most direct and reliable way to settle this ambiguity would be direct observation and analysis of individual magnetite grains. This method proved impractical, due mainly to the very low concentrations of remanence carriers and the ineffectiveness of magnetic separation in concentrating them, as discussed in section 3.5.6.1. On balance, it seems more likely that the two-component fit is an artefact of the model rather than a reflection of the mineralogy. For purposes of palaeomagnetic interpretation, it is sufficient to know that most or all of the remanence is carried by magnetite, or by a iron spinel oxide close in composition (and hence in magnetic properties) to magnetite: such a mineralogy strongly implies a detrital origin, since magnetite is unlikely to form authigenically under reducing conditions.

Both the thermal demagnetization and TDMS studies were valuable in excluding pyrrhotite and greigite, which have been reported in other marine sediments from south-eastern Zealandia (e.g. Roberts and Turner, 1993; Shipboard Scientific Party, 1999), and might be expected at least in the Fairfield sediments due to the presence of pyrite (Snowball and Torii, 1999). Since pyrrhotite and greigite have similar remanent coercivity spectra to magnetite (Peters and Dekkers, 2003), the IRM studies alone do not distinguish them reliably: in the absence of other data, the harder IRM component could be attributed to

pyrrhotite or greigite. Thermal studies resolve this ambiguity: pyrrhotite has a Curie point of around 320°C and greigite breaks down at around 200–250°C (Torii *et al.*, 1996), so their presence should be easily detectable by both stepwise thermal demagnetization and TDMS studies. None of the thermal studies in this thesis indicated their presence.

8.2.2 *Comparisons of magnetic mineralogy*

A notable feature of the sediments studied in this thesis is that iron sulphide minerals do not appear to be significant as remanence carriers. This observation contrasts with several previous studies of similar Neogene sediments (e.g. Roberts and Turner, 1993; Rowan and Roberts, 2005; Rowan and Roberts, 2006; Rowan and Roberts, 2008; Ohneiser *et al.*, 2008), where greigite and pyrrhotite have acted as significant palaeomagnetic recorders. Roberts and Turner (1993) and Turner (2001) noted that greigite and pyrrhotite are chiefly associated with fine-grained mudstones with low permeability. The inferred cause of this association is that greigite and pyrrhotite form as intermediate products during the pyritization process. In non-permeable sediments, pyritization is arrested by a lack of hydrogen sulphide, caused in turn by the inability of pore-water sulphate to diffuse down to the zone of pyritization; conversely, in siltstones and mudstones, an adequate hydrogen sulphide supply allows the conversion of all the available iron into pyrite. Complete pyritization appeared to have taken place in the sandy mudstones and muddy sandstones of Wilson and Roberts (1999) and in the siltstones of Turner (2001), none of which contained magnetic iron sulphides. Roberts and Turner (1993) reported strong greigite magnetizations in their fine mudstone samples; in their siltstone and sandstone samples, where the pyritization had progressed to completion, the NRM was much weaker, and was found to be carried mainly by detrital ferrimagnetic iron oxides. However, Vickery and Lamb (1995) inferred (from IRM data) the presence of both magnetite and pyrrhotite in Miocene and Pliocene siltstones, suggesting that silt/sand grain size does not always guarantee complete pyritization.

The sediments studied in this thesis have similar characteristics to the Neogene Wanganui basin sediments of Turner (2001): weak NRM; moderate susceptibility suggestive of a large paramagnetic component; a low concentration of remanence carriers, leading to difficulty in identifying them directly; a lack

of remanence-carrying iron sulphides; soft remanent coercivity spectra; and high disordering temperatures.

It appears from the lack of pyrrhotite and greigite that most of the mudstones and siltstones studied in this thesis underwent complete pyritization. To some extent, this simplifies the interpretation of their palaeomagnetic data: since iron sulphides can form long after deposition (Rowan *et al.*, 2009), they necessitate great care in magnetostratigraphic interpretation. Iron spinel oxides can, in a reducing environment, be more safely assumed to be detrital, and dissolution of most of a magnetite population has been found not to affect the direction of the NRM (Karlin and Levi, 1985). On the other hand, the almost-complete dissolution of the detrital remanence carriers, and the lack of other remanence carriers, leads to NRMs which are very weak and difficult to measure accurately. It also raises the question of how the sparse remaining remanence carriers were able to survive: since there was evidently ample hydrogen sulphide for pyritization, how did any magnetite remain? I address this problem in section 8.2.6.

One useful analogue for the glauconitic sandstones and siltstones is the Oligocene Kokoamu Greensand directly above the Marshall Paraconformity, studied by Tinto (2010) and Dagg (2010). The unit is highly bioturbated and contains glaucony concentrations varying between 10% and 90%. IRM acquisition experiments by Tinto (2010) showed a dominant low-coercivity component, which was (with the aid of additional magnetic susceptibility and ARM measurements) inferred to be single-domain magnetite. Dagg (2010) conducted TDMS experiments whose results were also consistent with a dominant magnetite (or possibly maghaemite) component. Like most of the TDMS results in this thesis, those of Dagg (2010) showed dramatic (fourfold or greater) increases in room-temperature susceptibility after heating, indicating the formation of a new ferrimagnetic phase. As for most of my samples, the altered samples tended to show a clear but broad Hopkinson peak in the 400–500°C range. Dagg (2010) established that the source for this alteration product was not the glauconitic component of the sediments, and inferred that pyrite was the most likely candidate.

The most obvious analogue for the Tucker Cove Formation is the widespread Amuri Limestone, of which it is a equivalent (Cook *et al.*, 1999), albeit with some variation in age. Vickery and Lamb (1995) studied Late Palaeocene

Amuri Limestone and inferred the presence of both magnetite and haematite (with possible goethite) from IRM acquisition and thermal demagnetization experiments. My limestone samples did not show any similar high-coercivity, high-temperature components, except in the single case of sample D03 from Limestone Point, where IRM acquisition indicated a minor haematite component which was not corroborated by TDMS experiments. The Early Oligocene Otekaike Limestone examined by Tinto (2010) was also found to have a mixture of low- and high-coercivity magnetic components.

8.2.3 *The role of glaucony*

A major goal of my rock magnetic studies was to investigate the relationship between glaucony and remanent magnetism. The results showed that, while glaucony has a significant influence in rock magnetic experiments, the glauconitic grains themselves are not associated with remanence-bearing minerals. This observation simplifies the palaeomagnetic interpretation of glauconitic sediments: since glauconitic grains form authigenically over time periods of up to 1 Ma (Odin and Matter, 1981), a remanence carried by a glauconitic grain would require careful interpretation, involving the maturity and origin (autochthonous or allochthonous) of the grains. However, since the glaucony does not carry remanence, it has the effect of weakening the NRM, making it more difficult or potentially impossible to measure with sufficient accuracy for a palaeomagnetic study.

While high glaucony concentrations do not affect the interpretation of palaeomagnetic data, they do complicate rock magnetic experiments, as discussed in section 3.5.5 (p. 84). A significant problem is in the application of parameters and biplots, such as the widely used 'King plot' (King *et al.*, 1982), which require the assumption that the susceptibility of a sample is dominated by its remanence carriers, and that the contribution of the paramagnetic components to the overall susceptibility is negligible. For many natural samples, this is indeed the case, but the assumption is often made implicitly, and sometimes in cases where it does not hold (Yamazaki and Ioka, 1997). For highly glauconitic (and thus highly paramagnetically susceptible) samples with very low concentrations of remanence carriers, it does not hold. Tinto (2010) and Dagg (2010) both used the King *et al.* (1982) plot for magnetic grain size determination of glauconitic Oligocene sediments from southern New Zeal-

and, and concluded that the estimated grain size had been significantly influenced by the strong paramagnetic component. Similar problems occurred in the application of the mineralogy biplot of Peters and Thompson (1998) to the same sediments.

8.2.4 *Demagnetization behaviours*

Throughout the thesis, the samples I analysed showed common features of magnetic behaviour. NRMs were low, in the 10^{-5}–10^{-4} A/m range, and demagnetization showed that they were dominated by an overprinted secondary component. The mean direction of the secondary component was always close to that which would be expected from a normal GAD field at the site's present location, implying that it is a viscous overprint imparted by the current normal chron. Demagnetization paths were noisy, and a significant proportion of samples at each site failed to yield reliably interpretable demagnetization data. Mineral alteration and low magnetization obscured the final component, except in the case of the few normally magnetized samples from Campbell Island. In all other cases, remagnetization great circles analysis was necessary to recover the detrital remanent magnetization. In a small number of samples, there were indications of more than two components[10], but the very low magnetizations and extensive overlap between the components precluded palaeomagnetic analysis in these cases.

Demagnetization behaviour types

Throughout the thesis, I classified demagnetization behaviours into one of five types; table 8.1 summarizes the distribution of these types at each of the studied sections. It is clear that the most common behaviour type at each section is SN (single component, not origin directed), which I have in all cases interpreted as a strong viscous magnetization overprinting a detrital remanence. Thermal alteration obscures the demagnetization path before the detrital remanence

[10] In some cases it can be difficult to distinguish between a three-component magnetization and a heavily overlapping two-component magnetization. However, a two-component demagnetization path is always confined to a plane; in the few cases where I hypothesized more than two components, the demagnetization path could not be contained in a plane. The interpretation of these samples is in any case not critical, since no directions were determined from them.

Section name	Number of samples	Distribution of behaviour types (%)				
		SO	SN	MC	NT	ND
Fairfield Quarry	201	17	60	9	14	0
Mid-Waipara River	80	0	57	24	19	0
Camp Cove	85	0	98	0	0	2
Limestone Point	103	14	59	0	27	0

Table 8.1 Comparison of demagnetization behaviours from the sections studied in this thesis. Behaviour codes: SO single component, origin directed; SN single component, not origin directed; MC multiple component; NT no discernible trend; ND no significant demagnetization

can be observed directly, hence the extensive use of remagnetization great circles analysis. At Camp Cove, 98% of the samples displayed this behaviour; at the other sections, 57–60% did so. The second most prevalent behaviour overall is NT (no discernible trend), which appeared in every section except for Camp Cove. Note that the higher proportion of NT-type samples at Limestone Point is in part due to the less precise demagnetization protocols applied during the magnetization of some of the samples (section 7.5.3.1, p. 225). The great majority of published palaeomagnetic studies on New Zealand sediments describe a similar population of uninterpretable samples, sometimes comprising a majority of the analysed material. The results from Camp Cove are unusual in this regard. Camp Cove is also the only section from which ND-type (non-demagnetizing) samples were retrieved; since the only two samples with this behaviour were from the same site, it was probably due to a localized variation in mineralogy.

SO-type (single-component, origin directed) behaviour was observed in some samples from Fairfield Quarry and from Limestone Point, but was interpreted differently at each of these sites. At Fairfield Quarry, the direction was generally inconsistent with any plausible combination of geomagnetic field and tectonics since the time of deposition. Many Fairfield SO-type samples had low-inclination demagnetization paths which could not have been acquired at the high latitudes which the area has occupied throughout the Late Cretaceous and Cenozoic. Further, the direction of Fairfield SO-type samples was not consistent with others from the same sampling sites. I therefore considered these samples uninterpretable. The SO-type samples from Limestone Point were different: they gave a direction corresponding to a normal geomagnetic field as exper-

ienced at Campbell Island, and showed consistency within sampling sites. Due to the high latitude and consequent high inclination of the magnetic field, the present and early-Cenozoic normal field directions experienced at the site are similar, so it is difficult to separate the two components. However, given the consistency between samples at a site and the agreement with geomagnetic and tectonic constraints, the interpretation of the SO-type samples at Limestone Point as normally magnetized is fairly reliable.

MC-type (multiple-component) behaviour was observed in samples from Fairfield Quarry and the Mid-Waipara River, and at the latter section they constituted almost a quarter of the analysed samples. Most MC-type samples were impossible to interpret reliably: the final observed component did not trend towards the origin, implying a further, hidden component. However, great-circle remagnetization analysis was more difficult than for SN-type samples, since the path representing the second component was usually short and noisy, leading to unreliable great-circle fits. In a small number of cases, both observed components moved along the same great circle, and in these instances a fit was usually possible; in these cases I interpreted the two observed components as viscous magnetizations acquired at different times, and the invisible component as the primary remanence. Apparent three-component demagnetization paths can sometimes be attributed to two components with a large amount of overlap; for most of my MC-type samples, the large angles between the two observed components, and between the second observed component and the final implied component, were sufficiently great to indicate three actual components.

Heating-induced alteration

Thermal alteration of samples at around 300–400°C, indicated by sharp increases in magnetization and/or susceptibility, has been observed in most New Zealand sedimentary thermal studies to date (e.g. Kennett and Watkins, 1974; Walcott and Mumme, 1982; the Micoene siltstones of Vickery and Lamb, 1995). Kennett and Watkins (1974) attributed this behaviour to dehydration of an iron oxyhydroxide, while Roberts and Turner (1993) and Turner (2001) ascribed it to alteration of paramagnetic clay minerals. In my samples, clay minerals are the more likely of these two, since oxyhydroxides would be unstable in a reducing environment (Florindo *et al.*, 2003). In the numerous glaucon-

itic samples, glaucony may be a candidate; however, the work of Dagg (2010) suggested that glaucony does not form strongly magnetic minerals on heating, and that pyrite is a more likely source for such alteration products in reduced sediments. In some samples, siderite may be responsible for the magnetic alteration products: siderite is known to form below the sulphate-reducing zone in reductive sedimentary environments (Roberts and Weaver, 2005); it can produce inverse magnetic fabrics (Hirt and Gehring, 1991) like those observed at Fairfield Quarry (section 5.4.2.2); and on heating it can produce magnetic alteration products with behaviours similar to my TDMS results (Housen *et al.*, 1996).

Demagnetization behaviours: comparison with previous work

It is unsurprising that interpretation of my demagnetization data was not straighforward: New Zealand sediments are well known as tricky targets for palaeomagnetic investigation. Lamb (2011), in a survey of Cretaceous-Cenozoic palaeomagnetic studies from New Zealand, noted that '[s]econdary magnetisations are common in sedimentary rocks in the New Zealand region… leading in some studies to an 80% failure rate in identifying any primary magnetisation at all.' In the studies reported by Mumme and Walcott (1985), for example, only 11 of the 52 sampled localities yielded a primary magnetization.

Given the apparent similarities in magnetic mineralogy between my samples and those of Turner (2001), it is interesting that the palaeomagnetic behaviours and interpretations are significantly different. Many of the samples of Turner (2001) showed two visible components, and a third inferred from non-origin-directed demagnetization; the initial component was identified as a thermoviscous remanent magnetization and the final component as a secondary chemical remanent magnetization (CRM), with the primary magnetization residing in the intermediate component. This diagnosis was based in part on evidence for an extra mineralogocial component with a higher coercivity in the samples which had a high blocking temperature. Despite careful analysis of IRM acquisition spectra, I was unable to find convincing evidence of more than one coercivity component, which supports the hypothesis that my high-blocking-temperature component does not represent a secondary CRM. The Neogene sediments analysed by Rowan *et al.* (2005) are perhaps a better analogue for the samples in this thesis. While some of them exhibited a

high-temperature CRM component like that observed by Turner (2001), many conformed to the two-component model adopted in this thesis: a strong VRM overprint followed by a primary detrital remanence. The DRM of Rowan *et al.* (2005) was sometimes obscured by thermal alteration, and in these cases great-circle remagnetization analysis was effective in determining it. The same two-component behaviour, with the primary magnetization residing in a final, frequently alteration-obscured component, was also observed in the type-B samples of Roberts and Turner (1993) and in the Pliocene sediments of Wilson and Roberts (1999), where great-circle remagnetization analysis was successfully applied to around half the samples.

As with the magnetic mineralogy, previous studies on the Amuri Limestone provide useful comparisons for the palaeomagnetic behaviour of the Tucker Cove Formation. As would be expected for limestone, both Tucker Cove Formation and Amuri Limestone NRM intensities are very low and demagnetization paths are noisy (e.g. Vickery and Lamb, 1995; Townsend, 2001; Randall *et al.*, 2011). Demagnetization has usually shown a two-component DRM/VRM model, lacking the hard secondary CRM component sometimes observed in New Zealand mudstones and siltstones. Amuri Limestone seems more thermally stable than the Tucker Cove Formation, at least at the studied localities, and the final component is often directly observable (e.g. Vickery and Lamb, 1995). Unusually for a New Zealand sediment, AF demagnetization has sometimes been found effective on the Amuri Limestone (e.g. Randall *et al.*, 2011); while I found that the Tucker Cove Formation responded better to AF treatment than did the other lithologies studied in this thesis, thermal treatment was still more effective.

Possible causes for poor response to AF treatment

As previously discussed, the poor response of New Zealand marine sediments to AF demagnetization has become so notorious that several more recent studies have even omitted AF demagnetization pilots. In some cases the behaviour can probably be explained by a GRM acquired by greigite, but it has also been observed even where the remanence is carried by magnetite (e.g. Turner *et al.*, 2007). To date, it appears that no investigations have been published into the causes of this behaviour. In the work described in this thesis, I used rock magnetism mainly to establish the fidelity of the palaeomagnetic signal, and did

not perform any experiments specifically to determine the mechanism of the poor AF response. In this section I speculate briefly on possible causes and how they might be investigated.

The response to AF demagnetization may be attributable to the presence of a magnetic mineral with a Curie point only slightly above room temperature, which would therefore have a very short (< 1 day) relaxation time. There are various candidates for such a role: magnetite or maghaemite with extensive cation substitution, an iron oxyhydroxide, or nonstoichiometric areas within pyrite grains. The low Curie temperature would mean that such a mineral would carry no palaeomagnetic remanence and be undetectable to thermal rock magnetic studies. The mineral would not have to hold remanence for very long: under a minute, the time between the application of an AF field and the measurement of the sample remanence.

The actual mechanism of remanence acquisition may be related to the time taken for mineral grains to respond to an applied field: if their response time is close to the frequency of the alternating field, they will not keep up with the fluctuations of the demagnetizing field, and a constructive interference pattern may be set up between the response frequency and the driving alternating field, imparting a spurious remanence. Such a mechanism would explain why no significant spurious remanences were observed when IRM was imparted on the same samples. However, the difference between AF and IRM response may also be related to the slightly longer time between treatment and measurement during the IRM experiments, which could allow a spurious remanence imparted by IRM treatment to relax before it is measured.

These hypotheses could be tested in various ways. The idea that part of the remanence is carried by swiftly relaxing magnetic minerals could be tested by remeasurement of AF-treated samples at set intervals for a few days after treatment. If low-Curie-temperature minerals are involved, their component of the magnetization should fall off significantly during this period. Determining the actual acquisition mechanism would be more difficult: it could be investigated by applying AF demagnetization at different frequencies, but this would require fairly specialized equipment, since most commercially available AF treatment systems operate at a single, fixed frequency.

8.2.5 *Analysis of demagnetization data*

In all of the palaeomagnetic studies within this thesis, I have relied heavily on great-circle remagnetization analysis (McFadden and McElhinny, 1988) in determining the final component of magnetization, which I also inferred to be the primary remanence. This technique was necessary as the magnetization is carried by magnetite, with a Curie temperature of 580°C, but thermal alteration generally occurred in the 300–400°C range, obscuring the demagnetization of the natural remanence.

The method of McFadden and McElhinny (1988) allows the combination of 'direct observations' (from samples where the magnetization does reach the origin before alteration takes place) with extrapolated great-circle paths. For almost all samples in this thesis, however, no direct observations were possible, and directions were determined entirely on the basis of great-circle intersections. The precision of the great-circle intersections varied between field areas, with the best fits from Campbell Island samples. In the best cases, Campbell Island sites showed four great circles converging almost exactly upon a single point. At the Fairfield Quarry and the mid-Waipara River sections, no fits of this quality were observed, and many sites were removed from consideration due to insufficiently good precision parameters or confidence intervals.

Stepwise heating is generally the demagnetization method of choice for New Zealand sediments (section 8.1.2.4), but they are notoriously prone to thermal alteration at temperatures well below the unblocking temperatures of many iron oxides. It is thus unsurprising that great circle remagnetization analysis has been used in several previous studies, most usually employing the popular algorithm described by McFadden and McElhinny (1988). McGuire (1989) thermally demagnetized Pliocene sediments from the Turakina River; demagnetization could not be usefully continued beyond 350°C, and he used great circle remagnetization analysis to calculate inferred endpoints. The reliability of the ensuing magnetostratigraphy was called into question by Turner (2001), who determined that the DRM resided in an intermediate component, and that the final component was a secondary CRM. In this case, however, the fault was not with the technique itself, which did successfully isolate the 'invisible' final component of the samples; it was simply that the final component did not carry the primary magnetization. For the analyses in this thesis, I have taken care to establish that the highest blocking temperature component rep-

resents the primary magnetization.

Roberts *et al.* (1994) made extensive use of great-circle remagnetization analyses, both with and (as in this thesis) without constraints from direct observations, for Miocene–Pliocene South Island sediments. In some cases, a secondary component with a high blocking temperature necessitated the use of unanchored principal component analyses instead. Great-circle remagnetization analysis was also successfully employed by Pillans *et al.* (1994), Wilson and McGuire (1995), and Wilson and Roberts (1999).

Great-circle remagnetization analysis has less frequently been used for tectonic studies than for magnetostratigraphy, due to concerns about accuracy of the resulting directions (Rowan *et al.*, 2005); some successful applications have been reported, however. Vickery and Lamb (1995) used it on Miocene siltstones. Rowan *et al.* (2005) applied it to Miocene rocks at the Hikurangi margin, and found the directions consistent with those determined by PCA for samples which demagnetized fully; however, as in Roberts *et al.* (1994), the presence of a high-temperature secondary component in some samples limited its applicability. Further successful applications of the technique were reported by Rowan and Roberts (2008).

8.2.6 *Remanence acquisition model*

There is relatively little published literature on the palaeomagnetism of sediments similar to those in this thesis – specifically, pyritized sediments which nevertheless retain a very weak NRM carried by magnetite. However, this may reflect a form of selection bias rather than actual scarcity of such mineralogies: with a current state-of-the-art cryomagnetometer, the NRMs encountered in this thesis are close to the limits at which usefully accurate measurements can be made, especially after partial demagnetization. It is likely that, until fairly recently, such material would have been deemed useless for palaeomagnetic study. Although IRM acquisition experiments can detect minute amounts of magnetic minerals even without a highly sensitive magnetometer, it is unlikely that such experiments would be carried out on rocks whose NRM is too low for useful palaeomagnetic work.

The magnetite-dominated magnetic mineralogy and reducing environment imply a fairly straightforward model of remanence acquisition: detrital magnetite grains acquired a depositional remanent magnetization, which was

then substantially weakened by the dissolution of most of the magnetite. However, the model needs to account for the survival of a small proportion of the magnetite. This survival could be explained by one of two hypotheses:

1. Pyritization may have been arrested by a lack of hydrogen sulphide to react with iron.

2. The magnetite may have been physically protected in some way from contact with corrosive pore waters.

Hypothesis 1: excess magnetite

Hypothesis 1 is generally consistent with the conclusions of Berner (1970), who found that iron is most often (though not always) in excess during pyritization reactions, so that the extent of pyritization is controlled by the availability of organic matter and sulphate. A form of hypothesis 1 was adopted by Roberts and Turner (1993) to account for the preservation of a low concentration of titanomagnetite grains in Neogene sediments of the Awatere Group: they suggested that a high sedimentation rate limited the downward diffusion of sulphate from sea-water, and the substantial amount of detrital iron was more than sufficient to react with all the available sulphate under these conditions.

In my samples, however, the first hypothesis seems unlikely, for several reasons. One problem is the lack of intermediate sulphides (greigite and pyrrhotite) which would be expected if pyritization had been interrupted (Roberts and Turner, 1993). Another problem is the very low concentration of magnetite: this would imply that the amount of available sulphide was *precisely* sufficient to dissolve all but a few parts per million of the available magnetite. Such a close correspondence between the quantities of the reactants is implausible.

Hypothesis 1 would also fail to account for the inferred grain size of the magnetite: in general, smaller magnetite grains should be dissolved first due to their higher ratio of surface area to volume. Thus, once pyritization is well advanced, the remaining grains should be the largest ones; this situation has been observed by, for example, Karlin (1990b) and Rowan and Roberts (2006). Such observations are difficult to reconcile with the inferred sub-micron size of the magnetite in my samples. Karlin and Levi (1985) proposed one possible

explanation for the presence of fine-grained magnetite in an extensively pyritized sediment. In their model, the initial population of fine-grained magnetite was entirely dissolved, but partial dissolution and dissection of large, multi-domain grains created a new population of single-domain and pseudo-single-domain grains. The mechanism is, in effect, the inverse of the usual mode of CRM acquisition: a single-domain grain is formed not by growing from a super-paramagnetic size, but by dissection from a multi-domain size. This mechanism could potentially account for the inferred small grain size of the remaining magnetite in my sediments, but does not dispel the other objections to hypothesis 1.

Hypothesis 2: protected magnetite

Hypothesis 2 is consistent with the finding in chapter 3 that the remanence appears to be carried by the less susceptible grains; this could be explained by magnetic inclusions within weakly paramagnetic or diamagnetic grains. Although magnetic inclusions have long been known in igneous rocks (e.g. Evans *et al.*, 1968; Wu *et al.*, 1974; Davis, 1981; Bogue *et al.*, 1995), it is only relatively recently that attention has been paid to their sedimentary counterparts. Hounslow and Morton (2004) defined four classes of iron oxide inclusion within sedimentary particles, but for palaeomagnetic purposes, the most important distinction is between two main types of inclusion: firstly, inclusions which were formed in a source rock before being transported and deposited as sediment; and secondly, inclusions which were formed *in situ* as a result of authigenic mineral growth. The importance of this distinction relates to the acquisition of DRM. The orientation of a magnetized grain settling onto an underwater surface is controlled by several factors: the torque exerted by the ambient magnetic field; the inertia of the grain; viscous torque from the water; and the torque resulting from contact with the surface (Dunlop and Özdemir, 1997, §15.2). Theoretical and experimental results show that, for pure SD and PSD magnetite grains, the magnetic force dominates, allowing the grain to align with the magnetic field and preserve a DRM. However, if magnetite is present only as inclusions within a larger grain, the magnetic torque will be correspondingly weaker and may not be sufficient to overcome the mechanical, inertial, and viscous forces. If, conversely, the inclusion is formed post-depositionally, the process of DRM acquisition is unaffected.

Both types of inclusion have been reported in palaeomagnetic and rock magnetic studies. Canfield and Berner (1987) found that in some cases pyrite itself, as an overgrowth on magnetite grains, protected the magnetite from further sulphidization. Karlin (1990b) reported the growth of protective coatings of amorphous silica on magnetite, and Rowan and Roberts (2006), in a study of Neogene New Zealand sediments, found similar coatings protecting greigite from further pyritization and allowing it to retain a remanence from its time of formation. Hounslow *et al.* (1995) gave the first description of magnetic inclusions in sedimentary quartz; in this case, the quartz protected the inclusions (inferred to be magnetite) from pyritization, but it was unclear whether the grains carried a palaeomagnetic remanence. A study of Pleistocene North Sea sediments by Maher and Hallam (2005) found abundant magnetic inclusions within silicates in Pleistocene North Sea sediments, but concluded that they carried a negligible palaeomagnetic signal. Heider *et al.* (1993) reported a DRM carried by titanomagnetite inclusions within volcanic ash particles.

Wilson and Roberts (1999) described remanence carriers which, while not involving discrete magnetic inclusions, do have strong parallels with them. They found that, in some heavily pyritized sediments from the Wanganui basin, remanence appeared to be carried by ilmenite grains, despite the fact that ilmenite is generally known to be paramagnetic. They concluded that the ilmenite contained sub-micron ferrimagnetic iron-enriched zones with a probable haemo-ilmenite mineralogy, as previously described by Lawson and Nord (1984) and Nord and Lawson (1989). In this case, the unreactive ilmenite had protected the ferrimagnetic zones from the strongly reducing conditions, and – given the successful preservation of a palaeomagnetic signal – the overall magnetic moment had evidently been sufficient to align the entire grain.

Given the low magnetite concentrations in my samples, the 'protected magnetite' hypothesis does not require inclusion to be a particularly common occurrence: only a very small proportion of the original detrital magnetite needs to survive to carry the weak remanences seen throughout this thesis.

In my material, as with many of the studies described above, magnetic inclusions were not directly observed, but were inferred from rock magnetic and sedimentological data. It is thus impossible to say from direct analysis whether the inclusions were formed *in situ*, giving them the potential to record a palaeomagnetic direction, or whether grains were deposited with pre-exist-

ing inclusions, which would mean that the orientation would probably be controlled mainly by mechanical rather than magnetic forces. However, previous studies show that inclusions definitely have the potential to record DRM in sediments. Directions obtained from the sediments can be subjected to palaeomagnetic tests, such as consistency between samples, alignment with a known palaeofield direction, or the fold test of Graham (1949). I discuss the application of such tests to my data in section 8.3.1.

8.3 New Zealand Palaeogene stratigraphy

The palaeomagnetic investigations in chapters 5 to 7 established significantly improved age constraints on the studied sections. In this section I discuss the reliability of the palaeomagnetic results, the relationships between the magnetostratigraphies, and the implications for sedimentation rates in the units I investigated.

8.3.1 *Validity of palaeomagnetic directions*

In this section I consider the reliability of the mean directions I determined from the palaeomagnetic measurements, and assess their validity using various approaches.

8.3.1.1 *Remanence acquisition model*

In section 8.2, I discussed the mineralogy of the sediments I studied and presented a model for remanence acquisition. It appears that most or all of the remanence is carried by magnetite. This model supports the presence of a primary remanence, since most of the sediments were deposited under reducing conditions where magnetite would be unlikely to form *in situ*. The remanence acquisition model developed in section 8.2.6 allows the possibility that the magnetite holds a DRM, but cannot conclusively show it: DRM acquisition depends on whether the magnetite grains are able to orient themselves during deposition. However, the model does mean that if the palaeomagnetic directions themselves are plausible, there is a mechanism by which they could have been acquired. The model helps to exclude other possible mechanisms which might produce a high-unblocking-temperature final remanence component: CRM is,

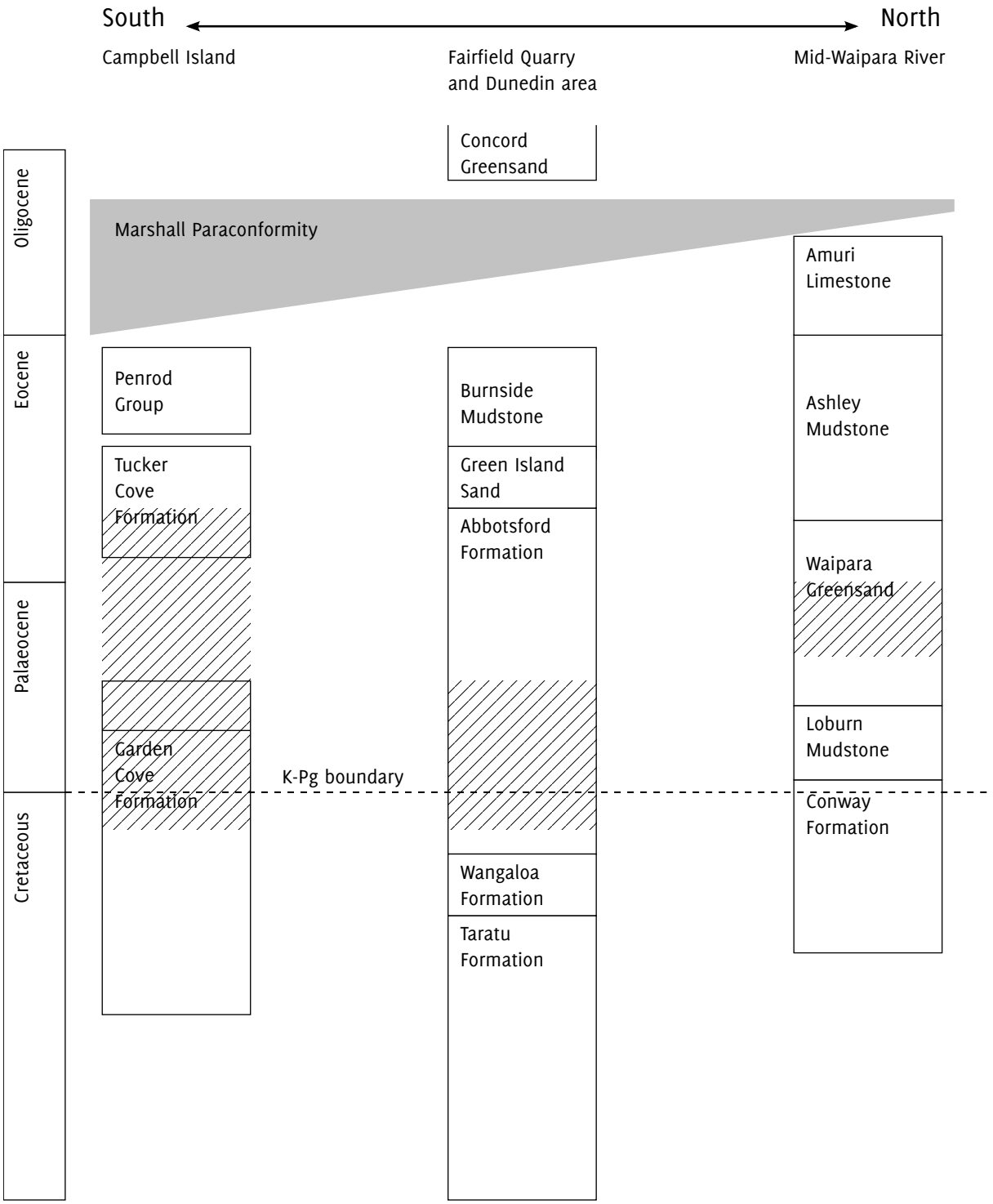

Figure 8.1 Schematic stratigraphic correlation of sections studied in this thesis (identical with figure 1.4 in the introduction). Hatched areas indicate the approximate extent of the sections I sampled.

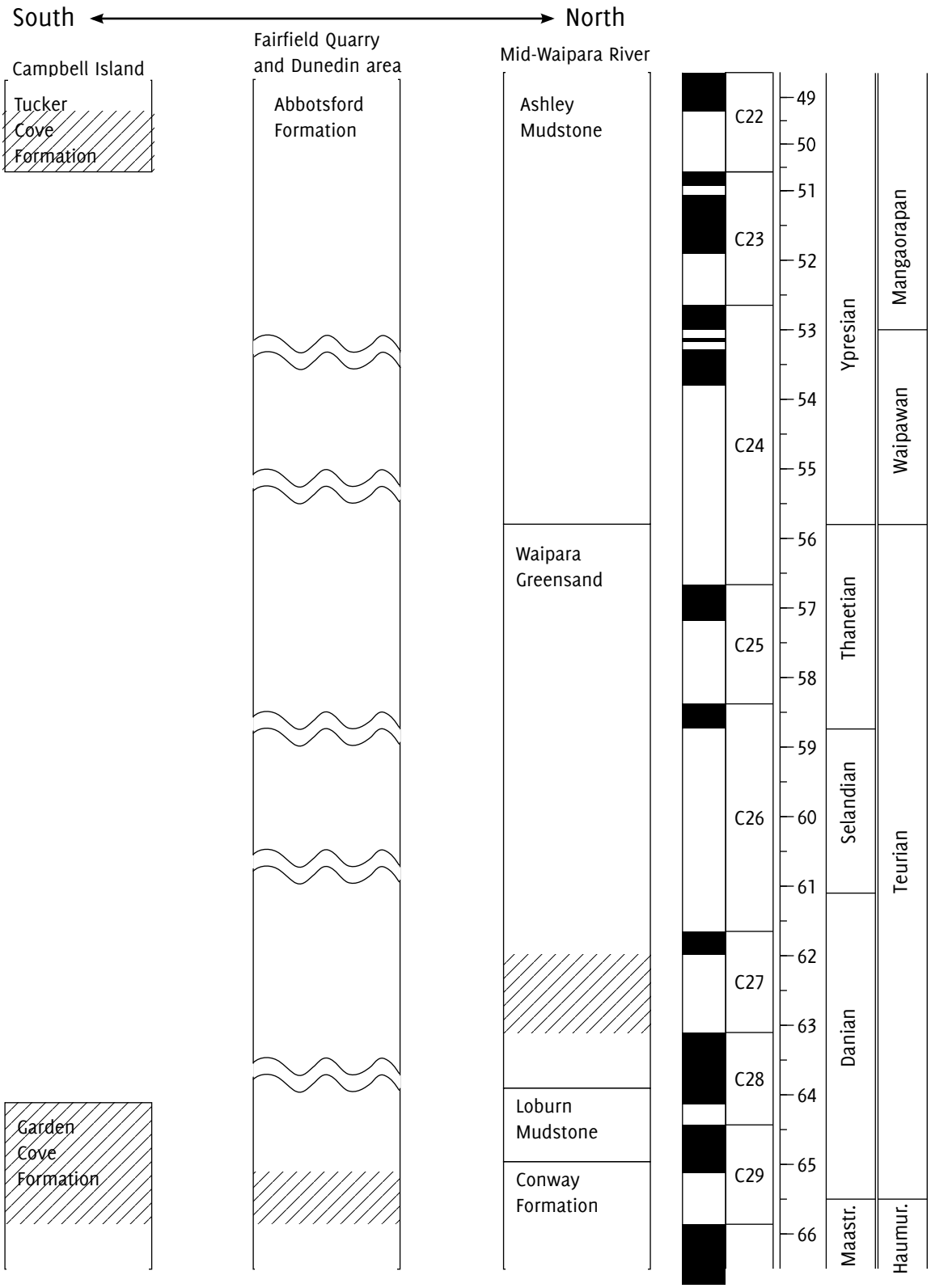

Figure 8.2 Correlated ages of all studied sections, determined by biostratigraphy and magnetostratigraphy. Hatched areas indicate the sampled regions. The breaks in the Abbotsford Formation column (not intended to correspond to specific time intervals) indicate schematically the multiple unconformities reported in the unit by McMillan (1993).

as stated above, unlikely when magnetite is the carrier, and the calculations in section 3.5.4 (p. 81) show that the thermal treatments should be sufficient to unblock any viscous magnetization.

8.3.1.2 *Site mean directions*

Provided that more than two great circles are used for a fit, the goodness of fit can be evaluated: the smaller the zone on which the circles converge, the better the fit. If multiple circles from samples at a single site converge to a single point (or sufficiently small area), it provides strong evidence that the final ('hidden') component is the same in all the samples. The great-circle remagnetization analysis algorithm provides goodness-of-fit measures (α_{95} and k), and I used these in all the palaeomagnetic studies to exclude sites where the circles did not appear to converge sufficiently.

A similar principle applies at the level of the formation mean direction: although site mean directions will vary somewhat due to secular variation, they should show a reasonable degree of clustering about the formation mean direction. This clustering can be measured using a Fisherian 95% confidence interval (α_{95}); for all but one of the sections, α_{95} was below 10°, indicating reasonable grouping of site means. Table 8.2 (p. 275) shows formation mean directions and Fisherian parameters.

8.3.1.3 *Field tests*

At the Fairfield Quarry and the mid-Waipara River, no field tests were possible, since bedding orientation was constant and no reversals were detected within the sections. At Campell Island, the Limestone Point section comprised one normal and two reversed zones, allowing me to carry out a reversals test. The data passed the test comfortably, although only two sites (totalling six samples) were available for the normal zone.

Since the Campbell Island study included two sites with different bedding attitudes, it was also possible to carry out a fold test. I carried out separate fold tests on the two formations sampled at Campbell Island, using the bootstrap formulation of the fold test described by Tauxe and Watson (1994). The results were mixed: for the Tucker Cove formation, the 95% confidence region for

optimal unfolding spanned −10% to 137%, indicating that no reliable determination could be made based on the available data. For the Garden Cove formation, the test was more successful: the 95% confidence interval was from 19% to 100%. While this is still a sizeable interval, it excludes (at the 95% confidence level) the possibility that the remanence was acquired post-depositionally.

8.3.1.4 *Tectonic and geomagnetic constraints*

The reliability of a palaeomagnetic direction can be assessed by comparing it with known constraints on the local geomagnetic field at the time and place of its formation. For a present-day viscous overprint, this is fairly easy: the time-average present-day GAD field and current position of the section are used. For all the studied sections, the mean direction of the inferred viscous component gave a reasonable match with the current GAD field.

For the primary component, it is necessary to consider the latitude and orientation of the locality at the time of formation; I defer this discussion to section 8.4 (p. 275).

8.3.2 *Sedimentation rates*

At Fairfield Quarry, I determined a minimum sedimentation rate of 44 mm/kyr for the lower part of the section; a high sedimentation rate is consistent with the extensive pyritization, and with good preservation of leaf fossils mentioned by Fordyce *et al.* (2009). Across the entire Abbotsford Formation, with a thickness of ~300 m and a duration of ~20 Myr (McKellar, 1990), the average sedimentation rate can be estimated at ~15 mm/kyr. It is probable that much of the 'missing' material implied by this discrepancy is accommodated in the unconformities detailed by McMillan (1993), which may be related to eustatic fluctuations; I discuss the significance of this in section 8.5 (p. 279).

The low minimum sedimentation rate of 5.5 mm/kyr determined at the mid-Waipara River may reflect a reduction of sedimentation caused by increased current flow. Again, I defer discussion of this relationship to section 8.5.

At Campbell Island, there appeared to be a sharp drop in sedimentation rate above the K-Pg boundary within the Garden Cove Formation; Hollis *et al.* (2003) reported contemporaneous reductions in sedimentation at Woodside

Creek, Flaxbourne River, and Branch Stream. In the Tucker Cove Formation, the minimum sedimentation rate of 3 mm/yr is compatible with the 3–20 mm range stated by Vickery and Lamb (1995) for the Amuri Limestone (of which the Tucker Cove Formation is a correlative) at Woodside Creek.

8.3.3 *Construction of magnetostratigraphies*

I constructed magnetostratigraphies constrained by existing biostratigraphic data, mainly from dinoflagellate cysts. In all cases the magnetic data significantly improved earlier age determinations. Figures 8.1 and 8.2 summarize the stratigraphic findings in this thesis: figure 8.1 reproduces the figure from the introduction showing the approximate zones which were sampled; figure 8.2 shows the same sections with a more precise temporal scale and magnetostratigraphic bounds on the ages of the sampled material.

Figure 8.2 summarizes the ages determined for the three sections I studied in this thesis. In all cases, magnetostratigraphy has allowed high-resolution age determinations. At Fairfield Quarry, all sites had reversed polarity and the entire sampled section was constrained to the C29r chron; while this implies that the sediments themselves are too old to show evidence of the suspected Palaeocene paraconformity, it gives a precise age for the bottom part of the Abbotsford Formation and thus helps to identify nearby targets for future sampling. The sedimentation rate is also consistent with the presence of conformities in the overlying parts of the Abbotsford Formation, as discussed above.

At Waipara, all the analysed sites were reversed, and magnetostratigraphy constrained the analysable portion of the studied section within the C26r chron.

At Campbell Island, the stratigraphy was somewhat more involved: there were two separate sections, each exposing two formations separated by a significant unconformity. The resulting magnetostratigraphy reconciled the two sections with each other, the biostratigraphy, and the GPTS, although there was some ambiguity in the assignment of two magnetozones to polarity chrons. At Campbell Island, the magnetostratigraphy narrowed the bounds on the ages of both the exposed formations. It determined that the start of the Palaeocene-Eocene unconformity is old enough for the unconformity to be associated with

Section	Declination	Inclination	α_{95}	k	# sites
Fairfield Quarry	102.6	72.6	6.7	16.1	31
Mid-Waipara River	168.7	62.1	17.6	9.5	9
Campbell Island A	173.2	83.3	8.1	32.8	11
Campbell Island B	253.2	78.8	9.2	28.7	10
Campbell Island C	166.6	69.7	7.1	61.9	10
Campbell Island D	201.5	74.2	7.4	67.5	7

Table 8.2 Formation mean directions for all sections studied in this thesis. The final column gives the number of site mean directions used to determine the formation mean.

the ice-rafted debris reported by Leckie *et al.* (1995); I discuss this further in section 8.5.1.2.

8.4 Tectonic rotations

In this section I discuss the formation mean directions from the various sections investigated, and relate them to the known tectonic history of southern New Zealand and the Campbell Plateau. Table 8.2 summarizes the formation means of all the sections. Note that, as in chapter 7, separate formation means are given for the four suites of samples from Campbell Island, since there is considerable variation between them.

8.4.1 *Possible sources of error*

Tectonic investigations have more stringent requirements than reversal magnetostratigraphy: rather than a binary normal/reversed determination (which can sometimes be made even if there is considerable imprecision in the mean direction), tectonic studies require determination of inclination and declination at a much finer level. In the sections studied in this thesis, there are several factors which may compromise the accuracy of the palaeomagnetic directions. The first is the high latitude of all the sections, especially at Campbell Island. Latitude has a dramatic effect on the precision with which declinations can be determined: the declination subtended by a circular confidence region is proportional to $1/\cos(I)$, where I is the inclination of the centre of the confidence region[11]. For example, a 10° confidence would subtend 20° of declination if I

= 60°, and nearly 58° of declination if I = 80°. Thus any uncertainties in the measurement of declination are in effect amplified by the high latitude and consequent high inclination of the geomagnetic field.

Secondly, my unavoidable reliance on great-circle remagnetization analysis may have contributed to the directional uncertainties; a direct observation of an origin-trending direction is preferable to a great-circle intersection, not least because each sample can independently provide an estimate of the site mean direction. Rowan *et al.* (2005) noted that, because of concerns about accuracy, great-circle remagnetization analysis has seldom been applied in tectonic studies; however, their study found that great-circle site directions reliably matched direct observations from origin-trending components at the same sites.

The third source of uncertainty is the relatively small number of successfully analysed sites. In the case of Campbell Island this was in part due to the short time available for fieldwork and the difficulty of access to the sections. Of the sites that were sampled, many were excluded because the data were not reliable enough. At Fairfield Quarry this was mitigated by the large number of sites originally sampled and the fact that the sub-sections often overlapped, but at Waipara the 21 sites originally sampled were reduced to 9 by data quality control. When a formation mean is determined from a small number of sites, it is less likely to average out secular variation and random measurement errors.

Finally, there may be some inaccuracy in the determination of bedding attitudes used to calculate the formation corrections. In most of the sections, the bedding structures were poorly defined. The most reliably determined bedding attitude was at Fairfield Quarry, where small-scale bedding structures were not visible, but the extensive exposure of laterally continuous glaucony beds made it possible to determine bedding at a larger scale using a range-finder (section 5.2.1, p. 126).

8.4.2 *Inclination and palaeolatitude*

The high-latitude 'amplification' of uncertainties does not apply to the inclination, and the formation mean inclinations generally show the expected trend

[11] This relation applies while the whole of the confidence region is below 90° latitude; once it includes the pole, declination is technically completely indeterminate at the given confidence level.

for the relative positions of the sections. Inclination increases with latitude, and (as discussed in the relevant chapters) is roughly consistent with the estimated palaeolatitudes of the sections. The only exception to this trend is suite C at Campbell Island (lower Limestone Point section), whose inclination of 69.7° is below that of the more northerly Fairfield Quarry site (72.6°).

8.4.3 *Tectonic reconstructions*

Sutherland (1995) and King (2000b) both gave reconstructions of rotations between the Australian and Pacific plates during the Cenozoic. King (2000b) determined an average anticlockwise rotation rate for the Pacific plate of around 1°/Myr for the past 40 Myr, and Sutherland (1995) gave a rate of 1.1°/Myr for the past 45 Myr. Prior to 45 Ma, plate motions are more poorly constrained, so there is some uncertainty in determining the expected declinations of the primary magnetization. The rotation is more poorly constrained prior to the formation of the plate boundary at around 45 Ma; assuming somewhat less rotation in the absence of a boundary gives a rough estimate of 50–60° for the Palaeocene. From this rotation rate, the expected magnetic declination for reversed magnetozones in the sections I investigated would be in the south-eastern quadrant, with a range of around 120–130°.

8.4.4 *Discussion of individual sections*

Fairfield Quarry

Fairfield Quarry provides the best agreement with known tectonic configuration at the time of deposition. This agreement is encouraging, since this section also has the largest number of successfully determined site means, the most reliably determined bedding orientation, and one of the smallest confidence intervals (α_{95}=6.7°). Nevertheless, due to the high inclination, the possible rotations (at 95% confidence) span a fairly large range, from 55° to 100°. The lower part of this range is consistent with the tectonic reconstructions discussed above.

Mid-Waipara River

At the mid-Waipara River section, the formation mean direction implies a lower latitude and lesser rotation than expected, but the substantial confidence region allows for a latitude of up to 70°. The rotation implied by the confidence region may be as high as 50°. Apart from inaccuracy, there may be another explanation for the anomolously low rotation: the mid-Waipara River section is relatively close to the Alpine Fault, and may have been subjected to clockwise rotations related to plate motion along the Hikurangi Margin over the past 20 Ma (e.g. Little and Roberts, 1997; Lamb, 2011), partially cancelling out the previous anticlockwise rotation.

Campbell Island

The mean declinations of the Campbell Island sections are not straightforward to interpret: there is considerable variation between them, and some are hard to reconcile with known tectonic rotations. It is likely that these difficulties are due in part to the various sources of uncertainty discussed in section 8.4.1.

Suite A (upper Camp Cove) is technically consistent with any rotation, since the confidence interval encompasses the pole; however, a northward-pointing declination would require an inclination of around 89° or above, which is inconsistent with the palaeolatitude. Most of the confidence region falls within the expected quadrant, and would be consistent with, say, a rotation of 50° and a palaeolatitude of 70°.

Suite B (lower Camp Cove) is perhaps the most problematic Campbell Island suite. The mean direction is not compatible with any anticlockwise rotation, and some error in its calculation must be suspected. Site means are well-constrained, and the most likely source of error is probably the bedding orientation: no bedding structures were apparent in the Garden Cove Formation at Camp Cove, so I corrected the directions using the bedding attitude of the overlying Tucker Cove formation. There may have been a slight angular unconformity between the two, or the Garden Cove Formation exposure may have been subjected to slight deformation caused by later volcanic activity (it was intruded by several dykes).

Suite C has a lower mean inclination than would be expected, but the confidence interval is consistent with palaeolatitudes up to 65°. The range of declina-

tions within the confidence interval (approximately 146°–187°) implies a lower rotation than expected, with a maximum clockwise rotation from present-day orientation of only 34°. This discrepancy may be connected to inaccurate formation correction or a too-small number of site mean directions, as discussed above.

The suite D formation mean direction was determined from only 7 site mean directions, so there is a strong chance that secular variation was not adequately averaged. As for suite B, the mean direction implies an implausible clockwise rotation since the time of deposition. The range of inclinations is reasonable, however.

8.5 Ice in the greenhouse

In this section I return to the hypothesis, introduced in chapter 1, that brief periods of Antarctic glaciation may have occurred prior to the inception of long-term ice sheet development in the Oligocene. I re-examine the expected effects of Antarctic glaciation on the sedimentary record and relate them to the findings presented earlier in the thesis.

8.5.1 *Possible effects of a glacial episode*

Section 1.1 (p. 1) outlined the effects that a transient Antarctic glaciation might be expected to have on ocean and climate, and the traces that these effects might leave in the sedimentary record. The Marshall Paraconformity in the mid-Oligocene (Fulthorpe *et al.*, 1996), associated with a short episode of Antarctic glaciation, form a rough template for the expected sedimentary record of such an event. Since the three sections studied in this thesis had different palaeogeographic and depositional settings, they would be expected to react differently to the effects of an Antarctic ice sheet.

8.5.1.1 *Eustatic sea-level changes*

Perhaps the most obvious large-scale effect of ice sheet formation – as recorded in marine sediments – is eustatic sea-level fall. Most other sedimentological signals, such as enhanced bottom-water flow and ice-rafted debris (IRD), are produced by a direct interaction between ice and water. But ice sheets tend to

grow from inland ice caps at high elevations, and will thus influence eustasy before they have a direct effect on the marine environment. If the ice sheet begins to shrink before reaching the coastline, the direct effects are of course never seen, leaving eustatic sea-level estimates and $\delta^{18}O$ records as the main evidence of ice (Miller *et al.*, 2005). In the case of early Cenozoic New Zealand sediments, eustatic signals will generally be superimposed on the gradual depth increase caused by continuing tectonic subsidence (King, 2000a), but the timescales of glaciation and deglaciation are so much shorter that this should not cause ambiguities in interpretation (Miller *et al.*, 2005).

There is evidence from the New Zealand region for eustatic sea-level falls during the Palaeocene. (Schiøler *et al.*, 2010) determined that the Tartan Formation of the Great South Basin and Canterbury Basin was deposited at the peak of a Late Palaeocene regression. On tectonic grounds and from correlation with similar events in the East Coast Basin, they argued that this regression was eustatic in origin. They identified it with the global sea-level fall at around 57 Ma recognized by Miller *et al.* (2005) and others.

Many of the sediments studied in this thesis might be expected to show a response to any sea-level fall of more than a few metres. Fairfield Quarry exposes the lowermost part of the Abbotsford Formation. McMillan (1993) interpreted the facies of this formation as indicative of estuarine to offshore depositional environments, with the Fairfield Quarry section mostly consisting of varying nearshore marine facies. McMillan (1993) tentatively correlated some unconformities in the Abbotsford formation with eustatic falls in the sea-level curves of Haq *et al.* (1987). The eustatic sea-level fall at 57–58 Ma, corresponding to the main hypothesized Palaeocene paraconformity, was not part of the sampled section at Fairfield Quarry. However, the facies variations at Fairfield, in particular the deposits of glaucony (often taken as an indicator of transgression), show that there was at least local relative sea-level variation around the time of the K-Pg boundary, and that the Abbotsford Formation sediments were responsive to it. The new magnetostratigraphic constraints on the time represented by the Fairfield Quarry section show that these variations were rapid (<1 Myr); this would be consistent with ice-sheet fluctuation as a driver of the sea-level variation, but large-scale correlation would be necessary to establish a eustatic cause.

The Mid-Waipara River section was deposited at inner to mid-shelf depths

(Hollis and Strong, 2003) and thus also has the potential to respond to sea-level fluctuations, albeit perhaps more weakly than the Fairfield Quarry section. A sea-level drop is one possible explanation for the apparent lack of palaeocurrent (as inferred from AMS) in the upper part of the section, as a more near-shore setting might be less influenced by large-scale, consistently directed ocean currents.

At Campbell Island, the long-term trend recorded in the Garden Cove Formation is one of gradually increasing depth as a result of tectonic subsidence. While the basal Garden Cove Formation is nonmarine, the uppermost portion (corresponding to the portion sampled in my study) has been identified as fully marine by the dinoflagellate analysis of G. J. Wilson in Hollis *et al.* (1997), implying a depositional depth exceeding that at Fairfield Quarry and similar to that at the Mid-Waipara River. (The depositional depth of the Tucker Cove Formation above the unconformity is of coure far greater, estimated at >1500 m by Hollis *et al.* (1997)). The unconformity between the Garden Cove and Tucker Cove formations encompasses most of the Palaeocene, including two short-term sea-level falls (Miller *et al.*, 2005) at around 57 Ma and 61 Ma, limiting the likelihood of its responding to eustatic change. There are no signs of a regression in the Garden Cove Formation.

8.5.1.2 *Ice-rafted debris*

If an Antarctic ice sheet reaches the margin of the continent, it can produce more direct sedimentological evidence, including IRD. Dropstones of Palaeocene age from the Whangai Formation in the eastern North Island have been reported by Leckie *et al.* (1995). They currently constitute perhaps the strongest evidence for Palaeocene Antarctic glaciation, and (unlike sea-level or isotopic records) directly imply a glaciation extensive enough to reach the Antarctic coastline. The dropstones were dated to ~62.5 Ma and are thus not correlatable with the eustatic sea-level fall at around 57 Ma (Miller *et al.*, 2005 and Schiøler *et al.*, 2010). The Campbell Island magnetostratigraphy presented in chapter 7 does, however, place the dropstone event within the time-span represented by the Garden Cove Formation/Tucker Cove Formation unconformity.

A number of lonestones were also found at the top of the Garden Cove Formation during the 2007 and 2009 Campbell Island expeditions (Andrew, 2010). While they have not yet been definitively identified as ice-rafted drop-

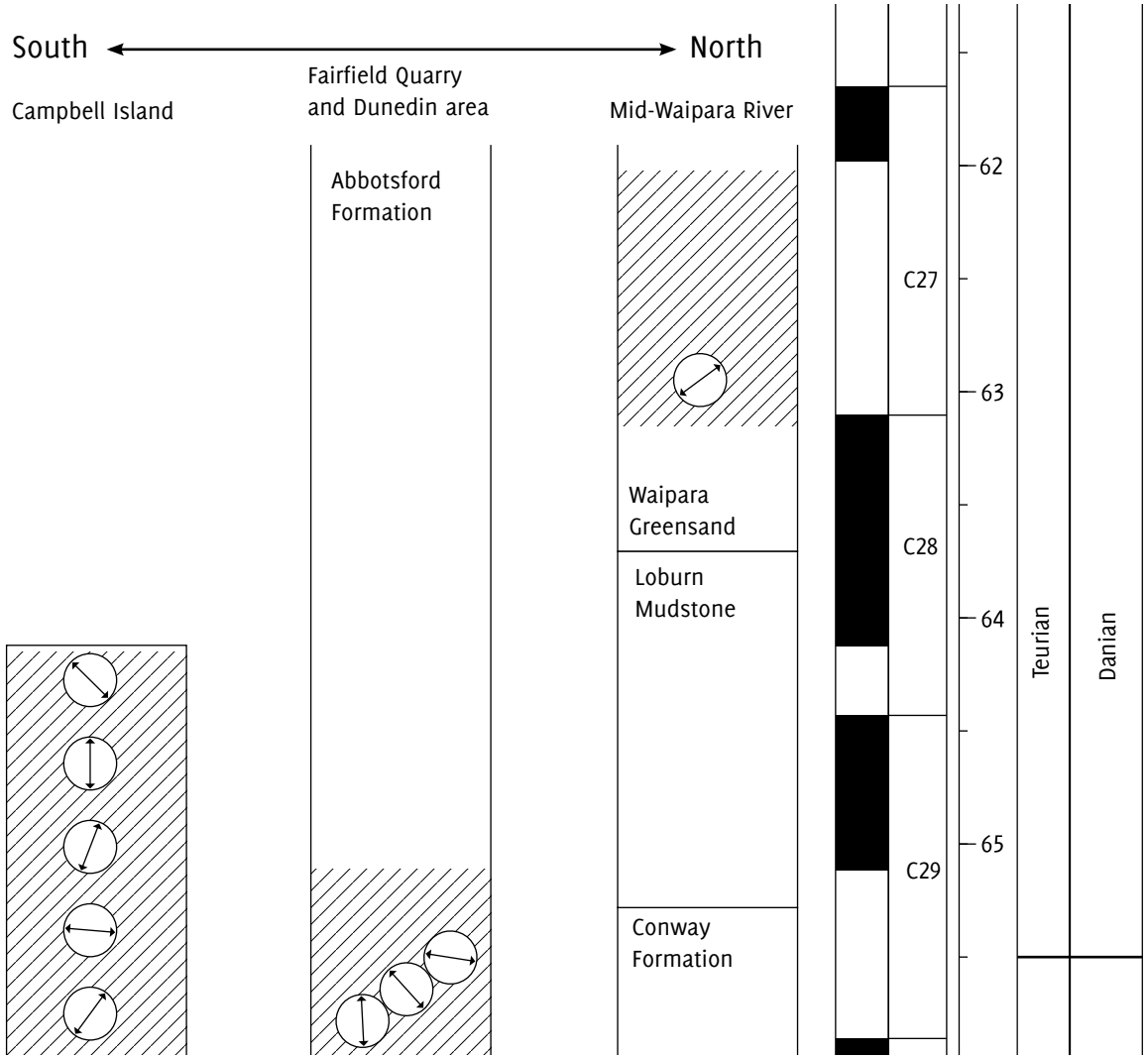

Figure 8.3 Palaeocurrent trends for all sampled sections. The two current directions determined from the Eocene Tucker Cove Formation at Campbell Island are omitted to permit a larger vertical scale.

stones, this at present seems the most likely explanation for their presence. If they are indeed dropstones, they would provide a link between the Garden Cove Formation/Tucker Cove Formation unconformity and the inception of Antarctic glaciation.

8.5.1.3 *Ocean currents*

If (as suggested by the IRD of Leckie *et al.*, 1995) ice did reach the Antarctic margin in the Palaeocene, it should have had an effect on ocean currents comparable to that seen at the Marshall Paraconformity. The present-day Antarctic ice sheet produces Antarctic bottom water (AABW), which, in the form of the powerful Deep Western Boundary Current (DWBC), controls ocean sediment-

ation along the eastern margin of Zealandia (Carter *et al.*, 2004). The DWBC is currently the largest single source of deep water for the world's oceans (Carter *et al.*, 1996). The mid-Oligocene Marshall Paraconformity shows that transient glaciation can have a similar effect, with the widepsread non-deposition and erosion attributed in part to invigorated ocean current flow.

Of the sections studied in this thesis, only those at Campbell Island have the potential to show effect from a proto-AABW flow, since the others were deposited at depths too shallow to be affected by ocean-bottom flow. It is possible that the Palaeocene-Eocene unconformity at Campbell Island is related to Antarctic glaciation, especially given the potentially ice-rafted lonestones at the top of the Garden Cove Formation. However, other factors are also likely to be involved, as temperatures in the earliest Eocene are too warm to be easily reconciled with a glaciated Antarctica (Zachos *et al.*, 2008).

Antarctic glaciation may still have an effect on current at the shallower sites, however: the present-day Antarctic ice sheet drives a complex system of interacting currents throughout the water column (e.g. Sverdrup *et al.*, 1942, chapter 15). The present-day Antarctic Circumpolar Current has a major influence on sedimentation at shallower depths (Shipboard Scientific Party, 2000). A similar stable shallow water flow might be produced by a Palaeocene glaciation, though prior to the opening of ocean gateways it could not take the form of a circumpolar current.

AMS results

Directions of maximum AMS axes – taken to represent palaeocurrent direction – are summarized in figure 8.3 (p. 282). Each direction is determined from several samples, usually at more than one sampling site. There is some apparent similarity between the current directions for Fairfield Quarry and the corresponding period at Campbell Island, but given the geographical separation of the sites and limited range of the comparison, it is probably coincidental.

The suite B results from Campbell Island show that the current directions are variable on a roughly 300 kyr timescale, suggesting a gradual change in factors affecting current flow; this may be connected to the continued subsidence responsible for the facies changes through the Garden Conve Formation. The suite A AMS measurements (figure 7.10, p. 213) show a lack of clear primary

direction immediately above the Garden Cove Formation/Tucker Cove Formation context, attributable to bioturbation and/or weakened current flow.

8.5.2 *The significance of glaucony*

Glaucony occurs in a number of settings in the studied sections. At Fairfield Quarry, the glaucony content varies rapidly and widely, from close to 0% to over 80%. This fluctuation suggests rapid variation in depositional environment, since glaucony only forms under particular conditions (Amorosi, 1997), including mid-shelf to slope depths and low sedimentation rates. Glaucony variability in the Abbotsford Formation may have been influenced by Antarctic glaciation in at least two ways: by eustatic sea-level variation, which can make the water depth more or less suitable for glaucony formation; and by changes in current flow, which can change the rate of deposition. McMillan (1993) associated some glauconitic horizons in the Abbotsford Formation with the onset of marine transgressions. At Campbell Island, glaucony is mainly concentrated in the region of the Palaeocene-Eocene unconformity, consistent with a period of low or no deposition. At Waipara, glaucony is present throughout the section in similar concentrations, suggesting a fairly uniform environment throughout the period of deposition.

8.5.3 *Summary*

Several lines of evidence – include eustasy, isotope curves, IRD, and unconformities – suggest the possibility of one or more brief episodes of Antarctic glaciation. The palaeomagnetic studies in this thesis have produced some new results with bearing on the question. At Campbell Island, the start of the Palaeocene-Eocene unconformity was constrained as older than 64 Ma; this means that the dropstones reported by Leckie *et al.* (1995) (dated to 62.5 Ma) were deposited during a time of non-deposition at Campbell Island. These dropstones are both the most direct evidence for Antarctic glaciation and the only evidence for glaciation reaching the coastline; however, compared to the other suspected glacial episode at 57–58 Ma, there has so far been limited corroborating evidence for an earlier glaciation. The association of the dropstones with the Campbell Island unconformity, which may also be glacially controlled,

provides a useful corroboration – especially given that suspected dropstones were also found at the Campbell Island unconformity surface itself.

The Fairfield Quarry section is too young to show direct evidence of either of the posited glacial events, but the sedimentation rates suggest that the younger unconformities in the Abbotsford Formation represent significant time-spans, and the variable lithology of the section shows that the formation would be responsive to eustatic fluctuations.

9 Conclusions

> What do we have? We have mud. And from mud we solve the problem of the world.
>
> – Christian Ohneiser, 2005

In this chapter I summarize the most significant outcomes of this thesis.

9.1 Rock magnetism of glauconitic sediments

Chapter 3 described an investigation into the magnetic properties of glaucony.

9.1.1 *Glaucony and remanence*

The rock magnetic experiments of chapter 3 examined the contribution of glaucony to the remanent and other magnetic properties of sediments. IRM experiments (section 3.4.1, p. 50) and other studies showed that, even by the weak standards of New Zealand marine sediments, glaucony is not a significant remanence carrier. This fact is helpful for palaeomagnetic interpretation. Given the slow rate of glaucony formation and the complex chemical processes involved (Odin and Matter, 1981), and the difficulty of distinguishing autochthonous and allochthonous grains (Amorosi *et al.*, 2007), a remanence carried by the glaucony itself might be subject to complex interpretations. With glaucony established as a non-remanent fraction, the magnetization of the other, detrital grains can more readily be interpreted as a depositional or post-depositional remanence. As a non-remanent component, glaucony was found to reduce the overall NRM of samples, making accurate magnetic measurement harder. The techniques and software described in chapter 4 are designed to deal with this problem.

9.1.2 *Glaucony and rock magnetic parameters*

While the effects of glaucony on remanence are fairly straightforward, its high susceptibility was found to complicate rock magnetic experiments. As discussed in sections 3.4.4 and 3.5.5, many analysis techniques are commonly applied with the assumption that bulk magnetic susceptibility is dominated

by the ferromagnetic remanence carriers in a sample, with the paramagnetic and diamagnetic components playing a negligible role. Two common examples are the frequency dependence of magnetic susceptibility and the χ_{ARM}/χ plot of King *et al.* (1982), both used to determine magnetite grain size. For my samples, the assumption is invalidated by a combination of two factors: firstly, the very low concentration of magnetite, which dilutes its magnetic susceptibility; secondly, the high susceptibility of glaucony and its high concentration in the samples, which makes the paramagnetic contribution to bulk susceptibility unusually large. The results from analyses assuming dominance of ferromagnetic susceptibility thus become invalid. It is possible, as King *et al.* (1982) pointed out, to separate the ferromagnetic and paramagnetic susceptibilities using hysteresis loop measurement, and this is occasionally done in practice (Yamazaki and Ioka, 1997). However, hysteresis measurement requires more equipment, effort, and time, partially negating a major original motivation for such tests – simplicity and speed of application.

9.1.3 *Magnetic separation*

It is usually the case that magnetic separation tends to concentrate remanence carriers, since ferromagnetic (*s.l.*) susceptibilities are in general much higher than paramagnetic susceptibilities, so ferromagnetic grains respond more strongly to external fields in magnetic separators. The opposite was in fact the case for the sediments studied in chapter 3. The remanence carriers were apparently embedded in low-susceptibility polycrystalline grains (section 8.2.6, p. 265); the low concentration of ferromagnetic components gave these grains a lower susceptibility than the strongly paramagnetic glaucony.

The primary aim of the separation was achieved: glaucony was isolated for magnetic analysis. The secondary goal of the separation was the concentration of remanence carriers for direct analysis. Direct observation or analysis of remanence carriers in a weakly magnetic sample – by means such as electron microscopy, microprobe analysis, or XRD – is very difficult unless they can be concentrated in some way. This goal was not achieved: although remanence carriers were indeed concentrated (albeit, unusually, in the less magnetically susceptible fractions), even the 'concentrates' had such low magnetite concentrations that none could be located microscopically (section 3.3, p. 40).

9.1.4 *Determining mineralogy of weakly magnetic samples*

The nature of the samples limited the range of applicable rock magnetic techniques: direct observation was precluded by difficulties in concentrating remanence carriers, and many bulk techniques using susceptibility were precluded due to the glaucony content.

The two most useful tools for determining sample mineralogy proved to be IRM acquisition spectra (section 3.4.1, p. 50) and TDMS measurements (section 3.4.6, p. 65). Both of these techniques were found effective even at very low concentrations of ferromagnetic minerals. IRM was effective because the intense fields used imparted an easily measurable remanence to even the least magnetic samples, especially since measurement was performed on a cryomagnetometer designed to detect weak natural remanences imparted by the geomagnetic field. TDMS was effective because the susceptibilities of the remanence carriers were amplified by the Hopkinson (1889) peak occurring just before the Curie point, and because the large, sharp drop in susceptibility after the Hopkinson peak was easy to identify even in noisy data. For example, the Tucker Cove Formation samples at Campbell Island had susceptibilities in the range $1–2 \times 10^{-5}$; this is a range typically seen in pure diamagnetic substances such as quartz and ice[12] (Hunt *et al.*, 1995), and is near the sensitivity limits of the MFK-1A kappabridge. Even here, though, the Hopkinson effect amplified the susceptibility of the magnetite component sufficiently to show the Curie point (figure 7.9, page 209).

Neither IRM nor TDMS is sufficient on its own to reliably determine magnetic mineralogy. IRM suffers from the fact that different magnetic minerals can have fairly similar coercivity spectra. If a 'composite' coercivity spectrum – one produced by a mixture of minerals – is measured, it is not always easy to determine the components unambiguously; considerable theoretical effort has been expended on this problem over the years, as I discussed in section 3.4.2.

Throughout this thesis, the IRM results gave strong indications of magnetite-dominated mineralogy, but on their own were often unable to rule out a minor contribution from pyrrhotite, which has a similar coercivity spectrum. I used the log-Gaussian analysis technique of Heslop *et al.* (2002) in order to distin-

[12] Diamagnetic substances, of course, have a negative susceptibility, but the absolute magnitudes are similar.

guish between single-component and multiple-component IRM spectra; while the technique produced more quantitative results than inspection of the acquisition curves, it could not definitively distinguish a single component from two extensively overlapping ones.

TDMS data is also frequently ambiguous due to thermal alteration of samples before they reach a Curie or Néel point. The strengths of IRM and TDMS are to an extent complementary. Minerals with similar coercivities often have very different disordering temperatures, for example magnetite and pyrrhotite, or haematite and goethite. In this thesis, TDMS was consistently useful in excluding the possibility of a pyrrhotite component suggested by the IRM results. Conversely, ambiguities in Curie temperature can be resolved using coercivity data; for example titanomagnetite with 60% titanium substitution (TM60) and goethite both have Curie points near to 150°C, but goethite's remanent coercivity is about 50 times greater.

9.2 Palaeomagnetic analysis software

I produced a software package, PuffinPlot, in order to deal with the low-intensity and sometimes complex magnetizations encountered in this thesis, and in other New Zealand sediments. PuffinPlot includes facilities for weakly magnetized samples, using special measurement protocols to increase the accuracy of magnetic measurements. It also facilitates investigation of complex magnetic behaviours by allowing both interactive, exploratory analysis of individual samples and uniform bulk analysis of large numbers of samples using preset parameters. As well as providing facilities for use in this thesis, PuffinPlot has many features which make it more generally useful, such as the ability to process long core data.

9.2.1 *Magnetic analysis of weakly magnetic material*

Most of the sediments I analysed for this thesis had magnetization intensities near the sensitivity limit of current SQUID-based cryomagnetometer systems. The cryomagnetometer at the OPRF is among the most sensitive in current use worldwide, but without the development of new measurement and analysis techniques it was still inadequate for palaeomagnetic study of these sediments. The repeated tray measurement protocol (section 4.5.3.3, p. 106), in particular,

made it possible to analyse samples which would otherwise not have yielded useful palaeomagnetic data. The PuffinPlot program includes facilities to apply these corrections automatically, so they do not involve any extra time or effort during data analysis.

9.3 Palaeomagnetic investigations

The results of the palaeomagnetic investigations had a number of common features: weak remanences, mitigated by the procedures discussed in section 9.2.1; low alteration temperatures, preventing demagnetization endpoints from being reached; and noisy demagnetization behaviour, particularly in the samples from the mid-Waipara River.

9.3.1 *Fairfield Quarry*

At Fairfield Quarry, I constructed a magnetostratigraphy based on 201 oriented samples from 58 sites, and informed by the dinoflagellate biostratigraphy of McMillan (1993). I also produced a detailed sedimentary log. Magnetostratigraphy constrained the entire section to the c29r chron, improving the age resolution from 6 Myr to about 0.75 Myr and allowing good estimates of sedimentation rates.

9.3.2 *Mid-Waipara River*

At mid-Waipara River, I used 80 samples from 17 sites to produce a magnetostratigraphy for 25 m of the section. As at Fairfield, all the analysed sites were reversed, and with the aid of nannoplankton biozonation I was able to correlate them unambiguously to the c26r chron.

9.3.3 *Campbell Island*

The Campbell Island stratigraphy was based on a total of 188 samples from 54 sites at two sections on different parts of the island. Each section exposed the Garden Cove Formation and the unconformably overlying Tucker Cove Formation. The magnetostratigraphy correlated the sections with each other and with the gpts, producing reasonably precise estimates for sedimentation

rates and improved constraints on the duration of the unconformity between the two formations.

The sampled (uppermost) portion of the Garden Cove Formation was correlated with the C29r, C29n, and C28r chrons, with all three corresponding magnetozones sampled at Limestone Point. At Camp Cove, only the two reversed magnetozones were sampled, and the C29n chron inferred to be present within an 8-metre sampling gap. The sampled (lowermost) portion of the Tucker Cove Formation was identified as most probably corresponding to C22r, although an alternative correlation with the final ~200 kyr of C23r is also a possibility.

9.3.4 *Magnetic mineralogies*

At every studied section, rock magnetic (IRM and TDMS) investigations indicated that the remanence was carried by very low concentrations of magnetite (possibly with slight oxidation or cation substitution), with negligible contributions from other magnetic minerals. As described in section 9.1.4, IRM and TDMS were the most useful techniques in determining mineralogy.

9.3.5 *Palaeomagnetic behaviours*

After comparative pilot studies with AF and thermal demagnetization, I used thermal treatment for all the palaeomagnetic studies. Most samples showed common features of magnetic behaviour: noisy demagnetization paths which failed to reach a stable endpoint, and thermally induced alteration usually at 300–400°C. The mean direction of the demagnetization path was close to the time-averaged present geomagnetic field, indicating that demagnetization was removing an overprint from the current normal chron. Since magnetite had been identified as the only demagnetization carrier, and magnetite is unlikely to form authigenically under reducing conditions, I inferred that the demagnetization paths were moving towards a primary magnetization component obscured by thermal alteration. I thus used great-circle remagnetization analysis (McFadden and McElhinny, 1988) to determine the directions of the final components.

The reliability of the great-circle fits varied between the field areas. At Fairfield Quarry and mid-Waipara River, a significant proportion of sites were discarded because of insufficiently reliable mean directions. At Campbell Island,

demagnetization paths tended to be shorter, but the mean directions determined by intersecting remagnetization great circles were usually very well constrained.

9.3.6 *Anisotropy of Magnetic Susceptibility*

Despite very low anisotropies (especially at the mid-Waipara River section), AMS measurements were generally successful in determining palaeocurrent flow directions. At mid-Waipara River, AMS recorded a cessation or weakening of current flow in the upper part of the section. At Campbell Island, AMS showed variations in current direction throughout the studied time period, with a greatly weakened signal both at the K-Pg boundary and immediately after the unconformity between the Garden Cove and Tucker Cove formations. At Fairfield Quarry, directions were determined for the bottom part of the section, but a strong inverse fabric dominated most of the section, preventing palaeocurrent analysis; the inverse fabric is probably caused by the presence of siderite.

9.3.7 *Remanence acquisition*

I developed a model for remanence acquisition to explain how a small remnant of detrital magnetite was able to survive in the reducing environments in which most of the sediments were deposited (section 8.2.6, p. 265). The model posits that a small proportion of the originally deposited magnetite was overgrown or encapsulated by an inert mineral, physically protecting it from the reducing environment. Provided that encapsulation occurred after deposition, the protected magnetite should still carry a DRM, albeit an extremely weak one.

9.4 Implications

9.4.1 *Palaeogene stratigraphy*

The magnetostratigraphic studies demonstrated the effectiveness of the remanence acquisition model, the measurement techniques, and the analysis software. They improved the dating of the sections and allowed more accurate determination of sedimentation rates.

9.4.2 *Tectonic rotations*

Most formation mean directions were broadly consistent with the expected direction from known constraints on the site's palaeolatitude and rotation. Two formation means from Campbell Island gave anomolous declinations, probably attributable to high inclination and insufficient averaging of secular variation.

9.4.3 *Ice in the greenhouse*

In this thesis I have developed and applied palaeomagnetic tools to investigate the hypothesis that Antarctica experienced glacial episodes before the Oligocene, and that ocean gateways are thus less vital to Antarctic glaciation than has commonly been assumed. The palaeomagnetic investigations gave improved age constraints for all the sections I studied, and the revised age constraints are consistent with pre-Oligocene Antarctic glaciation. At Campbell Island, magnetostratigraphy expanded the known duration of the major unconformity between the Garden Cove and Tucker Cove formations to 61.128–50.730 Ma, allowing the earlier part of this unconformity to be correlated with a previously reported occurrence of IRD (Leckie *et al.*, 1995). The magnetostratigraphically dated AMS results from the Campbell Island sections showed significant variation in bottom current direction and intensity before and after the unconformity, implying that it was related to a change in ocean currents. At Fairfield Quarry, the minimum sedimentation rate determined for the Palaeogene sediments implies the presence of significant unconformities higher in the Abbotsford Formation. At the mid-Waipara River, the magnetostratigraphy and AMS show evidence of a sharp change in bottom-water flow at around 59 Ma, which may represent a weaker response (due to the greater palaeodistance from Antarctica) to the same marine events which led to the unconformity on Campbell Island.

The palaeomagnetic interpretation of glauconitic horizons was a vital component of this thesis. At the rock magnetic level, I established that, while glauconony weakens the overall remanent magnetization, it does not acquire a post-depositional remanence, simplifying the palaeomagnetic interpretation. At the palaeomagnetic level, I developed methodologies for palaeomagnetic work on very weakly magnetic sediments, allowing directions to be determined from

samples which until recently would probably have been classed as 'nonmagnetic'. Central to these methodologies are improved measurement protocols and the development of a software application which can determine the actual sample remanence from these measurements. At the magnetostratigraphic level, this work enabled interpretation of the glauconitic horizons within the studied sections. The six horizons in the upper Fairfield Quarry section were shown to represent a relatively short interval of time (328 kyr), demonstrating the ability of magnetostratigraphy to improve on biostratigraphic age constraints in these sections; these results also showed that, while glauconitic horizons can represent intervals of reduced sedimentation, accurate chronostratigraphy is vital for their palaeoenvironmental interpretation.

The tools and techniques I developed were successful in dating the sections at the three field areas, allowing them to be interpreted together in the wider context of regional oceanographic changes during the early Palaeogene. The stratigraphic interpretations at Campbell Island and the mid-Waipara River support at least one late Palaeocene Antarctic glaciation correlated with a known deposit of IRD (Leckie *et al.*, 1995), and two of the glauconitic horizons at Fairfield Quarry may be attributable to brief glaciations in the early Palaeocene. The fluctuations in reported oxygen isotope values during the Palaeocene (Zachos *et al.*, 2008) might thus be explained, at least in part, by changes in global ice volume due to the growth and decay of ice sheets on Antarctica. Since neither the Drake Passage nor the Tasmanian Gateway had begun to open at this time, these results would then imply that ocean gateways are not necessary for the growth of Antarctic ice sheets.

Appendix A PuffinPlot user manual

This appendix forms a practical guide to the usage of the palaeomagnetic data plotting and analysis program PuffinPlot. It complements chapter 4, which gives theoretical background and implementation details, but few detailed notes on usage. This appendix is intended to be a comprehensive stand-alone manual, requiring no prior knowledge of chapter 4 for its use; it therefore incorporates two subsections (A.2.4 and A.3.3.5) reproduced from chapter 4.

A.1 Installation

This section describes the hardware and software requirements for running PuffinPlot, and gives instructions for installing and running it.

A.1.1 *Requirements*

PuffinPlot runs on the Java platform (version 5 or later), which is preinstalled or freely available for a variety of operating systems, including Windows, Linux, and Mac OS X. Instructions for installing Java are beyond the scope of this manual; please consult the documentation for your operating system or visit http://www.java.com/ for details.

A.1.2 *Obtaining and installing PuffinPlot*

PuffinPlot is distributed in two variants. The first is suitable for all operating systems. The second has identical functionality, but is tailored for easier installation and use on Mac OS X. Mac users are advised to use the second variant, although the first will also work for them.

A.1.2.1 *All operating systems*

The latest 'universal' version of PuffinPlot may be downloaded as a file named PuffinPlot.jar from http://talvi.net/PuffinPlot.jar . This file is recommended for Linux, Windows, and other non-Mac operating systems.

Figure A.I Two versions of the PuffinPlot icon; both depict an adult specimen of the Atlantic Puffin, *Fratercula arctica*. The old PuffinPlot icon (shown at left) was modified from a downloaded photograph of unknown provenance; the new PuffinPlot icon (shown at right, and used for version 0.95 and above) was cropped from an illustration by the Finnish artist Wilhelm von Wright (1810–1887), published in *Svenska fåglar, efter naturen och på sten ritade* (2nd ed., 1929).

The details of starting PuffinPlot vary between operating systems, but double-clicking on the file PuffinPlot.jar is the most common method. In some cases it may be necessary to right-click on the file and select 'Open with Java runtime' or some similar text from a menu.

A.1.2.2 *Mac OS X*

The latest Mac OS X version of PuffinPlot may be downloaded as a file named PuffinPlot.zip from http://talvi.net/PuffinPlot.zip. This file is packaged as a standard OS X application and conforms more nearly to OS X user interface standards than the 'universal' version described in the previous section.

After downloading PuffinPlot.zip, double-click on it to automatically extract the PuffinPlot application, denoted by an icon representing a puffin (shown in figure A.I). The application may then be dragged into the Applications folder, or any other convenient place.

PuffinPlot is started by double-clicking on its application icon.

A.2 Basic usage

This section gives a brief introduction to the PuffinPlot data model and to the features of its main window.

A.2.1 *A note on keyboard shortcuts*

PuffinPlot provides a large number of keyboard shortcuts for its various capabilities; most of them involve holding down the Ctrl key while pressing another key. On Mac OS X, these shortcuts use the ⌘ key rather than the Ctrl key, in accordance with Apple user interface guidelines. Throughout this manual, keyboard shortcuts will be given as (for example) 'Ctrl-A'. Users of Mac OS X should read these shortcuts as ⌘-A, etc.

A.2.2 *Opening a file*

To open a file, select Open… from the File menu. This function will allow you to choose one or more files to open from a standard file selection window. You may also select an entire folder; in this case every file within the folder will be opened.

A.2.3 *A tour of the main window*

Figure A.II shows an annotated screenshot of PuffinPlot's main window with a discrete sample data file open. The bulk of the window is devoted to the data display itself, and shows the four most popular data display methods for palaeomagnetic data: a table, a Zijderveld plot, an equal-area projection, and a demagnetization-intensity biplot (which also shows an overlaid magnetic susceptibility plot). The plots are interactive, in that individual data points may be selected by clicking or by dragging a rectangle with the mouse.

To the left of the main plot display area is the sample chooser, which shows a complete list of the samples within the suite, with the currently selected sample highlighted. Multiple samples may be selected at once allowing functions such as PCA calculation to be performed *en masse*. If a long core data file is loaded, the sample chooser is shown as a vertical slider indicating depth rather than a list of sample names.

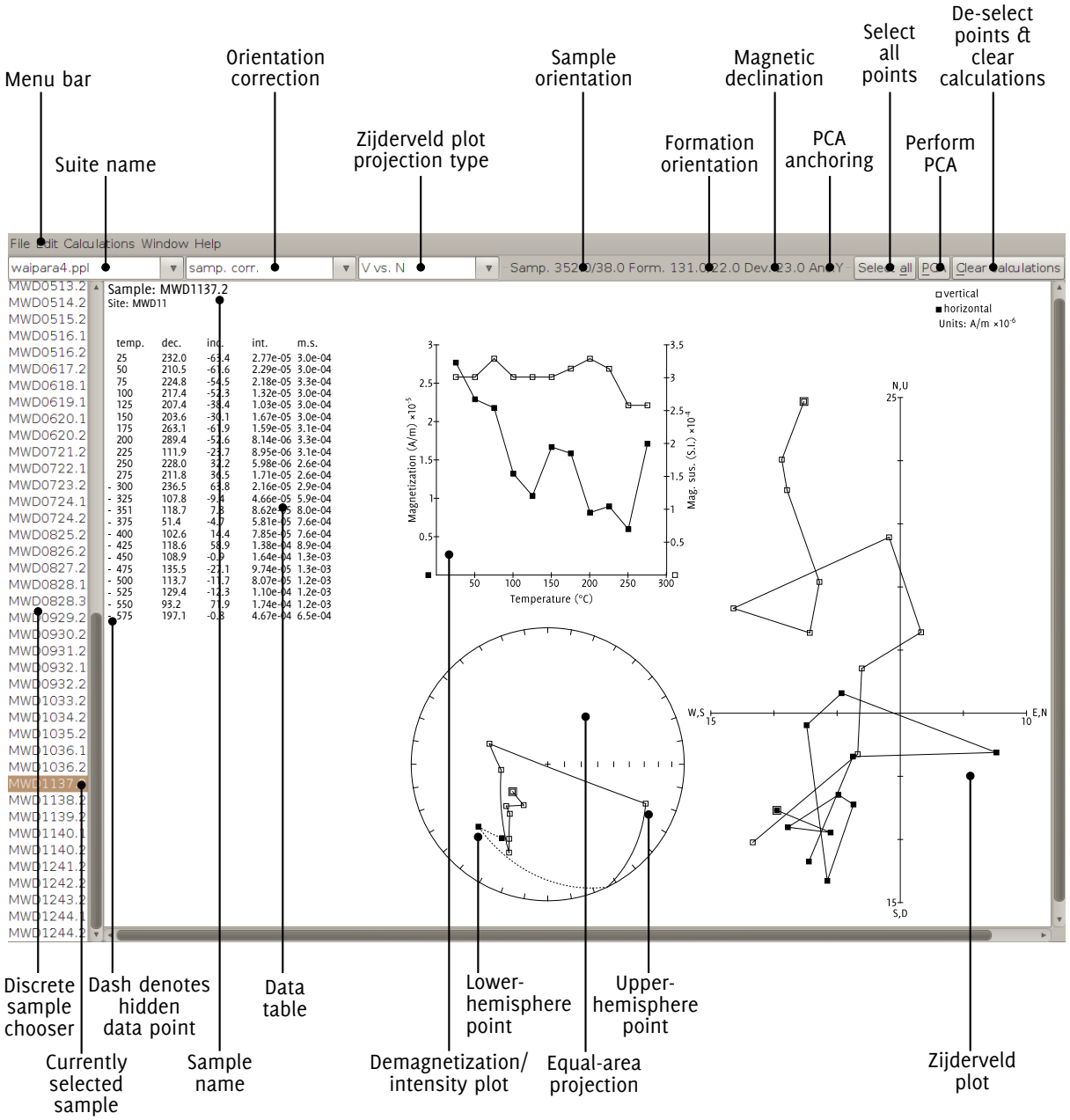

Figure A.II The main window of PuffinPlot with a discrete file loaded, showing the default data plot layout. Data plots, information displays, and controls are annotated. Note that several other data plots are available, but are not shown by default, and that the layout may be freely rearranged by the user. Data points above the 275°C demagnetization step have been hidden.

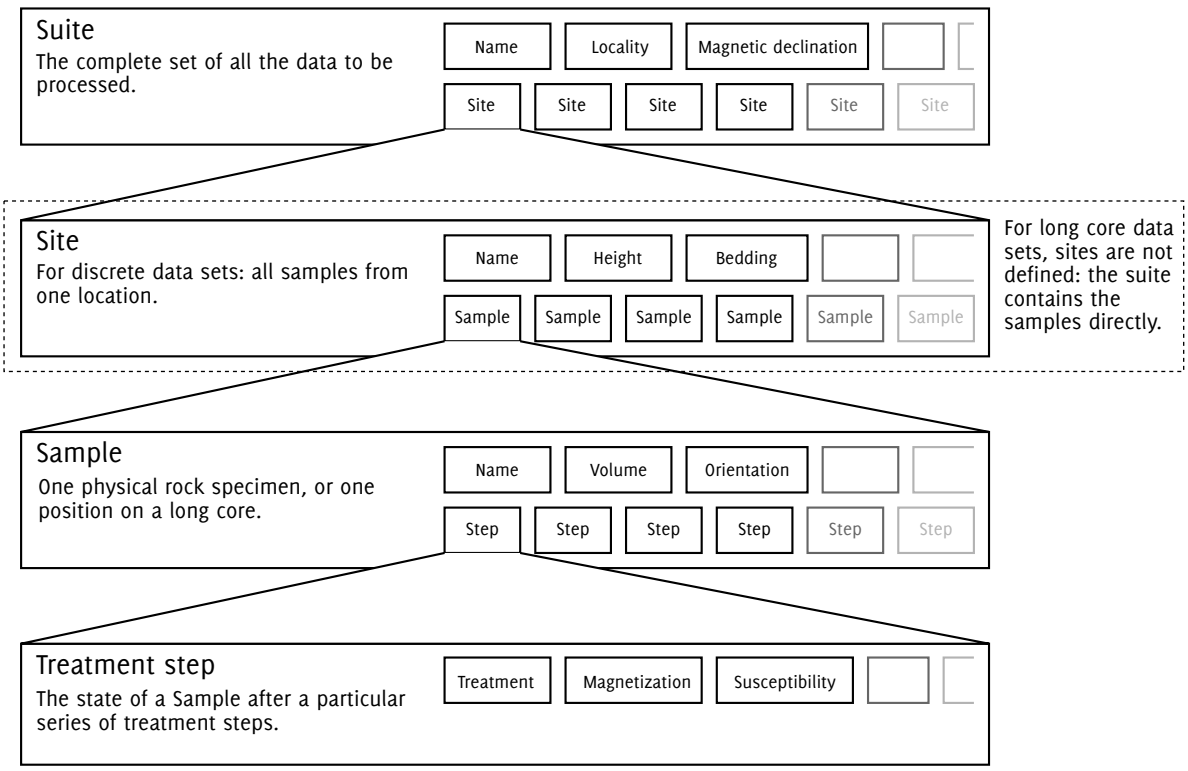

Figure A.III PuffinPlot's hierarchical data model. Each layer (except the lowest) contains multiple instances of the following layer.

Above the main plot area is the toolbar, which gives convenient access to some of the most frequently used facilities of the program. From left to right, these are: choosers for the currently displayed data suite, the orientation correction, and the Zijderveld projection type; displays of the sample and formation orientations and magnetic declination; and buttons for three of the most commonly performed actions.

At the top of the window is the menu bar, providing access to all the program's functions in a hierarchical manner. On Mac OS, the menu bar is at the top of the screen rather than the top of the window, and includes an extra menu at the left, entitled PuffinPlot.

A.2.4 *Data model*

This section is reproduced from chapter 4.

PuffinPlot uses a hierarchical data structure, with higher levels containing multiple instances of each lower level. The structure is summarized in figure A.III. At the top is the *suite*, which contains all the data to be analysed as

part of a particular study. For a discrete specimen study, this will typically correspond to a section in the field; for a long core study, it will correspond to a core. A suite is initially created by opening one or more data files from a magnetometer; it is saved as a file in PuffinPlot's own format. In a discrete study, a suite contains multiple *sites*. A site corresponds to a set of samples taken from one spot in a section. A site's associated data can include such things as bedding attitude and stratigraphic height, as well as calculated parameters such as the mean palaeomagnetic direction for all the samples at the site. For a long core study, sites are not defined: samples are contained directly within the suite.

Each site (or, for long core data, the suite) contains multiple *samples*. A sample corresponds to a small physical volume of rock. For a discrete study, this will usually be a typical palaeomagnetic 25 mm cylinder or IODP cube sample. For long cores, it is the portion of the core at a particular depth. The data associated with a sample consists of information specific to this physical unit which does not change with the application of demagnetization techniques – for example, a sample code or name (or, for long cores, a depth), the field orientation of the sample, and its volume. For discrete samples this data can also include a tensor representing anisotropy of magnetic susceptibility, which is imported separately from an AGICO kappabridge datafile and collated with the magnetization data by matching the sample names. The sample can also contain calculated parameters, such as a direction fitted by principal component analysis, or a best-fitting great circle.

Each sample contains multiple *demagnetization steps*. A *step* represents a sample at a particular point during the treatment protocol. Its associated data thus includes details of the treatment: the type (thermal, AF, IRM, etc.) and parameters (temperature, field strength, etc.). The data also includes the state of the sample itself – most importantly, the measured magnetization vector. For thermal studies, the magnetic susceptibility is usually also recorded after every heating cycle, and is also stored as part of the step.

A.2.5 *Main window features*

This section describes the parts and functions of the main PuffinPlot window, as shown in figure A.II.

A.2.5.1 *Plot area*

The plot area is the largest part of the window, and plots the data for the current sample using various plots. By default, four plots are shown: a demagnetization-intensity biplot, a Zijderveld plot, an equal-area projection, and a table of demagnetization steps. The plots can be moved and resized (see section A.3.3.2). Other plots are also available, and the preferences window can be used to control which plots are displayed (see section A.3.3.3).

A.2.5.2 *Sample chooser*

The sample chooser sits at the leftmost edge of the main window, and allows you to change the current sample (the one for which data is plotted) and the set of selected samples (most of PuffinPlot's functions operate on the currently selected samples). Often, the set of selected samples will consist only of the current sample.

The sample chooser takes two forms, depending on whether the current suite of data is for discrete samples or for a continuous long core measurement.

Using the discrete sample chooser

The discrete sample chooser shows the names of the samples in the current suite. The selected sample or samples are highlighted in a different colour. If more than one sample is selected, the first of them is displayed in the main plot area.

To select a single sample, click on its name. To select a contiguous range of samples, click at one end of the range, then hold down Shift while clicking at the other end of the range. To select multiple, non-contiguous samples, hold down Ctrl while clicking. To select all samples, press Ctrl-A.

Using the continuous sample chooser

The continuous sample chooser is a vertical grey bar representing the total length of the measured core, striped with horizontal white lines representing the individual measurements at each depth. (If there are too many measurements for all the requisite white lines to be displayed, they are omitted.) A black

triangle and line show the current depth. The selected samples are denoted with orange highlighting.

To select a single depth, click on the appropriate part of the sample chooser. To scroll rapidly through a range of samples, click and drag the mouse along the sample chooser. To select a range of samples, hold down Shift, then click, drag, and release the mouse on the chooser.

Keyboard shortcuts for sample selection

Use Ctrl-B and Ctrl-N to change the current sample. Use Ctrl-A to select all the samples in the current suite. You can also use the up and down arrow keys to change the sample.

A.2.5.3 *Toolbar*

The toolbar displays various data and provides several controls. From left to right, these are:

Suite chooser. This chooser shows the name of the current suite of data. If more than one suite of data has been opened, the suite chooser allows you to switch between them.

Orientation correction chooser. This chooser allows you to choose whether data is displayed in laboratory co-ordinates (uncorrected), in field co-ordinates, corrected for sample orientation (samp. corr.), or in tectonic co-ordinates, corrected for both sample orientation and bedding orientation (form. corr.).

Zijderveld projection type. This chooser controls the vertical projection used in the Zijderveld plot. The *y* axis always corresponds to the vertical direction; the chooser controls the *x* axis, which may correspond to North (V vs. N) or East (V vs. E). The third option, V vs. H, projects each data point separately, in the plane containing itself and the origin; this is sometimes referred to as a 'modified Zijderveld' plot.

Sample orientation (Samp). The first number is the azimuth of the sample orientation; the second is its dip. For a long core, all these values will usually be 0 and 90 respectively throughout the core.

Formation orientation (Form). The first number is the dip direction of the bedding; the second in the dip magnitude.

Magnetic declination (Dev). This is the angle between magnetic north and true north at the sampling site.

Select all selects all the points in the current sample.

PCA performs principal component analysis for the selected points of all the selected samples.

Clear calculations de-selects all the points in all the selected samples, and clears the results of any calculations done on them, such as PCA or great-circle analysis.

A.3 Detailed usage

This section gives a methodical account of PuffinPlot's features.

A.3.1 *Catalogue of functions*

This section lists all the items in PuffinPlot's menus, giving a brief description of the functionality associated with each one.

A.3.1.1 *File menu*

This menu contains functions connected with opening, closing, and saving files.

File › Open… loads one or more files of demagnetization data into PuffinPlot as a new suite. See section A.3.2.1 for details of supported filetypes.

File › Open recent file is a submenu which contains the names of the last eight files which have been opened in PuffinPlot, allowing them to be opened again with a single click.

File › Save saves the current suite as a PuffinPlot file. If the suite was opened from a PuffinPlot file or if it has been previously saved as a PuffinPlot file,

it will immediately be saved to that file. If no PuffinPlot file is associated with this suite yet, a standard 'save file' dialog box will prompt yo for a file name and location.

File › Save as... allows you to save the current suite to a different filename or location.

File › Close closes the current suite, removing it from PuffinPlot's data display.

File › Export data is a submenu allowing the export of various kinds of data to CSV files.

File › Export data › sample calculations... saves a file containing all the data associated with individual samples. Table A.I describes the fields which make up the file.

File › Export data › site calculations... saves a file containing (for suites with discrete samples) all the data associated with sites. Table A.II describes the fields which make up this file.

File › Export data › suite calculations... saves a CSV file containing only one line of data, which gives the mean inclination, mean declination, α_{95}, and k for the Fisherian mean direction calculated for the entire suite.

File › Export data › IRM data... saves files containing IRM acquisition data. It produces a folder of files, one for each sample in the suite. Each file is in tab-delimited text format, and each line within the file contains the IRM field strength and the magnetization intensity of the sample after application of that field.

File › Page Setup... opens a window allowing you to change the paper size, orientation, and margins for printing.

File › Print... opens a window allowing you to print the selected samples. Note that *only* the selected samples will be printed, so if you wish to print the whole suite use Edit › Select all first. On most systems this will also allow you to print to a PDF file; Windows users may need to install a virtual PDF printer, such as CutePDF Writer or Bullzip PDF Printer, in order to produce PDF files.

Field name	Description
Suite	Suite name
sample	Sample name
NRM intensity	NRM intensity (A/m)
MS jump temp.	For thermal demagnetization, the temperature step at which the first jump in magnetic susceptibility occurs, A jump is defined as an increase of 2.5 or more times the previous value.
Fisher inc.	Mean inclination (°)
Fisher dec.	Mean declination (°)
Fisher a95	α_{95} of mean direction (°)
Fisher k	*k*-value of mean direction
PCA inc.	Inclination of PCA direction (°)
PCA dec.	Declination of PCA direction (°)
PCA MAD1	The Maximum Angle of Deviation for the planar PCA fit; the smaller the value, the more coplanar the points.
PCA MAD3	The Maximum Angle of Deviation for the linear PCA fit; the smaller the value, the more collinear the points.
PCA anchored	'yes' if the PCA fit was anchored; 'no' if not
PCA start	Field or temperature of first demagnetization step used for PCA analysis (°C or mT)
PCA end	Field or temperature of last demagnetization step used for PCA analysis (°C or mT)
PCA contiguous	'yes' if all steps between the first and last were selected for PCA; 'no' if any were omitted
MDF half-intensity	half of the NRM
MDF demagnetization	the demagnetization level at which the NRM was reduced to half (°C or mT)
MDF midpoint reached	'yes' if magnetization intensity reached half the NRM intensity during demagnetization; 'no' otherwise
[annotations]	Any user-defined annotations are also exported as part of the sample export file. See section A.3.3.4 for details.

Table A.1 List of fields in exported sample data file, Note that, in addition to the predefined fields, any custom user annotations (see section A.3.3.4) will also be exported in this file.

Field name	Description
site	Name of site
Fisher inc.	Mean inclination of PCA directions (°)
Fisher dec.	Mean declination of PCA directions (°)
Fisher a95	α_{95} of mean PCA direction (°)
Fisher k	*k*-value of mean PCA direction
GC valid	'Y' if the great-circle fit is valid, blank otherwise. A fit is valid if it includes at least three circles, and has $\alpha_{95}<3.5$ and $k>3$.
GC inc.	Inclination of great-circle direction (°)
GC dec.	Declination of great-circle direction (°)
GC a95	α_{95} for great-circle direction (°)
GC k	*k*-value for great-circle direction
GC N	Number of great circles used in great-circle fit
GC M	Number of PCA directions used in great-circle fit
T1min	These four parameters give the ranges of demagnetization steps used to fit the circles. T1 is the first (lowest) demagnetization step in a circle path for an individual sample, and T2 the last (highest). T1min is the minimum of the T1 values across all the circles for the site, and T2 the maximum. Similarly, T2 is the last step used in a single circle, and T2min–T2max is the range of its values across all the samples at a site.
T1max	
T2min	
T2max	

Table A.II List of fields in exported site data file

File › Print Fisher... prints the contents of the separate window showing Fisher statistics of PCA directions through the suite; see Calculations › Fisher on suite in section A.3.1.3 for more details.

File › Print Great Circles... prints the contents of the separate great-circle fit window; see Calculations › Great circles in section A.3.1.3 for more details.

File › Import AMS imports AMS data from a file. The file must be in the .ASC format produced by the Safyr program distributed with AGICO kappabridges. The AMS data is assigned to the appropriate samples within the suite by matching the sample names specified in the ASC file with the sample names for the demagnetization data. If the AMS file contains data for samples not in the suite, these samples will be created and added to the suite. AMS data is not displayed by default; the equal-area plot of AMS data can be activated from the Preferences window.

File › Export SVG saves the current contents of the main data display as an SVG (Scalable Vector Graphics) file. As a vector graphics format, SVG is allows for high-quality reproduction at any size. It can also be easily edited and incorporated into other graphics using vector graphics programs such as Inkscape and Adobe Illustrator.

File › Export preferences... saves your current preferences to a file. In conjunction with the Import preferences feature, this allows you to transfer your preferences from one computer to another. It also allows you to keep multiple sets of preferences and switch between them as needed. Probably the most useful application is to save different plot layouts for different sets of data.

File › Import preferences... sets your preferences from a file saved using Export preferences. See the description of Export preferences for details.

File › Preferences... opens the preferences window. See section A.3.3.3 for details. On Mac OS X, this item is found on the PuffinPlot menu to the left of the File menu, rather than on the File menu.

File › Quit terminates PuffinPlot. On Mac OS X, this item is found on the PuffinPlot menu to the left of the File menu, rather than on the File menu.

A.3.1.2 *Edit menu*

The Edit menu provides various basic functions mainly to do with manipulation of data points.

Edit › Select all selects all the points in all the selected samples, excluding points which have been hidden (see Hide points below).

Edit › Clear selection de-selects all the points in all the selected samples.

Edit › Move plots allows you to reposition and resize the plots in the main display area. See section A.3.3.1 for details.

Edit › Reset layout resets the sizes and positions of all the plots to their default values.

Edit › Corrections… opens a window which allows you to change the sample orientation, formation orientation, and local magnetic declination for all the selected samples. Each correction type can be individually changed without affecting the values of the others.

Edit › Copy point selection takes the points which are selected for the current sample, and selects the corresponding points for all the selected samples. This functionality is useful, for example, for hiding the same points in a large number of samples without having to manually select them for each sample.

Edit › Hide points hides all the selected points in all the selected samples. They are removed from all the graphical plots (which will be rescaled to avoid unnecessary blank space), but not from the data table in the main plot window; on the data table, hidden data points are marked with a dash symbol (–) to their left. Hidden points can be restored using the

Edit › Show all points restores all hidden points in all the selected samples.

Edit › Edit custom flags… allows you to add or remove user-defined flags for the suite; see section A.3.3.4 for details.

Edit › Edit custom notes… allows you to add or remove user-defined note categories for the suite; see section A.3.3.4 for details.

Edit › Rescale mag. sus. scales all the magnetic susceptibility values for the suite by a specified factor. This feature is useful since magnetic susceptibility meters typically do not report values in standard S.I. units. Note that, unlike many PuffinPlot operations, the scaling is applied to the *entire suite*, not just the selected samples.

A.3.1.3 *Calculations menu*

The calculations menu provides facilities for calculating magnetic parameters and directions. Note that most calculations operate on all the selected samples, not just the current sample.

Calculations › PCA calculates a best-fitting line to all the selected points in all the selected samples, using principal component analysis (Kirschvink, 1980). The PCA direction is projected onto the Zijderveld plot.

Calculations › Anchor PCA is a menu item which may be toggled on or off. When it is on, PCA analyses are constrained to pass through the origin. In general, the PCA should be anchored when the analysed points are known to represent the final demagnetization component. Leaving it unanchored allows analysis of secondary components, provided that they are sufficiently well separated from other components.

Calculations › Fisher by sample calculates, for each selected sample, a Fisherian mean direction for all the selected points. This calculation can produce reasonable mean directions for origin-trending components, but principal component analysis is usually preferable.

Calculations › Fisher by site calculates a Fisherian mean direction for the PCA directions at each site.

Calculations › Fisher on suite calculates a Fisherian mean of the PCA directions for all the selected samples, and opens a new window showing an equal-area plot of the PCA directions, the mean direction, and the 95% confidence circle.

Calculations › MDF calculates the Median Destructive Field (or, for thermal demagnetization, the Median Destructive Temperature) of the selected

samples. This is the field (or temperature) at which the intensity of the sample's remanence has been reduced to half of its initial value. Once calculated, it is displayed on the demagnetization-intensity plot, and can be saved as part of the exported sample data.

Calculations › Clear calculations de-selects all the points in all the selected samples, and clears the results of any calculations done on them, such as PCA or great-circle analysis.

Calculations › Fit circle calculates and displays a best-fitting great circle for all the selected points in all the selected samples.

Calculations › Great circles calculates a best-fitting direction for all the great circles fitted at the current site, using the algorithm of McFadden and McElhinny (1988). The great-circle fit is shown both in the Great circles plot in the main window (if the plot has been activated in the preferences), and in a separate window which is opened automatically.

Calculations › Clear site calculations clears the results of any calculations associated with the selected *sites* (as opposed to samples); at present, this amounts to clearing the best-fit great-circle direction for each selected site.

Calculations › Reversal test performs a basic reversal test of *all* the currently open suites.

AMS calculations

PuffinPlot can show the results of statistical calculations on AMS tensors, giving mean directions and confidence ellipses for the principal axes by one of three methods; at present, however, these calculations cannot be performed by PuffinPlot itself. Instead, it makes use of two Python scripts from the PmagPy suite (Tauxe *et al.*, 2010), bootams.py and s_hext.py. In order to calculate AMS statistics, these scripts must first be installed on the computer running PuffinPlot, and the folder containing them must be specified in the Preferences window. The PmagPy programs may be obtained from http://earthref.org/PMagPy/.

All AMS calculations operate on the currently selected samples. Tauxe *et al.* (1998) and chapter 13 of Tauxe *et al.* (2010) give more details of tensor statistics, particularly with regard to the application of bootstrap methods.

Calculations › Calculate bootstrap AMS calculates bootstrap statistics using the bootams.py program, producing Kent error ellipses which are shown on the AMS plot in the main window.

Calculations › Parametric bootstrap AMS calculates bootstrap statistics using the bootams.py program, producing Kent error ellipses which are shown on the AMS plot. It differs from the previous function in employing a parametric bootstrap, which can provide more realistic confidence intervals for small numbers of samples on the (often reasonable) assumption that measurement uncertainties are normally distributed across the selected samples.

Calculations › Calculate Hext on AMS calculates Hext (1963) statistics using the s_hext.py program and displays the mean directions and error ellipses on the AMS plot.

Calculations › Clear AMS calculations Clears any previously done bootstrap and Hext calculations.

A.3.1.4 *Window menu*

This menu allows you to open or close two windows displaying extra data.

Window › Data table opens (or closes) a window showing all the demagnetization data for the current sample as a table. This table is far more extensive than the brief table displayed in the main window, and allows data to be selected and copied to the clipboard so that it can be pasted into a spreadsheet or text editor.

Window › Suite PCA plot opens (or closes) a window containing an equal-area plot of PCA directions; the plot is created by selecting the Calculations › Fisher on suite menu item, and may be printed using the File › Print Fisher... menu item.

A.3.1.5 *Help menu*

Help › About PuffinPlot displays some brief information about PuffinPlot, including the version. On Mac OS X, this item is also present on the PuffinPlot menu.

A.3.2 *Features*

This section presents PuffinPlot's features in moderate detail.

A.3.2.1 *Supported file types*

PuffinPlot can currently open three types of file: its own filetype (filename suffix ppl); data produced from 2G cryomagnetometers (filename suffix dat); and data from the Zplot program by Stephen Hurst (filename suffix txt). In general, support for other file formats is straighforward to add.

A.3.2.2 *Selecting points*

For most of PuffinPlot's functions, the data points of interest must be selected before anything can be done to them. You can select data points simply by clicking on them; if you click on a selected point it will be de-selected. Selected points are drawn in red to distinguish them from the black unselected points. Note that the notional data point itself is the thing being selected, not the visual representation that you click on. Thus, if you click on a point in one plot, the corresponding point in all the visible plots will also turn red, since they are visual representations of the same datum.

Since data points are relatively small, clicking accurately on them can be inconvenient. PuffinPlot offers two alternative selection methods to alleviate this problem. Firstly, by holding down the Shift key, you can select a point simply by left-clicking near it; holding Shift and right-clicking will de-select nearby points instead. Secondly, you can click, hold the button, and drag the pointer across the graph, creating a rectangle. Any point within the rectangle will be selected.

A.3.2.3 *Working with multiple samples*

Since most PuffinPlot operations are automatically applied to all the selected samples, repetitive analysis work can often be done automatically using the Copy point selection feature. For example, if you wish to apply a PCA to the 100–250°C demagnetization range of a series of 50 samples, it can be done in four quick steps:

1. For the first sample, select the points corresponding to the 100–250°C demagnetization range.

2. Select the 50 samples using the sample chooser, keeping the first sample as the current one.

3. Use Copy point selection on the Edit menu (or press Ctrl-Shift-C to select the corresponding points in all the selected samples.

4. Select PCA from the Calculations menu, or press Ctrl-R.

This procedure will immediately perform PCA on all 50 selected samples.

A.3.3 *Plot types*

This section lists and briefly describes the available plot types in PuffinPlot. Some of them are not displayed by default, but these may be activated via the preferences window (see section A.3.3.3). Note that the term 'plot' is used rather loosely in this manual to refer to any movable element displaying data within the main window. Thus, the 'plots' listed below include textual elements such as legends.

Equal-area is a Lambert azimuthal equal-area projection showing the directions of the current sample's magnetization vectors. Successive points are connected by great-circle segments. Points in the upper hemisphere are shown as unfilled (white) and connected by solid lines; points in the lower hemisphere are filled (black) and connected by dashed lines. If a great circle fit has been calculated for the sample, it is shown on this plot.

Zplot is a Zijderveld plot, overlaying an orthographic projection in the horizontal plane with an orthographic projection in a chosen vertical plane.

The vertical plane can be controlled using the chooser on the toolbar; see section A.2.5.3 for details. The horizontal projection is shown with filled points, and the vertical projection with unfilled points. If a PCA fit has been calculated for this sample, the two projections of the PCA lines are overlaid on the plot in blue. (If the V vs. H vertical projection is selected, only the horizontal projection of the PCA line is shown, since V vs. H effectively uses a different vertical projection for each point.)

Zplot key is a legend for the Zijderveld plot, showing the interpretations of the filled and unfilled points and giving the units in which the axes are calibrated.

Demag. is a plot of demagnetization step (in mT or °C) versus intensity of magnetization (in A/m), shown as a line of filled points. If magnetic susceptibility measurements have been taken, they are overlaid on the same plot as unfilled points, with the scale shown on the right of the graph.

Data table is a table in which each row represents one demagnetization step for the current sample. The columns, from left to right, give the demagnetization step, declination, inclination, intensity, and magnetic susceptibility. Selected points are denoted by an asterisk (*) to their left; hidden points are denoted by a dash (–) to their left.

PCA shows the results of PCA textually, if PCA has been carried out for the current sample; otherwise it is invisible. When visible, it shows the inclination and declination of the first principal component, which corresponds to a least-squares linear fit. It also shows the maximum angular deviation (MAD) values MAD1 and MAD3, which function as goodness-of-fit parameters (smaller is better) for planarity and collinearity respectively. Kirschvink (1980) gives more detail of the interpretation of MAD values.

Title simply shows the name of the current sample and the current site, for a discrete suite. For a continuous (long core) suite, it shows the current depth.

Fisher shows the parameters of the per-sample Fisherian analysis, if one has been carried out; otherwise it is invisible. It gives the mean inclination and declination and the α_{95} and k parameters.

AMS is a lower-hemisphere equal-area plot of AMS data, if any has been imported. Maximum, intermediate, and minimum anisotropy axes are shown as squares, triangles, and circles respectively. If AMS statistics have been calculated (see section A.3.1.3), the mean directions and confidence ellipses are also shown.

Ternary demag. is an experimental ternary plot designed to display data from triaxial IRM demagnetization experiments conducted according to the method of Lowrie (1990). The position of a point on the plot reflects the relative strengths of the three axes of magnetization, which in turn correspond to high, medium, and low coercivity components. The path produced by points at successive demagnetization steps thus shows the relative effects of thermal unblocking and alteration on these components.

Great circles shows all the great circles fitted at the current sample's site, along with a best-fit direction calculated by the method of McFadden and McElhinny (1988).

Formation mean shows all the site means for the suite, and a Fisherian mean and 95% confidence interval for them. If two polarities are present in the suite, two means are calculated and shown.

NRM Histogram shows a histogram of NRM intensities across the whole suite.

A.3.3.1 *Arranging the plots*

PuffinPlot allows the plots to be freely rearranged and resized within the display area; they can also be switched on and off as required (see section A.3.3.3). To arrange the plots, select Move plots from the Edit menu. A tick appears next to the menu item, and the plots are overlaid by pale orange rectangles, allowing you to manipulate them. Each plot is also annotated with its name, which helps to identify plots that are not currently displaying any data (e.g. the 'PCA directions' display if no PCA has been performed. To resize a plot, click on an edge or corner of its rectangle and drag it to the desired size. To move a plot, click in its central area and drag it to the desired location. Plots may be overlapped freely. When manipulating overlapping plots, mouse clicks only affect the smallest plot in the 'pile'.

Once the plots are arranged to your satisfaction, click Move plots on the Edit menu again to untick the menu item and resume normal operation.

A.3.3.2 *Changing the layout*

You can change the size and arrangement of the plots in the main window by choosing Move plots from the Edit menu. This action puts PuffinPlot temporarily into a special mode where plots become moveable: a tick appears next to the Move plots menu item, and the plots themselves are overlaid by translucent coloured rectangles. The name of the plot is also displayed at the top left corner of each rectangle; this can be useful for identifying plots which are currently invisible – for example, the table of PCA values if no PCA has been performed.

In Move plots mode, you can resize a plot by clicking and dragging on one of the darker-coloured edges or corners of the plot. You can move the whole plot by clicking and dragging in its more lightly coloured central zone. Plots can overlap one another freely. When you click in an area where two or more plots overlap, the smallest plot is treated as the 'topmost', and this is the one which will be moved or resized.

A.3.3.3 *The preferences window*

The preferences window is divided into three tabs.

The Loading tab

This tab contains options connected with reading data from .DAT files produced by the 2G 'Long Core' software.

SQUID sensor lengths. When reading a 2G file, PuffinPlot uses the 'X corr', 'Y corr', and 'Z corr' fields to determine the magnetization vector. However, for long core measurements, these values are not corrected for effective sensor length, which is determined by the response function of each SQUID and must be determined empirically when setting up the machine. To produce an accurate magnetization vector for long core files, PuffinPlot corrects the SQUID readings for the configured sensor lengths when opening the file.

Protocol gives the measurement protocol used in taking the readings. A protocol is a particular sequence of empty tray measurements and sample measurements in defined orientations, undertaken for each set of measured samples. The tray and sample measurements are combined by PuffinPlot as it reads the file, providing a more accurate, corrected moment measurement for each sample. (Magnetic susceptibility measurements, if present, are also automatically associated with the preceding magnetic moment measurement or measurements.) Table A.III describes the available protocols.

The Plots tab

This tab shows a list of plots which PuffinPlot can display. You can control which plots are shown by ticking the boxes next to the plot names. The plot types are detailed in section A.3.3.

The Misc. tab

Demag y axis allows to you customize the text which labels the *y* axis of the demagnetization-intensity plot.

PmagPy folder sets the location of the PmagPy programs. If you wish to do calculations of AMS statistics within PuffinPlot, it is necessary to have the PmagPy programs bootams.py and s_hext.py installed (see section A.3.1.3 for details). This box allows you to specify to PuffinPlot the folder in which the programs are installed.

Font allows you to change the font used in the plots: enter a font family name into the box. PuffinPlot must be restarted for the change to take effect. If the specified font cannot be found, a default fallback font is used.

A.3.3.4 *Annotations*

Annotations are a feature allowing short, categorized notes to be added to each sample in a suite. The categories can be freely chosen. Annotations come in two varieties, *custom flags* and *custom notes*. Custom flags embody a true/false

Protocol	Description
NORMAL	No extra tray or sample measurements are made. Each measurement run consists simply of measuring the samples once in their normal orientation.
TRAY_NORMAL	Before each sample-measurement run, an empty tray measurement run is made. The input file thus consists alternately of empty-tray lines and sample-measurement lines. Each tray measurement is used to correct the subsequent sample measurement.
NORMAL_TRAY	As TRAY_NORMAL, but the tray measurement is made after the sample measurement rather than before it.
TRAY_NORMAL_YFLIP	As TRAY_NORMAL, but adding an extra sample measurement as a third step. In the extra measurement, the sample is rotated 180° around its y axis, so that the x and z measurements are inverted. Combining these readings improves not only the precision but also the accuracy of the magnetic moments measured on the x and z axes, since any systematic bias should be cancelled out by the inversion. For the y axis, accuracy is not affected but precision is improved by averaging the two measurements.
TRAY_FIRST	This is the simplest tray correction: the tray is measured once at the start, and all subseuent measurements are sample measurements. PuffinPlot corrects each sample measurement using the initial tray measurement.
TRAY_NORMAL_IGNORE	This option reads a file measured using the TRAY_NORMAL protocol, but (like TRAY_FIRST) makes all sample corrections using the initial tray measurement, and ignores all subsequent tray measurements. The main intended use for this option is to allow direct comparison between the TRAY_FIRST and TRAY_NORMAL protocols, to avoid the extra work of using the TRAY_NORMAL protocol on sample suites for which it is unnecessary.

Table A.III A catalogue of measurement protocols for 2G data files.

value and are intended for when a sample fulfils some criterion – for example, 'messy', 'low-temperature alteration', or 'multiple components'. Custom notes are intended for adding short items of information which are not automatically inferred by PuffinPlot – for example, 'number of components' or 'behaviour type'.

Adding annotation categories

Annotations categories are defined by selecting the Edit custom flags… or Edit custom notes… item from the Edit menu. A window will appear allowing you to add, rearrange, or remove the annotation categories. If an annotation category is removed, all annotations made within that category will be lost.

Using annotations

When custom flags or notes have been defined, an extra panel appears at the right-hand side of the main window. For each custom note category there is a text box into which text may be typed. For each custom flag category there is a tick box which may be selected or de-selected.

Annotations are saved with the rest of the data in the PuffinPlot file; they are also exported in the sample data CSV file produced by the File › Export data › Export sample calculations menu item.

A.3.3.5 *Scripting*

This section is reproduced from chapter 4.

PuffinPlot's graphical desktop interface is intended to be the primary way to interact with the program. However, it is often useful to be able to interact with a program using a scripting language, in order to extend its capabilities, integrate it conveniently with other programs, or process large amounts of data without manual intervention. The Java platform upon which PuffinPlot is built supports a number of scripting languages which can easily interface with PuffinPlot. Perhaps most usefully, an implementation of the Python programming language – named Jython (Juneau *et al.*, 2009) – has been developed for the Java platform. Since Python is widely used in scientific programming and

scripting, and familiar to a large number of scientists, this should provide a convenient route for anyone wishing to integrate PuffinPlot with other data processing steps. Using Jython, PuffinPlot can be controlled either from a pre-written script, or interactively from a command shell which accepts and executes commands one at a time from the user.

Currently, the main barrier to controlling PuffinPlot from another program or from an interactive shell is that its internal structure is very poorly documented; for many parts, the source code itself constitutes the only documentation. However, the source code is cleanly written and clearly laid out, so careful perusal of it should provide enough understanding to interface with most of PuffinPlot's facilities.

Figure A.IV shows a very simple script demonstrating the use of PuffinPlot from within a Python environment. The script opens a data file, calculates the mean NRM, and produces a file containing a PCA direction for each sample. Note that virtually all of PuffinPlot's data and functionality is available to the Python script, so far more complex examples are possible.

```
### Import the required libraries.
from net.talvi.puffinplot import PuffinApp
from net.talvi.puffinplot.data import Suite
from java.io import File

### Start PuffinPlot and open a data file.
puffin = PuffinApp()
input_file = File("example.ppl")
suite = Suite([input_file])
samples = suite.getSamples()

### Calculate and display the mean NRM.
total_nrm = sum([sample.getNRM() for sample in samples])
print total_nrm / suite.getNumSamples()

### Perform a PCA calculation for each sample.
for sample in samples:          # do this for each sample:
    sample.selectAll()          # select all points in the sample
    sample.useSelectionForPca() # and mark them for use in PCA
suite.doSampleCalculations()    # perform PCA for each sample

### Save the results of the PCA calculation.
output_file = File("example-results.csv")
suite.saveCalcsSample(output_file)
```

Figure A.IV A simple Python script to demonstrate the use of PuffinPlot from a scripting environment. This script first opens a data file. It then calculates the mean NRM of all the samples and displays it. Then it calculates a PCA direction for each sample in the suite, and saves the results to a CSV file. Explanatory comments in the script are preceded by the character #. This figure is reproduced from figure 4.III.

Appendix B Definitions

B.1 Magnetic parameters

Symbol	Unit	Term	Definition	Reference
H_c	T	Coercive force	the reverse field which reduces the magnetization of a saturated sample to zero (during continued application of the field)	O'Reilly (1984), p. 56
H_{cr}	T	coercivity of remanence	the reverse field which reduces the *remanent* magnetization of a saturated sample to zero (after removal of the field)	O'Reilly (1984), p. 56
H'_{cr}	T	remanent acquisition coercive force	the field which magnetizes a sample to one half of its saturation magnetization	Dankers (1981), p. 448
M_{rs}, SIRM	A/m	Saturation Isothermal Remanent Magnetization	The remanence of a sample after removal of a saturating field	O'Reilly (1984), p. 56
MDF	T	Median Destructive Field	the alternating field necessary to reduce the remanent intensity by one half.	Opdyke and MacDonald (1973), p. 40

Table B.1 Magnetic parameters

B.2 Abbreviations

Abbreviation	Meaning
ACC	Antarctic Circumpolar Current
AF	Alternating-field
AMS	Anisotropy of Magnetic Susceptibility
ARM	Anhysteretic Remanent Magnetization
CLG	Cumulative Log-Gaussian
CRM	Chemical Remanent Magnetization
DRM	Depositional Remanent Magnetization
EDS	Energy Dispersive X-ray Spectroscopy
EPMA	Electron Probe Microanalysis
GAD	Geocentric Axial Dipole
GPTS	Geomagnetic Polarity Timescale
GRM	Gyromagnetic Remanent Magnetization
IRD	Ice-Rafted Debris
IRM	Isothermal Remanent Magnetization
MAD	Maximum Angular Deviation
MD	Multi-Domain
NRM	Natural Remanent Magnetization
OPRF	Otago Palaeomagnetic Research Facility
PCA	Principal Component Analysis
PDRM	Post-Depositional Remanent Magnetization
PSD	Pseudo-Single Domain
SD	Single Domain
SIRM	Saturation Isothermal Remanent Magnetization
SQUID	Superconducting Quantum Interference Device
SSD	Stable Single Domain

Table B.IIa Abbreviations

Abbreviation	Meaning
TDMS	Temperature Dependence of Magnetic Susceptibility
TVRM	Thermo-Viscous Remanent Magnetization
VGP	Virtual Geomagnetic Pole
VRM	Viscous Remanent Magnetization
XRD	X-Ray Diffraction

Table B.IIb Abbreviations

Appendix C Details of equipment and software used

> It is worth remembering that although the capability of analytical equipment has never been greater, never has it been so easy to produce bad data at such high speed and with so little effort.
>
> – James V. P. Long (1995)

In this appendix, to avoid duplication of material, I detail the equipment and software used for the rock magnetic study and three palaeomagnetic studies described in the body of the thesis.

Field equipment

I drilled cores using either an electric hand drill (modified Makita) or a small petrol drill (modified chainsaw). Both drills used diamond-tipped 25 mm bits, cooled and lubricated with water from a pressurised tank. I oriented the cores using a Pomeroy orienting fixture fitted with a Brunton compass and transported them to the laboratory in mu-metal shields.

Laboratory equipment

I cut specimens from rock cores using a circular saw with diamond-edged copper blades. Specimens were stored in the magnetically shielded room (ambient field <150 nT) at the oprf, which also houses the cryomagnetometer and demagnetizing oven.

Several of the studies involved heavily jointed or friable specimens. I reassembled these using cyanoacrylate, uhu glue, or uhu contact cement. While nonmagnetic, these glues have limited thermal stability (usually 100–200°C) so for higher heating steps samples were reglued between every step. I also experimented with the use of Ceramabond 571-l adhesive, manufactured by Aremco of New York; although it was entirely heatproof within the required range, it carried too high a magnetic remanence to be useful with weakly magnetized samples. To cement powder samples into cubes for the rock magnetic experiments of chapter 3, I used Grade N sodium silicate solution supplied by Clark Products of Napier.

I took magnetic remanence measurements using a 2G Enterprises cryogenic magnetometer with three Applied Physics Model 581 SQUID units. The magnetometer assembly also includes a 2G600 triaxial sample degaussing system and a 2G model 615 ARM magnetizer.

Thermal treatment was applied in a model TD-48SC thermal specimen demagnetizer manufactured by ASC Scientific. Thermally-induced alteration was monitored using a Bartington MS2 magnetic susceptibility meter with a 47 mm loop sensor fitted to the magnetometer track.

Isothermal remanent magnetizations were imparted with an ASC Scientific IM-10 impulse magnetizer.

For accurate measurements of bulk magnetic susceptibility, and for measurement of the anisotropy of magnetic susceptibility, I used an AGICO MFK-1A kappabridge operating at 976 Hz. For measurements of the temperature dependence of magnetic susceptibility, I used the same kappabridge fitted with a CS-3 furnace apparatus. All heating was carried out in an argon atmosphere of 99.999% purity with a flow rate of approximately 100 ml per minute.

Optical microscopy was undertaken on an Olympus BX-41 polarizing microscope equipped with a reflected-light illuminator and a Zeiss AxioCam MRc digital camera.

Electron microscopy and microprobe analysis were performed using the JEOL JXA-8600 electron microprobe analyser at the University of Otago Geology department.

Software

I made palaeomagnetic analyses and plots using the PuffinPlot package described in chapter 4 and appendix A. More specialized plots, such as the rock magnetic plots in chapter 3, were made with custom scripts written in Python (Beazley, 2009) using the matplotlib graphing library (Tosi, 2009). I analysed IRM data using version 2.2 of the Irmunmix program by Heslop *et al.* (2002). I produced graphical section logs with custom Python scripts making use of the Cairo graphical library, and with the Inkscape vector drawing program (Bah, 2011).

Appendix D Data

A CD-ROM containing the data from this thesis, along with a copy of the Puffin-Plot program, is included inside the back cover. The contents are listed in table D.I.

Folder	Contents
kappabridge	Data obtained from kappabridge
kappabridge/ams	AMS data
kappabridge/tdms	TDMS data
magnetometer	Data obtained from cryomagnetometer
magnetometer/campbell	Campbell Island palaeomagnetic data
magnetometer/fairfield	Fairfield Quarry palaeomagnetic data
magnetometer/waipara	Mid-Waipara River palaeomagnetic data
magnetometer/rock-mag	Magnetometer data from rock magnetism study (chapter 3)
puffinplot-files	Palaeomagnetic data in PuffinPlot format
puffinplot-files/campbell	PuffinPlot files for Campbell Island
puffinplot-files/fairfield	PuffinPlot files for Fairfield Quarry
puffinplot-files/waipara	PuffinPlot files for Mid-Waipara River
optical-micrographs	Optical micrographs of slides analysed in chapter 3
electron-micrographs	Electron micrographs of slides analysed in chapter 3
probe-analyses	Microprobe data from slides analysed in chapter 3
software	The PuffinPlot application described in chapter 4
software/puffinplot-packaged	The packaged, executable PuffinPlot software
software/puffinplot-source	The complete Java source code for PuffinPlot

Table D.1 Contents of data CD-ROM

Appendix E Access to thesis materials

All the samples used for this thesis are stored in the field-free room at the Otago Palaeomagnetic Research Facility at the Geology Department of Otago University. The collection includes both the fully demagnetized samples and additional oriented core samples suitable for further palaeomagnetic study. (Note that the demagnetized samples are unlikely to be of use for any future studies, since the heat treatment caused major mineralogical changes as well as demagnetizing the samples.) In addition to the oriented core samples, the collection includes bagged, unoriented offcuts from the cores, suitable for non-palaeomagnetic analysis. The collection also includes the samples used for the rock magnetic investigations of chapter 3.

For access to the thesis materials, please contact the OPRF manager or the Geology Department curator.

References

> 'But, Sir, is it not somewhat singular that you should happen to have Cocker's Arithmetick about you on your journey? What made you buy such a book at Inverness?' He gave me a very sufficient answer. 'Why, Sir, if you are to have but one book with you upon a journey, let it be a book of science. When you have read through a book of entertainment, you know it, and it can do no more for you; but a book of science is inexhaustible.'
>
> – James Boswell, *Life of Johnson*, vol. 5 (Boswell, 1791)

Abreu, V. S. and Anderson, J. B. (1998). Glacial eustasy during the Cenozoic; sequence stratigraphic implications. *AAPG Bulletin, 82*(7), 1385–1400.

Abreu, V. S., Hardenbol, J., Haddad, G. A., Baum, G. R. and Droxler, A. W. et al. (1998). Oxygen isotope synthesis: a Cretaceous ice-house? In de Graciansky, P.-C., Hardenbol, J., Jacquin, T. and Vail, P. R., editors, *Mesozoic and Cenozoic sequence stratigraphy of European basins*, number 60 in SEPM Special Publications, pages 75–80. SEPM (Society for Sedimentary Geology).

Acton, G. (2011). *ZPLOTIT Software Users' Guide, version 2011-01*. http://paleomag.ucdavis.edu/software-Zplotit.html. Retrieved 1 February 2011.

Alvarez, L. W., Alvarez, W., Asaro, F. and Michel, H. V. (1980). Extraterrestrial cause for the Cretaceous-Tertiary extinction. *Science, 208*(4448), 1095–1108.

Amorosi, A. (1993). Use of glauconies for stratigraphic correlation: review and case histories. *Giornale di Geologia, 55*(1), 117–137.

Amorosi, A. (1995). Glaucony and sequence stratigraphy: a conceptual framework of distribution in siliciclastic sequences. *Journal of Sedimentary Research, 65*(4 b), 419–425.

Amorosi, A. (1997). Detecting compositional, spatial, and temporal attributes of glaucony: a tool for provenance research. *Sedimentary Geology, 109*(1-2), 135–153.

Amorosi, A., Sammartino, I. and Tateo, F. (2007). Evolution patterns of glaucony maturity: A mineralogical and geochemical approach. *Deep Sea Research Part II: Topical Studies in Oceanography, 54*(11-13), 1364–1374.

Andrew, B. (2010). Sedimentary facies and unconformity analysis of some Paleocene-Eocene sections, Marlborough and Campbell Island, New Zealand. Master's thesis, Waikato, New Zealand: University of Waikato.

Arnold, K., Gosling, J. and Holmes, D. (2005). *The Java™ Programming Language*. 4th edition. Prentice Hall.

As, J. A. and Zijderveld, J. D. A. (1958). Magnetic cleaning of rocks in palaeomagnetic research. *Geophysical Journal of the Royal Astronomical Society, 1*(4), 308–319.

Babbage, C. (1864). *Passages from the Life of a Philosopher*. London: Longman, Green, Longman, Roberts, & Green.

Backus, J. W., Beeber, R. J., Best, S., Goldberg, R. and Haibt, L. M. et al. (1957). The FORTRAN automatic coding system. In *Papers presented at the February 26-28, 1957, Western Joint Computer Conference: Techniques for reliability* IRE-AIEE-ACM '57 (Western), pages 188–198. New York, NY, USA.

Bah, T. (2011). *Inkscape: Guide to a Vector Drawing Program*. 4th edition. Upper Saddle River, New Jersey: Prentice Hall.

Bailey, A. M. and Sorensen, J. H. (1962). *Subantarctic Campbell Island*, volume 10 of *Proceedings*. Denver: Denver Museum of Natural History.

Ballance, P. F. (1993a). The paleo-Pacific, post-subduction, passive margin thermal relaxation sequence (Late Cretaceous–Paleogene) of the drifting New Zealand continent. In Ballance, P. F., editor, *South Pacific Sedimentary Basins*, number 2 in Sedimentary Basins of the World, pages 93–110. Amsterdam: Elsevier.

Banerjee, S. K. (1991). Magnetic properties of Fe-Ti oxides. In Lindsley, D. H., editor, *Oxide Minerals: Petrologic and Magnetic Significance*, number 25 in Reviews in Mineralogy, pages 107–128. Washington, D. C.: Mineralogical Society of America.

Barker, P. F., Filippelli, G. M., Florindo, F., Martin, E. E. and Scher, H. D. (2007). Onset and role of the Antarctic Circumpolar Current. *Deep Sea Research Part II: Topical Studies in Oceanography, 54*(21-22), 2388–2398.

Barker, P. F. and Thomas, E. (2004). Origin, signature and palaeoclimatic influence of the Antarctic Circumpolar Current. *Earth-Science Reviews, 66*(1-2), 143–162.

Beazley, D. M. (2009). *Python Essential Reference*. 4th edition. Boston: Addison-Wesley.

Beggs, J. M. (1976). Sedimentary and metamorphic geology of Campbell Island, southwest Pacific Ocean. PGDipSci Thesis, Dunedin, New Zealand: University of Otago.

Beggs, J. M. (1978). Geology of the metamorphic basement and Late Cretaceous to Oligocene sedimentary sequence of Campbell Island, southwest Pacific Ocean. *Journal of the Royal Society of New Zealand, 8*, 161–177.

Benson, W. N. (1968). *Dunedin District 1:50,000*, volume 1 of *N.Z. Geological Survey Miscellaneous Map Series*. Wellington, New Zealand: Department of Scientific and Industrial Research.

Bentor, Y. K. and Kastner, M. (1965). Notes on the mineralogy and origin of glauconite. *Journal of Sedimentary Research, 35*(1), 155–166.

Berner, R. A. (1970). Sedimentary pyrite formation. *American Journal of Science, 268*(1), 1–23.

Berner, R. A. (1972). Sulfate reduction, pyrite formation, and the oceanic sulfur budget. In Dyrssen, D. and Jagner, D., editors, *The Changing Chemistry of the Oceans: Nobel Symposium 20*, pages 347–361.

Berner, R. A. (1984). Sedimentary pyrite formation: An update. *Geochimica et Cosmochimica Acta, 48*(4), 605–615.

Bice, K. L., Birgel, D., Meyers, P. A., Dahl, K. A. and Hinrichs, K.-U. et al. (2006). A multiple proxy and model study of Cretaceous upper ocean temperatures and atmospheric CO_2 concentrations. *Paleoceanography, 21*(2), PA2002.

Bina, M., Corpel, J., Daly, L. and Debeglia, N. (1991). Transformation de la pyrrhotite en magnetite sous l'effet de la temperature: une source potentielle d'anomalies magnétiques. *Comptes Rendus de l'Académie des Sciences, Paris, 313(II)*, 487–494.

Bingham, C. (1974). An antipodally symmetric distribution on the sphere. *The Annals of Statistics, 2*(6), 1201–1225.

Bogue, S. W., Gromme, S. and Hillhouse, J. W. (1995). Paleomagnetism, magnetic anisotropy, and mid-Cretaceous paleolatitude of the Duke Island (Alaska) ultramafic complex. *Tectonics, 14*(5), 1133–1152.

Bornemann, A., Norris, R. D., Friedrich, O., Beckmann, B. and Schouten, S. et al. (2008). Isotopic evidence for glaciation during the Cretaceous Supergreenhouse. *Science, 319*(5860), 189–192.

Borradaile, G. J., Fralick, P. W. and Lagroix, F. (1999). Acquisition of anhysteretic remanence and tensor subtraction from AMS isolates true palaeocurrent grain alignments. In Tarling, D. H. and Turner, P., editors, *Palaeomagnetism and diagenesis in sediments*, number 151 in Geological Society Special Publications, pages 139–145. London: Geological Society.

Borradaile, G. J. and Jackson, M. (2004). Anisotropy of magnetic susceptibility (AMS): magnetic petrofabrics of deformed rocks. In Martín-Hernández, F., Lüneburg, C. M., Aubourg, C. and Jackson, M., editors, *Magnetic Fabric: Methods and Applications*, number 238 in Special publications, pages 299–360. London: Geological Society.

Boswell, J. (1791). *The Life of Samuel Johnson, LL.D.* London: Charles Dilly.

Brennan, W. J. (1993). Origin and modification of magnetic fabric in fine-grained detrital sediment by depositional and post-depositional processes. In Aïssaoui, D. M., McNeill, D. F. and Hurley, N. F., editors, *Applications of Paleomagnetism to Sedimentary Geology*, number 49 in Special Publications, pages 17–27. SEPM.

Breza, J. and Wise, S. W. (1992). Lower Oligocene ice-rafted debris on the Kerguelen Plateau: Evidence for East Antarctic continental glaciation. In *Proceedings of the Ocean Drilling Program, Scientific Results*, pages 161–178.

Brooks, R. R., Hoek, P. L. and Reeves, R. D. (1986). Geochemical delineation of the Cretaceous/Tertiary boundary in some New Zealand rock sequences. *New Zealand Journal of Geology and Geophysics, 29*(1), 1–8.

Browne, G. H. and Field, B. D. (1985). *The lithostratigraphy of Late Cretaceous to Early Pleistocene rocks of Northern Canterbury, New Zealand*, volume 6 of *New Zealand Geological Survey Record*. New Zealand: Department of Scientific and Industrial Research.

Brynjólfsson, A. (1957). Studies of remanent magnetism and viscous magnetism in the basalts of Iceland. *Advances in Physics, 6*(23), 247–254.

Bucha, V. (1963). Verification of applicability of rocks in palaeomagnetism. *Studia Geophysica et Geodaetica, 7*(2), 183–191.

Buchanan, J. (1884). Campbell Island and its flora. *Transactions of the New Zealand Institute, 16*, 398–400.

Butler, R. F. (1992). *Paleomagnetism: Magnetic Domains to Geologic Terranes*. Oxford: Blackwell Scientific.

Campbell, A. S., Schwertmann, U. and Campbell, P. A. (1997). Formation of cubic phases on heating ferrihydrite. *Clay Minerals, 32*(4), 615–622.

Cande, S. C. and Kent, D. V. (1995). Revised calibration of the geomagnetic polarity timescale for the Late Cretaceous and Cenozoic. *Journal of Geophysical Research, 100*(B4), 6093–6095.

Canfield, D. E. and Berner, R. A. (1987). Dissolution and pyritization of magnetite in anoxic marine sediments. *Geochimica et Cosmochimica Acta, 51*(3), 645–659.

Cañón-Tapia, E. (1994). Anisotropy of magnetic susceptibility parameters: Guidelines for their rational selection. *Pure and Applied Geophysics, 142*(2), 365–382.

Carter, L., Carter, R. M. and McCave, I. N. (2004). Evolution of the sedimentary system beneath the deep Pacific inflow off eastern New Zealand. *Marine Geology, 205*, 9–27.

Carter, R. M. (1988a). Plate boundary tectonics, global sea-level changes and the development of the eastern South Island continental margin, New Zealand, Southwest Pacific. *Marine and Petroleum Geology, 5*(2), 90–107.

Carter, R. M. (1988b). Post-breakup stratigraphy (Kaikoura Synthem: Cretaceous-Cenozoic) of the continental margin off southeastern New Zealand. *New Zealand Journal of Geology and Geophysics, 31*(4), 405–429.

Carter, R. M., Carter, L. and McCave, I. N. (1996). Current controlled sediment deposition from the shelf to the deep ocean: the cenozoic evolution of circulation through the SW Pacific gateway. *Geologische Rundschau, 85*(3), 438–451.

Carter, R. M. and Landis, C. A. (1972). Correlative Oligocene unconformities in southern Australasia. *Nature Physical Science, 237*(70), 12–13.

Channell, J. E. T. (1982). Palaeomagnetic stratigraphy as a correlation technique. In Odin, G. S., editor, *Numerical Dating in Stratigraphy, part 1*, pages 81–103. New York: Wiley.

Chapman, F. R. (1890). The outlying islands south of New Zealand. *Transactions of the New Zealand Institute, 23*.

Cisowski, S. (1981). Interacting vs. non-interacting single domain behavior in natural and synthetic samples. *Physics of The Earth and Planetary Interiors, 26*(1-2), 56–62.

Clark, D. A. (1984). Hysteresis properties of sized dispersed monoclinic pyrrhotite grains. *Geophysical Research Letters, 11*(3), 173–176.

Cogné, J. P. (2003). PaleoMac: A Macintosh™ application for treating paleomagnetic data and making plate reconstructions. *Geochemistry, Geophysics, Geosystems, 4*(1), 1007.

Collinson, D. W. (1965). Origin of remanent magnetization and initial susceptibility of certain red sandstones. *Geophysical Journal of the Royal Astronomical Society, 9*(2-3), 203–217.

Collinson, D. W. (1977). Experiments relating to the measurement of inhomogeneous remanent magnetism in rock samples. *Geophysical Journal of the Royal Astronomical Society, 48*(2), 271–275.

Collinson, D. W., Creer, K. M. and Runcorn, S. K., editors (1967). *Methods in Palaeomagnetism*, Number 3 in Developments in Solid Earth Geophysics. Amsterdam: Elsevier.

Constable, C. and Tauxe, L. (1990). The bootstrap for magnetic susceptibility tensors. *Journal of Geophysical Research, 95*(B6), 8383–8395.

Cook, R. A., Sutherland, R., Zhu, H. and others (1999). *Cretaceous-Cenozoic geology and petroleum systems of the Great South Basin, New Zealand*, volume 20 of *Institute of Geological and Nuclear Sciences monograph*. Lower Hutt, New Zealand: Institute of Geological & Nuclear Sciences.

Cooper, R. A., editor (2004). *The New Zealand Geological Timescale*, Number 22 in Monographs. Lower Hutt, New Zealand: Institute of Geological and Nuclear Sciences.

Cox, A. and Doell, R. R. (1960). Review of paleomagnetism. *Geological Society of America Bulletin, 71*(6), 645–768.

Creer, K. M. (1959). A. C. demagnetization of unstable Triassic Keuper marls from S. W. England. *Geophysical Journal of the Royal Astronomical Society, 2*(4), 261–275.

Creer, K. M., Irving, E. and Runcorn, S. K. (1954). The direction of the geomagnetic field in remote epochs in Great Britain. *Journal of Geomagnetism and Geoelectricity*, pp. 163–168.

Dagg, R. (2010). The greensand at the Marshall Paraconformity. Master's thesis, Dunedin, New Zealand: University of Otago.

Daniel, I. L. (1961). The Wangaloan strata in the Brighton-Abbotsford area. Master's thesis, Dunedin, New Zealand: University of Otago.

Dankers, P. (1981). Relationship between median destructive field and remanent coercive forces for dispersed natural magnetite, titanomagnetite and hematite. *Geophysical Journal of the Royal Astronomical Society, 64*(2), 447–461.

Dankers, P. H. M. and Zijderveld, J. D. A. (1981). Alternating field demagnetization of rocks, and the problem of gyromagnetic remanence. *Earth and Planetary Science Letters, 53*, 89–92.

Davis, K. E. (1981). Magnetite rods in plagioclase as the primary carrier of stable NRM in ocean floor gabbros. *Earth and Planetary Science Letters, 55*(1), 190–198.

de Wall, H. and Nano, L. (2004). The use of field dependence of magnetic susceptibility for monitoring variations in titanomagnetite composition – a case study on basanites from the Vogelsberg 1996 drillhole, Germany. *Studia Geophysica et Geodaetica, 48*(4), 767–776.

Deaver, B. S. and Goree, W. S. (1967). Some techniques for sensitive magnetic measurements using superconducting circuits and magnetic shields. *The Review of Scientific Instruments, 38*(3), 311–318.

DeConto, R. M. and Pollard, D. (2003a). A coupled climate–ice sheet modeling approach to the Early Cenozoic history of the Antarctic ice sheet. *Palaeogeography, Palaeoclimatology, Palaeoecology, 198*, 39–52.

DeConto, R. M. and Pollard, D. (2003b). Rapid Cenozoic glaciation of Antarctica induced by declining atmospheric CO_2. *Nature, 241*, 245–249.

Dekkers, M. (1988). Magnetic properties of natural pyrrhotite part I: Behaviour of initial susceptibility and saturation-magnetization-related rock-magnetic parameters in a grain-size dependent framework. *Physics of the Earth and Planetary Interiors, 52*(3-4), 376–393.

Dekkers, M. J. (1989). Magnetic properties of natural pyrrhotite II. high- and low-temperature behaviour of j_{rs} and TRM as function of grain size. *Physics of The Earth and Planetary Interiors, 57*(3-4), 266–283.

Dekkers, M. J. (1990). Magnetic monitoring of pyrrhotite alteration during thermal demagnetization. *Geophysical Research Letters, 17*(6), 779–782.

Dekkers, M. J. (1990). Magnetic properties of natural goethite – III. magnetic behaviour and properties of minerals originating from goethite dehydration during thermal demagnetization. *Geophysical Journal International, 103*(1), 233–250.

Dekkers, M. J., Passier, H. F. and Schoonen, M. A. A. (2000). Magnetic properties of hydrothermally synthesized greigite (Fe_3S_4) – II. high- and low-temperature characteristics. *Geophysical Journal International, 141*(3), 809–819.

Dempster, A. P., Laird, N. M. and Rubin, D. B. (1977). Maximum likelihood from incomplete data via the EM algorithm. *Journal of the Royal Statistical Society. Series B (Methodological), 39*(1), 1–38.

Doell, R. R. and Cox, A. (1967). Analysis of palaeomagnetic data. In Collinson, D. W., Creer, K. M. and Runcorn, S. K., editors, *Methods in Palaeomagnetism*, number 3 in Developments in Solid Earth Geophysics, pages 340–346. Amsterdam: Elsevier.

Dunlop, D. (1979). On the use of Zijderveld vector diagrams in multicomponent paleomagnetic studies. *Physics of the Earth and Planetary Interiors, 20*(1).

Dunlop, D. J. (1972). Magnetic mineralogy of unheated and heated red sediments by coercivity spectrum analysis. *Geophysical Journal of the Royal Astronomical Society, 27*(1), 37–55.

Dunlop, D. J. (1986). Coercive forces and coercivity spectra of submicron magnetites. *Earth and Planetary Science Letters, 78*(2-3), 288–295.

Dunlop, D. J. (1995). Magnetism in rocks. *Journal of Geophysical Research, 100*(B2), 2161–2174.

Dunlop, D. J. (2003). Stepwise and continuous low-temperature demagnetization. *Geophysical Research Letters, 30*(11), 1582.

Dunlop, D. J. and Özdemir, Ö. (1993). Thermal demagnetization of VRM and pTRM of single domain magnetite: No evidence for anomalously high unblocking temperatures. *Geophysical Research Letters, 20*(18), 1939–1942.

Dunlop, D. J. and Özdemir, Ö. (1997). *Rock magnetism: fundamentals and frontiers*, volume 3 of *Cambridge studies in magnetism*. Cambridge University Press.

Dunlop, D. J., Schmidt, P. W., Özdemir, Ö. and Clark, D. A. (1997). Paleomagnetism and paleothermometry of the Sydney Basin 1. thermoviscous and chemical overprinting of the Milton Monzonite. *Journal of Geophysical Research, 102*(B12), 27271–27283.

Efron, B. (1979). Bootstrap methods: Another look at the jackknife. *The Annals of Statistics, 7*(1), 1–26.

Efron, B. (1982). *The jackknife, the bootstrap and other resampling plans*, volume 38 of *CBMS-NSF Regional Conference Series in Applied Mathematics*. Philadephia, Pennsylvania: Society for Industrial and Applied Mathematics.

Egli, R. (2003). Analysis of the field dependence of remanent magnetization curves. *Journal of Geophysical Research, 108*(B2), 2081.

Egli, R. and Lowrie, W. (2002). Anhysteretic remanent magnetization of fine magnetic particles. *Journal of Geophysical Research, 107*(B10), 2209.

Ellwood, B. B. (1980). Application of the anisotropy of magnetic susceptibility method as an indicator of bottom-water flow direction. *Marine Geology, 34*(3-4), M83–M90.

Emiliani, C. and Edwards, G. (1953). Tertiary ocean bottom temperatures. *Nature, 171*(4359), 887–888.

Enkin, R. (2008). Software – paleomagnetic analysis. http://gsc.nrcan.gc.ca/sw/paleo_e.php. Retrieved 25 April 2011.

Ernst, R. E. and Pearce, G. W. (1989). Averaging of anisotropy of magnetic susceptibility data. In Agterberg, F. P. and Bonham-Carter, G. F., editors, *Statistical Applications in the Earth Sciences*, pages 297–305. Geological Survey of Canada. Paper 89-9.

Evans, M. E. (2005). Nanophase magnetism and past global change. *Journal of Physics: Conference Series, 17*, 150–153.

Evans, M. E. and Heller, F. (2003). *Environmental magnetism: principles and applications of enviromagnetics*. San Diego: Academic Press.

Evans, M. E., McElhinny, M. W. and Gifford, A. C. (1968). Single domain magnetite and high coercivities in a gabbroic intrusion. *Earth and Planetary Science Letters, 4*(2), 142–146.

Exon, N., Kennett, J. and Malone, M. (2000). The opening of the Tasmanian gateway drove global Cenozoic paleoclimatic and paleoceanographic changes: Results of Leg 189. *JOIDES Journal, 26*(2), 11–18.

Facer, R. A. (1976). PALMAGFISHERANAL, a computer program using Fisher's analysis to analyze paleomagnetic directions – or other directions distributed on a sphere. *Computers & Geosciences, 1*, 325–330.

Fernández, O. (2005). Obtaining a best fitting plane through 3D georeferenced data. *Journal of Structural Geology, 27*(5), 855–858.

Field, B. D., Browne, G. H. and others, editors (1989). *Cretaceous and Cenozoic sedimentary basins and geological evolution of the Canterbury Region, South Island, New Zealand*, Number 2 in New Zealand Geological Survey Basin Studies. Lower Hutt: New Zealand Geological Survey.

Filhol, H. (1885). *Mission de l'Île Campbell*, volume 3 of *Recueil de mémoires, rapports et documents relatifs à l'observation du passage de Vénus sur le Soleil*. Firmin-Didot.

Finlay, H. J. (1950). Fossil foraminifera from Campbell Island. In *The Geology of Campbell Island*, pages 45–46. Wellington, New Zealand: Department of Scientific and Industrial Research.

Fisher, N. I. and Hall, P. (1989). Bootstrap confidence regions for directional data. *Journal of the American Statistical Association, 84*(408), 996–1002.

Fisher, N. I., Lewis, T. and Embleton, B. J. J. (1987). *Statistical Analysis of Spherical Data*. Cambridge University Press.

Fisher, R. (1953). Dispersion on a sphere. *Proceedings of the Royal Society of London. Series A, Mathematical and Physical Sciences, 217*, 295–305.

Fleming, C. A., editor (1959). *Lexique stratigraphique international. Vol. VI, Oceanie, Fascicule 4, New Zealand*. Paris: CNRS.

Florindo, F., Roberts, A. P. and Palmer, M. R. (2003). Magnetite dissolution in siliceous sediments. *Geochemistry, Geophysics, Geosystems, 4*(7), 1053.

Forbes, C. (1855). On the geology of New Zealand; with notes on its carboniferous deposits. *Quarterly Journal of the Geological Society, 11*(1-2), 521–530.

Fordyce, R. E., Lee, D. E. and Wilson, G. S. (2009). Field trip 3: Cretaceous–Paleogene stratigraphy of the Canterbury Basin. In *Climatic and Biotic Events of the Paleogene Conference Field Trip Guides*, number 17 in GNS Science Miscellaneous Series, pages 92–129. 6–21 January 2009, Te Papa, Wellington, New Zealand.

France, D. E. and Oldfield, F. (2000). Identifying goethite and hematite from rock magnetic measurements of soils and sediments. *Journal of Geophysical Research, 105*(B2), 2781–2795.

Fraser, H. L. (2009). Glacial extent on Campbell Island at the last glacial maximum. Master's thesis, Dunedin, New Zealand: University of Otago.

Freeman, R. (1986). Magnetic mineralogy of pelagic limestones. *Geophysical Journal of the Royal Astronomical Society, 85*(2), 433–452.

Fuller, M. D. (1962). A magnetic fabric in till. *Geological Magazine, 99*(03), 233–237.

Fulthorpe, C. S., Carter, R. M., Miller, K. G. and Wilson, J. (1996). Marshall Paraconformity: a mid-Oligocene record of inception of the Antarctic Circumpolar Current and coeval glacio-eustatic lowstand? *Marine and Petroleum Geology, 13*(1), 61–77.

Galeotti, S., Rusciadelli, G., Sprovieri, M., Lanci, L. and Gaudio, A. et al. (2009). Sea-level control on facies architecture in the Cenomanian-Coniacian Apulian margin (Western Tethys): A record of glacio-eustatic fluctuations during the Cretaceous greenhouse? *Palaeogeography, Palaeoclimatology, Palaeoecology, 276*(1-4), 196–205.

Gehring, A. U. and Heller, F. (1989). Timing of natural remanent magnetization in ferriferous limestones from the Swiss Jura mountains. *Earth and Planetary Science Letters, 93*(2), 261–272.

Gehring, A. U. and Hofmeister, A. M. (1994). The transformation of lepidocrocite during heating: a magnetic and spectroscopic study. *Clays and Clay Minerals, 42*(4), 409–415.

Gilbert, W. (1600). *De magnete*. London: Peter Short.

Goguitchaichvili, A. (1999). A simple, alternative presentation of paleomagnetic demagnetization data. *Geofísica Internacional, 38*(4), 285–290.

Goldman, M. I. (1922). Basal glauconite and phosphate beds. *Science, 56*(1441), 171–173.

Gómez-Paccard, M., Catanzariti, G., Ruiz-Martínez, V. C., Núñez, G. M. J. I. and Osete, M. L. et al. (2006). A catalogue of Spanish archaeomagnetic data. *Geophysical Journal International, 166*, 1125–1143.

Goree, W. S. and Fuller, M. (1976). Magnetometers using RF-driven squids and their applications in rock magnetism and paleomagnetism. *Reviews of Geophysics and Space Physics, 14*(4), 591–608.

Gradstein, F. M., Ogg, J. G. and Smith, A. G., editors (2004). *A Geologic Time Scale 2004*. Cambridge: Cambridge University Press.

Graham, J. W. (1949). The stability and significance of magnetism in sedimentary rocks. *Journal of Geophysical Research, 54*(2), 131–167.

Graham, J. W. (1954). Magnetic susceptibility anisotropy, an unexploited petrofabric element. *Geological Society of America Bulletin, 65*(12), 1257–1258.

Grange, L. I. (1921). Geology of the Green Island coalfield. *Transactions of the New Zealand Institute, 53*, 157–174.

Grommé, C. S., Wright, T. L. and Peck, D. L. (1969). Magnetic properties and oxidation of iron-titanium oxide minerals in Alae and Makaopuhi lava lakes, Hawaii. *Journal of Geophysical Research, 74*(22), 5277–5293.

Groshong Jr., R. H. (2006). *3-D Structural Geology: A Practical Guide to Quantitative Surface and Subsurface Map Interpretation*. 2nd edition. Berlin: Springer.

Haast, J. v. (1871). On the geology of the Waipara District, Canterbury, with geological maps and sections. *Geological Survey of New Zealand, Reports of Geological Explorations during 1870–71*, pp. 5–19.

Haast, J. v. (1879). *Geology of the Provinces of Canterbury and Westland, New Zealand: a report comprising the results of official explorations*. Christchurch: 'Times' Office.

Hall, L. S., Lamb, S. H. and Mac Niocaill, C. (2004). Cenozoic distributed rotational deformation, South Island, New Zealand. *Tectonics, 23*, TC2002.

Hallam, D. F. and Maher, B. A. (1994). A record of reversed polarity carried by the iron sulphide greigite in British early Pleistocene sediments. *Earth and Planetary Science Letters, 121*(1-2), 71–80.

Halls, H. C. (1976). A least-squares method to find a remanence direction from converging remagnetization circles. *Geophysical Journal of the Royal Astronomical Society, 45*(2), 297–304.

Hamilton, N. (1963). Susceptibility anisotropy measurements on some Silurian siltstones. *Nature, 197*(4863), 170–171.

Hamilton, N. and Rees, A. I. (1970). The use of magnetic fabric in palaeocurrent estimation. In Runcorn, S. K., editor, *Palaeogeophysics*, pages 445–463. London: NATO Advanced Study Insititute.

Hansen, J. M. (2009). *On the origin of natural history: Steno's modern, but forgotten philosophy of science*, volume 203 of *Memoir*, pages 159–178. Boulder, Colorado: Geological Society of America.

Haq, B. U., Hardenbol, J. and Vail, P. R. (1987). Chronology of fluctuating sea levels since the Triassic. *Science, 235*(4793), 1156.

Haubold, H. (1999). Alteration of magnetic properties of Palaeozoic platform carbonate rocks during burial diagenesis (Lower Ordovician sequence, Texas, USA). , *151*, 181–203.

Hector, J. (1896). Note on the geology of the outlying islands of New Zealand. *Transactions of the New Zealand Institute, 28*, 736–738.

Heider, F., Körner, U. and Bitschene, P. (1993). Volcanic ash particles as carriers of remanent magnetization in deep-sea sediments from the Kerguelen Plateau. *Earth and Planetary Science Letters, 118*(1-4), 121–134.

Henkel, O. (1964). Remanenzverhalten und Wechselwirkungen in hartmagnetischen Teilchenkollektiven. *Physica Status Solidi, 7*(3), 919–929.

Henry, B. (2007). Magnetic mineralogy, changes due to heating. In Gubbins, D. and Herrero-Bervera, E., editors, *Encyclopedia of Geomagnetism and Paleomagnetism*, pages 512–515. Berlin: Springer.

Henry, B., Jordanova, D., Jordanova, N., Souque, C. and Robion, P. (2003). Anisotropy of magnetic susceptibility of heated rocks. *Tectonophysics, 366*(3-4), 241–258.

Henry, S. G. (1979). Chemical demagnetization: methods, procedures, and applications through vector analysis. *Canadian Journal of Earth Sciences, 16*(9), 1832–1841.

Henshaw Jr., P. C. and Merrill, R. T. (1980). Magnetic and chemical changes in marine sediments. *Reviews of Geophysics and Space Physics, 18*(2), 483–504.

Heslop, D., Dekkers, M. J., Kruiver, P. P. and Van Oorschot, I. H. M. (2002). Analysis of isothermal remanent magnetization acquisition curves using the expectation-maximization algorithm. *Geophysical Journal International, 148*(1), 58–64.

Heslop, D., McIntosh, G. and Dekkers, M. J. (2004). Using time- and temperature-dependent Preisach models to investigate the limitations of modelling isothermal remanent magnetization acquisition curves with cumulative log Gaussian functions. *Geophysical Journal International, 157*(1), 55–63.

Hext, G. R. (1963). The estimation of second-order tensors, with related tests and designs. *Biometrika, 50*(3-4), 353–373.

Hirt, A. and Lowrie, W. (1988). Paleomagnetism of the Umbrian-Marches orogenic belt. *Tectonophysics, 146*(1–4), 91–103.

Hirt, A. M. and Gehring, A. U. (1991). Thermal alteration of the magnetic mineralogy in ferruginous rocks. *Journal of Geophysical Research, 96*(B6), 9947–9953.

Hoffman, K. A. and Day, R. (1978). Separation of multi-component NRM: A general method. *Earth and Planetary Science Letters, 40*(3), 433–438.

Hollis, C. J. (2003). The Cretaceous/Tertiary boundary event in New Zealand: profiling mass extinction. *New Zealand Journal of Geology and Geophysics, 46*(2), 307–321.

Hollis, C. J., Beu, A. G., Raine, J. I., Strong, C. P. and Turnbull, I. M. et al. (1997). Integrated biostratigraphy of Cretaceous-Paleogene strata on Campbell Island, southwest Pacific. Technical Report Lower Hutt, New Zealand: Institute of Geological & Nuclear Sciences.

Hollis, C. J., Dickens, G. R., Field, B. D., Jones, C. M. and Strong, C. P. (2005). The Paleocene–Eocene transition at Mead Stream, New Zealand: a southern Pacific record of early Cenozoic global change. *Palaeogeography, Palaeoclimatology, Palaeoecology, 215*(3-4), 313–343.

Hollis, C. J., Field, B. D., Rodgers, K. M. and Strong, C. P. (2003). Stratigraphic, paleontological, and geochemical data from Upper Cretaceous and lower Paleocene strata in southeastern Marlborough, New Zealand. Technical Report Lower Hutt, New Zealand.

Hollis, C. J., Handley, L., Crouch, E. M., Morgans, H. E. and Baker, J. A. et al. (2009). Tropical sea temperatures in the high-latitude south pacific during the eocene. *Geology, 37*(2), 99–102.

Hollis, C. J. and Manzano-Kareah, K. (2005). Source rock potential of the East Coast Basin (central and northern regions). In *Petroleum Report 3179*, pages 1–156. New Zealand: Ministry of Economic Development.

Hollis, C. J. and Strong, C. P. (2003). Biostratigraphic review of the Cretaceous/Tertiary boundary transition, mid-Waipara River section, North Canterbury, New Zealand. *New Zealand Journal of Geology and Geophysics, 46*(2), 243–253.

Hollis, C. J., Waghorn, D. B., Strong, C. P. and Crouch, E. M. (1997). Integrated paleogene biostratigraphy of DSDP site 277 (leg 29); foraminifera, calcareous nannofossils, radiolaria, and palynomorphs. *Institute of Geological and Nuclear Sciences Science Report, 97/7*, 87.

Hood, T. H. C. (1870). Geological observations on the Waipara River, New Zealand. *Quarterly Journal of the Geological Society, 26*(1-2), 409–413.

Hopkinson, J. (1889). Magnetic and other physical properties of iron at a high temperature. *Philosophical Transactions of the Royal Society of London. A, 180*, 443–465.

Hornibrook, N. de B. (1962). The Cretaceous-Tertiary boundary in New Zealand. *New Zealand Journal of Geology and Geophysics, 5*, 295–303.

Hospers, J. (1951). Remanent magnetism of rocks and the history of the geomagnetic field. *Nature, 168*(4287), 1111–1112.

Hounslow, M. (2001). *Palaeomag-Tools*. http://geography.lancs.ac.uk/cemp/resources/software/pmagtool.htm. Retrieved 29 May 2011.

Hounslow, M. W. and Maher, B. A. (1996). Quantitative extraction and analysis of carriers of magnetization in sediments. *Geophysical Journal International, 124*(1), 57–74.

Hounslow, M. W. and Maher, B. A. (1999). Laboratory procedures for quantitative extraction and analysis of magnetic minerals from sediments. In Walden, J., Smith, J. and Oldfield, F., editors, *Environmental Magnetism: A Practical Guide*, number 6 in QRA Technical Guides, pages 139–184. London: Quaternary Research Association.

Hounslow, M. W., Maher, B. A. and Thistlewood, L. (1995). Magnetic mineralogy of sandstones from the Lunde Formation (late Triassic), northern North Sea, UK: origin of the palaeomagnetic signal. In Turner, P. and Turner, A., editors, *Palaeomagnetic Applications in Hydrocarbon Exploration and Production*, number 98 in Geological Society Special Publications, pages 119–147. London: Geological Society.

Hounslow, M. W. and Morton, A. C. (2004). Evaluation of sediment provenance using magnetic mineral inclusions in clastic silicates: comparison with heavy mineral analysis. *Sedimentary Geology, 171*(1-4), 13–36.

Housen, B. A., Banerjee, S. K. and Moskowitz, B. M. (1996). Low-temperature magnetic properties of siderite and magnetite in marine sediments. *Geophysical Research Letters, 23*(20), 2843–2846.

Howarth, R. J. (1996). History of the stereographic projection and its early use in geology. *Terra Nova, 8*(6), 499–513.

Hrouda, F. (1994). A technique for the measurement of thermal changes of magnetic susceptibility of weakly magnetic rocks by the CS-2 apparatus and KLY-2 kappabridge. *Geophysical Journal International, 118*(3), 604–612.

Hrouda, F. (2003). Indices for numerical characterization of the alteration processes of magnetic minerals taking place during investigation of temperature variation of magnetic susceptibility. *Studia Geophysica et Geodætica, 47*, 847–861.

Hrouda, F. and Janák, F. (1976). The changes in shape of the magnetic susceptibility ellipsoid during progressive metamorphism and deformation. *Tectonophysics, 34*(1-2), 135–148.

Hu, S., Appel, E., Hoffmann, V., Schmahl, W. W. and Wang, S. (1998). Gyromagnetic remanence acquired by greigite (Fe_3S_4) during static three-axis alternating field demagnetization. *Geophysical Journal International, 134*, 831–842.

Huggett, J. M. and Gale, A. S. (1997). Petrology and palaeoenvironmental significance of glaucony in the Eocene succession at Whitecliff Bay, Hampshire Basin, UK. *Journal of the Geological Society, 154*(5), 897–912.

Hughes, J. C. (1982). High gradient magnetic separation of some soil clays from Nigeria, Brazil and Colombia. *Journal of Soil Science, 33*(3), 509–519.

Hunt, C. P., Moskowitz, B. M. and Banerjee, S. K. (1995). Magnetic properties of rocks and minerals. In Ahrens, T. J., editor, *Rock physics and phase relations: a handbook of physical constants*, number 3 in AGU Reference Shelf, pages 189–204. American Geophysical Union.

Hutton, C. O. and Turner, F. J. (1936). The heavy minerals of some Cretaceous and Tertiary sediments from Otago and Southland. *Transactions and Proceedings of the Royal Society of New Zealand, 66*(3), 255–275.

Ihmlé, P. F., Hirt, A. M., Lowrie, W. and Dietrich, D. (1989). Inverse magnetic fabric in deformed limestones of the Morcles nappe, Switzerland. *Geophysical Research Letters, 16*(12), 1383–1386.

Irving, E., Robertson, W. A., Stott, P. M., Tarling, D. H. and Ward, M. A. (1961). Treatment of partially stable sedimentary rocks showing planar distribution of directions of magnetization. *Journal of Geophysical Research, 66*(6), 1927–1933.

Ising, G. (1942a). Den varviga lerans magnetiska egenskaper. *Geologiska Föreningens i Stockholm Förhandlingar, 64*(2), 126–142.

Ising, G. (1942b). On the magnetic properties of varved clay. *Arkiv för Matematik, Astronomi, och Fysik, 29A*(5), 1–37.

Jackson, M. (2007). Magnetization, isothermal remanent. In Gubbins, D. and Herrero-Bervera, E., editors, *Encyclopedia of Geomagnetism and Paleomagnetism*, pages 589–594. Berlin: Springer.

Jelínek, V. (1978). Statistical processing of anisotropy of magnetic susceptibility measured on groups of specimens. *Studia Geophysica et Geodætica, 22*(1), 50–62.

Jelínek, V. (1981). Characterization of the magnetic fabric of rocks. *Tectonophysics, 79*, T63–T67.

Jelínek, V. (1996). Measuring anisotropy of magnetic susceptibility on a slowly spinning specimen – basic theory. AGICO Print 10, Brno, Czech Republic: Agico.

Jones, C. H. (2002). User-driven integrated software lives: "Paleomag" paleomagnetics analysis on the macintosh. *Computers & Geosciences, 28*, 1145–1151.

Jones, M. P. (1987). *Applied mineralogy: a quantitative approach*, chapter 3, pages 39–43. London: Graham & Trotman.

Juneau, J., Baker, J., Munoz, L. S., Wierzbicki, F. and Ng, V. (2009). *The Definitive Guide to Jython*. New York: Apress.

Karlin, R. (1990a). Magnetic mineral diagenesis in suboxic sediments at Bettis Site W-N, NE Pacific Ocean. *Journal of Geophysical Research, 95*(B4), 4421–4436.

Karlin, R. (1990b). Magnetite diagenesis in marine sediments from the Oregon continental margin. *Journal of Geophysical Research, 95*(B4), 4405–4419.

Karlin, R. and Levi, S. (1983). Diagenesis of magnetic minerals in Recent haemipelagic sediments. *Nature, 303*(5915), 327–330.

Karlin, R. and Levi, S. (1985). Geochemical and sedimentological control of the magnetic properties of hemipelagic sediments. *Journal of Geophysical Research, 90*(B12), 10373–10392.

Kennett, J. P. (1977). Cenozoic evolution of Antarctic glaciation, the circum-Antarctic ocean, and their impact on global paleoceanography. *Journal of Geophysical Research, 82*(27), 3843–3860.

Kennett, J. P., Burns, R. E., Andrews, J. E., Churkin Jr., M. and Davies, T. A. et al. (1972). Australian-Antarctic continental drift, palaeocirculation changes and Oligocene deep-sea erosion. *Nature Physical Science, 239*, 51–55.

Kennett, J. P., Houtz, R. E., Andrews, P. B., Edwards, A. R. and Gostin, V. A. et al. (1975). Site 277. *Initial Reports of the Deep Sea Drilling Project, 29*, 45–120.

Kennett, J. P. and Watkins, N. D. (1974). Late Miocene–early Pliocene paleomagnetic stratigraphy, paleoclimatology, and biostratigraphy in New Zealand. *Geological Society of America Bulletin, 85*(9), 1385–1398.

Kennett, J. P., Watkins, N. D. and Vella, P. (1971). Paleomagnetic chronology of Pliocene-early Pleistocene climates and the Plio-Pleistocene boundary in New Zealand. *Science, 171*(3968), 276–279.

Kent, D. V. and Lowrie, W. (1974). Origin of magnetic instability in sediment cores from the central North Pacific. *Journal of Geophysical Research, 79*(20), 2987–3000.

Kent, D. V. and Lowrie, W. (1975). On the magnetic susceptibility anisotropy of deep-sea sediment. *Earth and Planetary Science Letters, 28*, 1–12.

Kent, J. T. (1982). The Fisher-Bingham distribution on the sphere. *Journal of the Royal Statistical Society. Series B (Methodological), 44*(1), 71–80.

King, J., Banerjee, S. K., Marvin, J. and Özdemir, Ö. (1982). A comparison of different magnetic methods for determining the relative grain size of magnetite in natural materials: some results from lake sediments. *Earth and Planetary Science Letters, 59*(2), 404–419.

King, J. W. and Channell, J. E. (1991). Sedimentary magnetism, environmental magnetism, and magnetostratigraphy. *Reviews of Geophysics (Supplement), 29*, 358–370.

King, P. R. (2000a). New Zealand's changing configuration in the last 100 million years: plate tectonics, basin development, and depositional setting. In *New Zealand Oil Exploration Conference Proceedings*, pages 132–146. Wellington: Ministry of Economic Development.

King, P. R. (2000b). Tectonic reconstructions of New Zealand: 40 Ma to the present. *New Zealand Journal of Geology & Geophysics, 43*, 611–638.

King, P. R., Naish, T. R., Browne, G. H., Field, B. D. and Edbrooke, S. W. (1999). *Cretaceous to Recent sedimentary patterns in New Zealand*, volume 1 of *Folio Series*. Lower Hutt, New Zealand: Institute of Geological & Nuclear Sciences.

Kirschvink, J. L. (1980). The least-squares line and plane and the analysis of palaeomagnetic data. *Geophysical Journal of the Royal Astronomical Society, 62*(3), 699–718.

Kissel, C., Barrier, E., Laj, C. and Lee, T.-Q. (1986). Magnetic fabric in 'undeformed' marine clays from compressional zones. *Tectonics, 5*(5), 769–781.

Kostadinova, M., Jordanova, N., Jordanova, D. and Kovacheva, M. (2004). Preliminary study on the effect of water glass impregnation on the rock-magnetic properties of baked clay. *Studia Geophysica et Geodaetica, 48*(3), 637–646.

Kruiver, P. P., Dekkers, M. J. and Heslop, D. (2001). Quantification of magnetic coercivity components by the analysis of acquisition curves of isothermal remanent magnetisation. *Earth and Planetary Science Letters, 189*(3-4), 269–276.

Kushiro, I. (1960). γ→α transition in Fe_2O_3 with pressure. *Journal of Geomagnetism and Geoelectricity, 11*(4), 148–151.

Lamb, S. (2011). Cenozoic tectonic evolution of the New Zealand plate-boundary zone: A paleomagnetic perspective. *Tectonophysics, 509*(3–4), 135–164.

Lambert, J. H. (1772). Anmerkungen und Zusätze zur Entwerfung der Land- und Himmelscharten. In *Beitrage zum Gebrauch der Mathematik und deren Anwendung III*, pages 105–199. Berlin: Buchhandlung der Realschule.

Lawrence, K. P., Tauxe, L., Staudigel, H., Constable, C. G. and Koppers, A. et al. (2009). Paleomagnetic field properties at high southern latitude. *Geochemistry, Geophysics, Geosystems, 10*(1), Q01005.

Lawson, C. A. and Nord, G. L. J. (1984). Remanent magnetization of a "paramagnetic" composition in the ilmenite-hematite solid solution series. *Geophysical Research Letters, 11*(3), 197–200.

Lawver, L. A. and Gahagan, L. M. (2003). Evolution of Cenozoic seaways in the circum-Antarctic region. *Palaeogeography, Palaeoclimatology, Palaeoecology, 198*(1-2), 11–37.

Lawver, L. A., Gahagan, L. M. and Coffin, M. F. (1992). The development of paleoseaways around Antarctica. In Kennett, J. P. and Warnke, D. A., editors, *The Antarctic Paleoenvironment: A Perspective on Global Change*, pages 7–30. Washington, D.C.: American Geophysical Union.

Leckie, D. A., Morgans, H., Wilson, G. J. and Edwards, A. R. (1995). Mid-Paleocene dropstones in the Whangai Formation, New Zealand – evidence of mid-Paleocene cold climate? *Sedimentary Geology, 97*(3-4), 119–129.

Leslie, B. W., Lund, S. P. and Hammond, D. E. (1990). Rock magnetic evidence for the dissolution and authigenic growth of magnetic minerals within anoxic marine sediments of the California continental borderland. *Journal of Geophysical Research, 95*(B4), 4437–4452.

Lewis, D. W. (1992). Anatomy of an unconformity on mid-Oligocene Amuri Limestone, Canterbury, New Zealand. *New Zealand Journal of Geology and Geophysics, 35*(4), 463–475.

Lienert, B. R., Christoffel, D. A. and Vella, P. (1972). Geomagnetic dates on a New Zealand Upper Miocene-Pliocene section. *Earth and Planetary Science Letters, 16*(2), 195–199.

Lindsay, W. L. (1867). On the tertiary coals of New Zealand. *Transactions of the Royal Society of Edinburgh, 24*, 167–174.

Lisle, R. J. (1989). The statistical analysis of orthogonal orientation data. *The Journal of Geology*, pp. 360–364.

Little, T. A. and Roberts, A. P. (1997). Distribution and mechanism of Neogene to present-day vertical axis rotations, Pacific-Australian plate boundary zone, South Island, New Zealand. *Journal of Geophysical Research, 102*(B9), 20447–20468.

Livermore, R., Hillenbrand, C.-D., Meredith, M. and Eagles, G. (2007). Drake Passage and Cenozoic climate: An open and shut case? *Geochemistry, Geophysics, Geosystems, 8*(1), Q01005.

Long, J. V. P. (1995). Microanalysis from 1950 to the 1990s. In Potts, P. J. and others, editors, *Microprobe Techniques in the Earth Sciences*. London: Chapman & Hall.

Løvlie, R., Lowrie, W. and Jacobs, M. (1972). Magnetic properties and mineralogy of four deep-sea cores. *Earth and Planetary Science Letters, 15*(2), 157–168.

Lowrie, W. (1990). Identification of ferromagnetic minerals in a rock by coercivity and unblocking temperature properties. *Geophysical Research Letters, 17*(2), 159–162.

Lowrie, W. and Heller, F. (1982). Magnetic properties of marine limestones. *Reviews of Geophysics and Space Physics, 20*(2), 171–192.

Macmillan, S. and Maus, S. (2005). International geomagnetic reference field – the tenth generation. *Earth, Planets, and Space, 57*(12), 1135–1140.

Maher, B. A. (1988). Magnetic properties of some synthetic sub-micron magnetites. *Geophysical Journal, 94*(1), 83–96.

Maher, B. A. (2007). Environmental magnetism and climate change. *Contemporary Physics, 48*(5), 247–274.

Maher, B. A. and Hallam, D. F. (2005). Magnetic carriers and remanence mechanisms in magnetite-poor sediments of Pleistocene age, southern North Sea margin. *Journal of Quaternary Science, 20*(1), 79–94.

Maher, B. A., Thompson, R. and Hounslow, M. W. (1999). Introduction. In Maher, B. A. and Thompson, R., editors, *Quaternary Climates, Environments and Magnetism*, pages 1–48. Cambridge University Press.

Maier, F. and Bachtadse, V. (1998). *Palmag*. http://www.geophysik.uni-muenchen.de/~valerian/palmag/. Retrieved 29 May 2011.

Marshall, P. and Browne, R. (1909). The geology of Campbell Island and the Snares. In *The subantarctic islands of New Zealand*, pages 680–704. Wellington, New Zealand: J. Mackay, Government Printer.

Márton, E., Bradák, B., Rauch-Włodarska, M. and Tokarski, A. (2010). Magnetic anisotropy of clayey and silty members of tertiary flysch from the Silesian and Skole nappes (Outer Carpathians). *Studia Geophysica et Geodaetica, 54*(1), 121–134.

McCormack, A. (2005). Plotcore, Version 2. http://pcwww.liv.ac.uk/~sg01/Software/Plotcore/. Retrieved 29 May 2011.

McElhinny, M. W. (1973). *Palaeomagnetism and Plate Tectonics*. Cambridge University Press.

McElhinny, M. W. and McFadden, P. L. (2000). *Paleomagnetism: Continents and Oceans*. San Diego: Academic Press.

McFadden, P. L. and McElhinny, M. W. (1988). The combined analysis of remagnetization circles and direct observations in palaeomagnetism. *Earth and Planetary Science Letters, 87*, 161–172.

McGuire, D. M. (1989). *Paleomagnetic stratigraphy and magnetic properties of Pliocene strata, Turakina River, North Island, New Zealand*. PhD thesis, Wellington, New Zealand: Victoria University.

McIntosh, G., Rolph, T. C., Shaw, J. and Dagley, P. (1996). A detailed record of normal-reversed-polarity transition obtained from a thick loess sequence at Jiuzhoutai, near Lanzhou, China. *Geophysical Journal International, 127*(3), 651–664.

McKellar, I. E. (1990). Geology of the southwest Dunedin urban area. NZ Geological Survey DSIR, Lower Hutt, New Zealand. Booklet accompanying geological map of New Zealand miscellaneous series map 22: southwest Dunedin urban area 1:25000.

McMillan, S. G. (1993). *The Abbotsford Formation*. PhD thesis, Dunedin, New Zealand: University of Otago.

McMillan, S. G. (1995). Report on the Fairfield Estate drillhole (FE1) near Dunedin, Otago. Report 95/17, Lower Hutt, New Zealand: Institute of Geological and Nuclear Sciences.

McMillan, S. G. and Wilson, G. J. (1997). Allostratigraphy of coastal south and east Otago: a stratigraphic framework for interpretation of the Great South Basin, New Zealand. *New Zealand Journal of Geology and Geophysics, 40*, 91–107.

McNab, T. K., Fox, R. A. and Boyle, A. J. F. (1968). Some magnetic properties of magnetite (Fe_3O_4) microcrystals. *Journal of Applied Physics, 39*(12), 5703–5711.

McNish, A. G. and Johnson, E. A. (1938). Magnetization of unmetamorphosed varves and marine sediments. *Terrestrial Magnetism and Atmospheric Electricity, 43*(4), 401–407.

Miller, K. G., Fairbanks, R. G. and Mountain, G. S. (1987). Tertiary oxygen isotope synthesis, sea level history, and continental margin erosion. *Paleoceanography, 2*(1), 1–19.

Miller, K. G., Kominz, M. A., Browning, J. V., Wright, J. D. and Mountain, G. S. et al. (2005). The Phanerozoic record of global sea-level change. *Science, 310*, 1293–1298.

Miller, K. G., Wright, J. D. and Browning, J. V. (2005). Visions of ice sheets in a greenhouse world. *Marine Geology, 217*(3-4), 215–231.

Miller, K. G., Wright, J. D. and Fairbanks, R. G. (1991). Unlocking the ice house: Oligocene-Miocene oxygen isotopes, eustasy, and margin erosion. *Journal of Geophysical Research, 96*(B4), 6829–6848.

Morgans, H. E. G., Jones, C. M., Crouch, E. M., Field, B. D. and Hollis, C. J. et al. (2005). Upper Cretaceous to Eocene stratigraphy and sample collections, mid-Waipara River section, North Canterbury. Science Report 2003/08, Wellington: Institute of Geological and Nuclear Sciences.

Morris, P. A. (1976). The igneous geology of Campbell Island, south west Pacific Ocean. BSc (Hons) Thesis, Dunedin, New Zealand: University of Otago.

Moskowitz, B. M. (1981). Methods for estimating Curie temperatures of titanomaghemites from experimental J_S-T data. *Earth and Planetary Science Letters, 53*(1), 84–88.

Moskowitz, B. M., Frankel, R. B. and Bazylinski, D. A. (1993). Rock magnetic criteria for the detection of biogenic magnetite. *Earth and Planetary Science Letters, 120*(3-4), 283–300.

Moskowitz, B. M., Jackson, M. and Kissel, C. (1998). Low-temperature magnetic behavior of titanomagnetites. *Earth and Planetary Science Letters, 157*(3-4), 141–149.

Mountain, G. S., Burger, R. L., Delius, H., Fulthorpe, C. S. and Austin, J. A. et al. (2007). The long-term stratigraphic record on continental margins. In Nittrouer, C. A., Austin, J. A., Field, M. E., Kravitz, J. H. and Syvitski, J. P. M. et al., editors, *Continental Margin Sedimentation: From Sediment Transport to Sequence Stratigraphy*, number 37 in Special Publications, pages 381–458. Oxford: Blackwell Publishing.

Mumme, T. C., Lamb, S. H. and Walcott, R. I. (1989). The Raukumara paleomagnetic domain: constraints on the tectonic rotation of the East Coast, North Island, New Zealand, from paleomagnetic data. *New Zealand Journal of Geology and Geophysics, 32*(3), 317–326.

Mumme, T. C. and Walcott, R. I. (1985). Paleomagnetic studies at Geophysics Division 1980–1983. Geophysics Division Report 204, Wellington, New Zealand: Department of Scientific and Industrial Research.

Muxworthy, A., Williams, W. and Virdee, D. (2003). Effect of magnetostatic interactions on the hysteresis parameters of single-domain and pseudo-single-domain grains. *Journal of Geophysical Research, 108*(B11), 2517.

Muxworthy, A. R. (1999). Low-temperature susceptibility and hysteresis of magnetite. *Earth and Planetary Science Letters, 169*(1-2), 51–58.

Néel, L. (1949). Théorie du traînage magnétique des ferromagnétiques en grains fins avec applications aux terres cuites. *Annales De Géophysique, 5*(2), 99–136.

Néel, L. (1955). Some theoretical aspects of rock-magnetism. *Advances in Physics, 4*(14), 191–243.

Nelson, F. (2011). *Paleomagnetic records of the last two million years of climate and oceanographic change in the New Zealand sector of the South Pacific*. PhD thesis, Dunedin, New Zealand: University of Otago.

Newell, A. J., Dunlop, D. J. and Enkin, R. J. (1990). Temperature dependence of critical sizes, wall widths and moments in two-domain magnetite grains. *Physics of The Earth and Planetary Interiors, 65*(1-2), 165–176.

Nittrouer, C. A., Austin, J. A., Field, M. E., Kravitz, J. H. and Syvitski, J. P. M. et al. (2007a). Writing a Rosetta Stone: Insights into continental-margin sedimentary processes and strata. In Nittrouer, C. A., Austin, J. A., Field, M. E., Kravitz, J. H. and Syvitski, J. P. M. et al., editors, *Continental Margin Sedimentation: From Sediment Transport to Sequence Stratigraphy*, number 37 in Special Publications, pages 1–48. Oxford: Blackwell Publishing.

Noël, M. and Rudnicki, M. D. (1988). A computer program for determining current directions from rock magnetic data. *Computers & Geosciences, 14*(3), 321–338.

Nord, G. L. and Lawson, C. A. (1989). Order-disorder transition–induced twin domains and magnetic properties in ilmenite-hematite. *American Mineralogist, 74*(1-2), 160–176.

Odin, G. S. (1982). How to measure glaucony ages. In Odin, G. S., editor, *Numerical Dating in Stratigraphy, part 1*, chapter 20, pages 387–403. New York: Wiley.

Odin, G. S. and Matter, A. (1981). De glauconiarum origine. *Sedimentology, 28*(5), 611–641.

Odin, G. S. and Morton, A. C. (1988). Authigenic green particles from marine environments. In Chilingarian, G. V. and Wolf, K. H., editors, *Diagenesis, II*, number 43 in Developments in Sedimentology, chapter 4, pages 213–264. Amsterdam: Elsevier.

Ohneiser, C. (2011). *Late Neogene Antarctic ice sheet and climatic evolution of magnetic proxies*. PhD thesis, Dunedin, New Zealand: University of Otago.

Ohneiser, C., Wilson, G. S., Field, B. D. and Crundwell, M. P. (2008). A new high-resolution, middle Miocene magnetostratigraphy from western Southland, New Zealand. *New Zealand Journal of Geology & Geophysics, 51*, 261–274.

Oldfield, F. (1999). The rock magnetic identification of magnetic mineral and magnetic grain size assemblages. In Walden, J., Smith, J. and Oldfield, F., editors, *Environmental Magnetism: A Practical Guide*, number 6 in QRA Technical Guides, pages 98–112. London: Quaternary Research Association.

Oliver, R. L. (1950). Preliminary report on the geology of Campbell Island. In *The Geology of Campbell Island*, pages 1–44. Wellington, New Zealand: Department of Scientific and Industrial Research.

Oliver, R. L., Finlay, H. J. and Fleming, C. A. (1950). *The Geology of Campbell Island*. Wellington, New Zealand: Department of Scientific and Industrial Research.

Ongley, M. (1939). *The geology of the Kaitangata-Green Island Subdivision, Eastern and Central Otago Divisions*, volume 38 of *New Zealand Geological Survey Bulletin*. Wellington, New Zealand: Government Printer.

Opdyke, N. D. and Channell, J. E. T. (1996). *Magnetic Stratigraphy*, volume 64 of *International Geophysics*. San Diego: Academic Press.

Opdyke, N. D. and MacDonald, W. D. (1973). Paleomagnetism of Late Cretaceous Poços de Caldas alkaline complex, Southern Brazil. *Earth and Planetary Science Letters, 18*(1), 37–44.

O'Reilly, W. (1984). *Rock and Mineral Magnetism*. Glasgow: Blackie.

Owen, R. (1861). On the remains of a plesiosaurian reptile *(Plesiosaurus australis)* from the Oolitic Formation in the Middle Island of New Zealand. *Reports of the British Association for the Advancement of Science*, pp. 122–123.

Özdemir, Ö., Dunlop, D. J. and Moskowitz, B. M. (1993). The effect of oxidation on the Verwey transition in magnetite. *Geophysical Research Letters, 20*(16), 1671–1674.

Ozima, M., Akimoto, S., Yukutake, T., Sawada, M. and Yabu, T. et al. (1964). Low temperature characteristics of remanent magnetization of magnetite – self-reversal and recovery phenomena of remanent magnetization. *Journal of Geomagnetism and Geoelectricity, 16*, 201.

Pagani, M., Zachos, J. C., Freeman, K. H., Tipple, B. and Bohaty, S. (2005). Marked decline in atmospheric carbon dioxide concentrations during the Paleogene. *Science, 309*(5734), 600–603.

Papamarinopoulos, S., Readman, P. W., Maniatis, Y. and Simopoulos, A. (1982). Magnetic characterization and Mössbauer spectroscopy of magnetic concentrates from Greek lake sediments. *Earth and Planetary Science Letters, 57*(1), 173–181.

Park, J. (1910). *The geology of New Zealand: an introduction to the historical, structural, and economic geology*. Christchurch: Whitcombe and Tombs.

Pauthenet, R. and Bochirol, L. (1951). Aimantation spontané des ferrites. *Le Journal de Physique et le Radium, 12*, 249–251.

Pearson, K. (1901). On lines and planes of closest fit to systems of points in space. *Philosophical Magazine, 2*(6), 559–572.

Pearson, P. N., Foster, G. L. and Wade, B. S. (2009). Atmospheric carbon dioxide through the Eocene-Oligocene climate transition. *Nature, 461*(7267), 1110–1113.

Peters, C. and Dekkers, M. J. (2003). Selected room temperature magnetic parameters as a function of mineralogy, concentration and grain size. *Physics and Chemistry of the Earth, Parts A/B/C, 28*(16-19), 659–667.

Peters, C. and Thompson, R. (1998). Magnetic identification of selected natural iron oxides and sulphides. *Journal of Magnetism and Magnetic Materials, 183*(3), 365–374.

Petersen, N., von Dobeneck, T. and Vali, H. (1986). Fossil bacterial magnetite in deep-sea sediments from the South Atlantic Ocean. *Nature, 320*(6063), 611–615.

Petrovský, E. and Kapička, A. (2006). On determination of the Curie point from thermomagnetic curves. *Journal of Geophysical Research, 111*, B12S27.

Pillans, B. J., Roberts, A. P., Wilson, G. S., Abbott, S. T. and Alloway, B. V. (1994). Magnetostratigraphic, lithostratigraphic and tephrostratigraphic constraints on Lower and Middle Pleistocene sea-level changes, Wanganui Basin, New Zealand. *Earth and Planetary Science Letters, 121*(1-2), 81–98.

Pitman, W. C. I. and Golovchenko, X. (1983). The effect of sea level change on the shelf edge and slope of passive margins. In Stanley, D. J. and Moore, G. T., editors, *The Shelfbreak: Critical Interface on Continental Margins*, number 33 in Special Publications, pages 41–58. SEPM.

Plado, J., Preeden, U., Pesonen, L. J., Mertanen, S. and Puura, V. (2010). Magnetic history of Early and Middle Ordovician sedimentary sequence, northern Estonia. *Geophysical Journal International, 180*, 147–157.

Potter, D. K. and Stephenson, A. (1988). Single-domain particles in rocks and magnetic fabric analysis. *Geophysical Research Letters, 15*(10), 1097–1100.

Pullaiah, G., Irving, E., Buchan, K. and Dunlop, D. (1975). Magnetization changes caused by burial and uplift. *Earth and Planetary Science Letters, 28*(2), 133–143.

Puranen, R. (1977). Magnetic susceptibility and its anisotropy in the study of glacial transport in northern Finland. In Lawrence, L. K., editor, *Prospecting in Areas of Glaciated Terrain*, pages 111–119. London: Institution of Mining and Metallurgy.

Radhakrishnamurty, C. and Likhite, S. (1970). Hopkinson effect, blocking temperature and Curie point in basalts. *Earth and Planetary Science Letters, 7*(5), 389–396.

Randall, K., Lamb, S. and Niocaill, C. M. (2011). Large tectonic rotations in a wide zone of Neogene distributed dextral shear, northeastern South Island, New Zealand. *Tectonophysics, 509*(3-4), 165–180.

Rao, B. N. and Krishna, P. R. (1994). MAGPROS: An interactive FORTRAN-77 PC program for magnetic data processing. *Computers & Geosciences, 20*(5), 681–717.

Raynal, F. E. (1870). *Les naufragés, ou, Vingt mois sur un recif des Îles Auckland: recit authentique*. Paris: Hachette.

Raynal, F. E. (1875). *Wrecked on a Reef; or, twenty months among the Auckland Isles; a true story*. Edinburgh: T. Nelson and Sons.

Readman, P. W. and O'Reilly, W. (1972). Magnetic properties of oxidized (cation-deficient) titanomagnetites (Fe, Ti, □)$_3$O$_4$. *Journal of Geomagnetism and Geoelectricity, 24*, 69–90.

Reeburgh, W. S. (1983). Rates of biogeochemical processes in anoxic sediments. *Annual Review of Earth and Planetary Sciences, 11*(1), 269–298.

Reed, J., Cervato, C. and Fils, D. (2006). CHRONOS's PSICAT: a graphical core-logging tool for the 21st century. *GeoSpectrum, 5*(2), 33–34.

Rees, A. I. (1961). The effect of water currents on the magnetic remanence and anisotropy of susceptibility of some sediments. *Geophysical Journal of the Royal Astronomical Society, 5*(3), 235–251.

Rees, A. I. (1965). The use of anisotropy of magnetic susceptibility in the estimation of sedimentary fabric. *Sedimentology, 4*(4), 257–271.

Reisheck, A. (1889). Notes on the islands to the south of New Zealand. *Transactions of the New Zealand Institute, 21*.

Richter, C., Acton, G., Endris, C. and Radsted, M. (2007). Handbook for shipboard paleomagnetists. ODP Technical Note 34, Texas A&M University, College Station, Texas, USA: Ocean Drilling Program.

Righi, D. and Jadault, P. (1988). Improving soil clay minerals studies by high-gradient magnetic separation. *Clay Minerals, 23*(2), 225–232.

Roberts, A. (1992). Paleomagnetic constraints on the tectonic rotation of the southern Hikurangi margin, New Zealand. *New Zealand Journal of Geology and Geophysics, 35*(3), 311–323.

Roberts, A. P. (1995). Magnetic properties of sedimentary greigite (Fe_3S_4). *Earth and Planetary Science Letters, 134*, 227–236.

Roberts, A. P. and Pillans, B. J. (1993). Rock magnetism of Lower/Middle Pleistocene marine sediments, Wanganui Basin, New Zealand. *Geophysical Research Letters, 20*(9), 839–842.

Roberts, A. P. and Turner, G. M. (1993). Diagenetic formation of ferrimagnetic iron sulphide minerals in rapidly deposited marine sediments, South Island, New Zealand. *Earth and Planetary Science Letters, 115*, 257–273.

Roberts, A. P., Turner, G. M. and Vella, P. P. (1994). Magnetostratigraphic chronology of late Miocene to early Pliocene biostratigraphic and oceanographic events in New Zealand. *Geological Society of America Bulletin, 106*(5), 665–683.

Roberts, A. P. and Weaver, R. (2005). Multiple mechanisms of remagnetization involving sedimentary greigite (Fe_3S_4). *Earth and Planetary Science Letters, 231*, 263–277.

Robertson, D. J. (1993). Discrimination of tephra using rockmagnetic characteristics. *Journal of Geomagnetism and Geoelectricity, 45*(2), 167–178.

Robertson, D. J. and France, D. E. (1994). Discrimination of remanence-carrying minerals in mixtures, using isothermal remanent magnetisation acquisition curves. *Physics of The Earth and Planetary Interiors, 82*(3-4), 223–234.

Roncaglia, L., Field, B. D., Raine, J. I., Schiøler, P. and Wilson, G. J. (1999). Dinoflagellate biostratigraphy of Piripauan-Haumurian (Upper Cretaceous) sections from northeast South Island, New Zealand. *Cretaceous Research, 20*(3), 271–314.

Rosenthal, Y., Boyle, E. A. and Slowey, N. (1997). Temperature control on the incorporation of magnesium, strontium, fluorine, and cadmium into benthic foraminiferal shells from Little Bahama Bank: Prospects for thermocline paleoceanography. *Geochimica et Cosmochimica Acta, 61*(17), 3633–3643.

Rowan, C. J. (2006). *Neogene paleomagnetism and geodynamics of the Hikurangi margin, East Coast, New Zealand*. PhD thesis, University of Southampton.

Rowan, C. J. and Roberts, A. P. (2005). Tectonic and geochronological implications of variably timed magnetizations carried by authigenic greigite in marine sediments from New Zealand. *Geology, 33*(7), 553–556.

Rowan, C. J. and Roberts, A. P. (2006). Magnetite dissolution, diachronous greigite formation, and secondary magnetizations from pyrite oxidation: Unravelling complex magnetizations in Neogene marine sediments from New Zealand. *Earth and Planetary Science Letters, 241*, 119–137.

Rowan, C. J. and Roberts, A. P. (2008). Widespread remagnetizations and a new view of Neogene tectonic rotations within the Australia-Pacific plate boundary zone, New Zealand. *Journal of Geophysical Research, 113*(B3), B03103.

Rowan, C. J., Roberts, A. P. and Broadbent, T. (2009). Reductive diagenesis, magnetite dissolution, greigite growth and paleomagnetic smoothing in marine sediments: A new view. *Earth and Planetary Science Letters, 277*(1-2), 223–235.

Rowan, C. J., Roberts, A. P. and Rait, G. (2005). Relocation of the tectonic boundary between the Raukumara and Wairoa Domains (East Coast, North Island, New Zealand): Implications for the rotation history of the Hikurangi margin. *New Zealand Journal of Geology and Geophysics, 48*(1), 185–196.

Sagnotti, L., Roberts, A. P., Weaver, R., Verosub, K. L. and Florindo, F. et al. (2005). Apparent magnetic polarity reversals due to remagnetization resulting from late diagenetic growth of greigite from siderite. *Geophysical Journal International, 160*(1), 89–100.

Scheidegger, A. E. (1965). On the statistics of the orientation of bedding planes, grain axes, and similar sedimentological data. *US Geological Survey Professional Paper, 525*, 164–167.

Schieber, J. and Ellwood, B. B. (1988). The coincidence of macroscopic paleocurrent indicators and magnetic lineation in shales from the Precambrian Belt Basin. *Journal of Sedimentary Research, 58*(5), 830–835.

Schiøler, P., Rogers, K., Sykes, R., Hollis, C. J. and Ilg, B. et al. (2010). Palynofacies, organic geochemistry and depositional environment of the Tartan Formation (Late Paleocene), a potential source rock in the Great South Basin, New Zealand. *Marine and Petroleum Geology, 27*(2), 351–369.

Schmidt, P. W. (1982). Linearity spectrum analysis of multi-component magnetizations and its application to some igneous rocks from south-eastern Australia. *Geophysical Journal of the Royal Astronomical Society, 70*(3), 647–665.

Schmidt, W. (1925). Gefügestatistik. *Tschermaks Mineralogische und Petrographische Mitteilungen, 38*, 395–399.

Schouten, S., Hopmans, E. C., Schefu, E. and Damsté, J. S. S. (2002). Distributional variations in marine crenarchaeotal membrane lipids: a new tool for reconstructing ancient sea water temperatures? *Earth and Planetary Science Letters, 204*(1-2), 265–274.

Schulze, D. G. and Dixon, J. B. (1979). High gradient magnetic separation of iron oxides and other magnetic minerals from soil clays. *Soil Science Society of America Journal, 43*(4), 793–799.

Seward, D., Christoffel, D. A. and Lienert, B. (1986). Magnetic polarity stratigraphy of a Plio-Pleistocene marine sequence of North Island, New Zealand. *Earth and Planetary Science Letters, 80*(3-4), 353–360.

Shandley, P. D. and Bacon, L. O. (1966). Analysis for magnetite utilizing magnetic susceptibility. *Geophysics, 31*(2), 398–409.

Shaw, J., Yang, S., Rolph, T. C. and Sun, F. Y. (1999). A comparison of archaeointensity results from Chinese ceramics using microwave and conventional Thellier's and Shaw's methods. *Geophysical Journal International, 136*(3), 714–718.

Sherwood, G. J. (1989). MATZIJ – a BASIC program to determine paleomagnetic remanence directions using principal component analysis. *Computers & Geosciences, 15*(7), 1173–1182.

Shipboard Scientific Party (1999). Site 1120: Central Campbell Plateau. In Carter, R. M., McCave, I. N., Richter, C., Carter, L. and others, editors, *Initial Reports*, number 181 in Proceedings of the Ocean Drilling Program. College Station, Texas: Ocean Drilling Program.

Shipboard Scientific Party (2000). Leg 189 preliminary report. The Tasmanian Gateway between Australia and Antarctica – paleoclimate and paleoceanography. ODP Preliminary Report 89, Ocean Drilling Program. http://www-odp.tamu.edu/publications/prelim/189_prel/189prel.pdf.

Shoemake, K. (1985). Animating rotation with quaternion curves. *ACM SIGGRAPH Computer Graphics, 19*(3), 245–254.

Silverman, B. W. (1985). Some aspects of the spline smoothing approach to non-parametric regression curve fitting. *Journal of the Royal Statistical Society. Series B (Methodological), 47*(1), 1–52.

Situmorang, M. (1978). The geology of the Fairfield-Waldronville area. Dipl. Sci. thesis, Dunedin, New Zealand: University of Otago.

Smith, W. F. and Hashemi, J. (2006). *Foundations of Materials Science and Engineering*. 4th edition. New York: McGraw-Hill.

Snowball, I. and Torii, M. (1999). Incidence and significance of magnetic iron sulphides in Quaternary sediments and soils. In Maher, B. A. and Thompson, R., editors, *Quaternary Climates, Environments and Magnetism*, pages 199–230. Cambridge University Press.

Snowball, I. F. (1997). The detection of single-domain greigite (Fe_3S_4) using rotational remanent magnetization (RRM) and the effective gyro field (*Bg*): mineral magnetic and palaeomagnetic applications. *Geophysical Journal International, 130*, 704–716.

Sørensen, J. (1982). Reduction of ferric iron in anaerobic, marine sediment and interaction with reduction of nitrate and sulfate. *Applied and Environmental Microbiology, 43*(2), 319–324.

Spinu, L. and Stancu, A. (1998). Modelling magnetic relaxation phenomena in fine particles systems with a Preisach-Néel model. *Journal of Magnetism and Magnetic Materials, 189*(1), 106–114.

Spreitzhofer, G., Fierz, C. and Lehning, M. (2004). SN_GUI: a graphical user interface for snowpack modeling. *Computers & Geosciences, 30*(8), 809–816.

Stacey, F. D. (1961). Theory of the magnetic properties of igneous rocks in alternating fields. *Philosophical Magazine, 6*(70), 1241–1260.

Stacey, F. D. (1962). A generalized theory of thermoremanence, covering the transition from single domain to multi-domain magnetic grains. *Philosophical Magazine, 7*(83), 1887–1900.

Stacey, F. D. and Banerjee, S. K. (1974). *The Physical Principles of Rock Magnetism*, volume 5 of *Developments in Solid Earth Geophysics*. Amsterdam: Elsevier.

Steno, N. (1665). Discours de Monsieur Stenon sur l'anatomie du cerveau a messieurs de l'assemblée, qui se fait chez Monsieur Thevenot. Paris.

Stephenson, A. (1980). A gyroremanent magnetisation in anisotropic magnetic material. *Nature, 284*, 49–51.

Stober, J. C. and Thompson, R. (1979). Magnetic remanence acquisition in Finnish lake sediments. *Geophysical Journal of the Royal Astronomical Society, 57*(3), 727–739.

Stockhausen, H. (1998). Some new aspects for the modelling of isothermal remanent magnetization acquisition curves by cumulative log Gaussian functions. *Geophysical Research Letters, 25*(12), 2217–2220.

Strong, C. P. (1984). Cretaceous-Tertiary boundary, Mid-Waipara River section, North Canterbury, New Zealand. *New Zealand Journal of Geology and Geophysics, 27*, 231–234.

Sun, W. and Jackson, M. (1994). Scanning electron microscopy and rock magnetic studies of magnetic carriers in remagnetized early Paleozoic carbonates from Missouri. *Journal of Geophysical Research, 99*(B2), 2935–2942.

Sutherland, R. (1995). The Australia-Pacific boundary and Cenozoic plate motions in the SW Pacific: Some constraints from Geosat data. *Tectonics, 14*(4), 819–831.

Sverdrup, H. U., Johnson, M. W. and Fleming, R. H. (1942). *The oceans: their physics, chemistry and general biology*. Englewood Cliffs: Prentice-Hall.

Svoboda, J. (2004). *Magnetic Techniques for the Treatment of Materials*. Kluwer Academic Publishers.

Sweeney, R. E. and Kaplan, I. R. (1973). Pyrite framboid formation; laboratory synthesis and marine sediments. *Economic Geology, 68*(5), 618–634.

Symons, D. T. A. and Cioppa, M. T. (2000). Crossover plots: A useful method for plotting SIRM data in paleomagnetism. *Geophysical Research Letters, 27*(12), 1779–1782.

Takezawa, K. (2006). *Introduction to nonparametric regression*. Hoboken, New Jersey: John Wiley & Sons.

Tarling, D. H. (1976). Magnetic dating. *Nature, 262*, 8.

Tarling, D. H., Donovan, R. N., Abou-Deeb, J. M. and El-Batrouk, S. I. (1976). Palaeomagnetic dating of haematite genesis in Orcadian Basin sediments. *Scottish Journal of Geology, 12*(2), 125–134.

Tarling, D. H. and Hrouda, F. (1993). *The magnetic anisotropy of rocks*. London: Chapman & Hall.

Tauxe, L. (1998). *Paleomagnetic principles and practice*. Kluwer Academic Publishers.

Tauxe, L., Butler, R. F., Banerjee, S. K. and Van der Voo, R. (2010). *Essentials of paleomagnetism*. Berkeley: University of California Press.

Tauxe, L., Gee, J. S. and Staudigel, H. (1998). Flow directions in dikes from anisotropy of magnetic susceptibility data: the bootstrap way. *Journal of Geophysical Research, 103*(B8), 17775–17790.

Tauxe, L., Kylstra, N. and Constable, C. (1991). Bootstrap statistics for paleomagnetic data. *Journal of Geophysical Research, 96*(B7), 11723–11740.

Tauxe, L. and Watson, G. S. (1994). The fold test: an eigen analysis approach. *Earth and Planetary Science Letters, 122*(3-4), 331–341.

Tennyson, A. (1850). *In Memoriam*. London: Edward Moxon.

Thomson, J. A. (1920). The Notocene geology of the middle Waipara and Weka Pass district, north Canterbury. *Transactions of the New Zealand Institute, 52*, 322–415.

Tinto, K. (2010). *A geophysical investigation of the Marshall Paraconformity in South Canterbury, New Zealand*. PhD thesis, Dunedin, New Zealand: University of Otago.

Torii, M., Fukuma, K., Horng, C.-S. and Lee, T.-Q. (1996). Magnetic discrimination of pyrrhotite- and greigite-bearing sediment samples. *Geophysical Research Letters, 23*(14), 1813–1816.

Tosi, S. (2009). *Matplotlib for Python Developers*. Birmingham: Packt Publishing.

Townsend, D. (2001). *Neogene evolution of the Pacific–Australia plate boundary zone in NE Marlborough, South Island, New Zealand*. PhD thesis, Wellington, New Zealand: Victoria University.

Tudryn, A. and Tucholka, P. (2004). Magnetic monitoring of thermal alteration for natural pyrite and greigite. *Acta Geophysica Polonica, 52*(4), 509–520.

Turner, G. M. (2001). Toward an understanding of the multicomponent magnetization of uplifted Neogene marine sediments in New Zealand. *Journal of Geophysical Research, 106*(B4), 6385–6397.

Turner, G. M. and Kamp, P. J. J. (1990). Palaeomagnetic location of the Jaramillo Subchron and the Matuyama-Brunhes transition in the Castlecliffian stratotype section, Wanganui Basin, New Zealand. *Earth and Planetary Science Letters, 100*(1-3), 42–50.

Turner, G. M., Kamp, P. J. J., McIntyre, A. P., Hayton, S. and McGuire, D. M. et al. (2005). A coherent middle Pliocene magnetostratigraphy, Wanganui Basin, New Zealand. *Journal of the Royal Society of New Zealand, 35*(1-2), 197–227.

Turner, G. M., Michalk, D. M., Morgans, H. E. G. and Walbrecker, J. O. (2007). Early Miocene magnetostratigraphy and a new palaeomagnetic pole position from New Zealand. *Earth, Planets and Space, 59*(7), 841–851.

Turner, G. M., Roberts, A. P., Laj, C., Kissel, C. and Mazaud, A. et al. (1989). New paleomagnetic results from Blind River: revised magnetostratigraphy and tectonic rotation of the Marlborough region, South Island, New Zealand. *New Zealand Journal of Geology and Geophysics, 32*(2), 191–196.

Updike, J. (1969). *Midpoint and Other Poems*. New York: Alfred A. Knopf.

Urrutia-Fucugauchi, J. (2007). Magnetic susceptibility, anisotropy, effects of heating. In Gubbins, D. and Herrero-Bervera, E., editors, *Encyclopedia of Geomagnetism and Paleomagnetism*, pages 560–564. Berlin: Springer.

Vail, P. R., Mitchum Jr., R. M. and Thompson III, S. (1977). Seismic stratigraphy and global changes of sea-level, part 4: Global cycles of relative changes of sea-level. In Payton, C. E., editor, *Seismic stratigraphy – applications to hydrocarbon exploration*, number 26 in AAPG Memoir, pages 83–97. .

Vajda, V. and Raine, J. I. (2003). Pollen and spores in marine Cretaceous/Tertiary boundary sediments at mid-Waipara River, North Canterbury, New Zealand. *New Zealand Journal of Geology and Geophysics, 46*(2), 255–273.

Vali, H., von Dobeneck, T., Amarantidis, G., Förster, O. and Morteani, G. et al. (1989). Biogenic and lithogenic magnetic minerals in Atlantic and Pacific deep sea sediments and their paleomagnetic significance. *Geologische Rundschau, 78*(3), 753–764.

Verhoogen, J. (1959). The origin of thermoremanent magnetization. *Journal of Geophysical Research, 64*(12), 2441–2449.

Verosub, K. L. (1977). Depositional and postdepositional processes in the magnetization of sediments. *Reviews of Geophysics, 15*(2), 129–143.

Verwey, E. J. M. (1935). The crystal structure of γ-Fe_2O_3 and γ-Al_2O_3. *Zeitschrift für Kristallographie, 91*, 65–69.

Verwey, E. J. W. (1939). Electronic conduction of magnetite (Fe_3O_4) and its transition point at low temperatures. *Nature, 144*(3642), 327–328.

Vickery, S. and Lamb, S. (1995). Large tectonic rotations since the Early Miocene in a convergent plate-boundary zone, South Island, New Zealand. *Earth and Planetary Science Letters, 136*(1-2), 43–59.

Vine, F. J. and Matthews, D. H. (1963). Magnetic anomalies over oceanic ridges. *Nature, 199*(4897), 947–949.

Wack, M. (2010). A new software for the measurement of magnetic moments using SQUID and spinner magnetometers. *Computers & Geosciences, 36*(9), 1178–1184.

Walcott, R. I. and Mumme, T. C. (1982). Paleomagnetic study of the Tertiary sedimentary rocks from the east coast of the North Island, New Zealand. Geophysics Division Report 189, Wellington, New Zealand: Department of Scientific and Industrial Research.

Walton, D., Shaw, J., Share, J. and Hakes, J. (1992). Microwave demagnetization. *Journal of Applied Physics, 71*(3), 1549–1551.

Webb, P. (1973a). Paleocene foraminifera from Wangaloa and Dunedin. *New Zealand Journal of Geology and Geophysics, 16*, 109–157.

Webb, P. (1973b). A re-examination of the Wangaloan problem. *New Zealand Journal of Geology and Geophysics, 16*, 158–169.

Weeks, R., Laj, C., Endignoux, L., Fuller, M. and Roberts, A. et al. (1993). Improvements in long-core measurement techniques: applications in palaeomagnetism and palaeoceanography. *Geophysical Journal International, 114*(3), 651–662.

Wehland, F., Alt-Epping, U., Braun, S. and Appel, E. (2005). Quality of pTRM acquisition in pyrrhotite bearing contact-metamorphic limestones: possibility of a continuous record of Earth magnetic field variations. *Physics of the Earth and Planetary Interiors, 148*(2-4), 157–173.

Weidler, P. G. and Stanjek, H. (1998). The effect of dry heating of synthetic 2-line and 6-line ferrihydrite: II. surface area, porosity and fractal dimension. *Clay Minerals, 33*, 277–284(8).

Westrich, J. T. (1983). *The consequences and controls of bacterial sulfate reducation in marine sediments*. PhD thesis, Yale University.

Willumsen, P. S. (2003). *Marine palynology across the Cretaceous-Tertiary Boundary in New Zealand*. PhD thesis, Wellington, New Zealand: Victoria University.

Willumsen, P. S. and Vajda, V. (2010). A new early Paleocene dinoflagellate cyst species, *Trithyrodinium partridgei:* its biostratigraphic significance and palaeoecology. *Alcheringa, 34*(4), 523–538.

Wilson, D. D. (1963). Geology of Waipara subdivision (Amberley and Motunau sheets S68 and S69). Bulletin 64, New Zealand Geological Survey.

Wilson, G. J. (1967). Microplankton from the Garden Cove Formation, Campbell Island. *New Zealand Journal of Botany, 5*(2), 223–240.

Wilson, G. J. (1972). Age of the Garden Cove Formation, Campbell Island. *New Zealand Journal of Geology and Geophysics, 15*(1), 184–185.

Wilson, G. J. and McMillan, S. G. (1996). Late Cretaceous-Tertiary stratigraphic sections of coastal Otago, South Island, New Zealand: a summary of biostratigraphic and lithostratigraphic data. Report 96/39, Lower Hutt, New Zealand: Institute of Geological and Nuclear Sciences.

Wilson, G. S. (1993). *Ice induced sea-level changes in the late Neogene*. PhD thesis, Wellington, New Zealand: Victoria University.

Wilson, G. S. and McGuire, D. M. (1995). Distributed deformation due to coupling across a subduction thrust: Mechanism of young tectonic rotation within the south Wanganui basin, New Zealand. *Geology, 23*(7), 645–648.

Wilson, G. S. and Roberts, A. P. (1999). Diagenesis of magnetic mineral assemblages in multiply redeposited siliclastic marine sediments, Wanganui basin, New Zealand. In Tarling, D. H. and Turner, P., editors, *Palaeomagnetism and diagenesis in sediments*, number 151 in Geological Society Special Publications, pages 95–108. London: Geological Society.

Wilson, R. L. (1961). Palaeomagnetism in Northern Ireland. Part I: The thermal demagnetization of natural magnetic moments in rocks. *Geophysical Journal of the Royal Astronomical Society, 5*(1), 45–58.

Wohlfarth, E. P. (1958). Relations between different modes of acquisition of the remanent magnetization of ferromagnetic particles. *Journal of Applied Physics, 29*(3), 595–596.

Wright, I. C. and Vella, P. P. (1988). A New Zealand Late Miocene magnetostratigraphy: glacioeustatic and biostratigraphic correlations. *Earth and Planetary Science Letters, 87*(1-2), 193–204.

Wu, Y. T., Fuller, M. and Schmidt, V. A. (1974). Microanalysis of N.R.M. in a granodiorite intrusion. *Earth and Planetary Science Letters, 23*(3), 275–285.

Xuan, C. and Channell, J. E. T. (2009). UPmag: MATLAB software for viewing and processing u channel or other pass-through paleomagnetic data. *Geochemistry, Geophysics, Geosystems, 10*(10), Q10Y07.

Yamazaki, T. and Ioka, N. (1997). Environmental rock-magnetism of pelagic clay: Implications for Asian eolian input to the North Pacific since the Pliocene. *Paleoceanography, 12*(1), 111–124.

Zachos, J. C., Breza, J. R. and Wise, S. W. (1992). Early Oligocene ice-sheet expansion on Antarctica: stable isotope and sedimentological evidence from Kerguelen Plateau, southern Indian Ocean. *Geology, 20*(6), 569.

Zachos, J. C., Dickens, G. R. and Zeebe, R. E. (2008). An early Cenozoic perspective on greenhouse warming and carbon-cycle dynamics. *Nature, 451*(7176), 279–283.

Zachos, J. C., Lohmann, K. C., Walker, J. C. G. and Wise, S. W. (1993). Abrupt climate change and transient climates during the Paleogene: A marine perspective. *The Journal of Geology, 101*(2), 191–213.

Zervas, D., Nichols, G. J., Hall, R., Smyth, H. R. and Lüthje, C. et al. (2009). SedLog: A shareware program for drawing graphic logs and log data manipulation. *Computers & Geosciences, 35*(10), 2151–2159.

Zhang, C. and Ogg, J. G. (2003). An integrated paleomagnetic analysis program for stratigraphy labs and research projects. *Computers & Geosciences, 29*, 613–625.

Zijderveld, J. D. A. (1967). A. C. demagnetization of rocks: Analysis of results. In Collinson, D. W., Creer, K. M. and Runcorn, S. K., editors, *Methods in Palaeomagnetism*, number 3 in Developments in Solid Earth Geophysics, pages 254–286. Amsterdam: Elsevier.

This dissertation was set in Minion by Robert Slimbach and Delicious by Jos Buivenga, using the ConTEXt typesetting system by Hans Hagen and others; my thanks go to all of them, and to the members of the ConTEXt mailing list who assisted me during production.

❧

Finally: It was stated at the outset, that this system would not be here, and at once, perfected. You cannot but plainly see that I have kept my word. But I now leave my… System standing thus unfinished, even as the great Cathedral of Cologne was left, with the cranes still standing upon the top of the uncompleted tower. For small erections may be finished by their first architects; grand ones, true ones, ever leave the copestone to posterity. God keep me from ever completing anything. This whole book is but a draught – nay, but the draught of a draught. Oh, Time, Strength, Cash, and Patience!

– Herman Melville, *Moby-Dick*